SERDP

FINAL REPORT

Recycling and Reuse of Metal Alloys by a Single Solid-State Additive Manufacturing and Repair Process

Paul Allison
J. Brian Jordon
The University of Alabama and Baylor

Kevin Doherty
Army Research Laboratory

Nanci Hardwick
Aeroprobe Corporation

December 2022

SERDP Project WP18-1323

DISTRIBUTION STATEMENT A
This document has been cleared for public release.

This report was prepared under contract to the Department of Defense Strategic Environmental Research and Development Program (SERDP). The publication of this report does not indicate endorsement by the Department of Defense, nor should the contents be construed as reflecting the official policy or position of the Department of Defense. Reference herein to any specific commercial product, process, or service by trade name, trademark, manufacturer, or otherwise, does not necessarily constitute or imply its endorsement, recommendation, or favoring by the Department of Defense.

REPORT DOCUMENTATION PAGE

Form Approved
OMB No. 0704-0188

The public reporting burden for this collection of information is estimated to average 1 hour per response, including the time for reviewing instructions, searching existing data sources, gathering and maintaining the data needed, and completing and reviewing the collection of information. Send comments regarding this burden estimate or any other aspect of this collection of information, including suggestions for reducing the burden, to Department of Defense, Washington Headquarters Services, Directorate for Information Operations and Reports (0704-0188), 1215 Jefferson Davis Highway, Suite 1204, Arlington, VA 22202-4302. Respondents should be aware that notwithstanding any other provision of law, no person shall be subject to any penalty for failing to comply with a collection of information if it does not display a currently valid OMB control number.
PLEASE DO NOT RETURN YOUR FORM TO THE ABOVE ADDRESS.

1. REPORT DATE *(DD-MM-YYYY)*	2. REPORT TYPE	3. DATES COVERED *(From - To)*
12/12/2022	SERDP Final Report	5/3/2018 - 5/3/2022

4. TITLE AND SUBTITLE

Recycling and Reuse of Metal Alloys by a Single Solid-State Additive Manufacturing and Repair Process

5a. CONTRACT NUMBER
18-C-0025

5b. GRANT NUMBER

5c. PROGRAM ELEMENT NUMBER

6. AUTHOR(S)
Paul Allison and J. Brian Jordon: University of Alabama and Baylor

Kevin Doherty: Army Research Laboratory

Nanci Hardwick: Aeroprobe Corporation

5d. PROJECT NUMBER WP18-1323

5e. TASK NUMBER

5f. WORK UNIT NUMBER

7. PERFORMING ORGANIZATION NAME(S) AND ADDRESS(ES)
University of Alabama
Dept. of Mechanical Engineering
Box 870276
Tuscaloosa, AL 35487-0276

8. PERFORMING ORGANIZATION REPORT NUMBER
WP18-1323

9. SPONSORING/MONITORING AGENCY NAME(S) AND ADDRESS(ES)
Strategic Environmental Research and Development Program
4800 Mark Center Drive, Suite 16F16
Alexandria, VA 22350-3605

10. SPONSOR/MONITOR'S ACRONYM(S)
SERDP

11. SPONSOR/MONITOR'S REPORT NUMBER(S)
WP18-1323

12. DISTRIBUTION/AVAILABILITY STATEMENT
DISTRIBUTION STATEMENT A. Approved for public release: distribution unlimited.

13. SUPPLEMENTARY NOTES

14. ABSTRACT

Additive Friction Stir Deposition (AFSD) provides a rapid, flexible, and robust metal recycling option that can be applied to manufacture large-scale multi-material components and/or repair damaged structures (i.e. vehicles, armor systems, etc.) while in-theatre, at the point-of-need, thus reducing the associated logistical challenges. This research report summarizes a combined experimental and computational investigation of two specific metal waste streams from the deployed Military Occupational Specialty (MOS) units: (1) scrap metal from machine chips generated by maintenance-MOS activities, and (2) expeditionary airfield (EAF) aluminum landing mats from EAF-MOS activities. These two waste streams typically generate chips and metal strips, respectively, and were used as the pilot case for feedstock in the AFSD process. Processing of the materials was performed on new and recycled feedstock material that allowed for the development of a Smooth Particle Hydrodynamic AFSD-Simulation tool to elucidate processing parameter influence on material flow, temperature, and localized stress and strain states. Additionally, multiscale characterization was performed from the nano- to the macroscale using a suite of analytical tools to understand intrinsic structural evolution of the as-deposited material. Furthermore, X-ray Computed Tomography (CT) analyses demonstrated that fully-dense epositions were achieved with isotropic mechanical behavior observed in a large 203 mm diameter by 44 mm tall helical build in large test articles. In addition, the in-depth experimental datasets characterizing microstructure, residual stresses, and mechanical performance were used to develop multiscale computational models for predicting material performance. To demonstrate the ability to recycle waste streams, strips were extracted from damaged airfields mats to use as a secondary feedstock to repair simulated forklift puncture damage on the aluminum airfield mat core top extrusion skin. Four-point bend experiments of the repaired mat core confirmed no knockdown in performance when compared to new mat core four-point bend results. These results provide a starting point for the scientific community to begin assessing this new DAR paradigm for using battle-damaged material as secondary feedstock for Point-of-Need Manufacturing and Repair that eases logistic burdens. In conclusion, additional developments are likely required for deployment to FOBs with this DAR AFSD approach and technology, where the maturation of AFSD software needs to include automation of the AM process flow that would be integrated with a digitally driven approach for parameter prediction and optimization through a simulation based tool framework. The fundamental understanding compiled on this study could serve as the groundwork to transition AFSD to a potential Austere Location Manufacturing and Repair (ALM&R) technique.

15. SUBJECT TERMS
Additive manufacturing, corrosion and repair technologies, structural repair, surface preparation, recycling, metal alloys, recycle and re-use

16. SECURITY CLASSIFICATION OF:			17. LIMITATION OF ABSTRACT	18. NUMBER OF PAGES	19a. NAME OF RESPONSIBLE PERSON
a. REPORT	b. ABSTRACT	c. THIS PAGE			Paul Allison
UNCLASS	UNCLASS	UNCLASS	UNCLASS	309	19b. TELEPHONE NUMBER *(Include area code)* 205-348-9271

Abstract

Additive Friction Stir Deposition (AFSD) provides a rapid, flexible, and robust metal recycling option that can be applied to manufacture large-scale multi-material components and/or repair damaged structures (i.e. vehicles, armor systems, etc.) while in-theatre, at the point-of-need, thus reducing the associated logistical challenges. This research report summarizes a combined experimental and computational investigation of two specific metal waste streams from the deployed Military Occupational Specialty (MOS) units: (1) scrap metal from machine chips generated by maintenance-MOS activities, and (2) expeditionary airfield (EAF) aluminum landing mats from EAF-MOS activities. These two waste streams typically generate chips and metal strips, respectively, and were used as the pilot case for feedstock in the AFSD process. Processing of the materials was performed on new and recycled feedstock material that allowed for the development of a Smooth Particle Hydrodynamic AFSD-Simulation tool to elucidate processing parameter influence on material flow, temperature, and localized stress and strain states. Additionally, multiscale characterization was performed from the nano- to the macroscale using a suite of analytical tools to understand intrinsic structural evolution of the as-deposited material. Furthermore, X-ray Computed Tomography (CT) analyses demonstrated that fully-dense depositions were achieved with isotropic mechanical behavior observed in a large 203 mm diameter by 44 mm tall helical build in large test articles. In addition, the in-depth experimental datasets characterizing microstructure, residual stresses, and mechanical performance were used to develop multiscale computational models for predicting material performance. To demonstrate the ability to recycle waste streams, strips were extracted from damaged airfields mats to use as a secondary feedstock to repair simulated forklift puncture damage on the aluminum airfield mat core top extrusion skin. Four-point bend experiments of the repaired mat core confirmed no knockdown in performance when compared to new mat core four-point bend results. These results provide a starting point for the scientific community to begin assessing this new DAR paradigm for using battle-damaged material as secondary feedstock for Point-of-Need Manufacturing and Repair that eases logistic burdens. In conclusion, additional developments are likely required for deployment to FOBs with this DAR AFSD approach and technology, where the maturation of AFSD software needs to include automation of the AM process flow that would be integrated with a digitally driven approach for parameter prediction and optimization through a simulation based tool framework. The fundamental understanding compiled on this study could serve as the groundwork to transition AFSD to a potential Austere Location Manufacturing and Repair (ALM&R) technique.

1. EXECUTIVE SUMMARY

Objective: Examine a circular economic approach for direct additive recycling (DAR) through a transformative hybrid solid-state additive manufacturing process, Additive Friction Stir Deposition (AFSD), as a new path to recycle metal waste/scrap at a forward operating base (FOB) to either fabricate or repair components. This research has investigated the processing-structure-property relations through a computation and experimental approach for two specific metal waste streams from the deployed Military Occupational Specialty (MOS) units as representative secondary feedstocks for this research: (1) scrap metal from machine chips generated by maintenance-MOS activities, and (2) expeditionary airfield (EAF) aluminum landing mats from EAF-MOS activities. These two waste streams generate chips and metal strips, respectively, that were used as AFSD feedstock to produce fully-dense deposits. During the novel solid-state AFSD process, the secondary metal feedstock in chips and stacked strips was compared to depositions from new solid rod that were all deposited additively layer-by-layer through a hollow rotating tool. Very importantly for FOB use, the AFSD process was examined as a viable pathway for direct additive recycling that does not require metal powders, which can be difficult, energy intensive, or impractical to produce in austere environments.

Technical Approach: The technical approach implemented a transformative solid-state deposition approach - AFSD, to test the hypothesis that *fully dense samples with isotropic wrought mechanical properties can be produced from two proposed (metal chips and stacked metal strips) waste streams*. This collaborative effort required a multidisciplinary team with a combined skill set of processing science, microstructural characterization, and mechanical characterization. The three-year research program was divided into three main complimentary technical tasks. Task 1 examined the feasibility of the process for this purpose by making fully dense deposits using recycled aluminum materials, including machine chip scraps and landing mats. Risks and constraints of the process were investigated in this task. Additionally, the researchers developed a smooth particle hydrodynamics simulation tool for modeling the AFSD process in Task 1 to specifically elucidate the role of oxide layer dispersion and refinement during the AFSD process. Furthermore, the AFSD process modeling subtask supported the fabrication and subsequent characterization tasks to establish a complete iterative feedback loop. Task 2 characterized the recycled material from the nano- to the macroscale. Finally, in Task 3, mechanical characterization and physics-based modeling build off the previous tasks where the monotonic and fatigue properties were quantified to understand dominant intrinsic and extrinsic structural features. The modeling in Task 3 aided in elucidating the role of oxide dispersion and microstructural evolution on performance of the AFSD recycled materials.

Results and Discussion: This project has resulted in a fundamental understanding of the processing-structure-property-performance (PSPP) relationships for new and secondary aluminum alloys feedstocks through a combined computational and experimental approach. Additionally, this research was the first to successfully deposit fully dense builds by recycling two secondary feedstock aluminum alloys (AA5083 machine chips) and (AA6061 discrete strips of damaged airfield matting) that compared the recycled feedstock depositions to depositions from new feedstock material.

Specifically, AA5083 and AA6061 are model alloys that have been investigated extensively over the past years for military component applications. AA5083 is a prominent alloy used on US ground combat vehicle platforms (Bradley, Assault Amphibious Vehicle, M113 Armored Personnel Carrier, etc.). AA6061 has ubiquitous use for a variety of military components such as Patriot Missile Systems and expeditionary airfield landing mats. These two alloys also represented an opportunity to develop and contrast the science of AFSD processing on two very different aluminum alloys families: AA5083 which is strengthened primarily by solid solution and cold work, and AA6061, which is strengthened primarily by precipitation strengthening.

For this controlled study, ARL produced machine chips from in-house commercial milling machines using stock AA5083. Specifically, ARL examined continuous vs discontinuous chips for dry and wet machining. Machine chips were deposited from both compacted bar feedstock and as loose chips fed through an auger feeding system. Processing greatly benefited from ball milling of the chips to adequately compact the loose chips into a compacted density that could be used as feedstock. Thus, experimental results from this project suggest that first feeding the loose chips through a friction stir extrusion machine would be an optimal way to produce compacted chip feedstock instead of ball milling chips then compacting in a press and die. The direct feeding of the machine chips required ball milling to achieve necessary densification of as-deposited material, and the auger system also suffered from an inability to deposit hard alloys due to internal wearing and durability issues. Additionally, to minimize machine downtime required to change between an auger system and solid rod deposition the added use of a friction stir extrusion machine to fabricate feedstock would be a valuable time savings at forward operating bases that could produce AFSD feedstock as well as wire and rod material as-required.

The UA researchers quantified oxide formation on the machine chips using energy dispersive X-ray spectroscopy (EDS) elemental analysis detectors on the scanning electron microscopes (SEM) at the UA Central Analytical Facility. However, in-theater, a commercial handheld X-ray fluorescence (XRF) device could be used to analyze scrap metals to determine the alloy/chemistry. Large depositions from both recycled and new feedstock material were tested monotonically to examine processing influence on stress-state dependence (compression and tension), strain rate effects (quasi-static and high strain rate), specimen orientation influence, and also fatigue behavior of the deposited material. The research team also investigated the as-deposited material properties for different deposition paths with uniform layer heights, non-uniform layer heights, and parallel pass depositions.

In addition, to complement the experimental processing tasks, an AFSD simulation framework was developed in conjunction with the research team colleagues at National Research Council Canada by modifying a FSW smooth particle hydrodynamic (SPH) framework to accurately simulate solid feedstock, strips of feedstock, and dissimilar material feedstock that was calibrated by X-ray CT, embedded thermocouples, and hardness maps for high fidelity simulations of material flow, temperature generations, and localized stress and strain, respectively.

The structure of the feedstock and recycled material in the initial state as well as the as-deposited and heat-treated material was quantified at the nano-, micro-, and macro-scale. In particular, the suite of experimental tools was able to ascertain grain size, texture, second phase precipitation and distribution of oxide layers under AFSD processing. Key finding from this work identified that for the β" (Mg_2Si) precipitate strengthened AA6061 material, the Local Electrode Atom Probe (LEAP) tomography quantified that the nanoscale, β" precipitates in the material were overaged from the heat input during deposition for both the new and recycled feedstock creating solute clusters resulting in a decrease in as-deposited strength from the T6 temper feedstock material. However, TEM did quantify that post-deposition heat treatments were able to retain the nano precipitates in the as-deposited material resulting in the ability of the material to retain that strengthening mechanism. For the AA5083, the dislocation accumulation from the strain hardened H131 feedstock material was eliminated due to the deposition temperatures effectively annealing the material during the process. At the microscale, the as-deposited material achieved a significant grain refinement in the as-deposited state for both aluminum alloys for the new and recycled feedstocks. This allowed the material to have an increase in Hall-Petch strengthening mechanisms compared to the wrought materials. At the micro- and macro-scales oxides were not readily observed on the new or recycled material. However, new AA6061 feedstock rods were anodized with 10-micron thick and 68-micron thick aluminum oxide layers. These anodized feedrods were then deposited creating a large deposit. A significant refinement of the aluminum oxide layer was observed in the as-deposited build with uniform size and distribution of the two oxide coatings applied through anodization were efficiently dispersed during the AFSD process, with oxide particles distributed throughout the microstructure. These oxide particles had median sizes of 1.8 and 3.5 μm^2, respectively.

Residual stress was also quantified for the first time during this research program for an AFSD deposition. Here, a large ($194 \times 49 \times 66$ mm^3) deposit of AA6061 was produced using AFSD with a rotational speed of 300 RPM and a translational speed of 127 mm/min. Three components of residual stresses were independently measured in the deposit using neutron diffraction on the VULCAN instrument at the Spallation Neutron Source in the Oak Ridge National Laboratory. The distribution of residual stress through the thickness of the deposit is relatively constant. All three residual stress components were tensile at the beginning and in the center of the deposit, but compressive at the completion of the deposit. The d_0-spacings measured from stress-relieved samples show a marked change in lattice constant in the top layers of the deposit. This change in lattice chemistry is attributed to the dissolution of β" (Mg_2Si) precipitates caused by the thermal cycles in the AFSD process. The residual stresses are much lower in the AFSD AA6061 build as compared to the fusion-based welding of AA6061-T6, but are still significant in light of the low yield strength of AFSD AA6061 in its as-deposited state.

The mechanical behavior of AFSD structures were assessed using a variety of experimental techniques including microhardness, uniaxial load frames, and split Hopkinson pressure bars. However, the experiments focused upon understanding key mechanical parameters for aluminum alloys. The team and experimental equipment quantified the monotonic behavior by determining quasi-static tensile properties of yield strength, tensile strength, and elongation to failure as a function of location in the additive deposits using miniature tensile specimens. In addition, these same tensile properties were measured from separate AFSD-produced deposits large enough for ASTM standard tensile specimens. Simultaneously the team performed basic, low-cycle fatigue (LCF) and high-cycle fatigue (HCF) characterization of the deposited material determining fundamental mechanisms responsible for fatigue damage. Complementing the experiments, optical and electron microscopy techniques elucidated the tensile damage mechanics along with the micro-mechanisms of the fatigue evolution in the AFSD material. Mechanical characterization was performed on the new solid rod feedstock AA6061 depositions, anodized AA6061 feedstock depositions, recycled AA6061 airfield landing mats stacked strip depositions, and AA6061 depositions after a T6 post-deposition heat treatment, new solid rod feedstock AA5083 depositions, and ground machine chip AA5083 depositions.

The Vickers microhardness maps performed on the deposition cross-sections for both alloys identified lower hardness in the bottom layers compared to the top layers that experienced less thermal cycling during the AFSD process. The mechanical results identified isotropic behavior (tensile and fatigue) for some of the large AA6061 depositions in the as-deposited state. However, for all the AA5083 there was a decrease in build direction tensile ductility due to kissing-bond type defects with a poor metallurgical bonding between layers due to aerosolized graphite embedded on the layers. This phenomenon was observed on some of the AA6061 as-deposited builds with certain parameters where the same graphite lubricant remnants was found on the fracture surfaces. This suggests that adequate cooling of the AFSD tools to control thermal expansion of the feed rod in the tool would be much preferred to the aerosol spray graphite being coated on the feedstock to minimize jamming of the feed rods inside the tool during depositions.

To adequately model the material performance with these materials containing specialized material history, microstructure sensitive material modeling was employed and calibrated to both the monotonic and cyclic experimental data. Specifically, physics-based material modeling of the mechanical behavior of additively manufactured aluminum alloys is paramount in the design of critical components for the automotive and aerospace industry. Furthermore, the development and resulting application of robust material models in finite element analysis (FEA) may significantly reduce cost and time for product development. A consistent methodology for the constitutive relations, kinematics, and thermodynamics is required for the development of a multiscale material modelling framework. The constitutive models employed in this project are based on microstructure-property relations that are constrained by the laws of thermodynamics have been shown to be effective for multiscale material modeling. Additionally, the models have been shown to capture the behavior of uniform wrought, cast, and additive materials. However, with the increase in use of additive manufacturing techniques there arises a need to capture material gradients that are exhibited due to microstructural changes resulting from intense thermal gradients. In this project, the constitutive model was adapted to capture the mechanical response of thermomechanically processed AFSD material. Here, the effect of precipitate size and distribution on mechanical response was performed on an AA6061 build fabricated with AFSD. To quantify the effect that the thermomechanical AFSD processing exhibits on the dynamic behavior of AA6061, quasi-static (QS) and high-rate (HR) tensile experimentation was performed on two different orientations in two different locations of the as-deposited build. As such, this is the first study to quantify the microstructural and mechanical property dependence on location and orientation of an as-deposited AA6061 structure processed with AFSD. Additionally, this is the first study to develop a constitutive model to capture the mechanical gradient in a material processed with AFSD as a function of precipitate size and distribution.

In order to predict the durability of the AFSD process, a microstructure-sensitive fatigue model was modified and calibrated for this unique processing history. The Multi-Stage Fatigue (MSF) model co-developed by PIs Allison and Jordon was used as the basic framework to elucidate the higher order microstructure effects on nucleation and small crack fatigue of the AFSD processed material. In particular, the fatigue model was used to capture fatigue crack incubation from microstructural features and defects (i.e., intermetallic particles, pores, etc) and microstructurally small crack growth in order to elucidate fatigue mechanisms in the AFSD process. In this project, the MSF model captured the underlining mechanisms of the fatigue performance of the AFSD depositions made from solid bar feedstock and recycled materials. Overall, in terms of fatigue behavior, the smaller grain size and higher strength of the AFSD-Recycled material was more resistant to crack propagation and nucleation than the AFSD-Solid bar materials. This experimentally observed attribute appears directly related to the refined grain size occurring as a result of the material dynamic recrystallization during AFSD.

Implications for Future Research and Benefits: (1) Recycling and Sustainability: Providing a flexible and robust metal recycling option that may be applied to both non-ferrous and ferrous material systems delivers the joint services a superior technological capability to manufacture components in the field and repair damaged structures/vehicles/armor with a new superior similar or dissimilar structural material, thus reducing time and energy for new components or repairs. This specifically benefits the warfighter by averting risk associated with transporting new components and reducing wait-time for critical components to ensure mission success. Additionally, the ability for a low-power metal recycling-to-component open-atmosphere fabrication process minimizes personnel and environmental hazards associated with dangerous chemicals involved in some fusion-based phase change metal recycling programs. (2) Basic science: The knowledge obtained through this research for processing recycled aluminum alloys via AFSD provides new insight on microstructural, texture, and phase evolution under non-conventional, environmentally friendly processing conditions.

TABLE OF CONTENTS

1. EXECUTIVE SUMMARY II

TABLE OF CONTENTS VIII

LIST OF FIGURES XII

2. OBJECTIVE 1

3. BACKGROUND 3

4. MATERIALS AND METHODS 11

4.1 Materials 11
4.1.1 Aluminum Alloy 6061 11
4.1.2 Aluminum Alloy 5083 12

4.2 Methods 13
4.2.1 Processing 13
AA6061 AFSD 13
AA5083 AFSD 14
New Solid Rod Feedstock AA5083 AFSD 14
AFSD of AA5083 Machine Chips 16
4.2.2 Nano- and Microstructure Characterization 16
4.2.3 Mechanical Property Characterization 17
Microhardness Experiments 17
Residual Stress Experiments 17
Monotonic Experiments 17
Fatigue Experiments 18
4.2.4 Modeling and Simulations 19
AFSD Process Simulations 19
Material Model 24
Thermal-mechanical Joining Contact 26
Monotonic Modeling 28
Microstructure-Sensitive Fatigue Model 28

5. RESULTS AND DISCUSSION 30

5.1 New Solid Bar Feedstock Processing Parameter Influence on As-Deposited AFSD AA6061 Nano- and Microstructure and Properties 30
5.1.1 Material and methods 30
5.1.2 Results and Discussion 32
5.1.3 Conclusion 40

5.2 Influence of Parallel Path Depositions of New Solid Bar Feedstock on the Microstructure and Tensile Behavior 41
5.2.1 Results and Discussion 43
Microscopic Observations 43

Mechanical Behavior 51
Fractography 53
Discussion of the Limits of Deposition Equation 55
5.2.2 Conclusions 56

5.3 Effect of Solutionizing and Artificial Aging on the Microstructure and Tensile Behavior of New AA6061 Feedstock AFSD **58**
5.3.1 Materials and Methods 59
5.3.2 Results and Discussions 60
5.3.3 Conclusions 63

5.4 Effect of New AA6061 Feedstock AFSD Processing on the As-Deposited Tensile and Fatigue Performance Capturing Orientation Behavior by Microstructure Sensitive Fatigue Modeling **64**
5.4.1 Materials 64
5.4.2 Test Specimens and Experimental Methods 64
5.4.3 Results and Discussion 66
Microstructure 66
Monotonic Tensile Results 68
Effect of Thermomechanical Processing on Monotonic Behavior 70
Strain-Control Fatigue Results 70
Post-Mortem Analysis of Fatigue Fracture Surfaces 72
MSF Model Results and Discussion 74
5.4.4 Conclusions 78

5.5 Influence of Post Deposition Heat Treatment on the Fatigue Behavior of New AA6061 Feedstock AFSD and Fatigue Modeling **80**
5.5.1 Material and Method 80
5.5.2 Results and Discussion 81
5.5.3 Conclusions 90

5.6 Tensile Behavior of Varying Orientations for a Large Circular Helical Build Deposition **92**
5.6.1 Material and Method 92
5.6.2 Results and discussions 94
5.6.3 Conclusions 97

5.7 Influence of Surface Oxides and Material Flow During AFSD of AA6061 ..... **98**
5.7.1 Materials and Methods 98
5.7.2 Results and Discussion 100
5.7.3 Conclusions 110

5.8 Residual Stress Distributions in AA6061 Feedstock AFSD Characterized by Neutron Diffraction **111**
5.8.1 Material and Method 111
Neutron diffraction measurement of AFSD AA6061 113
Residual Strain and Residual Stress Analysis 115
Microstructural Characterization and Hardness Measurement 115
5.8.2 Results and Discussion 115
5.8.3 Conclusions 125

5.9 New Solid Bar Feedstock Processing Parameter and Lubrication Influence on As-Deposited AFSD AA5083 Nano- and Microstructure and Mechanical Properties **126**
5.9.1 Materials and Methods 126
5.9.2 Results 128
Parameter Study 128
Mechanical Behavior of the Free-Standing Deposit 133
Post-Mortem Analysis 136
5.9.3 Conclusions 144

5.10 Microstructure, Tensile, and Fatigue Behavior of Direct Additive Recycling of AA5083 Machine Chips Captured by Monotonic and Fatigue Performance Models 145
5.10.1 Materials and Methods 145
Materials 145
Test Specimens and Experimental Methods 147
Static Strength Modeling: 148
5.10.2 Results and Discussions 149
Microstructure Characterization 149
Quasi-Static Tensile Test Results 151
Fatigue Behavior 154
Post-Mortem Analysis of Fatigue Fracture Surfaces 157
Multi-Stage Fatigue Modeling 160
5.10.3 Conclusions 163

5.11 Meshless AFSD Simulation Framework Development to Capture Material Flow and Temperature 164
5.11.1 Material and Method 164
5.11.2 Results and discussion 166
Temperature Model Calibration 166
Build Profile Model Calibration 169
Simulation Temperature Contours 171
Simulation Plastic Strain Contours 172
5.11.3 Concluding remarks 173

5.12 Constitutive Model Influence of Temperature and Strain Rate on the Mechanics of AFSD Aluminum Alloys 175
5.12.1 AFSD Processing Environment 176
AFSD Plastic Strain 177
AFSD Strain Rate 177
AFSD Temperature 177
5.12.2 Materials and Methods 178
Constitutive Models 178
5.12.3 Results and Discussion 182
Constitutive Model Behavior 182
AFSD Simulations 188
5.12.4 Conclusion 198

5.13 Computational and Experimental Study of Material Flow Behavior Prediction of External Particle Feedstock and Internal Particle Feedstock 200
5.13.1 Materials and Methods 202
Anodized Feedstock Depositions 202
Copper Wire Core Deposition 202
Microstructural Characterization of Depositions 202
SPH Methodology 203
AFSD SPH Simulations 205
5.13.2 Results and Discussion 208
Oxide Verification 209
Anodized Feedstock Experiment vs Simulation 210
Copper Wire Core Deposition 211
Copper Wire Core Experiment vs Simulation 212
Particle Paths 213
5.13.3 Conclusions 217

5.14 Modeling the Tensile and Fatigue Behavior of AFSD AA5083 and AA6061 219
5.14.1 Materials and Methods 220
Materials 220

Test Specimens and Experimental Methods 221
Internal State Variable Modeling: 223
5.14.2 Results and Discussions 227
Microstructure 227
Compression Test Results 229
Internal State Variable Modeling 235
5.14.3 Conclusions 237

5.15 Airfield Landing Mat Strip Feedstock for Point-of-Need Manufacturing and Repair of Airfield Landing Mat Skin Punctures **239**

6. CONCLUSIONS AND IMPLICATIONS FOR FUTURE RESEARCH **247**

LITERATURE CITED ..... **- 1 -**

APPENDIX ..... **- 25 -**

List of Publications: ..... **- 25 -**

List of Presentations: ..... **- 26 -**

LIST OF FIGURES

Figure 2.1 Schematic of proposed additive friction stir deposition (AFSD) manufacturing process for recycling of FOB metal waste. 1

Figure 3.1. (A) Cross section schematic of the beginning of the AFSD process where the tool plunges into a substrate while spinning at a predetermined rotational speed. (B) The tool is then raised to the layer height during which time an actuator drives a solid, or powder, feedstock through the tool as the tool traverses across the substrate, producing a layer. (C) At the completion of a layer, the spindle raises to the next layer height and repeats the process to build consecutive layers. (D) Photograph of the actual AFSD process applied to AA6061. (E) Image of the teardrop featured tool. 6

Figure 3.2. (a) Schematic diagram of the Additive Friction Stir Deposition (AFSD) process. (b) Representative AFSD deposition with multiple layers creating a large external feature. 8

Figure 4.1. Two AFSD processes featuring a) solid bar feedstock made from AA5083-H131 rolled plate and b) feedstock made from loose machine chips cut from AA5083-H131 rolled plate and fed through an auger. 16

Figure 4.2. (A) Schematic of the AFSD process where a non-consumable tool rotates and traverses along a substrate as a linear actuator extrudes material through the center of the tool. (B) The tool deposition path produced to create an overlapping, parallel raster. Arrows denote the tool path alternating directions after consecutive layers. (C) Image of the final deposit with sample layout depicted schematically. (D) Sample geometry (mm) to determine tensile response. (E) Bottom surface of 38.1 mm AFSD tool containing features. 18

Figure 4.3. Kernel function interpolation in the smoothed particle hydrodynamics (SPH) method 19

Figure 4.4. Flow stress model for AA6061-T6: (a) as a function of plastic strain and temperature; and (b) as a function of strain rate and temperature. 26

Figure 5.1 (A) Cross section schematic of the beginning of the AFSD process where the tool plunges into a substrate while spinning at a predetermined rotational speed. (B) The tool is then raised to the layer height during which time an actuator drives a solid, or powder, feedstock through the tool as the tool traverses across the substrate, producing a layer. (C) At the completion of a layer, the spindle raises to the next layer height and repeats the process to build consecutive layers. (D) Photograph of the actual AFSD process applied to AA6061. (E) Image of the teardrop featured tool. 31

Figure 5.2 (A) Parameter contour plot relating tool rotational and traversing speed to average deposition hardness. (B) Parameter contour plot relating tool traversing speed to deposition feed rate to average deposition hardness. (C) Vickers hardness plot of low-parameter AFSD deposit. (D) Vickers hardness plot of rapid-parameter AFSD deposit. 34

Figure 5.3 (A) 3-D representative EBSD map of virgin AA6061-T651 feedstock (100μm scale bar). (B) EBSD map of the cross section of the deposition with the slowest parameters. (C) EBSD map of the cross section of the deposition with the fastest parameters. (D) 3-D EBSD map of the slowest deposition depicting refined, equiaxed grains (50μm scale bars). (E) 3-D EBSD map of the fastest deposition depicting refined, equiaxed grains (50μm scale bars)..... 35

Figure 5.4 Grain boundary and grain reference orientation (GROD) plots observing cross sections of the low (A, B) and rapid parameter (C, D) deposits. Low angle grain boundaries (LAGB) with misorientation angles from 2° to 10° are represented by red lines. High angle grain boundaries (HAGB) were defined as boundaries with misorientation angles greater than 10°. .. 37

Figure 5.5(A) TEM bright field images of AA6061-T651 with conventional needle-shaped β" precipitates. (B) TEM micrograph of the low-parameter deposit showing Mg-Si solute clusters. (C) TEM micrograph of the rapid-parameter deposit exhibiting solute clusters. (D) APT analysis visualizing Mg-Si rich clusters (20x20x40nm^3 volume). 39

Figure 5.6 (A) Schematic of the AFSD process where a non-consumable tool rotates and traverses along a substrate as a linear actuator extrudes material through the center of the tool. (B) The tool deposition path produced to create an overlapping, parallel raster. Arrows denote the tool path alternating directions after consecutive layers. (C) Image of the final deposit with sample layout depicted schematically. (D) Sample geometry (mm) to determine tensile response. (E) Bottom surface of 38.1 mm AFSD tool containing features. 43

Figure 5.7 (A) OM cross-section of the as-deposited AA6061 raster, centered upon the overlapping region. Outlined regions depict specific locations deformed by the tool features. (B) Magnified view of two parallel layers and substrate developing a plume structure. (C) A continuous oxide layer (denoted by arrows) divides the layers and substrate. (D) SEM images depict similar small networks of particles. (E) A smaller, discontinuous network forming a web. 45

Figure 5.8 (A) OM image depicting the location of an oxide film separating the substrate from flash and freshly deposited material. (B) SEM reveals etch pits resulting from the NaOH caustic etchant selectively attacking oxides. (C) EDS qualitatively determines these particles (D) as trapped oxides. 47

Figure 5.9 (A) Oxides forming the outline of two parallel layers of AA6061. (B) Oxides in the raster interface are smaller than those at the substrate interface and form a discontinuous network. (C) EDS qualification of oxide particles..... 48

Figure 5.10 (A) Cumulative grain diameter frequency plot with correlating OM depicting EBSD scan locations. (B) EBSD depicts equiaxed grains at the center of the deposition path. (C) EBSD in the raster interface revealed slightly smaller, elongated grains as a result of twice as much severe plastic deformation from additional tool passes. 51

Figure 5.11 Vickers hardness map displays a reduction in hardness in the overlapping region compared to a single row deposition. 51

Figure 5.12 (A) Quasi-static stress-strain response of the as-deposited AFSD AA6061 deposited in parallel passes. (B) Schematic of the sample location with respect to the overlapping region (this study). (C) Schematic of a single row of AFSD AA6061. 52

Figure 5.13 (A) Side view of fractured sample 1. Significant necking is observed along with apparent delamination. (B) Optical microscopy of the cross-section of the fractured sample shows that the shelf that forms does not propagate throughout the width of the specimen. 53

Figure 5.14 (A) Macroscopic view of the fracture surface of sample 1. (B) High magnification SEM image outlining large oxide particles that coalesced along a ridge. (C) Delamination occurring at layer interfaces. (D) Submicron oxide particles are observed along the length of the cavity, outlined by ellipses. 55

Figure 5.15 Schematic of the cross-section of the tool depicting the effect of the feedstock expanding inside of the AFSD tool. 56

Figure 5.16 (a) AFSD process illustrations representing a featured tool, (b) featured tool face enlargement, (c) representative AA6061 AFSD build on AA6061-T651 substrate, and (d) schematic of specimen geometry and orientation detailing location of specimens within. 59

Figure 5.17 Representative grain size through use of inverse pole figure maps for (a) extruded wrought AA6061-T651 control samples, (b) AFSD AD, (c) AFSD SQ, and d) AFSD SQA 61

Figure 5.18 TEM bright field images show a) wrought AA6061-T651 control with strengthening precipitates, b) AFSD AD without strengthening precipitates and c) precipitates returning after heat treatment to AFSD AA6061 61

Figure 5.19 Experimental true stress-strain tensile test results of averaged wrought AA6061-T651 (3 specimens), AFSD AD (3 specimens), AFSD SQ (3 specimens), and AFSD SQA (4 specimens) with (b-e) representative fracture surfaces. 62

Figure 5.20 Sample geometry and layout from within the AFSD build. 65

Figure 5.21 Isometric view of EBSD maps of (a) AA6061-T651 feedstock and (b) as-deposited AFSD AA6061 with equiaxed grains. 66

Figure 5.22 (a) AFSD back-scatter electron (BSE) image showing iron rich particles generally spherical in nature, (b) 5000x magnification BSE image of a cluster of particles in the AFSD, (c) wrought AA6061-T651 feedstock BSE image with larger, amorphous iron intermetallic particles, and (d) a normal distribution contrasting the sizes of the iron particles in the AFSD and feedstock materials. 68

Figure 5.23 Monotonic stress-strain curve of wrought AA6061-T651, AFSD AA6061 as-deposited longitudinal direction, AFSD AA6061 as-deposited build direction, and the annealed wrought AA6061-O. 69

Figure 5.24 Strain amplitude versus cycles to failure plot of the AA6061-T651 feedstock, AA6061 AFSD as-deposited longitudinal direction, and AA6061 AFSD as-deposited build direction. 71

Figure 5.25 The evolution of the stress amplitude response to deformation for wrought AA6061-T651, as-deposited longitudinal direction AA6061, and as-deposited build direction AA6061 for specimens tested at 0.3 and 0.5%..... 72

Figure 5.26 Fracture surface of (a) AFSD as-deposited build direction sample tested at εa = 0.3% (Nf = 6,505 cycles) with (b) high magnification view of a crack initiation site, and fracture surface of (c) AFSD as-deposited longitudinal direction sample tested at εa = 0.3% (Nf = 67,983 cycles) with (d) higher magnification view of crack initiation site. 74

Figure 5.27 MSF model fit for (a) AFSD as-deposited AA6061 in the longitudinal direction and (b) AFSD as-deposited AA6061 in the build direction. 75

Figure 5.28 MSF model plots of the incubation and small crack growth contributions to the total fatigue life prediction for (a) AFSD AA6061 in the longitudinal direction and (b) AFSD AA6061 in the build direction. 76

Figure 5.29 Bound life MSF model plots for (a) AFSD AA6061 in the longitudinal direction and (b) AFSD AA6061 in the build direction. 77

Figure 5.30 Specimen Geometry and layout for post deposition heat treatment study of AFSD AA6061..... 81

Figure 5.31 Inverse pole figure map of post-deposition heat treated AFSD AA6061 demonstrating larger grains than the as-deposited AFSD AA6061 reported in the literature [66]. 82

Figure 5.32 Monotonic stress-strain curves comparing wrought AA6061-T651, AA6061-O, and AFSD AA6061 as-deposited in both the build and longitudinal directions. 83

Figure 5.33 Strain versus life plot for wrought AA6061-T651, as-deposited AA6061, and heat treated AFSD AA6061..... 84

Figure 5.34 Fracture surface of (a) a sample tested at ε_a = 0.3% (N_f = 47,470 cycles) and (b) a sample tested at ε_a = 0.5% (N_f = 1,432 cycles). Both surfaces demonstrate void coalescence at 1 mm increments believed to correspond to deposition layers. 85

Figure 5.35 Fracture surface of a sample tested at ε_a = 0.2% (N_f = 1,535,618 cycles) that exhibits signs of both ductile and brittle failure modes. 86

Figure 5.36 The fracture surface of a sample tested at ε_a = 0.3% (N_f = 47,470 cycles) with crack initiation observed to occur at the middle of top surface as well as an alternate initiation site in the bottom right corner..... 87

Figure 5.37 Total life results from MSF model calibration of AFSD AA6061..... 88

Figure 5.38 MSF model plot showing the contributions of the incubation stage and the microstructurally / physically small crack growth portions of the model. 89

Figure 5.39 MSF plot shown with upper and lower bounds that were generated from the distribution of constituent particles in AFSD AA6061..... 90

Figure 5.40 (a) Pictorial representation of fabricating helical build via the AFSD process, (b) and (c) front and top view of the completed AA6061 component. 92

Figure 5.41 Pictorial representation of (a) orientation of specimens with respect to the helical build, (b) geometrical dimensions of the tensile specimen. 93

Figure 5.42 Monotonic True Stress-strain curves with error bars of the specimens from three different orientation. 95

Figure 5.43 Representative microstructure images of (a) 0°, (b) 90° and (c) 45° orientation specimens. 95

Figure 5.44 EBSD maps of (a) wrought-feedstock AA6061, (b) 0° specimen, (b) 90° specimen and (c) 45° orientation specimen. 96

Figure 5.45 cross-section of square-rod feedstock AA6061-T6: a) as received; b) anodized with a 9.8-μm thickness; c) anodized with a 68-μm thickness..... 98

Figure 5.46 (a) The AFS-D build from anodized square-rod AA6061 feedstock; (b) the AFS-D tool with four “teardrop” protrusions on the shoulder surface. 99

Figure 5.47 SEM images and corresponded binary images analyzed via imageJ of alumina particles in the AFS-D build from anodized feedstock bars with an average thickness of a) & c) 9.8 μm; b) & d) 68 μm. 100

Figure 5.48 Optical images showing full consolidation of feedstock material AA6061 after AFS-D processing: a) AA6061-NA; b) AA6061-0.4%alumina; c) AA6061-2.8%alumina. The dark particles are aluminum oxide particles, not pores. 101

Figure 5.49 BSE images of AFS-D builds: a) AA6061-NA; b) AA6061-0.4%alumina; c) AA6061-2.8%alumina. 101

Figure 5.50 SEM images and EDS signals collected from a) & b): the AA6061-0.4%alumina deposition; c) & d): the AA6061-2.8%alumina deposition. The detected sulfur signal was from the sulfuric acid electrolyte used in the hard anodization process to prepare the anodized feedstock. 102

Figure 5.51 Alumina particle size distribution in a) AA6061-0.4%alumina deposition; b) AA6061-2.8%alumina deposition. 103

Figure 5.52 SEM images and EDS signals collected from a) & b): the AA6061-NA deposition; c) & d): the AA6061-0.4%alumina deposition; e) & f): the AA6061-2.8%alumina deposition. The peak at 0.1 keV is the noise peak from the spectrometer and should be disregarded. 104

Figure 5.53 Stress-strain curves of quasi-static monotonic tensile behavior of the AFS-D depositions in the a) longitudinal direction; b) build direction. The tensile data from AA6061 without anodization is included from Rutherford et al. [11]. 105

Figure 5.54 Tensile properties of the AFS-D builds as a function of the theoretical volume percentage of alumina in the deposition: a) Elongation; b) YS; c) UTS. The error bars represent the standard deviation among tested tensile coupons. 106

Figure 5.55 Fractography images of AA6061-NA (a, d); AA6061-0.4%alumina (b, e); AA6061-2.8%alumina (c, f) in longitudinal direction (a-c) and in build direction (d-f). 106

Figure 5.56 Schematic of AFSD process, modified from Avery et al.'s previous work [5] 112

Figure 5.57 (a) AFSD AA6061 deposit built on a 12.7mm-thick AA6061-T651 substrate, red box region indicates the location of sliced 'comb' sample in (b); (b) stress-relieved 'comb' sample for d_0-spacing measurement, cyan box region indicates the location of neutron beam measured on each tooth. 113

Figure 5.58 Schematic of the geometry for the neutron diffraction-based residual stress experiments. 114

Figure 5.59 Measured d_0-spacings from the stress-relieved "comb" sample sliced from the AFSD deposit. The "normal" direction is the same as the z direction. 116

Figure 5.60 Measured d-spacings from the AFSD deposit in: (a) starting position; (b) center region; (c) finishing position. 117

Figure 5.61 Calculated strain distribution in the AFSD deposit in: (a) starting position; (b) center region; (c) finishing position. 117

Figure 5.62 Residual stress distribution in the AFSD deposit in: (a) starting position; (b) center region; (c) finishing position. Note: the residual scale is different between sub-figures to allow better visualization of the changes in the residual stress profiles. 118

Figure 5.63 Stress-free lattice parameter (blue filled circles) and microhardness (black cross) in the z (normal) direction in the center region of the AFSD AA6061 deposit. Red arrows indicate the regions of EBSD inverse pole figure in Figure 5.64. 123

Figure 5.64 EBSD inverse pole figure mapping with respect to longitudinal direction mapping showing grain size in the AFSD deposit in the center region: (a) top surface; (b) mid-thickness (c) legend of crystal orientation; (d) cumulative area percentage as a function of grain diameter. 124

Figure 5.65 (A)Schematic of the AFS-D process denoting specific features and process control variables. (B) Schematic of the features located on the interaction face of the steel AFS-D tool. 127

Figure 5.66 Color contour plot contrasting the material volumetric feedrate to the RPM of the tool. (B) Deposition cross-sectional hardness versus average temperature. Key: circles correlate to 200 RPM, squares to 300 RPM, and triangles to 400 RPM. Blue data points correlate to deposition ratio of 0.55, black data points correlate to a deposition ratio of 0.65, and red data points correlate to a deposition ratio of 0.75..... 130

Figure 5.67 (A): Optical micrograph of wrought AA5083-H131 plate showing constitutive particles pancaked between the rolled grains. (B) Optical micrograph of as-deposited AA5083 after AFSD showing smaller, dispersed constitutive particles. 131

Figure 5.68 EBSD maps in 3-orientations of (A) the rolled AA5083-H131 feedstock and (B) as-deposited AA5083. Scale bars are 50 μm. 132

Figure 5.69 Comparative tensile stress-strain response of the wrought AA5083-H131 feedstock and as-deposited AA5083. 133

Figure 5.70 Vicker's hardness plot with respect to the sample geometry. 135

Figure 5.71 Low magnification overview of 45° fracture of AA5083-H131 sample. (B) Large voids, surrounded by microvoids, coalesced from fractured iron particles along rolling boundaries. 136

Figure 5.72 (A): Post-mortem analysis of tensile sample tested in the vertical build direction. (B) Contamination observed near delamination crack. (C) Material flow lines parallel the deposited layers with a larger void encasing a secondary-phase particle. 138

Figure 5.73 (A): Post-mortem analysis of tensile sample tested in the vertical build direction. (B) Contamination evidenced along the fracture surface. (C) High-magnification image of two locations compared via EDS. (D) EDS analysis comparing contaminant composition with respect to the matrix. EDS was performed at 5 keV. (E) Brittle fracture features observed. (F) Shallow dimples filled with carbon particles. 140

Figure 5.74 (A) Macroscopic image of the onion ring structure on the final layer of the deposit taken as observed directly below the tensile sample observed in (C). (B) High-magnification OM of the onion ring pattern depicting distances between rings. (C) SEM fractography correlating flow patterns with onion ring structures observed in OM. 141

Figure 5.75 (A): Overview schematic of the cross section of the AFSD tool, feedstock, and two layers. (B) Schematic of the material flow close to the tool exit hole. Carbon highlighted in red. (C) Schematic of the area near a tool teardrop feature. Carbon follows the path of the tool features rather than dissolving into the layers. (D) Carbon on the active layer becoming entrapped by the flash from excess material in the onion skin. 143

Figure 5.76 Two AFSD processes featuring a) solid bar feedstock made from AA5083-H131 rolled plate and b) feedstock made from loose machine chips cut from AA5083-H131 rolled plate and fed through an auger. 146

Figure 5.77 Representative a) image of solid bar build, b) specimen layout in solid bar build, c) specimen orientation relative to processing directions of solid bar build, d) fatigue specimen shape and dimensions, e) monotonic tensile specimen shape and dimensions, f) image of recycled build, g) specimen layout in recycled build, h) specimen orientation relative to processing directions of recycled build. 147

Figure 5.78 Imagery representative of grain structure for a) AA5083-H131 rolled plate wrought control, b) AFSD As-Deposited recycled chip build in the Longitudinal Direction (LD), and c) AFSD As-Deposited rolled plate feedstock build in the Longitudinal Direction (LD). 150

Figure 5.79 Monotonic true stress-strain curve of AA5083-H131 wrought control, AA5083 AFSD from solid bar feedstock, and AA5083 AFSD from recycled chip feedstock, with maximum and minimum errors represented and respective strength model calibration plots. .. 152

Figure 5.80 Stress amplitude vs. cycles to failure of AFSD AA5083 and AFSD AA5083 chip deposit in the LD Direction. 155

Figure 5.81 Low cycle fatigue fracture surfaces for a) wrought control AA5083-H131 (s =198 MPa, N_f = 30,808), b) AA5083 AFSD recycled chip (s =180 MPa, N_f = 29,789), and c) AA5083 AFSD solid bar (s =180 MPa, N_f = 26,709) specimens, where the red circles indicate observed crack initiation sites, and respective magnifications of primary crack initiation sites below (d-f). 158

Figure 5.82 High cycle fatigue fracture surfaces for a) AA5083-H131 (s =126 MPa, N_f = 346,732, b) AA5083 AFSD-Recycled (s = 144 MPa, N_f = 1,074,636), and c) AA5083 AFSD-Solid bar (s =126 MPa, N_f = 399,576) specimens, where the red circles indicate observed crack initiation sites, and respective magnifications of primary crack initiation sites below (d-f). 159

Figure 5.83 Multistage Fatigue (MSF) fit displaying stress-life plots for crack incubation (N_{inc}) and microstructurally and physically small crack growth ($N_{msc/psc}$) compared to total life (N_{total}) for a) AA5083-H131 wrought control, b) AA5083 AFSD Solid bar, c) AA5083 AFSD Recycled Chip, and d) MSF fit for total life (N_{total}) comparison previously mentioned materials. 161

Figure 5.84 Additive Friction Stir Deposition (AFSD) model used in this study. Smoothed particle hydrodynamic material points modeled the feedstock and substrate, and finite elements modeled the tool and base. 164

Figure 5.85 AFSD substrate temperature experimental setup depicting locations of thermal couples in the substrate to measure advancing side, middle, and retreating side temperatures. 166

Figure 5.86 Thermocouple temperature results for three test cases: (a) starved at 63.5 mm/min actuator feed rate, (b) optimal at 127 mm/min actuator feed rate, and (c) overfed 254 mm/min actuator feed rate. 168

Figure 5.87 Diagram illustrating the lower temperature zone directly beneath the tool caused by the reduction of the tool velocity vector and the feedstock heat sink. Temperature scale is in degrees Celsius. 169

Figure 5.88 Comparison between experiment and simulation build profiles for: (a) starved at 63.5 mm/min actuator feed rate, (b) optimal at 127 mm/min actuator feed rate, and (c) overfed 254 mm/min actuator feed rate. 170

Figure 5.89 Simulation temperature (°C) contours for: (a) starved at 63.5 mm/min actuator feed rate, (b) optimal at 127 mm/min actuator feed rate, and (c) overfed 254 mm/min actuator feed rate. 171

Figure 5.90 Effective plastic strain contours for: (a) starved at 63.5 mm/min actuator feed rate, (b) optimal at 127 mm/min actuator feed rate, and (c) overfed 254 mm/min actuator feed rate. 172

Figure 5.91 (a) Schematic of the AFSD process shows how feedstock rod is transformed into deposition by spinning and traversing tool. (b) Large multi-layer deposition created by the AFSD process [260]. 176

Figure 5.92 SMT001 Gleeble torsion samples used for constitutive model calibration. All dimensions are in millimeters. 180

Figure 5.93 AFSD model used in this study. Smoothed particle hydrodynamic material points modeled the feedstock and substrate, and finite elements modeled the tool and base. 181

Figure 5.94 Analysis zone in the SPH simulations used to highlight the effects different constitutive models have on the simulation environment. 182

Figure 5.95 Experimental effective stress and strain curves for AA6061-T6 vs constitutive models: (a) JC (b) FKS and (c) ST. FKS was the most accurate for AA6061-T6. 183

Figure 5.96 Experimental effective stress strain curves for AA6061-O vs compared models: (a) JC (b) FKS and (c) ST. FKS and JC captured the trend of AA6061-O stress-strain behavior. 184

Figure 5.97 Comparison between the constitutive models shows the importance of accounting for high plastic strain behavior when curve fitting. 185

Figure 5.98 Average effective stress differences for each constitutive model and temper compared with experimental data show the relative accuracy of FKS vs JC and ST. 186

Figure 5.99 Constitutive model yield strength evolution with temperature highlights different behaviors with each model. 187

Figure 5.100 Constitutive model yield strength evolution with strain rate shows similar behaviors with each model. 188

Figure 5.101 SPH simulation results of average peak (a) temperature, (b) effective stress, and (c) effective plastic strain values for each constitutive model show consistency of each constitutive model and provide a better comparison than single peak values. 189

Figure 5.102 (a) Legend of analysis zone. (b) Temperature contour plots for each constitutive model emphasize the unique thermal softening behavior of FKS. (c) Temperature percent difference contour plots for comparisons between each constitutive model show the drastic difference between FKS and the other constitutive models. 191

Figure 5.103 (a) Legend of analysis zone. (b) Effective stress contour plots for each constitutive model show the low stresses required to induce flow in the FKS simulation. (c) Effective stress percent difference contour plots for comparisons between each constitutive model show the large differences between FKS and the other constitutive models. 193

Figure 5.104 (a) Legend of analysis zone. (b) Effective plastic strain contour plots for each constitutive model show the relatively high plastic strains experienced in $JC_{0.23}$. (c) Effective plastic strain difference contour plots for comparisons between each constitutive model highlights the differences between $JC_{0.23}$ and the other constitutive models. 195

Figure 5.105 Build profiles for each constitutive model highlight differences between $JC_{0.23}$ and the other models. (a) $JC_{0.001}$ (b) $JC_{0.23}$ (c) FKS (d) ST. The similarity between $JC_{0.001}$, FKS, and ST indicates that changing processing temperature, effective stress, and effective plastic strain does not necessarily change output part appearance. 197

Figure 5.106 Description of AFSD process where a feedstock material is pushed through a spinning non-consumable tool onto a substrate. 201

Figure 5.107 SPH kernel function illustrating the influence domain of a particle and the neighboring particles that fall under the influence domain [40]. 204

Figure 5.108 SPH model of AFSD process with labeled parts used for model calibration. SPH points modeled the feedstock and substrate, and rigid finite elements modeled the tool and base. 206

Figure 5.109 SPH model of AFSD oxide and copper wire tagging for comparison with experimental AFS Depositions. 207

Figure 5.110 (a) Starved and (b) overfed AFS Depositions created with anodized rods for model calibration with labelled oxide analysis regions. Showing oxide analysis regions used in results section (revise). 208

Figure 5.111 (a) Region 2 micrograph of overfed anodized AFS Deposition with SEM image indicating EDS point scans. (b)-(g) EDS results from Region 2 of the overfed AFS Deposition confirm the appearance of anodized oxides. 210

Figure 5.112 Quantified AFSD oxide distributions for the anodized feedstock depositions per oxide analysis region show preference for retreating side in both (a) starved and (b) overfed builds for both experiments and simulations. The oxide analysis regions are labelled on the physical samples in Figure 5.110. 211

Figure 5.113 (a) Copper wire core deposition using AFSD for use in SPH model calibration. (b) Schematic showing construction of copper wire core feedstock. 212

Figure 5.114 (a) XRCT scan of copper wire core deposition using AFSD shows concentration of copper on the advancing side. (b) SPH simulation of AFSD process with copper wire core feedstock shows good agreement with experimental deposition. 213

Figure 5.115 (a) Location of tracked oxide particles at start of simulation on the outside of the feedstock. Oxide particle paths during (b) starved and (c) overfed simulations show three kinds of flow behaviors interact to determine particle movement: 1) rotational flow, 2) radial flow, and 3) traverse flow. 215

Figure 5.116 (a) Location of tracked copper particles at start of simulation at the center of the feedstock. (b) The central starting position of the copper particles results in a spiral flow out of the feedstock rotation circumference. 216

Figure 5.117 Representative images of (a) AFSD process using AA5083-H131 solid rod feedstock and (b) featured tool with “tear drop” protrusions on tool face that interacts with substrate surface. 221

Figure 5.118 Representative a) image of AFSD AA5083 build, b) specimen layout and orientation in AFSD build, and c) compression specimen shape and dimensions. 222

Figure 5.119 Graphical illustration of Split-Hopkinson Pressure Bar experiment setup including MATLAB Split-Hopkinson Pressure Bar Data Analysis Tool. 223

Figure 5.120 Representative grain structure of a) AA5083-H131 rolled plate wrought control in RD, ST, and LT directions and b) AFSD As-Deposited in LT, LD, and BD directions. 229

Figure 5.121 Representative sampling of raw data for AA5083-H131 wrought control including an a) oscilloscope trace displaying the amplified strain gage output voltage for the incident, transmitted, and reflected waves and b) oscilloscope trace converted to strain using strain-to-voltage factor 0.000614 e/V for incident and reflective waves and 0.0001228 e/V for transmitted wave. 230

Figure 5.122 Representative sampling of raw data for AA5083-AFSD including an a) oscilloscope trace displaying the amplified strain gage output voltage for the incident, transmitted, and reflected waves and b) oscilloscope trace converted to strain using strain-to-voltage factor 0.000614 e/V for incident and reflective waves and 0.0001228 e/V for transmitted wave. 232

Figure 5.123 Plasticity stress-strain response for AA5083-H131 and AA5083-AFSD-BD, -LT, and -LD at room temperature for HRC ($2000s^{-1}$) and AA5083-H131 and AA5083-AFSD-LT for QSC ($0.001s^{-1}$) with error bars to represent the resultant range for each test condition. 234

Figure 5.124 Comparison between ISV plasticity-damage model prediction and experimental data for a) QS compressive response at room temperature for AA5083-H131 wrought material and AA5083-AFSD-LT and b) HR compressive response at room temperature for AA5083-H131 wrought material and AA5083-AFSD-LT, -ST, and -LD directions. 235

Figure 5.125 Comparison between the modified ISV plasticity model prediction and the experimental data for AFSD AA6061. **(a)** Comparison between the Original ISV plasticity model prediction and experimental data under the top and bottom longitudinal orientation. **(b)** Comparison between the modified ISV plasticity model prediction and experimental data under top and bottom longitudinal orientation able to capture the material behavior. 237

Figure 5.126 The Direct Additive Recycling (DAR) paradigm for recycling secondary feedstocks at forward operating bases (FOBs) processed through the Additive Friction Stir Deposition (AFSD) process. 240

Figure 5.127 a) Battlefield scrap serving as bulk feedstock stream for subsequent deposition. b) Scrap recycled into compatible geometry for AFSD feedstock. c) Deposition using solid virgin material. d) Deposition using recycled strips from battlefield scrap. Both depositions exhibit similar build morphology and surface finish. 241

Figure 5.128 a,b) Cross-sectional X-ray CT confirming fully dense deposition for a) recycled strip deposition and b) solid feedstock deposition. c,d) Isometric X-ray CT confirming full density within near net shape deposit for c) recycled strip deposition and d) solid feedstock deposition. 242

Figure 5.129 a) Schematic depicting the three principal directions of the deposit. b) Deposition utilizing solid feedstock. c) Deposition utilizing recycled stacked strips. (d,e) Representative Electron Backscatter Diffraction at denoted locations in d) solid feedstock deposition and e) recycled stacked strip deposition. 243

Figure 5.130 a) Representative 44.5 kN rough terrain forklift used to transport mat bundles [304] b) Typical mat bundle configuration [305] c) Simulated fork puncture in mat skin. 244

Figure 5.131 a) Skin damaged component fixtured in machine for repair. b) Repaired skin damage after solid-state deposition of material. c) As-deposited material (red) and post-deposition machining (blue) to restore original component geometry. 244

Figure 5.132 Subcomponent four-point bed results depicting similar mechanical behavior between new matting (Base Material) and repaired matting (AFSD Repair) cross-sections. The experimental setup and location of the repair is denoted schematically within the graph. The cross-sectional geometry of the component is not publicly available and has therefore been omitted. 245

Figure 6.1 Comparison of build accuracy versus build rates for additive friction stir deposition (AFSD), powder bed, and direct energy deposition. 248

Figure 6.2 Successful AFSD depositions from recycled feedstock including compacted machine chips, loose machine chips, and strips of damaged material. 250

Figure 6.3 Limitations of current build comparing actual deposition time to machine downtime during a build. 252

Figure 6.4 Comparison between round and square feedstock depositions that are both fully-dense. 253

Figure 6.5 A vertically integrated Direct Additive Recycling (DAR) approach to fabricate or repair components without needing atomization of scrap machine chips. 254

Figure 6.6 Use of AFSD for repairing airfield landing mat components such as edge clamps fabricated from mat core top skins where strips of damaged landing mat built up the component thickness to required sizes. Left image from [306]. Center image from [304]..... 254

2. OBJECTIVE

The objective of this work is to understand and confirm the viability of the Additive Friction Stir Deposition (AFSD) process to successfully reuse multiple waste streams to produce fully dense components with robust material performance. To illustrate the robustness of this proposed solid-state additive manufacturing approach with AFSDeposition, we will focus on recycling two FOB waste streams: (1) metal machine shop chips and (2) damaged metal expeditionary airfield (EAF) matting systems, specifically AM2, as shown in Figure 2.1.

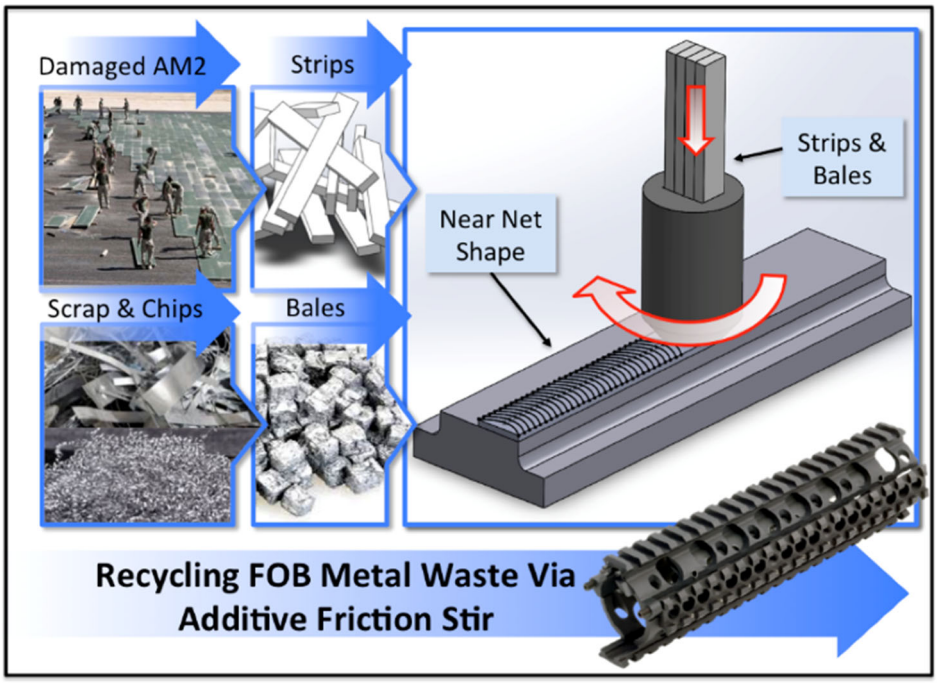

Figure 2.1 Schematic of proposed additive friction stir deposition (AFSD) manufacturing process for recycling of FOB metal waste.

To complete the objective the process-structure-property-performance (PSP^2) relations of a transformative forward operating base (FOB) metal recycling paradigm in which metal waste/scrap is reused for fabrication and repair of both constrained capacity resource (CCR) and non-CCR components using a novel solid-state additive manufacturing process. Two metal waste streams at FOBs were investigated in this study, but as suggested in the statement of need (SON), the proposed strategy is flexible and robust enough to be applied to additional waste streams such as salvaged battlefield scrap metal. Additionally, as requested in the SON, the proposed recycling methodology has low energy demands, minimized labor requirements, and a small logistical footprint to fabricate or repair fully-dense components for the Warfighter.

This novel solid state manufacturing approach, AFSD, offers several advantages for use in austere environments because the process is low-power, able to build small and large parts, can use a variety of metals in different forms, does not require secondary processing for densification or atmospheric controls, has superior build rates yielding enhanced mechanical properties, can be operated by a machine shop technician, and is ISO container transportable.

This research tested the hypothesis that (1) the powder range can be increased to include chips from a recycling stream and compacted machine chip bales and (2) stacks of waste metal strips from damaged airfield landing mat (AM2) as solid feedstock to produce fully dense samples with isotropic wrought mechanical properties through both waste stream approaches as depicted in Figure 2.1.

We tested the hypothesis by quantifying the relationship between microstructural evolution, mechanical properties and the processing parameters (e.g. shear forces, heat generation) for AFSD battlefield scrap feedstock (AM2 portable aluminum airfield landing mat and metal machining chips) samples. Particular focus was to fundamentally understand how oxide arrays due to surface area oxidation on multilayered or machine chip feedstock were broken-up and dispersed during AFSD. This fundamental investigation provides new scientific knowledge that may be applied to both non-ferrous and ferrous material systems to provide the joint services a superior technological capability to manufacture components in the field and repair damaged structures/vehicles/armor with an enhanced similar or dissimilar structural material.

3. BACKGROUND

FOB Metal Waste Streams: There are a variety of solid waste streams from deployed forces due to the different Military Occupational Specialty (MOS) units [1]–[6]. Two specific metal waste streams identified are (1) scrap metal from maintenance-MOS activities [2], [6] where metal machining chips are created at the FOB sites, such as Mobile Parts Hospital, Expeditionary Labs, and other ad hoc metal machining operations. The use of these chips for the AFS process at the FOB could eliminate their unacceptable disposal and/or cut the costly expenses related to their transportation to a recycling site. The second waste stream will be from (2) EAF-MOS [7] aluminum landing mats, where AM2 is reported to have a 10 percent refurbishment quantity. Even though there have been composite landing mat discussions, the Marine Corps is the largest user and still wants an all metal solution due to the robustness of metal solutions for VTOL sorties that have resulted in loss of life incidents when using non-metal landing pads [8]. New matting development efforts such as the lightweight-light duty, remote piloted aircraft (RPA), and AMX programs suggest matting systems will still be all metal solutions to support the Joint Services [9]. While we acknowledge that there are additional waste streams, successfully reclaiming these battlefield products will provide a quantifiable step forward in recycling objectives at FOBs.

Expeditionary airfields (EAF), including the aluminum alloy AM2, are an essential component of a FOB. The amount of AM2 at a typical FOB can vary but can be as significant as the 4,000 feet by 150 feet runway built at Camp Dwyer in Afghanistan (when initially a FOB) [10], [11]. Thus, the runway built at Camp Dwyer could generate a waste stream of over 1800 tons of aluminum. Depending on the operational use, AM2 can sustain significant damage, including failure of end connectors, skin punctures, etc. [12]–[14]. Therefore, the goal is to reuse damaged and unusable AM2 in theater that would otherwise be sent back to the US for refurbishment or be left behind in-theater.

FOB Additive Manufacturing Challenges: With significant thrusts such as the Army Net Zero Waste Program [1], [6], Reverse Logistics Programs [15], and other efforts to minimize potentially dangerous resupply convoys [16] there exists a large potential for in-theater manufacturing and repair of equipment at FOBs to ensure mission success. While processes such as selective laser melting (SLM), electron beam (EBeam), and laser engineered net shaping (LENS) can be used for current additive manufacturing, they lack the capability to repair or join large-scale metal components. These technologies, along with repair techniques such as cold-spray, are prohibitive because they are extremely energy intensive and require highly specialized environments (i.e. vacuum, nitrogen gas, helium gas) that are not feasible or necessarily safe to provide at a FOB. Additionally, these processes require significant energy and cost investments by the user to produce powder feedstock within a certain tolerance range, which is extremely more constrained than the powder used in AFSD machines. Furthermore, the AFSD process with either powder or solid filler rod uses low power for continuous solid-state joining or deposition without atmospheric control to enable additive manufacturing and repair. Since material is actually being deposited in the AFSD process, there are also significant advantages over other solid-state additive manufacturing processes like layered friction stir welding. In layered friction stir welding [17], a converted solid state joining process that produces layered microstructures, significant machining has to be performed between successive layers in-order to build up a fully-dense structure, which results in added time, energy, and additional waste for the build process.

Additionally, as metal manufacturing costs have increased, viable methods for producing complex geometries with high strength-to-weight ratios that produce limited waste has yielded numerous methods for metal additive manufacturing (AM) [18]. Fusion-based metal AM processes require the use of a focused, high energy source directed on to a wire [19]–[21] or a mixture of metallic powders [22]–[24] that either melts or sinters the feedstock material into consecutive layers. However, these fusion based AM processes produce intense thermal gradients that present significant challenges for traditionally difficult or unweldable alloys, namely aluminum or magnesium alloys. These fusion processes create technical barriers in producing as-deposited defect-free aluminum components with commercially available materials. In aluminum alloy 6061 (AA6061), selective vaporization can occur, resulting in change of composition from the loss of zinc, magnesium, and silicon, substantial alloying elements that characterize AA6061 precipitate strengthening and corrosion resistance [25], [26]. Additionally, rapid formation of oxides [27], [28] and ambient water vapor [29] requires inert atmospheres to prevent contamination and porosity during solidification, remedied by secondary solidification operations. An alternative solution to circumvent these obstacles has been to pre-alloy powders containing increased traces of silicon, scandium, or zirconium [28]–[30].

Microstructural analysis of fusion-based additively manufactured aluminum alloys has often produced preferential grain orientation and destruction of inherent precipitates induced by phase transformations [29], [31]. Thijs [32] and Croteau [33] observed fine, equiaxed grains at layer interfaces giving way to columnar, preferential grains parallel to solidification gradients in the center of the melt pools. Furthermore, strong fibrous textures in the <100> direction were reported leading to anisotropic behavior of as-deposited alloys [20], [30], [32]. Supplemental examination on the nanoscale determined traditional precipitates were dissolved due to the vaporization of magnesium [34]. Instead, pre-alloyed elements produced cubic or triangular particles at grain boundaries on the layer interface, which pinned the migration of grains and explained the refined particle distribution seen at the top of each layer.

As-deposited aluminum alloys exhibited varying microhardness measurements depending on alloying composition and densification. Uddin et al. [30] reported Vickers hardness measurements of the most dense specimens averaging at 90 ±6 Hv of laser powder bed fusion AA6061, but 119 ±6 Hv with secondary tempering. When Si, Sc, or Zr was included as an alloying element, hardness varied from 93 Hv [35] to 127 ±3 Hv [32] in the as-deposited state. The noted increase in hardness was determined to be the result of increased silicon and scandium, which produced diamond-shaped, silicon-rich precipitates and a larger distribution of Al_3Sc precipitates [24]. However, it is noted that despite the ever-improving mechanical and microscopic properties of these additive manufacturing processes, these additive powders remain difficult to produce and have been shown to require additional alloying elements to be structurally viable. This creates a technological gap in additively manufactured, commercially available aluminum alloys and the end uses.

AFSD is a solid-state, AM process that benefits from similar fundamental physics occurring in friction stir welding/processing (FSW/P) [36]–[39]. The solid-state nature of the AFSD process avoids deleterious effects that occur in fusion-based AM processes such as hot cracking, porosity, and columnar grain structures without the need for secondary densification post processing. As illustrated schematically in Figure 3.1(A-C), robust, metallurgical bonding is achieved between deposited layers by forcing a metallic powder or solid feedstock through a rotating, cylindrical tool. The tool, featuring 4 teardrop projections on the interaction face evident in Figure 3.1(E), generates frictional heat and pressure inducing high-shear, severe plastic deformation of the solid feedstock onto a substrate and subsequent layers. Additionally, the severe plastic deformation generated by the tool and material interaction instigates dynamic recrystallization (DRX) in the as-deposited material, which yields a refined grain microstructure [37], [39]–[41]. At the end of a predetermined path, the spindle raises by a user-defined layer height and traverses along the build route to deposit consecutive layers (Figure 3.1(C)), producing a near-net shaped component (Figure 3.1(D)).

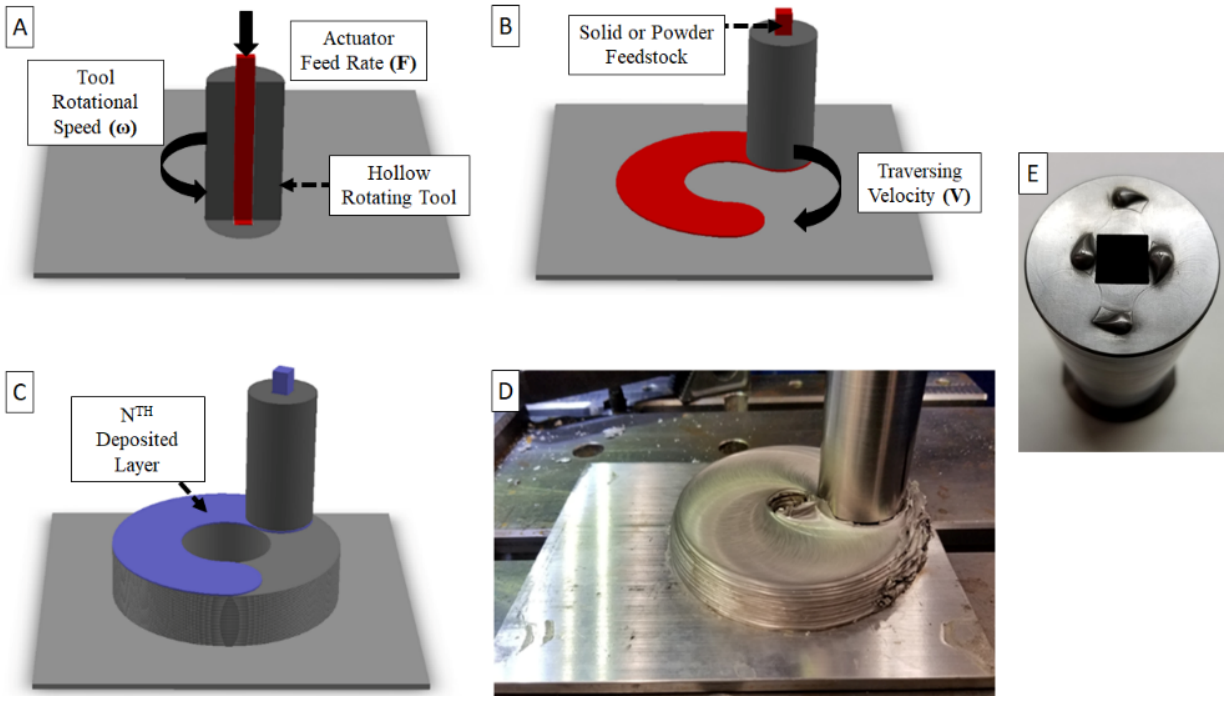

Figure 3.1. (A) Cross section schematic of the beginning of the AFSD process where the tool plunges into a substrate while spinning at a predetermined rotational speed. (B) The tool is then raised to the layer height during which time an actuator drives a solid, or powder, feedstock through the tool as the tool traverses across the substrate, producing a layer. (C) At the completion of a layer, the spindle raises to the next layer height and repeats the process to build consecutive layers. (D) Photograph of the actual AFSD process applied to AA6061. (E) Image of the teardrop featured tool.

Though the process principle appears to be similar to friction stir welding/processing, the material flow mechanism is different. In friction stir welding/processing, the existing material is transported by the tool pin in a manner influenced by the tool shape. During this process the surface oxide layer or contaminations are distributed into the nugget zone creating oxide array defects defined as 'lazy S', 'zigzag line' or 'kissing bond' [42], [43]. In AFSD, the material flows from the middle of the tool towards the outer edge of the tool. During this process, most of the surface contamination is expected to be expelled from the deposition region as flash, which has occurred for AFSD powder feedstock processing of aluminum alloys and magnesium alloys. However, failure to properly disperse the surface oxide layers in the AFSD process, from natural oxidation or anodization, may result in kissing bonds similar to the FSW process which are caused by a lack of metallurgical bonding in localized regions of the deposited material. The kissing bond defects may result in reduced static strength, impact strength, and fatigue life. Hence, the *Technical Barriers* proposed from using these new feedstock systems will be to quantify and fundamentally understand how interlayer oxides from filler materials, including multiple stacks of AM2 and baled aluminum scrap and chips, are dispersed to promote ideal microstructures.

AFSD Machine Specifications: Since the AFSD machines are modified milling machine platforms the energy usage is similar to conventional CNC milling machines and welding equipment used at FOBs. In addition, the AFSD process uses seven times less energy per unit build volume than a typical powder-based select laser melting (SLM) process, e.g. 47 Joules per cubic millimeter versus 325 Joules per cubic millimeter based on literature data. Currently, the AFSD machine capable of producing parts sizes up to 10" x 40" x 10" build volumes operates on 480V 3-Phase at 10A (5kW). As a comparison, at the Mobile Parts Hospital deployed at FOBs, the Mazak machining centers typically run on 3-phase, 400V at 50A (20kW). Thus, power requirements for AFSD machines are in line with current power usages at FOBs.

The AFSD system footprint can vary but is on the scale of milling machine platforms. The AFSD machine referenced in "Energy Usage" has a footprint of 144"W x 53"L but can easily be scaled up or down. In addition, 6 axis robotic arm platforms, portable platforms, and very large platforms to accommodate build sizes up to 16' x 13' x 3.5' have been recently proposed and demonstrate the flexibility of the AFSD process.

The AFSD technology has already been used for a variety of different solid, powder, and multi-material metallic systems. These include superalloys (Inconel 625), steels (ODS 14YWT/F82H, HY80, 300M, 4140, AerMat 100), aluminums (AA1xxx, AA2xxx, AA5xxx, AA6xxx, AA7xxx, Al-SiC MMC, Al-steel, Al-Fe MMC), magnesiums (AZ31, WE43, E675, AMX602, E21), coppers (Cu-Tungsten MMC, Cu-Tantalum, Cu-Niobium, Cu-Molybdenum MMC, Cu-Molybdenum), and nickel aluminum bronze. The current AFSD technology may be applicable to recycle the specific materials with limited or no surface preparation of waste metal components to make defect free additive components.

AFSD Process Modeling

The AFSD process is a nascent solid-state additive manufacturing approach providing layer-by-layer material deposition. The concept of the AFSD process was originally introduced as the hollow rotating tool Friction Stir Cladding (FSC) process described by Liu et al. [44] and Stelt et al. [45], where the FSC process is a derivative technology of friction stir welding (FSW) [46]. In FSW, the frictional heat generation derives from both the tool shoulder stirring against the top of the welded plates and the tool pin stirring within the welded material. In contrast, since the AFSD tool does not have a pin that plunges down into the material, the frictional heat generation derives primarily from the tool shoulder rotating above the substrate or deposited material (Figure 3.2). The benefit and necessity for the development of the AFSD and FSW solid state processes is motivated from prior work documenting that FSW is known to provide several advantages over traditional fusion-based welds [17], [47]–[62]: lower porosity, lower residual stresses, greater fatigue life, better ductility and toughness, no solidification or liquation cracking, and reduction in environmental and safety issues due to the temperature of the material remaining below the melting point.

Recently, the experimental investigations on the AFSD process has been demonstrated for a variety of different materials including hard alloys such as nickel-based super alloys [39], [41], copper [63], [64], lightweight metals like aluminum alloys [40], [63]–[69] and magnesium alloys [70]. Specifically, the physics of the process occurs through depositing material onto a substrate without the need for solid-to-liquid phase transformations of the material being deposited.

Currently, the AFSD process occurs by an actuator pushing a 300-mm long feedstock rod coated with a graphite lubricant through a rotating hollow tool onto a substrate as depicted in Figure 3.2 for a multilayer deposition. An offset between the bottom of the tool and the substrate is maintained to create a layer of deposited material. The rotating motion of the tool causes heat to be generated so the material softens and flows into the gap between the tool shoulder and previously deposited layers.

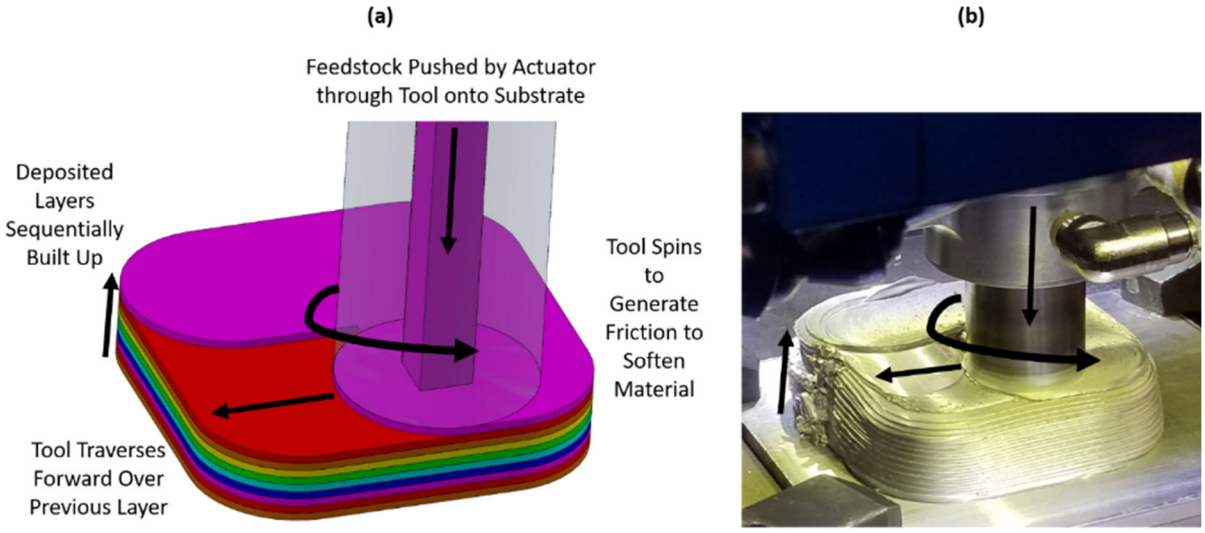

Figure 3.2. (a) Schematic diagram of the Additive Friction Stir Deposition (AFSD) process. (b) Representative AFSD deposition with multiple layers creating a large external feature.

Since AFSD is a burgeoning technology, computational approaches are beneficial to help elucidate and decouple the complex physical and thermal mechanics of the process. With AFSD sharing similar physics to FSW, computational methods in FSW provide a useful starting point to simulate the AFSD process. The most common method employed for simulating FSW is the Finite Element Method (FEM). In general, FEM simulations either use a Lagrangian mesh (mesh on part) or an Eulerian mesh (mesh in space). A Lagrangian approach, which is typically used for computational solid mechanics, uses the material coordinate system as the reference frame, which are the original coordinates of the nodes of the part. This approach naturally captures complex material movement and deformation but suffers from accuracy with excessive deformation. In particular, the determinant of the deformation gradient, the Jacobian, is a scalar quantity that can be related to the magnitude of element distortion. When the Jacobian is less than zero, the element has folded in on itself, which is physically unrealistic. Remeshing is one solution to this problem, where the elements are "re-drawn" to accommodate large deformation. However, this is a computationally expensive process and can produce unreliable results. Examples of Lagrangian simulations with remeshing in order to account for large element distortion are found in Chenot and Massoni [71] and Buffa et al. [72], [73].

Within FEM, one alternative to a Lagrangian approach is an Eulerian approach, which is typically used in computational fluid mechanics, tends to be more commonly used in FSW simulations by Hasan et al. [74] and Zhu et al. [75] because this approach ignores the problem of excessive distortion by having a fixed mesh in space. The material passes through the fixed mesh, which is

known as the spatial coordinate system. However, with an Eulerian approach, it is difficult to precisely track material movement, which leads to a decrease in accuracy in modeling the interface between the tool and the plates, as well as the inability to account for material history, which is important for modeling damage. To maintain accuracy while accommodating excessive deformation, the Lagrangian and Eulerian methods can be combined as in the Coupled Eulerian Lagrangian method (CEL) and the Arbitrary Lagrangian Eulerian method (ALE). In the CEL method, which was developed by Noh [76], involves using both methods simultaneously, where the tool is modeled with a Lagrangian mesh and the plates with an Eulerian mesh as utilized by Ajri and Shin [77] and Zhu et al. [78]. This approach opens up the possibility of modeling tool damage with material flow around the tool, and such has gained popularity for use in FSW simulations in recent years. The ALE method was developed by Franck and Lazarus [79] and Trulio [80] and later adapted to FEM. The ALE has been used for FSW simulations by van der Stelt et al. [81] and Meyghani et al. [82]. However, particle tracking in ALE is more difficult than with a true Lagrangian approach, as mentioned in the ALE material tracing algorithm in Dialami et al. [83].

The previously mentioned schemes are known as mesh-based methods, where elements are geometric shapes with nodes as the points, but sometimes meshless methods are beneficial. Meshless methods fall into two main categories: pseudo-meshless and true-meshless. Pseudo-meshless methods still require a background mesh for spatial integration, and the governing PDEs are reduced to a weak formulation. One such pseudo-meshless method is the Natural Element Method (NEM), created by Traversoni [84]. NEM uses Voronoi tessellation around an array of points to automatically generate a background mesh. Cells are generated around the nodes based on the distance to the background nodes. Values at nodes are interpolated based on the overlap of a node cell with the background Voronoi cells [85]. NEM has been utilized for FSW by Alfaro et al. [86]. Another pseudo-meshless method is the Element-Free Galerkin Method (EFG), created by Belytschko et al. [87]. EFG uses weight functions to interpolate field variables at nodes based on the influence of neighboring nodes. As in the Galerkin Method, EFG requires a background mesh to perform numerical integration. EFG has been successfully applied to FSW by Wu et al. [88]. True-meshless methods, however, do not require a background mesh for spatial integration. This mesh independence reduces the computational burden of the simulation. The true-meshless method used in this study is Smoothed Particle Hydrodynamics (SPH).

SPH is an advanced Lagrangian mesh-free simulation method that has applications in a wide variety of dynamic problems such as astrophysics, magneto-hydrodynamics (MHD), computational fluid dynamics (CFD) and computational solid mechanics (CSM). This method was originally proposed by two independent research groups within the same year, Gingold and Monaghan [89] showed that the method could be used to simulate non spherical stars and Lucy [90] used the method to test the theory of fission for rotating protostars. Interestingly, both groups based their methods on statistical approaches to estimate probability densities. The original SPH schemes proposed in 1977 were developed for applications to astrophysics problems and did not conserve linear and angular momentum as explained by Monaghan [91]. Later in 1982, Gingold and Monaghan modified the formulation to conserve momentum by using the Lagrangian to describe the conservation laws for a compressible dissipative fluid [92]. Since its inception, SPH has been used for a variety of large deformation problems such as FSW in studies by Fraser et al. [93], or machining in studies by Xi et al. [94].

4. MATERIALS AND METHODS

4.1 Materials

4.1.1 Aluminum Alloy 6061

Aluminum Alloy 6061 (AA6061) is a highly versatile and commonly used general-purpose alloy. It is used in a broad range of applications due to its ability for welding and heat treatment, high strength to weight ratio, and general availability. As industry moves toward light-weighting to increase fuel efficiency and vehicle handling, the use of aluminum alloys like AA6061 will only become more prevalent. The main constituents of AA6061 aside from Aluminum (97.9%) are Silicon (0.6%) and Magnesium (1.0%). The Mg-Si elements allow for precipitation hardening, which increase the strength of the material by growing strengthening precipitates. The mechanical properties associated with AA6061 are due to the microstructural morphology of the hardening precipitates within the material matrix, in this case the β" (Mg_2Si) [95]–[98]: The following is the simplified, generic precipitation for Al-Mg-Si alloy s[95]–[98]:

$$SSSS \rightarrow GP \rightarrow \beta'' \rightarrow \beta' \rightarrow \beta \cdot Mg2Si \tag{4-1}$$

where 'SSSS' stands for the super-saturated-solid-solution, 'GP' indicates the Guinier-Preston zones which are developed in the initial stages of precipitation and whose structure depends on the Mg/Si ratio of the alloy, the β" needle-like precipitates are associated with peak hardness, the β' rod-like precipitates are associated with over-aging and the final β -Mg_2Si phase is considered an equilibrium phase in the sequence.

Heat treatment is a common method for achieving optimized strength in precipitate strengthened 6xxx series aluminum alloys. In AA6061, a T6 temper provides the alloy with an ultimate tensile strength of 310 MPa, a tensile yield strength of 276 MPa and an elastic modulus of 70 GPa. Tempering AA6061 is a three-step process: solutionizing, followed by a rapid quench, and finally artificial aging. Solutionizing involves heating the alloy above the solvus line, into the alpha phase, and holding for set amount of time. This process dissolves the strengthening precipitates [65]. Next, quenching preserves the supersaturated solid solution by preventing diffusion and formation of a second phase. Finally, artificial aging allows for the growth of precipitates, which hinder dislocation motion and in turn, increase the strength and hardness of the alloy. In AA6061, these strengthening phases are the b" precipitates, where the finer and more numerous the particles, the more effective they are at increasing the strength of the alloy.

Many studies have been performed on AA6061 as processed through FSW. A loss of hardness and reduction in tensile strength of AA6061 has been reported in similar solid state materials processes such as FSW [99]. A microstructural study by Boonchouytan et al. revealed the Mg_2Si particles necessary for strength recover were uniformly dispersed through the stir zone [100]. Feng et al. observed the build material AA6061 used in their FSW fatigue study exhibited the b" primary strengthening precipitates prior to processing and that post-processing those precipitates dissolved [101]. Efforts to recover post processing strength have shown that full strength recovery of FSW AA6061 is achievable through post weld heat treatment (PWHT) [102] and that solutionizing combined with aging that produced a uniform distribution of b" precipitates [103].

4.1.2 Aluminum Alloy 5083

Aluminum alloy 5083 (AA5083) is a commercially available strain hardened alloy, frequently used in the transportation sector because of its high performance under harsh conditions, providing resistance against chemical and corrosive environments. The main constituent of AA5083 aside from Aluminum (95.6%) is Magnesium (4%) with trace amounts of other elements like Manganese, Chromium, and Copper. AA5083 possesses the highest strength of the aluminum alloys that are not heat-treatable as well as a high fatigue-fracture resistance. The ultimate tensile strength is 317 MPa with a tensile yield strength of 228 MPa and an elastic modulus of 70.3 GPa. Typical applications include marine vessels, rail cars, vehicle bodies and pressure vessels. AA5083 is known for having a high notch-yield ratio and very low Peierls stresses making it an attractive alloy for applications where toughness is key[104], [105].

AA5083 is a strain-hardened alloy. Strain hardening, or work hardening, is a strengthening process where dislocations are formed in the material through plastic deformation[106]. Those dislocations are then forced to move along slip planes until they reach an obstacle that prevents movement. The dislocation continues to flow until it is no longer free to move, often wrapping itself around the obstacle that created the pinning. When this occurs, a new dislocation is formed and the process repeats itself until the dislocations can no longer flow. When movement is impeded, strength is increased. Strain hardening, while increasing strength, allows for a loss in ductility and increases the potential for brittle failure. Tucker et al. [107] evaluated the plasticity, damage, and fracture characteristics of both AA5083 and AA6061 varying the stress states (tension, compression and torsion) and strain rates (monotonic and high rate). Flow stress, damage and fracture were observed to be dependent on the stress state more so than the strain rate.

Huskins et al. [108] sought to determine the mechanical response and strain rate sensitivity as well as explore the strengthening mechanisms in AA5083. Compression tests of varying strain rates (1000-6000s^{-1}) were performed using a Kolsky bar. Uniform deformation was observed for all high strain rate specimens, while non-uniform shearing deformations were observed in many of the monotonic specimens. Strain hardening was observed with increasing strain rates. Dynamic strain aging (DSA) was determined to have occurred as indicated by the evidence of serrated flow and negative strain rate sensitivity of the monotonic compression test. DSA is an interaction between flowing solute atoms and pinned dislocations. In AA5083, stress fields create a clustering of Mg solute atoms around the dislocation core, which generates a drag force and hinders dislocation movement. The applied stress to overcome the interference of the dislocation motion determines the strength of a material. While investigating the strengthening mechanisms, it was determined the Mg remained in a solid solution while Mn formed rod-like precipitates, both solid- and solute-dislocation interactions resulting in significant strengthening. Ultimately, it was determined the dominant strengthening mechanism for AA5083 was due to dislocation sub-domains and for an increase in strength to occur, plastic work and grain size refinement were key.

Numerous studies have been performed on FSW AA5083. Behngagh et al. investigated the microstructural evolution of FSW AA5083-O and observed grain refinement of 70% on average from 10 mm to 3 mm due to DRX [109]. Additionally, Peel et. al. [110] observed the mechanical properties and residual stresses of FSW AA5083 and determined that weld properties obtained from FSW were more dominated by thermal input to the weld than the deformation of the tool and tensile residual stresses were found in both the longitudinal and transverse directions. In another study, Liu et al. performed a study on the influence of FSW on AA5083 where it was determined the strength of the weld is highly dependent on the weld parameters and under optimum operational parameters, a softening occurred that led to a loss of 27% of strength [111]. Torzewski et al. [112] observed the microstructural and low cycle fatigue properties of AA5083 after FSW. Ultrafine grains were observed in the stir zone due to dynamic recrystallization as well as an increase in hardness in the stir zone. When subjected to low cycle fatigue, the FSW AA5083 experienced a 66% reduction in cycles to failure as compared to the base material. Tensile results, however, only experienced a 10% reduction in strength as compared to the base material. Vilaca et al. [113] discovered that the microstructural characteristics and hardness profiles were not affected by tool shoulder geometry. In a study of the fatigue of FSW and friction stir processed AA5083, the primary mode of failure was ductile with micro void coalescence being the dominant failure mechanism [114].

4.2 Methods

4.2.1 Processing

AA6061 AFSD

A B8 AFSD machine produced by Aeroprobe Corp. (now MELD) deposited square, nominally 9.53 mm solid AA6061-T651 (nominally Al, 1.16 wt% Mg, 0.51 wt% Si, 0.27 wt% Cu) feedstock rods fed through a hollow, 38.1 mm diameter, rotating tool with four “teardrop” protrusions on the tool face onto a 6.35 mm thick AA6061-T651 fixed substrate. Four 88.9 mm long consecutive layers were deposited in alternating directions at 1 mm layer heights to construct each build. As illustrated schematically in Figure 3.1, tool rotational speed (ω) varying between 300 to 420 RPM, feed rates (F) ranging from 66 to 122 mm/min, and traversing velocity (V) alternating from 127 to 229 mm/min were applied as a 3-factor approach to produce each build. Fabricated cross-sections from each build were observed for lack of cohesion, voids, and galling, which assessed the success of the build for ensuing evaluation.

Significant challenges exist with highly popular fusion based AM applications for aluminum alloys predominantly regarding the effects of the energy source on aluminums. Aluminums are widely regarded for their preferred corrosion resistance compared to heavier metals due to their rapid formation of oxide films. These films, however, are detrimental in AM as they induce balling, which along with aluminum’s high conductivity and reflectivity, give way to large, uneven melt pools [115].

The selective laser melting process (SLM) provides a potential method to additively manufacture aluminum components with complex geometries and high dimensional resolution. The process fabricates components by selectively melting consecutive layers of extremely fine particles, in a work-bed of powder, via a high-energy laser in an inert atmosphere [27], [116], [117]. However,

the fusion-based, and thus the resulting solid-liquid-solid phase transformation process, presents challenges in terms of precipitation and solidification-related defects [118], [119]. Louvis et al. [27] determined some of these solidification defects are the product of the traditional nature of aluminum oxide films to rapidly produce due to the higher melting point of the films, most commonly observed in conventional cast or welded aluminum products [28], [120]. Uddin et al. [30] suggests that rapid cooling invokes hot tearing due to occur, which significantly reduces the fracture toughness of the produced part. Additionally, the intense thermal gradient produces preferential, columnar grain orientations [20], [121], which was subsequently numerically corroborated [122], [123]. Moreover, traditional β" precipitates degraded to the less beneficial β phase as a result of prolonged heat input [30]. To subjugate some of these complications, elemental composition adjustments are made to base powders alleviate volumetric transformations. 10-wt% additions of Si, AlSi10Mg which more closely resembles common casting alloy A360, has been shown to reduce the solidification range and resists hot tearing effects without a significant loss in ductility [22]. The resulting mechanical performance is promising as the SLM AlSi10Mg compares closely with the cast alloy with a slight increase in ductility thanks to the finer microstructure and Si distribution. However, Kempen et al. [124] notes that samples produced in the build-direction (through direction) fractured prematurely due to cracks that form between layers, which is widely apparent throughout similar literature on fusion-based AM techniques [125]–[127].

Alternative options to thermal-based AM solutions include those in the solid-state processing regime such as cold gas dynamic spraying (CS). Cold spray, for short, employs a pressurized gas to accelerate metallic particles at supersonic velocities to produce enough kinetic energy to super-plastically deform upon impact on a workpiece [128]–[130]. Outside of adiabatic heating, elevated gas temperatures[131], or use of low-power lasers, to assist plastic deformation [132], CS remains solid state; thus, creating an substitute AM avenue for materials affected by phase transformation defects. In AA6061, refined, nanocrystalline grain structures were evident. Specifically, at deformed particle interfaces, dynamic recrystallization (DRX) occurs due to the severe plastic deformation occurring due to the high strain rates upon impact [133], [134]. Rokni et al. [135]–[137] studied various aspects of CS AA6061. The studies observed geometrically dynamic recrystallized grain sizes below 100 nm with indications of high residual stresses and distortion following deposition. An unexpected precipitation result of the process occurred where Mg and Si concentrated, lining grain boundaries. The authors suggested that the high strains induced dislocations and point defects in the form of vacancies, which were then filled by the two alloying elements. Subsequent mechanical testing revealed a considerable increase in UTS and YS at the cost of ductility. These traits were attributed to grain refinement and cold working mechanisms. Post-deposition heat treatment reacquired additional ductility while retaining the strength by precipitating the primary β" phase accompanied by limited grain growth and reduced dislocation density.

AA5083 AFSD

New Solid Rod Feedstock AA5083 AFSD

Despite the heavy use of fusion based welding of Al-Mg alloys [138], similar challenges to that of AA6061 have arisen as a result of fusion based AM processes. Galy et al. [119] classified these issues as gas entrapment and evaporation defects, which are particularly prevalent due to the lower

melting temperature of the primary alloying element, Mg. In Wire-Arc Additive Manufacturing (WAAM), a modified gas metal arc welding (GMAW, also known as MIG welding) apparatus is affixed to a robotic arm driven by machine code to deposit a feed wire in a continuous stream to produce consecutive layers via wire melting [139]. In the as-deposited state, Gu et al. [140] revealed thermally induced grain coarsening and porosity typically resulting from trapped gas and solidification cracking as seen in traditional welding studies [141]. However, Gu et al. could achieve fully dense deposits with recrystallized grains following an interlayer rolling technique that induced a compressive force after each layer was deposited. Wang et al. [142] further attempted to preclude these defects by introducing titanium powder between each layer, which increased recrystallization effects and marginally improved mechanical performance by 10% over standard WAAM AA5083.

As with Al-Mg-Si alloys, use of commercial grade AA5083 in AM is sparse without compositional additives [24]. This fact is noted by Zhou et al. [143] in regards to Laser Powder Bed Fusion (LPBF), which initially exhibited less than 90% density. The study determined this mass loss is a direct result of the vaporization of Mg in the melt pool surface. In SLS/M processes, an attempt to remedy thermal defects was by introducing zirconium as an additive, which is popular in AM of Al-Mg(-Si) systems [33], [144], [145]. By carefully adjusting processing conditions to manage heating effects, Croteau et al. [33] was capable of effectively replacing the vaporized Mg with Zr and retain near 99% density. The resulting deposit relied on Al_3Zr precipitation which not only nucleated refined grains, but also increased tensile strength by 40% to 332 MPa.

AFSD of AA5083 Machine Chips

In order to examine the effect of using reclaimed waste metal chips as feedstock in the AFSD process, metal machined chips were created through dry turning of AA5083-H131 bar stock on a CNC lathe [66]. Additionally, for comparison purposes, AFSD builds were also made using solid bar feedstock taken from the same AA5083-H131 rolled plate. For clarity of discussion in this present work, reference to AFSD processed materials from machine chips and solid bar stock are referred to as AFSD-Recycled and AFSD-Solid Bar, respectively. Figure 4.1 illustrates representative processes for the AFSD process for depositing solid feedstock bars (Figure 4.1a) and waste machine chips (Figure 4.1b). As indicated in Figure 4.1a, AA5083-H131 rolled plate was used to create the solid bar feedstock in a MELD Manufacturing B8 machine, while AA5083-H131 machine chips were fed through an auger feed system and forced through a K2 MELD Manufacturing machine for a separate AFSD build. The AFSD solid bar (AFSD-Solid bar) build was produced with the following parameters: 300 RPM tool rotation speed, 127 in/min traversing speed (along the longitudinal direction), 83 mm/min actuator feed rate, at a layer thickness of 1 mm. The AFSD deposition produced with machine chip waste (AFSD-Recycled) was produced using a proprietary set of processing parameters by MELD manufacturing.

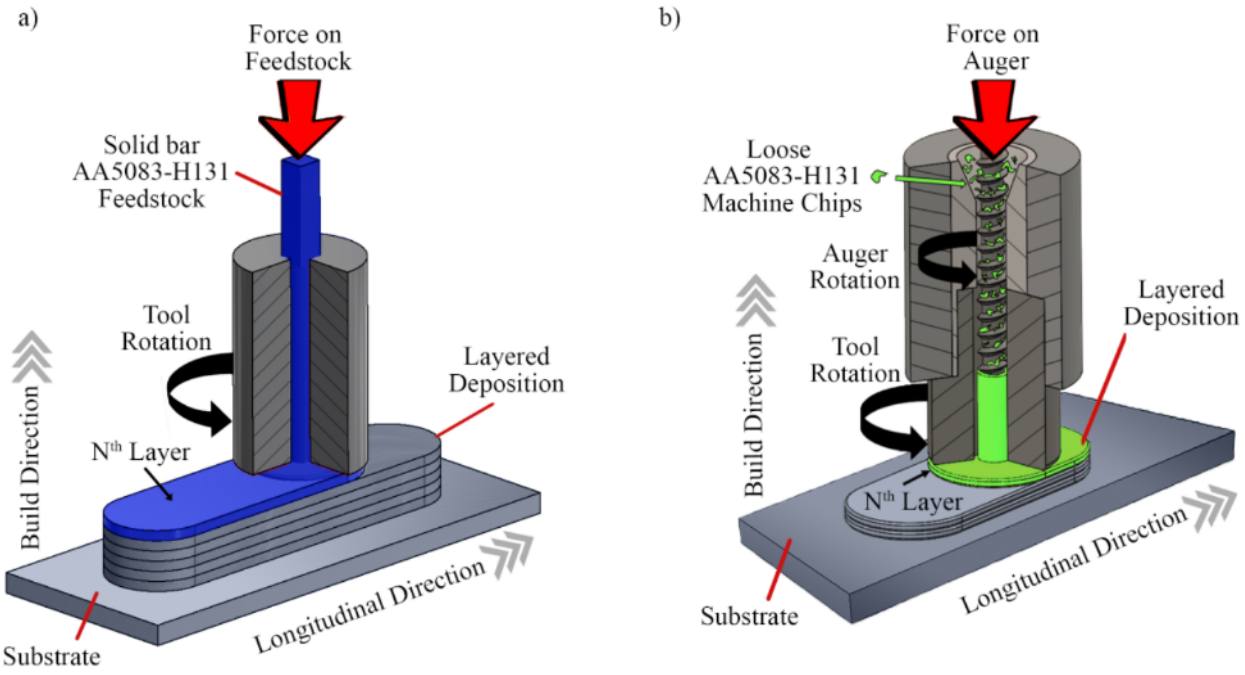

Figure 4.1. Two AFSD processes featuring a) solid bar feedstock made from AA5083-H131 rolled plate and b) feedstock made from loose machine chips cut from AA5083-H131 rolled plate and fed through an auger.

4.2.2 Nano- and Microstructure Characterization

Metallographic evaluation samples were extracted from depositions and feedstock material via high precision cut-off saws or EDMs, and were ground and polished step-wise down to a 3.0 μm diamond suspension. For higher magnification analysis the samples were subject to an additional 1 μm diamond suspension polish followed by vibratory polish with 0.5 μm colloidal silica. A Tescan Lyra FIB-FESEM affixed with an EDAX Hikari Super EBSD camera was employed to perform EBSD grain size analysis, conducted by producing scans complying with ASTM 2627-13 [146]. Subsequently, a FEI Tecnai F-20 TEM imaged nanostructure features and the evolution of precipitates from the feedstock and as-deposited AA6061. Deposited samples for atom probe field evaporation were fabricated by a focused ion beam (FIB) lift-out approach using a FEI Quanta Dual Beam FIB and a Lyra Tescan FIB. The tips were field evaporated in a Cameca Local Electrode Atom Probe (LEAP) 5000XS. The field evaporation process was conducted at 30K (voltage mode). Voltage pulse fraction and frequency was 20% and 200 KHz respectively. The clusters were depicted by 1.3 at.% Mg and 1.2 at.% Si iso-concentration surface.

4.2.3 Mechanical Property Characterization

Microhardness Experiments

For microhardness, successful depositions and feedstock material were ground and polished step-wise down to a 3.0 μm diamond suspension for Vickers hardness measurements. An 18 x 40 microindentation grid on a Struers Durascan at 0.2 kg indented the deposition cross-sections ensuring examination of both the as-deposited AA6061 and transient region between the deposit and substrate per ASTM E384-17 [147].

Residual Stress Experiments

The lattice strain was calculated from the following equation:

$$\varepsilon_i = \frac{d_i}{d_{0_i}} - 1 \qquad (4.1),$$

where ε is the lattice strain, i is one of the three orthogonal directions, which are longitudinal (x), transverse (y) and normal (z) directions, d is the stressed lattice spacing and d_0 is the unstressed lattice spacing.

Hooke's law was applied to calculate the residual stress from the following equation:

$$\sigma_i = \frac{E}{(1+\nu)}\left\{\varepsilon_i + \frac{\nu}{1-2\nu}(\varepsilon_x + \varepsilon_y + \varepsilon_z)\right\} \qquad (4.2),$$

where σ is the residual stress, ε is the lattice strain calculated from equation (4.1), E and ν are the elastic moduli and Poisson's ratio for reflection {3 1 1}, which are 69 GPa and 0.35 respectively adopted from the Reuss modeling scheme [148]. This analysis of residual stress measured from neutron diffraction were successfully adopted in other researches, e.g., AA6061-T6 after friction stir processing [149] and Inconel 625 after laser powder bed fusion [150]

Monotonic Experiments

Quasi-static tensile specimens were machined out of the build excluding the dwell and path reversal sections as an effort to exclusively characterize the overlapping interface, via a wire-EDM using geometry visible in Figure 4.2. Tensile testing was performed via an MTS 647 servo hydraulic load frame in displacement control. All samples used in this study were taken from the same height with respect to the top of the substrate. An MTS 632.29F-30 5 mm extensometer was placed on the specimen around the midpoint of the gage section to measure the induced strain during tensile testing.

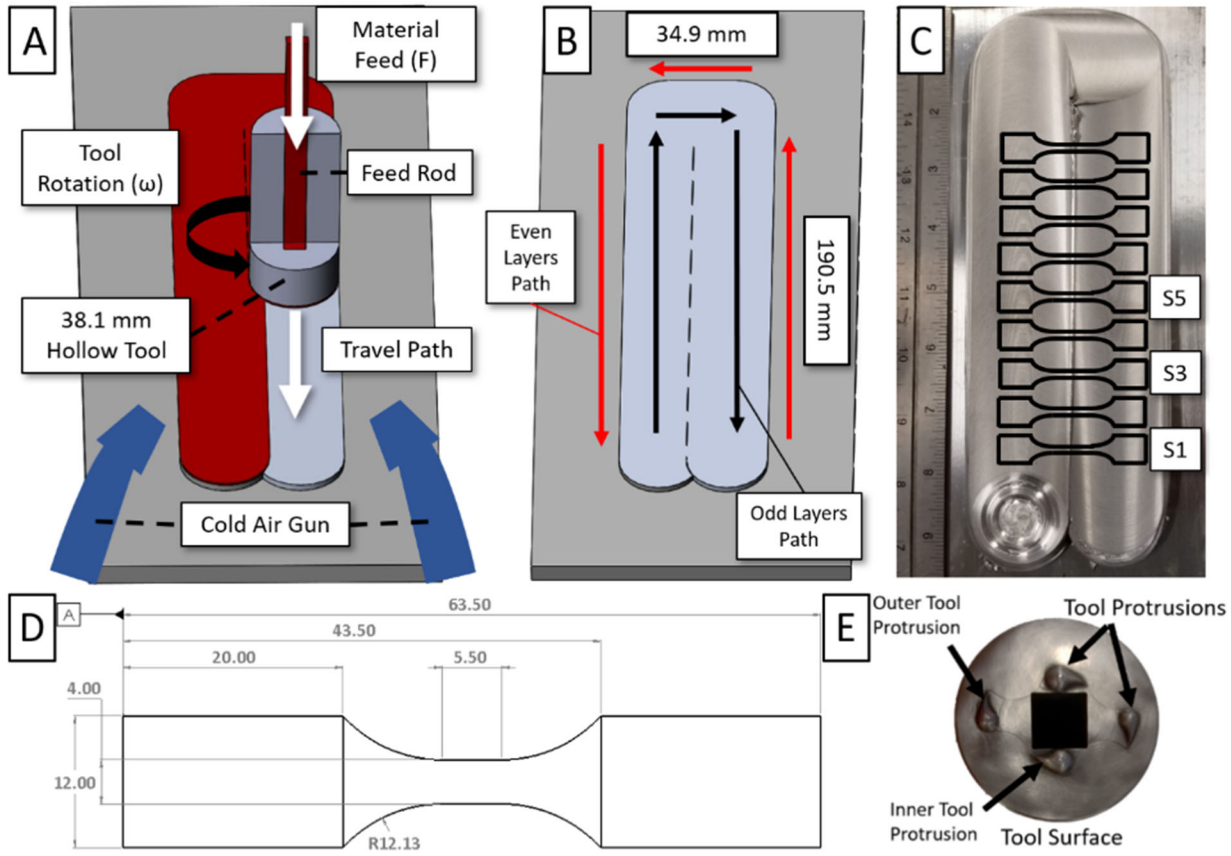

Figure 4.2. (A) Schematic of the AFSD process where a non-consumable tool rotates and traverses along a substrate as a linear actuator extrudes material through the center of the tool. (B) The tool deposition path produced to create an overlapping, parallel raster. Arrows denote the tool path alternating directions after consecutive layers. (C) Image of the final deposit with sample layout depicted schematically. (D) Sample geometry (mm) to determine tensile response. (E) Bottom surface of 38.1 mm AFSD tool containing features.

Fatigue Experiments

Fatigue tests were performed on a 25 kN MTS 307 landmark servo hydraulic load frame. A sub-sized fatigue specimen with a 3.0 mm gage width and 1.5 mm gage thickness was selected for this study. All fatigue specimens were mechanically ground and polished using 1200 grit SiC paper. The fully reversed tests were conducted in load control at five different amplitudes in triplicate and were tested at a frequency 5-30Hz depending on the amplitude.

4.2.4 Modeling and Simulations

AFSD Process Simulations

What makes the SPH method mesh-free is that the set of field equations (conservation equations for a solid body in this case) are solved by interpolation using a kernel, *W(r,h)*. The kernel operates on a set of "*j*" neighbor material points that are within a radius of influence of *h* (commonly called the smoothing length) of the particle of interest, "*i*". Figure 4.3 gives a graphical representation of this concept. Through this method, continuous field equations, or partial differential equations, can be transformed into a set of discrete ordinary differential equations.

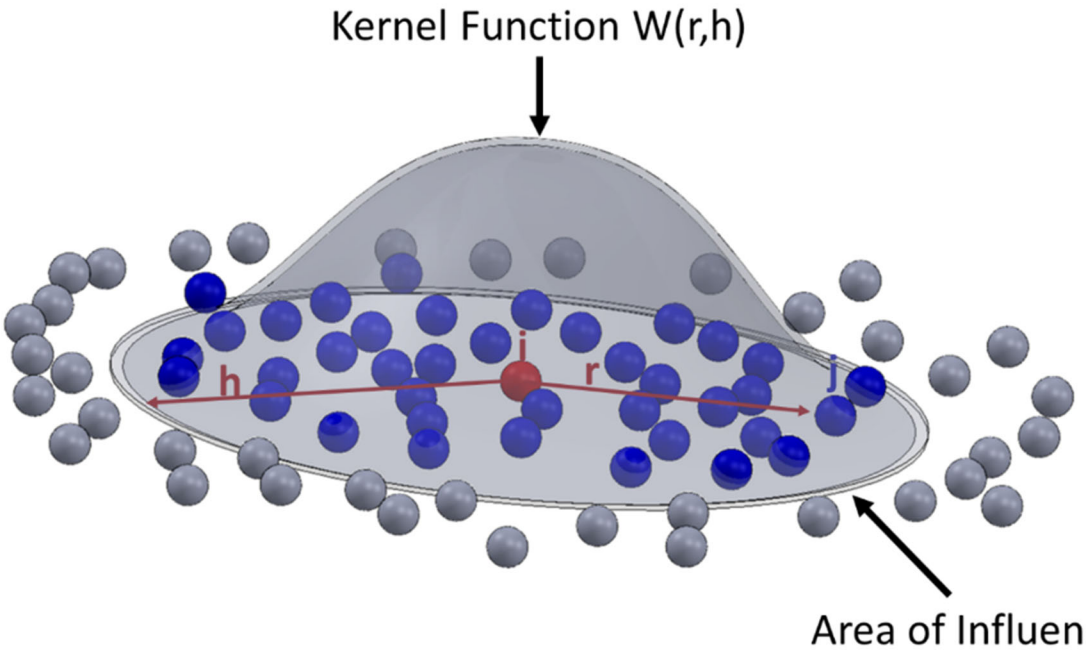

Figure 4.3. Kernel function interpolation in the smoothed particle hydrodynamics (SPH) method

Determining the neighbors list for each material point is a computationally expensive task. In this work, an adaptive cell based search is used as described in Fraser [151]. The entire domain is divided into cubic cells with sides of 2h. The material points are binned into these cells. Then, the neighbors search is performed by cycling over only the neighboring cells. In 3D space, a total of 27 cells are searched, in which the neighbor's information is stored and re-used for material points

with plastic strain increments below a threshold level, which is set to $1.0\text{x}10^{-6}$ in this present work. The adaptive neighbor search effectively reduces the time per calculation step spent on the neighbor search algorithm by over 50%.

Under the SPH formalism, a continuous function can be approximated by an interpolant through the use of a convolution integral:

$$f(\bar{x}) = \int f(\bar{x}')\, W(\bar{x} - \bar{x}', h) d\bar{x}' \tag{4.3}$$

where $\bar{x}$ is the calculation point and $\bar{x}'$ is the set of continuous interpolation locations. The integral equation can then be written for a set of discrete material points as:

$$f({x_i}^{\alpha}) = \sum_{j=1}^{N_i} \frac{m_j}{\rho_j} f({x_j}^{\alpha}) W(r, h) \tag{4.4}$$

In this sense, the value of the field variable at the material point location ${x_i}^{\alpha}$ is evaluated by summing the values at the N_i neighboring points located at ${x_j}^{\alpha}$. Einstein notation convention is used for the rank 1 and greater tensor variables, and as such, there should be no confusion between $\bar{x}$ (written with tensor notation) and x^{α}. The radial distance between points is $r = \left\|{x_{ij}}^{\alpha}\right\| = \left\|{x_i}^{\alpha} - {x_j}^{\alpha}\right\|$. The mass and density of the material point is m_j and ρ_j respectively. Throughout the rest of the text, the smoothing function will be written as:

$$W(r, h) = W(R) = W_{ij} \tag{4.5}$$

A change of variables had been introduced to normalize the smoothing function such that $R = \frac{r}{h} = \left\|{x_{ij}}^{\alpha}\right\|/h$. The gradient of the smoothing function with respect to the i^{th} material point can be written as:

$$\nabla_i W_{ij} = \frac{\partial W_{ij}}{\partial {x_i}^{\alpha}} = \frac{dW(R)}{dR} \frac{{x_{ij}}^{\alpha}}{h\left\|{x_{ij}}^{\alpha}\right\|} \tag{4.7}$$

The compactly supported smoothing function used in this work is the hyperbolic spline developed by Yang et al. [152]:

$$W_{ij} = \alpha_d \begin{cases} R^3 - 6R + 6, & 0 \le R < 1 \\ (2 - R)^3, & 1 \le R < 2 \\ 0, & R \ge 2 \end{cases} \tag{4.8}$$

In 2D simulations, the value of α_d is $1/3\pi h^2$ and in 3D is $15/62\pi h^3$. This smoothing function has been shown to improve the solution stability when strong compressive stress fields are present in the material, which is the case in AFSD. The gradient of a vector field at a material point can be discretized using the SPH approach:

$$\nabla f(x_i{}^{\alpha}) = \sum_{j=1}^{N_i} \frac{m_j}{\rho_j} f(x_j{}^{\alpha}) \nabla_i W_{ij} \tag{4.9}$$

The aforementioned equations form the basic building blocks of the SPH method and will be used to discretize the set of continuum mechanics equations. By using a continuum material strength approach, the elastic and plastic strain fields in the material can be calculated. This allows for an accurate determination of internal and surface defects as well as residual stresses. The set of field equations to be solved correspond to conservation of mass, conservation of momentum, velocity, rate of enthalpy change, total strain rate, spin rate, stress rate, and lastly a linear equation of state. These form a set of partial differential equations in the Lagrangian reference frame:

$$\frac{d\rho}{dt} + \nabla \cdot \rho \bar{v} - \rho \beta_{expand} \dot{T} = 0 \tag{4.10}$$

$$\frac{d\bar{v}}{dt} = \frac{1}{\rho} \nabla \cdot \bar{\bar{\sigma}} \tag{4.11}$$

$$\bar{v} = \frac{d\bar{x}}{dt} \tag{4.12}$$

$$\frac{\partial H}{\partial t} = \frac{1}{\rho} (\nabla \cdot (k \nabla T) + \dot{q}) \tag{4.13}$$

$$\dot{\bar{\bar{\varepsilon}}} = \frac{1}{2} (\nabla \otimes \bar{v} + (\nabla \otimes \bar{v})^T) \tag{4.14}$$

$$\bar{\bar{\Omega}} = \frac{1}{2} (\nabla \otimes \bar{\boldsymbol{v}} - (\nabla \otimes \bar{v})^T) \tag{4.15}$$

$$\dot{\bar{\bar{S}}} = 2G \left(\dot{\bar{\bar{\varepsilon}}} - \frac{1}{3} tr\left(\dot{\bar{\bar{\varepsilon}}}\right) \bar{\bar{\delta}} \right) + \bar{\bar{S}} \bar{\bar{\Omega}}^T + \bar{\bar{\Omega}} \bar{\bar{S}} \tag{4.16}$$

$$p = c^2 (\rho - \rho_0) \tag{4.17}$$

where t is time, β_{expand} is the volumetric coefficient of thermal expansion, $\dot{T}$ is temperature change rate, $\bar{\bar{\sigma}}$ is the total (Cauchy) stress tensor, H is enthalpy, T is temperature, $\dot{q}$ is a heat source term that is due to plastic and friction work, $\dot{\bar{\bar{\varepsilon}}}$ is the strain rate tensor, $\bar{\bar{\Omega}}$ is the spin rate tensor, $\dot{\bar{\bar{S}}}$ is the deviatoric stress rate, $\bar{\bar{\delta}}$ is the Kronecker delta, p is pressure, c is speed of sound, and ρ_0 is the reference state material density. The thermal conductivity, k, is a function of temperature of the form as taken from Mills [153]:

$$k = k_0 + k_1 T + k_2 T^2 + k_3 T^3 \tag{4.18}$$

The constants in Eq. 4.18 are $k_0 = 167\ [W/\,°C]$, $k_1 = 0.084\ [W/m\,°C^2]$, $k_2 = -4.14 \times 10^{-4}\ [W/m\,°C^3]$, and $k_3 = 3.13 \times 10^{-7}\ [W/m\,°C^3]$. Temperature measurements obtained during the AFSD process have shown that the temperature at the tool interface is typically very

close to the solidus, and in many cases we have observed evidence of a local layer of aluminum that has reached melting temperatures. This is why the rate of change of enthalpy is calculated instead of the commonly used heat diffusion equation. An energy based temperature law is used based on Valencia and Quested [154] and Tarwidi [155] that takes the form:

$$T = \begin{cases} T_m + \dfrac{H}{C_p}, & H < 0 \\ T_m, & 0 < H < L \\ T_m + \dfrac{H - L}{C_p}, & H \geq L \end{cases} \tag{4.19}$$

In Eq. 4.19, T_m is the melting temperature and L is the latent heat for aluminum and is considered to be 380 kJ/kg in this work. C_p is the heat capacity which is itself a function of temperature of the form taken from Mills [153]:

$$C_p = \begin{cases} C_{p0} + C_{p1}T + C_{p2}T^2, & T \leq T_m \\ 1120\ [J/kg\ K], & T > T_m \end{cases} \tag{4.20}$$

The constants in Eq. 4.20 are $C_{p0} = 896\ [J/kg\ °C]$, $C_{p1} = 0.145\ [J/kg\ °C^2]$, $C_{p2} = 1.18 \times 10^{-3}\ [J/kg\ °C^3]$. L is the latent heat of fusion of the aluminum alloy, which is 380 kJ/kg based on Valencia and Quested [154] for the alloy used in this work. Using Eq. 4.13 along with Eq. 4.19 provides a simple and efficient means to account for the energy associated with melting.

By applying the meshfree discretization equations described in Eq. 4.5 to Eq. 4.9, the set of continuum equations (Eq. 4.10 to Eq. 4.15) can be written for the i^{th} material point as:

$$\frac{d\rho_i}{dt} = \rho_i \sum_{j=1}^{N_i} \frac{m_j}{\rho_j} {v_{ij}}^{\alpha} \frac{\partial W_{ij}}{\partial {x_i}^{\alpha}} + \rho_i \beta_{expand} \dot{T}_i \tag{4.21}$$

$$\frac{d{v_i}^{\alpha}}{dt} = \sum_{j=1}^{N_i} m_j \left(\frac{{\sigma_i}^{\alpha\beta}}{{\rho_i}^2} + \frac{{\sigma_j}^{\alpha\beta}}{{\rho_j}^2} \right) \frac{\partial W_{ij}}{\partial {x_i}^{\beta}} \tag{4.22}$$

$${v_i}^{\alpha} = \frac{d{x_i}^{\alpha}}{dt} = {v_i}^{\alpha} + \tilde{v}_i^{\alpha} = {v_i}^{\alpha} + \varepsilon_{XSPH} \sum_{j=1}^{N_i} \frac{m_j}{\rho_{ij}} {v_{ji}}^{\alpha} W_{ij} \tag{4.23}$$

$$\frac{dH_i}{dt} = \frac{1}{\rho_i} \left[\sum_{j=1}^{N_i} \frac{m_j}{\rho_j} \frac{4k_i k_j}{k_i + k_j} \frac{(T_i - T_j)}{|x_{ij}|^2} {x_{ij}}^{\alpha} \frac{\partial W_{ij}}{\partial {x_i}^{\alpha}} + \dot{q}_i \right] \tag{4.24}$$

$$\dot{\varepsilon}_i{}^{\alpha\beta} = \frac{1}{2}\sum_{j=1}^{N_i}\left(\frac{m_j}{\rho_j}v_{ji}{}^{\alpha}\frac{\partial W_{ij}}{\partial x_i{}^{\beta}} + \frac{m_j}{\rho_j}v_{ji}{}^{\beta}\frac{\partial W_{ij}}{\partial x_i{}^{\alpha}}\right) \quad 4.25$$

$$\Omega_i{}^{\alpha\beta} = \frac{1}{2}\sum_{j=1}^{N_i}\left(\frac{m_j}{\rho_j}v_{ji}{}^{\alpha}\frac{\partial W_{ij}}{\partial x_i{}^{\beta}} - \frac{m_j}{\rho_j}v_{ji}{}^{\beta}\frac{\partial W_{ij}}{\partial x_i{}^{\alpha}}\right) \quad 4.26$$

The discrete versions of Eq. 4.21 to Eq. 4.26 do not require SPH interpolation, and as such are identical in continuum and discrete form. A filtered velocity, $\widetilde{v_i}^{\alpha}$, is introduced in Eq. 4.23 due to the XSPH approach from Monaghan [91], which has been shown to improve the stability of SPH simulation. The XSPH constant, ε_{XSPH}, can take a value between 0 and 0.5. In this work, $\varepsilon_{XSPH} = 0.01$ is chosen. This value has been found to improve the solution stability without introducing any noticeable dissipation. The velocity difference is $v_{ji}{}^{\alpha} = v_j{}^{\alpha} - v_i{}^{\alpha}$, and the average density is $\rho_{ij} = 0.5(\rho_i + \rho_j)$.

SPH has a known instability when the stresses in the material are primarily tensile. A number of authors have worked on different approaches to alleviate this problem. Monaghan [156] as well as Gray et al. [157] proposed an artificial stress approach that is able to suppress the tensile instability to a certain extent. In the case of small to medium levels of plastic deformation, the Total Lagrangian (TL-SPH) approach seen in Vignjevic et al. [158] is a suitable solution. However, under large plastic deformation with material advection (as is the case for AFSD), the TL-SPH method will break down. An interesting approach is the delta-plus method of Sun et al. [159]. This approach uses a material point shifting algorithm that can remove the tensile instability.

An approach similar to delta-plus method has been used in this work. We start by determining which material points are on the surface of each body, or part. The first step is to calculate the center of mass, $x_{COM_i}{}^{\alpha}$, of each neighbor cluster:

$$x_{COM_i}{}^{\alpha} = \frac{1}{M}\sum_{j=1,\, Part_j \neq Part_i}^{N_i} m_j x_{ij}{}^{\alpha} \quad 4.27$$

The $Part_j \neq Part_i$ statement makes sure that the i^{th} and j^{th} points are not in the same body, which will be important for the surface normal vectors. The total mass of the neighbor cluster is M. Next, a pre-selection of possible surface points is made based on:

$$Surface_{list} = \begin{cases} 1, & \left\|\bar{x}_{COM_i}\right\| \geq 0.05h_i \; and \; N_i \leq 20 \\ 0, & Otherwise \end{cases} \quad 4.28$$

The $\left\|x_{COM_i}\right\| \geq 0.05h_i$ conditional statement ensures that the center of mass of the cluster is shifted by at least 5% from the i^{th} material point position. The $N_i \leq 20$ statement ensures that the number of neighbors for that point are less than or equal to 20. These two conditions are chosen to provide a preselection of potential surface points that is not overly restrictive to make sure points

are not missed in sharp angle corners. Then, a truncated conical area with a cone angle of 40° and a height of $2h_i$ is scanned similar to the approach of Marrone et al. [160]. If another point is found in this cone area, then the point is removed from the surface list. This method is less computationally expensive since the eigenvalues of the renormalization matrix are not required. Furthermore, this approach is better suited for the GPU since finding the eigenvalues of a matrix is difficult to run in parallel.

With the surface list in hand, the next step is to perform the shifting algorithm. Each timestep, the material points that do not belong to the free surface are shifted slightly by $\bar{\delta}_{shift}$ from their pre-shifted location, $\bar{x}_{pre-shift}$. Our implementation is based on the work of Oger et al. [161], with some slight modifications:

$$\bar{x}_i = \bar{x}_{pre-shift} + \bar{\delta}_{shift} \tag{4.29}$$

$$\bar{\delta}_x = \varphi_{shift}\|v_i\|2h_{ij}dt\sum_{j=1}^{N_i} m_j \nabla_i W_{Lucy} \tag{4.30}$$

$$h_{ij} = 0.5\left(h_i + h_j\right) \tag{4.31}$$

$$\nabla_i W_{Lucy} = \frac{105}{16\pi {h_{ij}}^3}\begin{cases} -\left(\frac{12\bar{x}_{ij}}{h_{ij}\|\bar{x}_{ij}\|}\right) R(R-1)^2, & 0 \le R < 1 \\ 0, & R \ge 1 \end{cases} \tag{4.32}$$

One of the main differences with this approach is that the Lucy kernel [90] is compactly supported to $1.0R$ as opposed to $2.0R$ for typical kernels. This helps to prevent the solid body from expanding when the shifting algorithm is used, which is a common problem with other shifting approaches that use a $2R$ support radius.

Material Model

In order to simulate the AFSD process, a material law that accounts for flow stress change at different temperatures and plastic strain is needed. In this present work, the material model developed by Fraser et al. [93] is used, where this model provides an improved flow stress prediction for AA6061-T6 at high temperature and plastic strain levels compared to other commonly used material models such as Johnson–Cook (JC) [162], or more computationally intensive material models such as in McCullough et al. [163], Allison et al. [164], [165], Mason et al. [166]. The flow stress, σ_y, is predicted from:

$$\sigma_y(\varepsilon^p, \dot{\varepsilon}, T^*) = H(\varepsilon^p)\Lambda(\dot{\varepsilon}, T^*)\Theta(T^*) \tag{4.33}$$

which is a multiplicative combination of strain hardening, $H_{FKS}(\varepsilon^p)$; thermal softening, $\Theta(T^*)$; and strain rate stiffening, $\Lambda(\dot{\varepsilon}, T^*)$, of the form:

$$H_{FKS}(\varepsilon^p) = a_1 + a_2 tan^{-1}(a_3\varepsilon^p) \tag{4.34}$$

$$\Lambda(\dot{\varepsilon}, T^*) = 1 + \left[b_1 {T^*}^{b_2}\right]\left[b_3 ln\left(\frac{\dot{\varepsilon}}{\dot{\varepsilon}_0}\right)\right] \tag{4.35}$$

$$\Theta(T^*) = 1 - \frac{1}{(1 + e^{-c_1 T^*})^{\frac{1}{c_2}}} \quad 4.36$$

$$T^* = \frac{T - T_{melt}}{T_{melt} - T_{room}} \quad 4.37$$

The FKS material model introduced by Fraser et al. [93] is accurate for the range of plastic strain that is typically observed in FSW and AFSD processes. The flow stress as a function of plastic strain and temperature is shown in Figure 4.4a and as a function of strain rate and temperature in Figure 4.4b. Notice that the flow stress saturates at high plastic strain, this is found to be a critical feature for these processes. Flow stress saturation refers to the material behavior where, after initial strain hardening at low plastic strain, the flow stress plateaus after experiencing large plastic strain. Most constitutive models do not account for this behavior, and so are only valid for low plastic strain. Plasticity is accounted for in the simulation code by using the radial return algorithm. The plastic strain increment is found by taking a Taylor series expansion from the current time step. This leads to an efficient non-iterative plasticity scheme. The material parameters for AA6061-T6 are provided in Table 4.1. The parameters were determined in Fraser [167] by fitting compression stress-strain data to the FKS constitutive model.

Table 4.1 - FKS material model constants

Constant	Value	Units
a_1	277	MPa
a_2	71	MPa
a_3	32	-
b_1	1.7	-
b_2	2.4	-
b_3	0.1	-
c_1	4.86	-
c_2	0.176	-

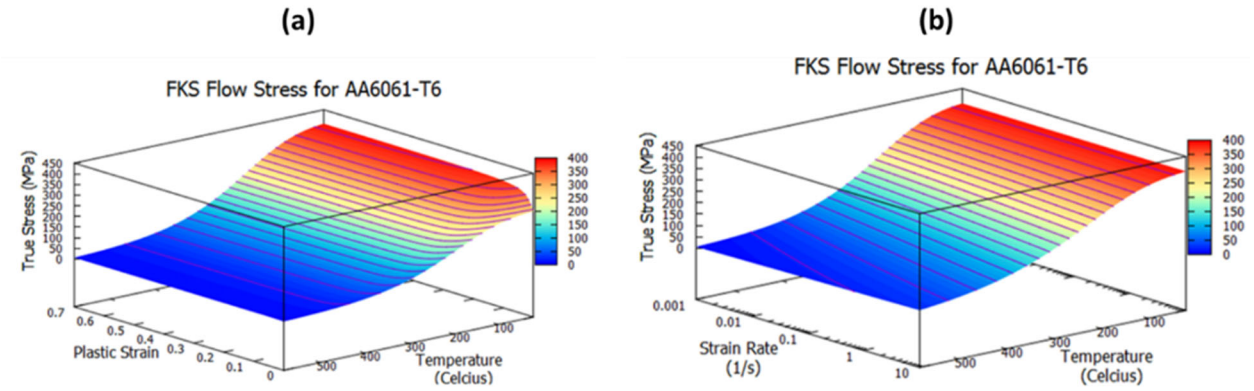

Figure 4.4. Flow stress model for AA6061-T6: (a) as a function of plastic strain and temperature; and (b) as a function of strain rate and temperature.

Thermal-mechanical Joining Contact

In order to suitably simulate the solid state additive manufacturing process, a joining algorithm is needed. The method needs to account for multi-body contact including friction prior to joining. At this point, only compressive stresses can develop at the interface, thus allowing the bodies to separate but not penetrate. Then once the conditions for joining have been met, the bodies must be treated as a continuum, and as such permitting shear, tension, and compression at the interface.

Before the bodies are joined, contact is treated through a penalty approach. First a list of potential contact pairs are established and stored in an array called *NeibContact*. Next, a surface normal vector is calculated by normalizing $\bar{x}_{COM}$ (which was found using Eq. 4.38):

$$\hat{n}_i = \begin{cases} \dfrac{\bar{x}_{COM_i}}{\left\|\bar{x}_{COM_i}\right\|}, & Surface_{list} = 1 \\ 0, & Otherwise \end{cases} \tag{4.38}$$

Then, the i^{th} material point's surface normal vector is smoothed out by taking the average of all the surface normals of the neighboring points, $\hat{n}_{i_s}$, that are also in the surface list.

$$\hat{n}_{i_s} = \frac{1}{N_s}\sum_{j=1}^{N_s} \hat{n}_j \tag{4.39}$$

where N_s is the total number of surface neighbors (included the i^{th} point as well). This surface normal smoothing is important to the success of the joining contact algorithm. The penalty contact force is given by:

$$\bar{F}_N = \left(K_{ij}\delta_{pen} + C_{ij}\dot{\delta}_{pen}\right)\hat{n}_{i_s} \tag{4.40}$$

$$K_{ij} = \frac{m_i m_j}{m_i + m_j}\left(\frac{PFAC}{dt^2}\right) \tag{4.41}$$

$$C_{ij} = DFAC\left(m_i + m_j\right)\sqrt{\frac{K_{ij}\left(m_i + m_j\right)}{m_i m_j}} \tag{4.42}$$

where δ_{pen} is the penetration distance, $\dot{\delta}_{pen}$ is the penetration rate, and dt is the timestep size that is chosen based on stability. $PFAC$ and $DFAC$ are the penalty and damping factor respectively and are both chosen to be 0.1 in this work.

If the material point energy state surpasses a predefined level, it is then considered to be joined and the interaction between the two parts occurs through the SPH kernel. That is to say that the parts are considered to be a continuum, and can develop compression, tension, and shear stresses. The joining criteria is such that:

$$Joined_i = \begin{cases} 1, & T_i \geq T_{join} \wedge \varepsilon^p \geq PS_{join} \\ 0, & Otherwise \end{cases} \tag{4.43}$$

This joining criteria is based on the authors experience with the friction stir welding process. In this study, $T_{join} = 400°C$ and $PS_{join} = 0.01$. Although this criteria is rudimentary in nature it captures the overall physics of the actual material joining. Further research is warranted to determine more precisely the joining energy criteria.

Monotonic Modeling

Microstructure-Sensitive Fatigue Model

The microstructure-sensitive fatigue (MSF) model, proposed by McDowell et al. [168] for automotive cast aluminum alloy and subsequently modified to account for mechanisms in other materials [169], [170] and materials processing methods [171], [172] including fusion-based AM [173], [174] was used to correlate the experimental fatigue results and to aid in elucidating the effect of microstructure evolution on fatigue mechanisms due to the AFSD process. The model aims to take into account various microstructural features, such as particle size, shape, nearest neighbor distance, grain size, crystallographic texture, etc. when modelling the fatigue behavior of a material. The model approach discretizes established stages of fatigue failure in distinct modeling stages. Namely, (1) crack incubation, (2) microstructurally small crack (MSC) growth and physically small crack (PSC) growth, and (3) long crack (LC) growth. The incubation stage involves the portion of the fatigue life spent developing a crack from a nucleation site, such as an inclusion or void. The microstructurally small crack growth refers to the portion of the life spent with a crack with a length on the order of microstructural features such as inclusions or small grains within the material. After the crack has grown to physically significant size, somewhat larger than microstructural features, but not yet long enough to be characterized as a long crack, as in Paris law fatigue crack growth, it is in the PSC growth stage. Once the crack has reached a size applicable to the fatigue crack growth (FCG) stage, which is generally multiple grain lengths long [169], the long crack growth portion has been reached. The LC portion of the model uses linear elastic fracture mechanics to model that portion of the life.

The total life of a component can then be expressed as a sum of the length of life spent in each stage of fatigue:

$$N_{total} = N_{inc} + N_{MSC/PSC} + N_{LC} \tag{4.46}$$

where N_{inc} represents the number of cycles in the incubation stage, $N_{MSC/PSC}$ represents the number of cycles spent in the combined MSC growth and PSC growth stages, and N_{LC} represents the number of cycles spent in the LC growth stage until failure.

The crack incubation contribution to fatigue life, N_{inc} from Equation 4.46 is found using a modified Coffin-Manson fit that takes microscale parameters into consideration to characterize the nucleation of a microscopic crack from a microscopic notch. The modified Coffin-Manson expression is given as:

$$C_{inc}N_{inc}^{\alpha} = \frac{\Delta\gamma_{max}^{p*}}{2} = \psi\bar{Y}[\varepsilon_a - \varepsilon_{th}]^q \tag{4.47}$$

where α and C_{inc} are the respective exponent and linear coefficients and the nonlocal plastic shear strain around an inclusion is represented by the remote applied strain amplitude (ε_a), the microplasticity strain threshold (ε_{th}), and ψ and ¥, which will be explained further in detail. ¥ is a model parameter that relates the development of local plastic shear strain from the applied remote strain amplitude expressed as the following:

$$\bar{Y} = Y = y_1 + (1 + R) * y_2 \quad 4.48$$

where R is the load ratio and y_1 and y_2 are model constants. When the localized plastic region around the inclusion reaches a certain size the $\bar{Y}$ is modified to include geometric effects by a parameter. More information on that process can be found in a prior study on AA6061 [37]. The parameter ψ relates observed microstructural features to the incubation behavior and is expressed as:

$$\psi = \left(\frac{(MPS^2)}{(NND)(GS)}\right)^{\lambda} \quad 4.49$$

where MPS is the maximum particle size, NND is the nearest neighbor distance, GS is the grain size, and λ is a sensitivity parameter.

The microstructurally/physically small crack growth portion of the fatigue life from Equation 4.46 is determined using a crack tip displacement crack growth model. The MSC/PSC contribution can be determined from the following expression:

$$\left(\frac{da}{dN}\right)_{MSC} = \chi(\Delta CTD - \Delta CTD_{th}), \qquad a_i = 0.625D \quad 4.50$$

where da/dN is the crack growth rate, initial crack length is 62.5% of the maximum particle size, χ is a constant related to the crack propagation rate, which typically falls between 0.33 and 0.5. ΔCTD_{th} is the threshold value for crack tip displacement and has been reported to be $2.85*10^{-4}$ μm for pure FCC aluminum [169]. ΔCTD is a parameter of crack tip displacement is given by the following equation:

$$\Delta CTD = C_{II}\psi\left(\frac{GS}{GS_0}\right)^{\omega}\left(\frac{U\Delta\hat{\sigma}}{S_{ut}}\right)^{\zeta} a_i + C_I\psi\left(\frac{GS}{GS_0}\right)^{\omega}\left(\frac{\Delta\gamma^p_{max}}{2}\right)^2 \quad 4.51$$

where C_I and C_{II} are material parameters for microstructure on MSC and PSC growth in low cycle and high cycle regimes respectively. $\Delta\hat{\sigma}$ is a parameter for load path and amplitude of multiaxial fatigue, which in this study is the uniaxial loading range. The parameter U is a loading ratio parameter given by U = 1/(1-R), GS is the grain size, GS_0 is the reference grain size, and ω is a material constant related to sensitivity of small crack growth to grain size.

5. RESULTS AND DISCUSSION

5.1 New Solid Bar Feedstock Processing Parameter Influence on As-Deposited AFSD AA6061 Nano- and Microstructure and Properties

This research provides the first description of the process parameter relationship to the microstructure/nanostructure and mechanical properties of Aluminum Alloy 6061 AFSD deposits. The solid-state, additive friction stir deposition, process provides a new path for coating, joining, and additively manufacturing materials with high deposition rates (20-30 lbs/hr) while avoiding liquid-solid phase transformation defects. As-deposited samples revealed the AFSD process reduced the average grain size by an order of magnitude over a range of processing conditions. Transmission Electron Microscopy (TEM) and Atom Probe Tomography (APT) analysis established β" precipitates were dissolved by the AFSD process and re-precipitated as Mg-Si solute clusters.

5.1.1 Material and methods

Additive Friction Stir Deposition (AFSD), commercially known as MELD, is a solid-state, AM process that benefits from similar fundamental physics occurring in friction stir welding/processing (FSW/P) [37], [39], [40]. The solid-state nature of the AFSD process avoids deleterious effects that occur in fusion-based AM processes such as hot cracking, porosity, and columnar grain structures without the need for secondary densification post processing. As illustrated schematically in Figure 5.1(A-C), robust, metallurgical bonding is achieved between deposited layers by forcing a metallic powder or solid feedstock through a rotating, non-consumable cylindrical tool. The tool, featuring 4 teardrop projections on the interaction face evident in Figure 5.1(E), generates frictional heat and pressure inducing high-shear, severe plastic deformation of the solid feedstock onto a substrate and subsequent layers. Additionally, the severe plastic deformation generated by the tool and material interaction instigates dynamic recrystallization (DRX) in the as-deposited material, which yields a refined grain microstructure [37], [39], [40]. At the end of a predetermined path, the spindle raises by a user-defined layer height and traverses along the build route to deposit consecutive layers (Figure 5.1 (C)), producing a near-net shaped component (Figure 5.1(D)).

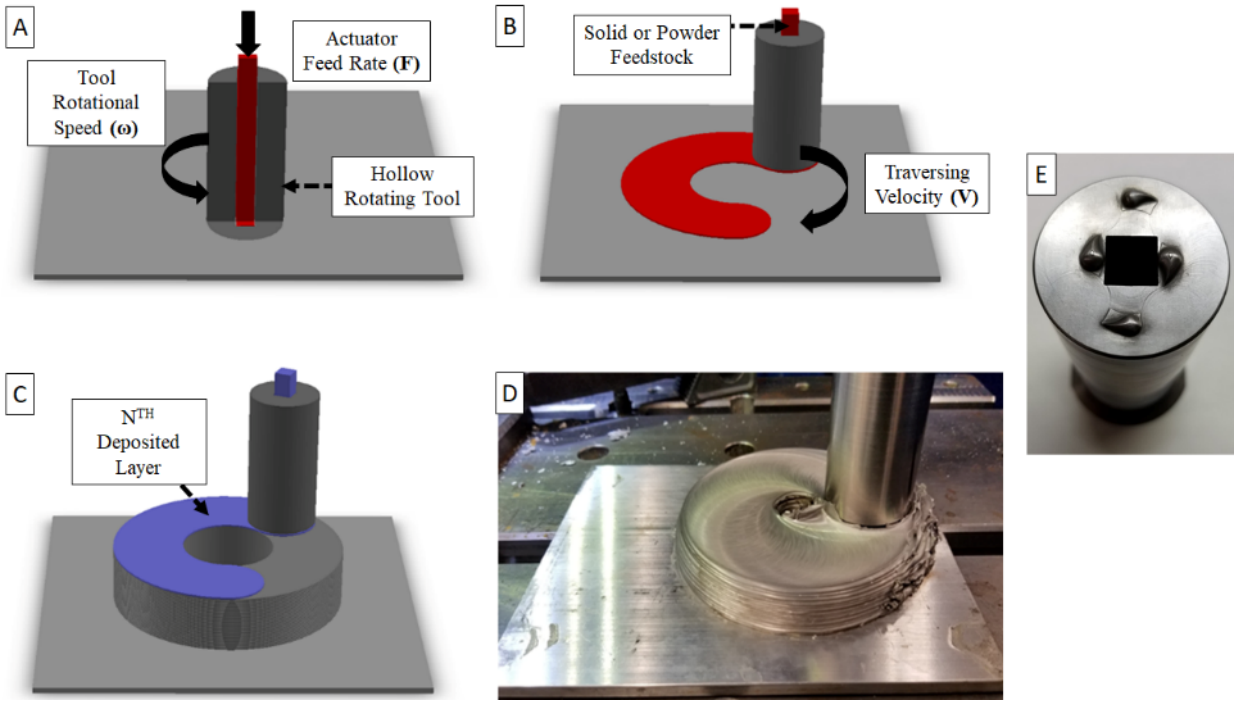

Figure 5.1 (A) Cross section schematic of the beginning of the AFSD process where the tool plunges into a substrate while spinning at a predetermined rotational speed. (B) The tool is then raised to the layer height during which time an actuator drives a solid, or powder, feedstock through the tool as the tool traverses across the substrate, producing a layer. (C) At the completion of a layer, the spindle raises to the next layer height and repeats the process to build consecutive layers. (D) Photograph of the actual AFSD process applied to AA6061. (E) Image of the teardrop featured tool.

This is the first study to quantify the integral process-microstructure-property relationships of as-deposited AA6061 using the AFSD process. Microhardness profiles were taken from the cross-section of builds to produce relationships between mechanical characteristics and machine parameters. Resulting average hardness values were plotted against the processing window and used to determine comparative samples for microstructural analysis. Electron backscatter diffraction (EBSD) and transmission electron microscopy (TEM) was conducted to characterize the microstructural evolution of depositions. This study provides a succinct, multiscale characterization of as-deposited AFSD AA6061 to expound the effect of the high-shear solid-state AM process.

To elucidate the fundamentals of the AFSD AM process, an investigation on the influence of varying processing parameters on the deposited material microstructure is necessary. Prominent processing parameters controlling quality of parts produced include spindle rotational speed (ω), deposition feed rate (F), and traversing velocity (V) of the tool. Significant work has been conducted by the FSW/P community establishing similar effects [175]–[179]. By understanding the relationship between process parameters and deformation mechanisms for AFSD, correlations can be made to effectively and efficiently deposit alternative materials at varying rates without diminishing part quality.

In the assessment of the processing parameters on the resulting structure-property relations, A B8 AFSD (Aeroprobe Corp. now MELD) machine deposited square, nominally 9.53 mm solid AA6061-T651 (nominally Al, 1.16 wt% Mg, 0.51 wt% Si, 0.27 wt% Cu) feedstock rods fed through a hollow, 38.1 mm diameter, rotating tool with four "teardrop" protrusions on the tool face onto a 6.35 mm thick AA6061-T651 fixed substrate. Four 88.9 mm long consecutive layers were deposited in alternating directions at 1 mm layer heights to construct each build. As illustrated schematically in Figure 5.1, tool rotational speed (ω) varying between 300 to 420 RPM, feed rates (F) ranging from 66 to 122 mm/min, and traversing velocity (V) alternating from 127 to 229 mm/min were applied as a 3-factor approach to produce each build. Fabricated cross-sections from each build were observed for lack of cohesion, voids, and galling, which assessed the success of the build for ensuing evaluation.

5.1.2 Results and Discussion

Figure 5.2 shows the correlation between varying process parameters and the average Vickers hardness contour plots obtained from the respective cross-sections. Specifically, in Figure 5.2(A), higher average hardness values are observed as rotation speed and traversing velocity increase. Figure 5.2(B) illustrates the processing boundaries between the actuator deposition feed rate (F) and traversing velocities (V). Builds that were manufactured with low material feed rates and high traversing velocities generated significant galling and voids as a result of insufficient material flow. Surface defects observed are associated with cold processing analogous with friction stir welding where insufficient material flow prevents consolidation and lack of fill on the advancing region of the tool path [180]. Conversely, operating with high material feed rates and lower traversing velocities yields reduced deposition efficiency as characterized by substantial material pushed externally from under the tool face as flash. Figure 5.2(C) displays the Vickers hardness contour plot of the deposit produced by the lowest operating parameters (ω = 300 RPM, V = 127 mm/min, 2.0 lb/hr) and Figure 5.2(D) illustrates the contour plot of the deposit operating at the highest parameters in the study (ω = 300 RPM, V = 228.6 mm/min). Figure 5.2(C) and Figure 5.2(D) represent specific samples further examined to understand the disparity seen in Figure 5.2(A). The highest

hardness exhibited in the build composed of the lowest processing parameters is observed in the final layers of the deposition measured at 73.6 ±3.2 Hv which is similar to hardness results observed in FSW stir zones [181]–[183]. The protrusions on the tool induce material flow beyond the freshly deposited layers, resulting in less definitive interfaces between the consecutive layers. This data is counter to results from Rivera et al. [40] due to the change from the featureless tool utilized in that study. Maximum hardness in the build with the highest investigated parameters was found to be 91.0 ±7.0 Hv; however, the deviation of hardness values in the cross section is significantly higher than that of the other examined deposit. The less consistent nature of the hardness data in this deposit infers additional process optimization would likely improve mechanical coherency. Nevertheless, maximum hardness found in the cross sections is 20% lower than that of the feedstock at 112 ±2.65 Hv suggesting dynamic recovery (DRV) or precipitate evolution is occurring from the intrinsic high shear mechanisms involved in the process [184], and is discussed in the proceeding sections.

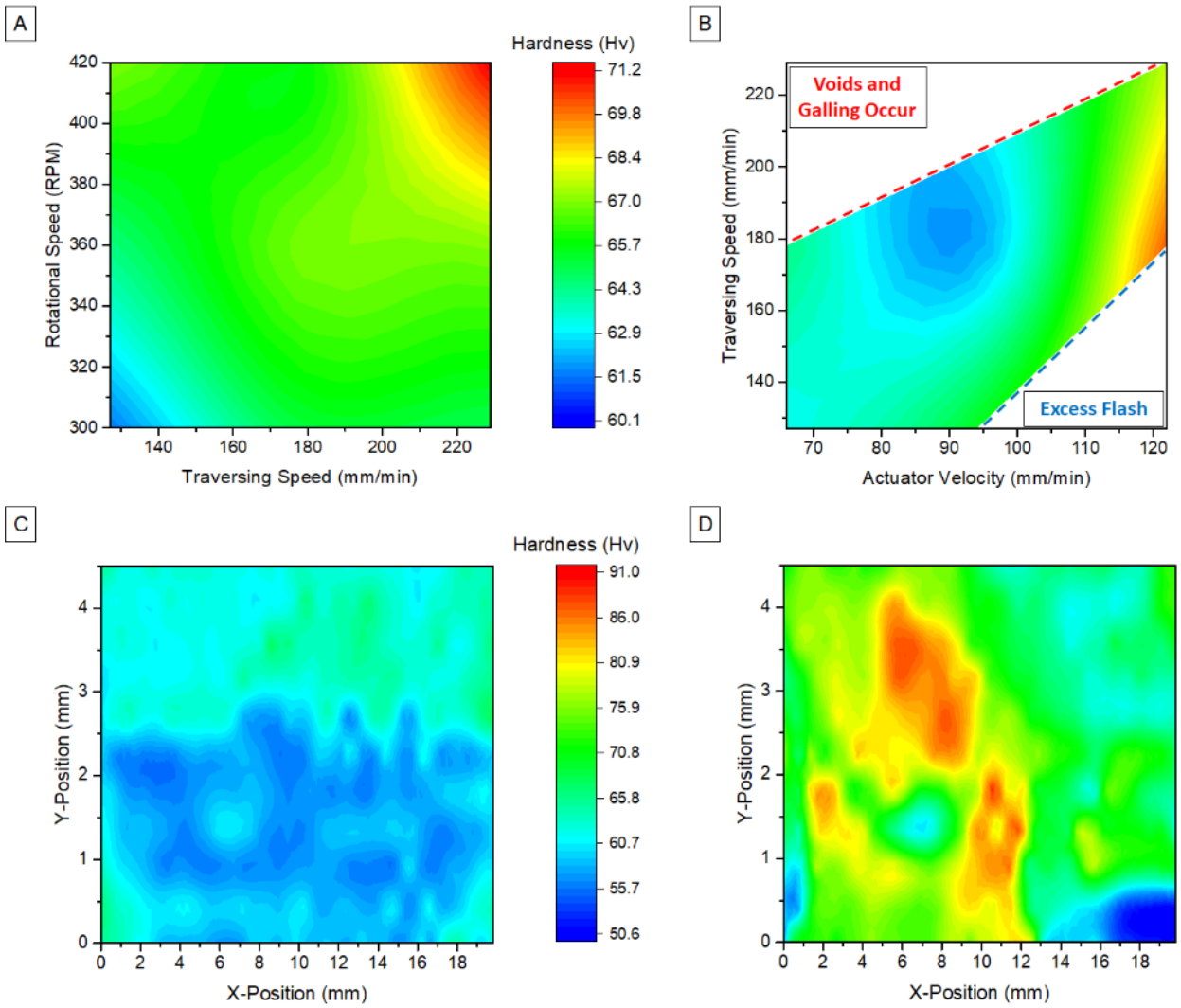

Figure 5.2 (A) Parameter contour plot relating tool rotational and traversing speed to average deposition hardness. (B) Parameter contour plot relating tool traversing speed to deposition feed rate to average deposition hardness. (C) Vickers hardness plot of low-parameter AFSD deposit. (D) Vickers hardness plot of rapid-parameter AFSD deposit.

Figure 5.3 depicts the comparative inverse pole figure grain orientation maps for the feedstock and as-deposited AA6061. Figure 5.3(A) shows the grain orientation map of the feedstock while Figure 5.3(B) and Figure 5.3(C) contrasts the angle EBSD maps and grain size transformation of the low and rapid-parameter as-deposited AFSD specimens, respectively. ASTM grain size analysis revealed a 93% average reduction in grain size from 200 µm observed in the feedstock to 15 ±4 µm in both as-built deposits. The substantial reduction is attributed to the DRX generated by the high normal and rotational shear strains induced by the AFSD tool during the deformation and deposition process. Rivera et al. [40] documented a similar rate of 90% reduction in grain size in AFSDeposited AA2219; however, the final grain size was smaller. This recrystallization mechanism is understood to be correlated to the attributes of the initial grain structure [185]. Elongated, preferential grains comprising the as-received, extruded feedstock rods were transformed into refined, equiaxed grains throughout the deposited microstructure. These grain sizes are comparable to grain sizes exhibited in AA6061 FSW weld nuggets [179], [182]. Studies

on traditional FSW found that minuscule decreases in both tool rotational speeds (50 RPM difference) and translational speeds (50 mm/min difference) resulted in grain sizes exhibiting a 50% greater reduction in the weld nuggets [186]. However, no such variance is observed in the evaluated AFSDeposits despite the variation in rotational and advancing speeds of 120 RPM and 102 mm/min respectively. While significant, the observed DRX is not as severe as that occurring in AFSD of IN625, which reported ultra-fine and nanocrystalline grains [38], [39]. This difference can be credited to the higher stacking fault energies inherent in aluminum alloys [40], [187], and is akin to other SPD processes such as FSW and high pressure torsion [181], [188]. These refined grains are equiaxed in shape as shown in Figure 5.3(D, E), which present 3-dimensional inverse pole figure orientation maps collected from three orthogonal surfaces of the as-deposited AFSD AA6061 produced with the lowest and highest defined parameter sets respectively. Thus, the process provides the driving mechanism to promote dislocations and consequently cultivating equiaxed grains.

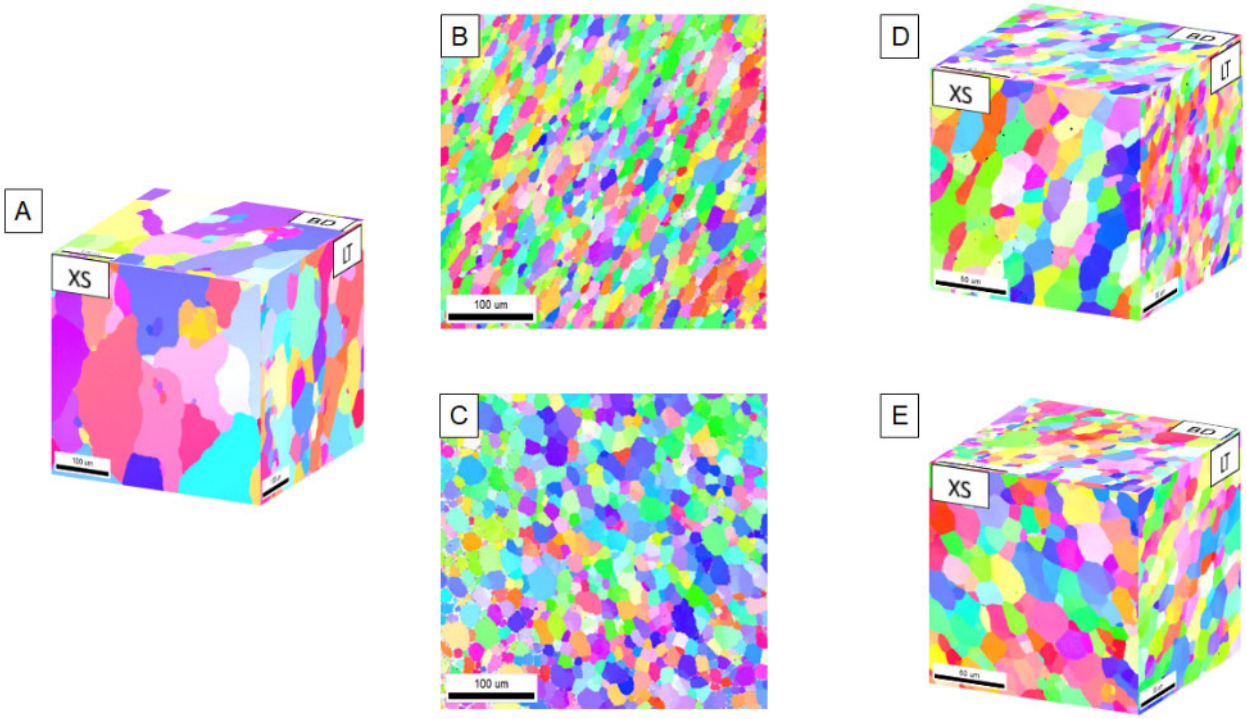

Figure 5.3 (A) 3-D representative EBSD map of virgin AA6061-T651 feedstock (100µm scale bar). (B) EBSD map of the cross section of the deposition with the slowest parameters. (C) EBSD map of the cross section of the deposition with the fastest parameters. (D) 3-D EBSD map of the slowest deposition depicting refined, equiaxed grains (50µm scale bars). (E) 3-D EBSD map of the fastest deposition depicting refined, equiaxed grains (50µm scale bars).

Figure 5.4 provides further supplementary visualization of the recrystallization occurring in representative grain boundary and grain reference orientation deviation (GROD) maps of the low (A, B) and rapid (C, D) parameter deposits. Low angle grain boundaries (LAGB), depicted as red misorientations from 2° to 10°, appear more frequently in the low-speed deposit and suggests a reduction in dislocation densities within grains. GROD maps further indicate this by measurement of intergranular misorientation where recrystallized grains are characterized by lower intergranular misorientation that are displayed as blue grains. By comparison, the low-parameter deposit exhibits 7.4% more recrystallized grains than that of the rapid-parameter deposit. Suhuddin et al. [189] hypothesized that misorientation distributions in FSW aluminum near the pin location were more continuous in nature by their increase in HAGB. However, it was also suggested that areas further away from the pin exhibited more discontinuous recrystallization due to the decrease in strain rate, temperature, and viscosity caused by the increased distance from the pin [190], [191]. This hypothetical effect is exaggerated in AFSD resulting from the lack of baseplate material ahead of the advancing tool that acts as a barrier for material flow in FSW. Consequently, particularly in the rapid parameter deposit that creates a larger wave front of deposited material, the combination of a greater deposition feed rate and lack of material pinning along the leading edge results in more discontinuous recrystallization and flashing. The resulting less consistent

dislocation pile-up inhibits grain movement; thus, revealing a higher hardness than the contrasted deposit.

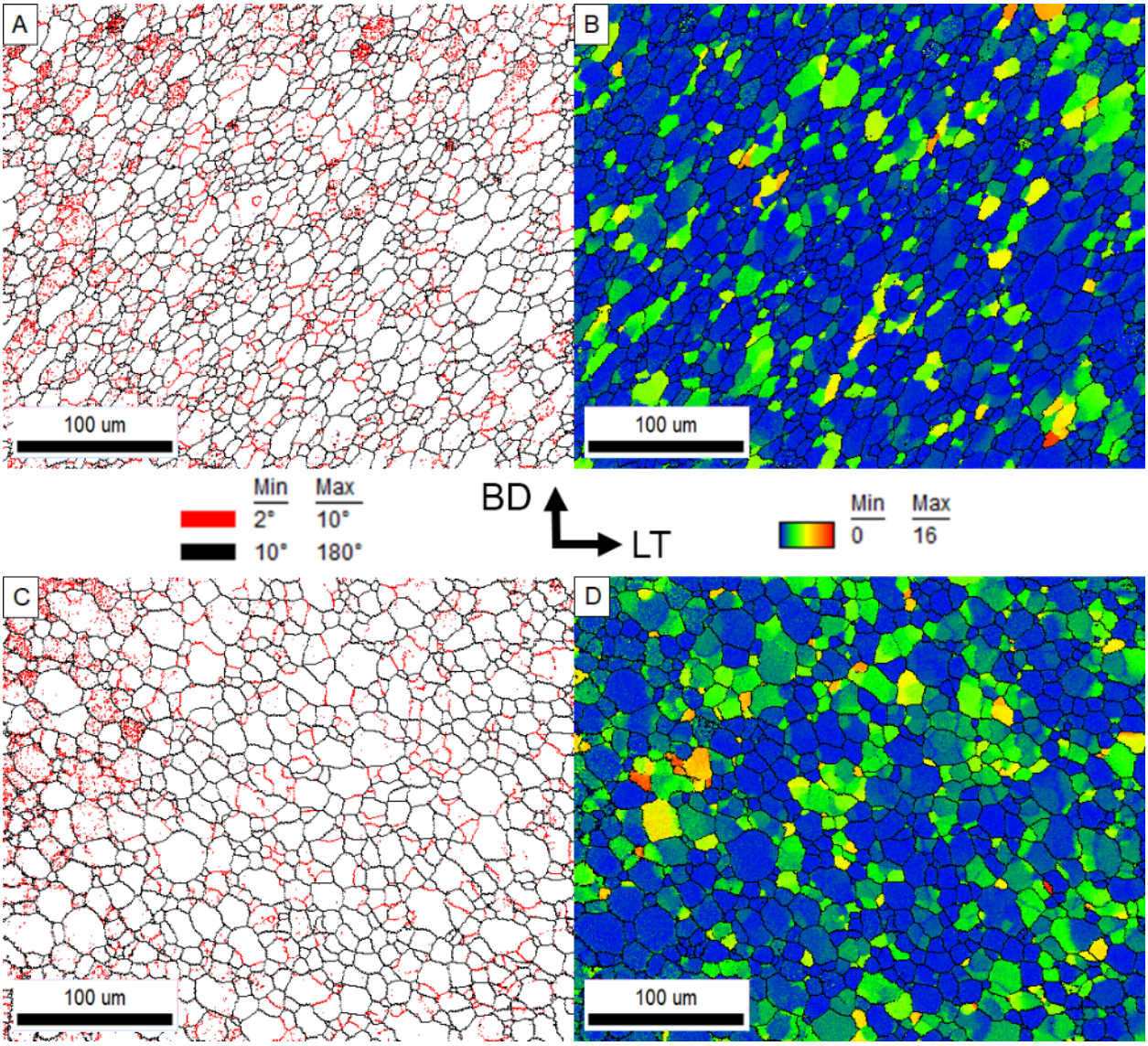

Figure 5.4 Grain boundary and grain reference orientation (GROD) plots observing cross sections of the low (A, B) and rapid parameter (C, D) deposits. Low angle grain boundaries (LAGB) with misorientation angles from 2° to 10° are represented by red lines. High angle grain boundaries (HAGB) were defined as boundaries with misorientation angles greater than 10°.

Comparative microstructural examination between the feedstock material and as-deposited AFSD precipitate behavior is depicted in bright field images in Figure 5.5(A) shows needle-shaped β" precipitates characteristically found in solution heat treated and artificially aged Al-Mg-Si alloys [192] in the as-received feedstock material. Figure 5.5(B,C) evaluate the precipitation behavior of the as-built AFSD deposits, which do not exhibit the same precipitation evident in the feedstock. Rather, observations of re-precipitation occurring in the form of Mg-Si solute clusters is evidenced in the two deposits, suggesting the process dissolves β precipitates back into the aluminum matrix during the AFSD process [40], [193], [194]. Atom probe tomography analysis in Figure 5.5(D) provided clear details of the size and distribution of the Mg-Si rich clusters taken from the cross section of the as-deposited samples. These clusters exhibit small size (~5 nm) and circular morphology, concurrent with TEM results. This nanostructural change can be attributed to the significant shear deformation and temperatures intrinsic of the process as AA6061 traditionally undergoes precipitation transformation at 803 K (530°C) , and re-precipitation is possible as Mg-Si solute clusters at 443 K (170°C) [194]–[196], similarly observed in FSW nuggets [179], [182]. Additional work is necessary to examine the temperature variation while depositing various materials to effectively quantify this observation, but is estimated to be analogous with FSW where $T < T_{melt}$ [186], [197]. Nevertheless, the dissolution of these traditional strengthening precipitates clarifies the reduced strength indicative in the hardness profiles, despite Hall-Petch strengthening resulting from the DRX. It is notable that despite the variance in processing parameters, the

resulting microstructure in both deposits remain similar in microstructural appearance at both the micro- (grain size and morphology) and nanoscales (solute clustering).

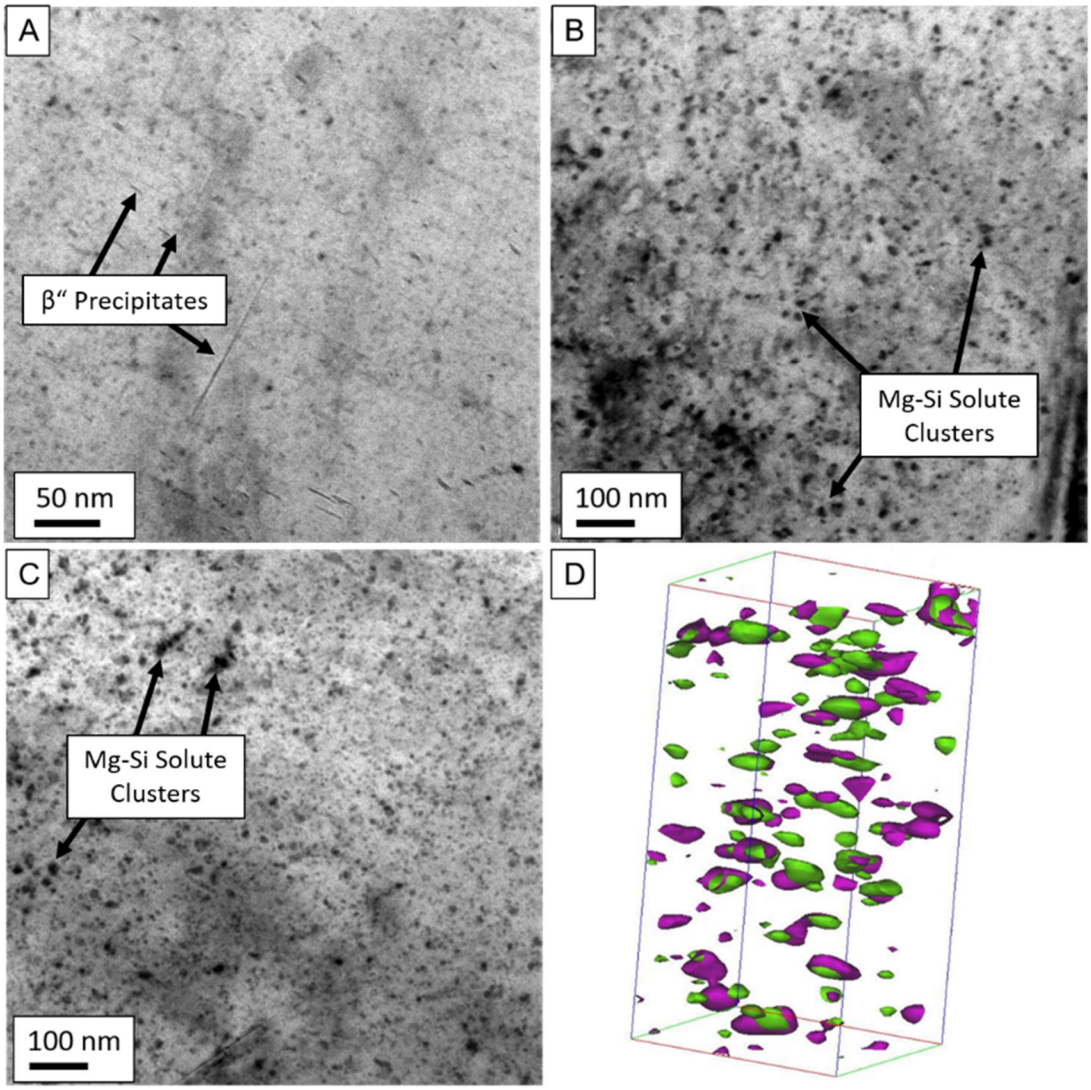

Figure 5.5(A) TEM bright field images of AA6061-T651 with conventional needle-shaped β” precipitates. (B) TEM micrograph of the low-parameter deposit showing Mg-Si solute clusters. (C) TEM micrograph of the rapid-parameter deposit exhibiting solute clusters. (D) APT analysis visualizing Mg-Si rich clusters (20x20x40nm^3 volume).

5.1.3 Conclusion

In conclusion, this study presents the first investigation to elucidate the fundamental mechanisms of the solid-state additive manufacturing process, AFSD, by quantifying the effects of varying process parameters on microstructural evolution of as-deposited AA6061 builds. The multiple deposits produced by AFSD and cross-sectioned revealed a 20% reduction in Vickers hardness from the feedstock AA6061-T651 material. EBSD analysis revealed significant grain size reduction from 200 μm in the feedstock to an average of 15 μm in both as-deposited AA6061 deposits resulting from the inherent high shear mechanisms in the process. The microstructure additionally revealed that the slower deposit contained a more recrystallized microstructure than that of the overfed build, which may be a result of the reduced strain and viscosity occurring near the edge of the rotating tool. Subsequent TEM and APT evaluation found the dissolution of β" strengthening precipitates and then re-precipitation of Mg-Si solute clusters in the as-deposited material, which explains the depreciated mechanical properties in the as-deposited AA6061 when compared to the feedstock. However, similarities between deposits suggests that microstructural evolution does not appear to be process dependent; thus, suggesting that visual, non-destructive inspection may be sufficient to determine deposition quality.

5.2 Influence of Parallel Path Depositions of New Solid Bar Feedstock on the Microstructure and Tensile Behavior

In this work, the effect of overlapping parallel additive depositions on microstructure and mechanical properties in Additive Friction Stir Deposition (AFSD) is explored. In particular, the AFSD process was employed to make parallel depositions of AA6061 with a 6.35 mm overlap to effectively bond the two parallel layers. The AFSD process draws on similar physics to friction stir welding in that frictional heat and plastic deformation is exploited to deposit metallic materials from the center of a hollow rotating tool as it traverses across the build table to produce consecutive metallurgically bonded layers. In this work, the microstructural aspects of the 6.35 mm overlapping raster interface were characterized using optical and scanning electron microscopy. Aluminum oxide particles are observed at the raster interface, which are located at layer boundaries. Additional grain refinement is also apparent as a direct result of multiple stirring passes within the overlapping deposition region. Mechanical characterization via microindentation and monotonic tensile testing observed a hardness gradient in the overlapping region, but comparable tensile strength to a single row of deposited AA6061. The influence of existing oxides on the mechanical results was observed to have limited effect on the properties longitudinally across the raster. The study determined that parallel layers of AA6061 can be successfully deposited via the AFSD technique. The resulting deposit exhibited a strong metallurgical bond across the parallel layers despite the presence of surface oxidation on the unprepared feedstock and substrate.

A commercially available model B8 AFSD machine was employed to deposit commercially sourced AA6061-T651 with 9.53 x 9.53 mm cross-section solid feedstock onto a 6.35 mm thick substrate fixed to the build table by 4 machine clamps. The substrate was placed in the as-received condition with no surface preparation. Prior to deposition, the feedstock was coated with a thermally resistant carbon-based lubricant to reduce friction between the feedstock and interior tool walls. The tool used for deposition was a H13 hardened tool steel with 4-teardrop protrusion features located on the interaction face of the tool which is the same tool utilized in a previous study by the authors, Phillips et al. [65]. A 1 m^3/min Vortec dual nozzle forced induction air gun was fixed to the build anvil near the layer initialization zones to cool the deposit as the build was produced.

Process parameters for the parallel-pass deposition was determined by establishing a linear material usage approximation, introduced for the first time here as the Limits of Deposition Equation (LOD). The two dominant process parameters that define deposition rate are the actuator feed rate, which governs the velocity that material is extruded through the bottom of the tool onto the workpiece, and the tool traversing velocity. These two machine parameters can be related to the length of feedstock required to deposit a layer of defined length and height. LOD is expressed as:

$$L = \sum F_R\left(d_{xyz}/V_{xyz}\right) + L_{dwell} \tag{5.2.1}$$

where L is the length of feedstock required to produce a deposition, F_R is the linear actuator speed (i.e. the feed rate), d_{xyz} is the coordinate direction distance the tool travels, V_{xyz} is the tool traversing velocity used to travel the respective distance, and L_{dwell} is the additional length of feedstock required to begin deposition following a reload. Implementation of the equation assumes that all material deposited via AFSD fills the full volume between the tool and substrate. To determine the total quantity of solid feedstock rods required for a given deposition path, the total number of layers at a predefined layer height can be multiplied by the LOD equation.

Eight-1 mm thick layers were deposited by traversing 190.5 mm parallel to the rolling direction of the substrate followed by a 90˚ turn to travel 34.9 mm. The machine then began the return pass by turning 90˚ and traversed parallel to the recently deposited material in the opposing direction as seen in Figure 5.6B. This geometry produced a 228.6 x 69.9 mm deposit with a 6.35 mm overlap to be evaluated. Tool rotation and traverse speeds were fixed at 300 rpm and 127 mm/min, respectively, as determined by previous work to produce a deposit with consistent build quality. In this work, the desired volume is defined by the projected build path in Figure 5.6B, which correlates to a total theoretical volume 159,121 mm^3. To balance the material feed on the return pass and maintain a volume balance, the deposition feed rate was reduced on the return path of the deposit from 69.9 mm/min to 63.5 mm/min. Since the diameter of the tool covers 3.18 mm (half of the overlapping region) of the deposit on the return pass, less material was necessary to fill in the area under the tool; thus, leading to the reduction in the material feed rate to prevent the material from jamming in the tool.

Specimens for visual examination and microindentation were cut from the center of the deposit in the transient region to contrast the variance between the overlap region and the center of the tool path. Specimens for optical microscopy (OM) and microhardness measurements were ground and polished stepwise down to 3 μm diamond suspension. To aid in flow visualization, the cross-section was chemically etched with a NaOH caustic etchant. Optical analysis was conducted on a Keyence VHX 1000 digital microscope. Energy dispersive X-ray spectroscopy (EDS) was conducted on a Tescan Lyra 3 scanning electron microscope (SEM) with an Octane Elite EDS system with subsequent particle analysis performed via ImageJ. Specimens were then polished with a 0.3 μm colloidal silica in a vibratory polisher for 20 hours for subsequent electron backscatter diffraction (EBSD) in an Apreo SEM affixed with an EDAX Hikari EBSD camera.

Vickers hardness measurements were recorded on a Buehler Wilson VH1202 microhardness tester at 200 gf and a 0.5 mm linear spacing. Indents were taken from the cross section of the deposit 2 mm below the top surface of the deposit and from the center of each tool path towards the interface. Indentation location was chosen at this location to record data at the same location in which tensile specimens were extracted. Quasi-static tensile specimens were machined out of the build excluding the dwell and path reversal sections as an effort to exclusively characterize the overlapping interface, via a wire-EDM using geometry visible in Figure 5.6D. Tensile testing was performed via an MTS 647 servo hydraulic load frame in displacement control. All samples used in this study were taken from the same height with respect to the top of the substrate. An MTS 632.29F-30 5 mm extensometer was placed on the specimen around the midpoint of the gage section to measure the induced strain during tensile testing.

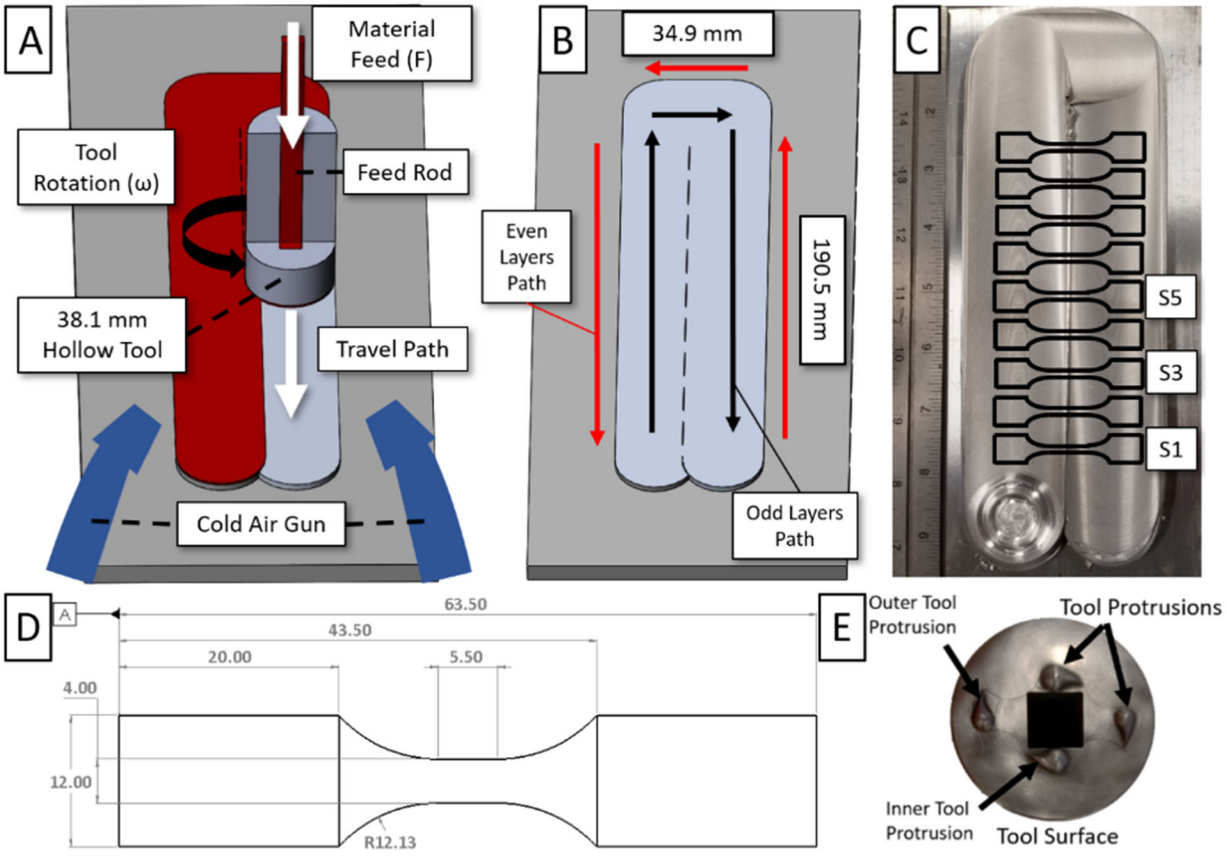

Figure 5.6 (A) Schematic of the AFSD process where a non-consumable tool rotates and traverses along a substrate as a linear actuator extrudes material through the center of the tool. (B) The tool deposition path produced to create an overlapping, parallel raster. Arrows denote the tool path alternating directions after consecutive layers. (C) Image of the final deposit with sample layout depicted schematically. (D) Sample geometry (mm) to determine tensile response. (E) Bottom surface of 38.1 mm AFSD tool containing features.

5.2.1 Results and Discussion

Microscopic Observations

OM observing the cross-section of the raster interface is presented in Figure 5.7A-E. Shear induced material deformation from the teardrop protrusions on the AFSD tool is observable from the flow lines located 5 and 15 mm from the centerline of the raster interface. These flow lines, which are not evident in the final layer of the deposit, demonstrate the purpose of the protrusions. The previous layer is restirred to effectively plasticize the existing layer and the freshly deposited material to produce a mechanical bond between the successive layers, which is outlined in Figure 5.7A. Additionally, this effect permeates the region between the substrate and deposited aluminum as evidenced by the discoloration in the substrate; thus, developing the bond between the substrate and deposition. Furthermore, this effect is neutralized in the raster interface due to the opposing restirring action occurring on the opposite side of the raster centerline.

At increased magnification, the interface of two parallel lines of deposited material develops a plume effect, seen in Figure 5.7B, in which multiple phenomena are occurring. At the deposit-to-substrate interface, residual surface treatment of the as-received AA6061 substrate assists in visualization of a plume of material that develops in the raster interface. When the first layer is deposited, the tool protrusions remove material from the substrate, creating grooves. The substrate material is then pushed by the protrusions outwards from the center of the tool and replaced with newly deposited material. As a result, the substrate is stirred to the outside radius of the deposition as flash due to the vertical constraints of the newly deposited material and AFSD tool. The displaced substrate is forced radially from the tool rotation and down creating the spiral effect at the substrate interface visible in Figure 5.7C. Observations made in this present work compliment recent studies by Perry et al. [198] and Garcia et al. [63], in which similar observations on aluminum flow in AFSD via X-ray computed tomography and optical imaging are presented. Closer inspection of the center of the overlapping regions of AA6061 reveals a discreet white line that segregates the flash from the substrate. Similar observations are made higher in the deposit, but more faintly as a line of fine particles in Figure 5.7D and as a web of the same particles in Figure 5.7E.

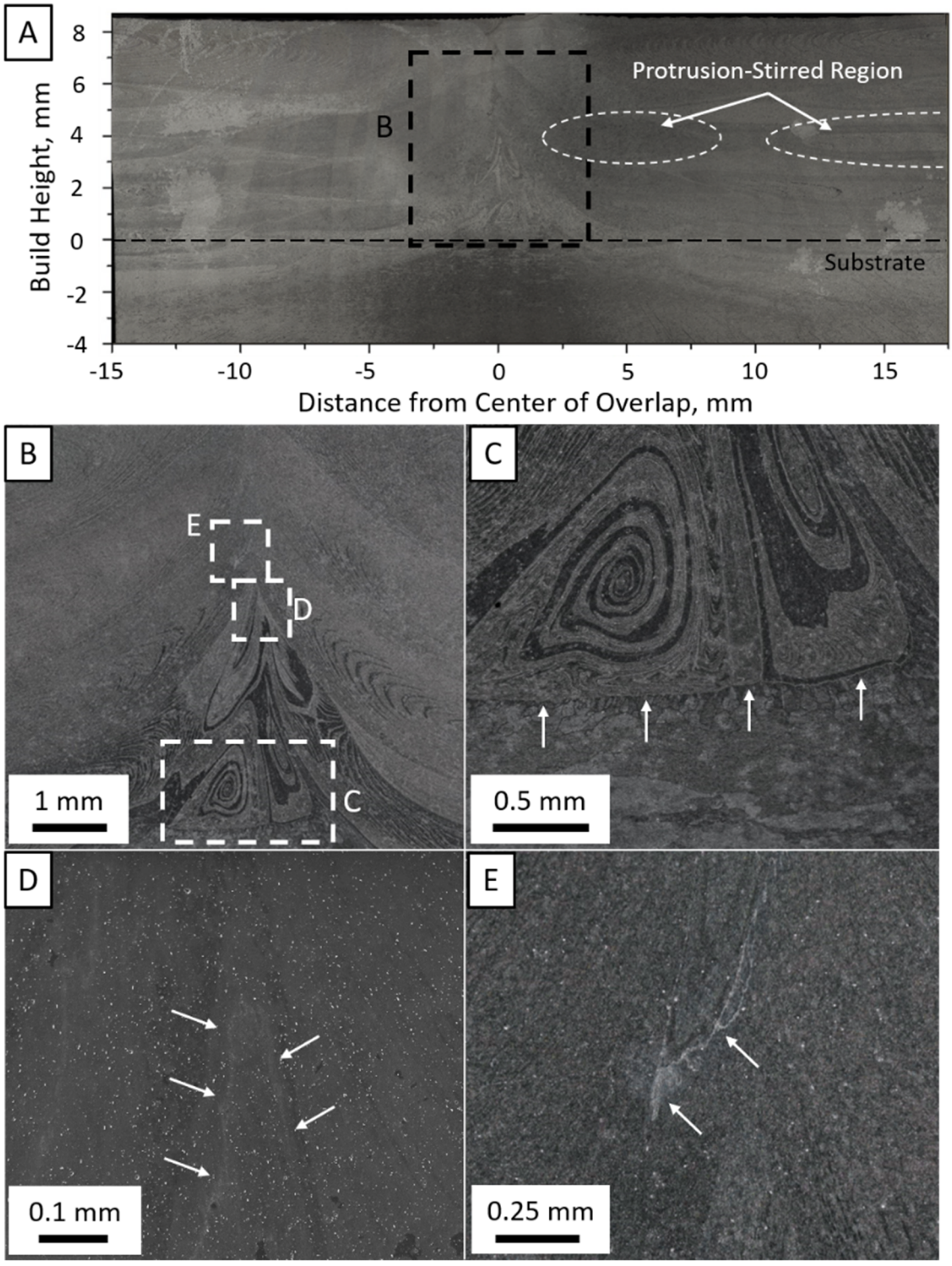

Figure 5.7 (A) OM cross-section of the as-deposited AA6061 raster, centered upon the overlapping region. Outlined regions depict specific locations deformed by the tool features. (B) Magnified view of two parallel layers and substrate developing a plume structure. (C) A continuous oxide layer (denoted by arrows) divides the layers and substrate. (D) SEM images depict similar small networks of particles. (E) A smaller, discontinuous network forming a web.

Evaluation of the separating line between the deposit and interface within the overlapping region is outlined in Figure 5.8A-C. SEM micrographs of this region show what appear to be large cracks forming at the substrate-deposition interface and a large particle developing a triple-point between the substrate, substrate-originated flash, and newly deposited material. Qualitative EDS analysis revealed that this particle, as well as the trace film remaining in the crack, is a 12 μm diameter aluminum-oxide (Al_2O_3) particle.

Okamura et al. [199] noted that NaOH etchants, such as that applied in the present work, will selectively attack thicker regions of oxides, which was investigated on FSW Al-Mg-Si alloy. The authors state that oxides that form are more soluble in acid and alkaline solutions and are more soluble than that of the aluminum matrix. In SEM images, these appear as large depressions that increase in width as the concentration and size of oxides as well as etching time increases. Liu et al. [200] identified that these oxides are typically in regions that develop FSW defects identified as zigzag lines and kissing bonds. The root cause of oxidation related FSW defects was determined to originate from surface preparation or lack thereof. Ren et al. [201] explained that rapid oxidation rates common in aluminum alloys permits oxide films to manifest in open atmosphere conditions, even after surface cleaning, and are thus unavoidable. However, Okamura et al. [199] suggested that these defects can be mitigated by specification of processing parameters, which govern the quantity of deformation imposed by the process necessary to dissipate the oxide. In AFSD, this occurrence corresponds to oxide layers that were once prevalent on the substrate and feedstock that are not decomposed well as the AFSD tool radius increases. Three-dimensional flow modeling of FSW by Nandan et al. [190] suggests that the strain rate of material under the tool surface decreases inversely to the tool radius. This results in a thin layer of oxides forming at the outer edge of the deposit that are insufficiently stirred by the AFSD tool.

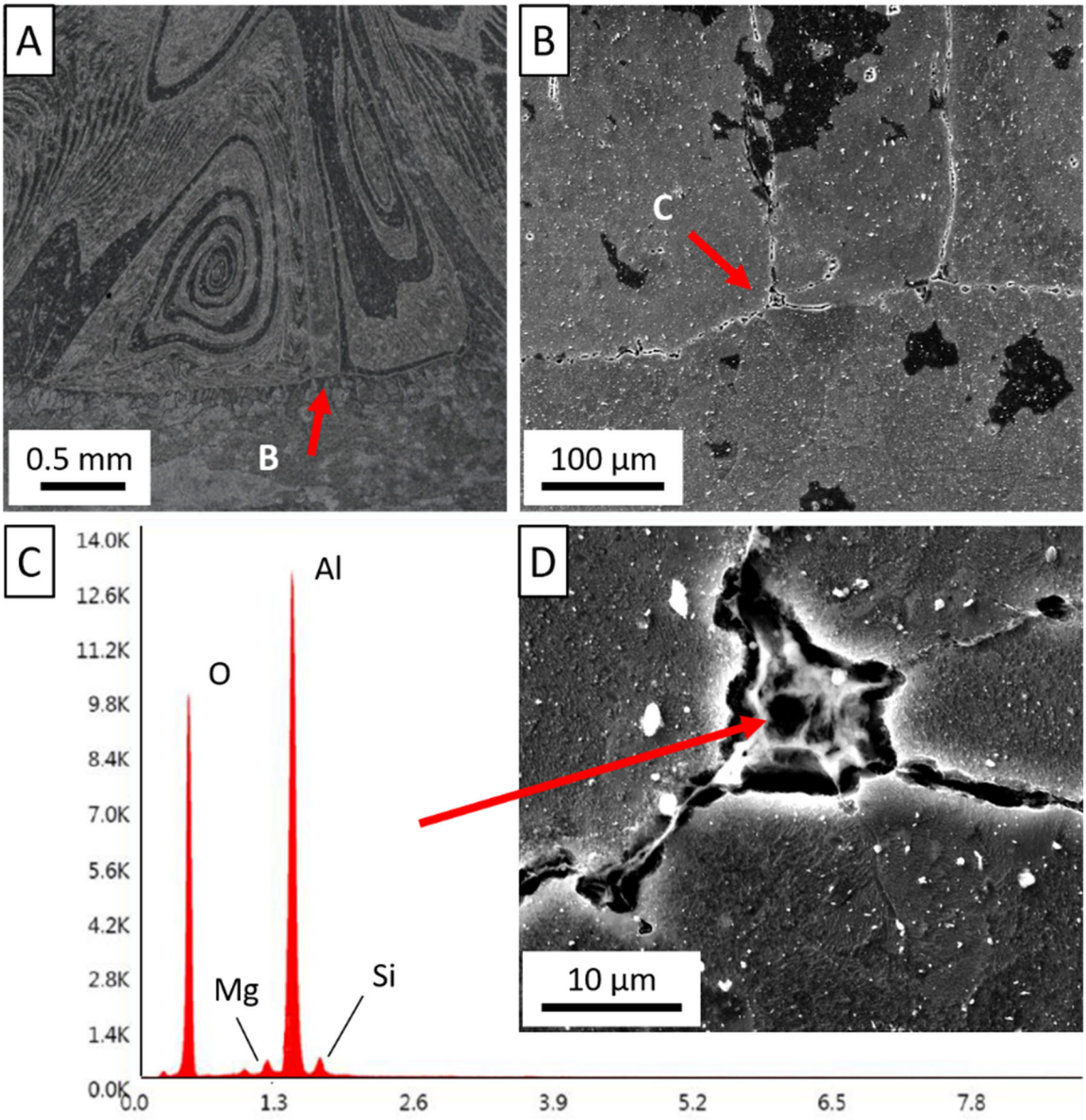

Figure 5.8 (A) OM image depicting the location of an oxide film separating the substrate from flash and freshly deposited material. (B) SEM reveals etch pits resulting from the NaOH caustic etchant selectively attacking oxides. (C) EDS qualitatively determines these particles (D) as trapped oxides.

Figure 5.9A-C shows a similar, but dissipated occurrence of Al_2O_3 particles forming a network, which is observed at approximately 1 mm intervals throughout the raster interface. Particle size and nearest neighbor distances are summarized in Table 5.2.1. In this region, the submicron amorphous particles do not produce etchant pits evident at the substrate. The high scatter in size shows that these particles are non-uniform in size with a range from 0.147 to 2.636 μm^2. Both the size and spacing along the plume suggests that these oxides originate from the feedstock material and create 15.7 ±1.38 µm bands of broken up oxides outlining the top and bottom of each layer. It is notable that these bands disappear as the distance to the center of the tool path decrease as a result of the tool features stirring together the existing and freshly deposited layer.

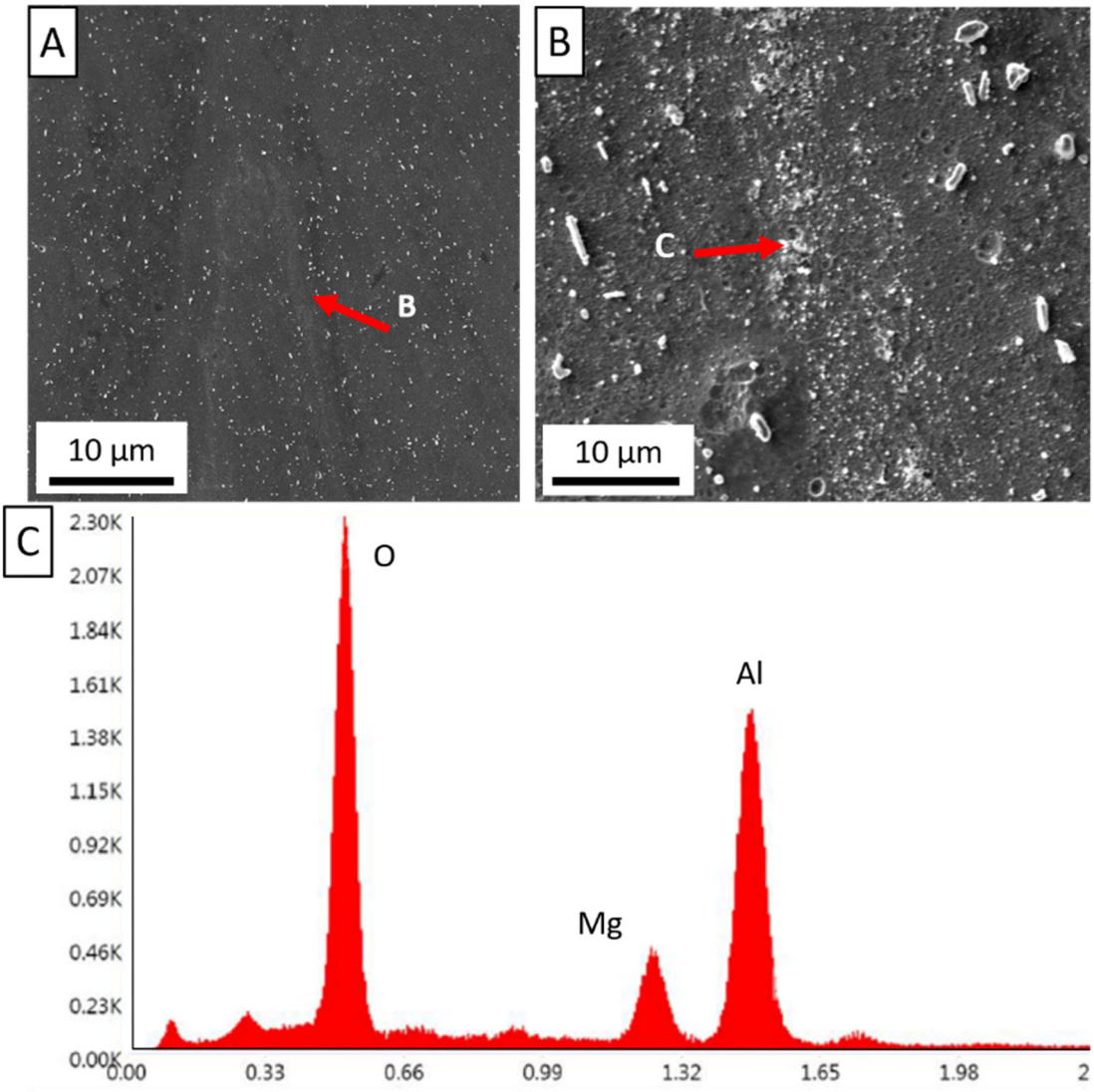

Figure 5.9 (A) Oxides forming the outline of two parallel layers of AA6061. (B) Oxides in the raster interface are smaller than those at the substrate interface and form a discontinuous network. (C) EDS qualification of oxide particles.

Table 5.2.1. Particle size and nearest neighbor evaluation from oxide bands in the overlapping region.

	Particle Size (μm²)			*Nearest Neighbor Distance (μm)*		
Location	*Average*	*Deviation*	*Max*	*Average*	*Deviation*	*Max*
Particle Band	*0.147*	*0.138*	*2.389*	*0.64084*	*0.329491*	*2.825*
Surrounding Matrix	*1.876*	*0.612*	*3.216*	*6.457688*	*3.25618*	*13.139*

Figure 5.10A shows the cumulative frequency plot of the as-deposited AA6061 grains evaluated at the center of the deposition path (Figure 5.10B) and center of the overlapping interface (Figure 5.10C). Grains exhibit refined and equiaxed grain morphology as a result of the AFSD process, consistent with previous AFSD work documented in literature, which is a direct result of the plasticity induced dynamic recrystallization. Grains evaluated in the overlapping region of the build measured 9.1 ± 5.8 μm in diameter, which are statistically similar to the grains located at the center of the deposition path measuring 10.6 ± 7.2 μm. The marginal refinement in the raster area is a direct cause of the repeated stirring created by the opposing rotational directions in the overlapping deposition pass, evident by the steeper slope of the frequency curve. It is observed that despite the repeated thermal cycles, grain growth did not appear to occur in either the center of the tool path or interface region of the deposited of AA6061, but instead decreased the deviation in grain diameter in the overlapping interface.

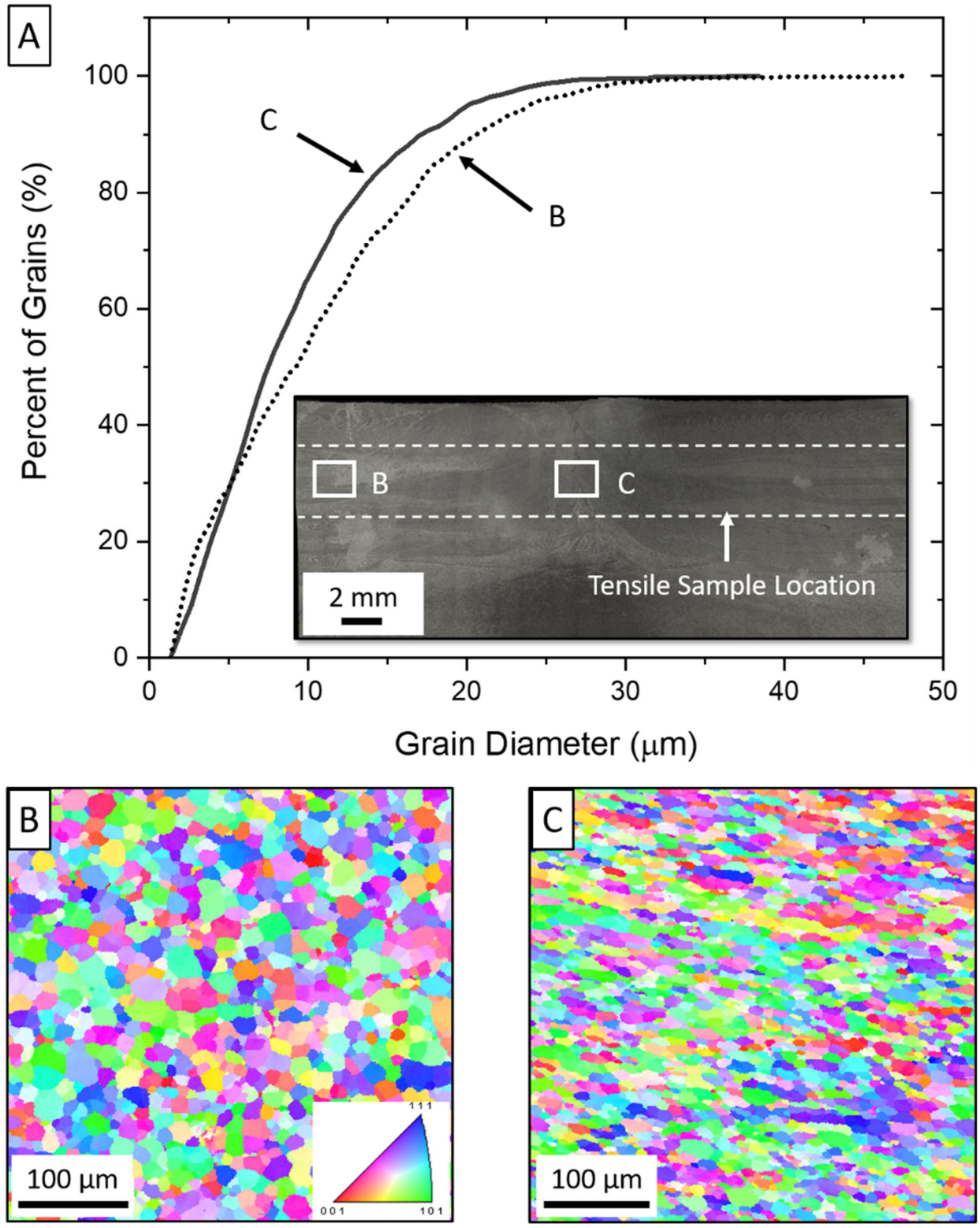
A
Percent of Grains (%)
Grain Diameter (μm)
C
B
B
C
2 mm
Tensile Sample Location
B
100 μm
111
001
101
C
100 μm

Figure 5.10 (A) Cumulative grain diameter frequency plot with correlating OM depicting EBSD scan locations. (B) EBSD depicts equiaxed grains at the center of the deposition path. (C) EBSD in the raster interface revealed slightly smaller, elongated grains as a result of twice as much severe plastic deformation from additional tool passes.

Mechanical Behavior

Figure 5.11 graphically illustrates the fluctuation in Vickers hardness present in the interface of the deposit as compared to the authors' previous study, Phillips et al. [65]. The average deposition hardness is 54 Hv, reduced from the 112 Hv in the AA6061-T651 feedstock. As observed in comparison to the optical image in Figure 5.7A, as the indentation measurements deviated from the center of the tool path and towards the interface between the raster interface, a stark 15 Hv reduction in hardness is exhibited. As addressed in FSW, repeated thermal cycles can significantly degrade aluminum strength, which is similar to the phenomena in this work. Ma et al. [202] observed a similar trend where the transition zone demonstrated diminished hardness as compared to the nugget zone in FSP. This occurrence is attributed to repeated thermal cycles dissolving strengthening precipitates back into the matrix in heat treatable alloys, such as AA6061. As observed in this present work, the hardness reduction is likely attributed to the repetitive heat generation in this region, which doubles when compared to a single row of deposited material.

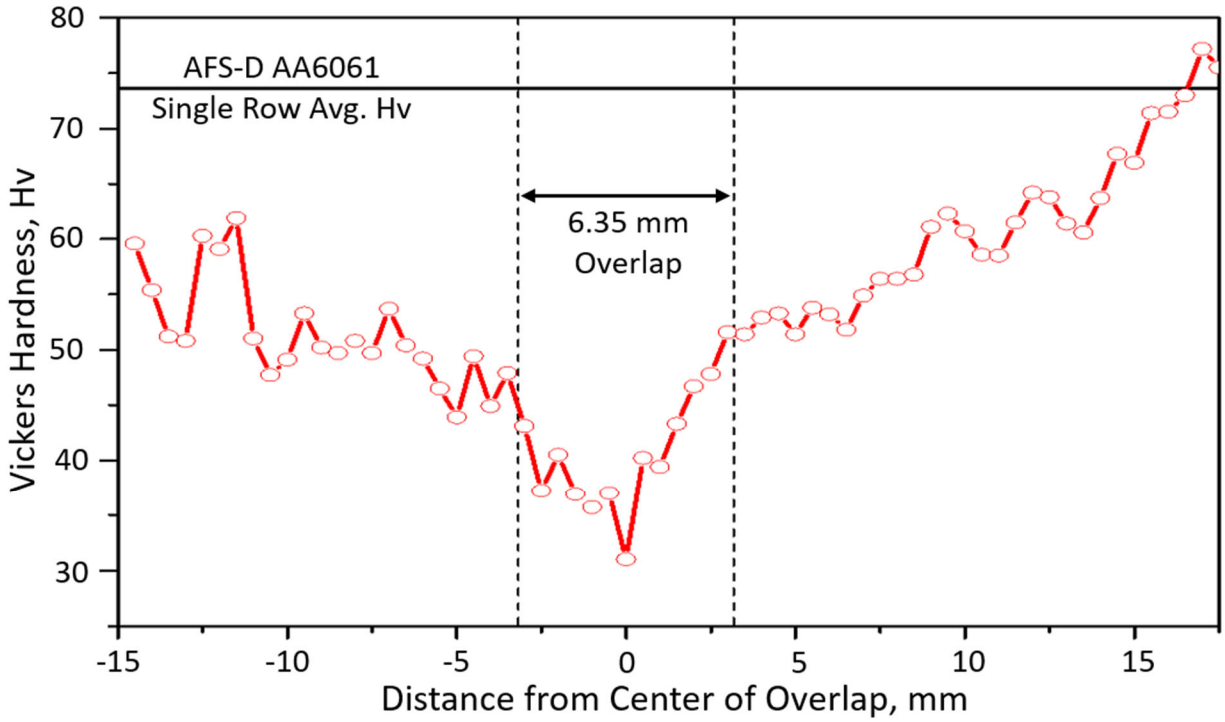

Figure 5.11 Vickers hardness map displays a reduction in hardness in the overlapping region compared to a single row deposition.

Figure 5.12A displays the stress-strain quasi-static tensile response of the as-deposited overlapping region of the deposit. Three specimens were selected for testing at random, schematically illustrated in Figure 5.12B, and averaged to generate a single curve with associated error bars. The resulting engineering stress and strain was compared to wrought AA6061-T651 substrate, as well as the longitudinal mechanical response of an as-deposited AFSD AA6061 produced as a single row in recent work Rutherford et al. [67], which is visually represented in Figure 5.12C. It is noted that the single row samples and their respective data only account for longitudinal samples taken from the final layers. As a result, samples compared in both studies are taken from similar locations with respect to the top of the deposit. Additionally, the same specimen geometry is used to contrast the AA6061 deposited in a single row, from Rutherford et al. [67], and material deposited with an overlap (this study). . All specimens exhibited lower mechanical strength than that of the feedstock AA6061-T651 as a result of the dissolution of the strengthening β”-phase back into the matrix, which was evaluated by Phillips et al. [65]. Additionally, this result is consistent with FSW studies of the same material, which elucidate the result as an effect similar to over-aging, which is explained by Baghdadi et al. [203] and Sauvage et al. [204]. However, specimens evaluated over the raster pattern exhibited on average a 20MPa increase in strength when compared to that of the single row deposit.

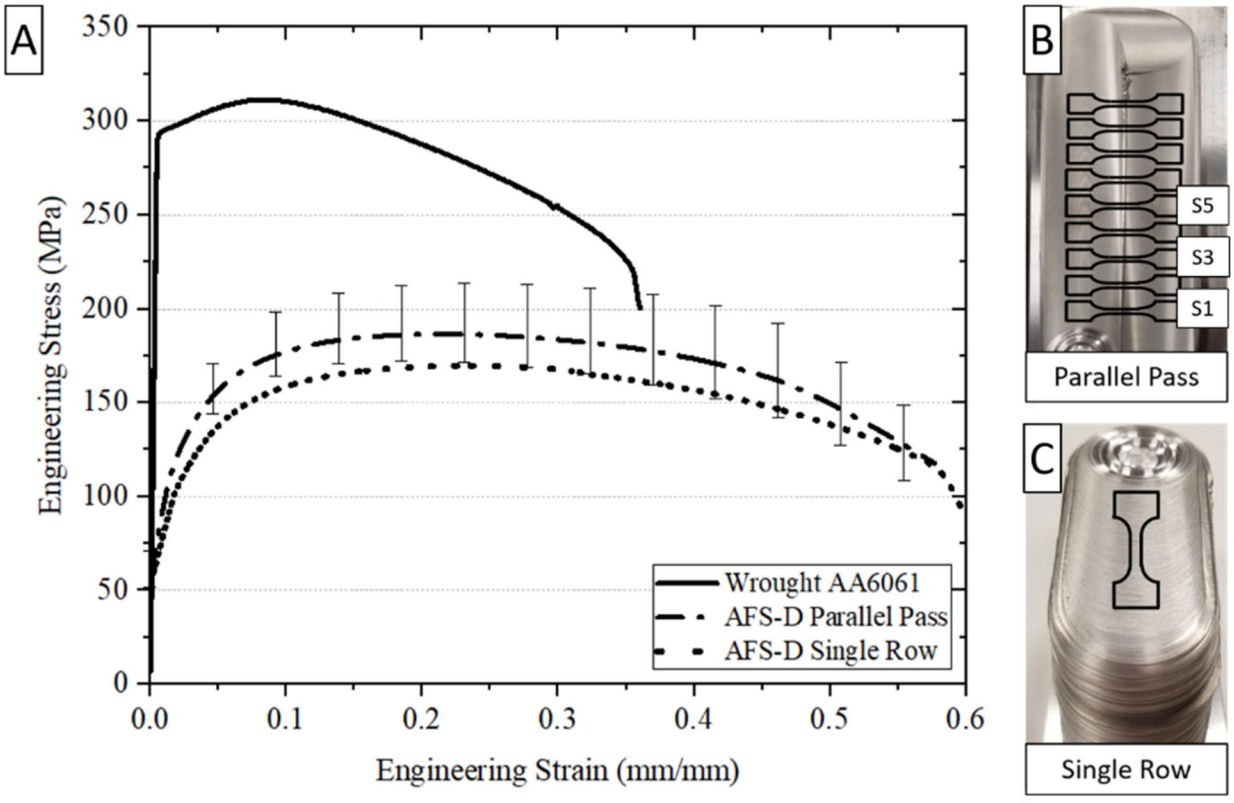

Figure 5.12 (A) Quasi-static stress-strain response of the as-deposited AFSD AA6061 deposited in parallel passes. (B) Schematic of the sample location with respect to the overlapping region (this study). (C) Schematic of a single row of AFSD AA6061.

Tensile evaluation in this work exhibited a 20 MPa increase in tensile strength when compared to the single row deposit. In their study, Rutherford et al. [67] note that the longitudinal direction observed a wide error band. This observation was attributed to the reduced thermal cycles the final layers experienced in the significantly taller, 64mm deposit suggesting a layer influence on mechanical behavior. In the present work, only a fraction of those layers were produced. Accompanied by increased cooling rates by forced cold air convection, the parallel pass deposit may have experienced reduced thermal degradation or subsequent overaging. This also assists in the explanation of the wide range of error exhibited in Figure 5.12(A). Specimens extracted closer to the forced air cooling (S1) exhibited greater strength than those near the middle of the deposit (S5), which were more comparable to the samples from the single row deposit. Additional work on mechanisms to moderate temperature during AFSD processing is suggested to inhibit thermal gradients in heat treatable material depositions.

Fractography

Optical images of tensile sample 1 (S1), shown in Figure 5.13(A-B), depict unconventional fracture behavior of AA6061 when compared to that of wrought AA6061. Near the bottom of the specimen, a sharp point is evident which appears to be delamination forming a tearing ridge. Observation of the cross-section in Figure 5.13(B) shows that this behavior does not propagate throughout the entire sample, but rather, is terminated 500 μm through the longitudinal direction (LD) of the sample. The location and shape of this fracture is directly correlated to the location of the webbed oxide network previously discussed in Figure 5.7(E). Failure likely occurred as a result of the oxide network coalescing with the oxides located at the layer boundary. The oxide network was not detected in other samples, which suggests that S1 may have been subjected to transient processing behavior due to the location of the sample with respect to the beginning of the deposit.

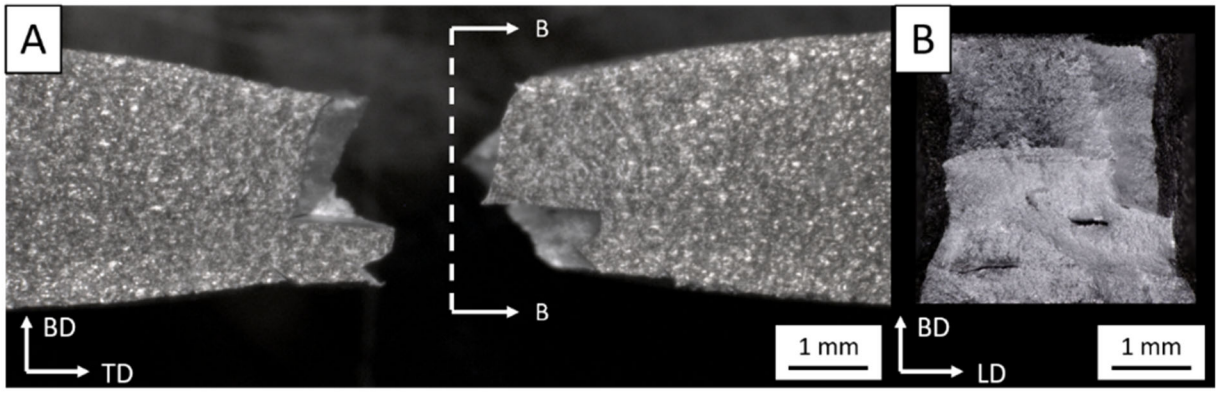

Figure 5.13 (A) Side view of fractured sample 1. Significant necking is observed along with apparent delamination. (B) Optical microscopy of the cross-section of the fractured sample shows that the shelf that forms does not propagate throughout the width of the specimen.

Figure 5.14A-D presents SEM post-mortem fractographic analysis of S1. Typical fracture progression in aluminum alloys is dominated by void nucleation, growth, and coalescence developing from secondary phases. The resulting fracture surface is covered by dimpled features as a result of the cavities that form from these constitutive particles, as observed in studies such as that from Dorbane et al. [205] and Ghahremaninezhad and Ravi-Chandar [206]. The overview of the specimen, Figure 5.14A, shows a more tumultuous fracture surface than that of typical wrought AA6061 fracture surface, characterized by a ridge and large cavities that develop outlining layers. Upon closer observation of the ridge that forms in Figure 5.14B, a distinct line of particles is observed. Iron-rich particles that typically define fracture behavior are refined and replaced by larger oxide particles that were not fully dispersed by the AFSD process; thus, becoming the dominant fracture mechanism. These are the same particles identified previously that were located along the oxide bands outlining the layers. These oxides are often irregular in sphericity and develop the 10 μm voids.

Large cracks are visible 1 mm apart in the low magnification overview of the fracture surface, which matches the individual layer heights of the deposit. Closer investigation into the cause of these large cavities, shown in Figure 5.14C-D, reveals that layer decohesion is occurring. Significant quantities of submicron oxide particles litter the separated surfaces. These particles match the relative size and spacing of particles observed in the cross-section in Figure 5.9. Several researchers have observed a similar occurrence in FSW. Ren et al. [201] observed the effects of surface preparation on Al-Zn-Mg-Cu butt-joints and reported small oxide cavities following flow lines at various points in the FSW nugget zone. The resulting fracture was directly attributed to the agglomeration of oxide particles along equiaxed grain boundaries forming zigzag defects. This is corroborated by similar studies on various aluminum alloys such as that by Liu et al. [200]. Additionally, Okamura et al. [199] and Chen et al. [207] determined that these oxidation defects could be rendered insignificant with proper process optimization. Both aforementioned studies determined that a reduction in ductility is possible as a result of the Al_2O_3 inclusions while retaining the expected tensile strength. In the present work, it is notable that the tensile strength was not directly affected by the oxide dispersion across the raster when compared to a single row of AFSD AA6061. However, it is possible that the delamination effect may be severely detrimental to the mechanical performance of the build (vertical) orientation. Additionally, larger overlaps may be necessary to permit the tool features to adequately dissipate or dissolve oxide networks to prevent interfacial decohesion related defects.

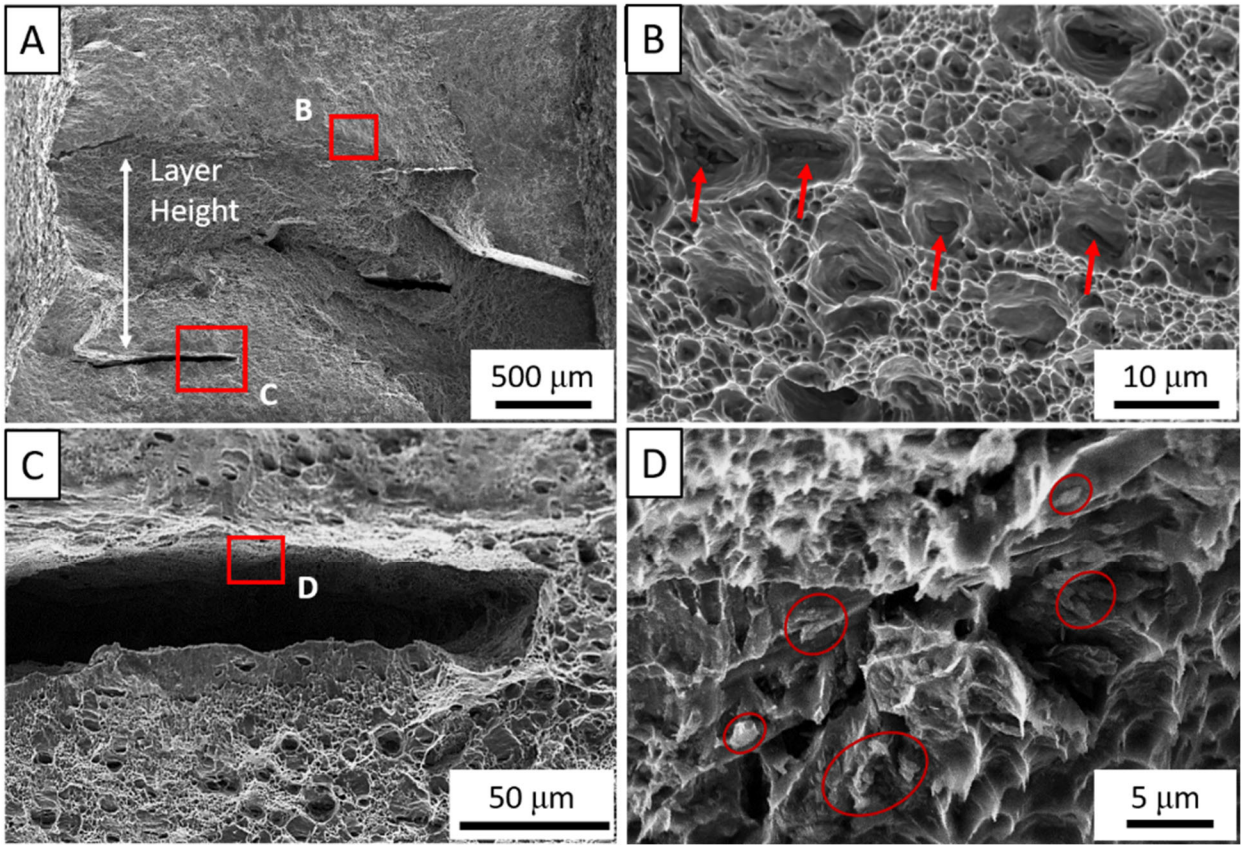

Figure 5.14 (A) Macroscopic view of the fracture surface of sample 1. (B) High magnification SEM image outlining large oxide particles that coalesced along a ridge. (C) Delamination occurring at layer interfaces. (D) Submicron oxide particles are observed along the length of the cavity, outlined by ellipses.

Discussion of the Limits of Deposition Equation

Table 5.2.2 presents a comparison between the estimated feedstock volume required to produce the deposit and the actual material quantity consumed. Data reflecting the actual feedstock spent was determined by monitoring the difference between the machine logged initial and final actuator mechanism position following the dwell period for each layer. The data shows good correlation between the estimated and actual feedstock consumption with an error of 2.28%.

Table 5.2.2. Comparison of LOD estimated material required versus actual material consumed.

AA6061 Feedstock Material Consumed			
	Average Per Layer, mm³	*Deviation*	*Total Consumption, mm³*
Theoretical	*19,890*		*159,121*
Actual	*20,343*	*1042.4*	*162,746*

The source of error can be attributed to the inherent thermo-mechanical nature of the AFSD process. The actuator mechanism is velocity driven and compensates for variances by adjusting the power draw to the actuator. The machine attempts to maintain the specified actuator velocity, which fluctuates near the user-defined value and can be inhibited by the reaction forces on the feedstock. The forces exerted on the feedstock are stress and temperature dependent; thus, leading to variability as deposition length increases. As a thermo-mechanical process, heat is transferred into the feedstock via friction to promote plasticity via shear. However, as the material continues to soften, the thermal gradient in the feedstock extends further into the length of the feedstock, which is constrained by the inner walls of the AFSD tool, illustrated as a schematic in Figure 5.15. This results in an expansion of the feedstock material in the tool and is not accounted for by the actuator position data. As the feedstock expands, the forces required to extrude the material from the tool increases due to the additional friction generated by the feedstock and interior tool walls; thus, resulting in inconsistent actuator velocity. The authors suggest investigating a method to monitor the feedstock and deposition temperature as a method for feedback control for the AFSD process.

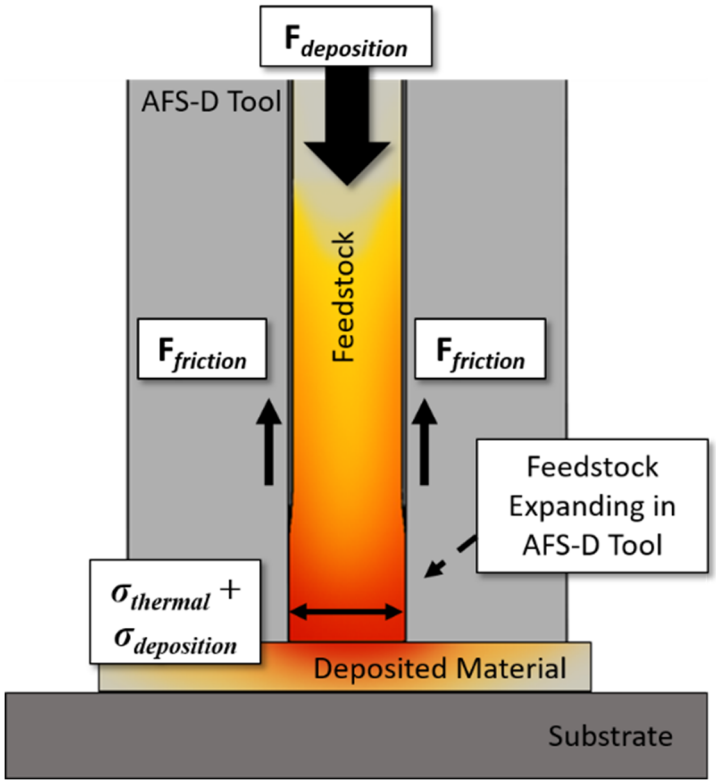

Figure 5.15 Schematic of the cross-section of the tool depicting the effect of the feedstock expanding inside of the AFSD tool.

5.2.2 Conclusions

This is the first study to investigate the AFSD deposits of AA6061 produced in a two-row, parallel raster pattern with a 6.35 mm tool overlap with an overall deposition width wider than the trackwidth of the tool The research found the following:

AA6061 was successfully deposited and metallurgically bonded using a raster pattern with a 6.35 mm tool overlap through to the introduction of the LOD equation to provide adequate material fill. The resulting region formed a fully dense bond between parallel layers of material.

Aluminum oxide particles that remained on the as-received substrate and feedstock were not as well dispersed in the raster interface and outlined the individual layers as compared to the bulk of the deposit. The stirring action by AFSD tool features were found to eliminate these networks of oxides. Pre-deposition surface preparation as performed before FSW may minimize surface oxides that get mixed in the deposition.

Continuous passes of the AFSD tool during deposition in opposing directions lead to refined grains in the overlapping region, while producing a smaller grain diameter as compared to the center of the tool path.

Monotonic testing demonstrated that the raster and oxide inclusions did not strongly influence the strength or ductility of the parallel pass deposit when compared to an AFSD AA6061 produced as a single row.

Fractographic analysis determined that fracture occurred due to oxide particles that were not fully dispersed in the raster interface. Partial delamination occurred as a result of submicron particles observed in large voids that opened up along the fracture surface.

The LOD equation was shown to be an effective tool to quantify feedstock consumption.

5.3 Effect of Solutionizing and Artificial Aging on the Microstructure and Tensile Behavior of New AA6061 Feedstock AFSD

In this study, the effect of post-deposition heat treatments on an Al-Mg-Si alloy processed with additive friction stir deposition (AFSD), a solid-state additive manufacturing process, is examined. Results reveal that wrought-like microstructure and mechanical properties are achievable in AFSD builds through the application of a post-deposition heat treatment.

The AFSD process has wide applicability and has been demonstrated on a range of materials [40], [41], [64], [66], [68], [208]. Phillips et al. [65] examined the AFSD process parameter window for AA6061 where they determined lower traversing velocities and rotational speed of the tool produced more consistent hardness throughout the build. Additionally, they observed AA6061-T6 β" strengthening precipitates were dissolved out of the matrix due to the elevated temperatures imposed by the AFSD process, yielding a 20% reduction in maximum hardness [65]. This loss of hardness and reduction in tensile strength of AA6061 has also been reported in similar solid-state materials processes such as FSW [99]. Efforts to recover post processing strength have shown that full strength recovery of FSW AA6061 is achievable through post weld heat treatment (PWHT)[102] and that solutionizing combined with aging produced a uniform distribution of □" precipitates [103].

While PWHT of solid-state processing can recover wrought-like mechanical properties, abnormal grain growth (AGG) has been reported [209]. Charit et al. [210] observed that AGG in FSW occurred after heat treatment due to the inhomogeneous deformation pattern created during the process and determined tool rotation rate and traverse rate could eliminate the AGG. Additionally, Attallah and Salem [211] observed lower rotation and higher traverse rates produced a higher probability of AGG. Despite the observation of AGG in PWHT of FSW, AGG was not necessarily detrimental to mechanical performance [209]. Furthermore, recent work by Yoder et al. [212] demonstrated that post deposition heat treatment (PDHT) of AA7xxx processed with AFSD can produce wrought-like properties, however the effect of PDHT on the microstructure including AGG was not reported.

In this present paper, the effect of PDHT on the AFSD as-deposited Al-Mg-Si alloy is characterized. To the best of the authors' knowledge, this study is the first to quantify how a standard PDHT affects the nanostructure, microstructure and mechanical properties of the AFSD as-deposited builds in an Al-Mg-Si alloy. In this work, a multi-layer build of AA6061 is fabricated with AFSD and subjected to a standard heat treatment schedule [213] including full solutionizing and aging.

5.3.1 Materials and Methods

A B8 machine produced by Meld Manufacturing was used to create additive builds using extruded AA6061-T651 feedstock for layer-by-layer deposition onto an AA6061-T6 plate substrate as shown in Figure 5.16. The build deposition (shown in Figure 5.16b) consisted of 33 layers with approximately 1 mm layer thickness. The specific build parameters are as follows: spindle rotation speed of 300 rpm, traversing speed of 127 mm/min, actuator feed rate of 66 mm/min, and build rate of 5mm/min with a featured tool (as displayed in Figure 5.16d). The normal forces observed during AFSD of AA6061 can range from 600-1,000lbf. During the deposition of the AA6061 in our present study, a force of 823 lbf was observed during steady-state deposition. Figure 5.16c displays the relative orientation and spatial location of the tensile specimens machined from the build along the longitudinal direction using wire electrical discharge machining.

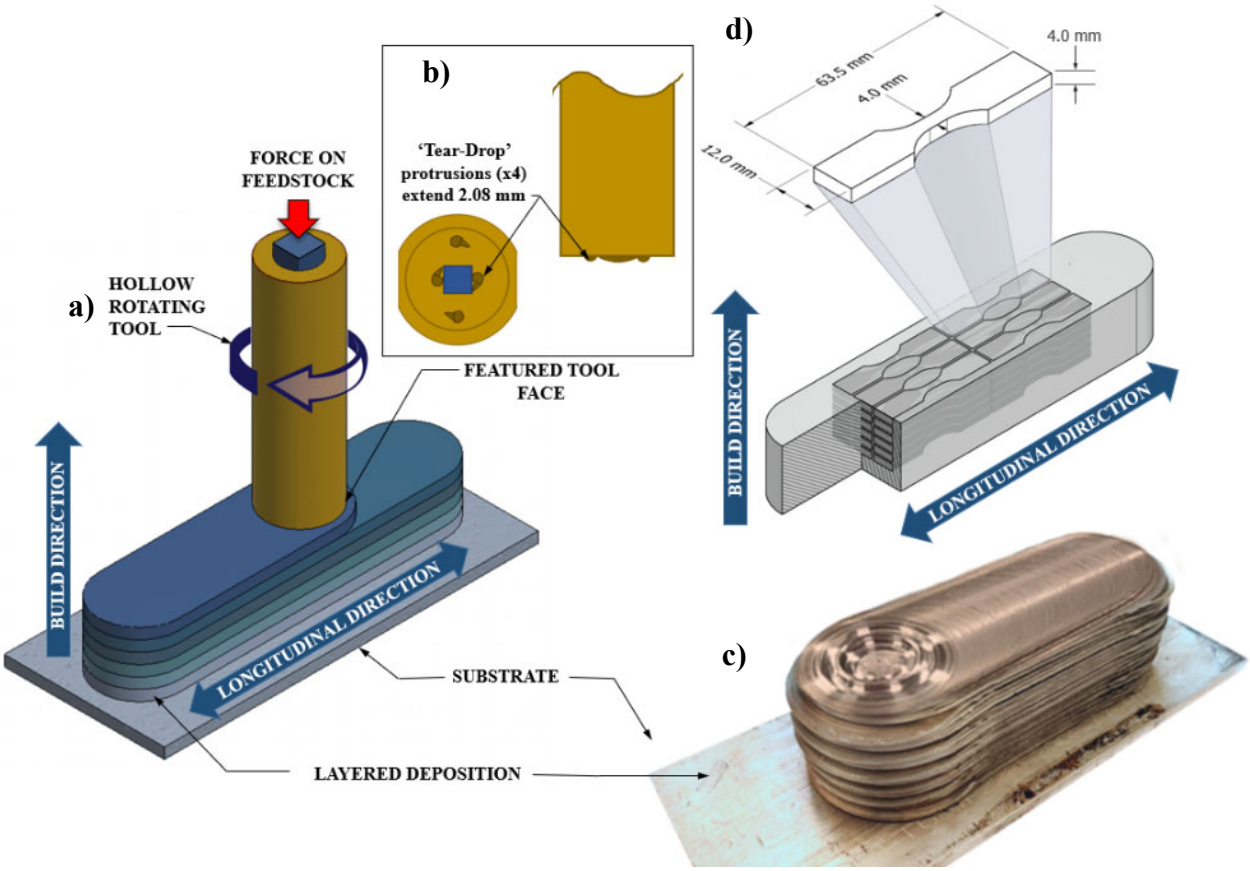

Figure 5.16 (a) AFSD process illustrations representing a featured tool, (b) featured tool face enlargement, (c) representative AA6061 AFSD build on AA6061-T651 substrate, and (d) schematic of specimen geometry and orientation detailing location of specimens within.

Following AFSD processing of the AA6061, PDHT was performed in accordance with ASTM B918-B91820-M Standard [213] for AA6061. First, tensile specimens were solutionized at a temperature of 565°C in an air furnace for 50 min. All specimens were then subjected to an ice water quench after solutionizing. To assess the effect of aging following the solutionization, several specimens were continued through the age hardening process at a temperature of 177°C for a duration of 8 hours.

To understand the effects the various phases of tempering had on the microstructural and mechanical properties of AFSD as-deposited AA6061, specimens were subjected to mechanical testing and microstructural analysis. Monotonic tensile testing was performed in displacement control with an approximate strain rate of 0.001 mm/mm/s using a servo-hydraulic load frame at room temperature. An axial extensometer was used to measure strain at the gage section. A minimum of three specimens were tested for each condition (wrought feedstock, as-deposited, solutionized, and artificially aged) to obtain an average value and uncertainty band of the resultant properties. All tensile specimens were subjected to post-mortem fractography. Metallographic samples extracted from the center of the build in the longitudinal direction were cold-mounted, ground, and polished down to 1mm using a diamond suspension followed by an additional vibratory polish with 0.5 mm colloidal silica to prepare for grain size analysis. Electron backscatter diffraction (EBSD), by means of a Tescan Lyra FIB-FESEM with an EDAX Hikari Super EBSD camera, was used for imaging the microstructure. The wrought AA6061-T651 control and AFSD heat-treated materials were also subjected to hardness testing using a Rockwell-B scale. A cross-section sample for TEM analysis was prepared using an SEM-focused ion beam (FIB) FEI Quanta 3D dual beam equipment, where Ar-ion milling in a Gatan precision ion polishing system (PIPS) was used to produce electron transparent thin specimens. An acceleration voltage of 30 kV was used during the FIB milling process. An acceleration voltage of 0.5 kV, incident beam angle of 5° and milling time of 45 sec were used in PIPS milling process for final thinning of the specimens. An FEI Tecnai F-20 TEM at 200 kV was used to obtain the bright field images.

5.3.2 Results and Discussions

Figure 5.17 displays the representative grain structure associated with each treatment stage observed in this study – wrought AA6061-T651 control, as-deposited (AD), solutionized/quenched (SQ), and solutionized/ quenched/ artificially aged (SQA). Shown in Figure 5.17a-b, dynamic recrystallization of the AFSD process caused a significant refinement in grain size from wrought to AFSD AD, reducing on average from 100 μm to 20 μm. After the SQ process, AGG developed as evident in Figure 5.17c. The SQA specimen also exhibited AGG along with refined grains (Figure 5.17d). Note that the orientation of the cross-sectional planes relative to the wrought feedstock and AFSD builds are indicated in Figure 5.17.

Figure 5.17 Representative grain size through use of inverse pole figure maps for (a) extruded wrought AA6061-T651 control samples, (b) AFSD AD, (c) AFSD SQ, and d) AFSD SQA.

Figure 5.18(a-c) displays the images of wrought AA6061-T651, AFSD AD material as well as heat treated AFSD material as characterized using TEM. The β" needlelike precipitates that can be observed in the wrought material (Figure 5.18a) are no longer present in the AFSD AD material (Figure 5.18b). Only the Mg-Si clusters are present as is expected due to the high temperatures (70-90% of the melting point) that occur during the AFSD process. Figure 5.18c displays the return of the numerous and evenly dispersed, needle-like β" precipitates that were re-precipitated during the SQA heat treatment process. These precipitates exhibited an average length of 46.7 nm and an average thickness of 4.13 nm.

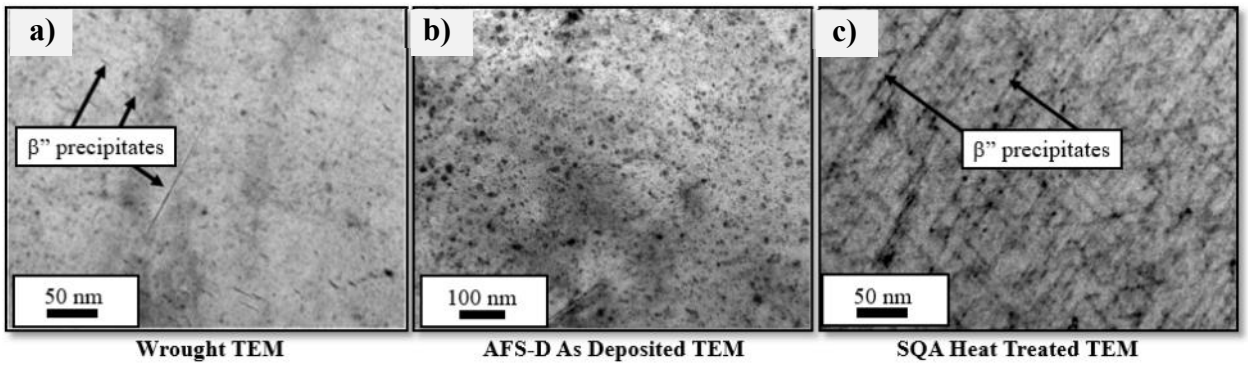

Figure 5.18 TEM bright field images show a) wrought AA6061-T651 control with strengthening precipitates, b) AFSD AD without strengthening precipitates and c) precipitates returning after heat treatment to AFSD AA6061

Figure 5.19 shows the results of the monotonic tensile tests along with representative SEM fractography displaying representative fracture surfaces. During the AFSD process, the wrought material undergoes microstructural changes including the dissolution of β" precipitates. The AFSD AD material exhibits a 47% reduction in the ultimate tensile strength as compared to the wrought material. Rutherford et al. attributed the increase in elongation to failure observed to the lack of dislocation pinning β", allowing for increased dislocation motion to occur.[67]. After SQ, the AFSD material regains 58% of strength at the loss of 10% ductility, despite the presence of AGG. After SQA, the strength and hardness characteristic of a T651 temper were realized due to the re-precipitation of the strengthening phases, ", as displayed in Table 5.3.1. Because AA6061 is a heat treatable alloy, the strength relies more on the growth of the strengthening precipitates that evolve during the PDHT. As displayed in the representative fracture surfaces, ductile fracture is the observed failure mode with characteristic dimples (primary and secondary voids) visible in each specimen. The dimples in the AFSD AD material (Figure 5.19b) exhibit fine and shallow features with some coalescence observed. After SQA, an increased damage rate due to the presence of increased primary void growth and coalescence is evident in Figure 5.19e.

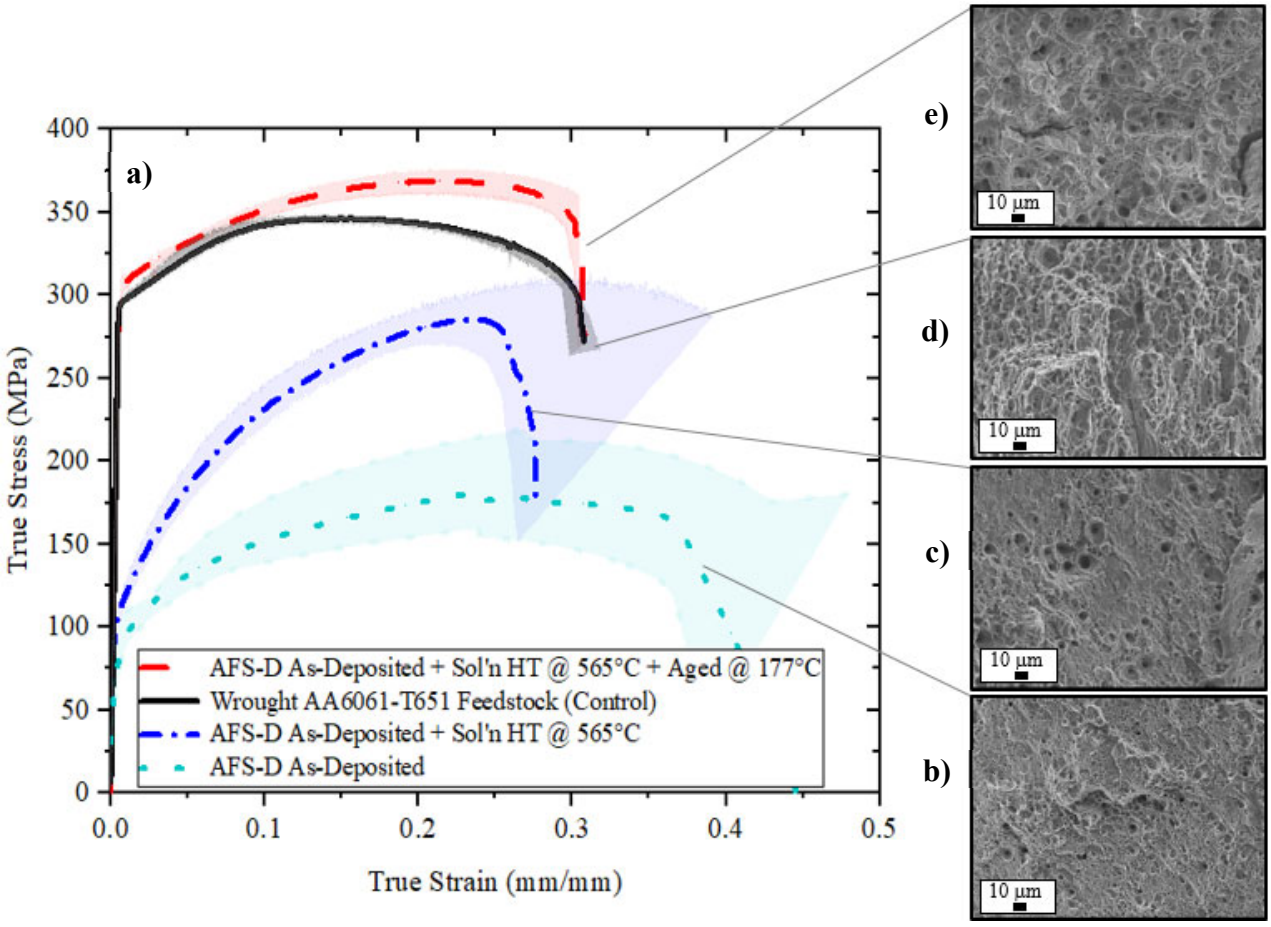

Figure 5.19 Experimental true stress-strain tensile test results of averaged wrought AA6061-T651 (3 specimens), AFSD AD (3 specimens), AFSD SQ (3 specimens), and AFSD SQA (4 specimens) with (b-e) representative fracture surfaces.

Table 5.3.1. Material properties as determined through true stress/strain relationships showing that HT of deposited material is able to obtain properties similar to T651 HT.

Material	Treatment	Elastic Modulus (GPa)	0.2% Offset Yield Strength (MPa)	Ultimate Tensile Strength (MPa)	Elongation to Failure (%)	Hardness Range (Rockwell-B Scale)
AA6061	Wrought T651 Control	61 +/-1	296 +/-2	351 +/-2	31 +/-2	57 +/-4
	AFSD AD	42 +/-3	114 +/-2	185 +/-22	37 +/-11	___
	AFSD Solutionized at 565°F (50 min)	46 +/-5	147 +/-9	292 +/-19	33 +/-6	___
	AFSD Solutionized at 565°F (50 min) + Artificially Aged at 177 °C (8 Hrs)	62 +/-4	320 +/-2	371 +/-7	31 +/-3	67 +/-6

5.3.3 Conclusions

This study presents for the first time the influence of a standard PDHT on the nanostructure, microstructure, and mechanical properties of AA6061 processed via AFSD.

AFSD process produced refined grains due to dynamic recrystallization. Grain refinement remained after SQ, but AGG was observed after SQ and remained in SQA.

Tensile tests revealed ductile failure modes for all specimens. AFSD AD material resulted in a 47% reduction in ultimate tensile strength due to the dissolution of β”, allowing for increased dislocation motion. SQ yielded a 10% reduction in ductility and 58% improvement in ultimate tensile strength over AD. SQA resulted in strength, hardness, and ductility characteristic of a T6 temper with the regrowth of β” precipitates.

While AGG has been observed in other research to have a deleterious effect on strength and ductility, that was not observed for the artificial aged AFSD specimens, herein, the β” precipitates due to PDHT proved to play a more critical role to the strengthening mechanisms of AFSD AA6061.

The results from this work indicate that despite the AGG, PDHT increases the AD strength, hardness and ductility, producing peak aged mechanical behavior. In particular, we observed an 8% increase in yield and 6% in ultimate strength compared to the control.

5.4 Effect of New AA6061 Feedstock AFSD Processing on the As-Deposited Tensile and Fatigue Performance Capturing Orientation Behavior by Microstructure Sensitive Fatigue Modeling

This work presents, for the first time, an in-depth investigation of the structure-property-fatigue relationships of an Al-Mg-Si alloy (AA6061) processed via Additive Friction Stir Deposition (AFSD). As industry focus continues to shift for more efficient and lightweight structures, the need for quantitative studies on the cyclic performance of additively manufactured materials are needed. In this study, the AFSD processed AA6061-T6 was machined into specimens in two orthogonal orientations and subjected to monotonic and strain-controlled fatigue testing. The microstructural features of as-deposited AA6061 exhibited evidence of dynamic recrystallization and grain refinement. In addition, significant reduction of the intermetallic particles was observed after AFSD processing. The fatigue results demonstrate that the as-deposited material, particularly the longitudinal direction, exhibited similar fatigue performance to wrought AA6061-T6 in both low cycle and high cycle fatigue regimes, which is a promising result for additive manufactured material in the as-deposited condition. In contrast, as-deposited build direction orientation possessed slightly lower fatigue resistance than the wrought feedstock material. The AFSD material was observed to exhibit different damage mechanisms from porosity-based damage mechanisms observed in fusion based additively manufactured materials. Lastly, a microstructure-sensitive fatigue model was employed to capture the fatigue effects of the AFSD processing on the AA6061.

5.4.1 Materials

The feedstock material used in this study was rolled AA6061-T651 that was machined using a water jet into dimensions of 9.5 mm x 9.5 mm x 304.8 mm in order to fit into the hollow opening of the AFSD tool. A multi-layer deposition build was produced using parameters of 300 RPM spindle rotation speed, 127 mm/min traversing speed, 66 mm/min actuator feedrate, 5 mm/min Z velocity, and 1 mm layer thickness. We note that these set of AFSD build parameters were chosen based on the results of a prior study [65], where these parameters produced the most uniform hardness throughout the deposition.

5.4.2 Test Specimens and Experimental Methods

The geometry of the test specimens used in this work is presented in Figure 5.20. The specimens were machined via wire electro-discharge machining (EDM) from the deposition in two different spatial orientations in order to quantify any orientation dependence due to anisotropy in the as-deposited AFSD material. For this study, the specimens were machined directly from the deposition with no post-processing carried on the specimens or the deposition. The orientation and location of each specimen was labelled as the specimens were machined, such that every specimen could be traced back to where it was in the deposition prior to machining. The layout of the specimen's orientation is also shown in Figure 5.20. The specimens oriented with the long axis parallel to the long axis of the build will be referred to hereafter as the longitudinal direction, while the specimens oriented with the long axis perpendicular to the layers will be referred to as the build direction. In order to reduce the effect of surface roughness on the fatigue performance of the specimens, all fatigue specimens were mechanically ground and polished. The polishing procedure started at relatively low grit (~300) SiC paper and progressively increased to 2000 grit SiC paper.

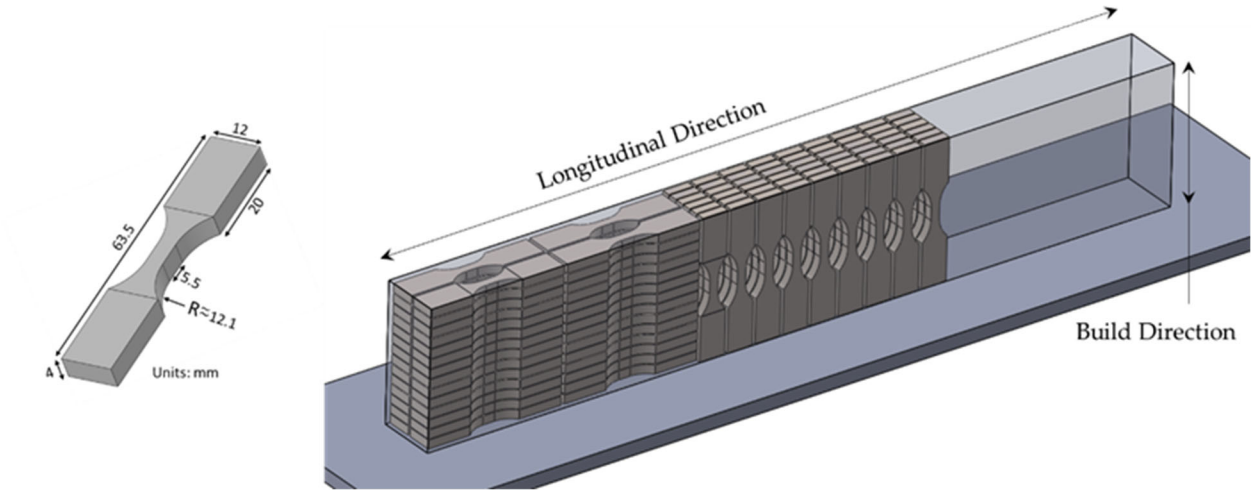

Figure 5.20 Sample geometry and layout from within the AFSD build.

Both the monotonic and fatigue experiments were carried out on a servo hydraulic load frame. The tests were conducted in lab air at room temperature. The monotonic tests were conducted in the quasi-static condition under displacement control with a strain rate of 0.001 mm/mm/s. Strain was measured using a 5 mm extensometer. Three data sets were generated: one from the wrought feedstock, one from samples oriented in the longitudinal direction of the as-deposited AFSD material, and one from samples oriented in the build direction of the AFSD deposition. The directions have been denoted on Figure 5.20. Every strain amplitude for every data set was tested on three samples to increase statistical confidence in the results. Fatigue testing was performed under a strain-control, fully-reversed (R = -1) condition until the hysteresis response of the material stabilized. The loading frequency for the strain-control portion of the test was 1 Hz. Once a stable hysteresis response was reached, the experiment was continued in load control using the stable hysteresis data to determine the loading parameters until the sample completely fractured. The loading frequency of the load-control portion of the test was kept at 1 Hz for specimens tested at 0.4, 0.5, and 0.6%, but was increased for specimens tested at 0.2% (20 Hz) and 0.3% (5 Hz). The change in frequency was made in the interest of time to conduct a fatigue test. The criterion used for determining stabilization was to run at least 1,000 cycles in strain control. Also note, in the tests at 0.6% the majority of the life is strain-controlled. Only for 0.4, 0.3, and 0.2% strain amplitude tests are the percentage of the life under strain-control less than 50%. It is worth mentioning that these tests were dominated by an elastic stress response that generally did not vary much after the first few hundred cycles. As such, a load-control test, which can be conducted at a much higher load frequency, was deemed acceptable.

Post-mortem fracture samples were prepped for SEM by mounting them to an observation stage via carbon tape and grounding the sample with copper tape to prevent charging during observation. The SEM used for fractography in this work was a TESCAN LYRA3 field emission SEM. Samples for microstructural analysis were ground and polished incrementally to a 1 μm diamond suspension polish that was followed by a vibratory polish using 0.5 μm colloidal silica. The grain size analysis was performed in compliance with the guidelines set forth in ASTM 2627-13 [214]. EBSD analysis was performed on a TESCAN LYRA3 field emission SEM with an EDAX Hikari Super EBSD camera.

5.4.3 Results and Discussion

Microstructure

The evolution of the grain size in AA6061-T651 due to the AFSD process is shown in the EBSD maps in Figure 5.21. In Figure 5.21, the orientation is denoted in the corner of each plane with XS representing the short transverse, LT representing the longitudinal direction, and BD representing the build direction. The microstructure associated with the build parameters used in this study have been demonstrated to exhibit a refined, equiaxed grain structure with predominantly high-angle grain boundaries as reported in a prior study [65]. The presence of refined, equiaxed grains and high-angle grain boundaries is indicative of dynamic recrystallization (DRX) as reported in a study on friction stir welded AA6061 by Feng and co-workers [101]. The refinement of the grain size is reported to be on the order of 93% reduction from 200 μm in the feedstock to 15 μm in the as-deposited material [65]. Likewise, transmission electron microscopy (TEM) and selected area electron diffraction (SAED) revealed complete dissolution of the strengthening β" precipitates [65], which is in agreement with Feng's study on FSW AA6061 [101]. It is important to note that 6xxx-series aluminum alloys, particularly alloys with magnesium and silicon as the major alloying elements, utilize precipitation hardening as a strengthening mechanism [215]. The alloying elements present in a given alloy, such as magnesium, silicon, iron, manganese, etc. influence the formation of intermetallic phases in the alloy [216]–[218]. The chemical composition of some coarse intermetallic phases have been identified as Al_7Cu_2Fe, Al_5FeSi, $Al_{12}(Fe,Cr,Mn)_3Si$, and Mg_2Si, which is the stable β phase and as such an intermetallic of particular interest [219]–[222].

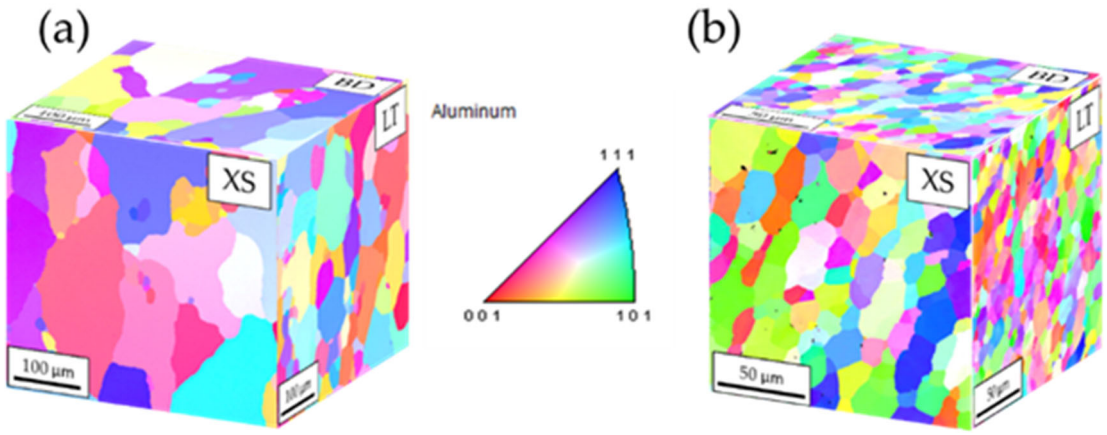

Figure 5.21 Isometric view of EBSD maps of (a) AA6061-T651 feedstock and (b) as-deposited AFSD AA6061 with equiaxed grains.

One inherent characteristic of AFSD is the refinement of the microstructural features, e.g. grain size, from the feedstock. This is similar to what is commonly observed in FSW, however, the AFSD material is analogous to the NZ in FSW. Avery et al. [21] observed the reduction in the average size and volume fraction intermetallic particles, which is attributed to severe plastic deformation of the AFSD process in refining the carbides into smaller particles. In particular, the size distribution for particles processed with AFSD was reported to be approximately 15 μm^2 while the feedstock was reported to be a size of approximately 55 μm^2 at the larger extreme tail of the size distribution [39]. Similarly, in the present study, the as-deposited AFSD and feedstock AA6061-T651 specimens were polished and observed under an SEM. The results of the SEM back-scatter electron (BSE) images for the AFSD and the feedstock are shown in Figure 5.22. Figure 5.22 (a) shows a 1500x BSE of the AFSD as-deposited sample while Figure 5.22 (b) shows a 5000x BSE of some particles in the AFSD sample. Figure 5.22 (c) shows the particles in the wrought AA6061 feedstock at 1500x using a BSE detector. Lastly, Figure 5.22 (d) shows a normal distribution curve of the constituent particle size in both as-deposited and feedstock specimens. These results show a similar particle refinement behavior to what was reported by Avery et al. [39], although the constituent particles in the feedstock of AA6061 were smaller than the carbide particles observed in the Inconel feedstock. The particles seen in the as-deposited material were generally spherical with no preferred orientation, while the wrought feedstock possessed larger, more amorphous intermetallic particles oriented randomly. This finding also suggests that the refinement of microstructural features, including defects, is inherent to the AFSD process and not material or alloy specific, although more material systems will need to be examined to verify this hypothesis. Table 5.4.1 shows the average particle size and standard deviation of the particle sizes in the wrought and as-deposited AFSD 6061 aluminum alloy. Table 5.4.1 also calculates the average particle size + and – half the standard deviation, which will be used in the modeling portion discussed later.

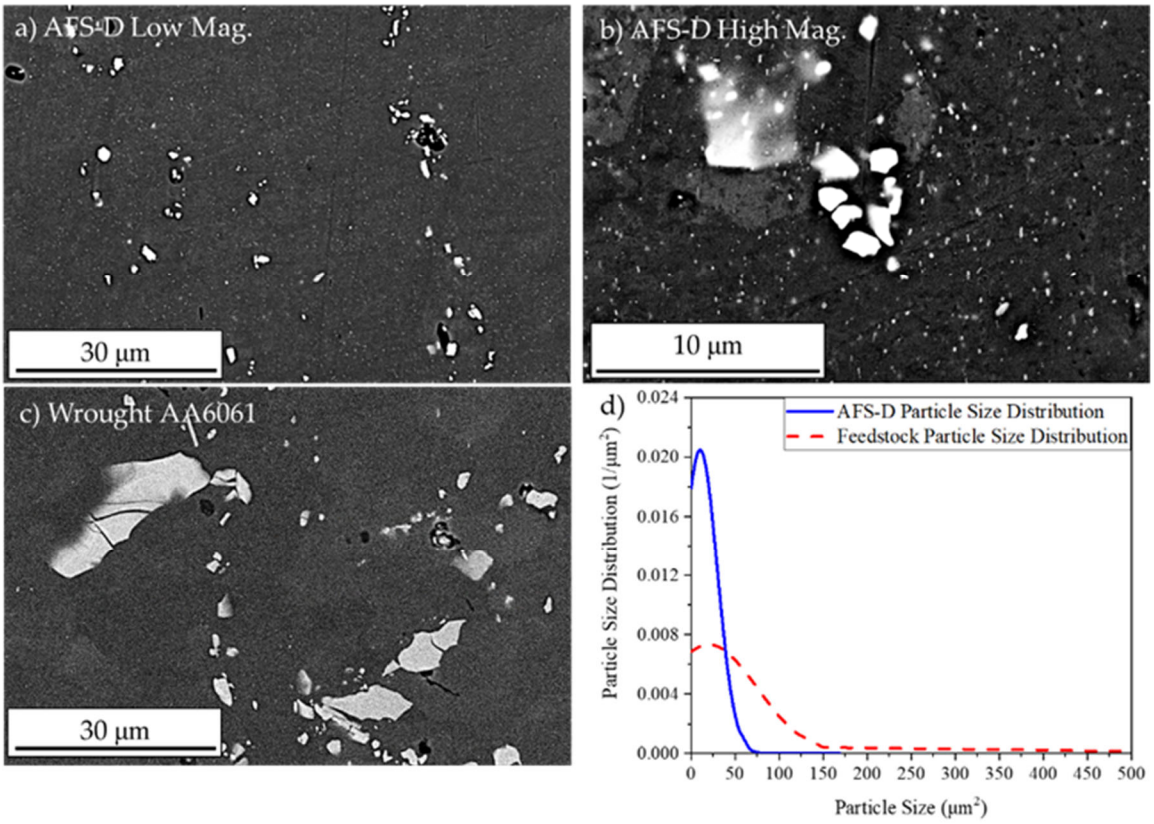

Figure 5.22 (a) AFSD back-scatter electron (BSE) image showing iron rich particles generally spherical in nature, (b) 5000x magnification BSE image of a cluster of particles in the AFSD, (c) wrought AA6061-T651 feedstock BSE image with larger, amorphous iron intermetallic particles, and (d) a normal distribution contrasting the sizes of the iron particles in the AFSD and feedstock materials.

Table 5.4.1. Average and standard deviation from particle distribution for wrought and as-deposited AFSD AA6061.

Material	AFSD (µm)	Wrought (µm)
Average Particle Size (Avg.)	2.89	4.10
Standard Deviation (Sdev.)	2.20	3.04
Avg. + 0.5*Sdev.	4.00	5.62
Avg. - 0.5*Sdev.	1.79	2.58

Monotonic Tensile Results

The results from the monotonic testing are presented in Figure 5.23. Each curve in Figure 5.23 is the averaged curve of the three discreet data sets with the error bars shown. As expected, the precipitation hardened feedstock experienced significantly higher strength than either of the as-deposited orientations with a yield and ultimate strength more than double the ultimate strength of either as-deposited orientations. The feedstock also exhibited a lower elongation to failure of approximately 34%. The as-deposited material exhibited a mostly isotropic mechanical behavior. Both the longitudinal and build direction have yield and ultimate tensile strengths that are within one standard deviation of the other as-deposited orientation. Additionally, both as-deposited orientations exhibit strength comparable to that of wrought AA6061-O, which makes sense based on the dissolution of the β" strengthening phases. In terms of elongation to failure, the longitudinal possessed the most ductile behavior at 60% while the build direction demonstrated an average elongation of approximately 45%. We note that the as-deposited longitudinal experimental results exhibited the largest error bars, and that is because of one specimen behavior performing anomalously. One of the longitudinal specimens taken from the very top surface of the build exhibited significantly higher strength than the other longitudinal specimens. This is likely due to the top layer experiencing the least thermal cycling and thus the least amount of dissolution of the strengthening phases. However, additional research is needed to understand the extent of spatial location on mechanical strength in the AFSD builds. The strength values (yield and ultimate) of the feedstock and as-deposited orientation is presented in Table 5.4.2.

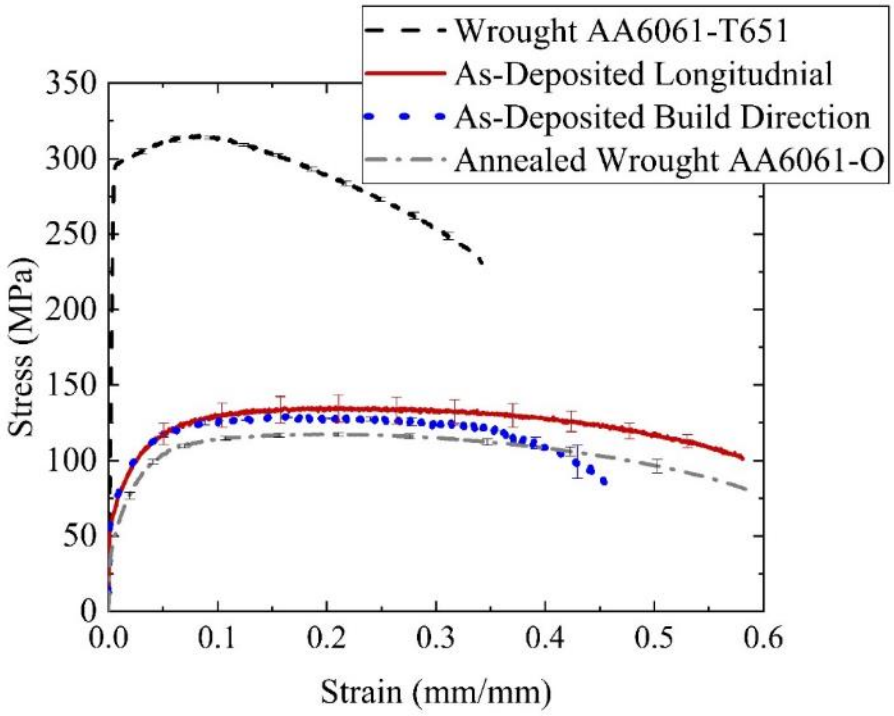

Figure 5.23 Monotonic stress-strain curve of wrought AA6061-T651, AFSD AA6061 as-deposited longitudinal direction, AFSD AA6061 as-deposited build direction, and the annealed wrought AA6061-O.

Table 5.4.2: Monotonic strength properties for feedstock and as-deposited AFSD material.

Material and Orientation	Yield Strength (MPa)	Ultimate Tensile Strength (MPa)
As-Deposited Longitudinal	61.3 ± 6.4	137.1 ± 14.8
As-Deposited Build Direction	63.9 ± 2.7	129.9 ± 3.5
Wrought AA6061-T651	295.8 ± 1.8	316.5 ± 2.2
AA6061-O	39.7 ± 0.2	118.1 ± 2.4

Effect of Thermomechanical Processing on Monotonic Behavior

The monotonic tensile curve of the as-deposited AA6061 presented in Figure 5.23 demonstrated significantly lower strength than the feedstock material. This result is expected behavior based on the evolution of the microstructure inherent in the thermomechanical processing of the AFSD process, due to the dissolution of Mg and Si into clusters within the material matrix [65], where the primary strengthening mechanism of AA6061 is fine β" (Mg_2Si) precipitates [223]. In addition to the lower strength in the as-deposited material due to the lack of dislocation pinning β" precipitates, the ductility of the as-deposited material in terms of elongation to failure is greater than what is observed in the feedstock [169]. This phenomenon may also be attributed to the lack of β" particles as the dislocations are allowed to move much more freely throughout the matrix. The annealing process for AA6061 per the ASM Handbook vol. 4 [224] is 2 – 3 hours are 415 °C. While the exact temperature of the AFSD process is unknown at this time, some unreported thermal measurements show the temperature is higher than 490 °C. Therefore, the as-deposited material in this study was subjected to thermal cycles in excess of 490 °C for several layers, although each layer deposition only took several minutes to complete. The as-deposited material also exhibited significant strain hardening, which suggests DRX occurs during the AFSD process, as a low dislocation density is a characteristic of DRX and would allow for extensive strain hardening during monotonic loading.

Strain-Control Fatigue Results

Figure 5.24 shows the results from the strain-controlled fatigue tests of the AA6061-T651 feedstock, AFSD as-deposited longitudinal direction, and as-deposited build direction. Similar to the tensile results, the wrought AA6061-T651 experimental fatigue data is included as a reference, as the as-deposited material is quite different in terms of strengthening precipitates to the wrought feedstock. At the highest strain amplitude tested, the fatigue performance of the as-deposited material was on the order of about 1,000 cycles for both orientations. Specifically, at the strain amplitude of 0.6%, the longitudinal direction exhibited cycles to failure that were only slightly higher than the build direction material. Similarly, the strain amplitude of 0.5% revealed both as-deposited orientations experienced similar fatigue lives. For the lower strain amplitudes tested, and in particular the 0.3% strain amplitude, the as-deposited build direction exhibited fewer cycles to failure than the as-deposited longitudinal orientation. Furthermore, it is noteworthy that the as-deposited longitudinal samples experienced run-outs (defined as $5x10^6$ cycles in this study) in all samples tested at 0.2% strain amplitude.

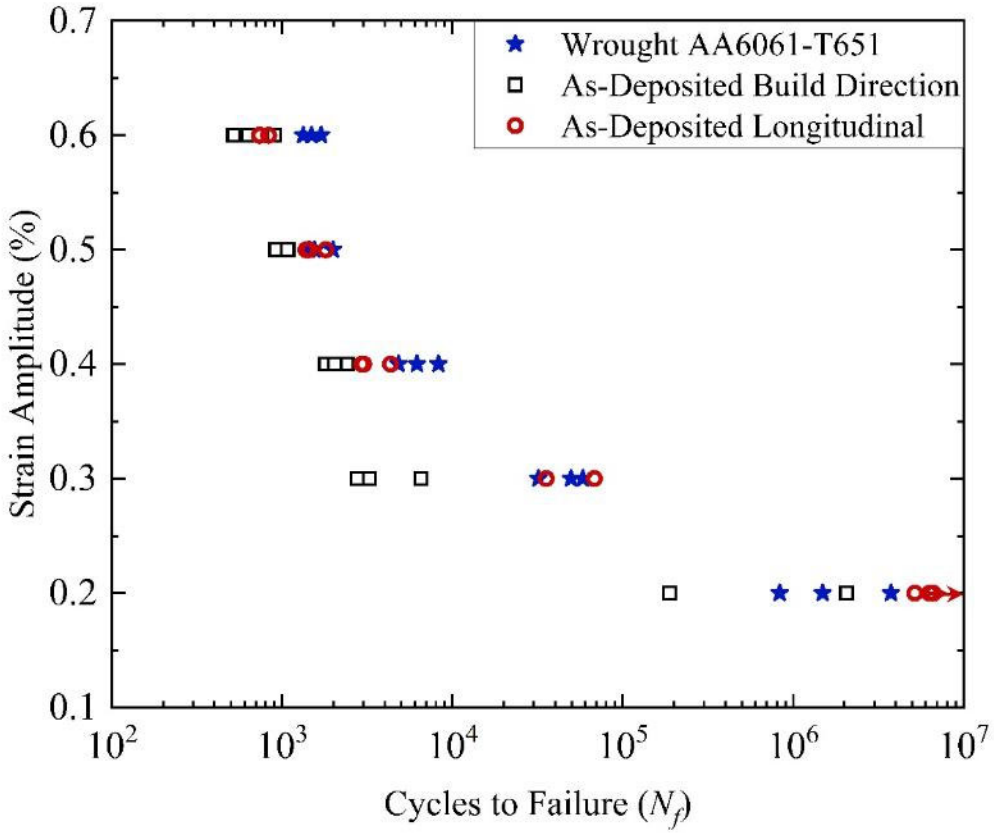

Figure 5.24 Strain amplitude versus cycles to failure plot of the AA6061-T651 feedstock, AA6061 AFSD as-deposited longitudinal direction, and AA6061 AFSD as-deposited build direction.

Figure 5.25 shows the evolution of the stress amplitude in response to two different applied strain amplitudes for wrought AA6061, as-deposited longitudinal, and as-deposited build direction. The 0.5% AFSD longitudinal direction (the gray stars) and the 0.5% AFSD build direction (the hollow blue triangles pointed right) did not stabilize. However, the fraction of the fatigue life for the 0.5% longitudinal is 73% and the 0.5% build direction sample failed at 914 cycles. The 0.5% wrought AA6061 cyclically softened but had stabilized by 1000 cycles. The fraction of the fatigue life under strain control was 65%. The 0.3% wrought AA6061, 0.3% AFSD longitudinal, and the 0.3% AFSD build direction all stabilized by the 1000 cycles.

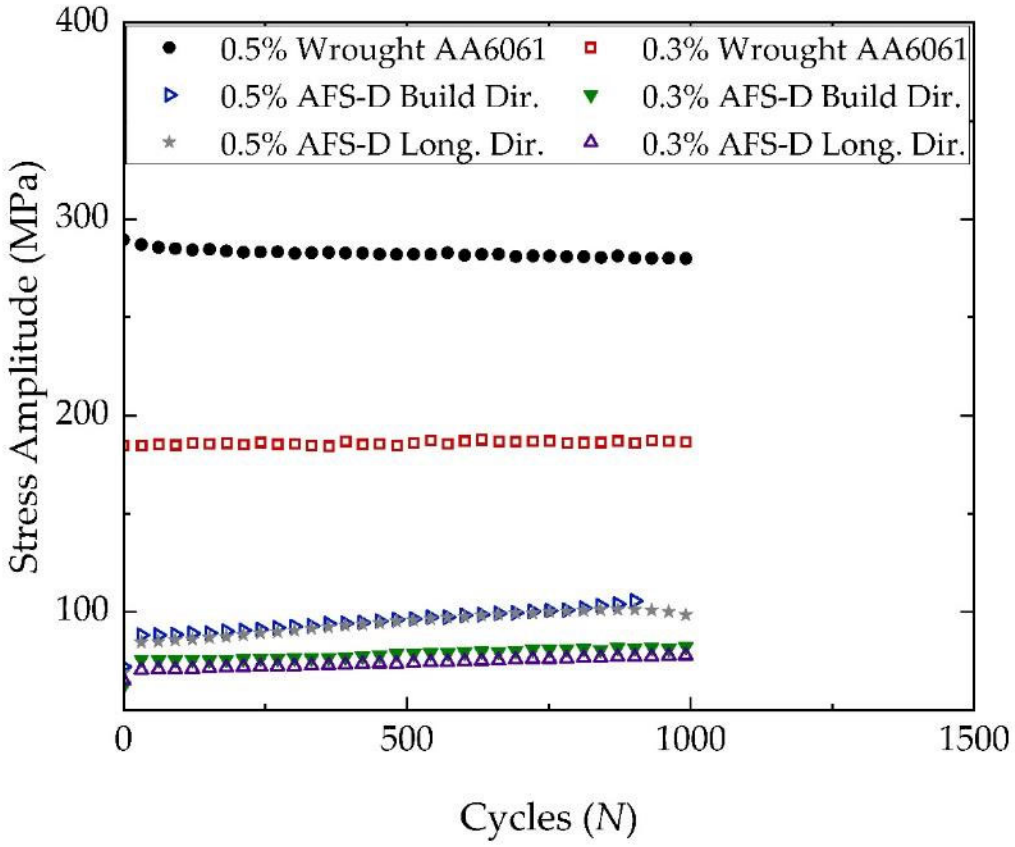

Figure 5.25 The evolution of the stress amplitude response to deformation for wrought AA6061-T651, as-deposited longitudinal direction AA6061, and as-deposited build direction AA6061 for specimens tested at 0.3 and 0.5%.

Post-Mortem Analysis of Fatigue Fracture Surfaces

Figure 5.26 shows representative fractography of the as-deposited fatigue specimens. The fractured surface shown in Figure 5.26 (a) and (b) was an as-deposited build direction specimen tested at ε_a = 0.3% and experienced a fatigue life of N_f = 6,505 cycles. The fracture surface exhibited evidence of multiple crack initiation sites noticeable in Figure 5.26 (a) where river patterns leading back to several areas can be seen. These areas include the lower left corner, the middle of the bottom surface, the top left corner, and the area in the top right to top middle region. There is no evidence of a fish eye type fracture in any samples investigated meaning both orientations of as-deposited and the feedstock experience crack initiation at near surface defects in the material. Figure 5.26 (b) shows an initiation region in the upper left corner crack initiation region from Figure 5.26 (a), where a void is observed that was likely caused by the fracturing of a particle that subsequently fell out of the specimen upon fracture. The parameters used in this study were identical to one set of parameters used in a study on the same material on the same AFSD machine [65]. That study reported fully dense depositions made with the same parameters, therefore the void likely developed as a result of the deformation that resulted from cyclic loading. Figure 5.26 (c) and (d) exhibit a fracture surface from an as-deposited longitudinal direction AFSD specimen tested at ε_a = 0.3% and experienced a fatigue life of N_f = 67,983 cycles. Figure 5.26 (c) shows crack initiation occurred from multiple initiation sites along the left surface and propagated across the surface of the specimen until final fracture occurred. The dark region show in Figure 5.26 (d) shows broken particles in the vicinity of the initiation on the surface of the specimen.

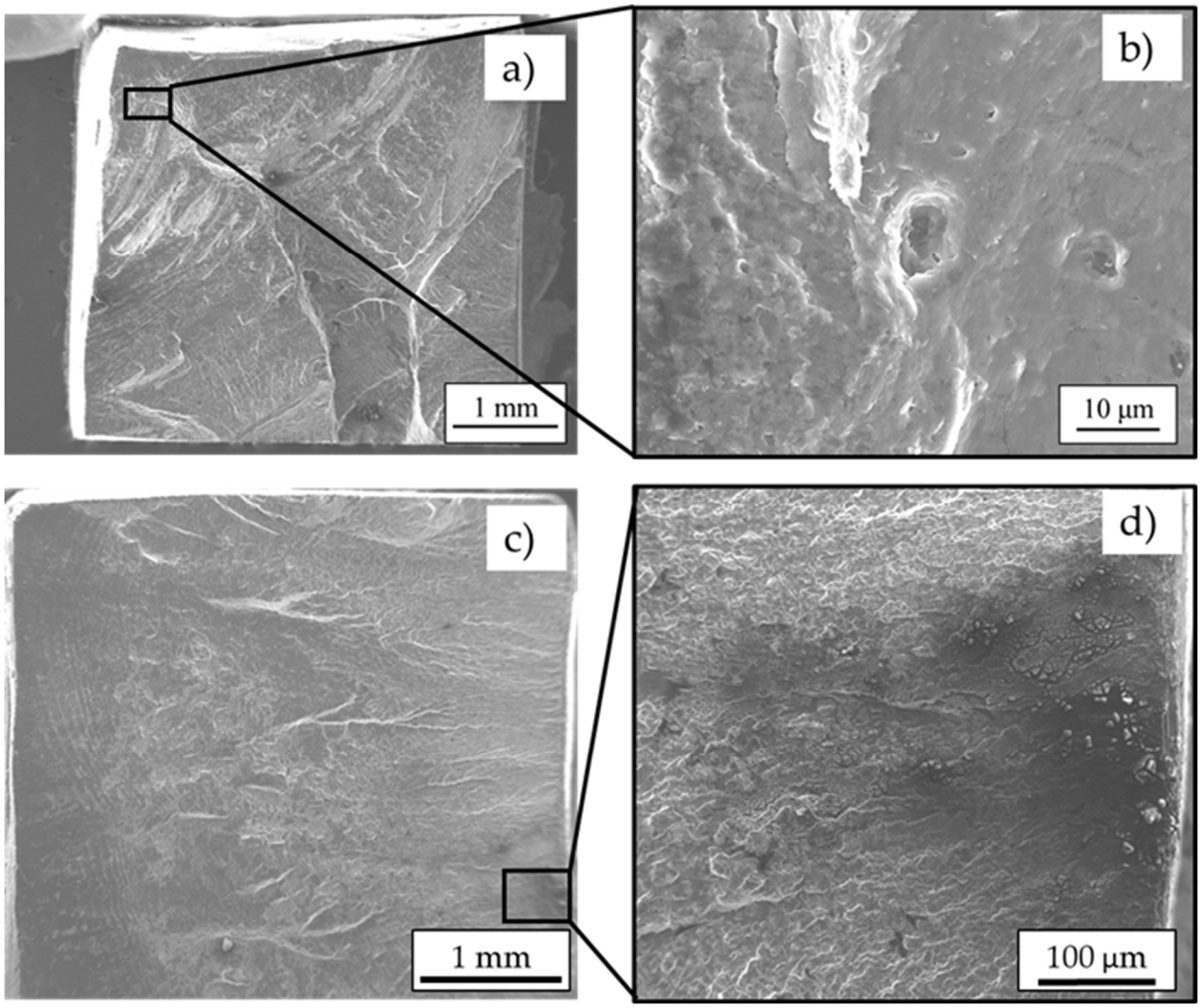

Figure 5.26 Fracture surface of (a) AFSD as-deposited build direction sample tested at εa = 0.3% (Nf = 6,505 cycles) with (b) high magnification view of a crack initiation site, and fracture surface of (c) AFSD as-deposited longitudinal direction sample tested at εa = 0.3% (Nf = 67,983 cycles) with (d) higher magnification view of crack initiation site.

MSF Model Results and Discussion

The results from the MSF model for the AFSD as-deposited longitudinal direction model correlation is provided in Figure 5.27 (a), and the AFSD as-deposited build direction model correlation is shown in Figure 5.27 (b). In both fatigue modeling results, the higher strain amplitude fatigue lives are dominated by small crack growth after a brief incubation stage. Likewise, all fatigue modeling results experienced incubation dominant fatigue behavior when subjected to lower strain amplitudes. The parameters used for the model fits of the longitudinal and build direction data are recorded in Table 5.4.2. In addition, it is important to note that the initial selection of the MSF model parameters where taken from a study of AA6061 conducted by McCullough et al [225]. By adjusting the material constants in the MSF model to fit the measured values from this study, such as Modulus of Elasticity, grain size, particle size, etc., as well as being informed by the constants in the study by McCullough et al. [225], such as crack tip displacement threshold for AA6061, MSF model fits were generated for each data set: wrought, AFSD as-deposited longitudinal, and AFSD as-deposited build direction. The parameters used for the model fits of the longitudinal and build directions are reported in Table 5.4.3 at the end of this section.

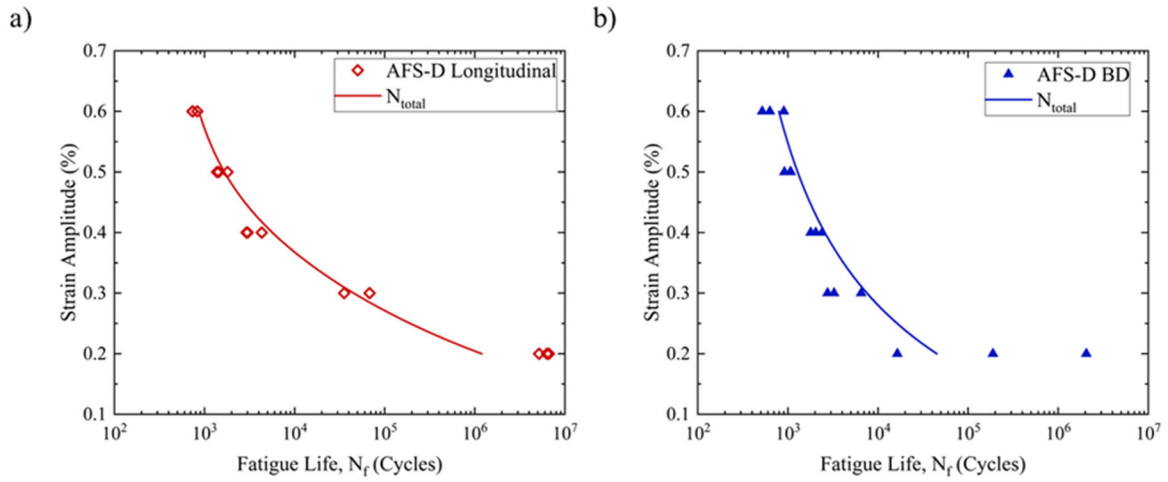

Figure 5.27 MSF model fit for (a) AFSD as-deposited AA6061 in the longitudinal direction and (b) AFSD as-deposited AA6061 in the build direction.

Figure 5.28 shows the contributions of the incubation (INC) and the microstructurally small crack growth and physically small crack (MSC/PSC) growth stages of the MSF model for (a) the longitudinal direction AFSD AA6061 and (b) the build direction (BD) AFSD AA6061. In each plot, the dotted line represents the INC contribution and in each condition the INC stage has less of an effect as the applied strain amplitude increases. However, as the strain amplitude becomes smaller, more of the fatigue life is controlled by the INC stage. This seems reasonable, as smaller strain amplitudes would need more cycles to progressively accumulate the local plastic strain needed to initiate a crack compared to larger applied strain amplitudes. As a result, in the presence of the larger strain amplitudes, the incubation stage occurs at lower number of cycles and the remaining life is dominated by the MSC/PSC stage, which is represented by the dashed line in each plot. The MSC/PSC contribution of the fatigue life tends to dominate the large strain amplitudes for the AFSD process materials observed in this study, and contributes a lower percentage of the total life in the lower strain amplitudes. Again, this seems reasonable as the number of cycles spent in MSC/PSC stage increases with lower strain amplitudes, but still at a rate lower than the INC stage. In addition, it is important to note that the INC stages tends to dominate the lower strain amplitudes of the AFSD processed materials. Due to the relatively small size of the specimens used in fatigue testing, the LC contributions to the fatigue life were negligible. By the time the crack grew to a length that would qualify as LC the specimens in the higher strain amplitudes had failed already, while the specimens tested under lower strain amplitudes experience only a few cycles of the LC stage before failure.

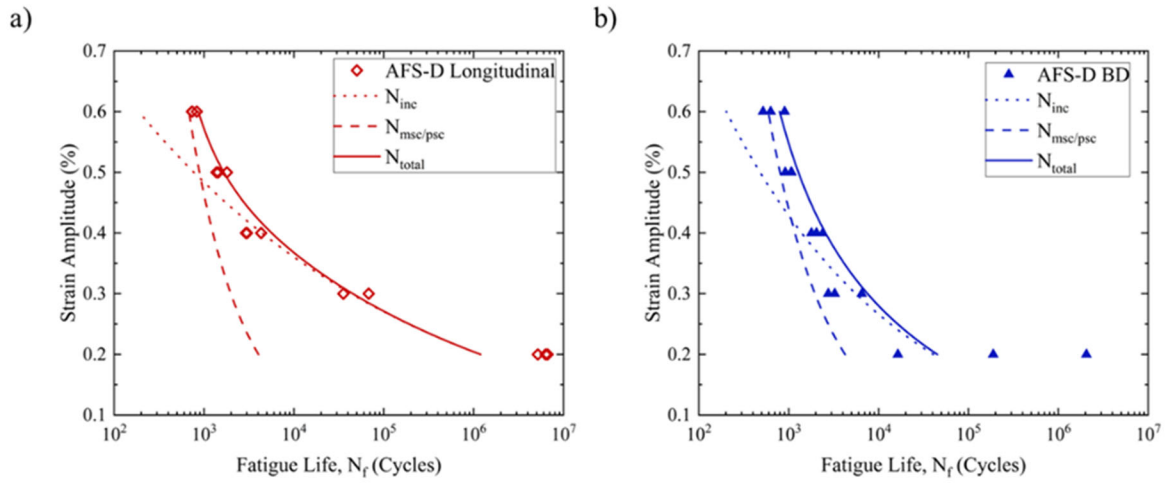

Figure 5.28 MSF model plots of the incubation and small crack growth contributions to the total fatigue life prediction for (a) AFSD AA6061 in the longitudinal direction and (b) AFSD AA6061 in the build direction.

Fatigue performance, particularly in the range of 10^5 cycles or more, is greatly affected by particle size within the sample. All other concerns being equal, a larger particle, when fractured due to mechanical loading, will release more energy than a smaller particle resulting in a larger stress intensity factor (SIF), and is therefore more likely to nucleate a fatigue crack, and will do so in fewer loading cycles than a smaller particle, the smaller average particle size coupled with the smaller standard deviation in the as-deposited material than the wrought results in a narrower distribution band of particle sizes.

This observation is likely the cause of the longitudinal as-deposited AA6061 performing with higher number of cycles to failure than the wrought AA6061-T651 at the strain amplitude of 0.2%, which would be otherwise expected to outperform the as-deposited material on account of the superior strength of the wrought samples. Additionally, the refined grain size inherent to the AFSD process also contributes to the performance of the AFSD as-deposited material, as a smaller grain size tends to provide better resistance to crack nucleation.

The effect of particle size on the fatigue behavior of AA6061 as-deposited material was then used to bound the total fatigue life fits of the MSF model on an upper and lower model prediction. To calculate the bounds, the only parameter varied in the model was the parameter for particle size, which was varied by ± ½ standard deviation based on characterization shown in Figure 5.22. The values of the averages and standard deviations used to make the upper and lower bounds are provided in Table 5.4.1. The bounded MSF model correlations are shown in Figure 5.29 for (a) longitudinal direction and (b) build direction. As can be seen, the effect of particle size in the MSF model can be used to account for the scatter observed in the longitudinal and build direction experimental fatigue results. A noteworthy finding from the results is that both the longitudinal and build direction data sets skew toward the lower bound. This makes sense in that the largest particle in a sample will likely exert the greatest effect on the performance of the sample. In other words, if all the particles in a sample are 2 μm except for one 15 μm particle, the large particle will cause the sample to perform more towards the lower bound. Another noteworthy behavior is that the width of the band between the lower and upper bound is larger in longitudinal samples. This finding suggests that specimens in the longitudinal direction may be affected differently than the build direction specimens by the deposition process with potential reasons associated with particle size effects, orientation of particle sizes, and interlayer effects. Further investigation of these effects is needed to fully elucidate the observed behavior.

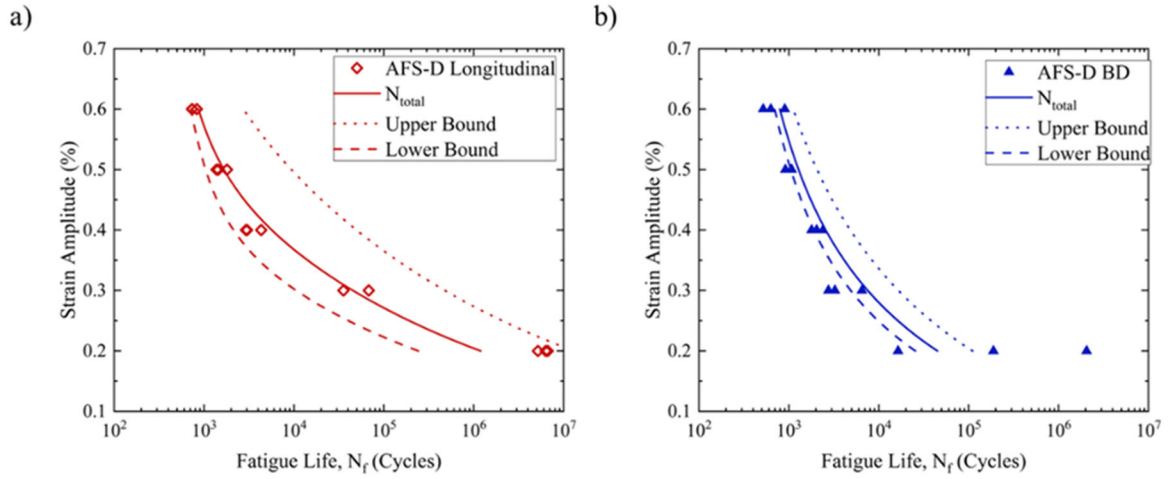

Figure 5.29 Bound life MSF model plots for (a) AFSD AA6061 in the longitudinal direction and (b) AFSD AA6061 in the build direction.

Table 5.4.3: MSF parameters for each data set.

Parameter	AFSD As-Dep. Long.	ASF-D As-Dep. Build
K’	340.9 MPa	449.05
n’	0.21	0.2731
C_{inc}	0.5	0.3
C_m	0.3	0.5
α	-0.3	-0.5
Q	2.24	2.33
y_1	577 MPa	577 MPa
y_2	1709 MPa	1709 MPa
ψ	4.6	4.6
R	0.4	0.4
E_{modex}	0	0
$Part_{exp}$	1.5	1.0
ω	$5*10^{-5}$	$5*10^{-5}$
a_i	1 μm	1 μm
Θ	0.8	0.8
Z	4	4
C_I	25000	25000
C_{II}	0.0002	0.00025
X	0.35	0.35
ΔCTD_{th}	$286*10^{-9}$	$286*10^{-9}$
a_f	2000 μm	2000 μm
DCS_{exp}	0	0
$PORE_{exp}$	0	0
GO_{exp}	0	0
GS	2.04	2.04
GS0	2.07	2.07

5.4.4 Conclusions

In this study, the fatigue properties of AFSD deposited AA6061 were investigated for the first time. Based on the experimental results and subsequent analysis from this study, the following conclusions are presented:

1. Microstructure of AFSD AA6061 possesses refined, equiaxed grain structure with predominantly high-angle grain boundaries indicative of DRX. In addition, AFSD process refines the size of the intermetallics particles.

2. Strain-control fatigue behavior of as-deposited AFSD AA6061 is reported for the first time. The longitudinal orientation exhibited slightly higher number of cycles to failure than the build direction, especially at lower strain amplitudes.

3. The as-deposited material exhibits generally homogeneous behavior with the exception of the top surface of the longitudinally oriented samples. This is likely due to fewer thermal cycles experienced by the top depositions layers compared to the bottom layers that experience more detrimental thermal exposure to the reinforcing particles.

4. As-deposited material experienced fatigue cracks that initiated from near surface defects such as intermetallic particles.

5. The fatigue crack nucleation and growth mechanisms associated with AFSD AA6061, like wrought material, are likely driven by constituent particles. This differs from porosity based fatigue mechanisms observed in fusion based additively manufactured material.

5.5 Influence of Post Deposition Heat Treatment on the Fatigue Behavior of New AA6061 Feedstock AFSD and Fatigue Modeling

The effects of post deposition heat treatment on an Al-Mg-Si alloy (AA6061) processed by Additive Friction Stir Deposition (AFSD) are investigated in-depth for the first time in this work. As lightweight, high efficiency structures remain an industry focus, studies focused on quantitative analysis of mechanical performance are necessary. In this work, heat treatment to recover the T6 temper is performed on AFSD AA6061 that is then subjected to monotonic and strain-controlled fatigue testing. Analysis of the microstructure revealed slight grain growth as a result of the heat treatment as well as the precipitation of the β" strengthening precipitates. Mechanical testing results indicate a full recovery of the strength of the AA6061-T6 temper, with comparable fatigue performance to the as-deposited AFSD AA6061. Fractography results revealed deformation mechanisms in the post deposition heat treatment not present in the as-deposited samples, however, these new deformation mechanisms do not significantly alter the fatigue resistance. A microstructure-sensitive fatigue model was implemented to capture the effects of the heat treatment process on the fatigue performance of the post deposition heat treated AFSD AA6061.

5.5.1 Material and Method

The material for this study was rolled AA6061-T651 that was cut into parallelepipeds with dimension 304.8 mm x 9.5 mm x 9.5 mm and processed into a deposition via AFSD. The process parameters used in the AFSD process were a rotational speed of 300 RPM, traversing speed of 127 mm/min., an actuator feedrate of 66 mm/min., a layer thickness of 1 mm, and a Z velocity of 5 mm/min. The deposition was made 419.1 mm long from the center of the tool at the start of a pass to the center of the tool at the end of a pass and was 63 layers tall. The samples for this study were cut from the deposition via wire electro-discharge machining (EDM) in two orientations: the longitudinal direction and the build direction, as shown in Figure 5.30. Also show in Figure 5.30 is the geometry of samples tested, which has been modified from ASTM-E606.

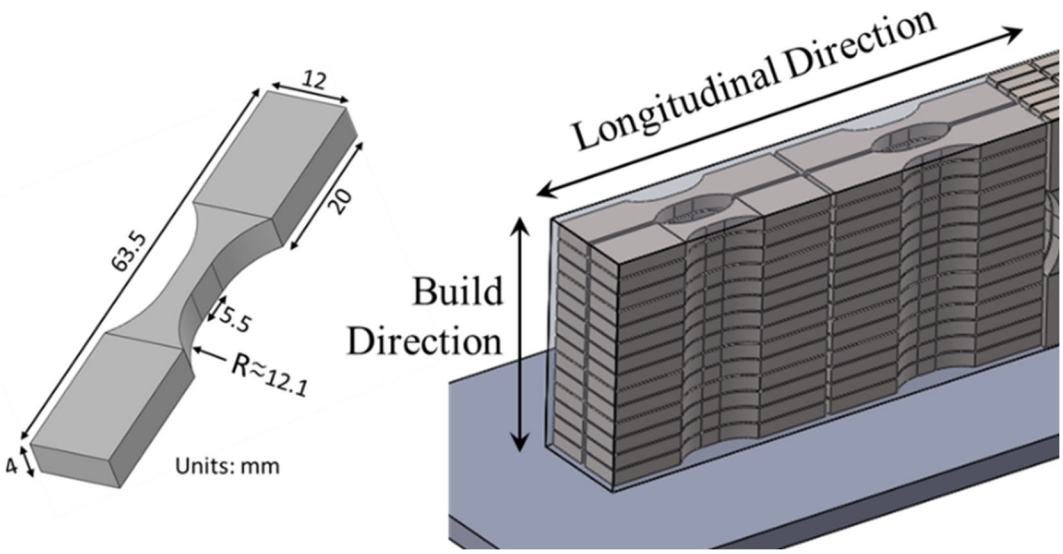

Figure 5.30 Specimen Geometry and layout for post deposition heat treatment study of AFSD AA6061.

The heat treatment procedure used in this study is based on the ASM handbook Volume 4 for AA6061 and the results of another study on AFSD AA6061. The as-deposited AFSD AA6061 samples were solutionized at 560 ˚C for 50 minutes followed by a water quench. After the quench, the samples were stored in a freezer until the heat treatment process could be performed in order to prevent natural aging. The heat treatment was carried out at 160 ˚C for 15 hours [224].

Mechanical testing was performed on a servo-hydraulic load frame. The extensometer used to measure axial strain had a nominal gage length of 5 mm. Due to this small gage length, the pump system for the hydraulics to the load frame was run at relatively low pressure to reduce the vibration in the lines running to the load frame, as the 5 mm gage length is much more sensitive to vibrations than a 12.7 mm or 25 mm gage length. Monotonic tensile testing was run under quasi-static loading conditions in displacement control at room temperature. The yield strength of each monotonic tensile test sample was measured using the 0.2% offset method. Fatigue testing was conducted under strain-controlled conditions. The fatigue tests were fully-reversed (R = -1), uniaxial, and run at five different strain amplitudes: 0.2%, 0.3%, 0.4%, 0.5%, and 0.6% all with a frequency of 1 Hz. After the first several thousand cycles, once the hysteresis response had been observed to stabilize, the test was paused, and the extensometer was removed. The test would then be continued under load-controlled conditions based on the stable hysteresis response of that sample at a frequency of 5 Hz.

The multi-stage fatigue model implemented in this study is unchanged from that of the one presented in several recent studies [39], [68], [174], [226]. The model was originally proposed by McDowell et al. [168], and has been expanded upon for other materials, processing methods including fusion-based AM and AFSD [169]–[174], [225]. In order to aid the understanding of the reader the basis of the model is briefly described as follows: the overall fatigue life is modeled as three discreet parts. The first is the incubation (INC) phase, which is the portion of the fatigue life that is characterized by the build up of damage prior to the nucleation of a crack. This portion of the model is informed by micromechanics on the local plasticity of microstructural features. The second portion of the model is the microstructurally small crack (MSC/PSC) growth phase, which is characterized as the portion of the fatigue life in which a crack has been nucleated, but is on the length scale similar to that of individual grains in the material. The msc phase is informed by empirically observed crack growth near crack initiation sites on fracture surfaces. The final portion of the model is the long crack (LC) growth phase. This phase is characterized by empirical Paris Law data from linear elastic fracture mechanics (LEFM).

5.5.2 Results and Discussion

The results of the electron backscatter diffraction (EBSD) scan are shown in Figure 5.31. The grain size in the heat treated AFSD AA6061 samples is about 25 μm. This indicates grain growth from the 15 μm observed in the as-deposited grain size [5][as-deposited paper] occurred as a result of the heat treatment process. Figure 5.31 also shows equiaxed grain structure, at least in the plane shown.

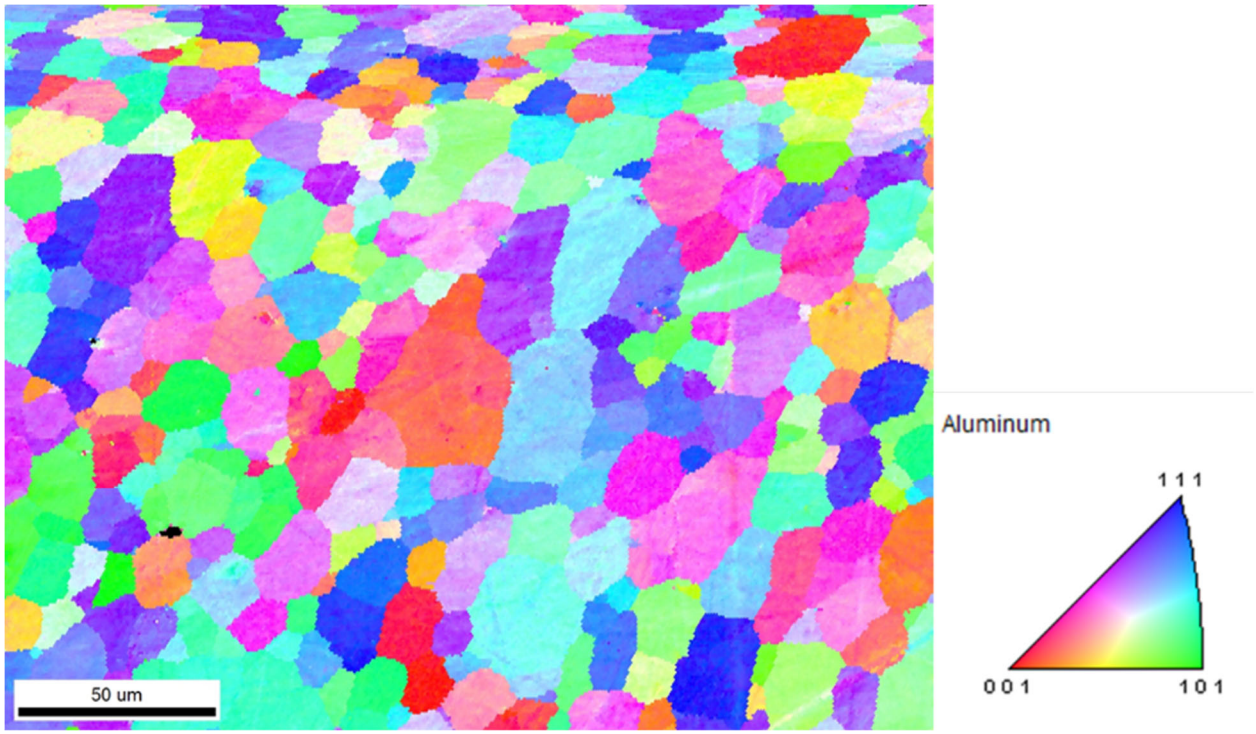

Figure 5.31 Inverse pole figure map of post-deposition heat treated AFSD AA6061 demonstrating larger grains than the as-deposited AFSD AA6061 reported in the literature [65].

Grain growth due to heat treatment was expected and appears to be relatively small. While the grains did grow roughly 66% larger, when compared to the reported size of the AA6061 feedstock of 200 μm [5] the grain refinement of the AFSD process and subsequent heat treatment is a reduction in grain size of about 88% to 25 μm. This result is desirable as one of advantages of the AFSD manufacturing process is grain refinement and the refinement is retained in AA6061 even after post deposition heat treatment. Furthermore, the grain growth from the heat treatment process did not change the equiaxed nature of the microstructure from the as-deposited AFSD AA6061.

The monotonic tensile test data is shown in Figure 5.32. The wrought AA6061-T651 used as the feedstock of the deposition is shown as a comparison to the heat treated AFSD AA6061. The yield strength of the wrought material shown here was measured as 295.8 ± 1.8 MPa while the ultimate tensile strength of the wrought was measured as 316.5 ± 2.2 MPa. The elongation to failure of the wrought sample was observed to be around 35%. The yield strength of the heat treated AFSD AA6061 was recorded to be 308.5 ± 12.0 MPa, and the ultimate strength was observed to be 332.8 ± 8.1 MPa. The ductility of the heat treated AFSD samples was measured to be around 30%.

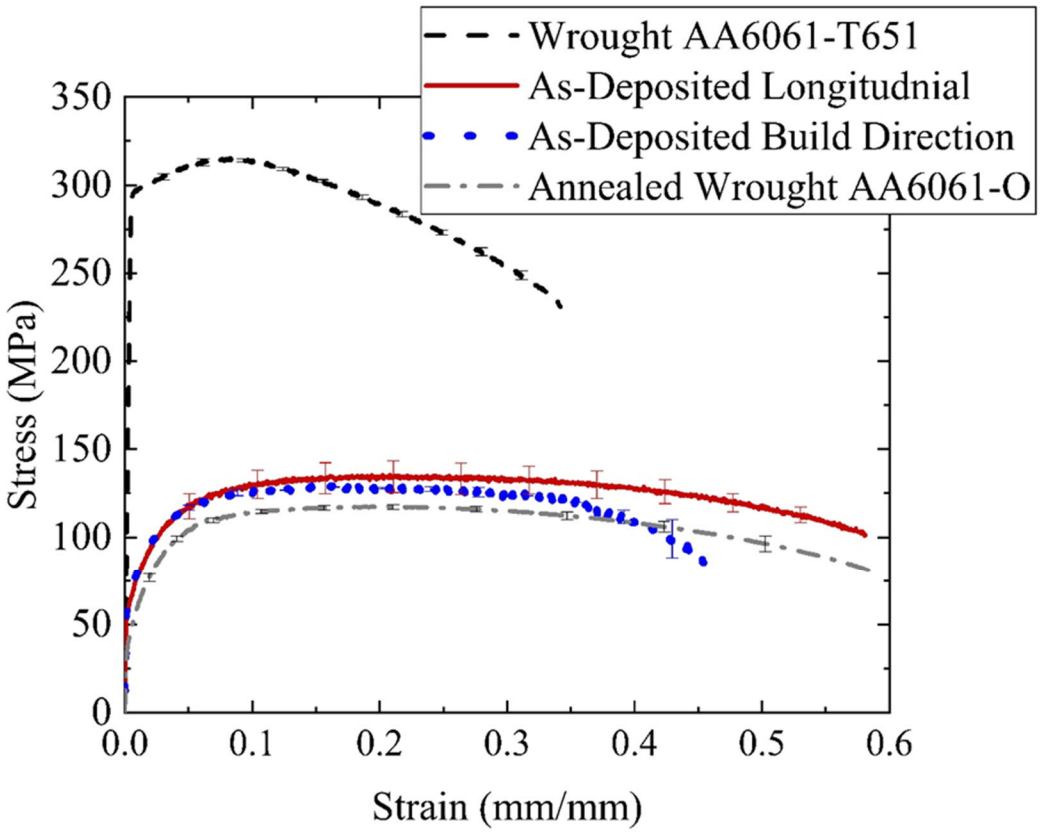

Figure 5.32 Monotonic stress-strain curves comparing wrought AA6061-T651, AA6061-O, and AFSD AA6061 as-deposited in both the build and longitudinal directions.

From the monotonic results, it has been demonstrated that the effectiveness of the post deposition heat treatment on the AFSD AA6061 successfully recovered the strength of the T6 temper possessed by the wrought AA6061-T651 material. The heat treated AFSD samples exhibited a 4.3% increase in yield strength and a 5.2% increase in ultimate strength compared to the wrought material. It is worth noting the heat treated AFSD AA6061 experienced less ductility in that the elongation to failure was observed as about 30% compared to the wrought elongation to failure of about 35%. However, that result is still somewhat promising as AA6061 FSW in previous studies have been shown to exhibit inferior strength and ductility [227]. In Moreira's study the heat treated FSW was observed to have an ultimate tensile strength of 70% of the base material and a ductility of 50% of base material. The AFSD and FSW processes are certainly not the same, however, since AFSD is a derivative technology from FSW and there is a lack of published literature on the monotonic performance of heat treated AFSD at the time of this work, the FSW was the best available data from which to draw a hypothesis on the behavior of post deposition, heat treated AFSD material.

Figure 5.33 shows the results of the fatigue testing of the heat treated AFSD AA6061 specimens. The heat-treated samples tested at 0.6% experienced a fatigue life on the order of 10^3 cycles to failure. At 0.5% an 0.4% the heat-treated samples had fatigue lives on the order of 10^3 to 10^4. The strain amplitude of 0.3% saw heat-treated samples fail generally around 50,000 cycles, and the samples tested a 0.2% failed on the order of 10^6 or more cycles.

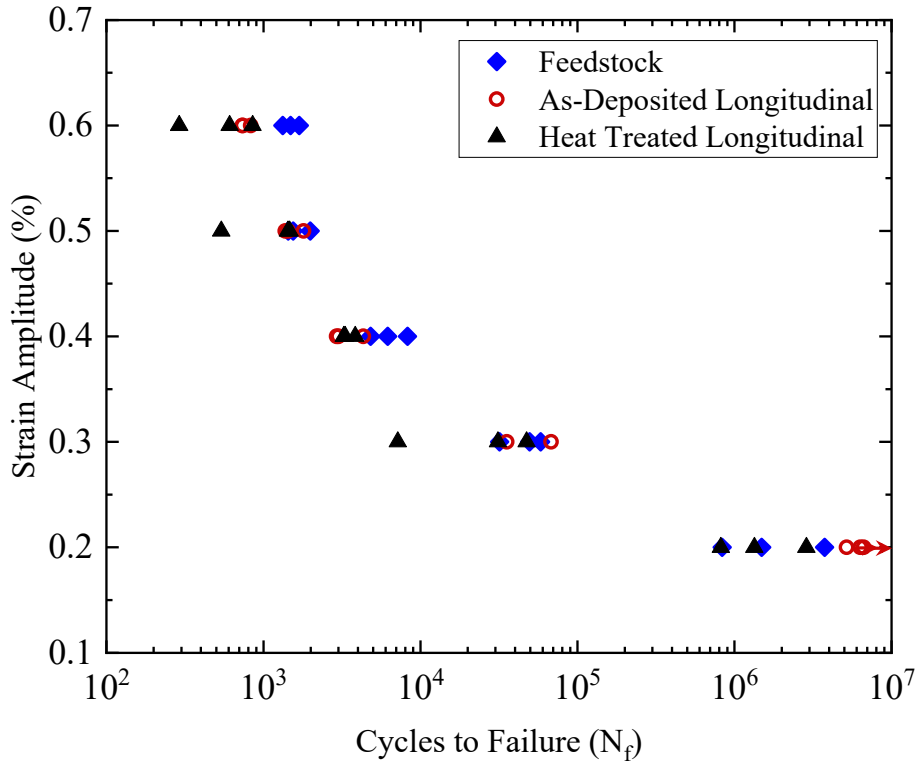

Figure 5.33 Strain versus life plot for wrought AA6061-T651, as-deposited AA6061, and heat treated AFSD AA6061.

Overall, the heat treated AFSD samples exhibited similar fatigue behavior to the as-deposited AFSD across the entire range of strain amplitudes investigated. At the strain amplitude of 0.2% it is noteworthy that the heat treated AFSD samples did not reach a runout of 5 million cycles, while the as-deposited did for every sample tested. This is likely due to the same reason the wrought AA6061 did not have a sample runout, which is that the smaller grain size in the as-deposited samples act to prevent crack nucleation. Without the mechanism of smaller grains it would be reasonable to expect both heat treated AFSD and wrought AA6061-T651 to perform better than the as-deposited as both possess higher load bearing capacity.

Figure 5.34 a) and b) shows the fracture surface for samples tested at ε_a = 0.3% (N_f = 47,470 cycles) and ε_a = 0.5% (N_f = 1,432 cycles), respectively. Both fracture surfaces exhibit a large area fraction with severe shear dimpling indicative of final fracture. Additionally, both surfaces have regions with vertically aligned void coalescence. From previous studies [65][my paper], the depositions made with these parameters have been shown to be fully dense, so these voids have developed as a result of cyclic deformation and rupture of the sample. What makes the nature of these voids interesting is that the different regions are typically spaced out along 1 mm horizontal increments. The deposition was made with a layer height of 1 mm, therefore it is likely that the observed void coalescence during cyclic deformation occurred along the layer boundaries. Despite this deformation, it appears that the cracks that precipitated failure began near the surface and closer to the bottom right corner on both of these samples. The interlayer void coalescence was not observed in the as-deposited AFSD AA6061 [my paper], so it is likely a result of heat treatment process on the treated AFSD AA6061.

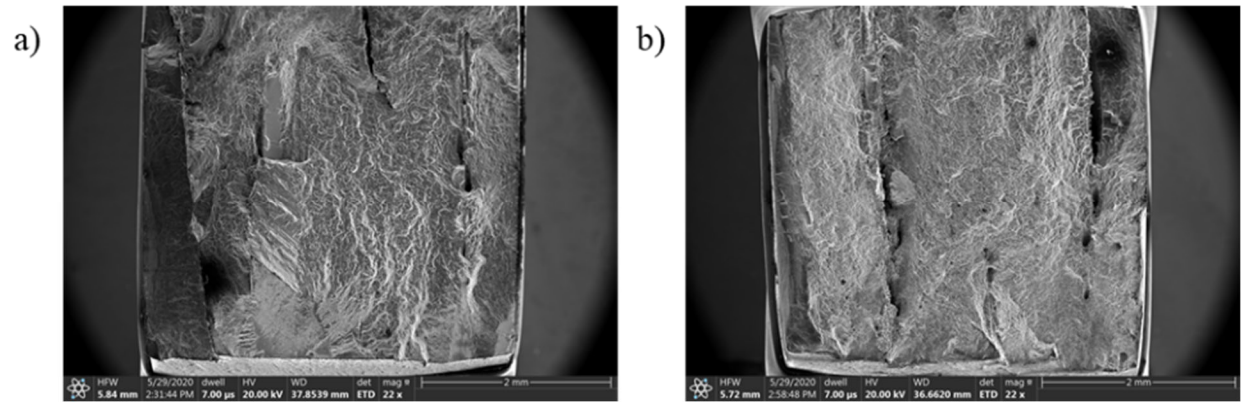

Figure 5.34 Fracture surface of (a) a sample tested at ε_a = 0.3% (N_f = 47,470 cycles) and (b) a sample tested at ε_a = 0.5% (N_f = 1,432 cycles). Both surfaces demonstrate void coalescence at 1 mm increments believed to correspond to deposition layers.

Some of the fracture surfaces investigated showed signs of mixed ductile and brittle failure modes, for example see Figure 5.35. It shows the fracture surface of a sample tested at ε_a = 0.2% (N_f = 1,535,618 cycles). The fracture observed in Figure 5.35 did not initiate from the brittle region, however, the mechanism behind the mixed failure mode may still have influenced crack growth and final fracture of the sample. Further study into the micro- and nano-scale mechanisms will be needed to fully understand this phenomenon.

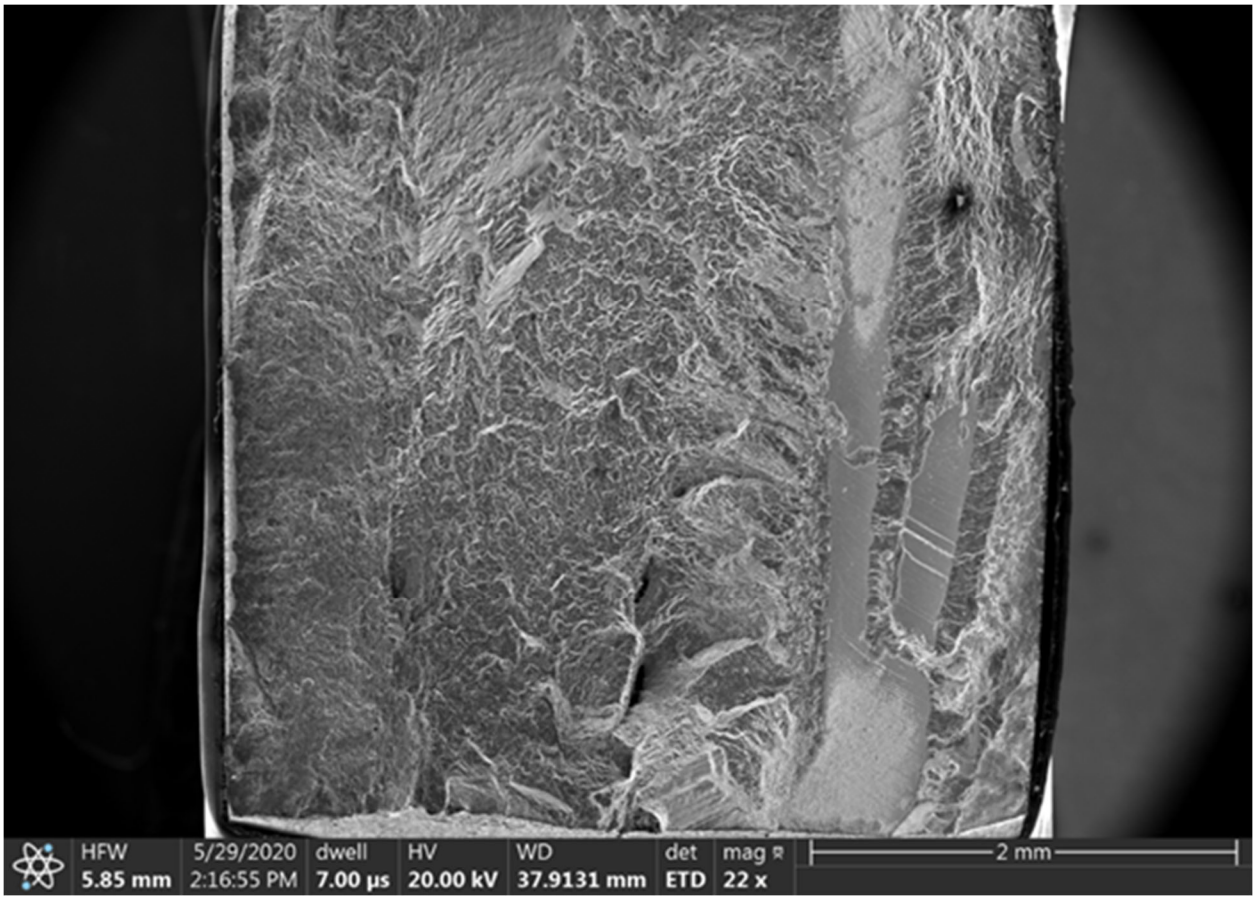

Figure 5.35 Fracture surface of a sample tested at ε_a = 0.2% (N_f = 1,535,618 cycles) that exhibits signs of both ductile and brittle failure modes.

For all the samples observed post mortem, the final fracture region of the fracture surface dominated the area fraction of the failure surface. This failure mode is common in components tested with higher nominal loads [228]. Shear dimpling can be observed in proximity to the top middle surface, but not at the free surface itself or within ~ 50 µm in Figure 5.36. This suggests the crack growth portion of the fatigue life was either relatively short in terms of the number of cycles or had a relatively slow crack growth rate. Once the crack reached the critical length, final rupture occurred, and it is clear that the critical length of the crack was relatively short. The fact that this behavior is normal for high nominal stresses is in agreement with the monotonic results that showed a recovery of the strength of the AA6061-T6 temper.

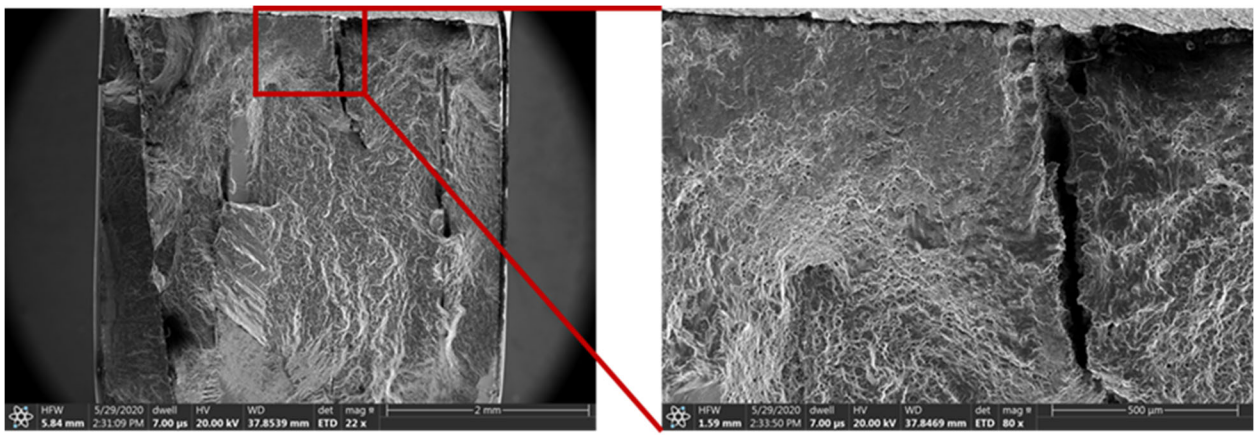

Figure 5.36 The fracture surface of a sample tested at ε_a = 0.3% (N_f = 47,470 cycles) with crack initiation observed to occur at the middle of top surface as well as an alternate initiation site in the bottom right corner.

The results of the multi-stage fatigue model are presented in Figure 5.37. The model shows good correlation with the data throughout the various strain amplitudes tested, demonstrating reasonable accuracy for fatigue behavior of post deposition heat treated AFSD AA6061. It is worth noting, similar to a previously published work [my paper], the MSF model parameters were informed by updating those of a previously published study on AA6061 [225]. By adjusting the empirically measured values, such as grain size, particle size, Modulus of Elasticity, ultimate tensile strength, and yield strength, as well as incorporating material properties like crack tip opening displacement, the MSF model was calibrated for post deposition heat treated AFSD AA6061.

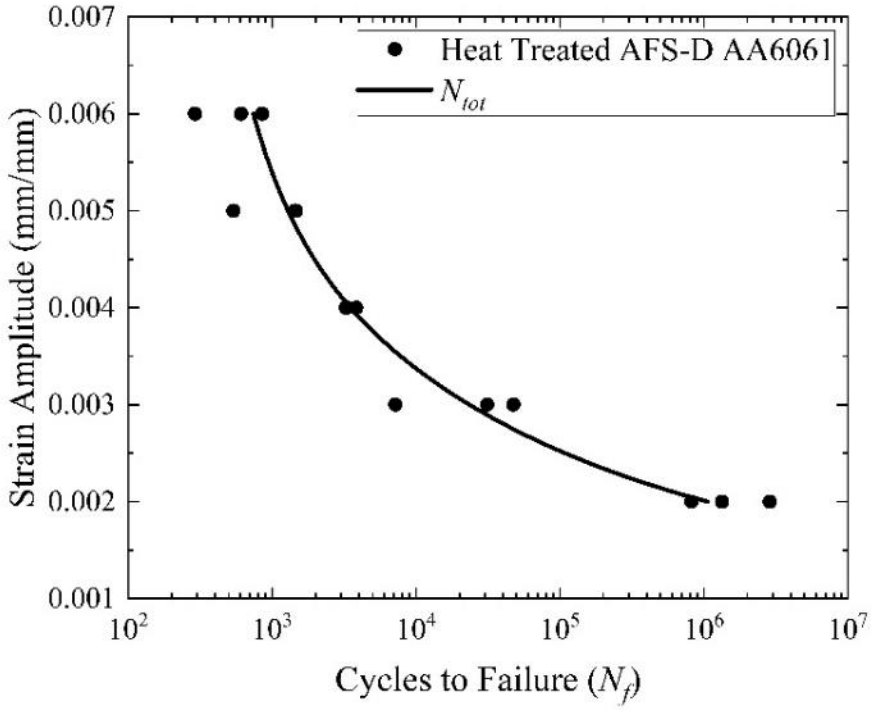

Figure 5.37 Total life results from MSF model calibration of AFSD AA6061.

Figure 5.38 exhibits the MSF model fit for the heat treated AFSD AA6061, as well as the contributions of the incubation portion of the fatigue life and the microstructurally / physically small crack growth portion of the fatigue life. At the larger strain amplitudes tested in this work, namely 0.006 and 0.005 mm/mm, the contribution of the incubation phase is relatively small compared to that of the msc/psc portion of the fatigue life. This is reasonable since, at larger deformation, more energy is imparted into the material which can allow a crack to quickly incubate, at which point the remainder of the life is dominated by small crack growth. If the specimens tested had been larger, it is possible the long crack growth portion of the MSF model would have had a noticeable effect. However, due to the relatively small length and width of the specimen geometry, any contribution of the long crack growth portion of the model was limited to a handful of cycles at most. Furthermore, at the lower strain amplitudes tested, primarily 0.002 and 0.003 mm/mm, the contribution of the incubation phase was observed to dominate the small crack growth phase. Again, this finding is reasonable, as the smaller applied deformation applies much less energy to the specimen. Therefore, the amount of time, and by extension cycles, to incubate and crack to nucleation is increased. Once a crack is nucleated it grows in the msc/psc phase, and while this phase is longer in terms of cycles than it was for the 0.006 mm/mm strain amplitude, it is still significantly smaller in terms of cycles than the incubation phase.

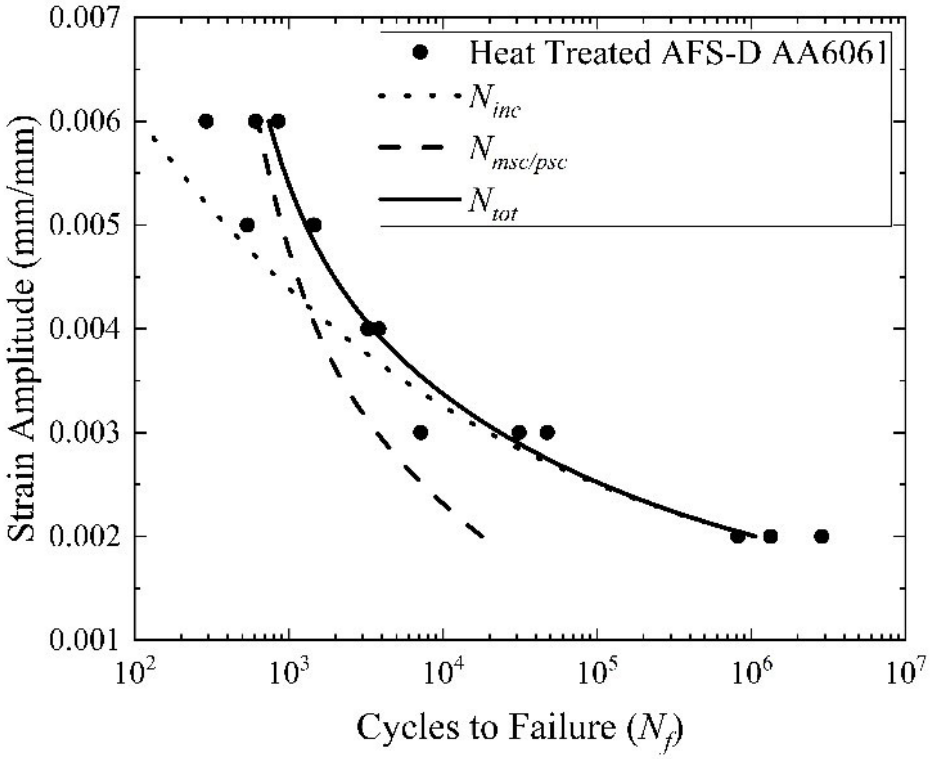

Figure 5.38 MSF model plot showing the contributions of the incubation stage and the microstructurally / physically small crack growth portions of the model.

Figure 5.39 shows the bounded plot of the MSF model. To generate the upper and lower bound of the plots shown in Figure 5.39, the particle size distribution must be utilized. For this work, it is assumed that the particle distribution in the post-deposition heat treatment is the same as it was prior to heat treatment. That is to say, identical to the distribution presented in the work by Rutherford et al. [my paper]. The upper bound is generated by holding all other constants equal and reducing the average particle size by one half the standard deviation of the particle distribution. Likewise, the lower bound is created by holding all other constants equal and increasing the average particle size by one half the standard deviation of the particle distribution. As can be seen on Figure 5.39, the bounding fits for the MSF prove reliably capable of capturing most of the fatigue data from the post deposition heat treated AFSD AA6061.

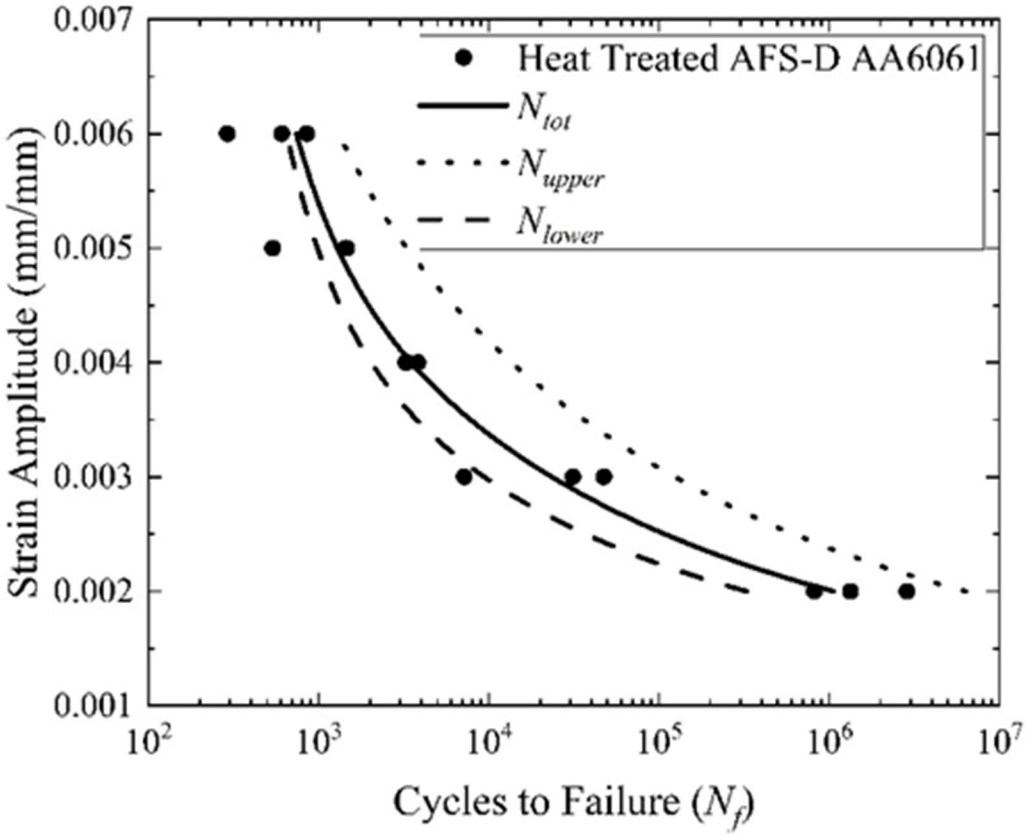

Figure 5.39 MSF plot shown with upper and lower bounds that were generated from the distribution of constituent particles in AFSD AA6061.

5.5.3 Conclusions

This work sought to determine the viability of post deposition heat treatment to effectively recover the material strength of AA6061 processed via AFSD to the wrought T6 temper. Based on the observations, experimental results, and the analysis performed the following conclusions can be drawn:

The post deposition heat treatment process proved viable to (recover the strengthening β" precipitates) and recover the strength of the T6 temper in AFSD AA6061.

The strain-controlled fatigue performance of the post deposition heat treated AFSD AA6061 remain comparable to the as-deposited AFSD AA6061, and the load bearing capacity of the post deposition heat treated AFSD AA6061 improved compared to the as-deposited AFSD AA6061.

The post deposition heat treatment of the AFSD AA6061 resulted in grain growth from 15 μm to 25 μm, but remained significantly refined compared to the grain size of the wrought AA6061-T651 feedstock at 200 μm.

An investigation of the fatigue fracture surface indicated higher nominal stresses in the post deposition heat treated AFSD samples compared to the as-deposited AFSD samples. Additionally, the post deposition heat treated AFSD samples exhibited deformation mechanisms not observed in the as-deposited samples, however, these deformation mechanisms did not have a significant impact on the fatigue performance.

A microstructure sensitive fatigue model was employed and found viable to model the performance of the post deposition heat treated AFSD AA6061.

5.6 Tensile Behavior of Varying Orientations for a Large Circular Helical Build Deposition

Additive friction stir deposition (AFSD) is a solid-state additive manufacturing technology with the capability to bulk deposit various alloys. In this work, AA6061 was bulk deposited in helical shape via AFSD. Tensile test specimens from three orientations with respect to build in 0°, 90° and 45° were extracted to evaluate the isotropic tensile behavior of the AFSD produced bulk structures. The test specimens from three orientation exhibit similar tensile strength and thereby suggesting isotropic nature in bulk AA6061 components produced via AFSD.

5.6.1 Material and Method

In this study, a B8 MELD machine (MELD Manufacturing, USA) was employed to deposit a 203 mm diameter by 44 mm tall helical build from a solid square feedstock made of AA6061 alloy. The feedstock measured 9.53 mm by 9.53 mm by 305 mm while the helical build was built in 44 layers with each layer measuring 1 mm in thickness. The depositions were made on a 305 mm by 6.35 mm thick AA6061-T651 square substrate using an AFSD tool made from high strength H13 steel, measuring 38.1 mm in diameter with four "teardrop" protrusions on the tool shoulder. The AFSD processing parameters measuring 300 RPM, 70 mm/min feed rate, and 127 mm/min traverse rate used in fabricating the helical build were chosen based on the work by Phillips et al. [65]. Figure 5.40(a) is a pictorial representation of the AFSD build process and Figure 5.40(b) and Figure 5.40(c) are the front and top views of the AFSD AA6061 helical build.

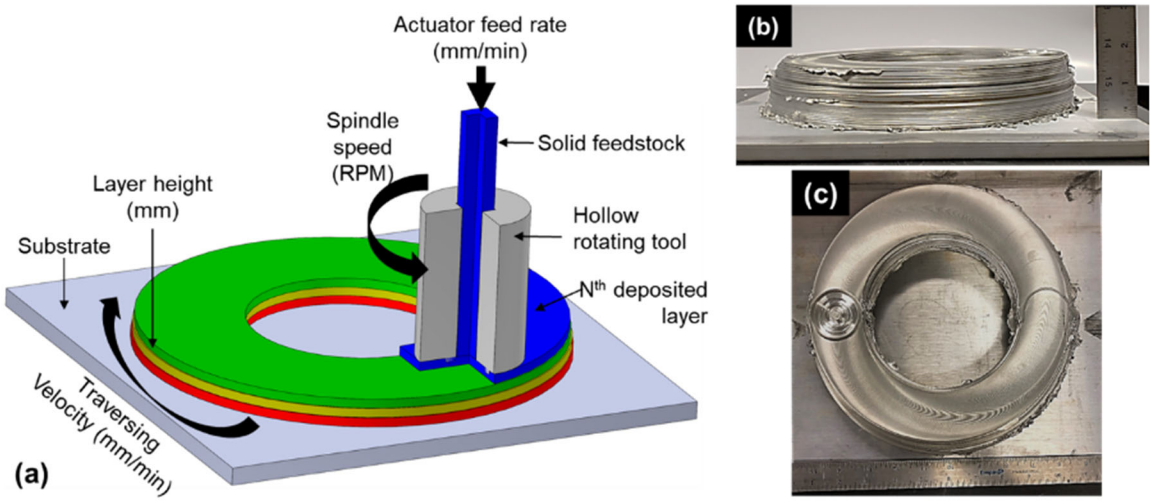

Figure 5.40 (a) Pictorial representation of fabricating helical build via the AFSD process, (b) and (c) front and top view of the completed AA6061 component.

The test specimens in this study were extracted via a Mitsubishi 1200 MV wire EDM (electrical discharge machine) from three unique directions (a) 0º (longitudinal direction), (b) 45º and (c) 90º (build direction). The pictorial in Figure 5.41(a) shows the orientation of each specimen with respect to the helical build. Figure 5.41(b) is the geometrical dimensions of the representative tensile specimens.

The monotonic tensile tests were performed on a Test Resources 100 series, electromechanical, screw type modular tensile test machine at a quasi-static strain rate of 0.001/s and at ambient room temperature. Due to the small nature of the tensile specimens, digital image correlation (DIC) was used in place of an extensometer to capture strain data in the material. An open source DIC MATLAB code was used to calculate the strain from the digital captured images. True stress-strain behavior was plotted to better understand material behavior and potential asymmetry in the build microstructure.

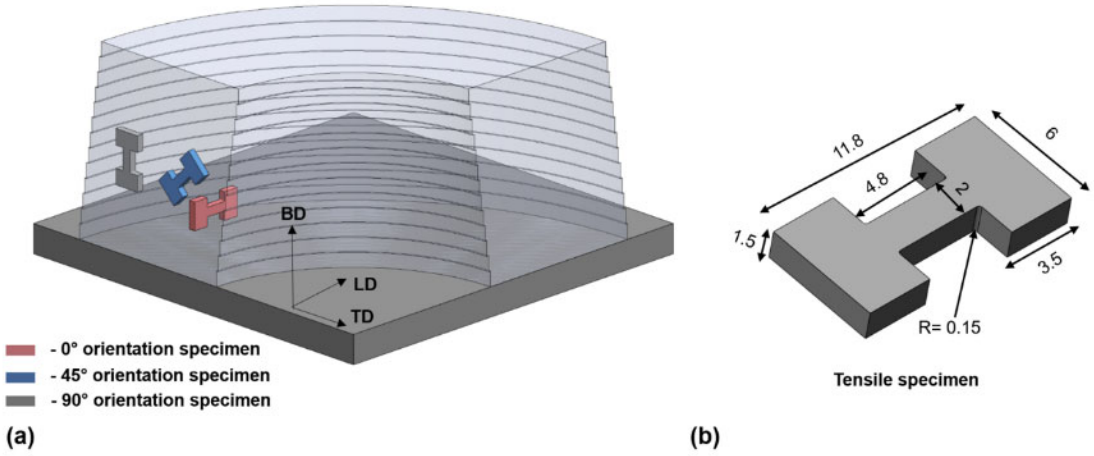

Figure 5.41 Pictorial representation of (a) orientation of specimens with respect to the helical build, (b) geometrical dimensions of the tensile specimen.

For metallographic analysis, the specimens were cold mounted in epoxy and standard metallographic sample preparation procedure was followed. The mounted specimens were finally polished using 0.05 μm colloidal silica on a vibratory polisher for 8 hours. For microstructure analysis, the polished specimens were etched with caustic etching (20% NaOH) for 120 seconds. An Apreo FE-SEM scanning electron microscope (SEM) equipped with an EDAX Hikari Super electron backscatter diffraction (EBSD) detector was used for EBSD analysis. The digital optical images were captured on Keyence VHX7000 microscope.

5.6.2 Results and discussions

The monotonic tensile true stress-strain response of the three specimens (0^o, 45^o and 90^o) are plotted and presented in Figure 5.42. Each curve in the plot with error bars is the averaged curve of three discrete tensile test results for individual specimens. The yield strength and ultimate tensile strength (UTS) of the three unique orientation specimens and wrought feedstock AA6061-T651 are provided in Table 5.6.1. The specimens from three build orientation exhibit near isotropic mechanical behavior in the elastic region. The ultimate tensile strength (UTS) however slightly varied between the three specimens. In consistent with observations made by Rutherford et al. [67], where the specimens in 0^o and 90^o exhibited similar tensile behavior, in the current work the 0°, 90° and 45° orientation specimens exhibit similar tensile behavior. Similar to previously made observations, the three unique orientation specimens exhibit lower tensile strength compared to wrought AA6061-T651 specimens with a UTS of 316.5 ± 2.2 MPa [67]. The lower yield and UTS of the as-deposited specimens is primarily due to dissolution of primary strengthening mechanism in AA6061 which is fine β" (Mg_2Si) precipitates. As observed by Rutherford et al. [67] and Phillips et al. [65] the dissolution of precipitates is expected during the thermomechanical processing under AFSD which ultimately resulted in lower UTS and yield strength as compared to wrought AA6061 feedstock material.

Table 5.6.1: Monotonic tensile strength properties of the fabricated and wrought AA6061.

Materials and orientation	Yield Strength (MPa)	Ultimate Tensile Strength (MPa)
Wrought AA6061-T651 [67]	295.8 ± 1.8	316.5 ± 2.2
Wrought AA6061-O [229]	63.6 ± 0.6	116.5 ± 1.3
0°orientation specimen	51.8 ± 6.82	128.5 ± 6.16
90° orientation specimen	51.3 ± 5.32	129.8 ± 3.3
45° orientation specimen	47.9 ± 11.92	132.1 ± 3.15

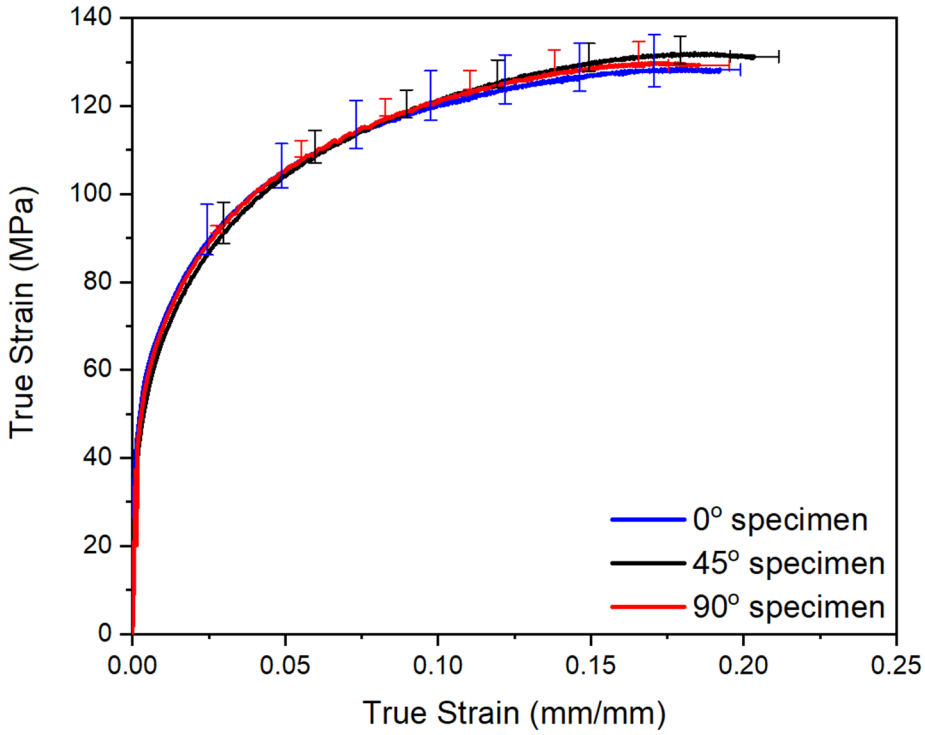

Figure 5.42 Monotonic True Stress-strain curves with error bars of the specimens from three different orientation.

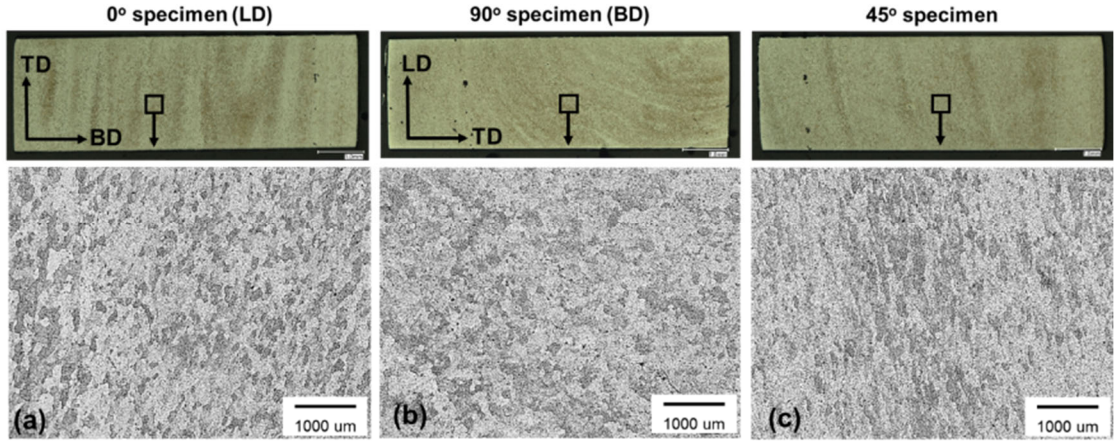

Figure 5.43 Representative microstructure images of (a) 0°, (b) 90° and (c) 45° orientation specimens.

The digital optical micrographs, comparing the microstructure of the AFSD AA6061 from three different build orientation are presented in Figure 5.43. The 0º specimen (Figure 5.43a) and the 90º specimen (Figure 5.43b) exhibits pancake shaped grains and the 45º specimen (Figure 5.43c) exhibits a mix of elongated and pancake shaped grains.

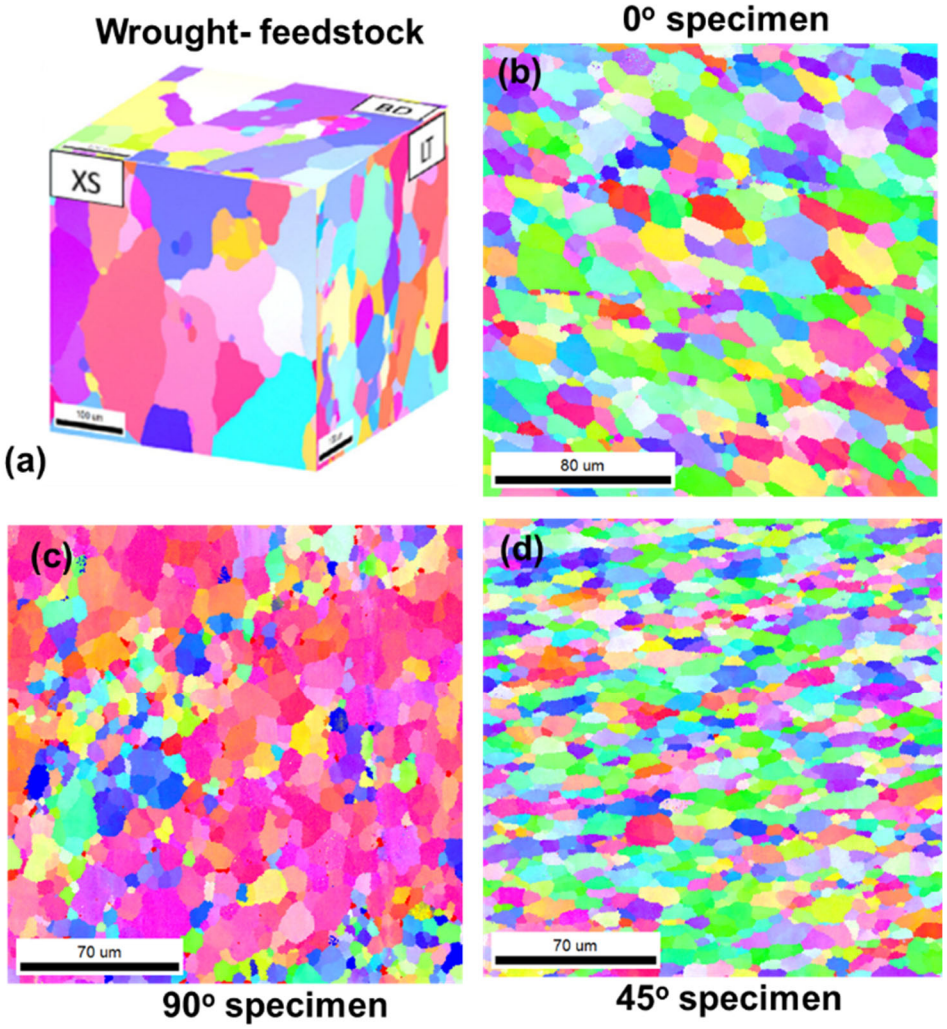

Figure 5.44 EBSD maps of (a) wrought-feedstock AA6061, (b) 0° specimen, (b) 90° specimen and (c) 45° orientation specimen.

Further, a detailed EBSD analysis of the three specimens are presented to further characterize the grains and impact of AFSD in AA6061. Figure 5.44(a) [65] is the 3D grain size and orientation map of the feedstock and Figure 5.44(b), Figure 5.44(c) and Figure 5.44(d) are the EBSD grain maps of the representative specimen extracted from 0º (LD), 45º and 90º (BD) orientations. The evolution of grain size and structure due to the AFSD process of AA6061 is appreciated in the EBSD maps shown in Figure 5.44. As noted in previous work [65], [67] on the AFSD process, the grain size is reduced to a fine equiaxed grain structure. This material showed a grain size reduction from a 200 µm grain size in the feedstock to a grain size of 15 ± 5 µm in the as deposited material which is a reduction of 93%. The reduction in grain size is attributed to the dynamic recrystallization (DRX) being done by the high shear strains and elevated temperatures during the deposition process. The AFSD process creates a fine equiaxed grain structure although the same grain size and structure was not observed in the three different orientations that were tested and mapped. The 0° orientation map is visible in Figure 5.44b with an average grain size of 15.2 ± 7.2 µm. The 90° orientation EBSD map is seen in Figure 5.44(c) with an average grain size of 20.1 ± 14.2 µm. There is a split of grains sizes below 15 µm and above 30µm within the sample, wherein the smaller grains are clustered together, and the large grains are clustered together as evident in Figure 5.44(c). Generally, the build direction or 90° oriented specimens in additively manufactured components exhibit lower tensile strength compared to longitudinal direction or 0° orientation specimen. However, in AFSD fabricated AA6061 component, the dynamic recrystallization of grains in deposited layers resulted in clustering or grains as evident from the EBSD maps in Figure 5.44(c). This may have contributed to build direction specimens exhibiting tensile strength that were comparable to those of longitudinal direction specimens. Figure 5.44(d) shows the 45° build direction EBSD map with the smallest average grain size at 9.3 ± 4.3 µm. The 45° orientation exhibited the smallest average grain size and the least amount of distribution amongst the three different orientations. Along with the consistent grain size observed in the 45° orientation, the 45° sample also exhibited the lowest amount of texture of the three tested orientations, which contributed to slightly higher UTS compared to other two orientation specimens.

5.6.3 Conclusions

Specimens from 0°, 90° and 45° orientation were extracted from an AA6061 helical build fabricated via additive friction stir deposition (AFSD). To verify the isotropic properties, the specimens were tensile tested and grain size and texture analysis were performed using EBSD. The following conclusions are made.

AFSD fabricated AA6061 components exhibit isotropic tensile properties which were verified by monotonic tensile test performed on specimens extracted from three unique orientations with respect to build direction.

The UTS is influenced by the grain size and texture. The 45° orientation specimens with smaller grain size and texture exhibited the maximum UTS of the three specimens tested.

The dynamic recrystallization that occurs during AFSD process, produced refined grains compared to the feedstock material. This ultimately improved the overall tensile strength of the AFSD built component.

5.7 Influence of Surface Oxides and Material Flow During AFSD of AA6061

This work examines the impact of oxide coatings on the surfaces of feedstock material used for Additive Friction Stir Deposition (AFSD). The AFSD process is a solid-state additive manufacturing process that uses severe plastic deformation and frictional heating to build bulk depositions from either metallic rod or powder feedstock. Since aluminum alloys naturally form an oxide layer, it is important to determine the influence of the feedstock surface oxide layer on the resultant as-deposited microstructure and mechanical properties. In this study, three AA6061 square-rod feedstock materials were used, each with a different thickness of aluminum oxide coating: non-anodized, 10-micron thick, and 68-micron thick. Macroscale depositions were produced with these feedstock rods using the AFSD process. Optical and electron microscopy showed that the two oxide coatings applied through anodization were efficiently dispersed during the AFSD process, with oxide particles distributed throughout the microstructure. These oxide particles had median sizes of 1.8 and 3.5 μm^2, respectively. The yield and tensile strengths of these materials were not measurably impacted by the thickness of the starting oxide coating. While all three feedstock material variations failed by ductile rupture, the elongation-to-failure did decrease from 68% to 55% in the longitudinal direction and 60% to 43% in the build direction for the thickest initial oxide coating, 68 microns.

5.7.1 Materials and Methods

In this research, two batches of square-rod AA6061-T6 feedstock bars (9.5 mm × 9.5 mm × 305 mm) were anodized in sulfuric acid by D & J Enterprises (Huntsville, Alabama) (Figure 5.45). The naturally occurring oxide layer (a few nanometers thick) on the non-anodized feedstock bars was not observable at low magnification (Figure 5.45a). The average thickness of the anodized layers on the feedstock bars was 9.8 ± 0.5 µm and 68 ± 10 µm for each of two batches, respectively (Figure 5.45b and Figure 5.45c). Three pieces of anodized feedstock were selected randomly from each batch, and on each piece three cross-sections (two at the edges and one in the center) were used to measure the thickness of anodized layers. In total, the layer thickness was measured at least 36 times at 9 cross-sections on three pieces of feedstocks of each batch. The anodized layers exhibited uniformity in thickness on the feedstock bars with 5% and 15% variation respectively. These two thicknesses were chosen based on the average grain size (15 µm) of AFS-D builds from non-anodized AA6061 feedstock [8].

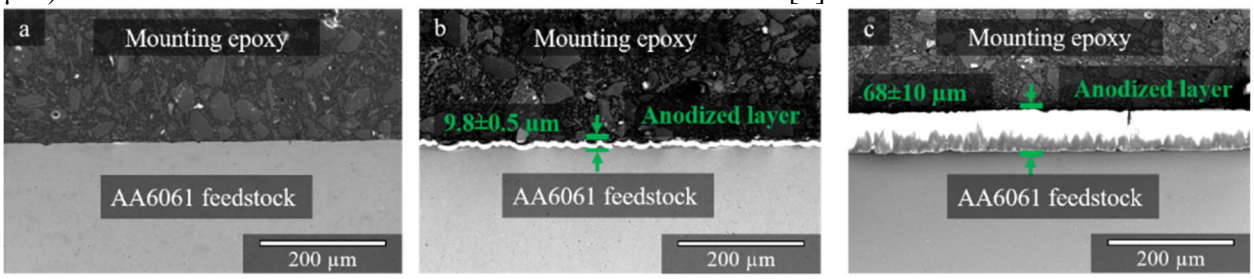

Figure 5.45 cross-section of square-rod feedstock AA6061-T6: a) as received; b) anodized with a 9.8-µm thickness; c) anodized with a 68-µm thickness

A commercial B8 AFS-D machine was used to produce two AFS-D builds with a geometry of 121 mm × 51 mm × 76 mm from the two batches of the anodized feedstocks (Figure 5.46a). In this present study, processing parameters developed in the work by Philips et al. were used for the two depositions: 300 RPM for the rotational speed, 127 mm/min for the tool traverse speed,

and 66 mm/min for the actuator feed rate [8]. Each piece of the square-rod feedstock produced four 1-mm-thick layers with alternating traverse directions, and a total of 18 pieces of feedstock were used for each deposition. The substrate was AA6061-T651 with a 6.35 mm thickness. No distortion of the substrate was observed after removing the depositions from clamping. A typical AFS-D tool was used for the depositions consisting of a 38.1 mm diameter with four "teardrop" protrusions on the shoulder surface to enhance material mixing between deposited layers during the process as detailed in Fig 2b. The microstructures and mechanical properties from these anodized feedstock depositions were compared to laboratory data from the non-anodized AA6061-T6 feedstock, and the processing parameters and the AFS-D tool were the same for all depositions [11].

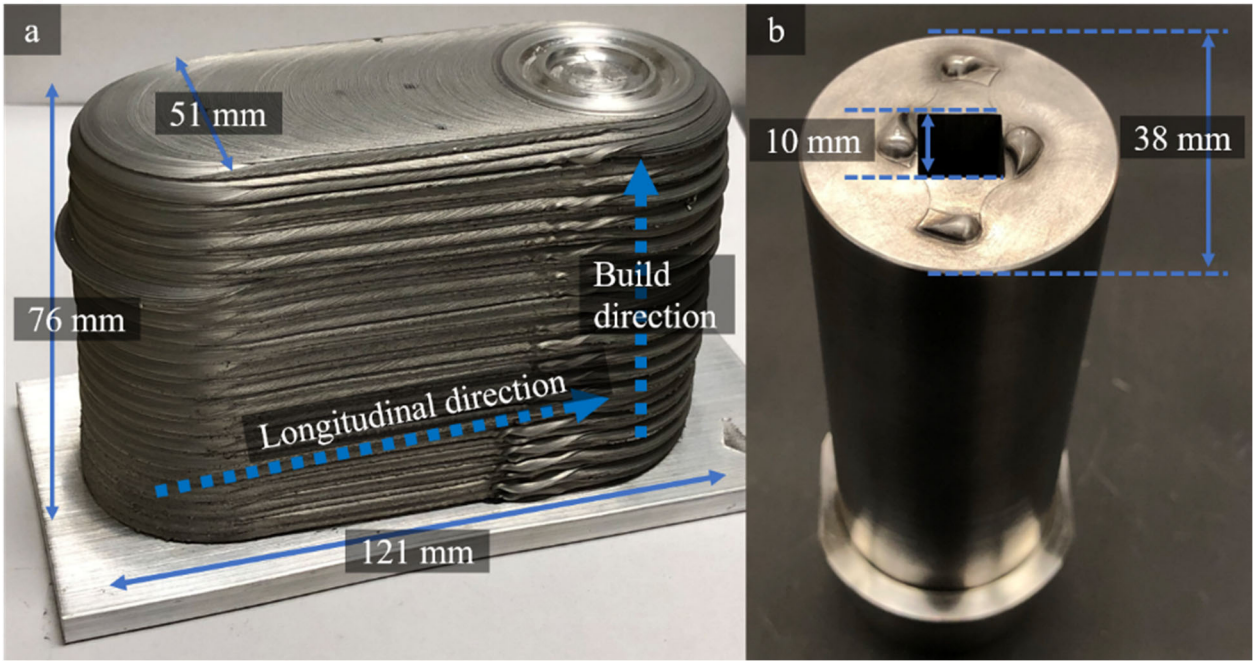

Figure 5.46 (a) The AFS-D build from anodized square-rod AA6061 feedstock; (b) the AFS-D tool with four "teardrop" protrusions on the shoulder surface.

Wire electrical-discharge machining (EDM) fabricated tensile coupons in both the longitudinal direction and the build direction for each deposition feedstock condition. Each tensile coupon was 63.5 mm in length, 12 mm in width and 4 mm in thickness corresponding to a modified ASTM E8 coupon as used previously [10,11]. The gauge length for each was 5.5 mm. Quasi-static ($\dot{\varepsilon}$ = 0.001 mm/mm/s) monotonic tests were carried out in triplicate on a servo hydraulic load frame under displacement control. A 5 mm extensometer was used to record the strain in the gauge section. Thus, allowing for the tensile mechanical properties of the AFS-D builds from non-anodized and anodized feedstocks to be directly compared.

Cross-sections parallel to the build direction from each deposition were used for microstructural analysis. Those samples were mounted, ground, and polished using standard metallographic techniques. A final polish was performed using a four-hour-long vibratory polish with a 0.02 colloidal silica slurry. A Thermo Fisher Scientific Apreo scanning electron microscope (SEM) was used to obtain the microstructure images at 20 kV and 6.4 nA with a working distance of 10 mm. For each deposition, 12 backscattered electron (BSE) images were collected at 65X magnification to analyze particle size and distribution. Compositional identification of particles

was made with energy dispersive x-ray spectroscopy (EDS) at 20kV and 0.4 nA using an EDAX system. A Tescan Lyra FIB-FESEM was used to take the fractography images at 20 kV and 0.3 nA with a working distance of 40mm.
The particle distribution was analyzed via ImageJ based on the BSE images (Figure 5.47). A median filter was used to reduce noise in the SEM images by replacing each pixel with the median of the neighboring (radius of 2 pixels) pixel values. Then the image was converted to a black and white binary image (Figure 5.47c & Figure 5.47d). Only particles with a size larger than 4 pixels were included in the analysis.

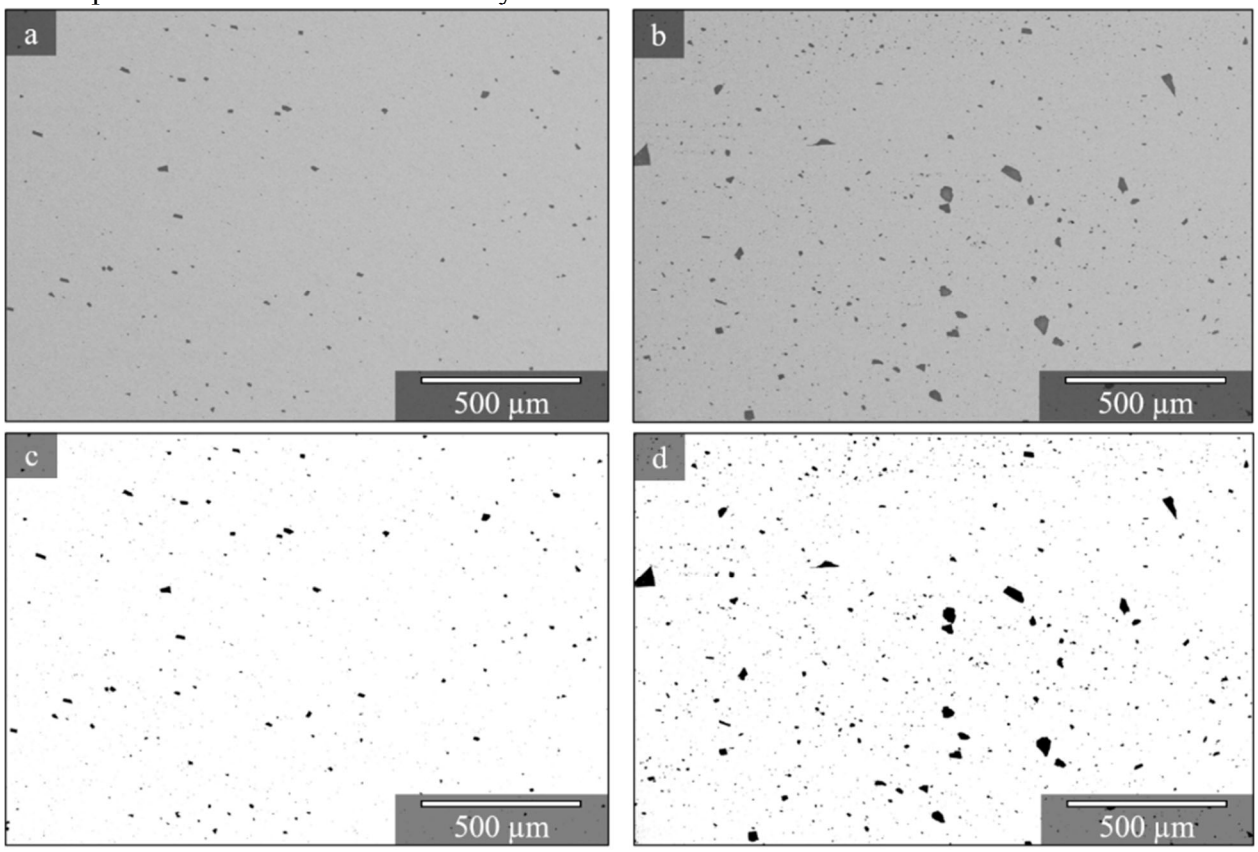

Figure 5.47 SEM images and corresponded binary images analyzed via imageJ of alumina particles in the AFS-D build from anodized feedstock bars with an average thickness of a) & c) 9.8 µm; b) & d) 68 µm.

In this paper, we will refer to the two depositions from anodized AA6061 feedstock as AA6061-0.4%alumina and AA6061-2.8%alumina, respectively. The values of 0.4% and 2.8% represent the theoretical percentage of alumina in the deposited material. These theoretical values were calculated based on the ratio of the measured area of oxide layers to the remaining area of the AA6061 matrix. The data from non-anodized AA6061-T651 feedstock will be termed AA6061-NA (no alumina).

5.7.2 Results and Discussion

The anodized feedstocks produced fully dense AFS-D builds without apparent porosity or cracks (Figure 5.48). Black particles in the microstructure were alumina from the anodized layers on the feedstock (Figure 5.48b and Figure 5.48c). Such large alumina particles were not observed in the

non-anodized AA6061 material (Figure 5.48a). Despite the presence of alumina particles in depositions from anodized feedstock, the material was fully consolidated within the aluminum matrix, and there were no pores or crevices along the boundaries between the alumina particles and the matrix. Larger alumina particles were observed in the AA6061-2.8% alumina deposition, which was produced from the feedstock with thicker anodized layers (68 μm) (Figure 5.48c).

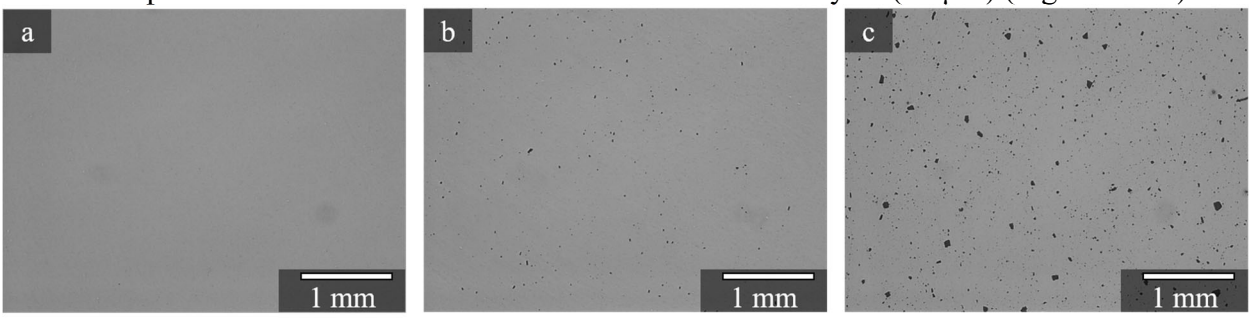

Figure 5.48 Optical images showing full consolidation of feedstock material AA6061 after AFS-D processing: a) AA6061-NA; b) AA6061-0.4%alumina; c) AA6061-2.8%alumina. The dark particles are aluminum oxide particles, not pores.

Irregular-shaped alumina particles (diameter > 9.8 μm) were observed in both depositions from anodized feedstock, and their sizes and area fractions were proportional to the thickness of anodized layers on the feedstocks (Figure 5.49b and Figure 5.49c). In the AA6061-2.8%alumina deposition, the particle sizes were distinctly larger, and the amount of both large particles (> 68 μm) and small particles was increased. The distribution of alumina particles was relatively uniform, with no obvious agglomeration. In the deposition from non-anodized feedstocks (Figure 5.49a), no alumina particles were observed at this same low magnification.

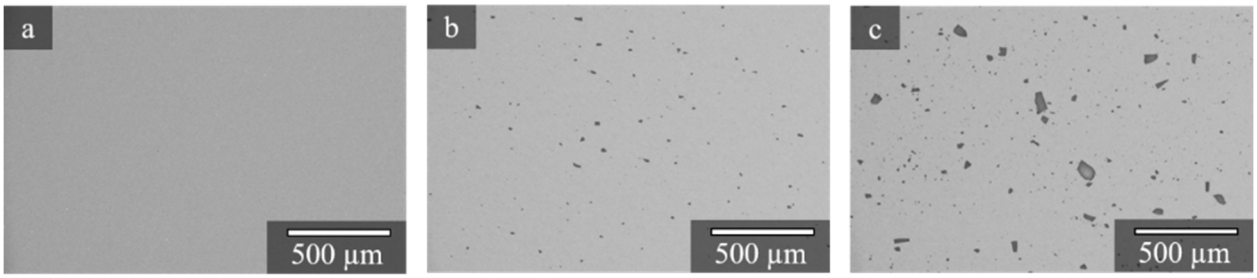

Figure 5.49 BSE images of AFS-D builds: a) AA6061-NA; b) AA6061-0.4%alumina; c) AA6061-2.8%alumina.

The larger black particles (Figure 5.49 and Figure 5.50) showed x-ray signals consistent with being alumina. All of these particles showed an enhanced oxygen signal in the EDS spectra. The larger particles (>9.8 μm in diameter) exhibited a strong oxygen signal in all EDS results from multiple particles. Figure 5.50b and Figure 5.50d are examples of EDS signals collected at the alumina particles point 1 and point 2, as circled in Figure 5.50a and Figure 5.50c. The detected sulfur signal was from the sulfuric acid electrolyte used in the hard anodization process to prepare the anodized feedstock.

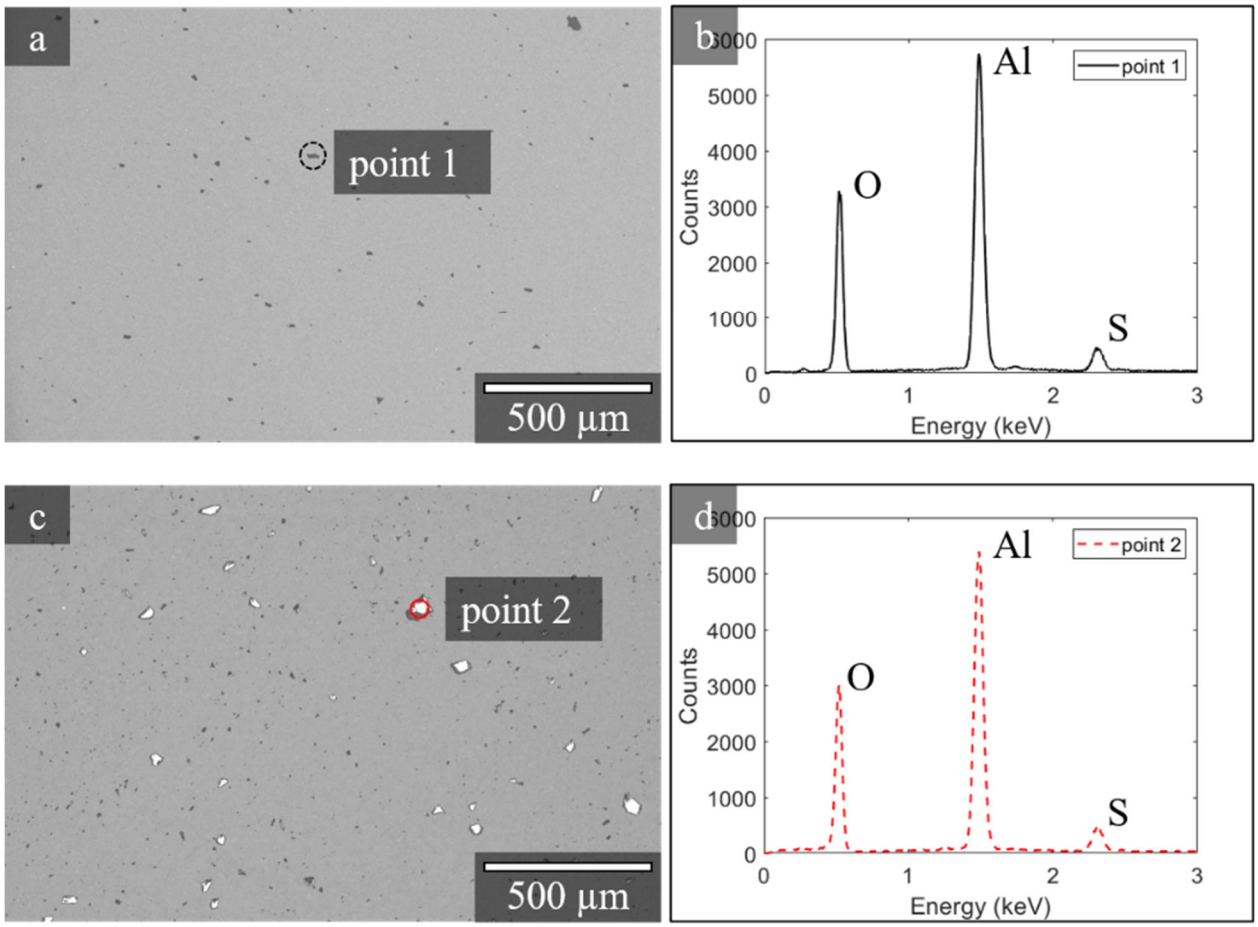

Figure 5.50 SEM images and EDS signals collected from a) & b): the AA6061-0.4%alumina deposition; c) & d): the AA6061-2.8%alumina deposition. The detected sulfur signal was from the sulfuric acid electrolyte used in the hard anodization process to prepare the anodized feedstock.

The AFS-D process clearly refines and disperses the alumina coatings on the anodized feedstock into small particles throughout the deposition (Figure 5.51a and Figure 5.51b). Note those particles were positively identified as alumina with the EDS signals shown in Figure 5.50b and Figure 5.50d. The frequency of particles sharply decreased with increasing particle size, shown by the red cumulative frequency curve in the Figure 5.51. Nevertheless, a few particularly large alumina particles were observed: in both depositions, less than 5% of the alumina particles were larger than 100 μm^2. In the AA6061-0.4%alumina deposition, the maximum particle size observed was 528 μm^2; in the AA6061-2.8%alumina the largest particle size was 10,100 μm^2. Descriptive statistics of alumina particles sizes are summarized in Table 5.7.1.

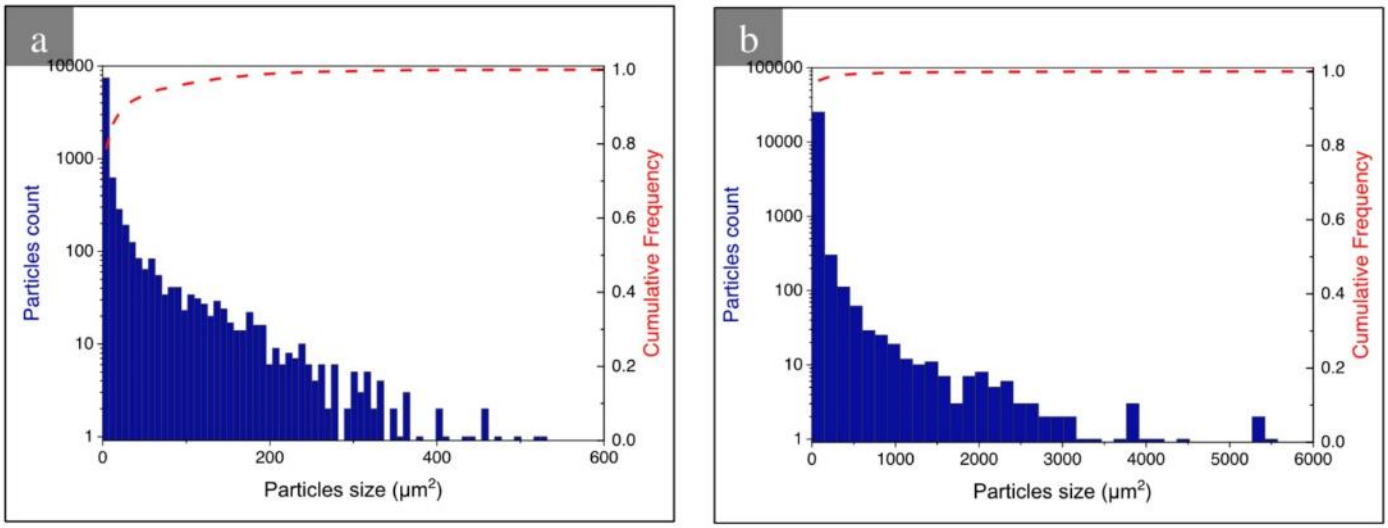

Figure 5.51 Alumina particle size distribution in a) AA6061-0.4%alumina deposition; b) AA6061-2.8%alumina deposition.

Table 5.7.1 Average and median alumina particle size and percentage of area covered by alumina particles.

Sample	Average size (μm²)	Median size (μm²)	Area fraction (%)
AA6061-0.4%alumina	14 ± 41	1.8	0.4%
AA6061-2.8%alumina	25 ± 164	3	2.1%

Additionally, depositions from all three feedstocks showed another set of even smaller (around 3 μm diameter) oxide particles (Figure 5.52). EDS spectra showed enhanced oxygen signals on all of the small particles measured, which implies that these small, black particles were also oxides (points 1, 3, 5). Due to their small size, it is important to consider the interaction volume of the electron beam and the resultant x-ray generation, which limits the spatial resolution for collecting oxygen signals from those particles. Monte Carlo modelling in NIST DTSA-II was used to simulate the interaction volume of the characteristic x-rays of oxygen Kα in an Al_2O_3 bulk sample. The resulting x-ray generation volume was 15.9 μm^3. From this simulation, assuming a spherical interaction volume, the spatial resolution in EDS is sufficient for collecting the oxygen signal from Al_2O_3 particles larger than 3.2 μm in diameter. While oxygen signals were detected in particles smaller than 3.2 μm in diameter, it must be noted that this signal may also be from material outside of the particles and higher spatial resolution techniques will be required for a more accurate determination. It should be noted that all of these smaller particles, unlike the larger ones, showed clearly enhanced Mg and Si signals in addition to the oxygen. This combination of aluminum, magnesium, silicon, and oxygen may suggest the presence of a magnesium aluminosilicate phase; however, further investigations would be required to confirm the crystallographic identity of this phase. There was no noticeable difference in the small black particles among the three depositions; the size, shape, and distribution were all similar.

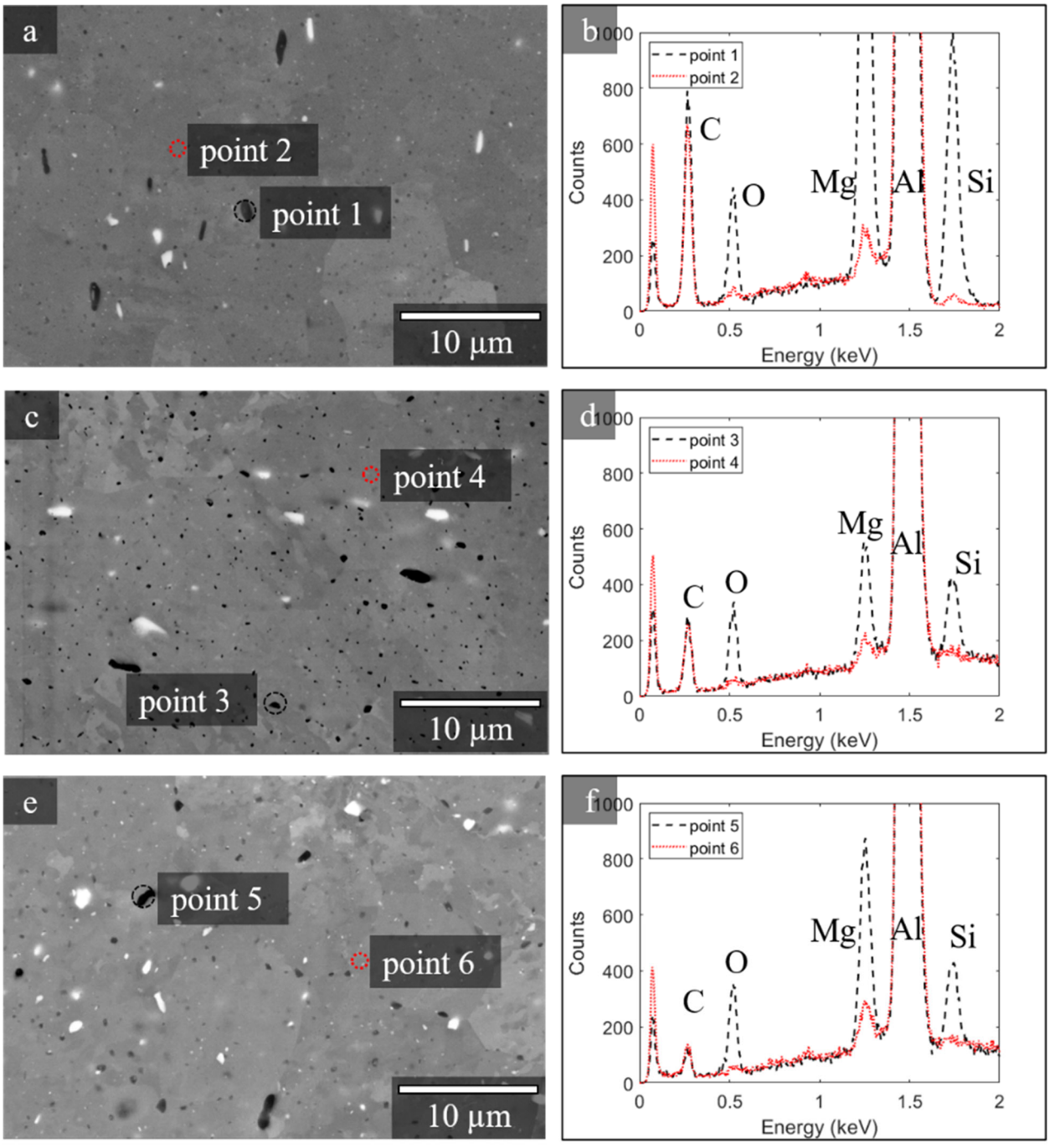

Figure 5.52 SEM images and EDS signals collected from a) & b): the AA6061-NA deposition; c) & d): the AA6061-0.4%alumina deposition; e) & f): the AA6061-2.8%alumina deposition. The peak at 0.1 keV is the noise peak from the spectrometer and should be disregarded.

The tensile properties of the two depositions produced by anodized feedstock (red and blue curves) yielded similar tensile behavior to the non-anodized feedstock material depositions presented by Rutherford et al. [11], shown in Figure 5.53. The YS and UTS did not measurably change as a function of the feedstock-type. The average UTS of the three depositions in the longitudinal direction were between 134 and 144 MPa, and in the build direction were between

125 to 136 MPa (Table 5.7.2). The elongation-to-failure did decrease somewhat with increased volume fraction of alumina in the depositions. Note that Figure 5.53 shows the stress-strain curves until a 40% reduction from the maximum stress was reached. As the volume of alumina increased in the depositions, the average elongation-to-failure was decreased from 68% to 55% in the longitudinal direction and decreased from 60% to 43% in the build direction (Table 5.7.2).

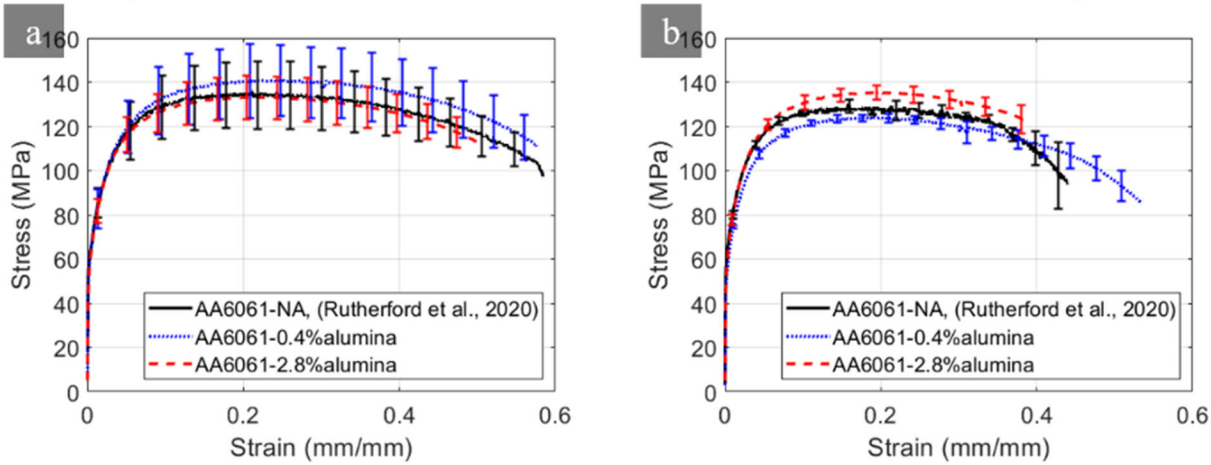

Figure 5.53 Stress-strain curves of quasi-static monotonic tensile behavior of the AFS-D depositions in the a) longitudinal direction; b) build direction. The tensile data from AA6061 without anodization is included from Rutherford et al. [11].

Table 5.7.2 Mechanical properties of AFS-D builds in longitudinal and build directions.

AFS-D Builds	**AA6061-NA [11]**	**AA6061-0.4%alumina**	**AA6061-2.8%alumina**
Orientation	**Longitudinal Direction**		
YS (MPa)	61 ± 6	58 ± 9	54 ± 1
UTS (MPa)	137 ± 15	144 ± 17	134 ± 11
Elongation to failure	68% ± 4%	62% ± 4%	55% ± 8%
Orientation	**Build Direction**		
YS (MPa)	64 ± 3	55 ± 4	55 ± 5
UTS (MPa)	130 ± 3	125 ± 2	136 ± 4
Elongation to failure	60% ± 6%	54% ± 1%	43% ± 5%

The elongation to failure of AFS-D builds was larger in the longitudinal direction than the build direction, but the YS and UTS did not show such a correlation (Figure 5.54). For the three AFS-D builds with different volume fractions of alumina (0%, 0.4 % and 2.8%), elongation to failure in the longitudinal direction was consistently about 10% higher than in the build direction. The UTS did not show an appreciable change between the longitudinal direction and the build direction. The UTS in the longitudinal direction was slightly larger than the build direction in the depositions with 0% and 0.4% of alumina. However, in the deposition with 2.8% of alumina, the UTS is almost the same (134 MPa vs. 136 MPa). In each deposition, the measured UTS in the build direction had less variation (standard deviation of 4 MPa), compared to a standard deviation of 14 MPa in the longitudinal direction.

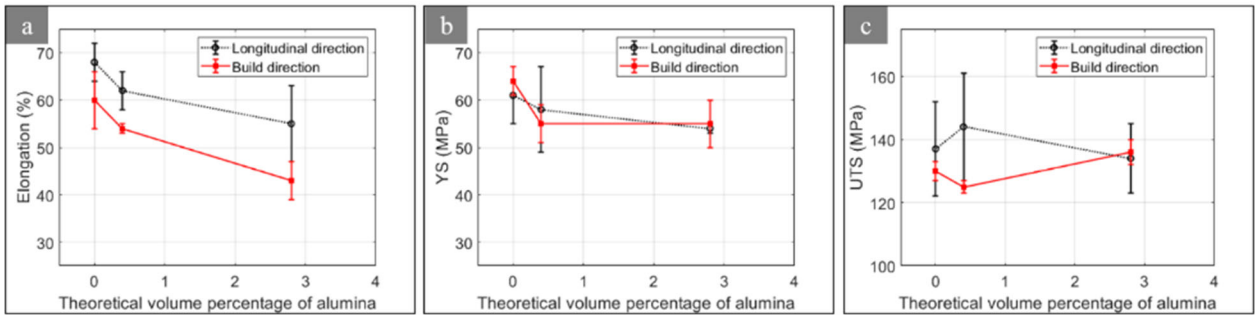

Figure 5.54 Tensile properties of the AFS-D builds as a function of the theoretical volume percentage of alumina in the deposition: a) Elongation; b) YS; c) UTS. The error bars represent the standard deviation among tested tensile coupons.

Ductile fracture was the main failure mechanism observed in both the longitudinal directions (LD) and build directions (BD) for all the three depositions. Extensive microvoids coalescence was observed on the fracture surfaces of all samples (Figure 5.55). The size of microvoids increased with increasing percentage of alumina in the depositions. Large alumina particles can clearly be seen within the large voids on the fracture surface of the AA6061-2.8%alumina deposition (Figure 5.55c and Figure 5.55f). More microvoids per unit area were observed in the longitudinal direction (Figure 5.55a-Figure 5.55c) than the build direction (Figure 5.55d-Figure 5.55f) in all three depositions.

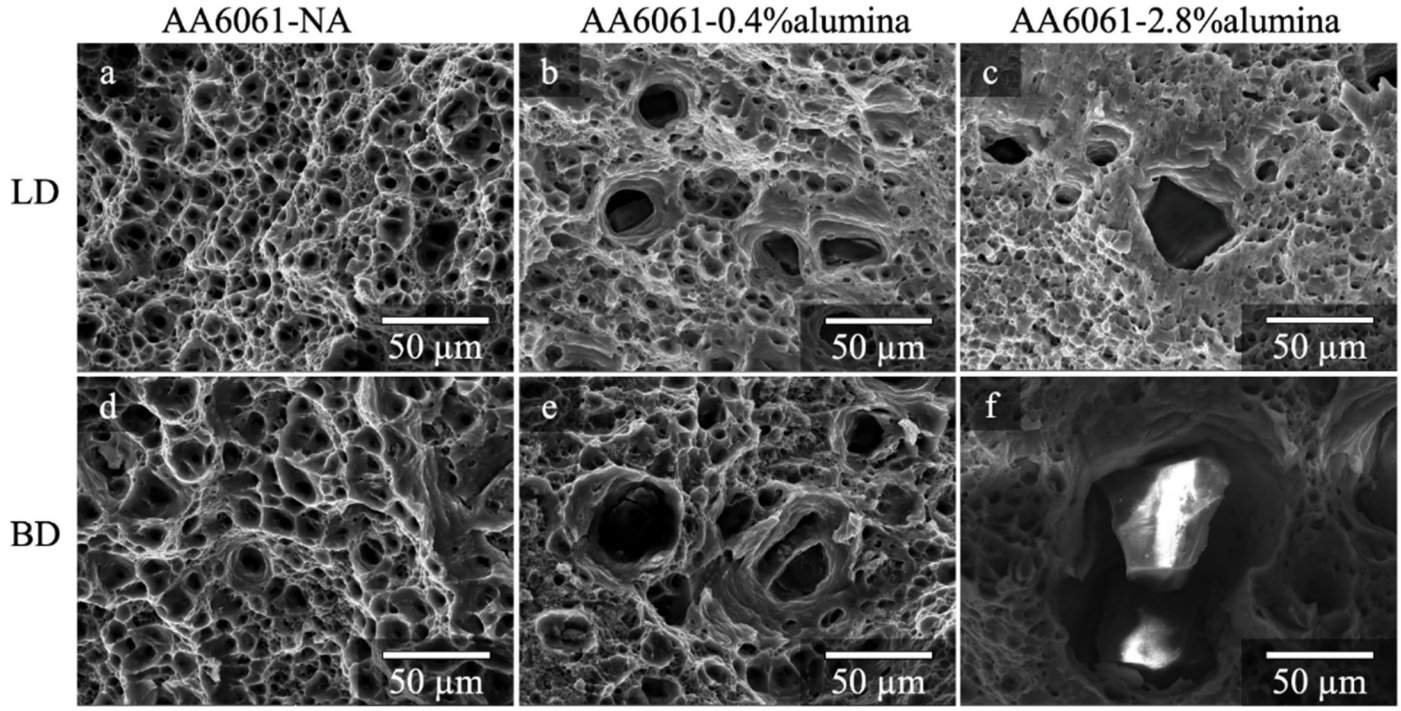

Figure 5.55 Fractography images of AA6061-NA (a, d); AA6061-0.4%alumina (b, e); AA6061-2.8%alumina (c, f) in longitudinal direction (a-c) and in build direction (d-f).

This study answered the concern that oxide layers on the surface of the AFS-D feedstock bars do not measurably increase or decrease the strength of the deposited material. The tensile results

from the AFS-D deposits clearly show that the level of difference in strength between non-anodized and anodized feedstock materials is within the scatter of the measurements (Figure 5.52b & Figure 5.52c). Furthermore, the variation in strength in the build direction is barely measurable. For comparison, other researchers have found that the addition of aluminum oxides/alumina would increase the strength of friction stir welded aluminum alloys compared to the welds without alumina. In the study of friction stir welded AA6061 from Singh et al., an addition of theoretical 3 vol.% of Al_2O_3 particles effectively increased the hardness, YS, and UTS in the nugget zone [19-21]. Tashkandi et al. showed increased UTS of friction stir welded AA6061 from the addition of 2 to 6 vol.% of alumina particles [22]. The increase of hardness of friction stir welded aluminum alloys with reinforcement particles was widely observed: Mazaheri et al. showed increased hardness of A356 with different sizes of Al_2O_3 particles after FSW [23]; Panaskar and Sharma showed increased hardness in friction stir processed aluminum with nanometer-scale (< 50nm) alumina [24]; in the study from Singh et al. [19], the microhardness in the nugget zone was effective increased with increasing the amount of Al_2O_3 particles in the AA6061 after FSW; in the other research from the same group, such increased hardness in the nugget zone was also observed by using TiO2 as the reinforcement material [20]. In those studies, the alumina particle size was either in nanometers [19-21,23,24] before FSW or refined from 25-63 μm to less than 10 μm (as observed from micrographs) [22,23] after FSW. In both cases, the small alumina particles in the friction stir welds served as dispersed, second phase particles that pinned the grain growth and increased the sub-grain boundary strengthening (Hall-Petch relationship) in the aluminum alloys after FSW [25], also known as the Zener pinning effect introduced by Rohrer [26]. Such a correlation between particle size and material strength was not observed in the current AFS-D AA6061 deposits because of some relatively large alumina particles in the deposits (Figure 5.55). The larger, observed alumina particles in the AFS-D deposit is likely for two major reasons. First, the *initial* alumina in this research was not micro-sized particles but was in the form of oxide layers around the feedstock bars. The thickness of those layers was 9.8 μm and 68 μm respectively but the length of those layers was much larger, scaling with the dimensions of the square feedstock bars with a side length 9500 μm, or 9.5mm. Second, the parameters of the AFS-D process had a higher traverse speed (V) and a lower rotational speed (ω) as compared to the FSW process: the weld pitch (V/ ω) in the AFS-D was 0.42 mm/RPM compared to 0.013-0.125 mm/RPM in all the FSW studies discussed above. Low weld pitch in FSW allowed for more stir interaction time between the tool pin and the substrate embedded with alumina particles, thus potentially generating a smaller alumina particle size. Although there is no improvement of the mechanical strength in the AFS-D AA6061 deposit with additional alumina, there was also no observed degradation in strength, as the measured level of difference in strength was within the scatter of measurements.

In addition, there was no measured correlation between the amount of alumina in the AFS-D AA6061 deposits and the measured strength of the deposited material. The volume percentage (vol.%) of alumina for the two AFS-D deposits with anodized coatings was between 0.4% and 2.8%, but the measured yield and ultimate tensile strengths in those deposits were not measurably different (Figure 5.52b & Figure 5.52c). Similar results were also found in friction stir welded aluminum alloys with a low volume fraction of alumina (<6 vol.%): the YS and UTS did not consistently increase with increasing the amount of alumina. In the research of friction stir processed AA6061 with added Al_2O_3 (initial particle size: 40-50 nm), the YS increased from 172.7 MPa to 184.5 MPa with increasing the Al_2O_3 amount from 2 vol.% to 4 vol.%, but then sharply decreased to 129.2 MPa with 6 vol.% of Al_2O_3 [27]. In another research of friction stir

welded AA6061 with added alumina particles (initial particle size: 25 μm), the UTS also increased at first with an increasing amount of alumina particles from 2 vol.% to 4 vol.% in the welds, but then the UTS decreased in the weld with 6 vol.% of alumina [22]. In both studies, the maximum increase in strength, as compared to AA6061 plate without alumina, was observed for 4 vol% alumina before decrease for loading of 6% or greater. In considering the strength of AA6061 material produced by AFS-D, one should also consider the other potential strengthening mechanisms. As FSW and AFS-D process raise the temperature of the material from the frictional heat, the nanoscale, strengthening precipitates (β") in AA6061 were dissolved in the aluminum matrix revealed by transmission electron microscopy in AFS-D AA6061 from Phillips et al. [8] and in friction stir welded AA6061 from Feng et al. [28], thus reducing the strength of the material as compared with wrought plate. If fine enough, alumina particles could contribute to added strength through grain and substructure strengthening and Orowan strengthening, discussed in the review of metal matrix composites from Lloyd [29] and validated with prediction models from Kim et al. [30]. In future research, changes to the AFS-D parameter which increase the stir time for a given volume of material, could decrease the alumina particle size and possibly strengthen the material as observed from the FSW literature.

In contrast, the alumina coatings on the feedstock do decrease the ductility since the fragmented alumina particles in the AFS-D AA6061 deposits served as additional nucleation sites on the fracture surface (Figure 5.55). The alumina particles present in the AFS-D deposits did not change the failure mechanism between materials, as all the samples clearly showed ductile rupture with microvoid coalescence (Figure 5.55). The fractography images clearly show that the alumina particles on the fracture surface were fully embedded in the large voids without any fracture surfaces or cracks inside those alumina particles: the material failed either within the AA6061 matrix or along the boundaries between the matrix and the alumina particles. The presence of the alumina particles appears to generate few, larger microvoids. The decreased ductility of AFS-D AA6061-alumina deposits compared to the non-alumina AFS-D deposit could be attributed to the increased amount of fragmented alumina particles from the oxide layers. A larger amount of alumina particles would reduce the density of microvoids and further decrease the ductility. In the research on FSW of AA6061 from Pirondi et al., the addition of 20 vol.% of alumina particles decreased the elongation from 18% in the AA6061 welds to 4% in the AA6061-alumina welds [31]. Parumandla and Kumar did not observe a constant increased mechanical strength in friction stir welded AA6061 with reinforcement particles, but the elongation was constantly decreased from 8.4% to 4.6%, as the Al_2O_3 amount increased from 2 vol.% and 6 vol.% [27]. For a constant amount of alumina particles, a smaller average size of alumina particles could potentially increase the ductility. Gustafson et al. found the flow stress of AMCs with magnesium aluminate spinel was dependent on the metal ligament size while the reinforcement particles amount remained the same [32]. In a related approach, Yang et al. used FSP to refine the size of alumina particles in initially cold sprayed AA2024-Al_2O_3, and they reported an increase in elongation [33]. The research from Lee et al. on FSP of Si-reinforced aluminum revealed that elongation of welds constantly decreased from 27% to 6% as the amount of Si reinforcement particles increased from 12 vol.% to 34 vol.% with a similar average size (1.26 to 1.51 μm) [34]. In a different study using B_4C reinforcement, decreasing the particle size from 83 μm to 9.3 μm with a similar volume percentage of particles (51-58%) did improve the AMC elongation from 1.5% to 3% [35]. This correlation was not observed in the AMC with Al_2O_3 as the reinforcement particles in the same study. Finally, Li et al. also studied the impact of B_4C reinforcement, with a constant amount (20 wt.%) and a similar size (between 5 and 6 μm)

of the reinforcement particles, and they did not observe a meaningful change in the elongation (4.3% to 4.7%) [36].

The AFS-D process caused multiple fragmentations to the alumina coatings on the feedstock bars into micro-size alumina particles, resulting in a median particle size of 1.8 and 3 μm^2 respectively. The large, irregular alumina particles were uniformly distributed in the AFS-D builds without any agglomeration (Figure 5.48-Figure 5.50). Griffith et al. also observed a uniform distribution of reinforcement particles (silicon carbide) using the same AFS-D process but with metal powders as the feedstock material [17]. In the current study, the oxygen signal shown in the EDS spectra positively identified the larger black particles as alumina (Figure 5.50). Those alumina particles did not show a preferential shape, such as circular or square. Such irregular-shaped reinforcement particles have also been observed in friction stir welded AA6061 with SiC from the review of Gan et al. [37] and in friction stir welded AA6061 with 20 vol.% of Al_2O_3 particles from Marzoli et al. [38]. If these larger particles were produced by a simple, single fragmentation event during AFS-D, then the largest possible width of those alumina particles would be the thickness of the oxide layers (9.8 μm and 68 μm) on the feedstock bars. Assuming square-shaped alumina particles, the largest possible cross-sectional area would be 96 μm^2 and 4624 μm^2 respectively. From our stereology, 95% of the alumina particles were smaller than 96 μm^2 in the AA6061-0.4%alumina deposition (Figure 5.51a), and 99.9% of the alumina particles were smaller than 4624 μm^2 in the AA6061-2.8%alumina deposition (Figure 5.51b). Based on this observation, the AFS-D process seems to refine the particles through multiple fragmentations. This multi-fragmentation in AFS-D is likely from the stirring action of materials beneath the shoulder surface, with applied frictional force from the rotating and plunging tool shoulder. In a similar way, studies from Yang et al. [33] and Hodder et al. [39] suggested that the FSP could effectively refine the size of Al_2O_3 particles in the cold sprayed aluminum deposits. In the AFS-D builds, there are a few alumina particles with a particular larger size indicates those particles were likely being fragmented only once during the friction stirring process. Those largest alumina particles with a length larger than the thickness of the anodized layer, were rectangular in shape with a width limited by the upper scale of the original thickness of the anodized layer. Approximately, there were 5% and 0.1% of those particles in AA6061-0.4%alumina deposition and AA6061-2.8%alumina deposition respectively, and they could be clearly observed in the fractography images (Figure 5.55). In the AA6061-2.8%alumina deposition, the largest alumina particle (10,100 μm^2) was rectangular with the width around 80 μm (upper scale of the anodized layer thickness) and the length around 130 μm. A similar observation was found in the AA6061-0.4%alumina deposition, for which the largest particle (528 μm^2) had a rectangular shape with the width around 17 μm and the length around 31 μm. Those large alumina particles were likely to be fragmented only once during the AFS-D process, which resulted a rectangular shape with the length larger than the original thickness of the anodized layer. However, those large rectangular alumina particles were less than 5% of the total particles observed in both builds.

The data in this paper also indicates a second population of smaller, more complex oxides in the AFS-D AA6061 builds. EDS spectra exhibited enhanced oxygen, magnesium and silicon signals on those particles comparing to the aluminum matrix, which suggest, that these smaller particles have a more complex composition, and are likely not alumina (Figure 5.52). Similar, small particles were observed in the wrought feedstock material, thus suggesting that the smaller particles were not generated by the AFS-D process. Further crystallographic investigation would

be necessary to confirm that smaller particles are indeed carried over from the wrought feedstock.

Given these results, one might consider AFS-D as a solid-state means of producing AMCs. This paper is the first work using AA6061 feedstock bars with anodized alumina layers to produce consolidated AMCs via AFS-D. The optimized AFS-D processing parameters for AA6061 from Phillips et al. [8], also produced sound aluminum alloys depositions using anodized feedstock material. As previously described in the literature, AMCs produced from FSW can require laborious preparation: most of the reinforcement materials were nanoscale particles; substrates required pre-machining with grooves or drilled holes to load the reinforcement particles [40]. In contrast, AFS-D has successfully produced AMCs by two approaches: previous work showed by Griffiths et al. [17] using a continuous powder feeding system, and this work using the solid square-rods feeding system. In the paper from Griffith et al., the AFS-D system used powder feedstocks, which required fine meshed powders and a pre-mixture of matrix powders and reinforcement particles. The approach to AFS-D in this work used commercially available, solid square-rod feedstock (9.5 mm × 9.5 mm × 305 mm) with the alumina reinforcement material provided by anodization. Despite the simplicity and low-cost of the anodized feedstock approach, the current loading of the alumina reinforcement phase will need to be increased beyond 3 volume percent in order to achieve a higher level of composite strengthening. This increase in reinforcement loading must be balanced against any decrease in ductility. Future work will consider feedstock designs which balance these needs.

5.7.3 Conclusions

This work using a systematic control of anodized feedstocks demonstrates that when investigating the influence of oxide films on secondary aluminum feedstock such as recycled chips and waste strips of material suggest these waste streams are viable candidates for the AFS-D approach to solid state AM with minimal or no degradation of mechanical properties from wrought feedstock. From the results and discussion, below are the conclusions addressed from this research:

Oxide layers on the surface of the AFS-D feedstock bars do not measurably impact the strength of the deposited material but may degrade the ductility: increasing the amount of alumina from 0% to 2.8% in the deposit decreased the elongation in the longitudinal direction from 68% to 55%, and in the build direction from 60% to 43%.

The microstructures produced by AFS-D exhibit two populations of oxide particles: the larger particles were generated by fragmentation and refinement of the anodized oxide coating by the AFS-D process, and the second population of smaller, more complex oxides were from the feedstock materials. The larger alumina particles may be acting as additional and larger nucleation sites on the fracture surface which decreased the elongation to failure in both orientations.

Similar to FSW, The AFS-D process has the ability to refine reinforcement materials added to the feedstock materials: a majority (>95%) of the alumina particles in the deposit had been fragmented multiple times and resulted a width less than the thickness of the anodized layer on the feedstock bars.

Additionally, this work suggests that AFS-D is a solid-state near-net shape AM means of producing a metal matrix composite from non-powder feedstock materials.

5.8 Residual Stress Distributions in AA6061 Feedstock AFSD Characterized by Neutron Diffraction

This work provides the first description of the residual stress distribution in a 66 mm-thick AA6061 deposit produced by additive friction stir deposition (AFSD). The AFSD process is being developed as a solid-state additive manufacturing technique and has been successfully applied to a wide range of alloys including aluminum, nickel, and magnesium alloys. In this study, a large ($194 \times 49 \times 66$ mm^3) deposit of AA6061 was produced using AFSD with a rotational speed of 300 RPM and a translational speed of 127 mm/min. Three components of residual stresses were independently measured in the deposit using neutron diffraction on the VULCAN instrument at the Spallation Neutron Source in the Oak Ridge National Laboratory. The distribution of residual stress through the thickness of the deposit is relatively constant. All three residual stress components were tensile at the beginning and in the center of the deposit, but compressive at the completion of the deposit. The d_0-spacings measured from stress-relieved samples show a marked change in lattice constant in the top layers of the deposit. This change in lattice chemistry is attributed to the dissolution of β" (Mg_2Si) precipitates caused by the thermal cycles in the AFSD process.

5.8.1 Material and Method

The feedstock materials used in this study before the deposition process were AA6061-T6 square bars with a dimension of $9.5 \times 9.5 \times 304.8$ mm^3. The nominal chemical composition of this alloy is shown in Table 5.8.1. A commercial B8 AFSD machine manufactured by MELD Manufacturing was used to produce a large AFSD build (Figure 5.57a) with a dimension of $194 \times 49 \times 66$ mm^3 on a 12.7 mm thick AA6061-T6 substrate. The AFSD processing parameters adapted from previous research was used in this study: 300 rotations per minute (RPM) for the rotational speed, 127 mm/min for the tool traverse speed, and 66 mm/min for the actuator feed rate [10, 24, 25]. Each deposited layer consumed one feedstock bar and the translational direction of the tool was always moving from starting position to the finishing position (Figure 5.57a). An initial dwell time of 30 s at the starting position of the deposit provided sufficient frictional heat to soften the feedstock material.

Table 5.8.1. Nominal chemical composition of feedstock square bars AA6061-T6 [26].

Aluminum Association designation	Composition, wt. %							
	Si	Fe	Cu	Mn	Mg	Zn	Cr	Al
6061	0.4-0.8	<0.7	0.15-0.40	<0.15	0.8-1.2	<0.25	0.04-0.35	Bal.

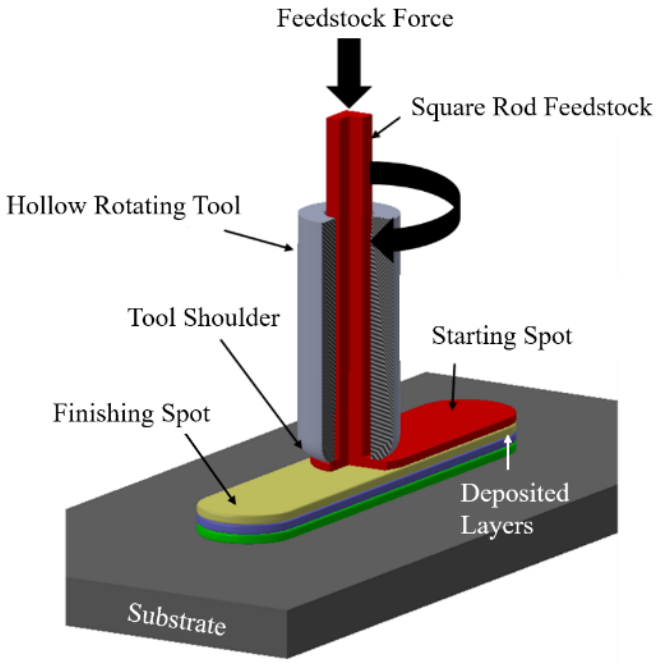

Figure 5.56 Schematic of AFSD process, modified from Avery et al.'s previous work [5] .

Neutron diffraction measurement of AFSD AA6061

Lattice spacings (d-spacings) of the AFSD deposit (Figure 5.57a) were measured via neutron diffraction from the VULCAN diffractometer at the Spallation Neutron Source at Oak Ridge National Laboratory. The d-spacings from the {3 1 1} diffraction peak were measured and processed using the VDRIVE software [27] with a least squares refinement subroutine in GSAS [28]. The d-spacings in all three directions were measured respectively: as shown in Figure 5.58, the d-spacings in transverse direction was measured by detector bank 1 and the d-spacings in normal direction was measured by detector bank 2. Then the AFSD deposit was rotated for 90º, which in this mounted orientation, the d-spacings in longitudinal direction were measured by detector bank 1. A 2 × 2 × 6 mm^3 gauge volume was defined by the incident beam slits. The scan was performed from the bottom of the substrate to the top of the deposit with a 2 mm step size. The d-spacings were measured in three distinctive regions in the AFSD deposit showed in Figure 5.58: starting position, where was the starting position of each deposited layer; the center region of the AFSD deposit; and the finishing position, where was the finishing position of each deposited layer.

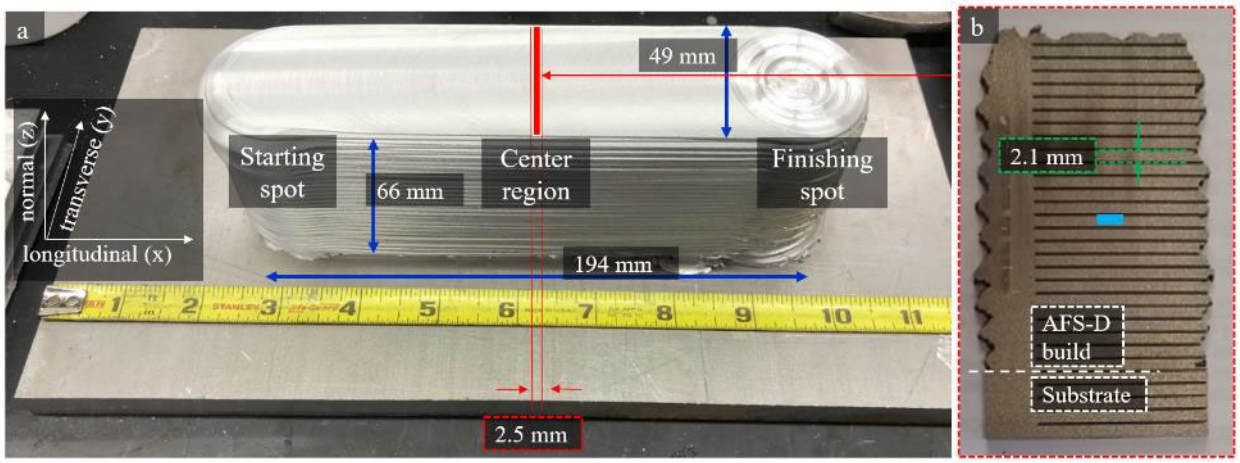

Figure 5.57 (a) AFSD AA6061 deposit built on a 12.7mm-thick AA6061-T651 substrate, red box region indicates the location of sliced 'comb' sample in (b); (b) stress-relieved 'comb' sample for d_0-spacing measurement, cyan box region indicates the location of neutron beam measured on each tooth.

Unstressed lattice spacings (d_0-spacings) from the {3 1 1} diffraction peak were measured from the stress-relieved 'comb' samples (Figure 5.57b). Those 'comb' samples were machined by electrical discharge machining from the AFSD AA6061 deposit in the location where the stressed lattice spacings were measured. For example, the 'comb' sample shown in Figure 5.57b was machined from the center region indicated with a red bar in Figure 5.57a. Two other 'comb' samples were machined from the starting position and finishing position respectively. The thickness of each comb sample was 2.5 mm. The stress-relieved cuts were at least 38-mm-long and parallel to the transverse direction (y). The first stress-relieved cut was performed along the boundary between the deposit and the substrate. The stress relieving cuts on the 'comb' sample in the normal (z) direction resulted a tooth width of 2.1 mm, showed in Figure 5.57b. Neutron diffraction data with the same gauge volume ($2 \times 2 \times 6$ mm^3) was collected in the center of each tooth between two adjacent cuts on the 'comb' sample along the transverse (y) direction, as marked with a cyan box in Figure 5.57b. The scan was performed from bottom of the substrate to top of the deposit on each of the three 'comb' samples.

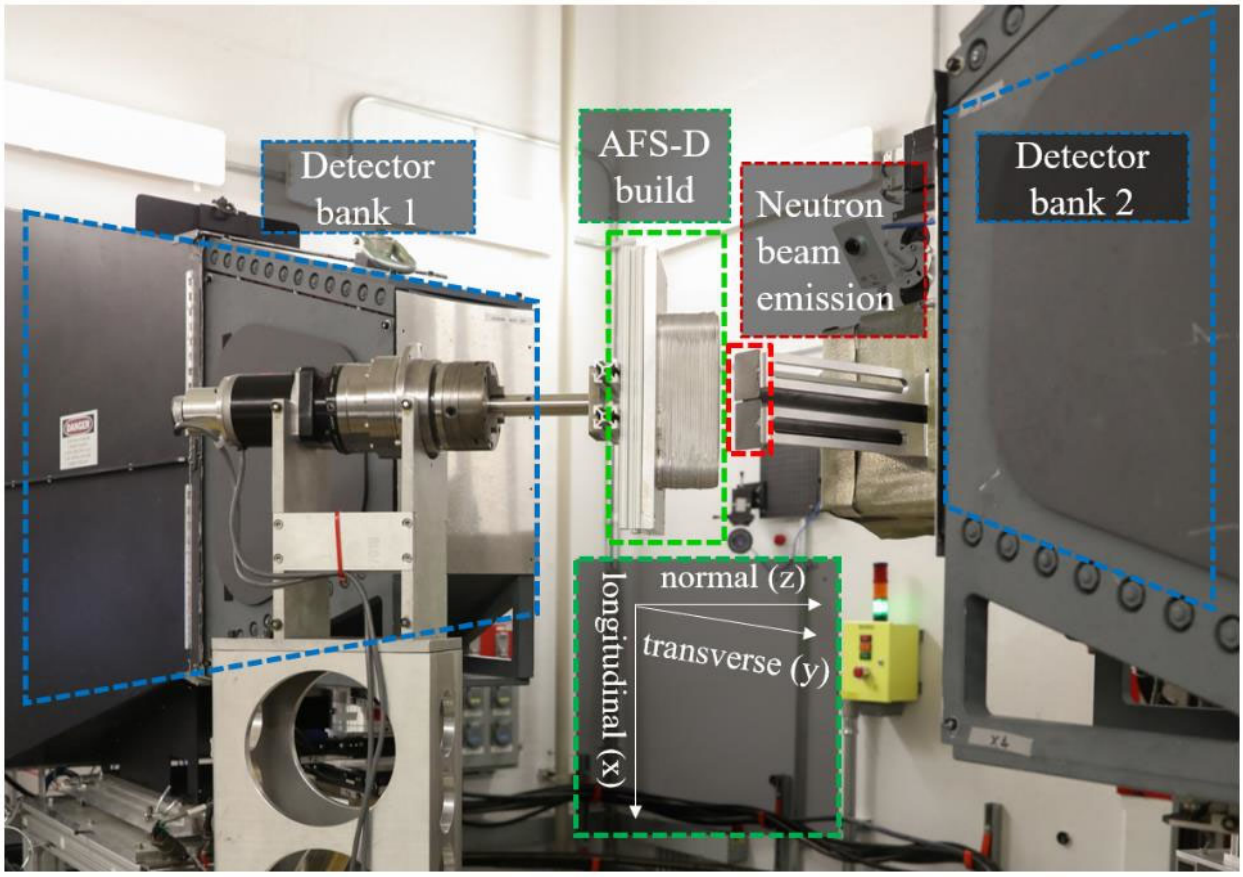

Figure 5.58 Schematic of the geometry for the neutron diffraction-based residual stress experiments.

Residual Strain and Residual Stress Analysis

The lattice strain was calculated from the following equation:

$$\varepsilon_i = \frac{d_i}{d_{0_i}} - 1 \qquad 5.8.1$$

where ε is the lattice strain, i is one of the three orthogonal directions, which are longitudinal (x), transverse (y) and normal (z) directions, d is the stressed lattice spacing and d_0 is the unstressed lattice spacing.

Hooke's law was applied to calculate the residual stress from the following equation:

$$\sigma_i = \frac{E}{(1+\nu)}\left\{\varepsilon_i + \frac{\nu}{1-2\nu}(\varepsilon_x + \varepsilon_y + \varepsilon_z)\right\} \qquad 5.8.2$$

where σ is the residual stress, ε is the lattice strain calculated from equation (1), E and ν are the elastic moduli and Poisson's ratio for reflection {3 1 1}, which are 69 GPa and 0.35 respectively adopted from the Reuss modeling scheme M.T. Hutchings [29]_ENREF_29. This analysis of residual stress measured from neutron diffraction were successfully adopted in other researches, e.g., AA6061-T6 after friction stir processing [18] and Inconel 625 after laser powder bed fusion [30].

Microstructural Characterization and Hardness Measurement

Cross-sections parallel to the normal (z) direction from the center region in the deposit were used for microstructural analysis. Those samples were cold mounted, ground, and subsequently polished with 3 μm, 1 μm diamond suspensions and final vibratory polished for 4 hours with 0.02 μm colloidal silica. The electron backscatter diffraction (EBSD) measurements were collected on an Apreo scanning electron microscope (Thermo Fisher Scientific, Waltham, MA, USA) at 20 keV and 6.4 nA using the APEX system (EDAX, Draper, UT, USA) with a 0.5 μm step size in a 150 × 150 μm^2 region. Cleanup on the EBSD measurements was performed on the OIM analysis package (EDAX) with the standard grain dilation type using a minimum grain size of 9 pixels. Microhardness were measured using an automated microhardness tester (Clemex, Quebec, Canada) with an axial load of 200gf and a dwell time of 10 seconds. A 5 × 72 hardness indentation grid was taken in the center region in the AFSD build and the substrate. The spacing between the microhardness indentation is 500 μm, which is more than three times of the indentation diameter around 100 μm.

5.8.2 Results and Discussion

The unstressed lattice spacings (d_0-spacings) measured from the "comb" samples showed three distinct regions beginning from the substrate through the deposit in the z direction (Figure 5.59). In each case, no significant variation in the x direction was observed. The substrate, represented by the negative values in normal direction from -13 mm to 0 mm in Figure 5.59, exhibited a uniform, and slightly larger, d_0-spacing than the main deposit. The first 50 mm of the deposit (0 mm to 50 mm) in the z direction showed a slight, almost linear increase in d_0-spacing. From 50 mm to the top of the deposit (50 mm to 66 mm), a sharp, nonlinear increase in d-spacing was observed. One should note that the d_0 distribution for a 'comb' sample with no stress and no change in chemistry would be flat across the entire deposit. The observations here indicate a possible change of the solute (Mg and Si) distribution in the aluminum matrix along the z direction in the deposit. The distribution of d_0-spacings measured along the z direction from the two ends and the middle of the build showed very similar trends.

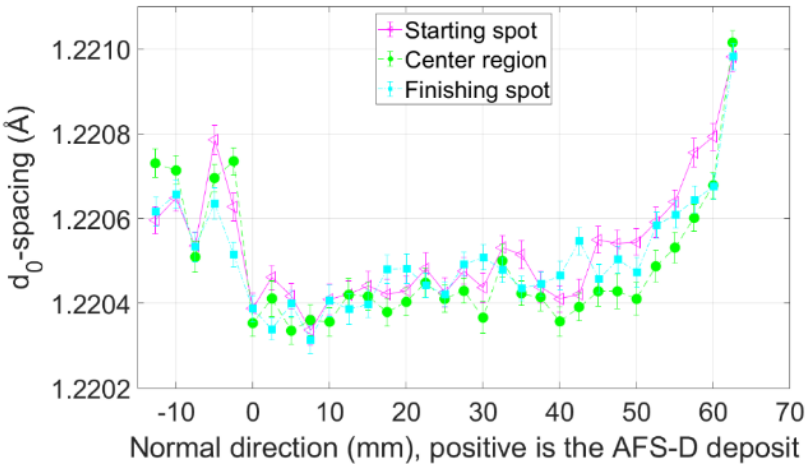

Figure 5.59 Measured d_0-spacings from the stress-relieved "comb" sample sliced from the AFSD deposit. The "normal" direction is the same as the z direction.

The measured lattice spacings and associated strains in the AFSD produced builds showed clear variation with respect to position in the build and the direction of the measurement (Figure 5.60 and Figure 5.61). In the substrates (normal direction: -13 mm to 0 mm) considerable strains were observed in all three directions, with tensile strains in the x and y directions and compressive strain in the z direction (Figure 5.61). In the first 50-60 mm (normal direction) of the build, the strain values were much smaller, but again increase in magnitude in the top 6-16 mm. The strain components did vary as a function of longitudinal (x) position in the build, e.g., from the starting position to the center region and then to the finishing position. For the starting position of the build (Figure 5.61a), the normal (z) component of strain was nearly zero for the first 60 mm of the build before becoming positive for the top 6 mm of the build. The distribution of y-component strain was similar except that the strain became compressive in the top 6 mm of the build. The x-component of strain was tensile throughout the build before becoming compressive at the top of the build. In the center region of the build (Figure 5.61b), the normal (z) component strain component was quite similar to the starting position of the build. The y component, however, was now tensile throughout the build and the x component was even more tensile than at the start. At the build finishing position, the x component was now slightly compressive, while the y and z component were clearly more compressive than in other regions of the build.

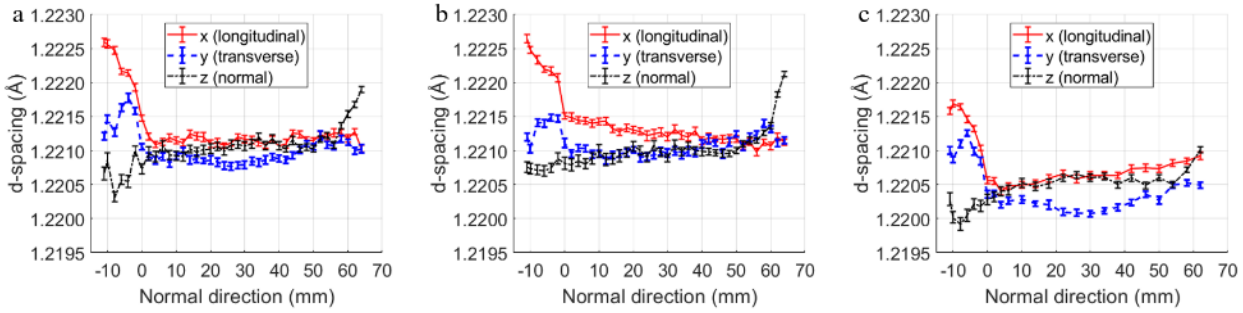

Figure 5.60 Measured d-spacings from the AFSD deposit in: (a) starting position; (b) center region; (c) finishing position.

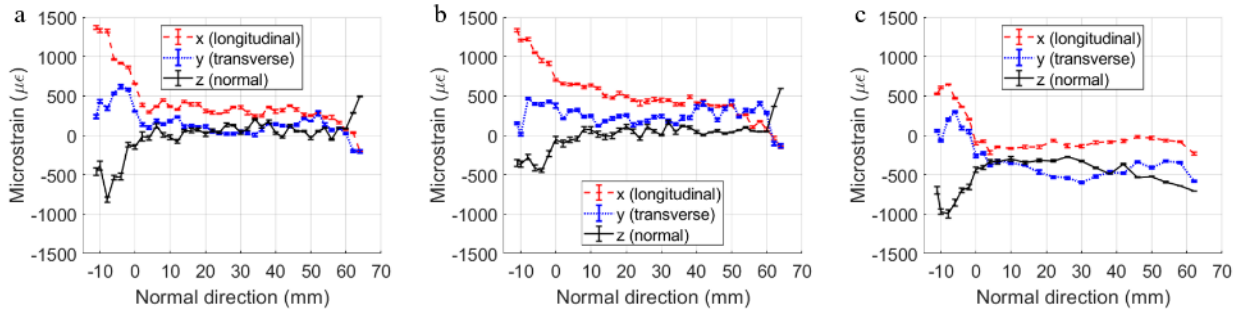

Figure 5.61 Calculated strain distribution in the AFSD deposit in: (a) starting position; (b) center region; (c) finishing position.

Using a Hooke's law analysis of the stresses based upon the measured strains, clear residual stresses were observed for all three (x, y, z) components in all regions of the build. In all three directions, the calculated residual stresses were tensile in the starting position and center region; and then changed to compressive in the finishing position (Figure 5.62). Clear differences in the x, y, and z components were noted in the substrate, particularly at the starting and center positions. Within the build, all three stress components closely tracked each other. The stress components were quite stable in value for the first 50-60 mm of the build before evolving in the top 6-16 mm of the build. This change at the top of the build was particularly clear for the finishing position.

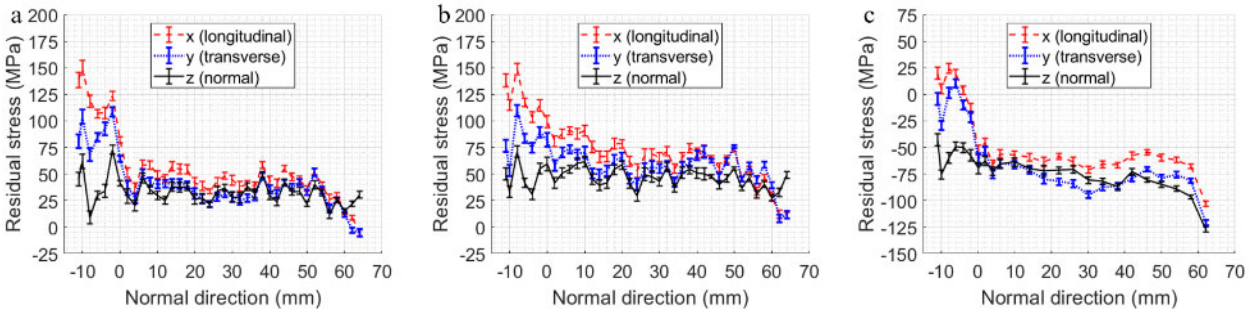

Figure 5.62 Residual stress distribution in the AFSD deposit in: (a) starting position; (b) center region; (c) finishing position. Note: the residual scale is different between sub-figures to allow better visualization of the changes in the residual stress profiles.

These neutron diffraction results provide the first evidence for residual stresses in material produced by AFSD. Authors in the recent literature have pointed out that materials produced by solid-state additive manufacturing exhibit comparatively lower levels of distortion and residual stresses [1]. These new neutron diffraction results are important because it is quite possible to have significant residual stresses in a material without exhibiting distortion. In fact, components often distort in order to relieve their internal residual stresses. For example, Richter-Trummer's research of clamping force effect on the distortion and residual stress in friction stir welded AA2198 revealed that highly distorted welds exhibited lower residual stress, whereas less distorted welds exhibited higher residual stress [31].

The residual stresses (RS) measured here in the AFSD AA6061 build at the starting position and center region are generally tensile and comparable to the tensile residual stress in the SZ reported in the extensive literature from friction stir welding/processing (FSW/P) of AA6061 (Table 5.8.2), but the region of balancing compressive residual stress is clearly different. In FSW/P, the peak tensile longitudinal (x) residual stress is usually observed outside the SZ, at a distance from the weld center line slightly larger than the radius of the tool shoulder. Thus, a better comparison is to compare the measurements from the SZ of friction stir welded material with the AFSD builds, as the physics and microstructures generated are closest for these regions. A wide range of residual stress values has been reported in the SZ in FSW/P of AA6061-T6: the longitudinal residual stresses are between -40 and 160 MPa, and the transverse residual stress are between -100 and 50 MPa (Table 5.8.2). These measurements are based upon different welding conditions and different measurement techniques, and generally measured in the center region along the FSW/P path. In this AFSD AA6061 build at the starting position and center region, the longitudinal residual stress ranges between -5 and 91 MPa and the transverse residual stresses is between -5 to 76 MPa, within the range reported for FSW/P of AA6061. In both FSW and AFSD of AA6061, the longitudinal (x) residual stress is generally tensile and larger than the transverse (y) residual stress [18,32] and the normal (or short transverse, z) residual stress is the lowest among the three component of residual stress. It is worth mentioning that the region of balancing compressive residual stress is clearly different in AFSD AA6061 build comparing to FSW/P of AA6061. Generally, in the FSW of aluminum alloys, the compressive residual stresses are along the longitudinal (x) direction in the HAZ and base metal [12,14,18,20] to balance the tensile residual stress in the SZ and TMAZ. The mechanism of developed tensile residual stress and balancing compressive residual stress can be explained by a three-bar arrangement illustration from Kou [33]. However, in the AFSD build, there is no HAZ or base metal region outside of the stir zone, thus the balancing compressive residual stresses have to be somewhere inside the build, or in the substrate. As a result, the finishing position exhibited compressive residual stresses in all three components between -127 and -46 MPa throughout the thickness from bottom of the substrate to top of the build, with tensile longitudinal residual stresses in the substrate of slightly less than 25 MPa. In FSW/P of AA6061, compressive residual stresses in the SZ were also observed in multiple studies, and generally they were distributed along the transverse direction [22,23,34].

Table 5.8.2. Residual stresses in the AFSD AA6061 and FSW/P of AA6061-T6 from the literature. Unless specific values were given from the authors, residual stresses in FSW/P of AA6061 were estimated from the plots.

Process	Method	Location in the normal direction	Location in the welding direction	Longitudinal RS		Transverse RS		Normal RS		Ref
				min	max	min	max	min	max	
AFSD	Neutron diffraction	Through thickness	Starting position of layers	-5	59	-5	51	12	49	This research
			Center region of layers	11	91	8	76	27	61	
			Finishing position of layers	-103	-46	-121	-54	-127	-63	
FSW/P	Neutron diffraction	Mid-thickness	Center region of the FSW path	70	110	0	50	0	30	[18]
	Contour	Mid-thickness		125	150	-	-	-	-	[20]
				30	150	-	-	-	-	
	X-ray diffraction	Top surface		-40	5	-30	-20	-	-	[22]
				-	-	-100	-70	-	-	[23]
				-	-	-15	10	-	-	[34]
				-	-	-15	0	-	-	
	Hole-drilling			105	130	30	50	-	-	[32]
				115	150	15	50	-	-	
				115	160	30	40	-	-	

All three components of residual stress are relatively consistent through the thickness (normal direction) at the starting position and center region of the AFSD AA6061 build, but such consistency is not observed at the finishing position, particularly in the top 10 mm of the build (Figure 5.62). In FSW/P of AA6061-T6, mixed results were reported to show the residual stress variation in the normal direction of the welds. In Woo et al.'s study, all three components of residual stresses were relatively consistent at the top surface, mid-thickness and bottom surface in the SZ, and the slightly variation of those residual stresses in the normal direction were within the error bars [18]. The homogenous distribution of residual stress in the normal direction were contributed to the 6.23-mm pin (95.8% of the welds thickness) acted as a heat-transfer medium in the 6.5-mm-thick welds. On the other hand, Liu et al. reported that in the weld centerline of friction stir welded AA6061-T6, mid-thickness longitudinal residual stress is larger than those near the top and bottom surface, and the peak residual stress was at a depth of 37.5% of the welds thickness below the top surface [20]. Note although both Woo et al. and Liu et al. used a similar travel speed between 250 to 282 MMPM, Woo et al. used 150% higher rotational speed of 1250 rpm comparing to 500 rpm used by Liu et al. One of the origins of residual stress is the thermal misfit stresses which arise from the temperature gradient [35]. The higher rotational speed in Woo et al.'s study provided more frictional heat, and consequently a lower temperature gradient, and resulted a homogenized distribution of residual stress through the thickness. The contribution from thermal misfit stresses to residual stresses in the AFSD build were likely be more significant than in FSW/P, since all regions in AFSD build experienced plastic deformation, similar to the SZ in the FSW/P. In other words, the plasticity gradient in AFSD should be less than in FSW/P, so residual stress generation would be dominated by thermal gradients. In this research, the bottom part of the AFSD build experienced more thermal cycles, since the AFSD is an additive manufacturing technique that deposit materials layer-upon-layer. The previously deposited layers at the bottom experienced multiple thermal cycles from the subsequent newly depositing layer. Those multiple, repeating thermal cycles were likely to result in a more homogeneous distribution of the temperature (less temperature gradient) in the bottom and middle parts of the build. The top few layers did not experience such repeated thermal cycles, so the temperature gradient was likely larger. Additionally, at the finishing position, the top few layers experienced the least amount of time at elevated temperature from the frictional heat. There was a 30s dwelling time at the starting position of each layer, and the total amount of time to build a single layer is about 100s including the dwelling time. The combination of fewer thermal cycles and less dwell time at elevated temperature resulted in the largest magnitudes of residual stress being observed at the top of the build.

These residual stresses are significant in light of the low yield strength of the AFSD material in its as-deposited state. When evaluating residual stress values, it is critical to reference them to the yield strength of the material [12]. For example, fully aged (T-651) AA6061 has a yield strength of 275 MPa, while fully annealed AA6061 (O temper) only has a tensile yield strength of 55 MPa [19]. It is more appropriate comparing the residual stress to the yield strength of the welds and not the parent material, since the yield strength often decreases after FSW of T6 heat-treated aluminum alloys due to coarsening of precipitates from the frictional heat. For example, the yield strength of FSW/P of AA6061-T6 decreased from 275 MPa to between 125 and 194 MPa in the transverse direction (perpendicular to the welding path) [22,23,34], and decreased to 105 MPa in the longitudinal direction (parallel to the welding path) [23]. Previous work on the mechanical properties of AA6061 produced by AFSD under the same conditions as those used in this paper produced material with a yield strength of 61.3 ± 6.4 MPa in the longitudinal direction and 63.9 ± 2.7 in the normal direction [24]. Clearly this yield strength is much closer to the O temper than a T-651 temper. Looking again at the residual stresses measured in the build (around 50 MPa, Figure 5.62), the residual stress level is close to the yield strength. In some cases, e.g., in the top 10 mm from the finishing position of the build (Figure 5.62c), the residual stress is estimated to be in excess of this yield strength. This discrepancy may be either from a lack of accuracy in the neutron diffraction generated residual stresses, or more likely, in the use of a single bulk average value for the yield strength in the AFSD build. For example, in a related study on AFSD of AA7075, the hardness (flow strength) gradually increased from 65 Hv at the bottom to 105 Hv at the top of the build, indicating an increase of yield strength in the normal direction [36]. The increasing hardness in the normal direction is also observed in this research of AFSD AA6061 (Figure 5.63). Thus, the apparent discrepancy of residual stresses exceeding the yield strength of the material is most likely due to a changing yield strength of the deposit material through its thickness. To authors' understanding of literature, there are few studies of residual stress distribution in fusion-based additive manufacturing of AA6061. However, the residual stress in fusion-based welding of AA6061-T6 is generally larger: Maisonnette at al. applied thermal loadings on AA6061-T6 to represent the welding cycles in the electron beam welding and discovered the tensile longitudinal residual stress is around 100 MPa in the fusion zone and 250 MPa in the HAZ [37]; Xu et al.'s numerical finite element model predicted tensile longitudinal residual stress between 200 and 280 MPa in the weld zone of AA6061-T6 after laser and gas metal arc hybrid welding [38];

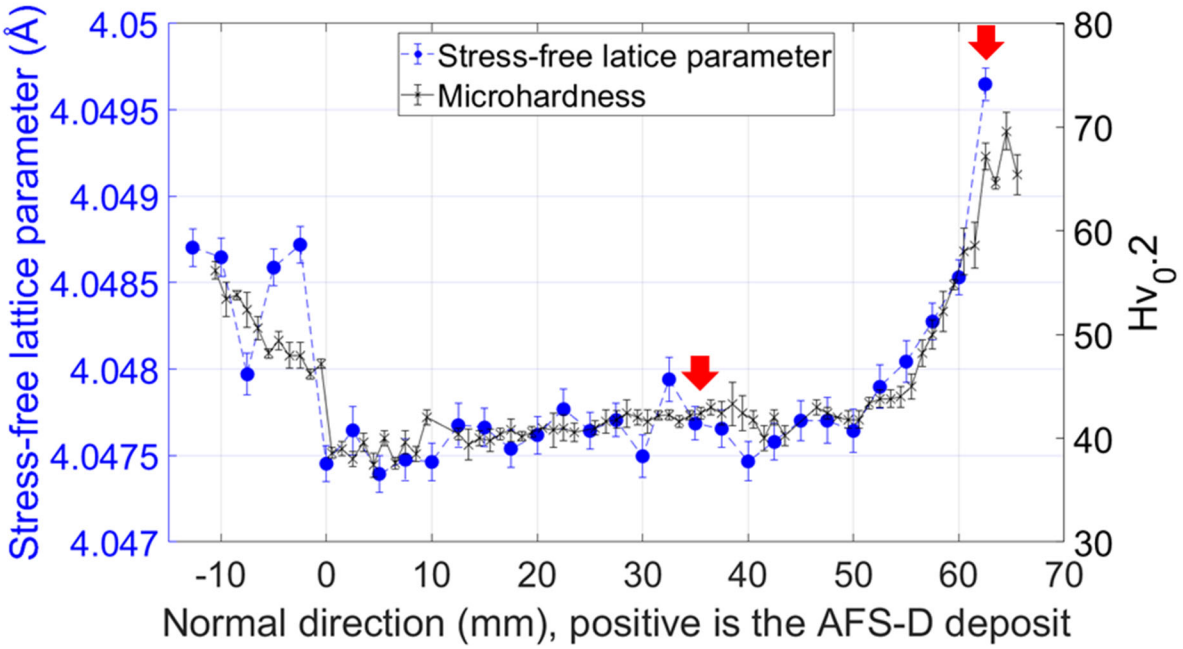

Figure 5.63 Stress-free lattice parameter (blue filled circles) and microhardness (black cross) in the z (normal) direction in the center region of the AFSD AA6061 deposit. Red arrows indicate the regions of EBSD inverse pole figure in Figure 5.64.

The neutron diffraction measurement of lattice parameter poses an interesting question in light of this discussion of yield strength/hardness gradient through the AFSD build. In Figure 5.63, we have plotted the measured hardness distribution on top of the measured, stress-free lattice parameter distribution. It is clear that the gradients in hardness and lattice-parameter track closely together. What does this correlation mean in terms of mechanical properties and residual stresses for the AA6061 AFSD build? The change in lattice parameter indicates that the top 16 mm of the build experiences a change in α aluminum (FCC) matrix chemistry. It has been noted in several, recent papers on AA6061 material produced by AFSD that the β" precipitates present in the feedstock material are dissolved during the deposition process [10,24,25]. The dissolution of these precipitates will release the Mg and Si atoms back into solid solution, thus changing the composition and the lattice parameter of the α aluminum matrix. The loss of the β" precipitates is the primary factor in explaining the loss of yield strength in the AFSD produced material compared with the T6 tempered feedstock. The grain size of the feedstock is refined by the AFSD process, and in this research, the average grain size in the mid-thickness was 13.9 ± 8.9 μm, slightly larger than the grain size of 12.3 ± 5.5 μm in the top surface in the AFSD AA6061 build (Figure 5.64d). This small difference in grain size cannot explain the measured difference in hardness observed in Figure 5.63. A more likely explanation is that the top of the build has naturally aged after deposition, thus increasing its hardness. The middle of the build experience prolonged heating which allowed for the coarse, β phase particles to precipitate, which does not provide strength to the material. Further investigation into the evolution of the strengthening phases in large AFSD AA6061 builds will provide insight into this complex phase evolution.

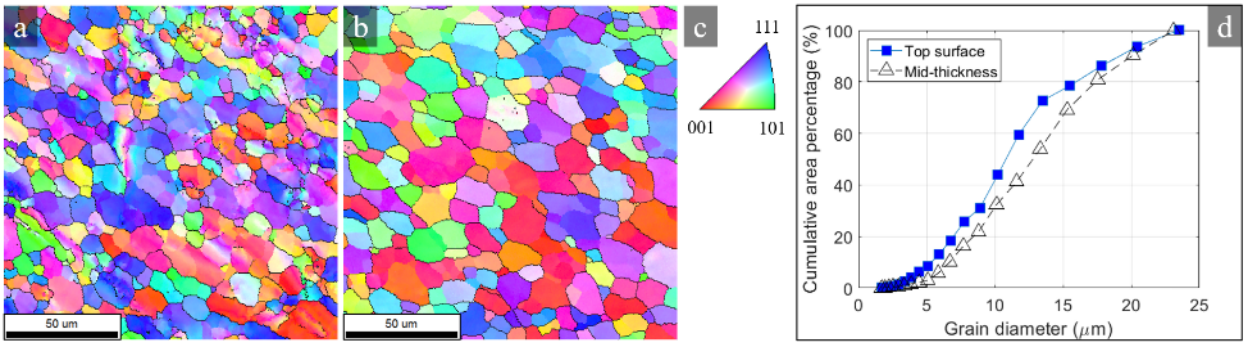

Figure 5.64 EBSD inverse pole figure mapping with respect to longitudinal direction mapping showing grain size in the AFSD deposit in the center region: (a) top surface; (b) mid-thickness (c) legend of crystal orientation; (d) cumulative area percentage as a function of grain diameter.

5.8.3 Conclusions

This work provides the first characterization of residual stresses in material produced by AFSD.

The residual stresses measured in the AFSD AA6061 at the starting position and center region of the build are generally tensile, and the longitudinal residual stresses are between -5 and 91 MPa and consistently larger than the transverse residual stresses between -5 and 76 MPa. Both longitudinal and transverse residual stresses are within the range of residual stresses reported in the literature for the stir zone of AA6061-T6 produced by friction stir welding or processing (FSW/P). However, unlike the compressive residual stresses observed in the HAZ and base metal after FSW/P of AA6061, the balancing compressive residual stress (between -127 and -46 MPa) in the AFSD AA6061 are observed at the finishing position of the build. The largest tensile stresses were consistently observed in the support substrate for the build.

All three components of residual stress are distributed homogeneously throughout the AFSD AA6061 build except at the top surface. The deposit in this region experienced the least thermal cycles and the least amount of aging time at elevated temperature from the frictional heat, thus resulted the largest residual stress (-127 MPa) in the AFSD build.

The residual stresses are much lower in the AFSD AA6061 build as compared to the fusion-based welding of AA6061-T6, but are still significant in light of the low yield strength of AFSD AA6061 in its as-deposited state.

The measured lattice parameter distribution in the build direction of the material indicates that the precipitates are substantially evolving through the build thickness. This variation in lattice parameter does correlate with a measured gradient in hardness in the build direction, but the exact connection between the evolution of the precipitates and change in the yield strength and residual stresses must be further clarified in future research.

5.9 New Solid Bar Feedstock Processing Parameter and Lubrication Influence on As-Deposited AFSD AA5083 Nano- and Microstructure and Mechanical Properties

Additive friction stir deposition (AFSD) is a transformative, metallic additive manufacturing (AM) process capable of producing near-net shape components with a wide variety of material systems. The solid-state nature of the process permits many of these materials to be successfully deposited without the deleterious phase and thermally activated defects commonly observed in other metallic AM technologies such as hot cracking, porosity, and vaporization. This work is the first to investigate the as-deposited microstructure and mechanical performance of a free-standing AA5083 deposition. An initial process parameterization was conducted to down-select optimal parameters for a large deposition to examine build direction properties. Optical microscopy revealed that constitutive particles were dispersed evenly throughout the matrix when compared to the rolled feedstock. Electron backscatter diffraction (EBSD) revealed a significant grain refinement as a result of the inherent dynamic recrystallization from the AFSD process. Monotonic tensile experiments determined a drop in yield strength, but an improvement in tensile strength of the longitudinal direction as a result of the microstructural refinement. However, a substantial reduction in tensile strength was observed in the build direction of the structure. Subsequent fractographic analysis provided insight into some of the potential issues of the process in regard to the build direction properties as well as a possible explanation into the root cause and potential improvements.

5.9.1 Materials and Methods

A B8 MELD machine affixed with a 4-teardrop hardened steel tool (Figure 5.65(B)) was employed to produce the deposits evaluated in this work. Feedstock material utilized in this study was wire-EDM cut into 9.53 x 9.53 x 254 mm rods parallel to the rolling direction from a 63.5 mm thick AA5083-H131 plate. The as-machined feedstock was then coated with a high-temperature graphite aerosol lubricant as instructed by the machine manufacturer to prevent friction within the walls of the AFSD tool while depositing material. The lubricant is established as a necessary part of the process to impede the tool from jamming during nearly all aluminum deposits. A 9-sample processing window, tabulated in Table 5.9.1, was produced altering the tool rotational speed from 200-400 RPM and linear actuator feedrate, expressed as volumetric feedrate, from 6,341-8,664 mm^3/min. Tool traversing velocity was maintained at 127 mm/min based off of prior aluminum alloy parameterization work by Phillips et al.[65], and to reduce the processing window size to evaluate the individual effects of weld pitch, expressed as V/ω by FSW, and deposition ratio, which is defined as A/V where A is the linear actuator velocity. To provide an estimate on processing temperatures, a thermocouple was placed in a pre-drilled hole half the thickness of the substate while a second thermocouple measured the ambient temperature. Deposits for the parameter study were 50.8 mm center-to-center and 4.064 mm tall. The follow-on free-standing larger deposit was manufactured to be 228.6 mm center-to-center in length and 66.04 mm in height to permit the full geometry of the tensile samples oriented in the build direction. A single tool steel non-consumable AFSD tool with 4 teardrop features was employed to deposit all 10 builds evaluated.

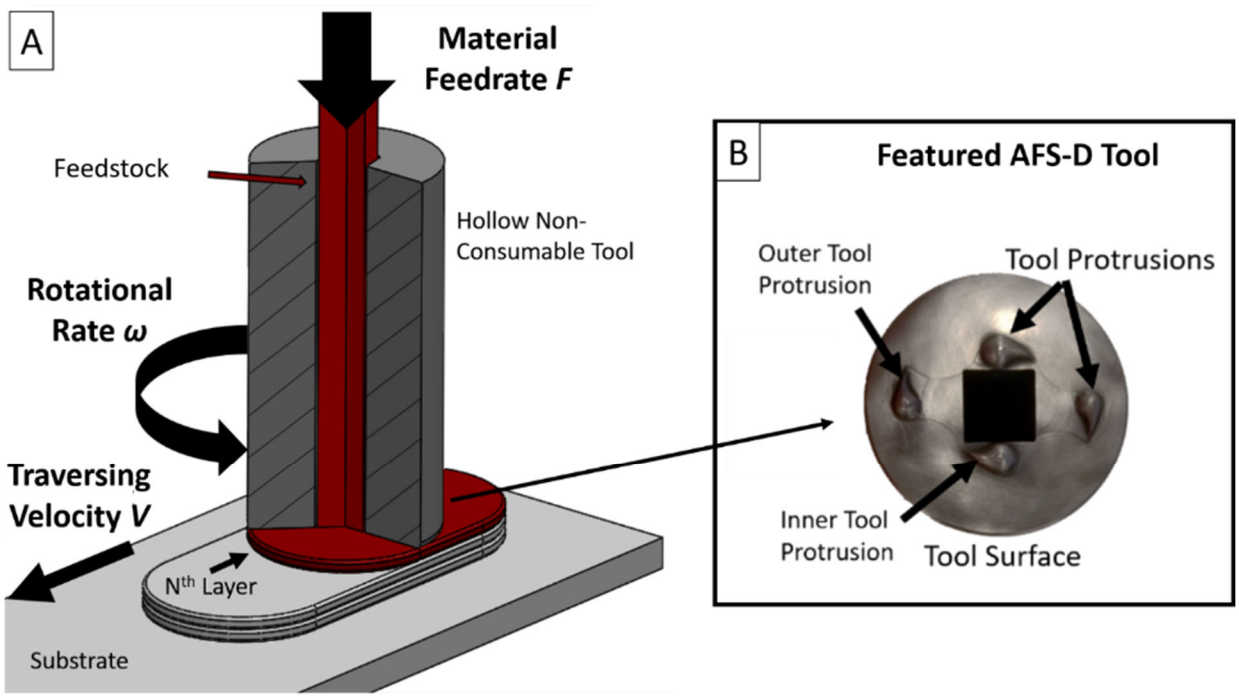

Figure 5.65 (A)Schematic of the AFS-D process denoting specific features and process control variables. (B) Schematic of the features located on the interaction face of the steel AFS-D tool.

Table 5.9.1. Sample set nomenclature and parameter specifications.

Parameter Set	Rotational Speed [RPM]	Vol. Feedrate [mm^3/min]	Weld Pitch [mm/rot]	Deposition Ratio
P1	200	6,341	0.635	0.55
P2	300	6,341	0.423	0.55
P3	400	6,341	0.318	0.55
P4	200	8,664	0.635	0.75
P5	300	8,664	0.423	0.75
P6	400	8,664	0.318	0.75
P7	200	7,494	0.635	0.65
P8	300	7,494	0.423	0.65
P9	400	7,494	0.318	0.65

Samples produced in the parameter study were cross-sectioned, ground stepwise down to a 4000p grinding disc, and polished with a 3 µm water-based diamond suspension. Samples were then tested on a Clemex CMT microindenter with 16 x 45 grid, 500 µm spacing, and 200 gf. Microscopy samples from the cross-sections were then polished further down with a 0.03 µm colloidal silica solution. Optical microscopy (OM) was performed on a Keyence VHX-7000 digital microscope. Scanning electron microscopy (SEM) was conducted on a Tescan Lyra FE-SEM with an Octane Elite EDS system and EDAX Hikari Super EBSD camera to perform chemical, grain morphological, and fractographic analysis. EBSD and fractographic analysis was performed at 20 keV while EDS was performed at 5-15 keV to evaluate lower energy elements within the deposits. Monotonic tensile tests were conducted on a MTS Landmark servo hydraulic load frame with a 25 kN load cell in ambient lab temperature and humidity. Three specimens were prepared from the same wrought AA5083-H131 plate as the feedstock parallel to the rolling direction using a wire-EDM. As-deposited AFSD AA5083 samples were prepared in the same manner in the longitudinal and build directions to evaluate any anisotropy. The experiments were run in displacement control with a 5 mm gage extensometer. The tests were conducted in the quasi-static regime with a displacement rate of 0.005 mm/s leading to a strain rate of 0.001 mm/mm/s across the gage section.

5.9.2 Results

Parameter Study

Figure 5.66(A) illustrates the correlation between the volumetric input of material into the deposit versus the AFSD tool rotational speed with respect to the average Vicker's hardness of the cross-section of each parameter set evaluated. The contour plot reveals, that maintaining a lower RPM and minimizing material input proved to retain 80% of the wrought AA5083-H131 feedstock hardness measured at 102 Hv. Additionally, the value of P1 lies between the Vicker's hardness of friction stir welds in the nugget and thermo-mechanically affected zone in AA5083 reported by various studies [110], [230], [231]. In the referenced works, processing speeds played a significant role in the severity and variation of the reduction in hardness where increases in rotational speed or a decrease in tool translational speed correlated to a lower weld pitch. The effect of low weld pitch is observed in this as well as evident by the reduced hardness in P6.

Figure 5.66(B) further evaluates this effect, which plots the deposition hardness from Figure 5.66(A) against the temperatures observed by the substrate embedded thermocouples. In Figure 5.66(B), circular symbols correlate to the low rotational rate conditions (200RPM), squares indicate the medium rate (300 RPM), and triangles represent the highest rotational rates evaluated (400RPM). Volumetric feedrates are classified by color where the minimal material input is denoted in blue, the median rate in black, and the highest feedrates in red. The figure further corroborates that an increase in RPM induces greater heat into the deposit while maintaining a constant tool traversing speed. Thus, similar relationships can be drawn in AFSD to FSW where weld pitch has a significant effect on mechanical properties when processing aluminum alloys, regardless of precipitate or work-hardening strengthening mechanisms. It is also notable that increases to material feedrate plays a role in the increase in deposition temperature. This effect was evaluated by Garcia et al. [63] in Cu and Al-Mg-Si resulting from the partial slipping-sticking state of the actively deposited aluminum's interaction to the AFSD tool face and features. The study notes that the friction coefficient between aluminum and steel is significant, which leads to greater material sticking between the deposited material and tool surface. In this work, greater material flow correlates to greater contact between the deposition layer and tool; and thus, an increase in temperature. From a macroscopic viewpoint, deposits that exhibited greater temperatures also presented rougher surface finishes, and in some cases, significant aluminum sticking to the tool causing some of these surface defects. To maintain the highest mechanically sound deposition based on the parameter study, P1 was determined to be the optimal parameter to be evaluated and employed in the subsequent, large-scale deposit at a Vicker's hardness of 82.9 ± 4.7 Hv.

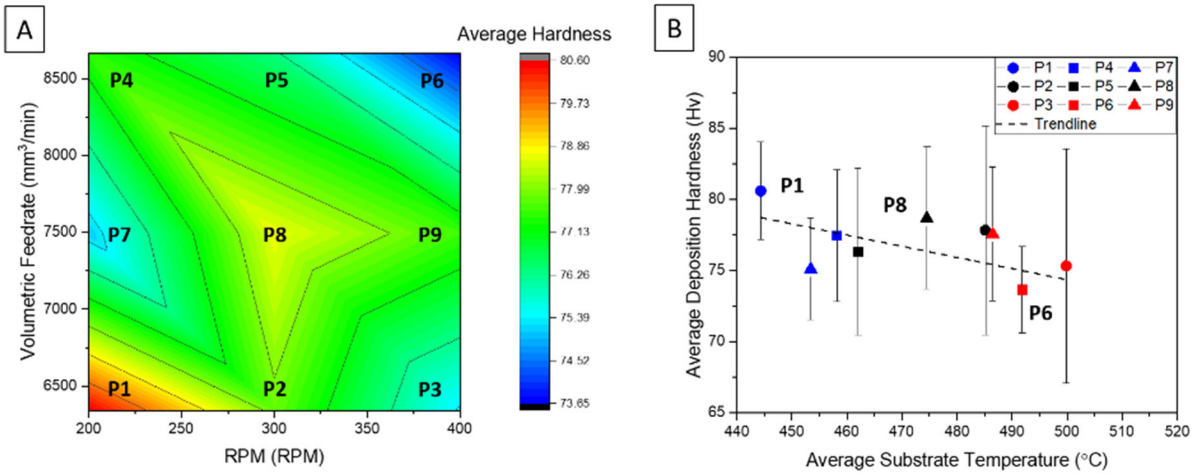

Figure 5.66 Color contour plot contrasting the material volumetric feedrate to the RPM of the tool. (B) Deposition cross-sectional hardness versus average temperature. Key: circles correlate to 200 RPM, squares to 300 RPM, and triangles to 400 RPM. Blue data points correlate to deposition ratio of 0.55, black data points correlate to a deposition ratio of 0.65, and red data points correlate to a deposition ratio of 0.75.

Optical micrographs of the wrought AA5083-H131 feedstock and as-deposited AA5083 are depicted in Figure 5.67(A) and (B), respectively. Despite surface defects caused by less desirable process parameters, the AFSD process fills in surface defects of the previous layers on the subsequent layers. As such, no volumetric defects were observed in the 9 cross-sections from the preliminary parameter evaluation. The size and distribution analysis of the constitutive particles is summarized in Table 5.9.2. The authors note that no statistical analysis was conducted delineating the Fe, Mn particles from the possible formation of β-phases. The feedstock exhibits typical rolled microstructural features where large constitutive particles are pancaked parallel to the rolling direction, which are observed as the dark particles in the figures. The result of the rolling process effectively creates stringers and layers of aluminum lined with these elongated Al_6Fe and Al_6Mn secondary phase particles. Once processed via AFSD, these 6.7 µm particles are fractured to nearly half their original size at 3.8 µm. The secondary phase is then dispersed homogenously throughout the microstructure due to the high levels of shear-induced plasticity from the process as evident by the lower deviation in nearest neighbor distance.

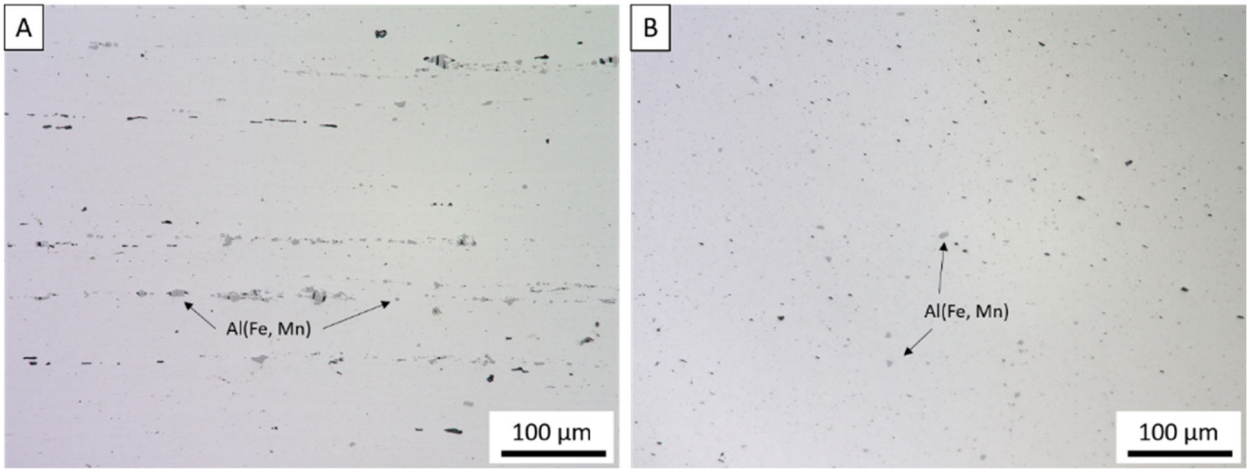

Figure 5.67 (A): Optical micrograph of wrought AA5083-H131 plate showing constitutive particles pancaked between the rolled grains. (B) Optical micrograph of as-deposited AA5083 after AFSD showing smaller, dispersed constitutive particles.

Table 5.9.2. Particle analysis comparing constitutive particles in the AA5083-H131 feedstock and AFSD AA5083.

Sample	Particle Size			Nearest Neighbor Distance		
	Max	Average	Standard Deviation	Max	Average	Standard Deviation
	µm²	µm²	µm²	µm	µm	µm
AA5083-H131	64.6	6.86	10.86	75.6	10.46	8.39
AFSD AA5083	56.3	3.80	6.13	42.2	8.30	5.99

Figure 5.14(A) and Figure 5.14(B) depict inverse pole figures displaying the stark reduction in grain size from the AA5083-H131 feedstock and as-deposited AA5083 in the longitudinal/rolling (top), long transverse (right), and short transverse/build (left) directions. The feedstock exhibits typical rolled grains along the longitudinal direction on the order of 250 µm with thin pancaked grains along the transverse directions. Following AFSD, these grains are refined into 3.16 µm diameter equiaxed grains with a standard deviation of 1.38 µm. As denoted by recent studies of Al-Cu [232], Al-Mg-Si [64], [65], [67], and Al-Zn Mg-Cu [68], [69], AFSD refines aluminum alloy grain structures via geometric, continuous dynamic recrystallization.

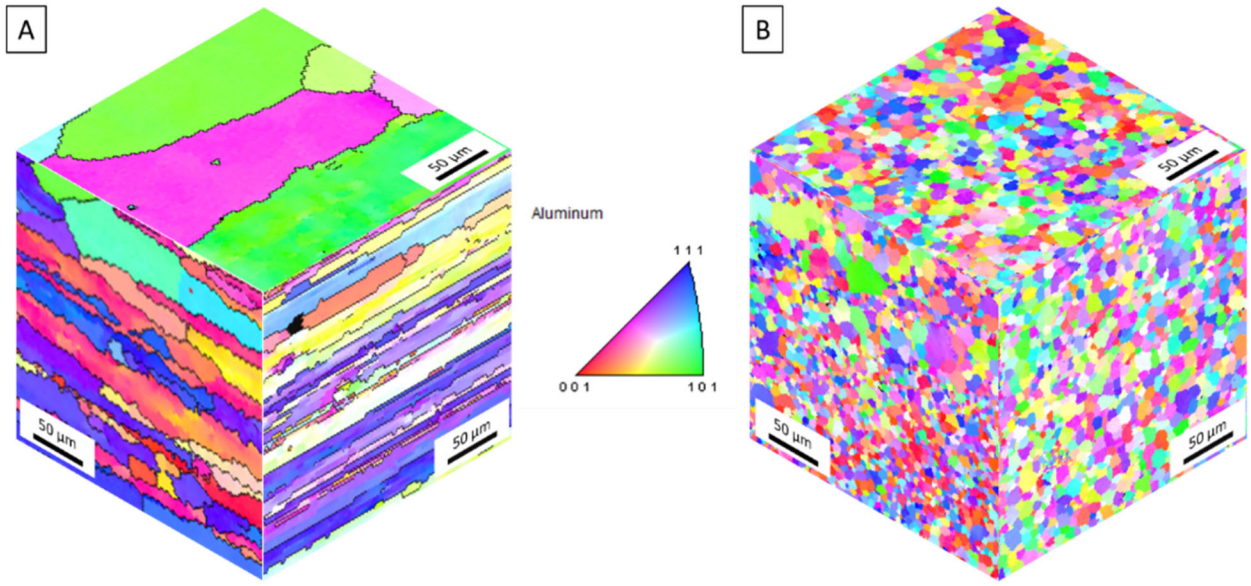

Figure 5.68 EBSD maps in 3-orientations of (A) the rolled AA5083-H131 feedstock and (B) as-deposited AA5083. Scale bars are 50 µm.

Mechanical Behavior of the Free-Standing Deposit

Bi-directional monotonic tensile properties of the as-deposited AFSD AA5083 versus the properties of the feedstock AA5083-H131 is compared in Figure 5.69. Additionally, the experimental data is available in Table 5.9.3. Samples tested in both the longitudinal (LD) and build directions (BD) exhibited areduction in yield strength resulting from the AFSD process. The thermo-mechanical processing shears grains through lattice rotation and annihilates dislocation structures. As a result, the refined grains lose their dislocations within the grains; and thus, any work hardening effects introduced by the H131 treatment. However, it is noted that beyond the yield point, the as-deposited material begins to strain-harden with increasing strain. In the longitudinal sample, we find that the ultimate tensile strength exceeds that of the feedstock AA5083-H131 material by approximately 20 MPa. This increase can be directly attributed to the reduction of grain size down to 3.1 µm, which the Hall-Petch relationship correlates to a 24.6 MPa increase in strength. The build direction, however, reveals a significant reduction in strength and ductility unlike any currently reported data on AFSD aluminums. Premature fracture occurring in the plastic regime of the material's response suggests that significant defects are present as a result of the layer-by-layer process.

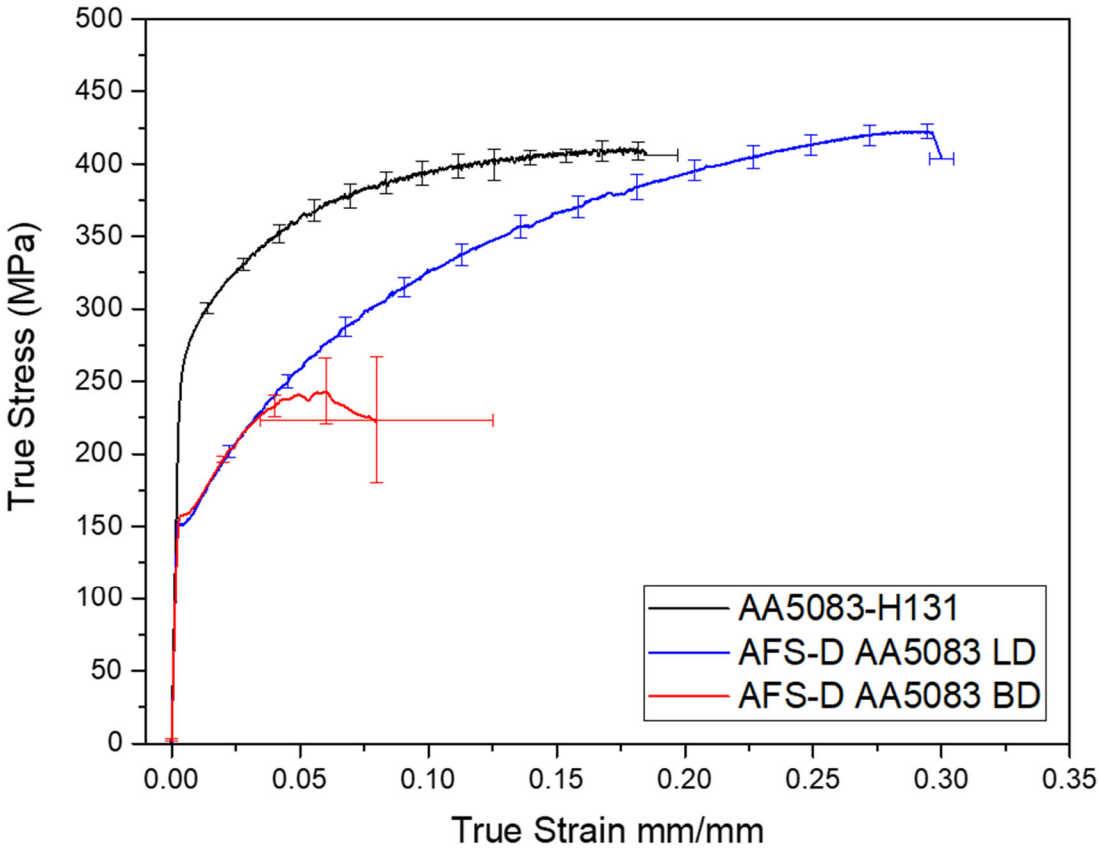

Figure 5.69 Comparative tensile stress-strain response of the wrought AA5083-H131 feedstock and as-deposited AA5083.

Table 5.9.3. Summary of AA5083-H131 feedstock and as-deposted AFSD AA5083.

Material (Direction)	E (GPa)	$\sigma_{YS,\ 0.2\%}$ (MPa)	σ_{UTS} (MPa)	ε_f
AA5083-H131	82.9 ± 0.9	273.7 ± 1.0	410 ± 6.1	0.15 ± 0.024
AFSD AA5083 (LD)	70.8 ± 5.2	151.3 ± 1.7	431.3 ± 1.9	0.30 ± 0.005
AFSD AA5083 (BD)	68.9 ± 5.8	157.7 ± 1.2	246.2 ± 45.9	0.08 ± 0.045

To determine the presence of a strength gradient in the build direction of the free-standing deposit, a section was extracted from the cross-section and indented as examined in Figure 5.70. The hardness plot compares the as-deposited AFSD AA5083 hardness to the measured feedstock values. As displayed, the recorded Vicker's hardness values are aligned to those previously evaluated in the parameter study at approximately 81 Hv. The consistency between parameter set P1 and the hardness data from the cross-section of the larger deposit suggest that the additional heat and plastic deformation induced as a result of the additional layers neither strengthens nor weakens the work-hardened AA5083. Additionally, no significant reduction in strength is exhibited in the gage section, which suggests that microstructural defects may exist between layers of the AFSD AA5083.

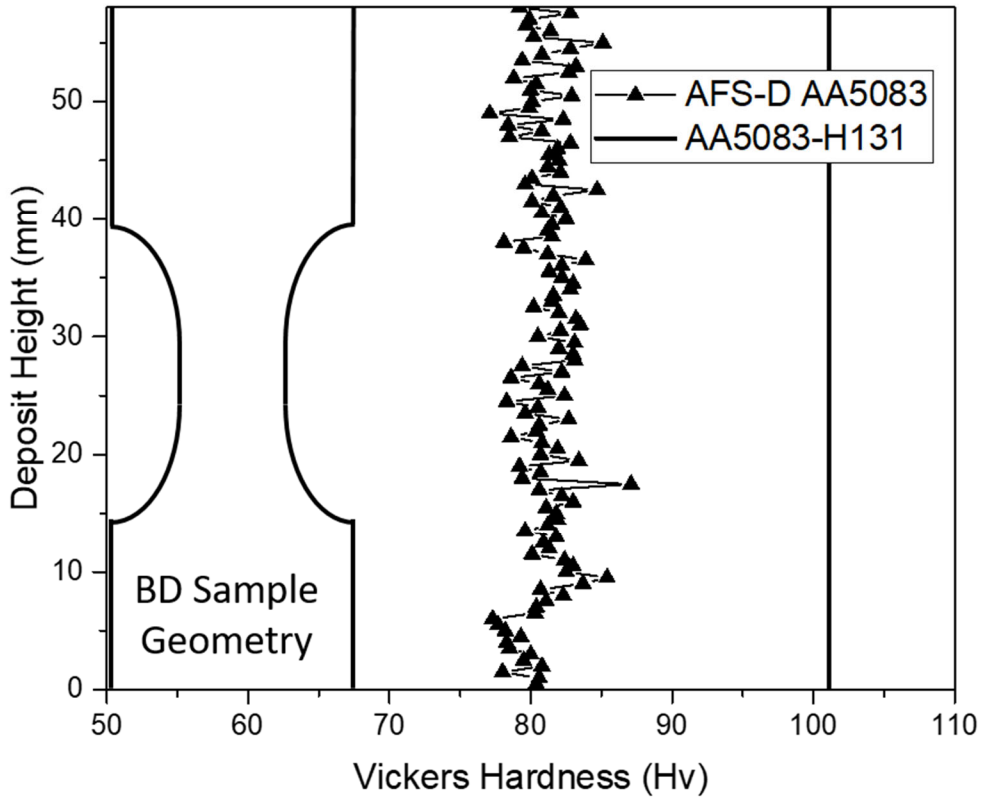

Figure 5.70 Vicker's hardness plot with respect to the sample geometry.

Post-Mortem Analysis

To evaluate and contrast the failure mechanisms between the feedstock material and as-deposited AA5083, Figure 5.71(A, B) present fractographic evaluation of the AA5083-H131 tested in the rolling direction of the plate. The fracture produced a fracture plane 45˚ with respect to the loading direction. The entirety of the fractured surface is dominated by microdimpling surrounding larger voids originating from brittle, cracked iron-rich inclusions such as those displayed in Figure 5.71(B). The smaller dimples are attributed to localized plasticity reaching critical strain while voids coalescing from constitutive particles develop until transgranular fracture occurs as is typical for wrought AA5083 [233].

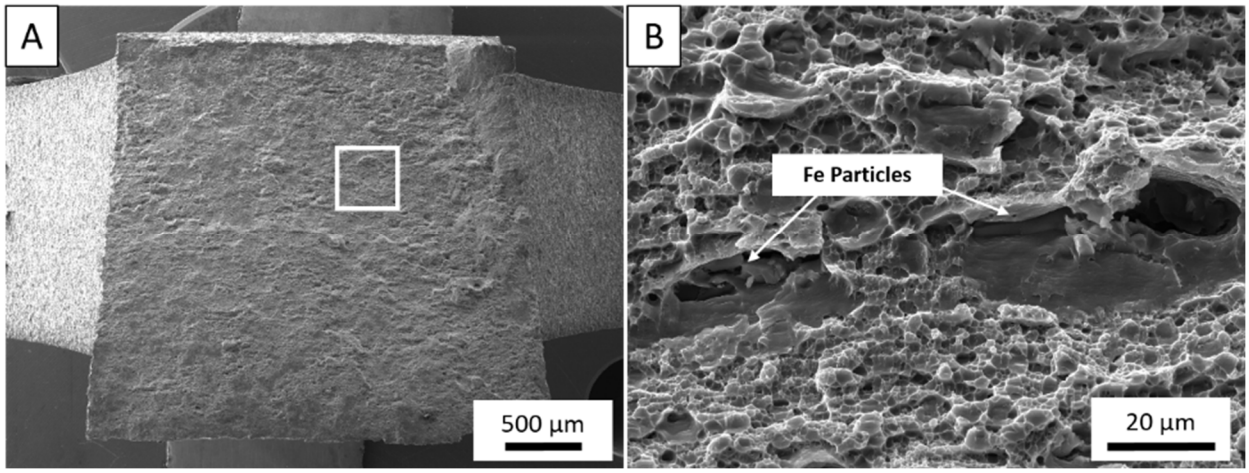

Figure 5.71 Low magnification overview of 45° fracture of AA5083-H131 sample. (B) Large voids, surrounded by microvoids, coalesced from fractured iron particles along rolling boundaries.

Figure 5.72(A-D) depicts a fractured sample tested from the longitudinal direction of the free-standing deposit. A few features are immediately evident in the macroscopic view in Figure 5.72(A). First, cracks appear to be forming approximately 1 mm apart, which is the approximate layer height for each layer in the deposit. Towards the center of the sample, the fracture comes to a point and gradually slopes to the exterior edges of the sample. These paths closely match the rotational pattern of the tool features as the tool traverses in the direction, observed collinearly with the loading direction of this sample. Next, highlighted in Figure 5.72(B), a dark, discolored region is observed at a large crack originating from the exterior surface of the sample. In this region, dimpling appears very shallow as the dark particles fill the dimples. Further discussion of this region is discussed later. Between the layer boundaries, material flow lines are observed in Figure 5.72(C) and at higher magnification in Figure 5.72(D). This region experiences more traditional fracture where transgranular dimpling surrounds larger voids nucleating from constitutive particles. However, it is observed that rather than uniquely $Al_6(Fe, Mn)$ particles, these platelets more closely resemble that of the β-phase precipitate. Yan et al. [234] found that β would often form as a result of dislocations diffusing Mg atoms towards high-angle grain boundaries (HAGB), particularly in the presence of Al_6Mn during deformation processes. In AFSD of aluminum alloys, it has been noted through various works that the high shear mechanisms of the process typically promote a high density of HAGB proportional to the strain governed by processing conditions [64], [65], [68]. As a result, the constitutive particles located at grain boundaries also provide preferential locations to precipitate β-phases. In loading conditions, larger voids can be expected to develop as a result of both $Al_6(Fe, Mn)$ and Al_3Mg_2 particles.

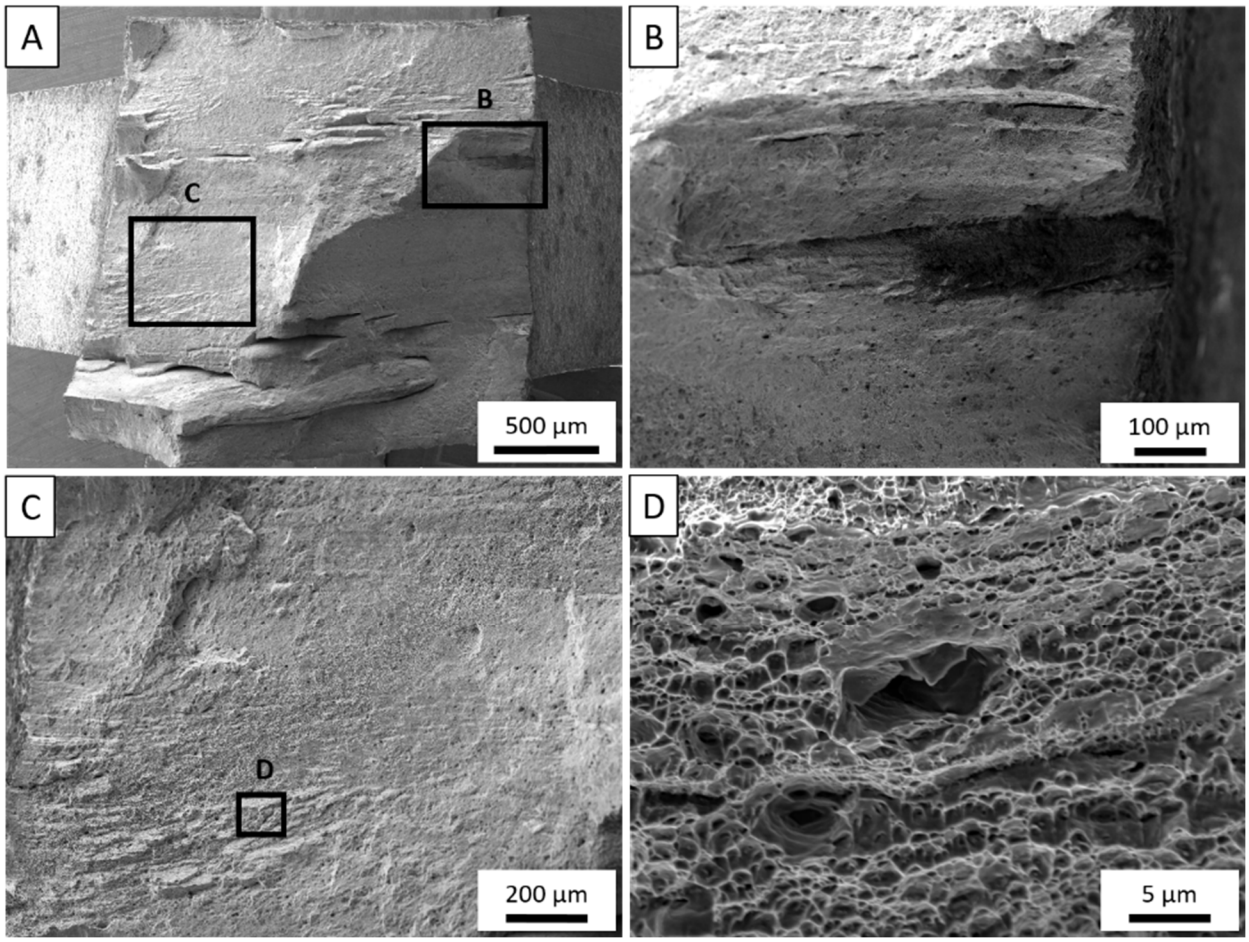

Figure 5.72 (A): Post-mortem analysis of tensile sample tested in the vertical build direction. (B) Contamination observed near delamination crack. (C) Material flow lines parallel the deposited layers with a larger void encasing a secondary-phase particle.

Figure 5.73(A-F) collates fractographic and EDS analysis of a sample tested in the build direction. The BD samples reveal a flat fracture surface, characteristic of a brittle failure, with tearing ridges separating thin layers of material. Near some ridges, the dark particles are observed in greater quantities such as those seen in Figure 5.73(B). Two regions were probed to determine the composition of the contaminants in Figure 5.73(C, D). As previously observed in the fractographic analysis of the LD samples, these dark regions are confirmed to be carbon contamination from the lubrication. Figure 5.73(E, F) show that even away from the ridges, the carbon particles sit within shallow dimples throughout the surface of the build direction samples.

Until this work, it was surmised that the carbon-based lubricant, employed to prevent sliding friction in the confines of the tool walls, were either burnt off during deposition or sufficiently mixed into the deposit by the repetitive stirring motion. Instead, it appears that this carbon displaces to the layer boundary and is only moderately coerced into the layer itself by the tool features on the subsequent passes as observed in Figure 5.72. The results of this analysis show that carbon does not distribute deep into layers, but rather remains on or near the surface of each layer produced. Moreover, the carbon does not diffuse into the matrix well, but rather becomes entrapped. The entrapped carbon hinders the diffusion between layers; thus, creating an interlayer defect and subsequent brittle behavior as evidenced in this work.

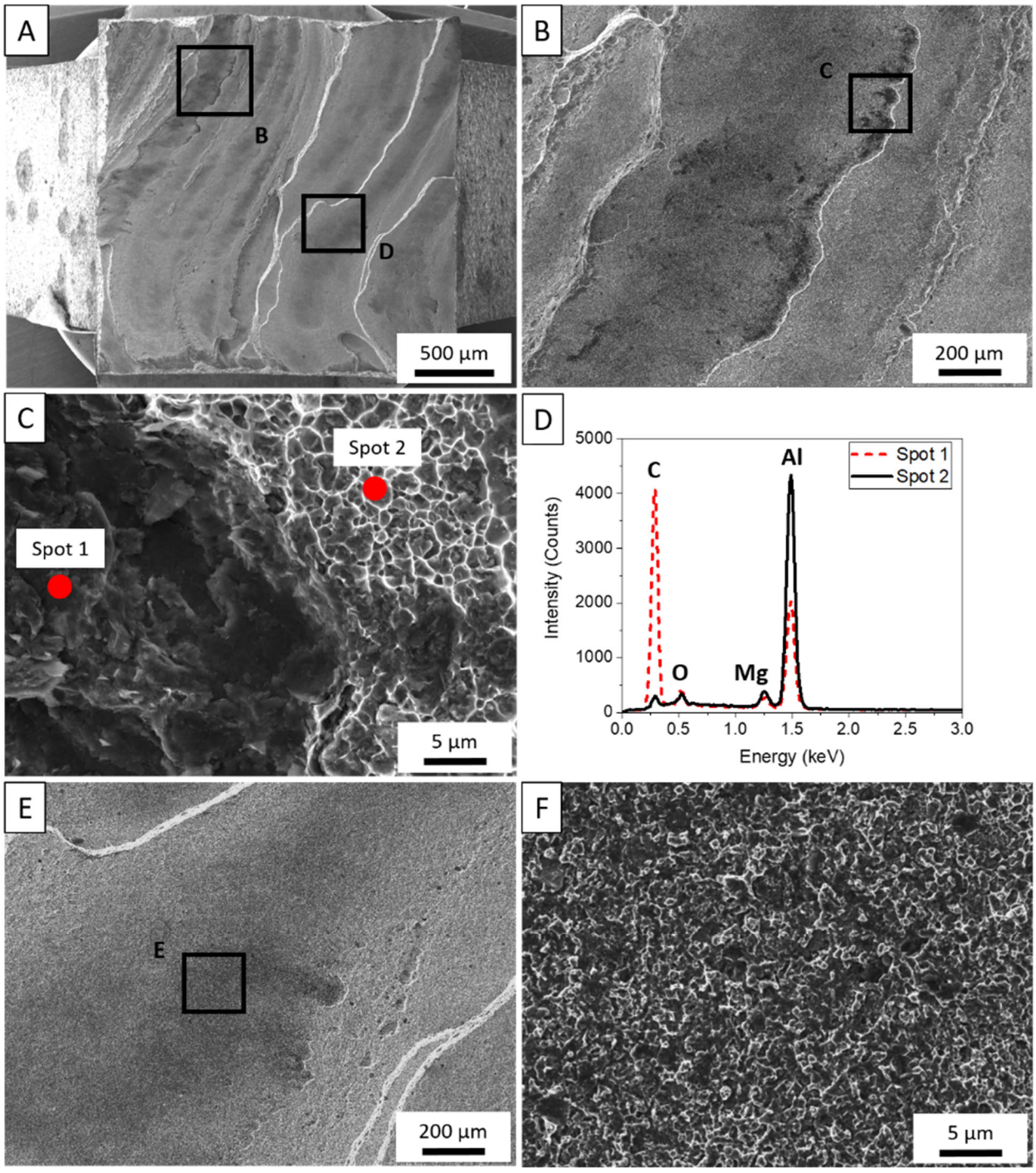

Figure 5.73 (A): Post-mortem analysis of tensile sample tested in the vertical build direction. (B) Contamination evidenced along the fracture surface. (C) High-magnification image of two locations compared via EDS. (D) EDS analysis comparing contaminant composition with respect to the matrix. EDS was performed at 5 keV. (E) Brittle fracture features observed. (F) Shallow dimples filled with carbon particles.

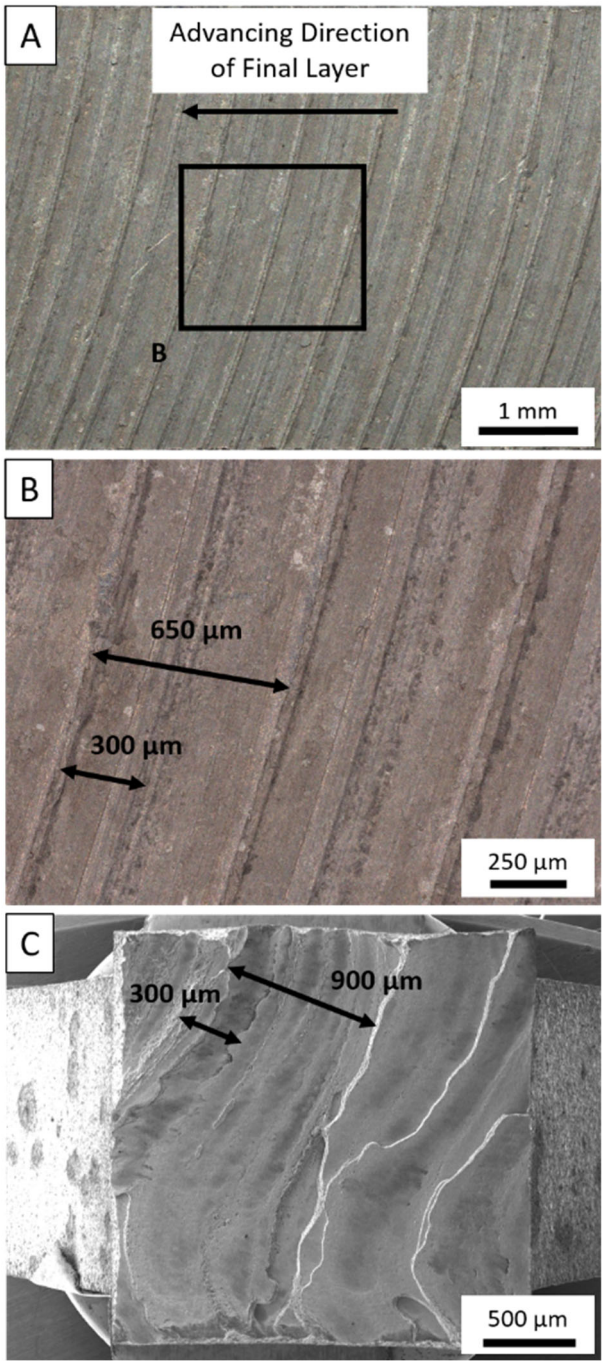

Figure 5.74 (A) Macroscopic image of the onion ring structure on the final layer of the deposit taken as observed directly below the tensile sample observed in (C). (B) High-magnification OM of the onion ring pattern depicting distances between rings. (C) SEM fractography correlating flow patterns with onion ring structures observed in OM.

The spacing of the ridges in the BD fractography provide insight into the carbon contamination, which is correlated in Figure 5.74(A-C). As is traditional in friction stir-based processes, an onion skin structure is observed on the surface of the deposit. As per Perry et al. [198], extraneous, unconstrained material flow develops a wave behind the tool generating a rough semicircular pattern. At tool movement speeds of 200 RPM and 127 mm/min, the spacing of these rings are 609 μm, which closely resembles the spacing measured on the top surface of the deposit where variance can be directly attributed to machine compliance. However, between each ring, a shallower second ring is developed approximately 300 μm from the leading onion ring. This second ring is excess material flowing from the edge of each individual ring, typically denoted as flash. Evaluating the spacing of the tearing ridges from the BD samples and the surface of the deposit, the features of the fracture surface match those of the onion rings.

The observations of both the fractography and top surface of the deposit paints a picture of the following phenomena hypothesized and graphically shown in Figure 5.75(A-D). First, as material is deposited, the material flows like a viscous fluid radially from the exit hole of the tool. However, since material is constrained, material flow is prohibited from mixing well in the vertical direction. This means that material towards the outer perimeter of the feedstock becomes compressed between the material ahead of the presently deposited layer, below the layer, and the tool interaction face. More specifically, the outer layer of carbon, which is located on the surface of the feedstock, becomes compressed and flows along the top surface of each layer as the layer is deposited (Figure 5.75(B)). Additionally, as the previously mentioned unconstrained wave of material develops the onion ring structure, it encases the now trapped carbon particles along the layer boundary in the 300 μm wave of flash, schematically shown in Figure 5.75(D). The theory behind Figure 5.75(B) is supported by similar techniques employed in FSP to generate surface composites in which powders or solutions are applied to the surface of a workpiece and subsequently mixed in via FSP [235]. However, rather than an existing solute on the surface of the substrate, AFSD introduces foreign material from the feedstock coating.

It is worth noting that tool features should disrupt and distribute the layer of carbon particles on the subsequent passes, particularly considering the central region of the deposit is stirred four-times per rotation. While true, the fractographic images of the LD from Figure 5.72 show that the features merely push the carbon particles into the grooves cut by the features and is shown schematically in Figure 5.75(C). The action does provide some distribution of carbon away from the layer boundaries, but the stirring motion is insufficient enough to completely disrupt the layer interfaces, at least at 200 RPM. This concept originates from FSW studies in which a contrasting marker material was placed into the workpiece prior to FSW before non-destructive evaluation. In AA2024, Schmidt et al. [236] used a copper strip to visualize the flow using X ray computed tomography to highlight the flow of the copper within the weld. The authors note that some of the copper is pulled downward into the cavity produced by the FSW pin. However at higher locations in the weld nugget, material rotates with the tool and remains relatively unchanged with respect to vertical location in the weld, similar to the findings of this study. To properly evaluate this phenomenon, the authors suggest an in-depth investigation on the effect of tool geometries on the mechanical stirring of the AFSD process as well as their influence on necessary lubrication.

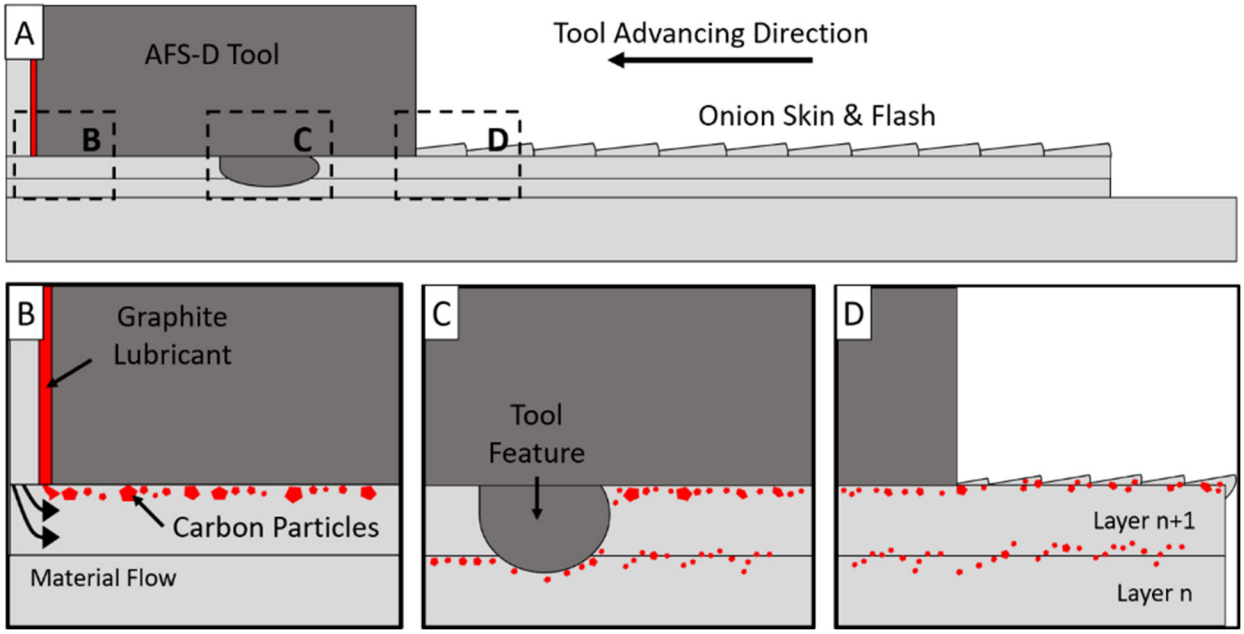

Figure 5.75 (A): Overview schematic of the cross section of the AFSD tool, feedstock, and two layers. (B) Schematic of the material flow close to the tool exit hole. Carbon highlighted in red. (C) Schematic of the area near a tool teardrop feature. Carbon follows the path of the tool features rather than dissolving into the layers. (D) Carbon on the active layer becoming entrapped by the flash from excess material in the onion skin.

5.9.3 Conclusions

This investigation is the first work to evaluate the microstructural and mechanical behavior of as-deposited AFSD AA5083. The study reached the following conclusions:

In processing AA5083 by AFSD, greater mechanical strength was expected with lower tool rotational rates due to less heat generation in the deposit as determined by microindentation experiments covering the cross-section of 9 deposits of varying processing conditions.

Equiaxed grains resulted from dynamic recrystallization and a 97% reduction in grain size was exhibited with an average grain size of 3.16 μm. While the thermal processing reduced the yield strength due to annihilation of dislocations, the ultimate tensile strength was improved due to the grain size reduction.

Build direction properties were greatly depreciated and macroscopic brittle fracture was observed.

The cause of premature failure in the build direction were attributed to the influence of carbon contamination preventing diffusion of the matrix between layers.

Carbon contamination originates from the aerosol lubricant, used to prevent friction within the tool during deposition, that becomes entrapped by the flash and material from the consecutive layers. Elimination of this contamination could provide consistency between the longitudinal and build directional mechanical performance.

As an immature process, more work is suggested to investigate the influence of tool geometry and design to assist in mitigating interlayer defects. Additional work should also include evaluation of alternatives to carbon-based lubrication techniques.

5.10 Microstructure, Tensile, and Fatigue Behavior of Direct Additive Recycling of AA5083 Machine Chips Captured by Monotonic and Fatigue Performance Models

In this study, the as-deposited microstructure and mechanical properties are examined for both the wrought strain hardened Al-Mg-Mn alloy (AA5083-H131) feedstock and the AA5083 machine chip waste feedstock processed with Additive Friction Stir Deposition (AFSD). Monotonic tensile and uniaxial fatigue experiments compared three specimen types: wrought AA5083-H131, AA5083 AFSD-Recycled, and AA5083 AFSD-Solid bar. Tensile and fatigue results demonstrated comparable performance between the recycled material and wrought control. Experimental results indicate the thermo-mechanical processing of AFSD resulted in an exchange of strengthening mechanisms – replacing the wrought material of strength from strain-hardening and replacing it with grain boundary strengthening from a refined as-deposited microstructure. Although strengthening mechanisms evolved in AA5083, the mechanical performance of the AFSD-Recycled material including improved fatigue performance over the wrought control samples illustrates the potential use of the AFSD process to reclaim waste machine chips into components or repairs while maintaining high mechanical performance requirements.

5.10.1 Materials and Methods

Materials

In order to examine the effect of using reclaimed waste metal chips as feedstock in the AFSD process, metal machined chips were created through dry turning of AA5083-H131 bar stock on a CNC lathe [66]. Additionally, for comparison purposes, AFSD builds were also made using solid bar feedstock taken from the same AA5083-H131 rolled plate. For clarity of discussion in this present work, reference to AFSD processed materials from machine chips and solid bar stock are referred to as AFSD-Recycled and AFSD-Solid Bar, respectively. Figure 5.76 illustrates representative processes for the AFSD process for depositing solid feedstock bars (Figure 5.76a) and waste machine chips (Figure 5.76b). As indicated in Figure 5.76a, AA5083-H131 rolled plate was used to create the solid bar feedstock in a MELD Manufacturing B8 machine, while AA5083-H131 machine chips were fed through an auger feed system and forced through a K2 MELD Manufacturing machine for a separate AFSD build. The AFSD solid bar (AFSD-Solid bar) build was produced with the following parameters: 300 RPM tool rotation speed, 127 in/min traversing speed (along the longitudinal direction), 83 mm/min actuator feed rate, at a layer thickness of 1 mm. The AFSD deposition produced with machine chip waste (AFSD-Recycled) was produced using a proprietary set of processing parameters by MELD manufacturing.

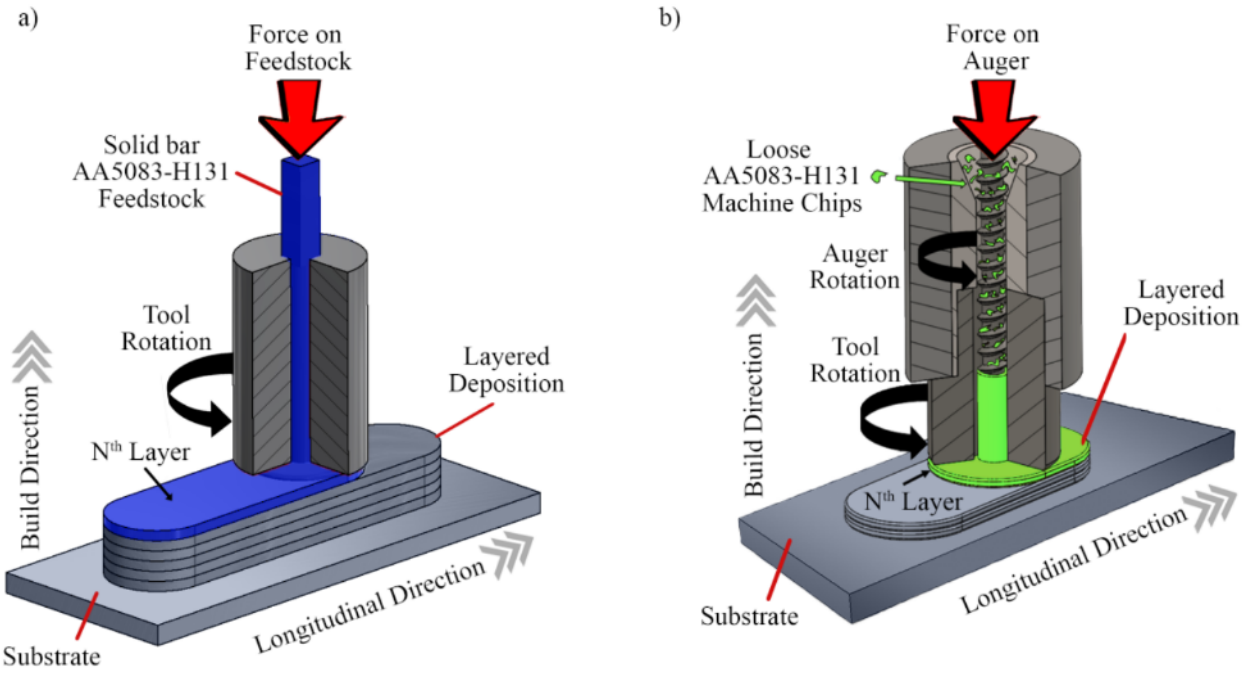

Figure 5.76 Two AFSD processes featuring a) solid bar feedstock made from AA5083-H131 rolled plate and b) feedstock made from loose machine chips cut from AA5083-H131 rolled plate and fed through an auger.

Test Specimens and Experimental Methods

Figure 5.77 shows the AFSD-Recycled and the AFSD- Solid bar builds with the corresponding specimen geometry and relative orientations in each build. The AA5083 AFSD deposition from the solid bar feedstock can be seen in Figure 5.77(a). The specimens were removed from the center of the build as illustrated in Figure 5.77(b). To better understand the orientation within the build relative to the AFSD processing directions, the specimens are presented with an axis emphasizing the build direction (BD), long transverse direction (LT), and longitudinal direction (LD) as shown in Figure 5.77(c). All specimens considered in this study were extracted from each build, using wire electrical discharge machining (EDM), parallel to the LD direction. Figure 5.77(d) and Figure 5.77(e) display the dimensions for the fatigue and monotonic specimens, respectively. The subscale specimen size was used to allow for direct property comparison to the smaller recycled chip (AFSD-Recycled) build, shown in Figure 5.77(f). The recycled specimens were extracted from the end of the build, toward the center, as shown in Figure 5.77(g), while Figure 5.77(h) displays the orientation within the build relative to AFSD processing directions used for each specimen. Prior to mechanical testing, specimens were cross-sectioned, mounted, ground and polished in preparation for EBSD using a Tescan Lyra FE-SEM with EDAX Hikari Super EBSD camera for grain morphology analysis.

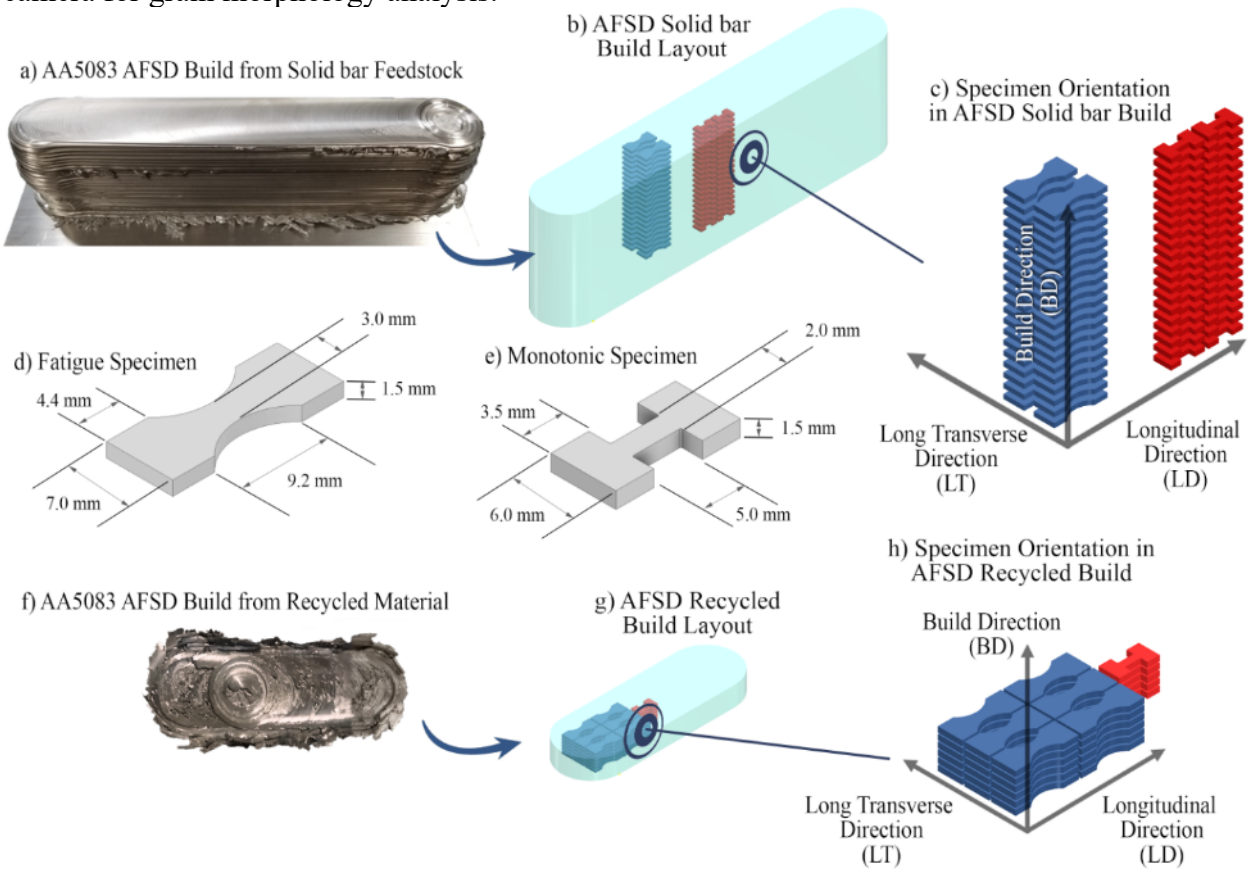

Figure 5.77 Representative a) image of solid bar build, b) specimen layout in solid bar build, c) specimen orientation relative to processing directions of solid bar build, d) fatigue specimen shape and dimensions, e) monotonic tensile specimen shape and dimensions, f) image of recycled build, g) specimen layout in recycled build, h) specimen orientation relative to processing directions of recycled build.

Experimental tensile testing was performed in the longitudinal direction on the AA5083-H131 wrought control, AA5083 AFSD-Recycled, and the AA5083 AFSD-Solid Bar specimens. The subscale sized tensile specimens had a flat dog bone geometry with a 5.0 mm gage length, a 2.0 mm width, and a 1.5 mm thickness. The specimens were tested in displacement control with an approximate strain rate of 0.001/s using a Test Resources 800LE Series electric mechanical load frame. An optical extensometer method and subsequent MATLAB® code was employed to capture strain data on all the monotonic tensile specimens, as discussed in previous research [41], [237]–[239].

Fatigue tests were performed on a 25 kN MTS 307 landmark servo hydraulic load frame. A sub-sized fatigue specimen with a 3.0 mm gage width and 1.5 mm gage thickness was selected for this study. All fatigue specimens were mechanically ground and polished using 1200 grit SiC paper. The fully reversed tests were conducted in load control at five different amplitudes in triplicate and were tested at a frequency 5-30Hz depending on the amplitude. Scanning electron microscopy (SEM) using a JEOL 7000 FE SEM was used to examine fracture surfaces and characterize microstructural features.

Static Strength Modeling:

To understand the effect the AFSD process has on strengthening mechanisms in AA5083, a static strength model, proposed by Huskins et al.[108], was used in this study. In the strength model, the proposed yield strength can be expressed as a linear combination of multiple strengthening mechanisms, including solute strengthening ($\Delta\sigma_{SS}$), precipitation strengthening ($\Delta\sigma_{prec}$), dislocation wall strengthening ($\Delta\sigma_{DW}$), and grain boundary strengthening ($\Delta\sigma_{GB}$) as follows:

$$\sigma_{YS} = \Delta\sigma_{SS} + \Delta\sigma_{prec} + \Delta\sigma_{DW} + \Delta\sigma_{GB}, \quad 5.10.1$$

As such, the yield expression can then be used in the strength model, such that the flow stress can be expressed as:

$$\sigma = \sigma_{YS}\left(\frac{\varepsilon}{\varepsilon_0}\right)^n, \quad 5.10.2$$

where ε_0 is the strain at yield and n is the strain hardening exponent. These parameters can be determined from experimental results.

Each of the strengthening mechanisms considered in this model cause interference with dislocation motion to enhance strength. During solid solution strengthening, or alloying, solutes can add strength to a material by acting as an obstacle to dislocation motion through "pinning" – the solute pins the dislocation at the point of contact, while the remaining dislocation continues in motion. Precipitation strengthening utilizes precipitates which are nucleated and grown within the matrix to hinder dislocation motion. Dislocation wall strengthening is due to dislocation walls generated from plastic deformation that act as obstacles to dislocation motion. Lastly, grain boundary strengthening affects dislocations through the interference of mobile dislocations with grain boundaries, where increased grain density promotes dislocation interference, yielding increased strength.

5.10.2 Results and Discussions

Microstructure Characterization

As shown in Figure 5.78, representative grain size and orientation for each material considered in this study was obtained from inverse pole figure (IPF) maps using electron backscatter diffraction (EBSD) with the SEM microscope. The AA5083-H131 wrought control, shown in Figure 5.78(a), exhibited an average grain size on the order of 250 mm diameter in the elongated rolling direction with flatter, pancake shaped grains in the long transverse direction (LT). The AFSD-Recycled build shown in Figure 5.78(b), exhibited refined, equiaxed grains with an average grain size of approximately 1.5 mm in diameter, whereas the AA5083 AFSD-Solid bar build, Figure 5.78(c), displayed an average grain size of 3.2 mm in diameter. While both the AFSD-Recycled and AFSD-Solid bar specimens demonstrated a significant grain size reduction with refined, equiaxed grain structure due to the dynamic recrystallization inherent in the AFSD process, the slightly larger grain size of the AA5083 AFSD-Solid bar build as compared to the AA5083 AFSD-Recycled build can be attributed to the smaller initial grain size of the chip waste induced by the dry turning machining process.

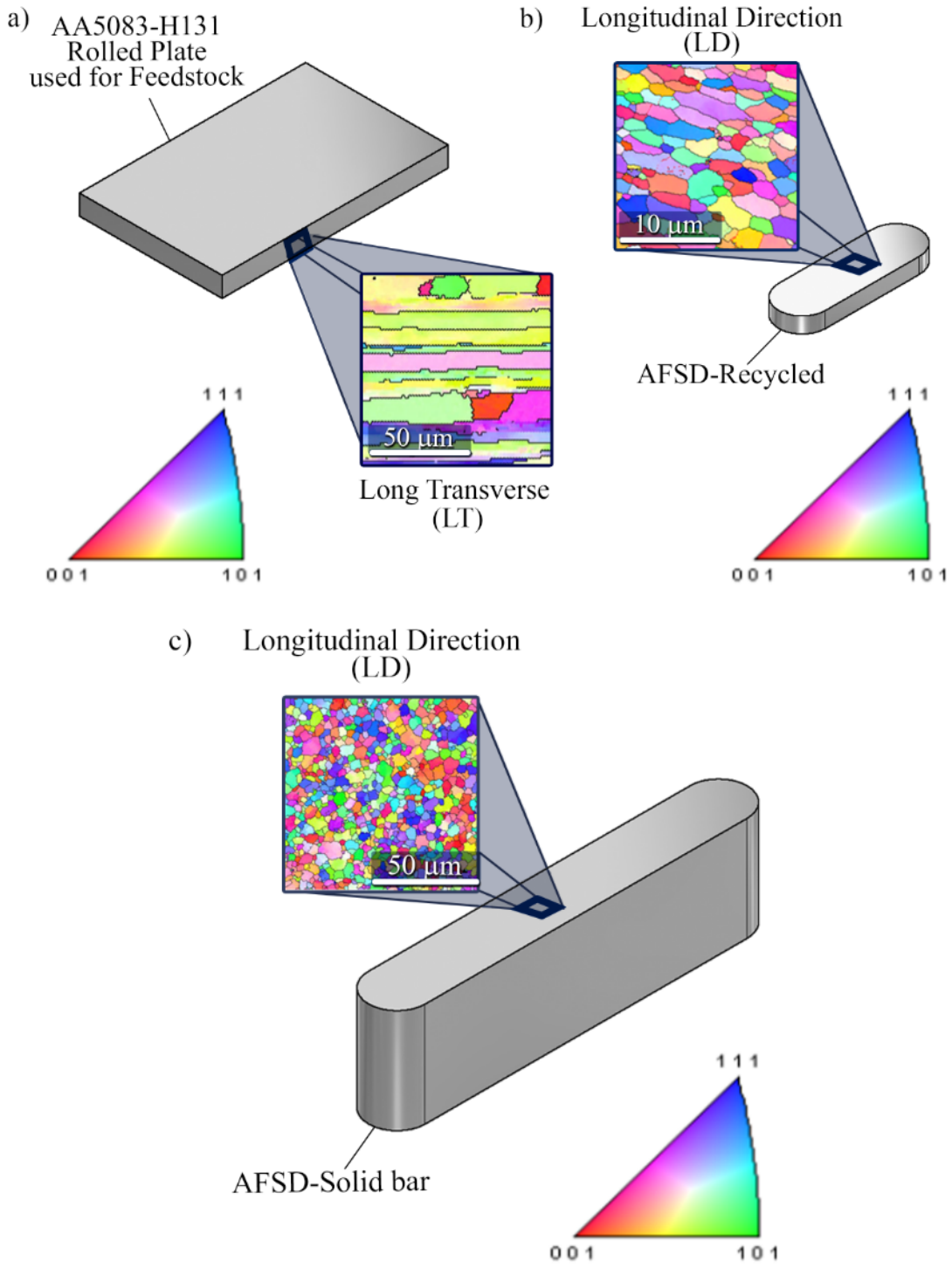

Figure 5.78 Imagery representative of grain structure for a) AA5083-H131 rolled plate wrought control, b) AFSD As-Deposited recycled chip build in the Longitudinal Direction (LD), and c) AFSD As-Deposited rolled plate feedstock build in the Longitudinal Direction (LD).

Quasi-Static Tensile Test Results

The experimental tensile results for the AFSD-Recycled, AFSD Solid bar, and the AA5083-H131 control specimens are shown in Figure 5.79 and summarized in Table 5.10.1. Each curve represents an average of three representative samples, where the error bars indicate the maximum and minimum scatter for each material. The thick solid lines in each color (black, green, and blue), represent the strength model for each material (AA5083-H131 wrought control, AA5083 AFSD-Recycled, and AA5083 AFSD-Solid bar, respectively). The wrought control exhibited mechanical behavior consistent with AA5083-H131 mechanical properties. The AA5083 AFSD-Recycled and AA5083 AFSD-Solid bar specimens exhibited a similar elastic modulus, reduced yield, and an equivalent, if not slightly higher, UTS and elongation to failure. The AA5083 AFSD-Recycled and AA5083 AFSD-Solid bar exhibited strain hardening while the AA5083-H131, did not. This is to be expected since the H131 temper indicates additional strain-hardening was applied to the AA5083. As such, the existence of this pre-existing strain-hardening in the elevated yield strength for the wrought specimens is observed. The reduction in yield strength observed in the AA5083 AFSD-Recycled and AA5083 AFSD-Solid bar, while achieving similar ultimate strength, suggests the elevated thermal input and plastic deformation from the AFSD processing reverses strain hardening and other strengthening mechanisms of the H131 temper of the feedstock and promotes an exchange of strengthening mechanisms.

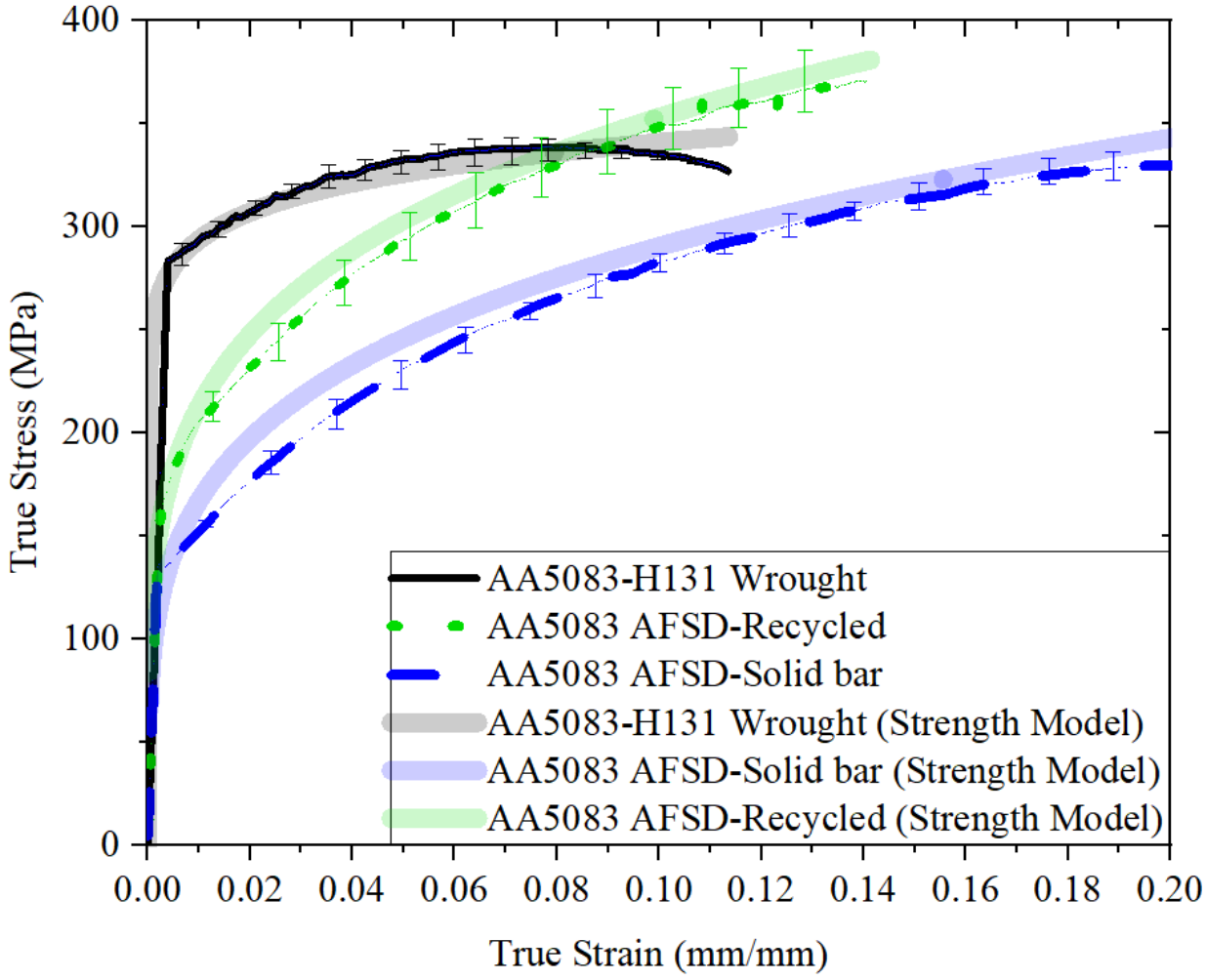

Figure 5.79 Monotonic true stress-strain curve of AA5083-H131 wrought control, AA5083 AFSD from solid bar feedstock, and AA5083 AFSD from recycled chip feedstock, with maximum and minimum errors represented and respective strength model calibration plots.

Table 5.10.2. Monotonic tensile strength properties of AA5083-H131 Wrought Control, AA5083 AFSD-Recycled, and AA5083-AFSD-Solid bar

Material	E (GPa)	YS, 0.2% (MPa)	UTS (MPa)	e to failure
AA5083-H131 Wrought	72.3 ± .2	286 ± 4	343 ± 5	0.14 ± 0.04
AA5083 AFSD-Recycled	70.4 ± .6	179 ± 8	368.0 ± 14	0.16 ± 0.02
AA5083 AFSD-Solid Bar	72.2 ± .4	133 ± 6	335 ± 12	0.24 ± 0.03

The strength model curves (with yield strength contributions from solid solution strengthening, precipitate strengthening, dislocation wall strengthening and grain boundary strengthening) present a good fit to the experimental data – with yield and ultimate strengths generally in agreement with the corresponding experimental data. Table 5.10.2 displays the strengthening mechanisms accounted for in each of the materials considered in this study and used to calibrate the strength model seen in Figure 5.79. It is evident that the only primary strengthening mechanism remaining in the AA5083 AFSD-Recycled and AA5083 AFSD-Solid bar material is the grain boundary strengthening. This can be calculated through the Hall-Petch equation, $\Delta\sigma_{GB} = k_y d^{-1/2}$, where d is the representative grain size and the Hall-Petch constant, $k_{y,}$ is taken [240]as 0.22 MPa-$m^{1/2}$[108]. After consideration of the Hall-Petch equation, it becomes clear that the significant increase in yield strength from AFSD-Solid bar to AFSD-Recycled is directly proportional to reduction in grain size (3.2 mm to 1.5 mm, respectively). The main contributor to solute strengthening in the wrought control is due to the Mg element. However, elevated temperatures have been observed to cause a preferential diffusion of the Mg to grain boundaries in AA5083 that b phase precipitates[234]. Huskins et al. observed that Mn, the other main alloying element in AA5083, did not remain in solid solution in AA5083-H131, but rather formed complex precipitates. The lack of a contribution from the precipitation strengthening mechanisms is also supported by work by Anderson-Wedge et al.[240] and Beck et al.[241] that demonstrated the dissolution of strengthening precipitates after AFSD processing due to the elevated temperatures achieved during deposition. In addition, transmission electron microscopy (TEM) investigation revealed a loss of strengthening precipitates and growth of Mg-Si solute clusters on the order of 5 nm is size[65]. Lastly, as for dislocation wall strengthening, it has been observed in AA2219 that the wrought material's dislocation networks were depleted due to AFSD processing[240].

Table 5.10.3. Strengthening mechanisms for AA5083-H131, AA5083 AFSD-Recycled, AA5083 AFSD-Solid Bar

Material	$\Delta\sigma_{SS}$ (MPa)	$\Delta\sigma_{prec}$ (MPa)	$\Delta\sigma_{DW}$ (MPa)	$\Delta\sigma_{GB}$ (MPa)	$\sigma_{YS,Calc}$ (MPa)	$\sigma_{YS,Exp.}$ (MPa)	n	ε_0
AA5083-H131	90	55	113	25	283	284	0.065	0.0059
AA5083 AFSD-Recycled	0	0	0	180	180	179	0.220	0.0045
AA5083 AFSD-Solid Bar	0	0	0	123	123	133	0.240	0.0038

Fatigue Behavior

The results from the fully reversible load-controlled fatigue tests of AA5083-H131 wrought control (black stars with gray shade), AA5083 AFSD-Recycled (green triangles with green shade), and AA5083-AFSD-Solid Bar (blue squares with blue shade) are shown in Figure 5.80 and summarized in Table 5.10.3. In addition, the colored shaded regions overlaid on the fatigue data represent the scatter bands of the experimental fatigue results. As indicated by the gray shaded region, the wrought control produced the least scatter in total life for the given stress amplitude. Like the tensile results, the AFSD-Recycled specimens experienced fatigue performance comparable to the wrought control specimens, but with a wider scatter in total number of cycles to failure. The solid bar specimens generally exhibited fewer cycles to failure relative to both the wrought control and the recycled specimens. The scatter in the AFSD-Solid bar was similar to that observed in AFSD-Recycled.

While aluminum alloys does not offer a clear endurance limit relationship as steel does, a general relationship is still present between fatigue strength and ultimate strength[242]. Given the tensile results, the AFSD-Recycled would be expected to experience the highest fatigue strength, followed by the AA5083-H131 wrought control, then AFSD-Solid bar. As the fatigue results show, the AFSD-Recycled performs similarly to the wrought control, and generally outperforms the AA5083-H131 wrought control in the high cycle regime, as predicted by the tensile strength.

Similar to the quasi-static tensile results of this present study, the experimental fatigue results of AA5083-AFSD-Recycled exhibited a higher resistance to fatigue in both the low and high cycle regimes than the AFSD-Solid Bar due to the strength gained from further reduction in grain size. Walley et al. performed a study on fatigue of two variations of ultra-fine-grained cryomilled AA5083 (one with a grain size of 315 nm and the other with a grain size of 240 nm) using AA5083-H131 as the control[243]. It was determined the cycles to failure of all three materials were equivalent at each of the plastic strain amplitudes tested and observed that crack nucleation occurred more rapidly in the AA5083-H131 material than cryomilled and hypothesized it was due to the high strength. The cryomilled study also exhibited similar tensile results where the finer the grain size, the higher the UTS. While the grain sizes reported in the cryomilled study are ultra-fine grains and roughly 10 times the size of those in the present study, the results suggest that the smaller the grain size becomes in the AFSD processing, the closer the fatigue performance is to achieving H131 like temper results.

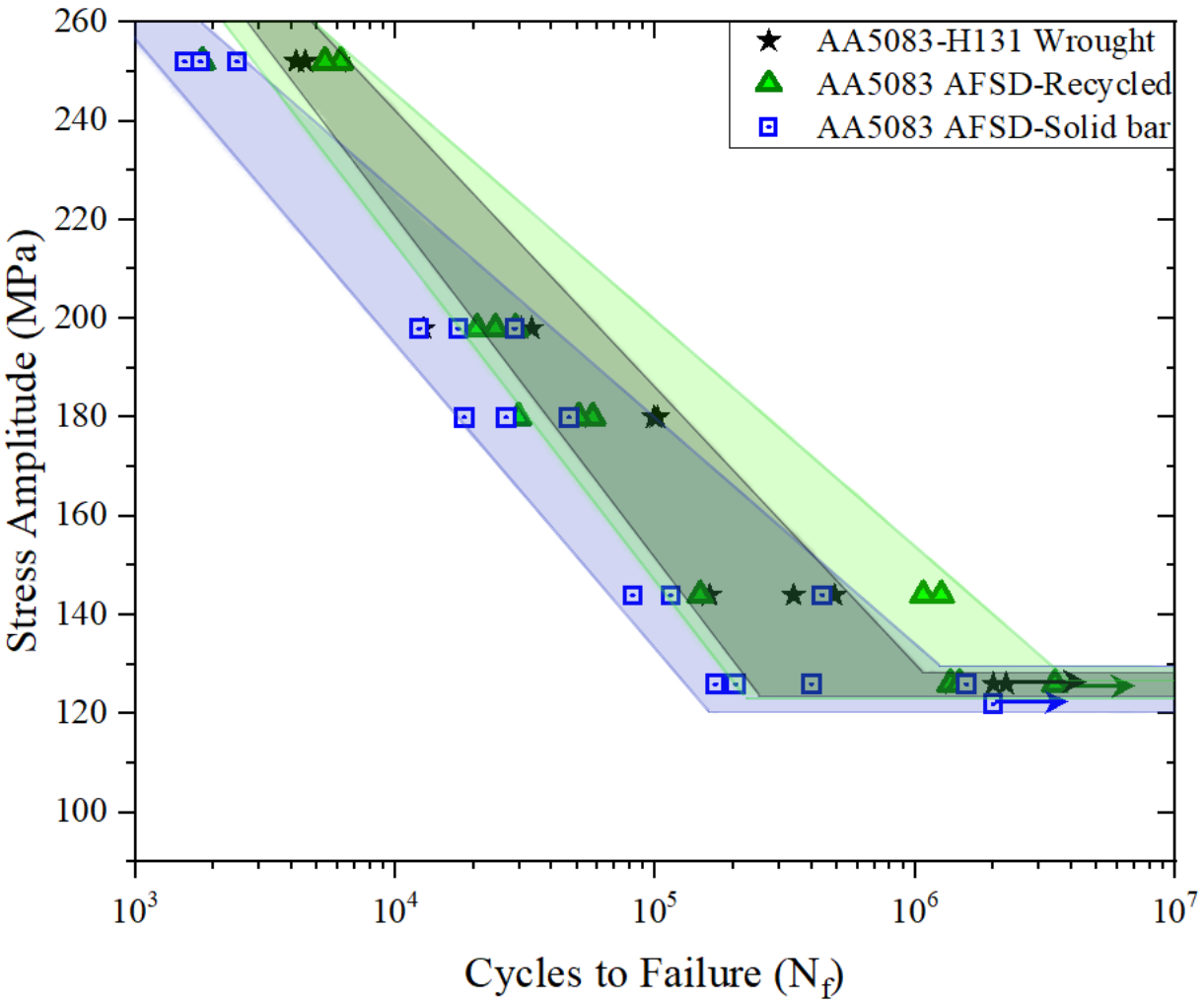

Figure 5.80 Stress amplitude vs. cycles to failure of AFSD AA5083 and AFSD AA5083 chip deposit in the LD Direction.

Table 5.10.4. Summary of comparative stress-life results of AA5083-H131 Wrought Control, AA5083 AFSD-Recycled, and AA5083 AFSD-Solid bar

	Specimen Cycles to Failure, N_f			
Stress Amplitude MPa	AA5083-H131 Wrought Control	AA5083 AFSD-Recycled	AA5083 AFSD-Solid Bar	Loading Ratio
252	6,021	1,814	629	-1
252	4,508	6,165	353	-1
252	4,153	5,367	338	-1
198	30,508	24,303	588	-1
198	12,877	29,052	716	-1
198	33,526	29,789	10,112	-1
180	50,671	57,560	14,381	-1
180	98,903	50,884	26,007	-1
180	102,084	148,962	22,821	-1
144	490,616	1,074,636	27,989	-1
144	341,049	1,261,425	39,786	-1
144	162,179	3,453,369	52,536	-1
126	2,000,000	1,368,313	639,458	-1
126	1,400,359	1,484,866	132,309	-1
126	2,240,000	2,130,539	1,882,929	-1

Post-Mortem Analysis of Fatigue Fracture Surfaces

Figure 5.81 displays representative low cycle fatigue (LCF) fracture surfaces of wrought control AA5083-H131, AA5083 AFSD-Recycled, and AA5083AFSD-Solid bar specimens. The wrought control, as shown in Figure 5.81(a), tested at s =198 MPa and experienced a fatigue life of N_f = 30,808, exhibits singular crack initiation from the middle edge of the specimen, with an enlargement of the initiation site in Figure 5.81(d). The AFSD specimens both exhibited evidence of multi-site crack initiation in LCF. Figure 5.81(b) displays the primary crack initiation for the AFSD-Recycled specimen, tested at s =180 MPa and experienced a fatigue life of N_f = 29,789 that is shown in Figure 5.81(b), occurred toward the bottom middle, while a secondary crack initiation was observed diagonally from that location on the top. An enlargement of the primary initiation site can be observed in Figure 5.81(e). Several crack initiations were observed on the fracture surface of the AFSD-Recycled, tested at s =180 MPa and experienced a fatigue life of N_f = 26,709, as shown in Figure 5.81(c). An enlargement of the primary initiation site, that occurred in the left middle of the specimen, can be observed in Figure 5.81 (f). Secondary initiation sites were observed on the top and bottom right-side corners. While the primary crack in the AA5083 AFSD-Solid bar specimen appears to initiate at a layer interface in the build, other AA5083 AFSD-Solid bar specimens indicate there is not a strong preference layer related initiation. All crack nucleation sites in LCF were observed at near surface defects in the material and do not appear to originate from voids or constituent particles. Phillips et al. observed constituent particles sandwiched between layers of rolled grains in wrought AA5083-H131 material with an average size of 7 mm in diameter. AFSD processing dispersed and reduced the particles to an average size of 4 mm, nearly the same diameter as the reduced average grain size.

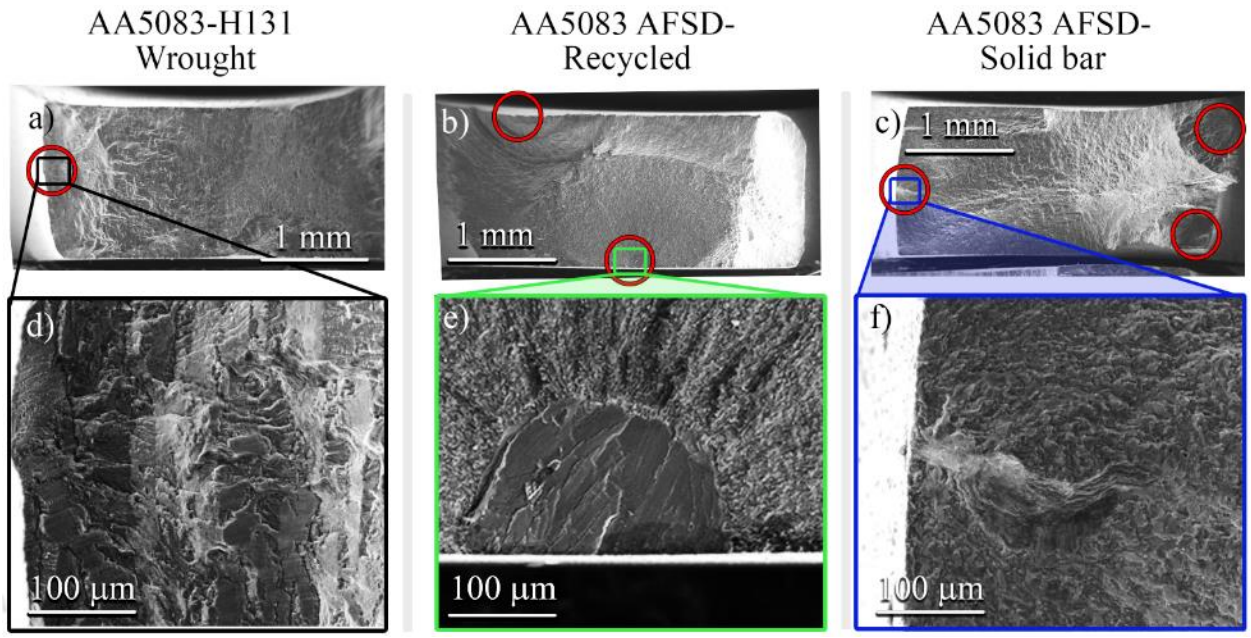

Figure 5.81 Low cycle fatigue fracture surfaces for a) wrought control AA5083-H131 (s =198 MPa, N_f = 30,808), b) AA5083 AFSD recycled chip (s =180 MPa, N_f = 29,789), and c) AA5083 AFSD solid bar (s =180 MPa, N_f = 26,709) specimens, where the red circles indicate observed crack initiation sites, and respective magnifications of primary crack initiation sites below (d-f).

Figure 5.82 displays representative high cycle fatigue (HCF) fracture surfaces of wrought control AA5083-H131, AA5083 AFSD-Recycled, and AA5083 AFSD-Solid bar specimens. As shown in Figure 5.82(a) and enlarged in Figure 5.82(d), the AA5083-H131 specimen tested at s = 126 MPa with a fatigue life of N_f = 346,732, experiences single crack initiation along the bottom middle surface. AA5083 AFSD-Recycled, tested at s =144 MPa with a fatigue life of N_f = 1,074,636, exhibits multi-site crack initiation with the primary crack along the left side toward the bottom left corner shown in Figure 5.82(b) and enlarged in Figure 5.82(e) and a smaller crack initiated toward the top right corner. After testing at s =126 MPa with a fatigue life of N_f = 399,576, the AFSD-Solid bar specimen's primary crack initiation site can be seen in the bottom right corner of Figure 5.82(c) and a magnified image is shown in Figure 5.82(f). The wrought control specimens in HCF generally presented with singular initiation sites, while both AA5083 AFSD-Recycled and AA5083 AFSD-Solid bar still exhibited some multi-site crack initiation, with nucleation occurring near surface defects in the material. Delamination was also evident in the fast fracture region of multiple AA5083 AFSD-Solid bar specimens during HCF indicating that while present, was not the site of crack initiation. This feature has also been observed in another AFSD study, where the delamination created stress risers leading to reduced life in AFSD IN625[11]. All specimens exhibit evidence of micro-void growth and coalescence.

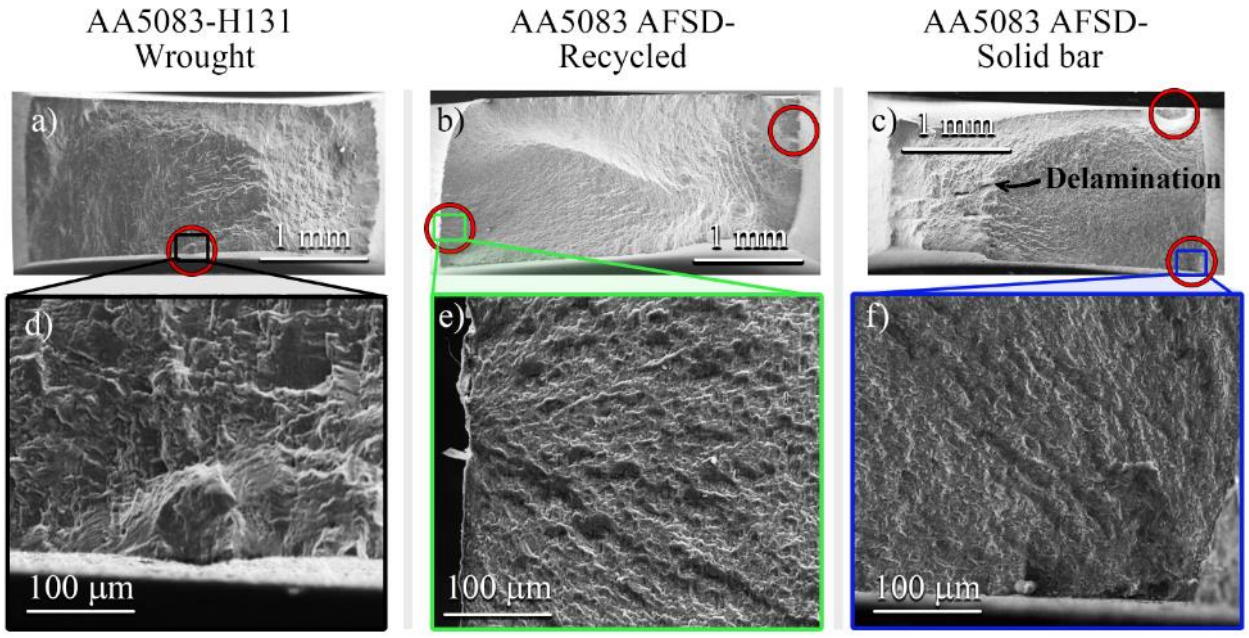

Figure 5.82 High cycle fatigue fracture surfaces for a) AA5083-H131 (s =126 MPa, N_f = 346,732, b) AA5083 AFSD-Recycled (s = 144 MPa, N_f = 1,074,636), and c) AA5083 AFSD-Solid bar (s =126 MPa, N_f = 399,576) specimens, where the red circles indicate observed crack initiation sites, and respective magnifications of primary crack initiation sites below (d-f).

Multi-Stage Fatigue Modeling

The calculated contributions of the crack incubation stage (INC) and the microstructurally and physically small crack growth stage (MSC/PSC) to the total life (N_{total}) can be observed in Figure 5.83 for the (a) AA5083-H131 wrought control, (b) AA5083 AFSD-Recycled material, and (c) AA5083-AFSD-Solid bar material, with direct comparisons of total life cycles shown in (d). For each curve (a-c), the INC is indicated by the dotted line, the dashed line represents MSC/PSC stage, while the solid line provides the MSF fit for N_{total}. Initially, the experimental data and parameters for AA5083-H131 wrought were input into the MSF modeling software. Constants were selected that dictated the impact of the microstructural features on the incubation and small crack growth stages of fatigue. The constants determined for AA5083-H131 were then compared to AA5083-AFSD-Solid bar experimental data, modified where appropriate, and were then applied to the AA5083-AFSD-Recycled experimental data, and again, modified as appropriate. The modeling parameters used to model the fatigue life of AA5083-H131 wrought control, AA5083 AFSD-Recycled, and AA5083 AFSD-Solid bar are presented in Table 5.10.4.

The MSF model provided a good correlation to the fatigue performance of the wrought control as well as both AFSD depositions. Each material shown in Figure 5.83 experienced a similar contribution from the INC stage and the MSC/PSC stages in the MSF model. At low stress amplitudes, fatigue life exhibited a high number of cycles and was controlled by the crack initiation stage. During the high cycle fatigue regime, repeated elastic deformation occurred. As the stress amplitude increased, the cycles to failure decreased; the incubation stage was increasingly less critical, while microstructurally and physically small crack growth increased in driving force. The fatigue life at higher stress amplitudes, characterized by fewer cycles to failure and repeated plastic deformation, was almost fully dominated by the MSC/PSC stage. Overall, in terms of fatigue behavior, the smaller grain sized and higher strength AFSD-Recycled material was more resistant to crack propagation and nucleation than the AFSD-Solid bar. This experimentally observed attribute this directly related to the refined grain size.

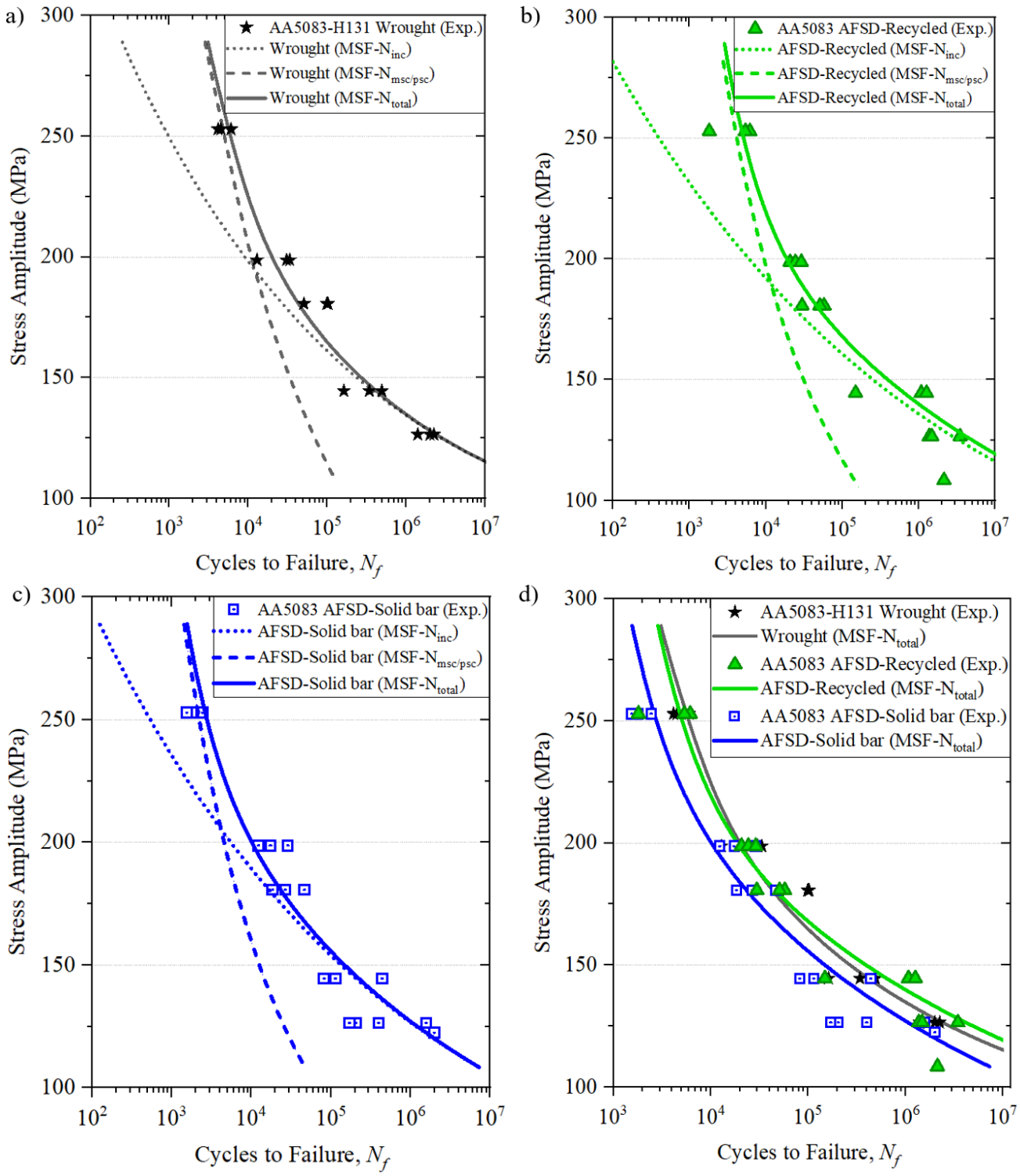

Figure 5.83 Multistage Fatigue (MSF) fit displaying stress-life plots for crack incubation (N_{inc}) and microstructurally and physically small crack growth ($N_{msc/psc}$) compared to total life (N_{total}) for a) AA5083-H131 wrought control, b) AA5083 AFSD Solid bar, c) AA5083 AFSD Recycled Chip, and d) MSF fit for total life (N_{total}) comparison previously mentioned materials.

Table 5.10.4. MSF parameters used for model fits.

Parameter	AA5083-H131 Wrought Control	AA5083 AFSD-Recycled	AA5083 AFSD-Solid bar
K'	400	617	544
n'	0.065	0. 22	0.24
C_{inc}	1.14	1.12	1.12
C_m	0.28	0.58	0.73
A	-0.35	-0.21	-0.24
Q	2.1	2.1	2.1
y_1	970	970	970
y_2	1600	1600	1600
Y	3.7	3.7	3.7
R	0.38	0.38	0.38
E_{mod}	72,260	70,400	72,200
S_{ULT}	343	368	335
S_{YLD}	286	179	133
SI_{exp}	1.5	1.5	1.5
W	5e-05	5e-05	5e-05
a_i	1	1	1
Q	0.5	0.5	0.5
Z	4	4	4
C_I	5e+06	5e+06	5e+06
C_{II}	0.0045	0.0045	0.0045
X	0.03	0.03	0.03
$DCTD_{TH}$	2.86e-10	2.86e-10	2.86e-10
a_f	2000	2000	2000
DCS_{exp}	1	1	1
$PORE_{exp}$	0.6	0.6	0.6
GO_{exp}	0	0	0
GS	10.86	1.5	3.16
GS_0	10	5	5

5.10.3 Conclusions

This study examined the effect of Direct Additive Recycling (DAR) of a strain-hardened Al-Mg-Mn alloy (AA5083) on the microstructure and mechanical properties including tensile and fatigue behavior.

The AFSD process produced a refined grain structure in both the solid bar and recycled machine chip depositions. The grain size was reduced from an average of 250 mm in the wrought material to 3.2 mm for AFSD-solid bar depositions and 1.5 mm for the AFSD-Recycled depositions. The additional grain size reduction of the recycled chip material as compared to the solid bar deposition is attributed to the initially reduced grain size of the machine chip feedstock relative to the wrought plate feedstock.

Tensile tests revealed comparable ultimate tensile strength results between wrought control AA5083-H131 and AFSD-Solid bar and a 7% increase for AFSD-Recycled specimens on average. Average yield strength for both AFSD-Solid bar and AFSD-Recycled were reduced by 37% and 53%, respectively. Elongation to failure increased by 14% and 71% for AFSD-solid bar and AFSD-Recycled, respectively. The tensile results are attributed to an apparent exchange of strengthening mechanisms (solute, precipitation, and dislocation wall strengthening for grain boundary strengthening) after AFSD processing due to extended time at elevated temperature (approximately 85% of the melt temperature) and severe plastic deformation.

Fatigue tests revealed comparable results between wrought control AA5083-H131 and AFSD-Recycled and slightly reduced for AFSD-solid bar specimens, all presenting similar crack initiation mechanisms. Fatigue performance closely mimics tensile performance with regard to the enhanced strength of the recycled material over the wrought AA5083-H131, likely due to the relationship between fatigue strength and ultimate strength with strength being improved by the grain size reduction which inherently increases the strain hardening induced during testing.

The MSF model was successfully calibrated for AA5083-H131 wrought control, AA5083-AFSD-Recycled, and AA5083-AFSD-Solid bar materials.

The results from this work indicate that solid-state AFSD is a viable option for generating components using AA5083 waste machine chips through DAR.

Future work to fully understand the contribution of solid solution strengthening in AFSD AA5083 through TEM characterization would further clarify the strengthening mechanisms of AFSD AA5083.

5.11 Meshless AFSD Simulation Framework Development to Capture Material Flow and Temperature

In this work, a fully coupled thermo-mechanical meshfree approach is developed for the first time to simulate a solid-state layer-by-layer additive manufacturing process, Additive Friction Stir Deposition (AFSD). The meshfree method in this present work uses a Lagrangian reference frame, which permits tracking of material point history. A solid mechanics formulation is used, allowing the resolution of both elastic and plastic strains. An explicit dynamics time stepping scheme is used to ensure that the code is robust for the large level of non-linearity native to the AFSD process. In this present work, a description of the meshfree method will first be described. Then a new thermo-mechanical joining contact algorithm will be introduced. Following that, a description of the experimental setup for the AFSD model calibration experimental one layer deposition cases is explained. Subsequently, the simulation model and results for three different parameter sets will be detailed and compared against the experimental results. Finally, temperature and strain rate gradients are revealed across the entire deposition elucidating spatial-temporal flow phenomena in the AFSD process.

5.11.1 Material and Method

The SPH model used in this study, which is comprised of a rigid fixed base, rigid rotating and translating tool, and deformable feedstock and substrate, is shown in Figure 5.84.

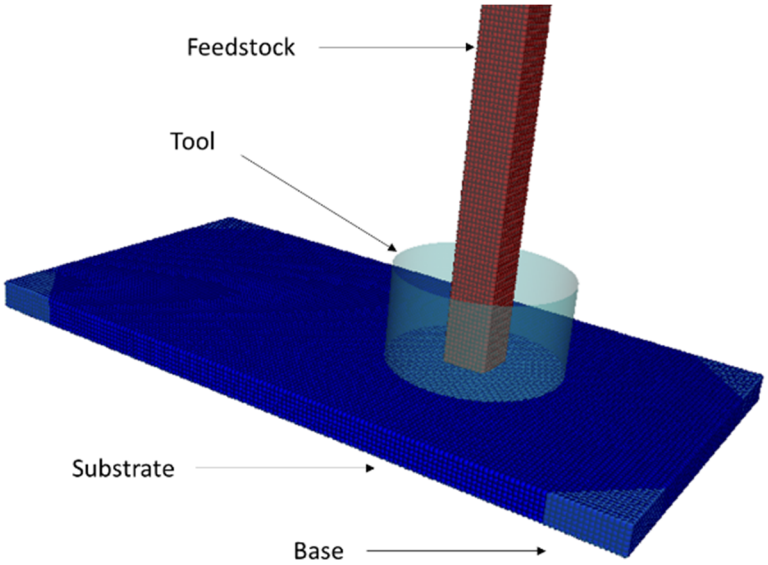

Figure 5.84 Additive Friction Stir Deposition (AFSD) model used in this study. Smoothed particle hydrodynamic material points modeled the feedstock and substrate, and finite elements modeled the tool and base.

The dimensions of the substrate were 76.2 x 152.4 x 6.35 mm^3, and the dimensions of the feedstock were 9.53 x 9.53 x 110 mm^3. The tool diameter was 38.1 mm. Here 11,000 and 69,312 material points were used to model the feedstock and substrate, respectively (total 80,312 material points). The SPH material points were spaced approximately 1 mm apart. 16,598 and 25,742 elements were used to model the tool and base, respectively (total 42,340 elements).” The nodes in the

elements were approximately 1 mm apart. The finite elements were employed to the rigid parts of the simulation to shorten the simulation times.

A commercially available B8 AFSD machine was employed to deposit 9.53 mm x 9.53 mm square cross-section solid wrought AA6061-T651 (nominally Al, 1.16 wt% Mg, 0.51% wt% Si, 0.27 wt% Cu) feedstock rods, which were pushed through a 38.1 mm hollow rotating tool with a flat interaction shoulder face, onto a constrained 6.35 mm thick aluminum substrate of the same composition. 50.4 mm center-to-center deposits were produced at 1.5 mm heights while varying deposition feed rate (F) multiplicatively from 63.5 mm/min to 254 mm/min. Tool rotational speed (ω) and traversing velocity (V) remained constant at 300 RPM and 127 mm/min, correspondingly. Process parameters were selected to produce three depositions of varying quality: proportional build, starved build, and an overfed build as shown in Table 5.11.1.

Table 5.11.1. AFSD parameter sets used for model calibration for the three experimental builds (starved, optimal, and overfed).

Case	Starved	Optimal	Overfed
Actuator Feed Rate (mm/min)	63.5	127	254
Tool Rotational Speed (RPM)	300	300	300
Tool Traverse Velocity (mm/min)	127	127	127

The starved build (63.5 mm/min actuator feed rate) was created by decreasing the actuator speed so that insufficient material was pushed through the tool, characterized by galling and/or a truncated build profile. Next, the overfed deposit (254 mm/min actuator feed rate) was created by increasing the actuator feed rate such that excess material was pushed through the tool, characterized by excessive flash and/or a wider build profile. All experiments were performed at room temperature (21 °C) in an open atmosphere. The experimental setup for the elucidation of AFSD processing temperature is shown in Figure 5.85.

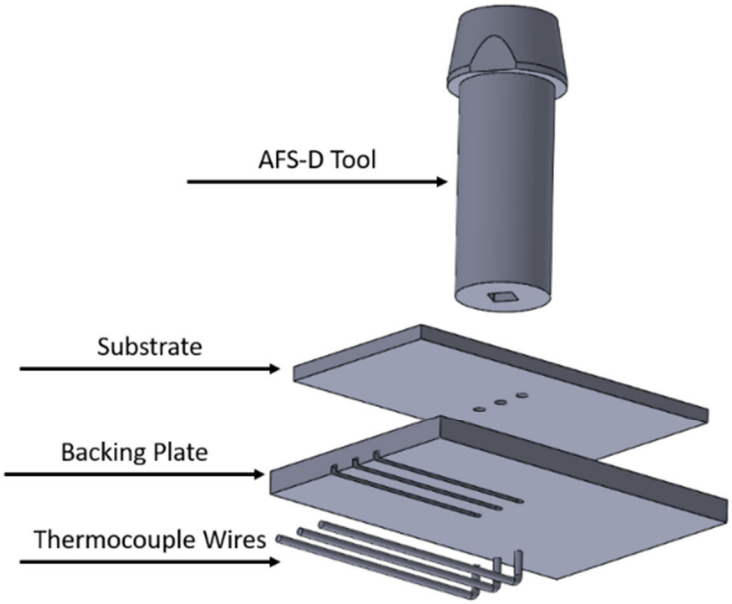

Figure 5.85 AFSD substrate temperature experimental setup depicting locations of thermal couples in the substrate to measure advancing side, middle, and retreating side temperatures.

A steel backing plate was created to protect the thermocouples from the force of the AFSD tool pushing down on the AA6061 substrate. Three channels were used to capture the advancing side, middle, and retreating side temperatures of the substrate by having thru-holes machined into a steel plate. Type K insulated thermocouples were inserted into the backing plate channels, with the tips protruding through to the 3 mm deep substrate holes. The holes were spaced 12.7 mm apart. During the builds, the temperature at the thermocouples was recorded by an Omega RDXL4SD datalogger at the midpoint location of the deposition. One layer was deposited for each test case. The rationale behind using single layer depositions are threefold: 1) significant reduction in simulation run time 2) limitation of GPU memory (11 GB) on the authors' local machine, which limits the total number of SPH material points 3) one layer is sufficient to demonstrate the ability of the code to capture the physics of the process.

5.11.2 Results and discussion

Temperature Model Calibration

The time to run each test case has been listed in Table 5.11.2. The simulations were run on a local machine using an EVGA GeForce GTX 1080 Ti GPU.

Table 5.11.2. SPH simulation run times for each test case.

Case	Starved	Optimal	Overfed
Run Time (hr:min)	36:46	38:48	37:55

The comparison for the experimental temperature results and the simulation results are shown in Figure 5.86 for the retreating side, middle, and advancing side of the deposition. The thermocouple data from the experiments are overlaid with the SPH simulation temperature data. The colors correspond to the measurement location relative to the traverse direction of the ASF-D tool: gray for retreating side, red for middle, and blue for advancing side. The horizontal axis shows the advancing phase time. The left vertical axis represents the temperature in Celsius, while the right vertical axis shows the temperature relative to the solidus temperature of AA6061. The starved condition comparison is provided in Figure 5.86a, the optimal deposition comparison is in Figure 5.86b, and the overfed condition comparison is in Figure 5.86c.

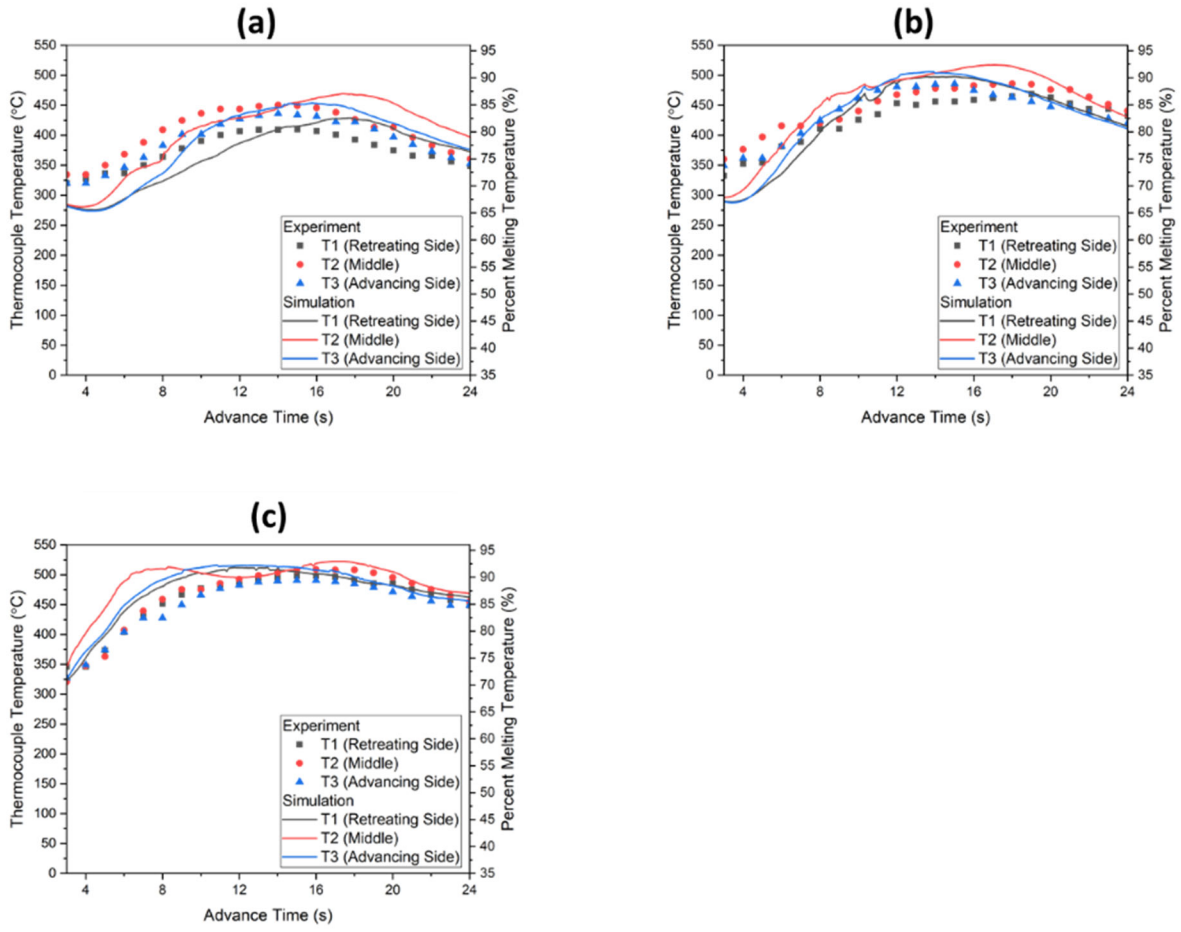

Figure 5.86 Thermocouple temperature results for three test cases: (a) starved at 63.5 mm/min actuator feed rate, (b) optimal at 127 mm/min actuator feed rate, and (c) overfed 254 mm/min actuator feed rate.

For all three conditions shown in Figure 5.86, the overall trend for the retreating, middle, and advancing side compared well between the experiments and SPH simulations. However, the temperature discrepancy between the simulations and experiments at the beginning of the deposition was a result of the simulations abbreviating the dwell phase to reduce simulation time. The dwell time was not observed to have a significant effect on simulation temperature after a few seconds of the advance phase. Processing temperature tended to peak between 90-95% of the AA6061 feedstock solidus temperature. However, this was only the peak of the thermocouple temperature, the true peak temperature in the stir zone-the region directly stirred by the tool-would have been hotter. The experiments and simulations showed that the advancing side experienced a higher temperature during the deposition than the retreating side, which is consistent with FSW. However, this temperature asymmetry tended to decrease with increasing deposition rate. This phenomenon was likely caused by the deposited material tending to favor the advancing side over the retreating side at lower deposition rates. So, as deposition rate increased, the profile widened out and covered the substrate over the thermocouples better, which both increased the temperature

and decreased the temperature asymmetry. Therefore, an asymmetry may have still existed at high deposition rates, but future studies with thermocouples spaced farther out from the SZ would be able to determine this more accurately. For all three conditions, there was a moment when the middle thermocouple temperature remained constant or even slightly decreased while the outer thermocouple temperatures continued to rise. A diagram illustrating this phenomenon is provided in Figure 5.87.

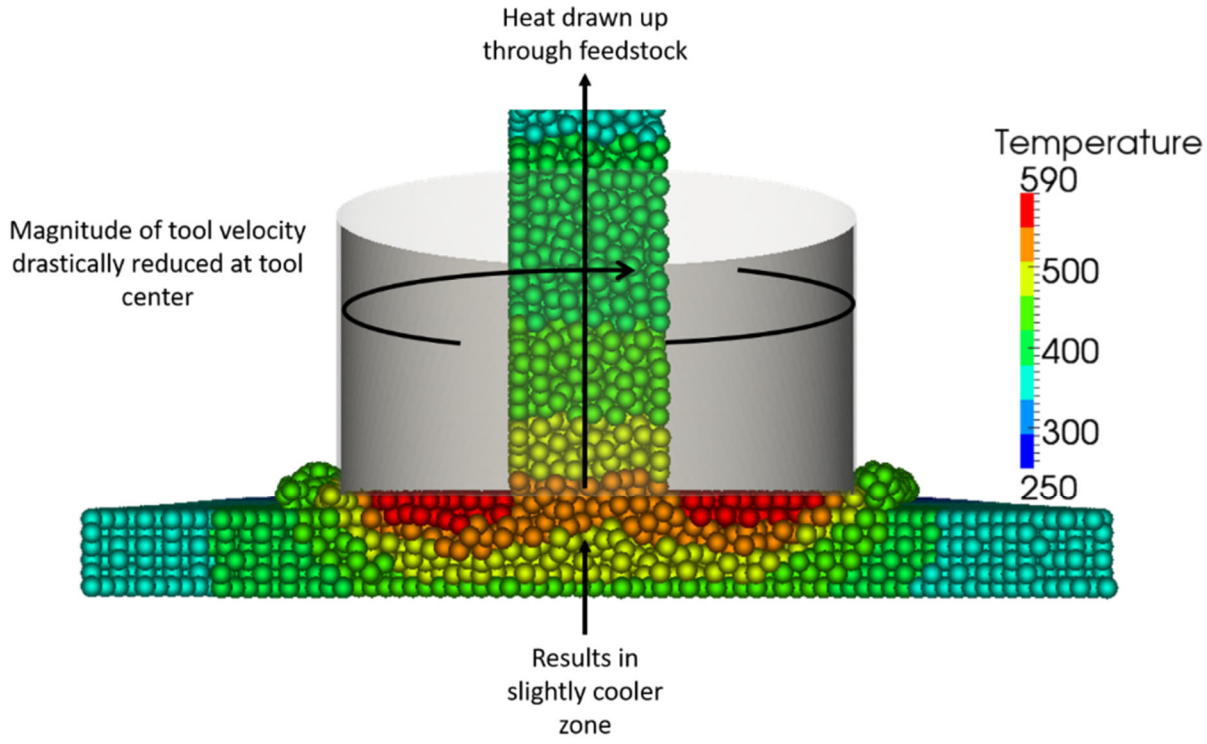

Figure 5.87 Diagram illustrating the lower temperature zone directly beneath the tool caused by the reduction of the tool velocity vector and the feedstock heat sink. Temperature scale is in degrees Celsius.

This reduction in the temperature at the middle along the deposition center was likely a combination of both the feedstock approaching the middle thermocouple and acting as a heat sink and the magnitude of the tool velocity vector decreasing towards the center of the tool, resulting in less frictional heat generated from the tool shoulder. The ability of the feedstock to draw heat away from the deposition increased with deposition rate, because a higher deposition rate forces the cooler top of the feedstock down into the build faster than a lower deposition rate.

Build Profile Model Calibration

The comparison between the experimental and simulated temperature profiles is shown in Figure 5.88a-c for the starved build, optimal build, and overfed build, respectively. The experimental AFSD depositions are overlaid with the opaque SPH simulation results to show how well the experiments and simulations match. The experimental depositions were isolated from the respective substrates through Photoshop. The SPH simulation profiles were taken from Paraview by isolating the deposition from the substrate. To ensure a uniform scale between each experiment

and simulation image, the size of the SPH images was adjusted to match 1) the crescent shape at the back of the deposition caused by the tool dwelling against the substrate 2) the circle at the center of the stir zone caused by the feedstock spinning against the deposition.

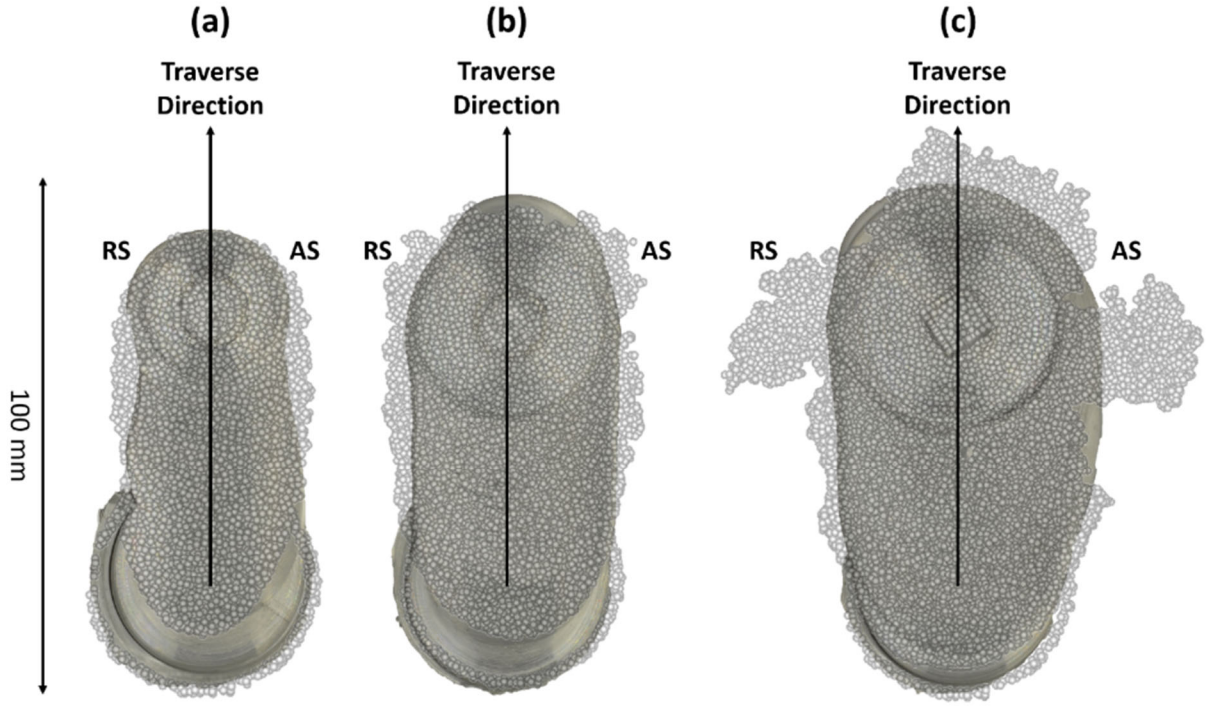

Figure 5.88 Comparison between experiment and simulation build profiles for: (a) starved at 63.5 mm/min actuator feed rate, (b) optimal at 127 mm/min actuator feed rate, and (c) overfed 254 mm/min actuator feed rate.

Good agreement exists between the experimental and simulation profile trends for all three build conditions as shown in Figure 5.88a-c. The experiments showed an advancing side bias for deposition, which was supported by the simulation build profiles and temperature profiles in the previous section. The asymmetry in both the experiment and simulations was quantified by dividing the advancing side area by the retreating side area for each case, the results of which are displayed in Table 5.11.3.

Table 5.11.3. Comparison of advancing-retreating side asymmetries between the experiments and simulations.

Case	Starved	Optimal	Overfed
Experiment AS/RS	1.16	1.06	1.06
Simulation AS/RS	1.23	1.02	1.16
% Difference	6.03	-3.78	9.43

The amount of asymmetry was predicted within 10% for all three cases, with the overfed case being the least accurate due to the large amount of flash predicted in the simulation. In all three cases the simulations predicted the crescent-shaped crater at the beginning, caused by the tool dwelling without depositing. The crescents shrank as actuator feed rate increased because higher feed rates push more material backwards at the start. The simulations tended to overpredict flash in the deposition, especially the overfed case. However, the overfed case used an extremely high deposition rate, which likely would not be used for actual parts. Flash formation may be dependent on material properties, as other studies have shown significant flash formation such as in Avery et al. [68]. SPH parameters may be adjusted to change the amount of flash formed, but this may result in simulation instability.

Simulation Temperature Contours

The comparison between the SPH simulation temperature contours is shown in Figure 5.89a-c. The temperature contours were generated in Paraview with a top down view of the simulated depositions. The feedstock was still visible in all three cases, but length of the remaining feedstock was inversely proportional to the actuator feed rate, so lower actuator feed rates resulted in longer leftover feedstocks. The temperature scale was measured in Celsius, with the temperature limits determined by the lowest and highest temperatures across all three test cases.

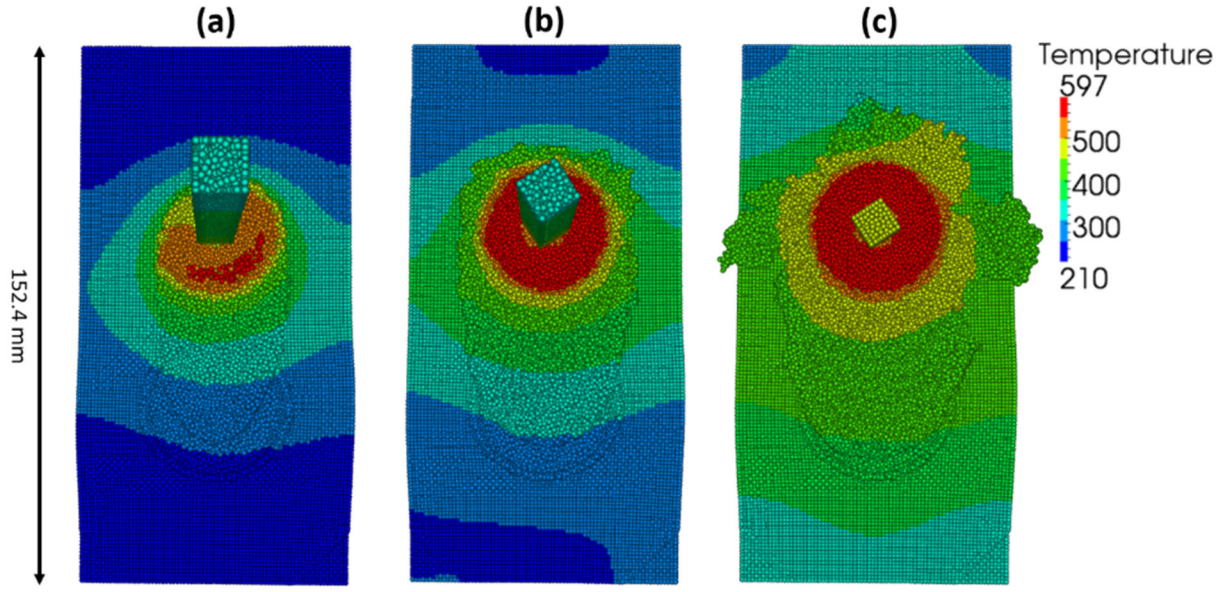

Figure 5.89 Simulation temperature (°C) contours for: (a) starved at 63.5 mm/min actuator feed rate, (b) optimal at 127 mm/min actuator feed rate, and (c) overfed 254 mm/min actuator feed rate.

In the temperature contour plots for the three conditions shown in Figure 5.89, the processing temperature was proportional to the actuator feed rate, with higher feed rates corresponding with increased temperatures. For the starved case in Figure 5.89a the low feed rate failed to provide adequate material flow to fill the stir zone, which resulted in less frictional heat generated between the tool and deposition reflected in the contour plot. The optimal and overfed cases, Figure 5.89b and 5.79c, respectively, had sufficient material flow to fill the SZs, but the overfed case in Figure 5.89c depicted a higher temperature contour. This temperature discrepancy was likely a result of

the higher actuator feed rate transferring relatively high force downwards generating more frictional heat in the overfed condition (Figure 5.89c). This mechanism also resulted in a relatively high thermal soak of the substrate for the overfed case. One conclusion of the temperature dependence on actuator feed rate was that actuator feed rate not only influenced output deposition appearance but also substrate material properties. A high feed rate may be desirable to limit thermal gradients across the entire part, which would result in lower residual stress and/or distortion. However, a low feed rate may be desirable for more localized heating, which, in a sufficiently large substrate, would result in a smaller heat affected zone. Thus, output part quality is not necessarily linked to part appearance, which was concluded in a previous study by Phillips et al. [65]. Another conclusion was that the processing temperature slightly exceeds the solidus temperature (592 °C). Machine operators have observed what could be considered a partially melted region in the SZ just below the tool. Future studies could confirm this by directly measuring the SZ temperature.

Simulation Plastic Strain Contours

The comparison between the simulated effective plastic strain contours for the three test cases is shown in Figure 5.90. A top down view of the depositions was taken in Paraview. The range of effective plastic strain varies from zero to the highest level of plastic strain experienced by any of the three test cases.

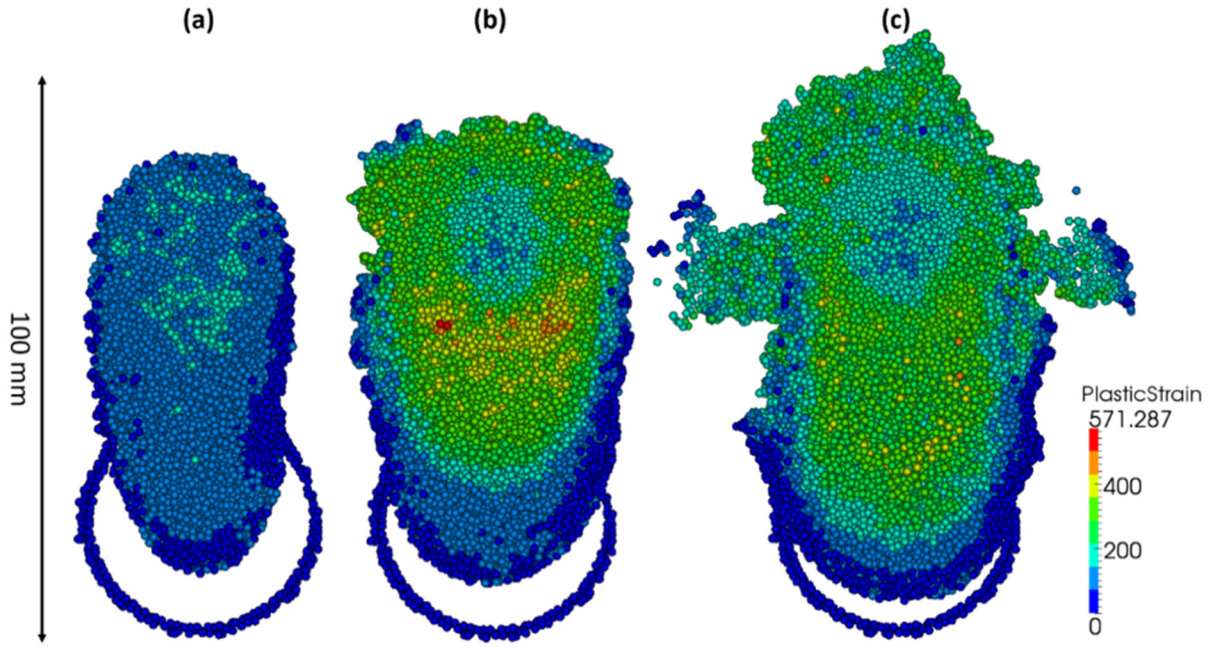

Figure 5.90 Effective plastic strain contours for: (a) starved at 63.5 mm/min actuator feed rate, (b) optimal at 127 mm/min actuator feed rate, and (c) overfed 254 mm/min actuator feed rate.

The simulation results of the deposition plastic strain for all three conditions plotted in Figure 5.90a-c do not show a strong preference for advancing or retreating side with respect to plastic strain, unlike the asymmetrical temperature distributions observed in previous sections. The starved plastic strain contour in Figure 5.90a showed relatively little deformation during deposition,

which likely correlates to the surface voids/galling observed experimentally due to lack of material-tool shoulder interaction. In contrast to the starved plastic strain contours, the optimal (Figure 5.90b) and overfed (Figure 5.90c) plastic strain contours exhibited similar results. The discrepancy between the starved case, the optimal case, and overfed case showed that there was likely a threshold value of actuator feed rate that divided insufficient from sufficient material mixing in the stir zone. The low actuator feed rate of the starved case failed to input sufficient material into the stir zone to ensure adequate material mixing. The medium actuator feed rate of the optimal case provided ample material flow in the stir zone. The high actuator feed rate of the overfed case failed to promote more material flow in the stir zone than the optimal case.

One implication of the relationship between actuator feed rate and plastic strain pertains to material mixing in the deposition. Material mixing would be proportional to effective plastic strain in the deposition. Therefore, more material movement would result in both higher plastic strain and greater material blending. If a very nonuniform feedstock-perhaps a result of recycling material or intentionally through mixing powder feedstock-was used, a low feed rate would likely result in a heterogeneous deposition. A starved build likely would not promote sufficient material mixing to create a homogeneous deposition. However, a medium to high actuator feed rate would result in a higher plastic strain gradient across the deposition, and therefore would result in greater material mixing, which would result in a more homogeneous deposition. The high actuator feed rate of the overfed case, rather, would not promote more material mixing than the medium actuator feed rate of the optimal case, and would actually result in wasted material due to excessive flashing. An interesting future study depositing dissimilar material could confirm this behavior of material mixing and may even pinpoint a threshold actuator feed rate for optimal mixing.

5.11.3 Concluding remarks

In this work, the authors present a meshfree formulation for AFSD simulations for the first time. The method uses a novel thermo-mechanical joining model that was able to handle the large plastic deformation. Other conventional methods would struggle to predict with good accuracy the temperature and build profiles of experimental builds. The SPH simulations showed good agreement with experimentally obtained temperature plots and build profiles. The physics captured the temperature dip in the middle of the SZ and temperature asymmetry between the retreating and advancing side caused by the magnitude of the tool velocity vector and the feedstock acting as a heatsink. The simulations exhibited the decreasing temperature asymmetry between the advancing and retreating sides as actuator feed rate increased, likely due from a higher volume of material deposited results in more material pushed outwards so the material better covers the substrate thermocouple locations. The model produced accurate build profiles on the starved and optimal cases, capturing the beginning crescent-shaped crater and advancing side bias, but future work could improve build profile simulations at higher actuator feed rates. The temperature contour plots demonstrate the dependence of spatial temperature distribution on actuator feed rate. The simulations showed that thermal bathing increased with increasing actuator feed rate. The overfed case provided the highest thermal soak, which could not only result in different mechanical properties in the substrate but also different residual stress and distortion profiles than the other two cases. The effective plastic strain contour plots show the dependence of material mixing on actuator feed rate. Lower actuator feed rate would likely result in a heterogeneous material, and higher actuator feed rate would likely result in a more homogeneous material. However, there was

evidence that a threshold for material mixing occurs and increasing actuator feed rate past that point would result in material waste through excessive flash.

The presented SPH model is a powerful tool for accompanying AFSD builds. The code can be used to predict output build quality using metrics such as temperature, profile, and effective plastic strain. Difficult to measure phenomena, such as temperature and plastic strain gradients across the entire build can aid researchers into elucidating the un-seen mechanisms occurring during AFSD processing of materials. This study paves the way for future, more comprehensive numerical studies into the nascent AFSD process.

5.12 Constitutive Model Influence of Temperature and Strain Rate on the Mechanics of AFSD Aluminum Alloys

In this study, the temperature and strain rate dependent physics of Additive Friction Stir Deposition (AFSD) are elucidated for the first time. Candidate constitutive models are selected to account for the severe plastic deformation and wide ranges of temperature and strain rate inherent to AFSD. Torsion mechanical tests are performed to capture AA6061 stress dependency on temperature and strain rate. Four constitutive models, including a low fidelity-calibrated one, are applied to single-layer AFSD simulations. The robust meshfree method, smoothed particle hydrodynamics (SPH), provided the framework for constitutive model comparison. Utilizing the SPH simulations, peak values, temperature contours, effective stress contours, effective plastic strain contours, build profiles, and simulation run time are all compared to reveal hidden mechanisms of AFSD processing

Simulating severe plastic deformation processes (SPDPs) necessitates the use of high fidelity constitutive models to successfully capture the dynamic temperature dependent flow behavior after severe plastic strain. Constitutive models are used to evolve the yield surface in a computer simulation by accounting for multiple factors such as strain rate, temperature, material history, or damage and the relevant factors vary for each scenario. The yield surface is an abstract 3D space which has the three principal stresses as the three dimensions [244]. As long as the coordinates of the principal stresses fall within the yield surface, yield has not occurred. However, once the coordinates reach the surface, yielding occurs. The shape of the yield surface varies based on the failure theory. For example, for isotropic materials, the von Mises yield surface results in a cylinder, and the Tresca yield surface results in a hexagonal prism [245]. In reality, the yield surface is rarely fixed, meaning that the yield surface can grow (isotropic hardening) or translate (kinematic hardening). The hardening occurs because of dislocation mechanics. To quantify the changing yield surface, engineers utilize constitutive models, which facilitate change through factors relevant to the real-life phenomenon they are simulating (thermal softening, strain rate sensitivity, and damage for example).

The simplest constitutive models are typically empirical, meaning that the equations have a limited basis in mechanics but typically match the trend of experimentally determined stress-strain curves. The Ramberg-Osgood equation (RO) only accounts for strain hardening [246]. RO is commonly inverted so strain is a function of stress [245], [247], and equations based on RO frequently appear in fatigue analysis [228], [248]. Johnson-Cook (JC), because of its simplicity, has been widely implemented in either the original or modified form [77], [249]–[253]. JC accounts for strain hardening, strain rate sensitivity, and thermal softening [162]. JC does not account for other factors that could be important, such as kinematic hardening, crystal structure, or grain size, which results in significant variance between studies [254]. The Zerilli-Armstrong (ZA) model was created to improve JC by accounting for different crystal structures [254]. ZA is based on dislocation mechanics. Some constitutive models are based on the Arrhenius equation, which describes the temperature dependence of a reaction [255]. The Arrhenius equation is the basis for the Zener-Hollomon parameter (Z), which relates stress to strain rate and temperature [256]. Multiple constitutive models utilize Z, such as the Medina-Hernandez model [257], the Sheppard-Wright model [258], and the Sellars-Tegart model [259]. One benefit of using Z is due to the relationship between the processing environment and grain size and hardness, which leads to a relatively easy method for model calibration [259].

The significant influence that constitutive models have on simulations necessitates further research into selecting appropriate models for AFSD simulations. Since limited literature exists for AFSD simulations [260], some candidate constitutive models will be selected from simulations for similar processes such as Friction Stir Welding (FSW). The constitutive models will be calibrated with torsion mechanical testing data for both AA6061-T6 and -O tempers. The models will then be compared against each other by contrasting relative temperature profiles, effective plastic strain profiles, effective stress profiles, build profiles, and run time within the Smoothed Particle Hydrodynamics (SPH) simulation framework.

5.12.1 AFSD Processing Environment

The AFSD process is a novel solid-state additive manufacturing process capable of rapidly producing near-net-shape parts. The solid-state attribute refers to the AFSD processing environment temperature remaining below the material melting point. Problems related to fusion-based process such as hot cracking and distortion are minimized in solid-state processes. A visual description of the AFSD process is provided in Figure 5.91.

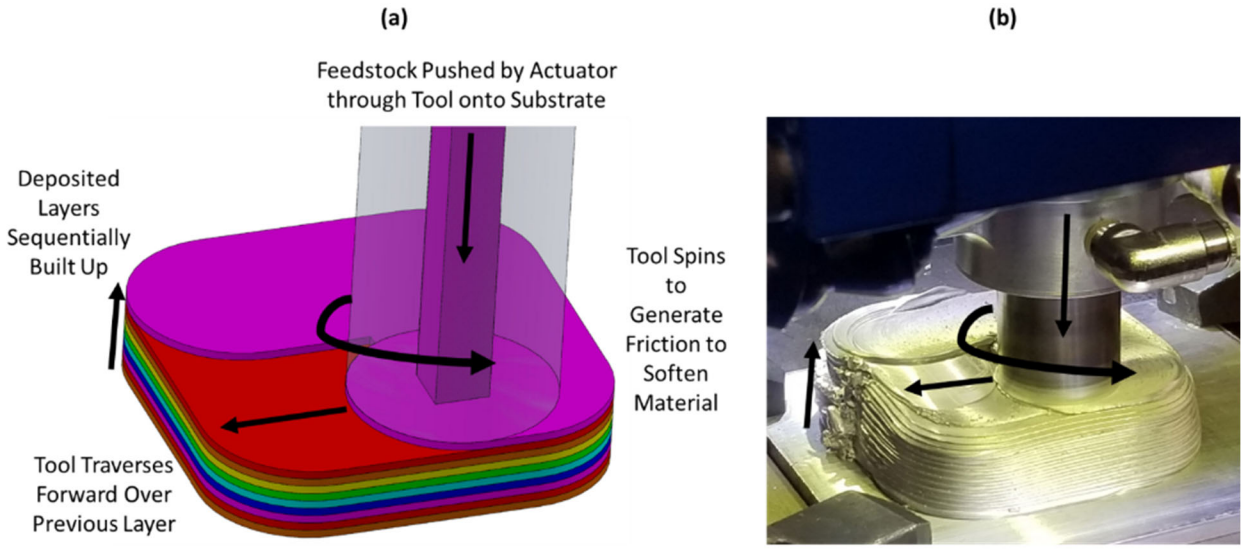

Figure 5.91 (a) Schematic of the AFSD process shows how feedstock rod is transformed into deposition by spinning and traversing tool. (b) Large multi-layer deposition created by the AFSD process [260].

In the AFSD process, the feedstock material is pushed through a hollow spinning tool onto a substrate. The tool traverses forward leaving behind a metallurgically bonded deposition. Directly underneath the tool is the stir zone, where the highest temperatures and plastic strains are experienced. Extruding material through the stir zone results in severe plastic deformation and high temperatures because of frictional heat generation between the tool and the deposition.

One of the challenges facing constitutive models is how to account for a wide range of behaviors with the minimum number of required parameters. Materials undergoing AFSD processing experience high plastic strain, wide ranges of strain rates, and temperatures ranging from room

temperature to near melting temperature. For accurate simulations, constitutive models need to account for these variables.

AFSD Plastic Strain

During AFSD, the deposited material undergoes severe plastic strain in the stir zone. While experimentally quantifying exact levels of plastic strain during the AFSD process would be challenging, secondary effects of severe plastic deformation such as significant grain refinement [64], [68], [212], [261] and breakup of particles [67], [68] and oxide films [262] were observed in previous AFSD studies. One computational study by Stubblefield et al. found a peak value of 571 for effective plastic strain [260].

AFSD Strain Rate

The actuator feed rate, tool rotational velocity, tool traverse velocity, and layer height determine the speed of material flow out of and under the tool. The material can flow faster as it leaves the center of the tool due to the increase of tangential velocity. An estimation of strain rate can be formulated using basic mechanics within the stir zone. Assuming the stir zone directly underneath the tool is a cylinder with the same diameter as the tool (38.1 mm) and a height the same distance from the tool to the substrate (1.5 mm). Given tool rotational velocity of 300 rpm (31.42 rad/s) and assuming that no slipping occurs between the tool and deposition, an estimate of effective strain rate can be formulated from shear strain rate as seen in Eq. 1.

$$\dot{\bar{\epsilon}} = \frac{\dot{\gamma}}{\sqrt{3}} = \frac{r\dot{\theta}}{l\sqrt{3}} = \frac{\left(\frac{1}{2}38.1mm\right)\left(31.42\frac{rad}{s}\right)}{(1.5mm)\sqrt{3}} = 230.38s^{-1} \qquad 5.12.1$$

$\dot{\bar{\epsilon}}$ is effective strain rate, $\dot{\gamma}$ is shear strain rate, r is tool radius, $\dot{\theta}$ is rotational velocity, and l is distance from the tool to the substrate. At the tool center, $r = 0$, the effective strain rate would be zero. Although slip would occur during the actual AFSD process, and the material would also experience strain flowing outward, the estimate shows the wide range of strain rates possible in AFSD.

AFSD Temperature

One of the most important factors of AFSD processing is frictional heat generation. As the tool spins against the deposited material, this generates significant frictional heat, enough to soften the material to initiate flow. Stir zone temperatures in the AFSD process have been measured experimentally, with Garcia et al showing 50-90% melting temperature based on a range of process parameters [63]. Similarly, Phillips et al reported 93% of the melting temperature based on precipitation transformation [65]. Additionally, Stubblefield et al showed in simulated stir zone that temperatures can exceed the melting temperature, which was confirmed with experimental observations of partially melted layers during deposition [260].

5.12.2 Materials and Methods

Constitutive Models

Johnson-Cook (JC)

JC is a constitutive model that was originally designed for ballistics-rate impact simulations and is provided in Eqs. 5.12.(2-4) [162], [263].

$$\sigma = [A + B\epsilon^n][1 + Cln(\dot{\epsilon^*})][1 - T^{*m}] \quad 5.12.2$$

$$\dot{\epsilon^*} = \frac{\dot{\epsilon}}{\dot{\epsilon_0}} \quad 5.12.3$$

$$T^* = \frac{T - T_{room}}{T_{melt} - T_{room}} \quad 5.12.4$$

Due to its ease of calibration and implementation, JC has been applied in a variety of studies, including FSW [77], [252], [264], [265]. A is the yield stress of the material. $\dot{\epsilon_0}$ is the reference strain rate, usually taken to be quasi-static strain rate. T_{melt} and T_{room} are the solidus temperature of the material and the room temperature, respectively. Matlab curvefitting software was used to calibrate JC for this study.

Fraser-Kiss-St-Georges (FKS)

FKS is an empirical model based on a series of Gleeble tests for AA6061-T6. The model was specifically created for FSW [93]. The equations for FKS are listed in Eqs. 5.12.(5-9).

$$\sigma(\epsilon^p, \dot{\epsilon}, T^*) = H(\epsilon^p)\Lambda(\dot{\epsilon}, T^*)\Theta(T^*) \quad 5.12.5$$

$$H(\epsilon^p) = a_1 + a_2 \tan^{-1}(a_3\epsilon^p) \quad 5.12.6$$

$$\Lambda(\dot{\epsilon}, T^*) = 1 + [b_1 T^{*b_2}]\left[b_3 \ln\left(\frac{\dot{\epsilon}}{\dot{\epsilon}_0}\right)\right] \quad 5.12.7$$

$$\Theta(T^*) = 1 - \frac{1}{(1 + e^{-c_1 T^*})^{\frac{1}{c_2}}} \quad 5.12.8$$

$$T^* = \frac{T - T_{room}}{T_{melt} - T_{room}} \quad 5.12.9$$

One major difference between JC and FKS is with the hardening portion: JC assumes a power law while FKS assumes an arctan law. The difference is magnified after severe plastic strain, where the effective stress in JC continues hardening and in FKS the effective stress saturates. Another major difference is the thermal softening behavior: JC assumes exponential decay while FKS assumes sigmoid decay. FKS also assumes that the material is strain rate independent at room

temperature, which is not a valid assumption for most materials, but it is valid for AA6061 and was employed by Stubblefield et al for AFSD simulations [260].

Sellars-Tegart (ST)

The ST model [266], modified by Sheppard and Wright [267], [268], has been used for a variety of high-temperature, high-strain applications such as FSW [259], [269], [270], Friction Stir Processing [271]–[275], and high-temperature deformation [276]–[281]. The ST equations are shown in Eqs. 5.12.(10-11).

$$\sigma = \frac{1}{\alpha}\sinh^{-1}\left[\left(\frac{Z}{A}\right)^{\frac{1}{n}}\right] \quad 5.12.10$$

$$Z = \dot{\epsilon}\exp\left(\frac{Q}{RT}\right) \quad 5.12.11$$

The inverse hyperbolic sine law accounts for effective stress saturation after severe plastic strain. One major benefit of using ST is the relation of Z to microstructural evolution [259], [280]–[283]. Calibrating ST is not as simple as calibrating JC or FKS, but it is still formulaic. The calibration process is outlined in Shi et al 2013 [278]. However, according to Shi et al, this process only works if the model parameters are constants and not functions of other variables such as temperature and strain rate [278]. For AA6061, both T6 and O tempers had this issue, so the usual calibration process was abandoned. Matlab curvefitting software was used instead. To the authors' best knowledge, ST has not been used for AFSD simulations.

Torsion Experiments

The constitutive models were calibrated using experimentally obtained torsion stress-strain curves. SMT001 Gleeble torsion samples shown in Figure 5.92 were manufactured from 15 mm diameter AA6061-T6 extruded rods. Half of the AA6061-T6 samples were heat treated to O temper using a standard procedure [284]. A Gleeble 3500 thermomechanical simulator was used to test both the AA6061-T6 and AA6061-O torsion samples at identical temperatures and strain rates. Both T6 and O tempers were tested to demonstrate the flexibility of each constitutive model for capturing different behaviors within the same alloy. The tests were conducted at temperatures varying from 25-500 °C and strain rates varying from 0.04-10 s^{-1}. The lower end of 0.04 s^{-1} for strain rate was based on the minimum rotational speed of the torsional motor. Only one test was conducted at room temperature per temper since AA6061 is strain rate insensitive at room temperature [93], [285], [286]. The room temperature tests were conducted at 0.1 s^{-1} as opposed to 0.04 s^{-1}. The mechanical testing data was converted to effective stress and strain using the Fields and Backofen method [287], because AA6061 is sensitive to temperature and strain rate at elevated temperature.

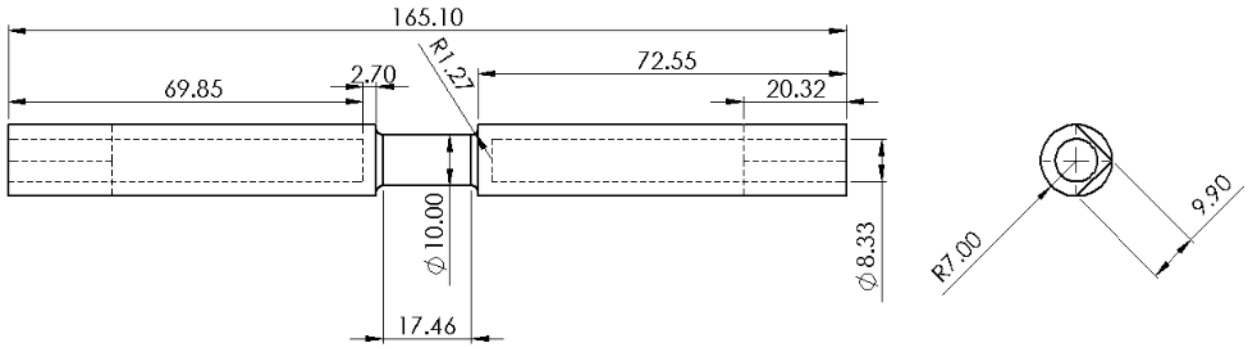

Figure 5.92 SMT001 Gleeble torsion samples used for constitutive model calibration. All dimensions are in millimeters.

AFSD Simulations

To test each constitutive model, AFSD simulations using the SPH framework were conducted. A visual description of the SPH model used in this constitutive model study is shown in Figure 5.93. The model was comprised of a rigid finite element base and tool, and deformable SPH feedstock and substrate. All finite elements were three-node triangular elements of zero thickness. The base was fixed in space, while the tool rotates, advances, and pushes the feedstock down. The tool diameter was 38.1 mm and was set 1.5 mm above the substrate, where the substrate was 76.2 x 152.4 x 6.35 mm^3, and the feedstock was 9.53 x 9.53 x 110 mm^3. The SPH material points were initially set 1 mm apart, and the nodes in the elements were meshed 1 mm apart. To demonstrate constitutive model flexibility, the feedstock had O temper properties and the substrate had T6 temper properties.

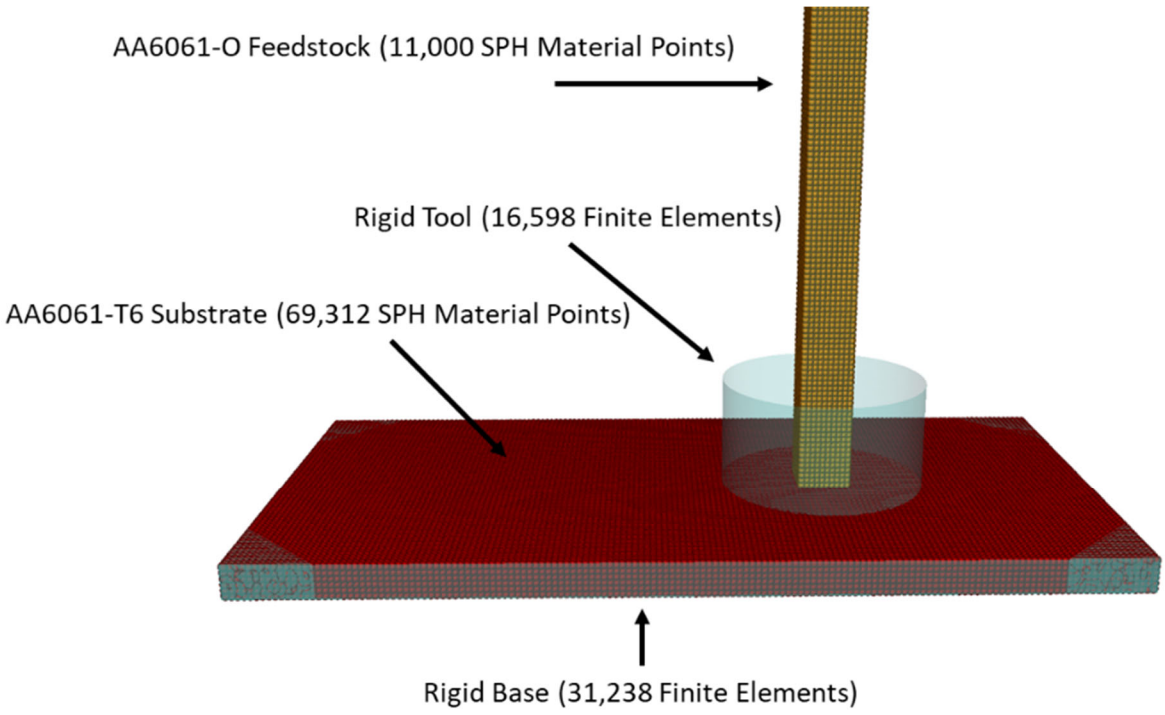

Figure 5.93 AFSD model used in this study. Smoothed particle hydrodynamic material points modeled the feedstock and substrate, and finite elements modeled the tool and base.

The constitutive models were evaluated in a zone shown in Figure 5.94. The 50 x 50 x 3 mm^3 analysis zone was centered around the tool axis horizontally and the top of the substrate vertically. The bottom of the zone was 1.5 mm below the surface of the substrate and the top of the zone 1.5 mm above the surface of the substrate.

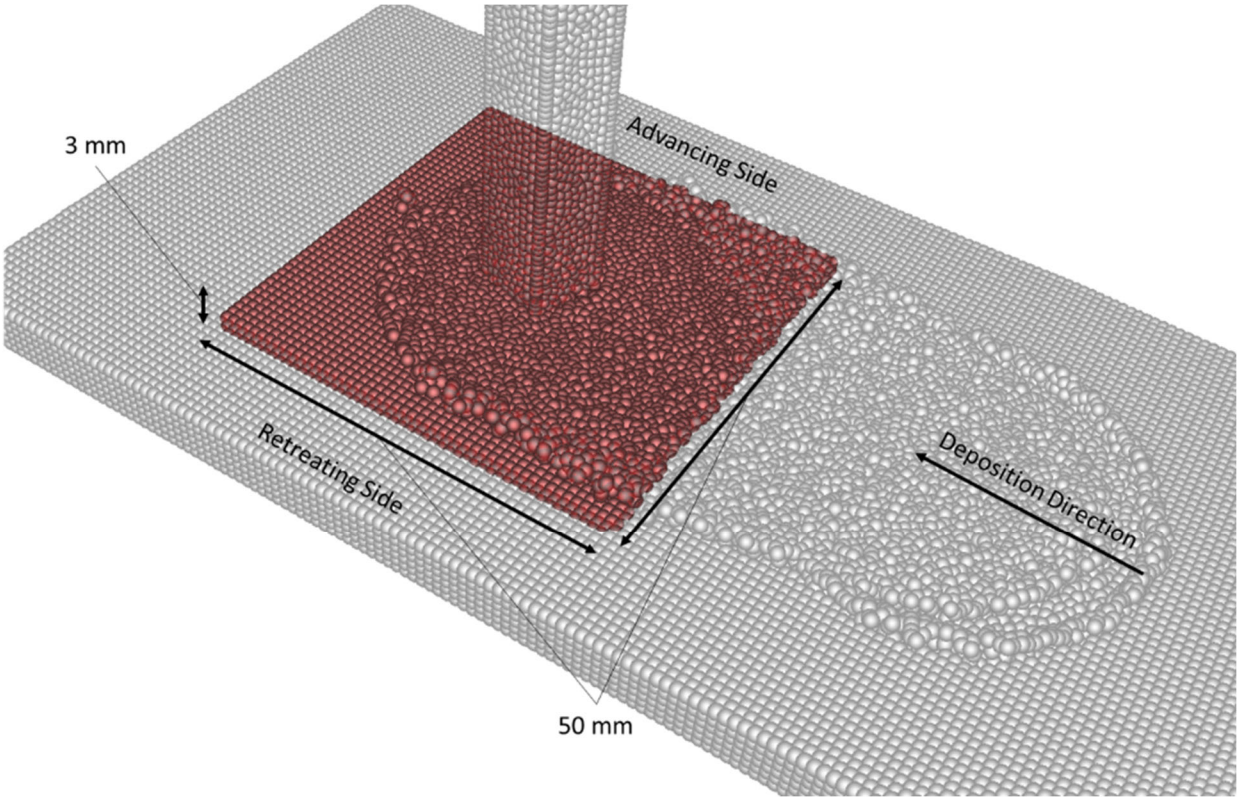

Figure 5.94 Analysis zone in the SPH simulations used to highlight the effects different constitutive models have on the simulation environment.

5.12.3 Results and Discussion

Constitutive Model Behavior

Effective Stress vs Effective Plastic Strain

The plastic portions of the stress-strain curves from the experimental data were isolated using the 0.2% offset method. The constitutive models compared with experimental data for AA6061-T6 are plotted in Figure 5.95. The strain to failure varied based on temperature and slightly based on strain rate. The 500 °C tests did not fail after two rotations. AA6061-T6 experienced little strain hardening before effective stress saturation, with increasing temperature shortening the strain hardening period as well as decreasing the effective stress. Although both JC and FKS can account for strain hardening, both curve fits exhibit perfectly plastic behavior due to the limited strain hardening observed experimentally. The FKS model was the most accurate at capturing the temperature and strain rate-sensitive behavior of AA6061-T6. However, the thermal softening function of JC was unable to capture the temperature sensitivity as well as the FKS model. The ST model had the least accurate fit of the three models; however, ST may be more suitable for other

materials.

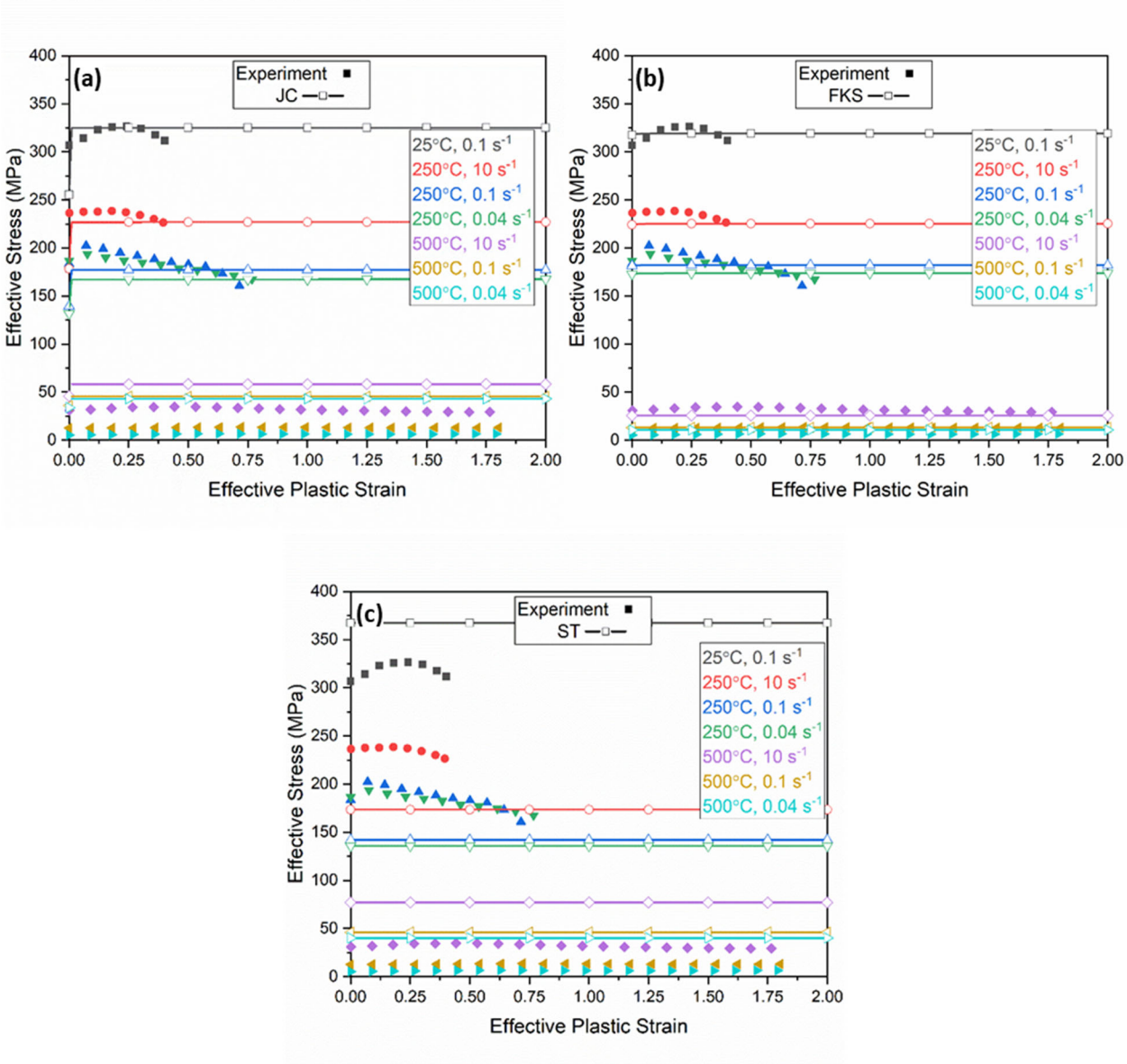

Figure 5.95 Experimental effective stress and strain curves for AA6061-T6 vs constitutive models: (a) JC (b) FKS and (c) ST. FKS was the most accurate for AA6061-T6.

The constitutive models compared with experimental data for AA6061-O are plotted in Figure 5.96. With the exception of the room temperature test, none of the AA6061-O torsion tests failed after two rotations. Like AA6061-T6, the high temperature AA6061-O curves did not experience much strain hardening, but unlike AA6061-T6, AA6061-O did experience significant strain hardening at room temperature and 250 °C. The overall stress response for the O temper was much lower than the T6 temper due to the lack of strengthening precipitates. The FKS and JC models capture the strain hardening trend well for AA6061-O. Since the ST model assumes perfect plasticity, the ST captures higher temperature data better than lower temperature data due to the lack of strain hardening at high temperature.

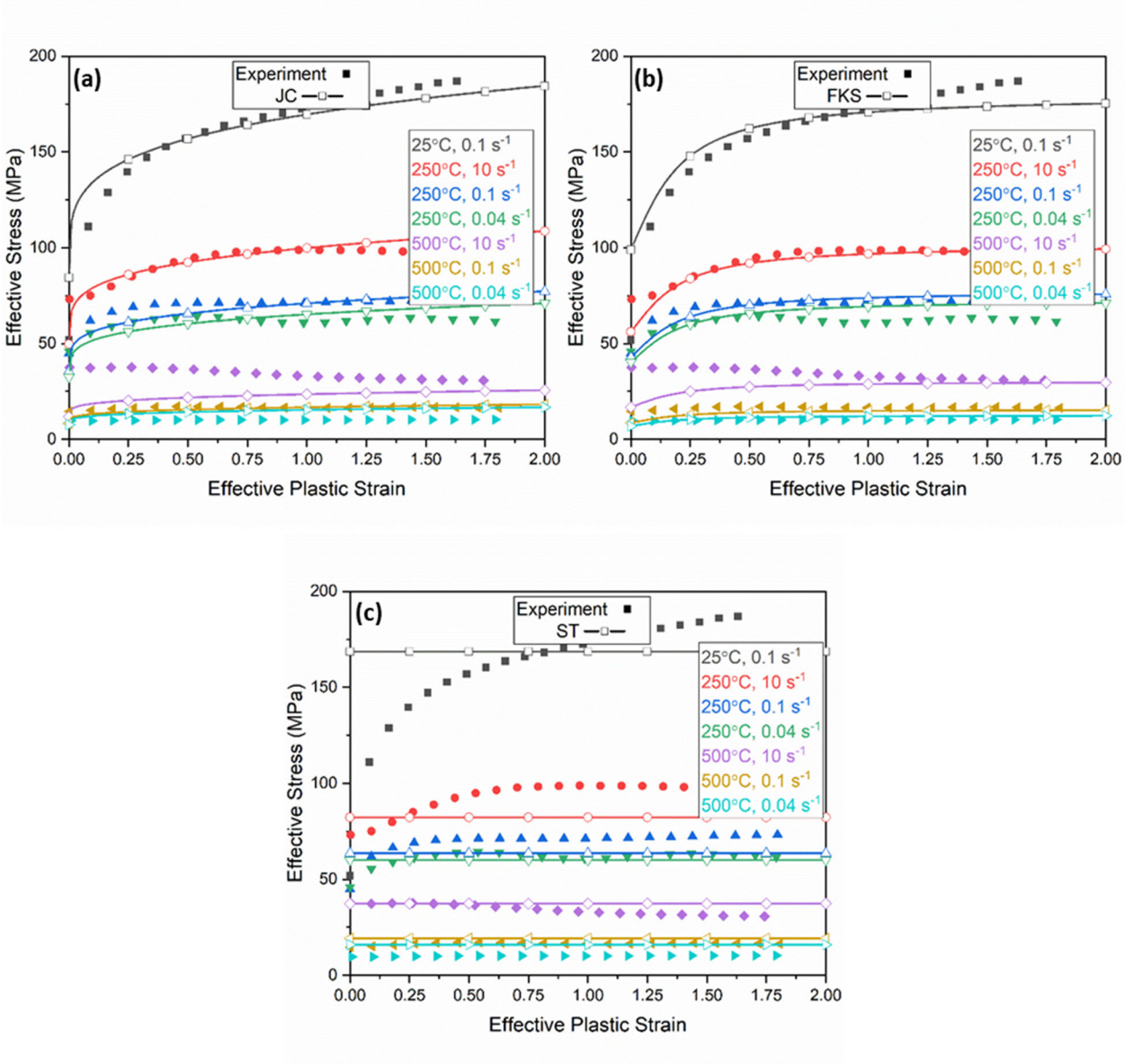

Figure 5.96 Experimental effective stress strain curves for AA6061-O vs compared models: (a) JC (b) FKS and (c) ST. FKS and JC captured the trend of AA6061-O stress-strain behavior.

For JC model fit of the O temper, the n constant had to be lowered from 0.23 to 0.001 due to excessive strain hardening after high plastic strain as shown in Figure 5.97. Note that a log scale was used for plastic strain to show strain hardening behavior at both low and high plastic strains. A temperature of 500 °C and strain rate of 10 s^{-1} was used for the models. Lowering the strain hardening parameter n in JC to 0.001 resulted in a higher jump at low effective plastic strain, but past an effective plastic strain of 1, the $JC_{0.23}$ model significantly overshot the $JC_{0.001}$ model. Considering the level of plastic strain experienced in a previous AFSD simulation study [260], JC model calibrated to low plastic strain data would result in significantly higher levels of stress than other constitutive models or a JC model calibrated with high plastic strain. It is important to note that the maximum level of plastic strain captured in the experiments was only 1.8. When large levels of plastic strain are expected in simulations, such as in AFSD, it is important to recognize

the strain limitations of mechanical testing and account for material behavior outside of the experimental limits. The stress in the FKS model saturates after high plastic strain because arctan asymptotically approaches π/2 as the argument goes to infinity. In contrast, the ST model is constant because of the perfect plasticity assumption. Additionally, both $JC_{0.001}$ and $JC_{0.23}$ models for the O temper are included because these models will be used in the constitutive model comparison analysis of this study. Furthermore, the T6 temper will only use one JC model since the calibration process produced an acceptable n value due to the limited strain hardening.

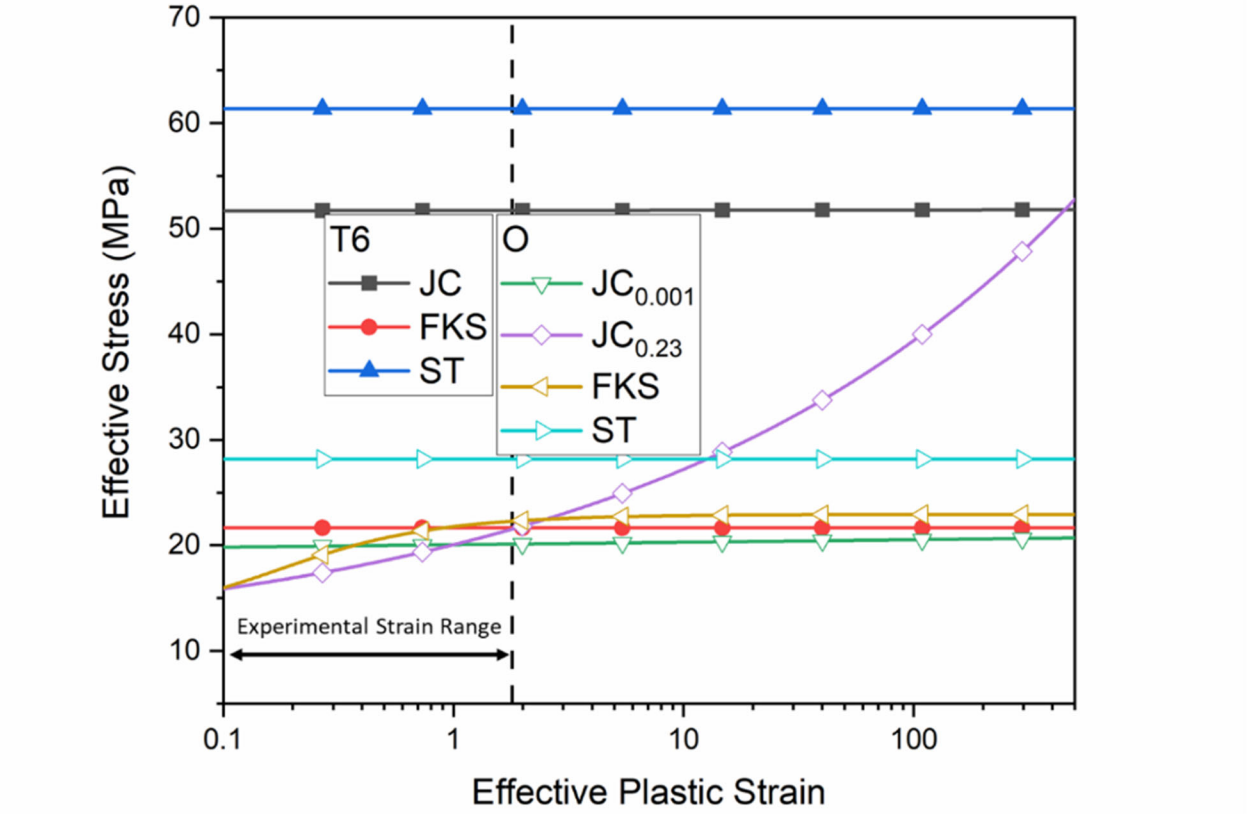

Figure 5.97 Comparison between the constitutive models shows the importance of accounting for high plastic strain behavior when curve fitting.

The average effective stress differences between the experiments and the constitutive models are shown in Figure 5.98. For the effective stress difference calculations, the absolute value of effective stress difference was taken at each strain point before taking the average. Percent difference calculations were not used since the low magnitude of effective stresses at 500 °C skewed the calculations. The absolute value was used so that over-predicting and under-predicting effective stresses do not cancel out. For the T6 temper, the FKS model was significantly more accurate and consistent compared to the other two constitutive models. As with the T6 temper, the results for O temper show that the FKS model was the most accurate and consistent, followed by JC and ST. However, the differences in accuracy and consistency between the constitutive models are much smaller for the O temper than with the T6 temper. The increase in accuracy and consistency with the O temper models was a consequence of the overall lower stresses relative to the T6 temper experimental results. The two different JC models for O temper were very similar when compared with experimental results.

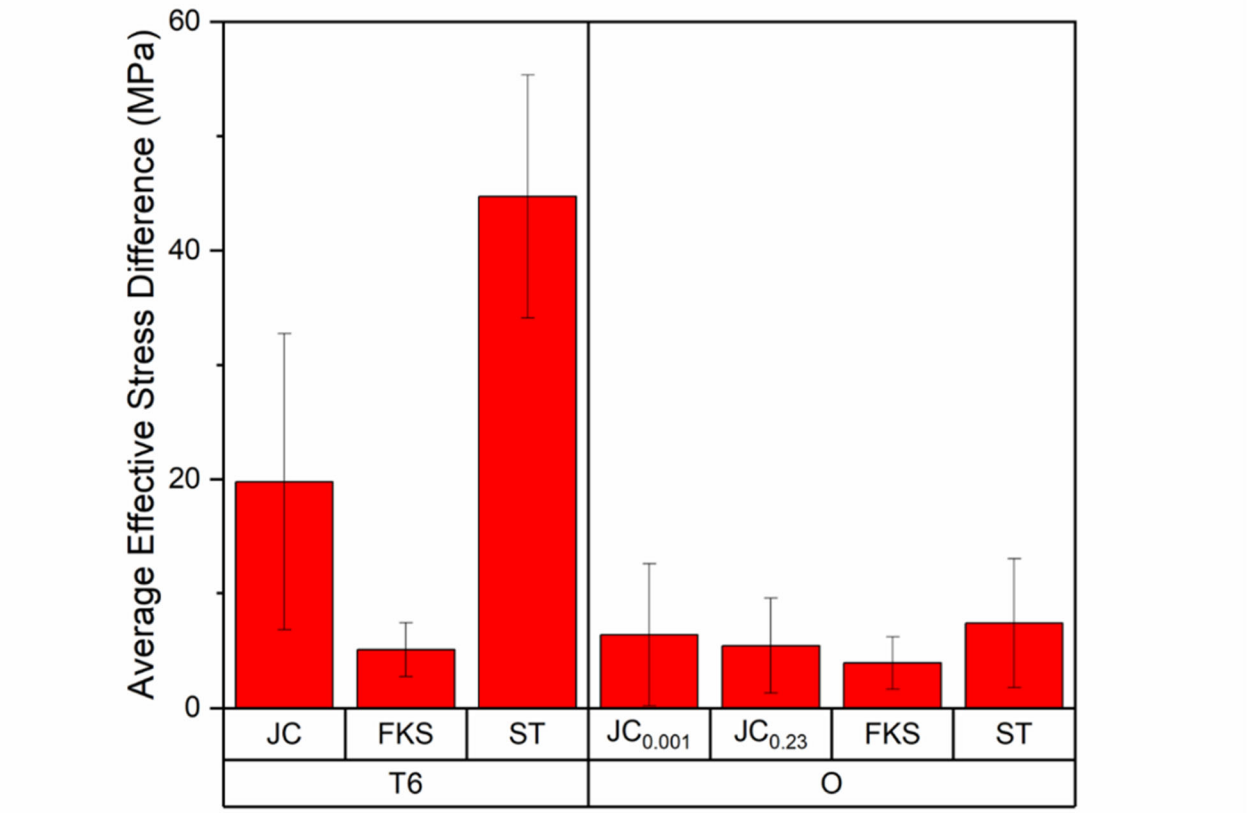

Figure 5.98 Average effective stress differences for each constitutive model and temper compared with experimental data show the relative accuracy of FKS vs JC and ST.

Yield Strength vs Temperature

While the constitutive models were calibrated against stress-strain curves, it is important to consider stress-temperature curves when analyzing constitutive models. The yield stress-temperature behavior for each model is shown in Figure 5.99. The T6 constitutive models were used to show the temperature behavior, where the plastic strain was set to 0, and the strain rate was set at 0.1 s^{-1} for each model. Experimental data from Allen [288] for AA6061-T651 are also included to show the sigmoid behavior of yield strength evolution with respect to temperature. The FKS model was well suited for fitting the sigmoid temperature behavior, which helps understand why it fit the experimental results better than the other constitutive models evaluated in this present study. Additionally, the exponential decay trends of JC and ST do not capture the yield strength evolution with respect to temperature for AA6061-T6, but perhaps JC and ST are good fits for other materials.

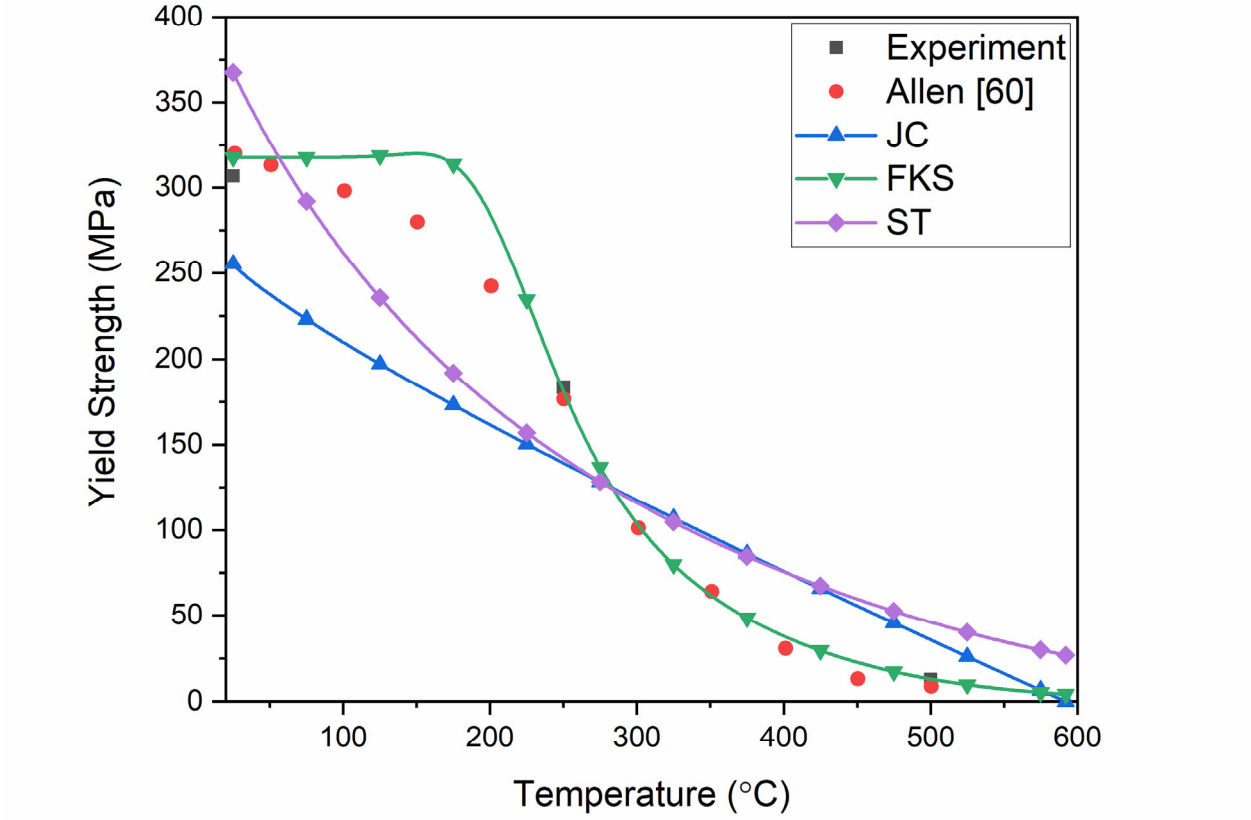

Figure 5.99 Constitutive model yield strength evolution with temperature highlights different behaviors with each model.

Yield Strength vs Strain Rate

In addition to stress-temperature curves, stress-strain rate curves are also important for analyzing constitutive model fidelity. The strain rate behavior for each model is shown in Figure 5.100. The T6 constitutive models were used to show the strain rate behavior. The plastic strain was set to 0, and the temperature was set at 500 °C for each model. Based on the results shown in Figure 5.100, all three constitutive models show a linear yield strength increase with the log increase of strain rate. The log behavior of yield strength evolution with respect to strain rate is a reasonable assumption given the torsion experimental data for AA6061. The discrepancy in values is due to the curve fitting seeking an average fit over all data points.

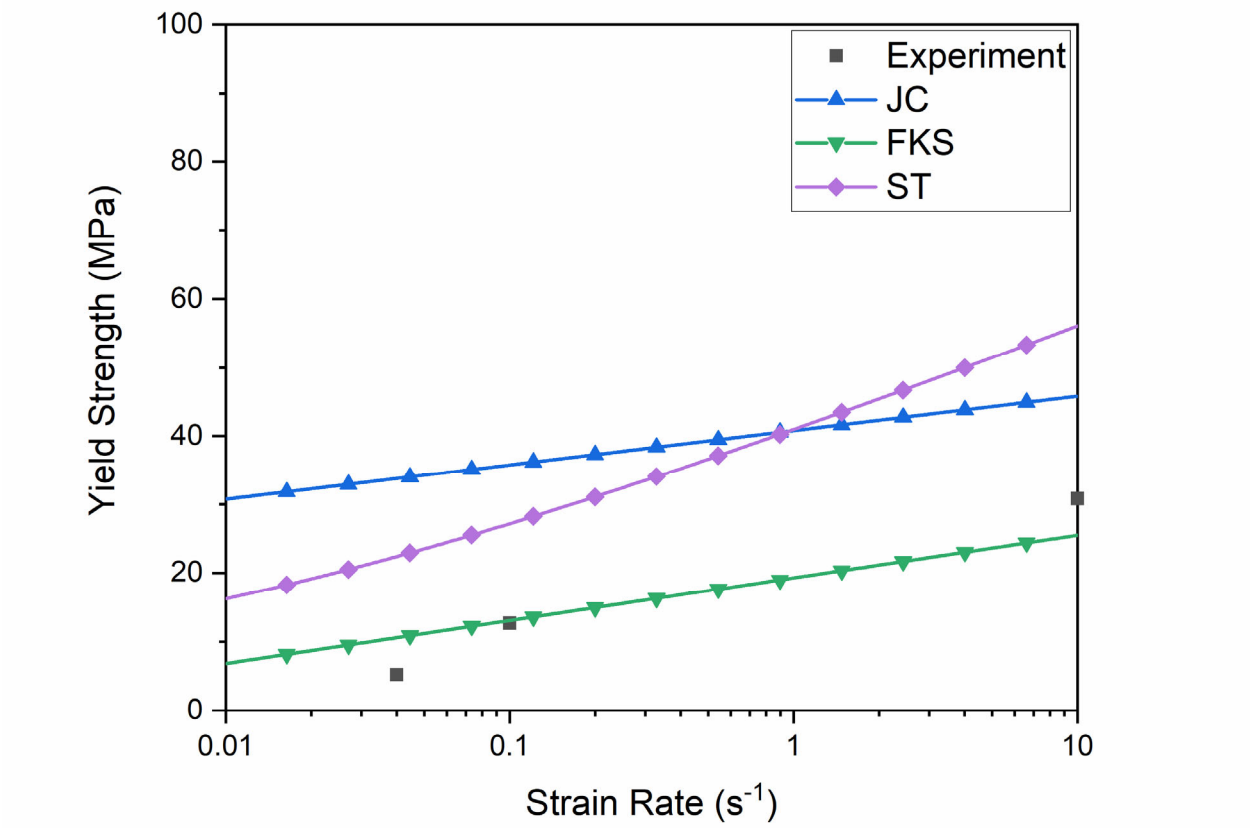

Figure 5.100 Constitutive model yield strength evolution with strain rate shows similar behaviors with each model.

AFSD Simulations

Peak Values

The average of five peak values in temperature, effective stress, and effective plastic strain are shown in Figure 5.101. It is important to note that showing the peak value at one particular timestep is not a good representative of simulations; peak values can change drastically after each timestep and the peak values may be outliers. To remedy this, the top five simulation peak values were averaged and plotted during the deposition phase for each constitutive model. The error bars represent one standard deviation in either direction. The peak values tended to level out as the simulation progressed, suggesting a transition from transient to steady state. Overall, FKS had the smallest ranges between the five peaks. FKS also had the lowest temperatures in Figure 5.101a and stresses in Figure 5.101b because of the sigmoid thermal softening behavior facilitating a rapid decrease in material strength. The $JC_{0.23}$ model exhibited the largest ranges between the five peaks in each category. The $JC_{0.23}$ model had the highest peak temperature in Figure 5.101a because of the significantly higher strain hardening compared to $JC_{0.001}$ and FKS models. ST had the second highest peak temperature in Figure 5.101a because the curve fitting in Figure 5.95c and Figure 5.96c, when attempting an average fit across all temperatures and strain rates, over-predicted high temperature stress for both tempers. Although the $JC_{0.23}$ simulation had the highest plastic strain in Figure 5.101c, those values appear to be outliers when compared to the lower peak values.

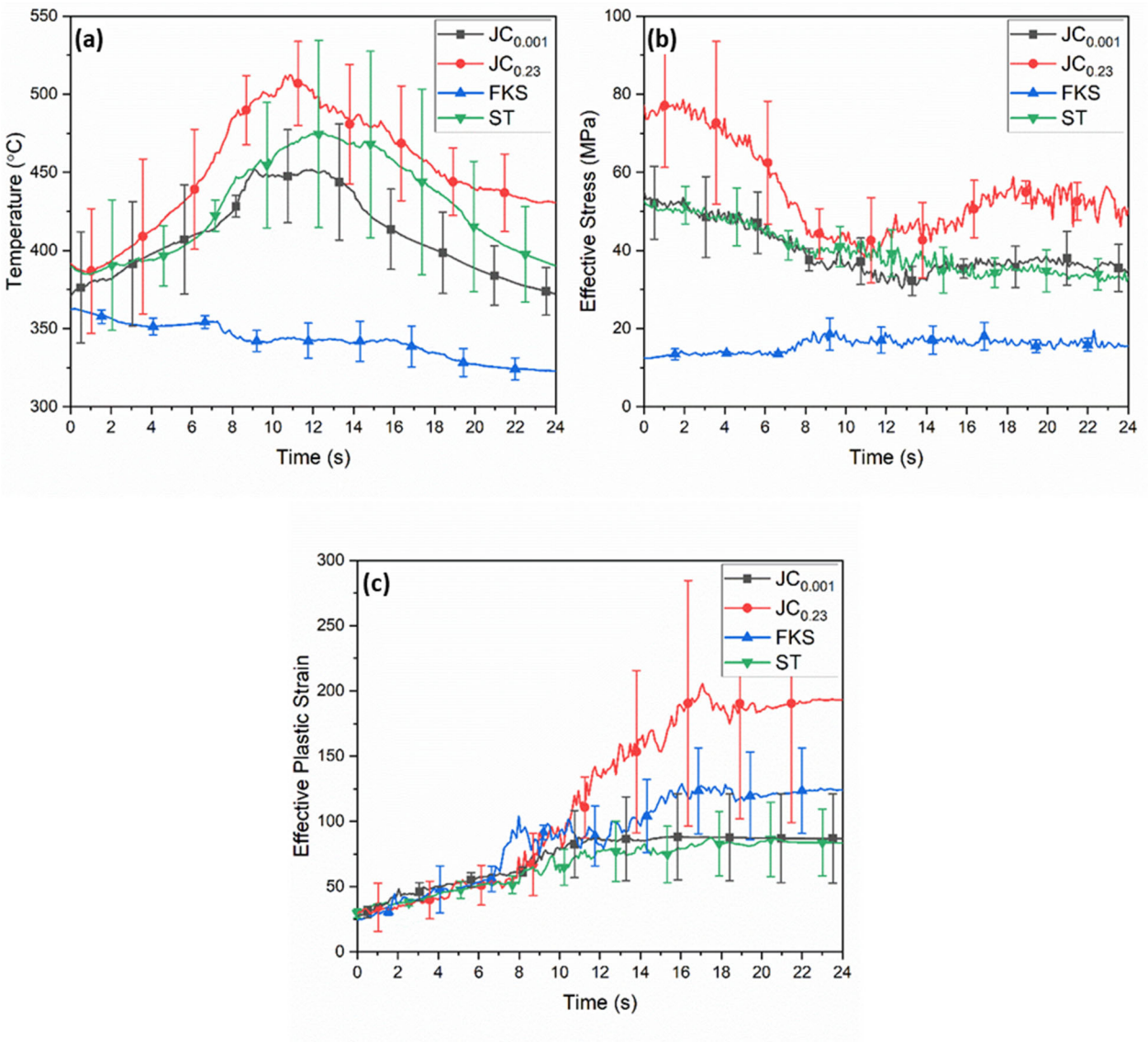

Figure 5.101 SPH simulation results of average peak (a) temperature, (b) effective stress, and (c) effective plastic strain values for each constitutive model show consistency of each constitutive model and provide a better comparison than single peak values.

Temperature Contours

The temperature contour plots taken within the analysis zone for each constitutive model are shown in Figure 5.102b. The temperature limits were determined from the minimum and maximum temperatures seen within the analysis zone across all simulations. The $JC_{0.23}$ simulation experienced the highest temperatures, followed by ST, $JC_{0.001}$, and then FKS models. The difference between $JC_{0.001}$ and $JC_{0.23}$ models highlights the effect changing the strain hardening constant n has on simulations. The excessive strain hardening of $JC_{0.23}$ model requires higher temperatures to soften the material for flow. Additionally, it is observed in Figure 5.102b that $JC_{0.23}$ and ST models behaved similarly, despite $JC_{0.23}$ model predicting excessive strain hardening and ST model predicting no strain hardening. In this study, the ST model curve fit in Figure 5.95c

and Figure 5.96c overpredicted high temperature effective stress for both T6 and O tempers. While the $JC_{0.23}$ model curvefit predicted lower effective stress than ST within the experimental plastic strain limits, the excessive strain hardening behavior combined with severe plastic strain inherent to AFSD resulted in the $JC_{0.23}$ model eventually reaching similar levels of effective stress as the ST model. All constitutive models experienced a ring of hotter material within the stir zone, which corresponds to the outer edge of the AFSD tool. The transverse velocity of the tool is highest on the outer edge, which translates into more friction and higher temperature. This phenomenon was captured by Stubblefield et al. [260] as well.

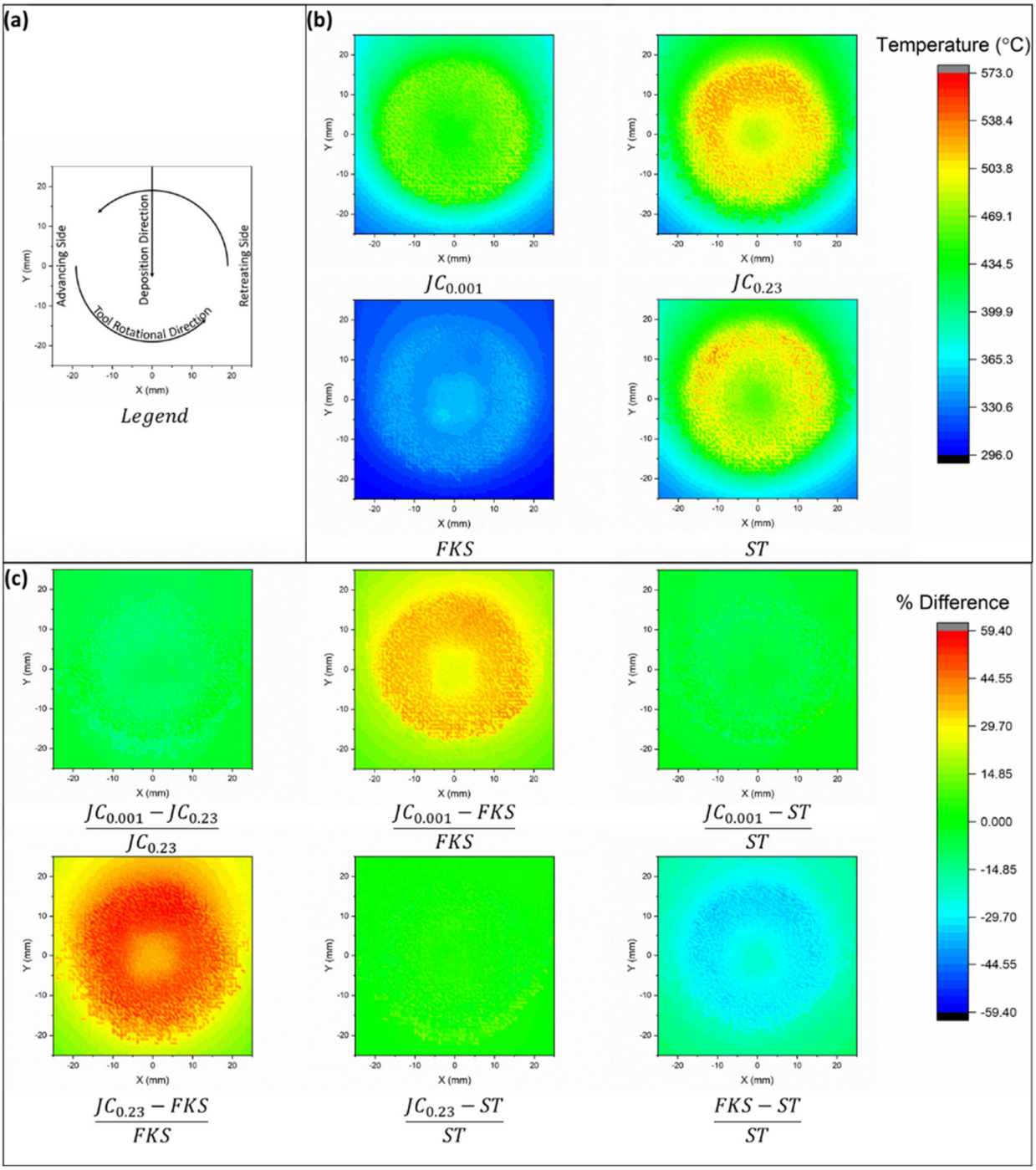

Figure 5.102 (a) Legend of analysis zone. (b) Temperature contour plots for each constitutive model emphasize the unique thermal softening behavior of FKS. (c) Temperature percent difference contour plots for comparisons between each constitutive model show the drastic difference between FKS and the other constitutive models.

The percent difference limits were chosen based on the largest value measured, which was then set as both extremes so that 0% was in the middle of the color scale (green), as shown in Figure 5.102c. The starkest contrasts were observed in all of the comparisons involving the FKS model,

which was a consequence of the sigmoid thermal softening behavior seen in Figure 5.99 resulting in a lower temperature requirement to induce material flow. The significantly lower temperatures of the FKS model in Figure 5.102b obscured the differences between the other constitutive models in Figure 5.102c. Beyond the stir zone, the temperatures experienced by the constitutive models were similar, suggesting that the temperature differences are localized within the stir zone.

Stress Contours

The effective stress (von Mises) contour plots taken within the analysis zone for each constitutive models are shown in Figure 5.103b. The effective stress limits were determined from the minimum and maximum effective stresses seen within the analysis zone across all simulations. For each simulation, the peak stresses were experienced just ahead of the stir zone where no material has been deposited yet. During the AFSD process, the substrates must be clamped down to prevent movement from considerable forces the spinning tool exerts on the deposition and substrate. However, since the peak temperatures are mostly localized in the stir zone, the high stresses ahead of the stir zone are yet to be relaxed. As such, the $JC_{0.001}$ model, and not $JC_{0.23}$ model, experienced the highest stresses ahead of the stir zone, since the T6 calibrated JC model is the same for both $JC_{0.001}$ and $JC_{0.23}$, which means the substrate material properties are identical between the two simulations. Given the hotter temperatures within $JC_{0.23}$ model and a larger temperature front seen in Figure 5.102b, the cooler temperatures in the $JC_{0.001}$ simulation mean that the substrate can support a higher stress than the $JC_{0.23}$ simulation in Figure 5.103b. The similar temperatures between $JC_{0.23}$ and ST models seen in Figure 5.102b correlate to similar stresses in Figure 5.103b. Although ST model predicts no strain hardening, and $JC_{0.23}$ model predicts significant strain hardening, the two constitutive models behave similarly for similar the levels of strain, strain rate, and temperature seen in the stir zone. The rings of high temperature in Figure 5.102b in the stir zone also correspond to regions of low stress in the stir zone in Figure 5.103b.

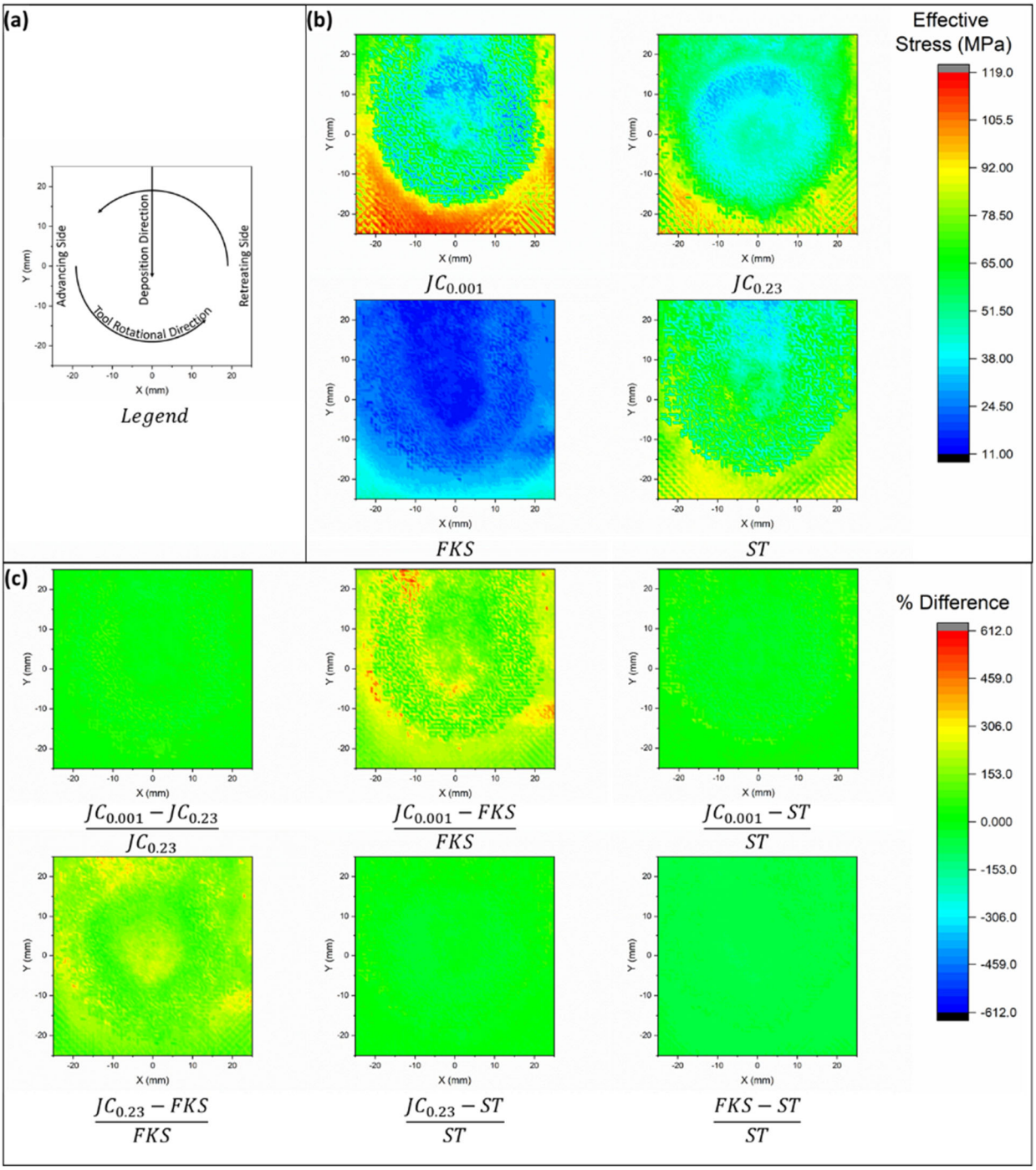

Figure 5.103 (a) Legend of analysis zone. (b) Effective stress contour plots for each constitutive model show the low stresses required to induce flow in the FKS simulation. (c) Effective stress percent difference contour plots for comparisons between each constitutive model show the large differences between FKS and the other constitutive models.

The percent difference limits in Figure 5.103c were chosen based on the largest value measured, which was then set as both extremes so that 0% was in the middle of the color scale (green). The largest differences in Figure 5.103c were experienced when comparing both $JC_{0.001}$ and $JC_{0.23}$ to

FKS in the center of the stir zone and just beyond the stir zone radius. The difference in the stir zone and the deposition just behind the stir zone correlates with the sigmoid thermal softening behavior of FKS model relative to $JC_{0.001}$ and $JC_{0.23}$ models. In addition, as shown in Figure 5.103c, both JC models had similar effective stress contours. Although there was a difference between FKS and ST models, that difference was marginal compared with the large differences between FKS and both JC models in Figure 5.103c.

Plastic Strain Contours

The effective plastic strain contour plots taken within the analysis zone for each constitutive model are shown in Figure 5.104b. The effective plastic strain limits were determined from the minimum and maximum effective plastic strains seen within the analysis zone across all simulations. $JC_{0.23}$ experienced the highest levels of effective plastic strain despite the stiff response predicted by the constitutive model. The high effective stress and effective plastic strain for the $JC_{0.23}$ simulation is likely a consequence of the relatively high minimum energy input for material flow resulting in softer regions more susceptible to plastic deformation. The substrates did not experience plastic strain ahead of the deposition, which explains the dark blue region ahead of the stir zone.

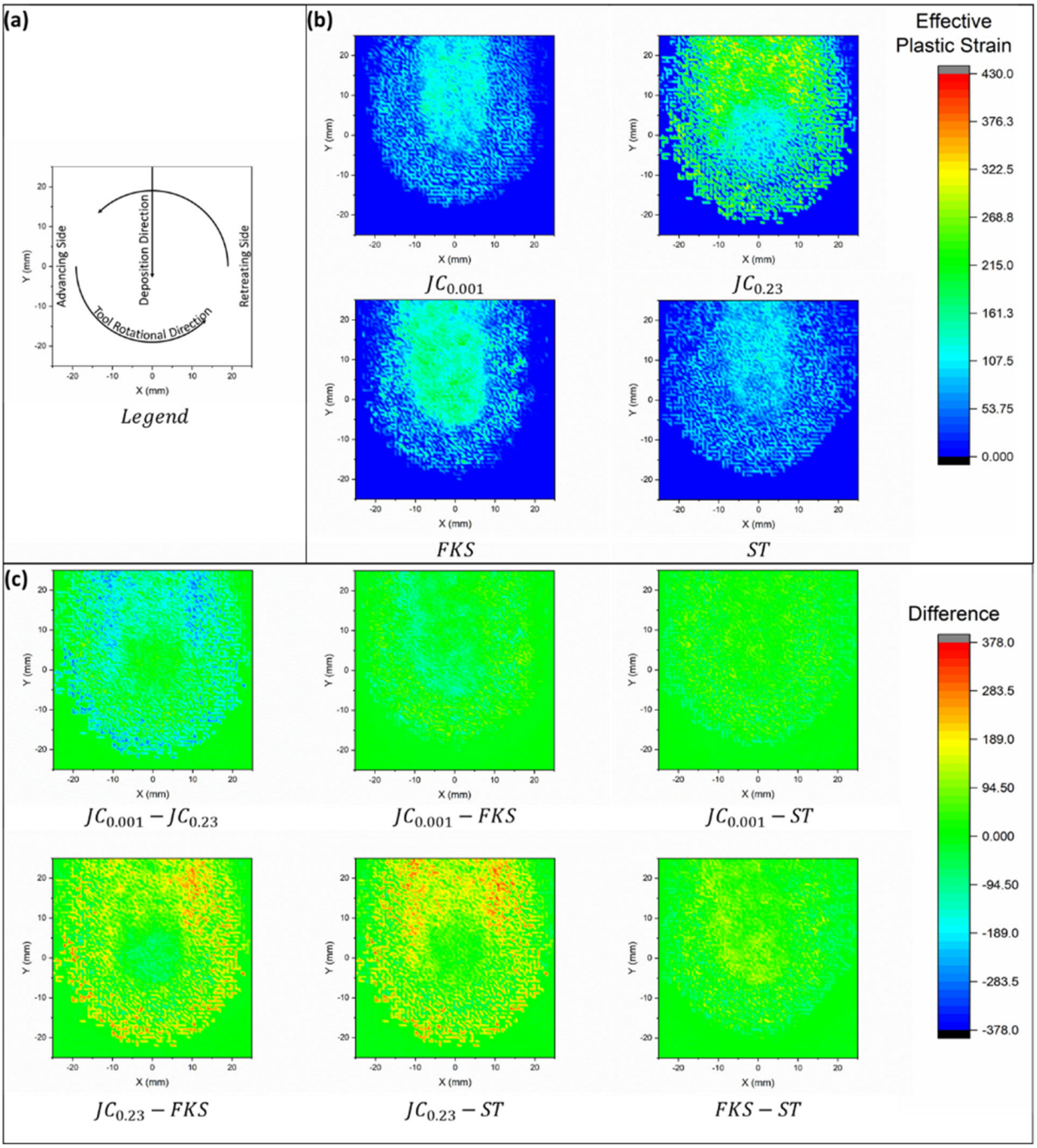

Figure 5.104 (a) Legend of analysis zone. (b) Effective plastic strain contour plots for each constitutive model show the relatively high plastic strains experienced in $JC_{0.23}$. (c) Effective plastic strain difference contour plots for comparisons between each constitutive model highlights the differences between $JC_{0.23}$ and the other constitutive models.

The effective plastic strain difference limits in Figure 5.104c were chosen based on the largest value measured, which was then set as both extremes so that 0 was in the middle of the color scale (green). Percent difference was not used because the near-zero values in the denominator of the percent difference formula resulted in extremely high values that obscured all other differences

between the simulations. For effective plastic strain, the largest differences were concentrated in the outer ring of the stir zone when compared with the $JC_{0.23}$ simulation. The other simulations had more similar plastic strain contours. The low level of strain hardening experienced by $JC_{0.001}$ model mimics the effective stress saturation experienced by FKS seen in Figure 5.95b and Figure 5.96b or perfect plasticity of ST models seen in Figure 5.95c and Figure 5.96c.

Build Profiles

The build profiles for each simulation are shown in Figure 5.105. All simulations had similar build profile appearances, with the exception of the $JC_{0.23}$ simulation seen in Figure 5.105b, which displayed a more jagged profile than the other simulations. Softer materials would flow more easily, which would result in a more uniform profile. In contrast, harder materials would not flow as easily, which would result in a less unform profile. Despite the differences between the models, the $JC_{0.001}$, FKS, and ST models in Figure 5.105a,c,d all displayed similar build profiles, indicating that processing environments, and by extension material properties, are not necessarily linked to output appearance. The crescent moon at the back of all the simulations in Figure 5.105 was a consequence of the tool pushing material out at the start of the deposition. As such, while this material is pushed out radially, the crescent moon at the front would have been deposited over and incorporated into the deposition.

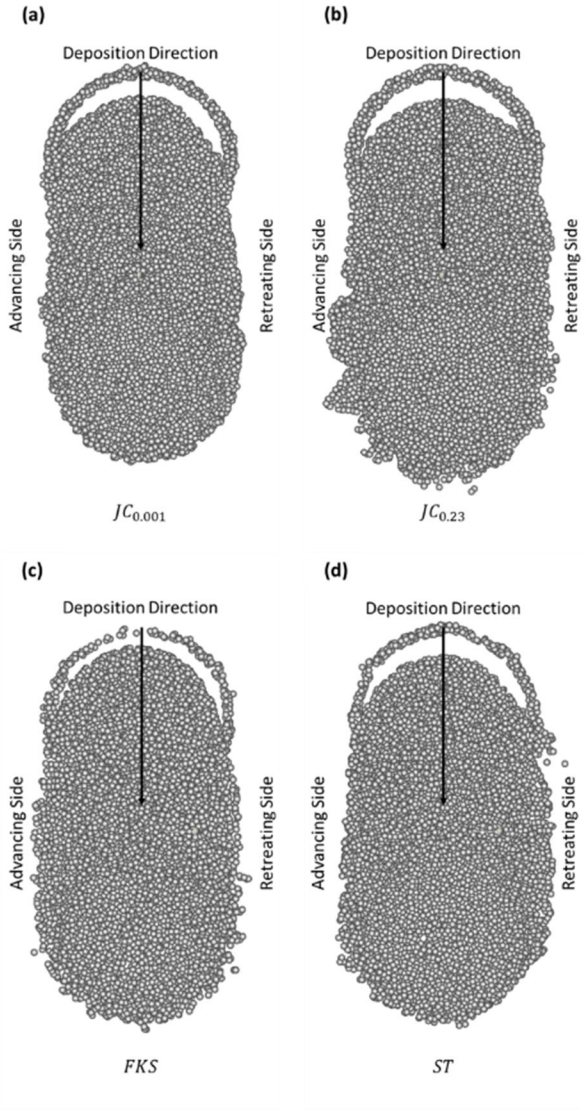

Figure 5.105 Build profiles for each constitutive model highlight differences between $JC_{0.23}$ and the other models. (a) $JC_{0.001}$ (b) $JC_{0.23}$ (c) FKS (d) ST. The similarity between $JC_{0.001}$, FKS, and ST indicates that changing processing temperature, effective stress, and effective plastic strain does not necessarily change output part appearance.

The ratio between the material deposited on the advancing side vs the retreating side for each constitutive model is shown in Table 5.12.5. The ratios were determined by summing the number of SPH material points on the advancing and retreating sides of the simulations. All simulations had a similarly balanced build profile, although the FKS simulation showed more advancing side bias than the other simulations. Although Stubblefield et al. [260] used AA6061-T6 feedstock calibrated with different experimental data, a similar bias towards the advancing side with the same processing parameters was observed. However, the softer properties of AA6061-O would result in a lower energy input threshold to induce flow than AA6061-T6. Future investigations should explore the effect different tempers have on the output build profile.

Table 5.12.5. Comparison of advancing-retreating side asymmetries between the constitutive models shows the balanced depositions of all constitutive models, except for a small advancing side bias for FKS.

Model	$JC_{0.001}$	$JC_{0.23}$	FKS	ST
AS	2423	2469	2451	2507
RS	2403	2461	2232	2423
AS/RS	1.01	1.00	1.10	1.03

Simulation Run Time

The total simulation run time for each constitutive model is shown in Table 5.12.6. The run times for each model were similar, indicating that simulation run time is not significantly dependent on constitutive model selected in this study. However, more sophisticated constitutive models may have an effect on simulation time compared to the models evaluated in this present study. For the SPH simulations, the largest bottleneck is not constitutive model calculation, but neighbor checking. In mesh-based methods, such as the finite element method, node neighbors are largely determined a priori based on mesh connectivity. However, in meshless methods involving severe plastic deformation, the SPH material points can travel great distances within the problem domain and change neighbors rapidly.

Table 5.12.6. Comparison of constitutive models displays lack of impact on simulation run time.

Model	$JC_{0.001}$	$JC_{0.23}$	FKS	ST
Run Time (hr:min)	29:45	29:11	30:24	29:06

5.12.4 Conclusion

In this work, a comparative analysis of constitutive models for AFSD was provided for the first time. Considering the severe plastic deformation as well as wide strain rates and temperatures inherent to the process, several candidate constitutive models were selected for this study. Descriptions of the constitutive models and calibration processes were provided and constitutive model temperature and strain rate behaviors were also shown. The constitutive models, including one intentionally low-fidelity model, were applied to single layer AFSD simulations. The particular constitutive model selection was found to have an significant effect on peak values, temperature contours, effective stress contours, and effective plastic strain contours. Regarding the FKS model, more consistent peak values in general relative to the other constitutive models was observed, while in contrast, the $JC_{0.23}$ had the most inconsistent peak values. While, the FKS model had the lowest temperatures and stresses, the $JC_{0.23}$ and ST models exhibited the highest temperature peaks in the stir zone. All constitutive models evaluated in this present study had similar peak stresses except for FKS model. In contrast, the $JC_{0.23}$ model had the highest peak plastic strain. With the temperature contour plots, all constitutive models experienced a ring of hotter material on the outer radius of the stir zone, corresponding to higher transverse tool velocity.

The FKS simulation also experienced the most different temperature contours than the other simulations, although all of the differences were localized within the stir zone. With the stress contour plots, the peak stresses for all constitutive models were experienced not in the stir zone, but just ahead of the deposition front because of the forces experienced during AFSD by the substrate. The rings of low stress correlated with the rings of high temperature. The FKS simulation was significantly softer than the $JC_{0.001}$ and the $JC_{0.23}$ simulations in the center of the stir zone and just outside the stir zone radius. The high minimum energy input for $JC_{0.23}$ model material flow was reflected in the plastic strain contours where, despite the overly stiff response predicted by the torsion stress strain curves, the $JC_{0.23}$ simulation experienced high plastic strain in softer regions caused by the high energy input in regions adjacent to the softer regions. In comparison with other models, the $JC_{0.23}$ simulation was the most different with respect to plastic strain, although the differences were isolated in the outer ring of the stir zone. Constitutive model selection was not found to have a significant effect on run time, although this present work was not intended to be a comprehensive study of all potential constitutive models, so other constitutive models may have a more significant effect on computational run time.

In summary, this present work is intended to aid future endeavors into AFSD simulations by evaluating potential constitutive models and the corresponding effects of such models have on the simulated AFSD processing environment. In particular, future investigations should explore alternate constitutive models such as internal state variable models [289], [290] and other feedstock materials [68], [212].

5.13 Computational and Experimental Study of Material Flow Behavior Prediction of External Particle Feedstock and Internal Particle Feedstock

In this study, a combined computational and experimental particle tracking investigation was performed for a solid-state additive manufacturing and repair process, Additive Friction Stir Deposition (AFSD). Specifically, smoothed particle hydrodynamics (SPH) simulations of AFSD were conducted in-order to elucidate deposition mechanics. The particle tracking of the SPH AFSD simulations was validated using experimental depositions of two feedstock varieties, including anodized AA6061-T6 feedstock to track external particles and AA6061-T6 copper wire core feedstock to track internal particles, to represent flow behavior from different regions of the feedstock. The X-Ray computed tomography (CT) experimental results revealed that the anodized oxides on the outside of the feedstock flowed to the retreating side, whereas the copper wire in the center of the feedstock migrated to the advancing side. Particle tracking results from the SPH simulations showed that, in general, particle movement is limited to directly beneath the feedstock. The rotational, radial, and traverse flow interactions visualized by AFSD simulations explained the advancing and retreating side biases experienced by the internal copper wire and surface oxides on the anodized feedstock. This work demonstrates the ability to predict AFSD material distributions, which has a significant impact on as-deposited material quality.

Non-fusion based additive manufacturing and repair techniques provide a complementary approach where melting of the feedstock is undesirable when lower heat inputs may be necessary to minimize residual stress and distortion in substrates and/or builds [1]–[3], or where a necessary microstructure may be required [4]–[6]. One solid-state technique gaining attention from the community, Additive Friction Stir Deposition (AFSD), depicted in Figure 5.106, is a nascent solid-state additive manufacturing and repair process, where the solid-state attribute refers to limiting processing temperature below the melting point, as opposed to fusion-based processes that exceed the melting point.

During the AFSD process, feedstock material is deposited through the square hole of a rotating tool onto a substrate or subsequent layers. The rotating tool generates frictional heat, which softens the feedstock material to facilitate material flow outwards while traveling forward to leave behind a plasticized layer of material. The rotating tool shoulder has been observed to break up surface oxides on the feedstock and substrate to create metallurgical bonds between the deposition and substrate [7]. Considerable research has been contributed towards AFSD in areas such as mechanical properties [8]–[15], machine learning [16], output microstructure [17]–[22], recycling material [23], repair capabilities [24], and processing temperature [25]. However, understanding material flow of deposited material, and especially of oxides, which may be difficult to remove from secondary feedstocks such as waste material in remote locations where the AFSD technique is gaining considerable interest for point-of-need manufacturing.

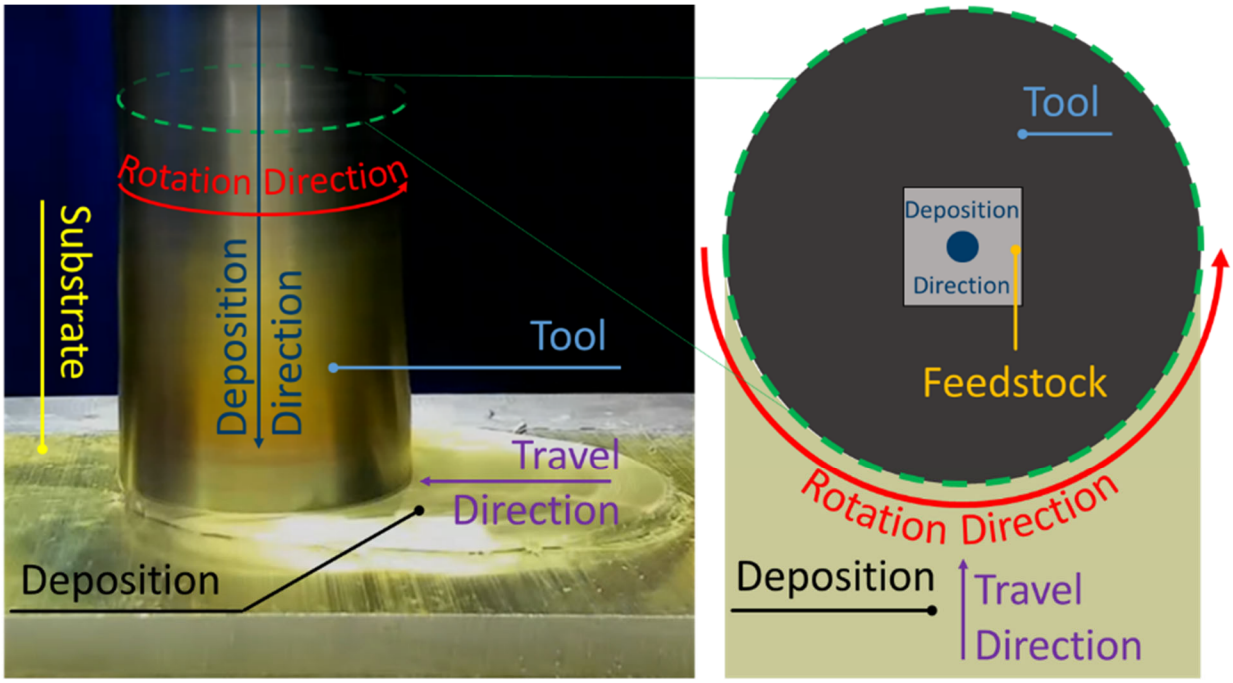

Figure 5.106 Description of AFSD process where a feedstock material is pushed through a spinning non-consumable tool onto a substrate.

It is well understood by the scientific community that metals can form surface oxides that must either be removed or broken up to facilitate metallurgical bonding [26]. Typically in FSW, the severe plastic deformation induced by the spinning tool breaks up the oxide films into smaller oxide particles, which are then trapped within the joined material [27]. However, poor processing parameters, which result in weak material flow, may fail to adequately break up the oxide film, resulting in kissing bonds or the lazy "s" feature [28]–[32]. These features may act as stress concentrations and crack nucleation sites within the FSW, which decrease fatigue performance [33], [34]. The oxide problem compounds when considering that oxide type defects are also difficult to detect without destructive testing [35]. Given the importance of oxide distribution in FSW plates, FSW tool manufacturers are particularly interested in oxide movement during FSW.

One solution to understanding the oxide problem in FSW is to utilize particle tracking simulations. Specifically, researchers have used particle tracking simulations in FSW to study material flow in the stir zone [36], [37]. FSW material flow behavior is beneficial to study, since the flow largely determines the finished weld bond strength, material homogeneity, weld asymmetry, and defect formation. One study by Fraser et al. used FSW simulations, validated by X-Ray computed tomography (XRCT), to identify wormhole defects in the stir zone of FSW [38]. Another study by Dialami et al. used FSW foil marker experiments in concert with simulations to visualize the lazy "s" feature formation in the weld nugget [39].

Given the deleterious effects oxides have on FSW parts, and the ability of particle tracking simulations to help understand the oxide problems, similar particle tracking of AFSD simulation studies need to be conducted to improve AFSD part quality. While most of the AFSD research to-date has focused on the materials science and mechanical performance side of AFSD, limited

studies have been carried out on the simulation of AFSD [40], [41]. The smoothed particle hydrodynamics (SPH) simulations previously developed by Stubblefield et al. [40], [41] provide the framework for particle tracking simulations. SPH is a prime candidate for particle tracking simulations, because SPH simulations naturally discretize the domain into smaller material points.

This study aims to explore AFSD particle tracking simulations to elucidate how feedstock material flows during the AFSD process. Two different types of experimental AFSD depositions were used for model calibration: anodized AA6061 rod feedstock with surface oxides to examine outer particle movement and AA6061 feedstock with copper wire cores to track material/particles from the center of the feedstock during deposition. The anodized feedstock rods contained a thick oxide layer, which, when deposited, resulted in the dispersal of aluminum oxides throughout the depositions. Optical microscopy was employed to quantify the surface area of oxides present in the experimental depositions. The copper wire core feedstock depositions resulted in the dispersal of copper throughout the depositions. XRCT scans mapped the copper distribution within the deposited aluminum matrix. Unique insight into particle flow behavior was also explored for each of the simulations.

5.13.1 Materials and Methods

Anodized Feedstock Depositions

Anodized feedstocks were utilized to represent material flow behavior from the outside of the feedstock. The anodized AA6061-T6 feedstock rod depositions have been detailed in a previous study by Ning et al. [7]. Specifically, to create the oxide surface, the feedstock rods were anodized in sulfuric acid resulting in an oxide layer approximately 69 μm thick. Two different depositions were created with the anodized feedstock rods. The tool rotational speed, traverse speed, and layer height were identical for both studies (300 rpm, 2.12 mm/s, 1.5 mm). To show how actuator feed rate would vary oxide distribution, the actuator feed rate was varied for each deposition. The first deposition, which will be referred to as the starved deposition, used a 1.06 mm/s actuator feed rate, which would result in a part with a narrow deposition width and significant surface galling. The second deposition, which will be referred to as the overfed deposition, used a 4.24 mm/s actuator feed rate, which would result in a part with large deposition width.

Copper Wire Core Deposition

While the anodized oxides represented material flow from the outside of the feedstock, the copper wire in the copper wire core depositions represented material flow from the center of the feedstock. The feedstock was created by cutting a 1 mm wide, 5.76 mm deep channel into a 9.53 mm square 152.4 mm long rod of AA6061-T6. A copper wire was pressed into the channel followed by a 1 mm wide, 4.76 mm tall, 152.4 mm long piece of AA6061-T6 to fill in the remainder of the channel. For the copper wire core deposition, the tool rotational speed, traverse speed, layer height, and actuator feed rate were 300 rpm, 2.12 mm/s, 1.5 mm, and 2.12 mm/s, respectively.

Microstructural Characterization of Depositions

The anodized feedstock samples were sectioned using Mitsubishi MV 1200S wire-cut electrical discharge machine and polished using 1 μm diamond suspension. A Keyence VHX 7100 Microscope was used to create micrographs at 150x magnification for oxide analysis. A Thermo

Fisher Scientific Apreo scanning electron microscope was used to perform energy dispersive x-ray spectroscopy (EDS) from EDAX to collect compositional information of the oxides at 20 kV and 0.4 nA with a working distance of 10 mm. The copper wire core deposition was analyzed using a North Star Imaging XRCT machine to highlight copper distributed throughout the AFSD builds.

SPH Methodology

When tasked with computer simulations, most researchers choose the finite element method (FEM) to approximate the governing equations. FEM is a powerful tool for handling problems with nonlinear geometry and complicated boundary conditions. FEM is based on the Galerkin method, which is a weighted residual method that approximates governing equations over the entire problem domain with a finite number of shape functions.

The FEM formulation discretizes simulated parts into a series of nodes and geometrical shapes called elements, and the connectivity between nodes and elements is known as the mesh. In contrast, SPH is a collocation method where the governing equations of AFSD are evaluated at a series of material points through the formulation shown in Eq. 5.13.1 taken from Liu and Liu 2003 [42].

$$f(x_i) = \sum_{j=1}^{N} \frac{m_j}{\rho_j} f(x_j) W(x_i - x_j, h) \qquad 5.13.1$$

Where $f(x_i)$ is the function to be evaluated at a particle of interest x_i, m_j and ρ_j are the mass and density of the neighboring particle x_j, N is the number of neighbors for the particle of interest x_i, and $W(x_i - x_j, h)$ is the smoothing function, which is evaluated based on the distance between the particle of interest and the neighboring particle $x_i - x_j$ and the smoothing length h, which is multiplied by particle radius to determine how far out the particle influence reaches. An illustration of the SPH method with a particle of interest, kernel (smoothing) function, and neighboring particles is provided in Figure 5.107.

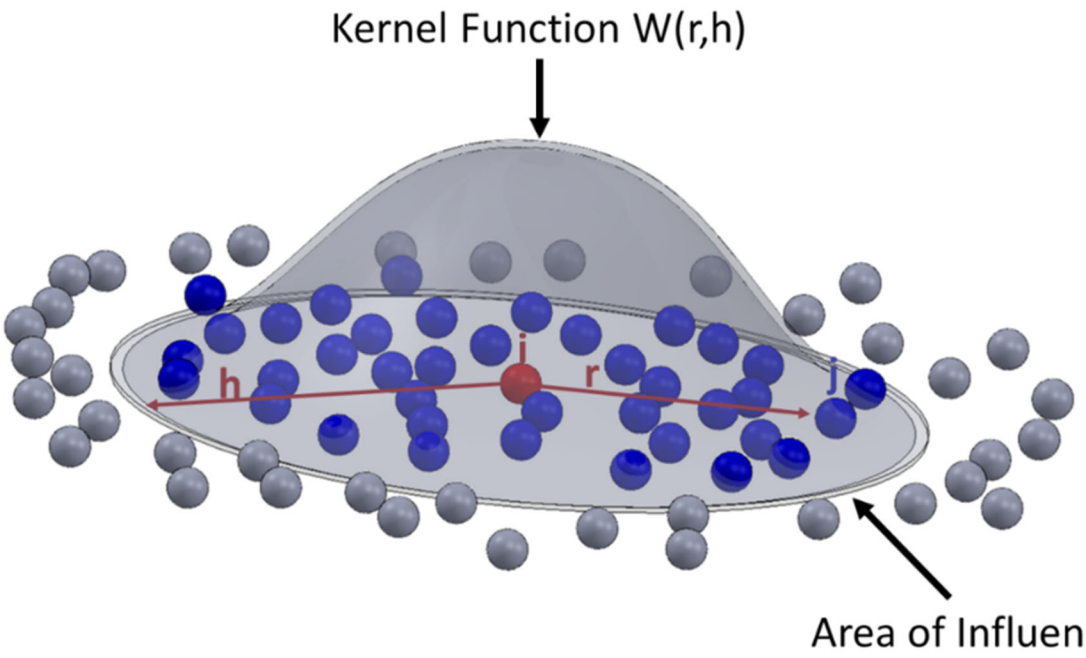

Figure 5.107 SPH kernel function illustrating the influence domain of a particle and the neighboring particles that fall under the influence domain [40].

Unlike with FEM, the SPH formulation does not include elements to discretize simulated parts, and therefore is known as a meshfree method. The smoothing function used in this study is the hyperbolic spline function taken from Yang et al. 2014 [43] and shown in Eqs. 5.13.(2-3).

$$W(s,h) = \alpha_d \begin{cases} s^3 - 6s + 6, & 0 \le s < 1 \\ (2-s)^3, & 1 \le s < 2 \\ 0, & s \ge 2 \end{cases} \quad 5.13.2$$

$$s = \frac{x_i - x_j}{h} \quad 5.13.3$$

Where α_d is the normalizing factor, which for 3D problems is $15/(62\pi h^3)$.

For particle tracking purposes, SPH is a natural candidate because SPH uses a Lagrangian reference frame, which provides a history of the movement of each particle over time. Also, SPH is more suitable than a Lagrangian FEM method for tracking particles over severe deformation, because SPH material points represent small particles that freely move within the problem domain, which are not constrained by a predefined mesh. The SPH approximation was applied to a series of continuum mechanics equations shown in [44]. The SPH methodology discretizes PDEs into ODEs, which can then be solved temporally with time integration, a sample of which can be seen in Table 5.13.7. Due to the nonlinearity that would arise during severe deformation, the authors in this study used the leapfrog forward difference method to temporally integrate the governing equations.

Table 5.13.7. Sample of PDEs approximated by the SPH method for use in AFSD simulations.

Name	PDE	SPH
Conservation of Mass	$\frac{D\rho}{Dt} + \rho\nabla \cdot \bar{v} = 0$	$\frac{D\rho_i}{Dt} = \rho_i \sum_{j=1}^{N_i} \frac{m_j}{\rho_j}(v_i{}^{\beta} - v_j{}^{\beta})\frac{\partial W_{ij}}{\partial x_i{}^{\beta}}$
Conservation of Momentum	$\frac{D\bar{v}}{Dt} = \frac{1}{\rho}\nabla \cdot \bar{\bar{\sigma}}$	$\frac{Dv_i{}^{\alpha}}{Dt} = \sum_{j=1}^{N_i} m_j \left(\frac{\sigma_i{}^{\alpha\beta}}{\rho_i{}^2} + \frac{\sigma_j{}^{\alpha\beta}}{\rho_j{}^2}\right)\frac{\partial W_{ij}}{\partial x_i{}^{\beta}}$
Jaumann Stress Rate	$\frac{d\bar{\bar{S}}}{dt} = 2G\left(\dot{\bar{\bar{\varepsilon}}} - \frac{1}{3}tr(\dot{\bar{\bar{\varepsilon}}})\bar{\bar{\delta}}\right) + \bar{\bar{S}}\bar{\bar{\Omega}}^T + \bar{\bar{\Omega}}\bar{\bar{S}}$	$\frac{dS^{\alpha\beta}}{dt} = 2G\left(\dot{\varepsilon}^{\alpha\beta} - \frac{1}{3}\delta^{\alpha\beta}\dot{\varepsilon}^{\gamma\gamma}\right) + S^{\alpha\gamma}\Omega^{\beta\gamma} + \Omega^{\alpha\gamma}S^{\gamma\beta}$
Stress Decomposition	$\bar{\bar{\sigma}} = \bar{\bar{S}} - p\bar{\bar{\delta}}$	$\sigma_i{}^{\alpha\beta} = S_i{}^{\alpha\beta} - p_i\delta^{\alpha\beta}$
Strain Rate	$\dot{\bar{\bar{\varepsilon}}} = \frac{1}{2}(\nabla^s\bar{v} + \bar{v}\nabla^s)$	$\dot{\varepsilon}_i{}^{\alpha\beta} = \frac{1}{2}\sum_{j=1}^{N_i}\left(\frac{m_j}{\rho_j}v_{ji}{}^{\alpha}\frac{\partial W_{ij}}{\partial x_i{}^{\beta}} + \frac{m_j}{\rho_j}v_{ji}{}^{\beta}\frac{\partial W_{ij}}{\partial x_i{}^{\alpha}}\right)$
Spin	$\bar{\bar{\Omega}} = \frac{1}{2}(\nabla^s\bar{v} - \bar{v}\nabla^s)$	$\Omega_i{}^{\alpha\beta} = \frac{1}{2}\sum_{j=1}^{N_i}\left(\frac{m_j}{\rho_j}v_{ji}{}^{\alpha}\frac{\partial W_{ij}}{\partial x_i{}^{\beta}} - \frac{m_j}{\rho_j}v_{ji}{}^{\beta}\frac{\partial W_{ij}}{\partial x_i{}^{\alpha}}\right)$
Conservation of Energy	$\frac{\partial T}{\partial t} = \frac{1}{\rho C_p}\nabla \cdot (k\nabla T) + \dot{q}$	$\frac{dT_i}{dt} = \frac{1}{\rho_i C_{p_i}}\sum_{j=1}^{N_i}\frac{m_j}{\rho_j}\frac{(4k_ik_j)}{(k_i+k_j)}\frac{(T_i - T_j)}{\lvert x_{ij}\rvert^2}x_{ij}\frac{\partial W_{ij}}{\partial x_i{}^{\beta}} + \dot{q}_i$

AFSD SPH Simulations

The simulation model set-up is shown in Figure 5.108. The SPH code, SPHriction-3D, was initially developed by Fraser [44] for FSW simulations, and was adapted by Stubblefield et al. [40] for AFSD simulations. The substrate was comprised of 69,312 SPH material points with

approximately 1 mm spacing. The feedstock was comprised of 11,000 SPH material points with approximately 1 mm spacing. The rigid tool was comprised of 16,598 triangular finite elements with approximately 1 mm spacing. The rigid base was comprised of 31,238 triangular finite elements with approximately 1 mm spacing. Rigid finite elements were employed to reduce simulation time. For the rigid tool boundary conditions, the tool was positioned 1.5 mm over the substrate, traversed over the substrate at a fixed rate of 2.12 mm/s, and had varying rotational velocities based on the test cases (1.06 mm/s, 2.12 mm/s, 4.24 mm/s). The rigid base was fixed in space.

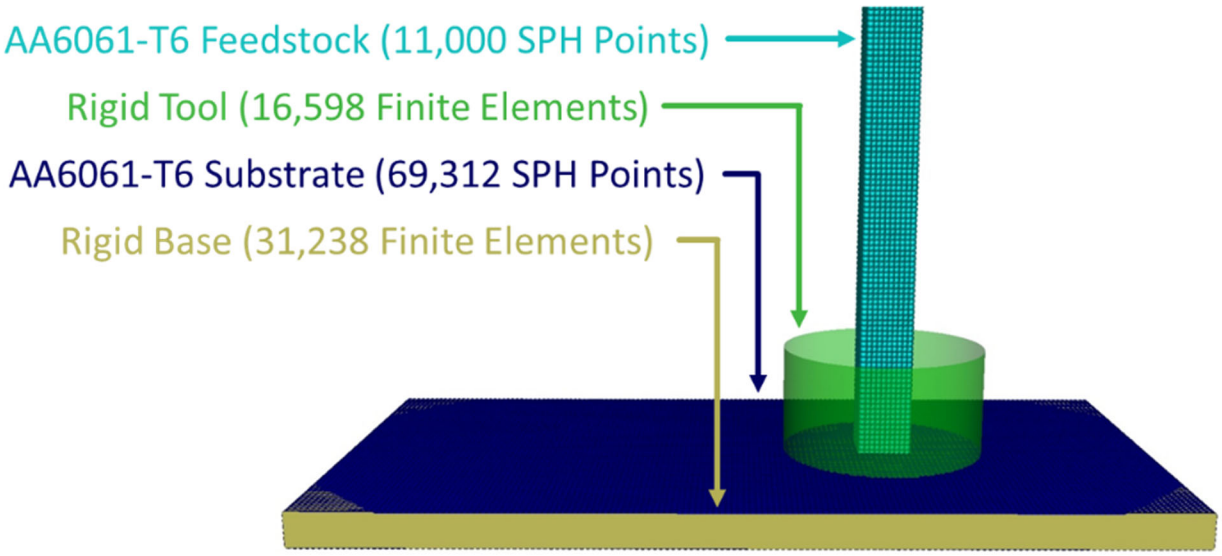

Figure 5.108 SPH model of AFSD process with labeled parts used for model calibration. SPH points modeled the feedstock and substrate, and rigid finite elements modeled the tool and base.

The particle tracking scheme is shown in Figure 5.109. SPH material points on the outer surface and center of the feedstock between 3 and 4 mm above the substrate were tagged to represent anodized oxides and copper wire, respectively. For computational efficiency of the simulations, the tagged points had the same material properties as the remainder of the AA6061-T6 feedstock. Each feedstock SPH material point had a representative diameter of 1 mm, but the oxide surface thickness on the anodized feedstock was an order of magnitude smaller at 69 μm. The main reason for this discrepancy is the computational intensity of SPH codes with available computer resources. Despite this shortcoming, the SPH model in this study is a valuable tool for predicting material flow and relative concentrations of oxides based on comparisons between experimental and computational results. Unlike the oxides, the 1 mm copper wire diameter is well represented by the 1 mm diameter SPH material points, although the copper wire would fragment into pieces smaller than 1 mm during the experimental deposition and not in the simulation deposition.

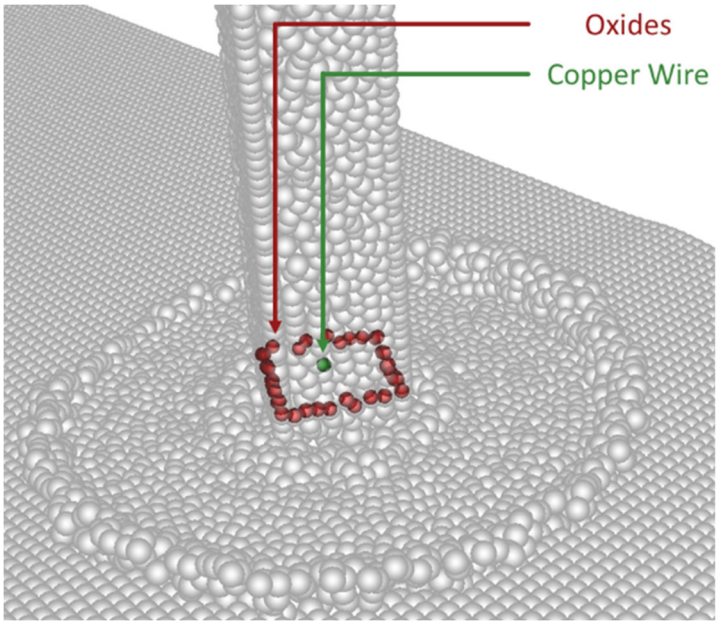

Figure 5.109 SPH model of AFSD oxide and copper wire tagging for comparison with experimental AFS Depositions.

Constitutive Model

Due to the significant plastic deformation inherent to the AFSD process, a constitutive model is necessary for the SPH simulations. In this work, the authors employed the Fraser-Kiss-St-Georges (FKS) constitutive model, previously used for FSW simulations [38], and AFSD simulations [40]. The FKS model is laid out in Eqns 5.13.(4-8):

$$\sigma_y(\epsilon^p, \dot{\epsilon}, T^*) = H(\epsilon^p)\Lambda(\dot{\epsilon}, T^*)\Theta(T^*) \quad 5.13.4$$

$$H(\epsilon^p) = a_1 + a_2 \arctan(a_3\epsilon^p) \quad 5.13.5$$

$$\Lambda(\dot{\epsilon}, T^*) = 1 + [b_1 T^{*b_2}] \ln\left(\frac{\dot{\epsilon}}{\dot{\epsilon}_0}\right) \quad 5.13.6$$

$$\Theta(T^*) = 1 - \frac{1}{(1 + \mathrm{e}^{-c_1 T^*})^{\frac{1}{c_2}}} \quad 5.13.7$$

$$T^* = \frac{T - T_{room}}{T_{melt} - T_{room}} \quad 5.13.8$$

$H(\epsilon^p)$ is the strain hardening parameter that depends on plastic strain ϵ^p and fitting constants a_1, a_2, and a_3. $\Lambda(\dot{\epsilon}, T^*)$ is the strain rate stiffening parameter that depends on homologous temperature T^*, strain rate $\dot{\epsilon}$, reference strain rate $\dot{\epsilon_0}$, and fitting constants b_1 and b_2. $\Theta(T^*)$ is the thermal softening parameter that depends on homologous temperature T^* and fitting constants c_1 and c_2. The values for the fitting constants were taken from torsion tests in Stubblefield et al. [41] and are shown in Appendix A.

5.13.2 Results and Discussion

The resulting anodized feedstock depositions with a provided schematic of the sectioned regions are shown in Figure 5.110. Oxide analysis regions, marked in Figure 5.110, were used to show the distribution of oxides within the depositions on the advancing and retreating sides from Regions 1-5. The advancing and retreating regions were each 15.88 mm wide. All samples were centered about the tool axis, not necessarily the center of the deposition.

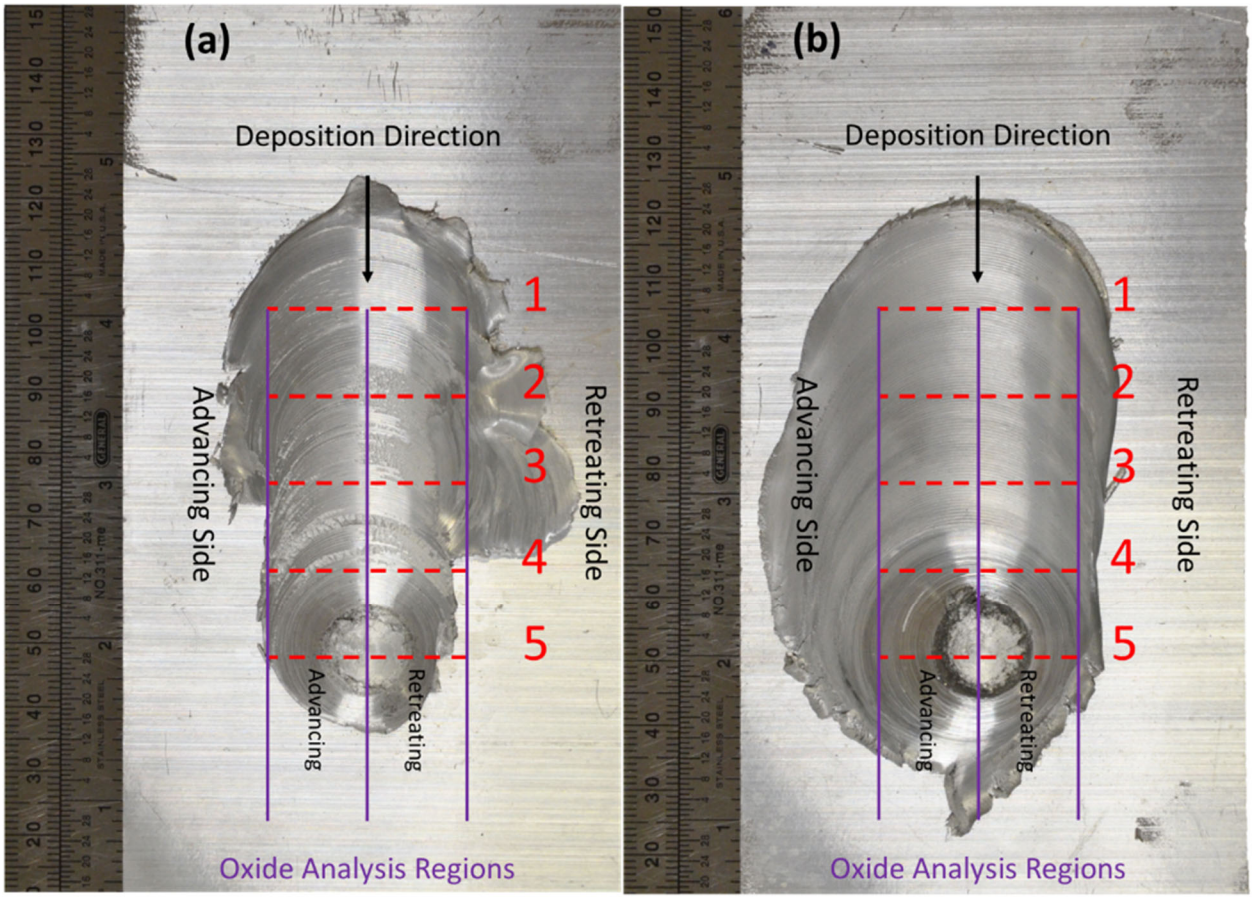

Figure 5.110 (a) Starved and (b) overfed AFS Depositions created with anodized rods for model calibration with labelled oxide analysis regions. Showing oxide analysis regions used in results section (revise).

The starved deposition in Figure 5.110a had a significant reduction in deposition width after the start of the deposition due to inadequate material input from the low actuator feed rate. To heat up the material initially, the hollow spinning tool is brought down into contact against the substrate. Once the material is softened, the spinning tool is slowly raised up while an actuator pushes the feedstock material through the center of the tool. The deposited material fills the gap between the tool and the substrate, which is seen at the start of the deposition. However, the low actuator feed rate relative to the tool traverse speed resulted in the reduction of deposition width once the tool moves past the initial dwell zone. In contrast, the overfed deposition in Figure 5.110b had a significantly wider deposition width than the starved deposition in Figure 5.110a due to the high

actuator feed rate. Similarly, the flash formed in Figure 5.110b was thicker than the flash formed in 4a due to the higher actuator feed rate in the overfed deposition relative to the starved deposition. The overfed build in Figure 5.110b showed a significant deposition bias towards the advancing side and no galling, but the starved build in 4a was more balanced and experienced significant surface galling.

ImageJ software was used to analyze the specific regions in Figure 5.110. First, the images were converted to black and white via the threshold tool. Next, the particle analysis tool was employed to obtain the size of each oxide in the images. The total oxide area for advancing and retreating sides was calculated by summing oxide particle areas. A minimum oxide area threshold was varied from 1 to 1000 μm^2 to account for noise in the small specks. The oxide ratio, which is the ratio of oxide surface area on the advancing side to the retreating side, was calculated by varying the minimum oxide area threshold and dividing the advancing side oxide area by the retreating side oxide area.

Oxide Verification

In each of the samples, dark particles visible under SEM dispersed throughout the top of the samples. In a similar study investigating the mixture of dissimilar aluminum-copper friction stir processing, Mehta et al. [45] used SEM imagery to highlight the aluminum- and copper-dense regions. The back-scattered electron image with corresponding EDS results is shown in Figure 5.111. The three spots analyzed were on the dark particles, and the last three spots were analyzed on the matrix. Spots 1-3 contained significant quantities of aluminum and oxygen, indicating the presence of aluminum oxides. The presence of sulfur was a result of the anodization process, implying that spots 1-3 were aluminum oxide particles specifically from the feedstock. Spots 4-6 taken on the gray background were comprised almost entirely of aluminum, with trace amounts of other elements such as silicon and magnesium, consistent with AA6061 composition.

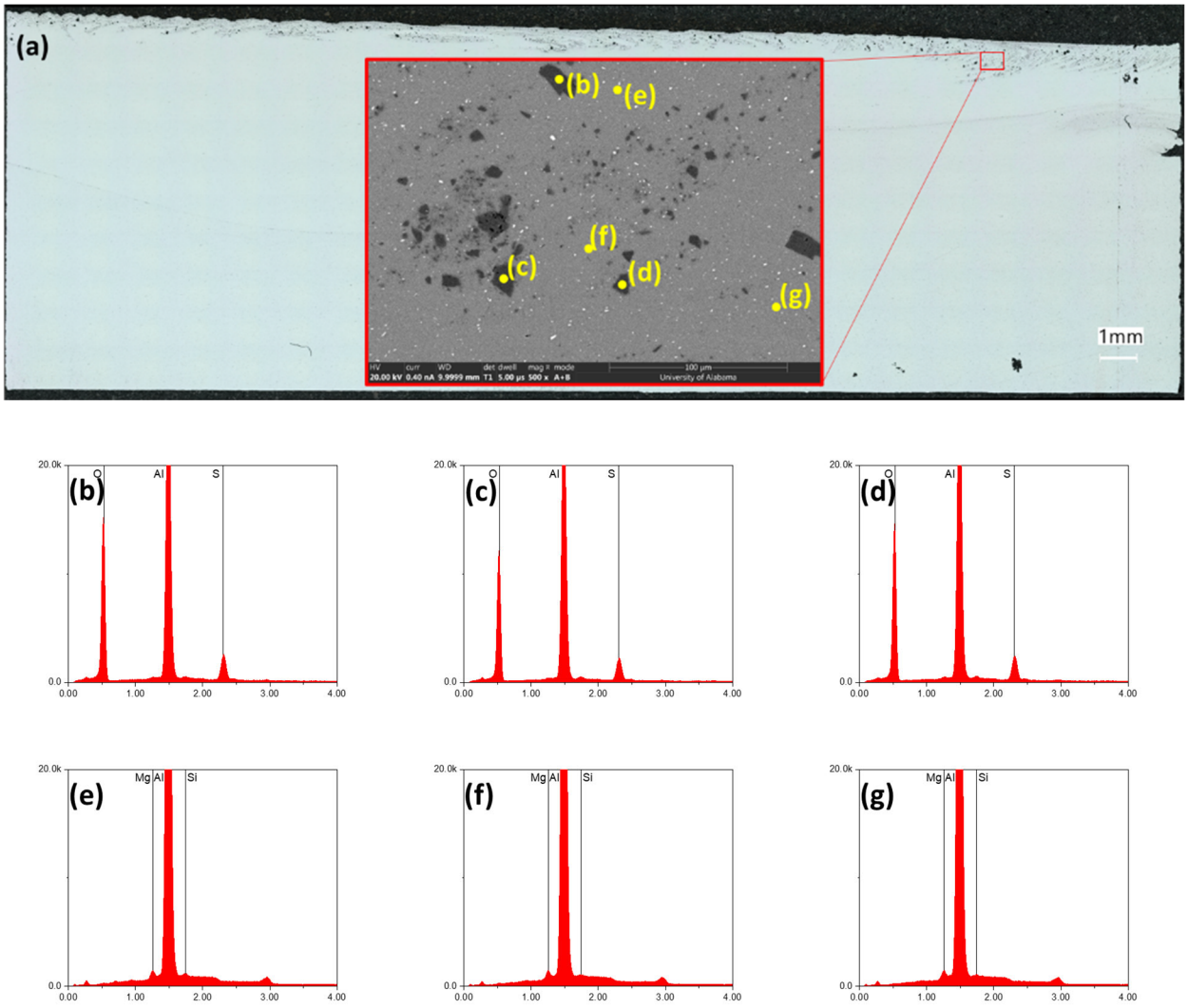

Figure 5.111 (a) Region 2 micrograph of overfed anodized AFS Deposition with SEM image indicating EDS point scans. (b)-(g) EDS results from Region 2 of the overfed AFS Deposition confirm the appearance of anodized oxides.

Anodized Feedstock Experiment vs Simulation

The quantified experimental oxide distributions are provided in Figure 5.112. Regions 1-5 on the horizontal axis correlate with the oxide analysis regions labelled in Figure 5.110. The oxide ratio on the vertical axis was calculated by dividing the total oxide surface area on the advancing side by the total oxide surface area on the retreating side for each oxide analysis region in Figure 5.110a,b. A high oxide ratio suggests that more oxides were found on the advancing side, and a low oxide ratio indicates that more oxides were found on the retreating side. Region 1 was the start of the deposition and region 5 was the finish of the deposition. Both the starved and overfed depositions showed a low oxide ratio in Regions 2-4, indicating a preference for the retreating side in the steady-state areas. The transient areas in Regions 1 and 5 had greater variances in the oxide

ratio. The discrepancy between experimental and simulated oxide distributions was anticipated and discussed in the previous section.

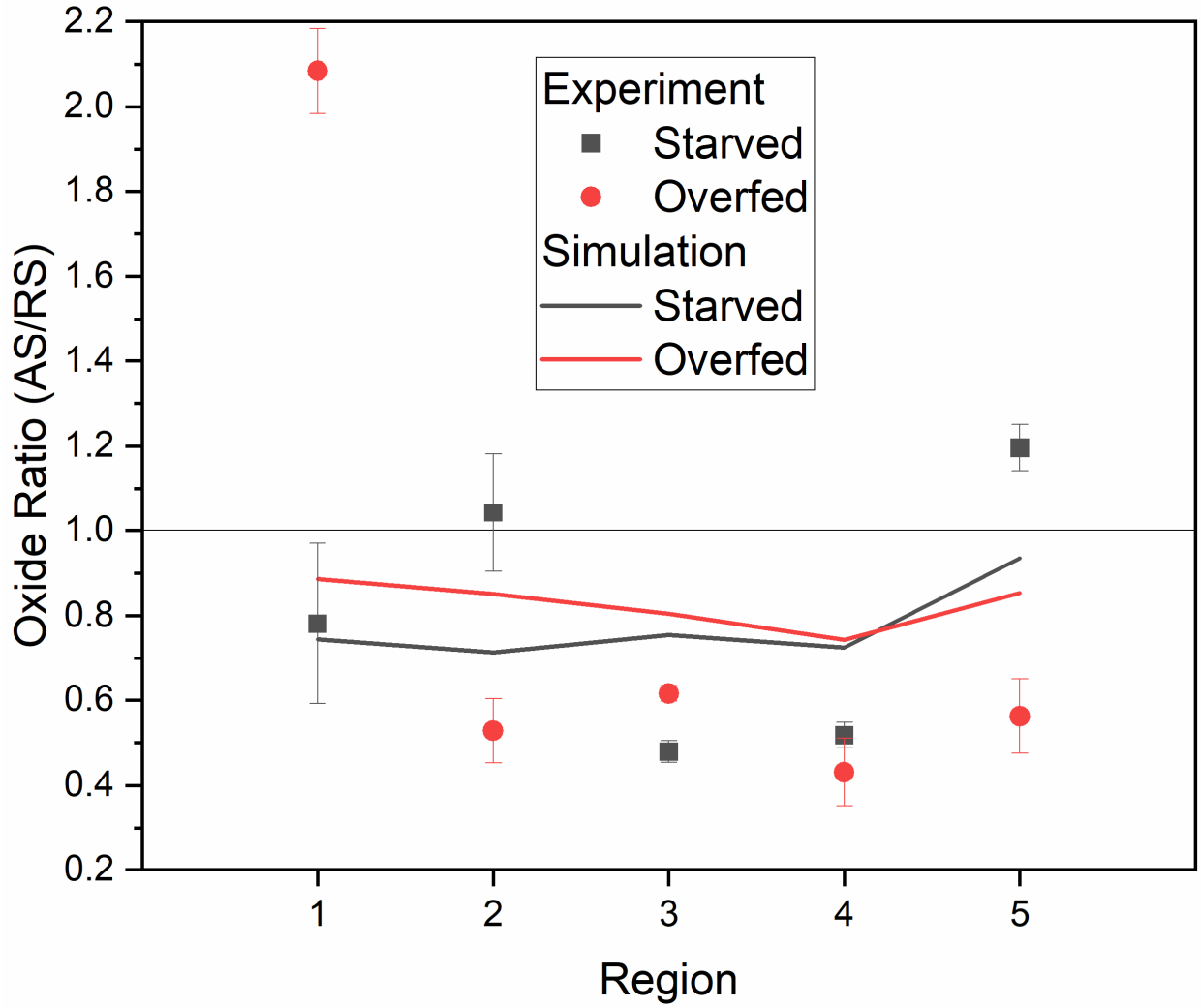

Figure 5.112 Quantified AFSD oxide distributions for the anodized feedstock depositions per oxide analysis region show preference for retreating side in both (a) starved and (b) overfed builds for both experiments and simulations. The oxide analysis regions are labelled on the physical samples in Figure 5.110.

Copper Wire Core Deposition

The resulting deposition with feedstock schematic is shown in Figure 5.113. Since the actuator feed rate of the copper wire core deposition in Figure 5.113a was between the actuator feed rates of the starved oxide deposition in Figure 5.110a and overfed oxide deposition in Figure 5.110b, the deposition width of the copper wire core deposition was also between the widths of the starved and overfed oxide depositions. The copper wire core deposition in Figure 5.113 also experienced some flash at the start of the deposition and relatively smaller flash features on the advancing and retreating side.

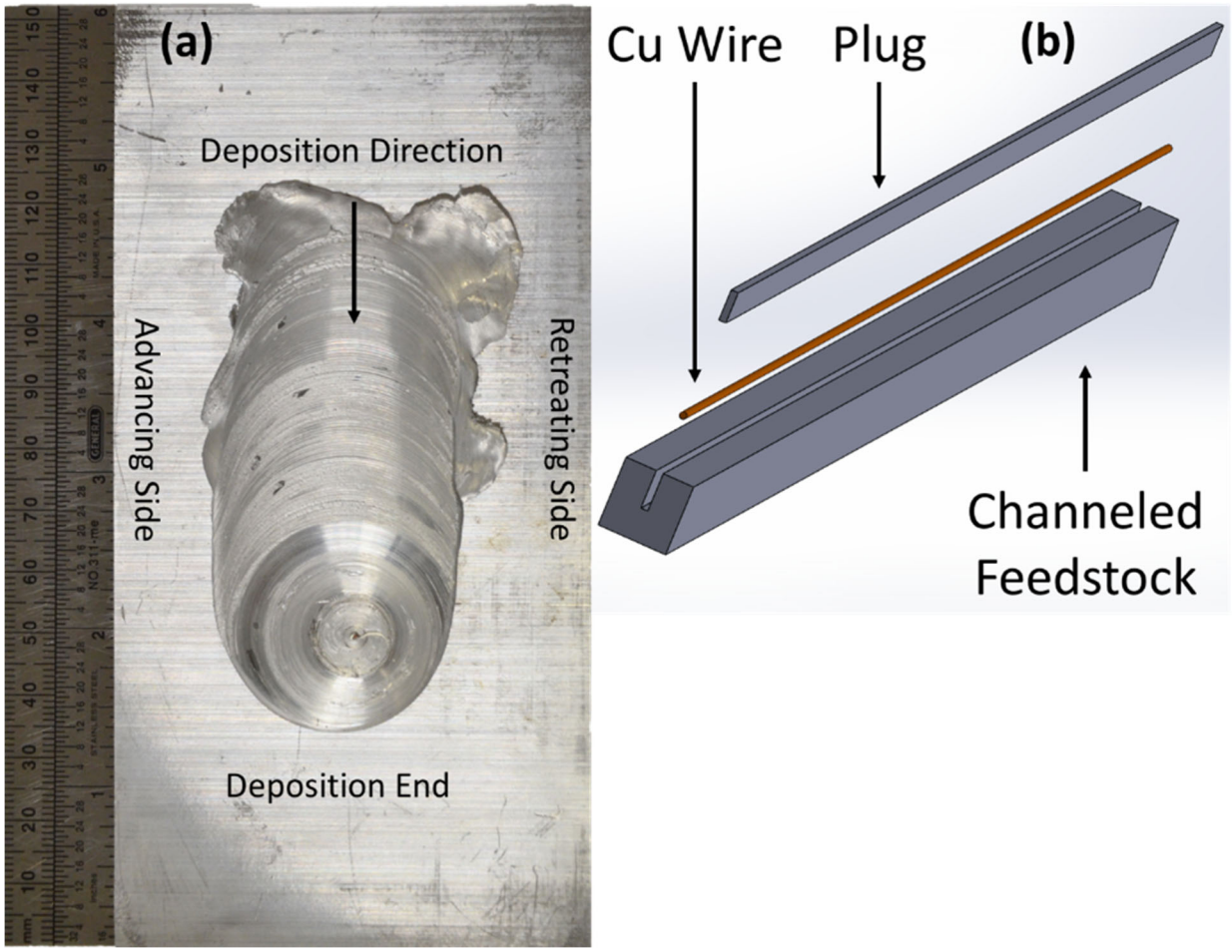

Figure 5.113 (a) Copper wire core deposition using AFSD for use in SPH model calibration. (b) Schematic showing construction of copper wire core feedstock.

Copper Wire Core Experiment vs Simulation

The XRCT scan of the copper wire core deposition is shown in Figure 5.114. The black areas are copper, and the transparent areas are aluminum. The SPH simulation in Figure 5.114b shows a curved copper concentration region that correlated well with the experimental deposition in Figure 5.114a. The shape of the copper concentration region was a consequence of copper fragments tending to flow to the advancing side as the copper flowed out from the center of the tool. Although the copper showed an advancing side bias, some fragments were scattered in the retreating side. A dissimilar aluminum-copper friction stir welding study by Zhou et al. [46] also showed particle fragments in the stir zone. Both the experiment and the simulation show a large cluster of copper at the end of the deposition, since the copper had not yet flowed outwards. Although the copper wire had been deformed and broken up, most of the copper wire fragments remained near other fragments, indicating a lack of material mixing. In contrast with the anodized oxides flowing to the retreating side in Figure 5.112, the copper wire showed an advancing side bias in Figure 5.114. This indicates a discrepancy in particle movement based on position within the feedstock, since the oxides started on the outside of the feedstock and moved to the retreating side, but the copper wire started in the center of the feedstock and moved to the advancing side.

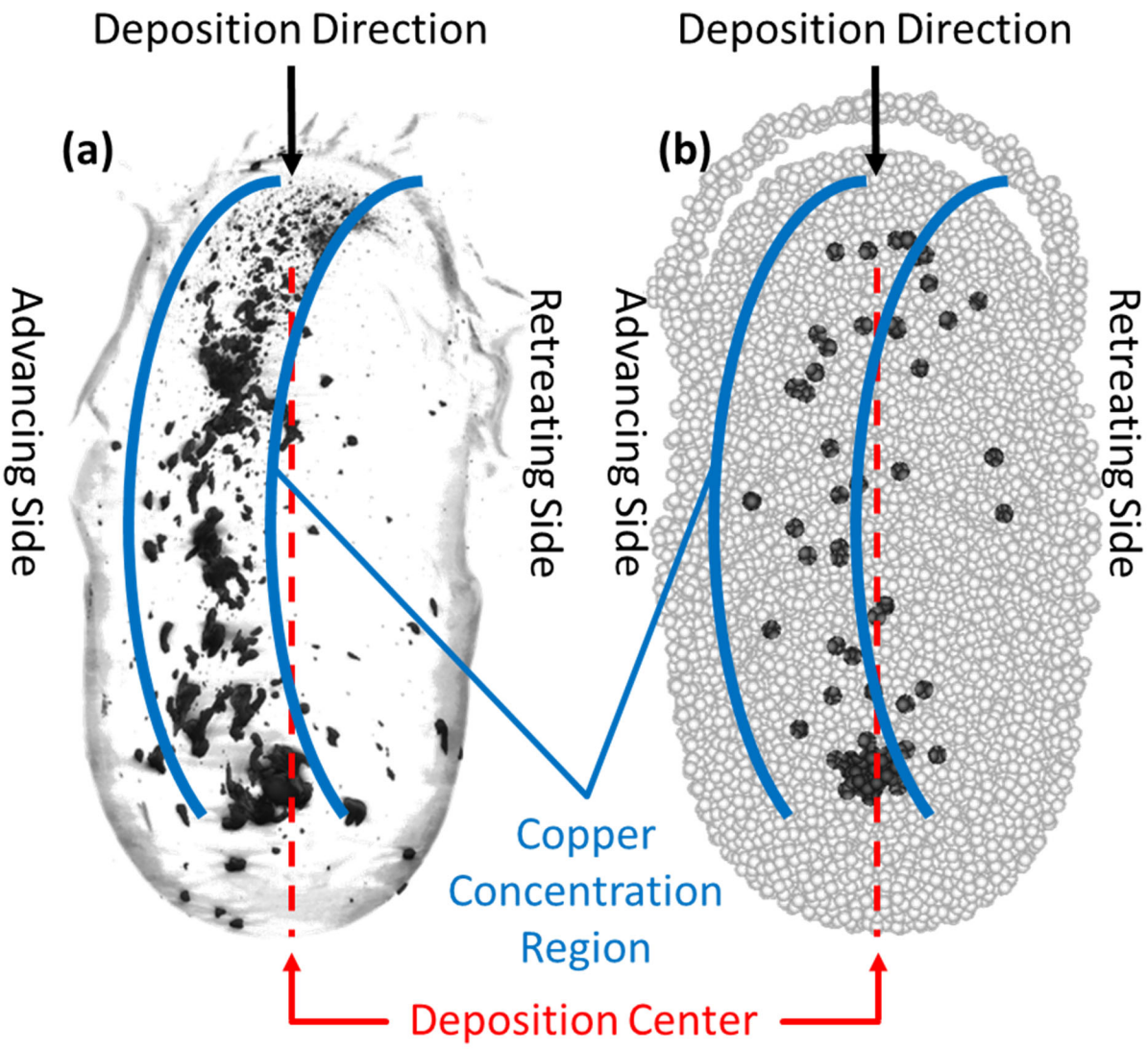

Figure 5.114 (a) XRCT scan of copper wire core deposition using AFSD shows concentration of copper on the advancing side. (b) SPH simulation of AFSD process with copper wire core feedstock shows good agreement with experimental deposition.

Particle Paths

Surface Oxide Particle Paths

The AFSD flow behavior for the oxide particles using the tool as a fixed reference frame is shown in Figure 5.115. The image in Figure 5.115a shows the experimental position of the deposited particles. The vertical axis represents the tool travel direction, the horizontal axis represents the advancing and retreating sides, and the deposition direction is going into the page. The feedstock rotation circumference is based on the diagonal width of the feedstock square cross-section. For both Figure 5.115b and Figure 5.115c there are three competing flows that dominate different regions under the tool: 1) rotational flow, 2) radial flow, and 3) traverse flow.

Rotational flow is caused by the spin of the tool and has a significant effect while the particle is still within the feedstock rotation circumference. The reason for this flow behavior is because the force pushing down on the feedstock is greatest directly beneath the feedstock, which results in minimal slip and maximum circular movement. However, once particles moved outside the feedstock rotation circumference, the rotation flow became much weaker, due to increased slip from decreased normal forces acting on the particles. The second type of flow is radial flow, which is caused by the actuator pushing feedstock material out of the tool and onto the substrate. Radial flow also occurs in FSW, as seen in Xie et al [47]. While initially moving down the center of the tool, the radial flow shifts 90° to move parallel to the substrate away from the center of the tool. The strength of the radial flow is dependent on the actuator feed rate, which is highlighted in the different flow behaviors of the starved simulation in Figure 5.115b and the overfed simulation in Figure 5.115c. The overfed simulation had a significantly higher actuator feed rate than the starved simulation (4.24 mm/s vs 1.06 mm/s), which resulted in oxides in the overfed deposition flowing outwards more than oxides in the starved simulation. Also, the high radial flow of the overfed simulation in Figure 5.115c interfered with the rotational flow more than in the starved simulation in Figure 5.115b, which helps explain the more erratic flow behavior of the overfed simulation in Figure 5.115c than the starved simulation in Figure 5.115b. The third type of flow is traverse flow, which is based on the travel speed of the AFSD tool over the substrate. Unlike rotational and radial flow, traverse flow only has a significant effect once the particles are outside of the feedstock rotation circumference.

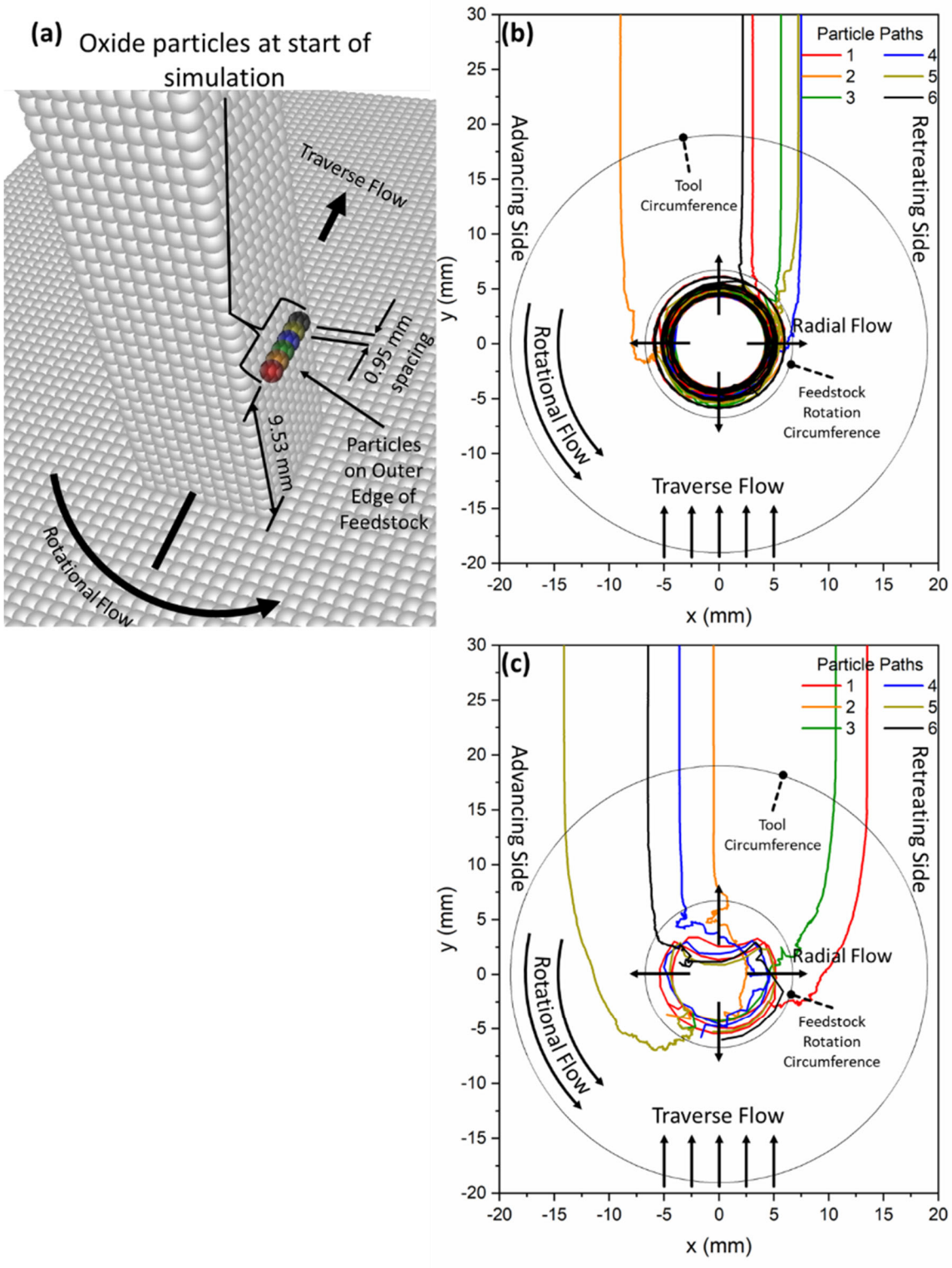

Figure 5.115 (a) Location of tracked oxide particles at start of simulation on the outside of the feedstock. Oxide particle paths during (b) starved and (c) overfed simulations show three kinds of flow behaviors interact to determine particle movement: 1) rotational flow, 2) radial flow, and 3) traverse flow.

Internal Copper Particle Paths

The AFSD flow behavior for the oxide particles using the tool as a fixed reference frame is shown in Figure 5.116. The original position of the particles is shown in Figure 5.116a. The vertical axis represents the tool travel direction, the horizontal axis represents the advancing and retreating sides, and the deposition direction is going into the page. The feedstock rotation circumference is based on the diagonal width of the feedstock square cross-section. As in Figure 5.115b and Figure 5.115c, the same three flows-rotational, radial, and traverse-are present in Figure 5.116b. Unlike with the surface oxide particles in Figure 5.115b and Figure 5.115c, the copper wire particles in Figure 5.116b began in the center of the feedstock and flowed outwards in a spiral pattern. Particle 5 did not escape the feedstock rotation circumference and would be present among the large cluster of copper at the end of the deposition as seen in Figure 5.114.

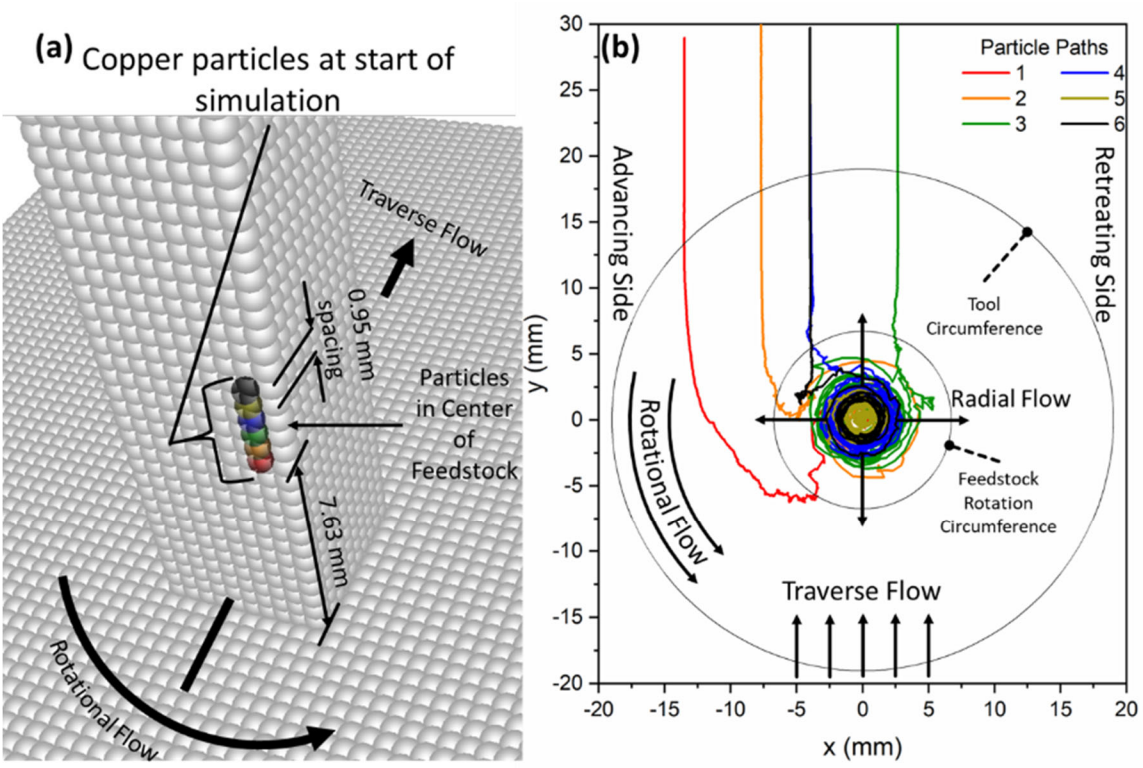

Figure 5.116 (a) Location of tracked copper particles at start of simulation at the center of the feedstock. (b) The central starting position of the copper particles results in a spiral flow out of the feedstock rotation circumference.

While the anodized feedstock depositions in Figure 5.112 showed a retreating side bias for oxide distribution, the copper wire core depositions in Figure 5.114 showed an advancing side bias for copper distribution. This indicates that the probability of a particle to end up on the advancing or retreating side is a function of starting position in the feedstock, since the oxides in Figure 5.115 were on the outer surface of the feedstock and the copper wire in Figure 5.116 was at the center of the feedstock. While all particles showed the most movement within the feedstock rotation circumference, the copper particles in Figure 5.116b experienced a significant drop in rotational flow while still within the feedstock rotation circumference. In contrast, the oxide particles in

Figure 5.115b and Figure 5.115c did not experience a significant drop in rotational flow until after exiting the feedstock rotation circumference.

The copper wire deposition in Figure 5.114 followed the general deposition trend towards the advancing side. However, the oxides gravitated to the retreating sides of the depositions as seen in Figure 5.112, despite the advancing side bias of the depositions in Figure 5.110. This behavior is explained by the interaction of rotational and traverse flow. On the advancing side, the rotational flow and the traverse flow run against each other, but on the retreating side, the rotational flow and the traverse flow run with each other. This suggests that a particle is more likely ejected from the feedstock rotation circumference on the retreating side, where the net flow is the strongest. However, for a particle starting in the center of the feedstock, the rotational flow weakens before the particle leaves the feedstock rotation circumference, because the particle is being incorporated into the deposition, which means that the traverse flow has a greater effect on particle movement. This results in the relatively stronger traverse flow pushing the particle back against the rotational flow. In this scenario, particles tend to spend more time on the advancing side where the two flows counteract each other, and therefore results in more particles that started in the center of the feedstock flowing to the advancing side.

The AFSD tool used in this study has a flat shoulder face, which may explain the lack of rotational flow in Figure 5.115b, Figure 5.115c, and Figure 5.116b outside of the feedstock rotation circumference. Perhaps an alternate tool design such as the four-teardrop tool in [8], [12], [14] or the two-protrusion tool in [20] would encourage more flow outside of the feedstock rotation circumference. Future work could also explore different composite feedstock configurations and investigate how the constitutive elements distribute within the AFSD depositions.

5.13.3 Conclusions

In this work, a particle tracking AFSD simulation using an SPH framework was presented for the first time. Experimental depositions using two anodized AA6061-T6 rods with external oxides on the feedstock and one AA6061-T6 copper wire core feedstock were created for SPH model calibration. The anodized feedstock simulations showed a bias towards the retreating side, which reflected experimental results. The copper within the copper wire core deposition was concentrated on the advancing side with fragments dispersed throughout the deposition. The copper in the copper wire core simulation showed a similar curved copper concentration region as the experimental copper wire core deposition. The particle tracking plots indicated that particle movement was mostly limited to directly beneath the feedstock. Varying actuator feed rate influenced particle flow behavior by increasing radial flow away from the tool. Also, the particle tracking plots revealed the interaction between different material flows: rotational, radial, and traverse flow. The discrepancy between oxide particles and copper particles flowing to the retreating and advancing sides, respectively, was explained by the interaction between the different material flows.

The presented SPH model is useful for analyzing material flow within AFS Depositions, which would be time-consuming and difficult to experimentally quantify with each deposition. One advantage of having validated computer simulations of a process is the predictive power simulations provide. If defects are present at oxides, researchers can use the SPH simulations to track oxides over a battery of simulations and select optimal process parameters to push oxides to

the outside of the deposition, where post-processing machining can remove the oxides. Another example involves composite feedstocks. Engineers can select optimal process parameters to ensure homogeneous mixing of different materials, without wasting resources on physical trials.

5.14 Modeling the Tensile and Fatigue Behavior of AFSD AA5083 and AA6061

In this study, the strain rate effect is quantified for a strain-hardened alloy Al-Mg-Mn alloy (AA5083-H131) as processed through Additive Friction Stir Deposition (AFSD) for multiple orientations in the deposited material. AA5083-H131 wrought control and AA5083 AFSD were subjected to quasi-static ($0.001s^{-1}$) and high rate ($2000s^{-1}$) compression loading. Experimental results revealed an increase in strain hardening of the AA5083 AFSD as compared to the AA5083-H131 wrought control. The rate of strain hardening was similar for each AFSD specimen orientation, although a decrease in flow stress for the build direction was observed. An increase in flow stress response with strain rate was observed for AA5083-H131 as well as the AA5083 AFSD material, indicating AA5083 in the compressive state is strain rate dependent. An internal state variable (ISV) history-dependent physics based material model was calibrated for the AA5083-H131 and AA5083 AFSD materials and the mechanical response was successfully captured.

Manufacturing at the point-of-need requires advanced manufacturing technologies that can be performed in remote or austere environments, and as such, manufacturers and engineers are presented with technical challenges to overcome, in particular, energy consumption and raw material logistics. Austere environments often have a limited power infrastructure, leaving power heavy equipment unusable. The logistical supply chain for raw materials might be inefficient, infeasible, or too costly. When considering vehicle repair in remote locations, replacement part lead-times could be several weeks out and on-site repair is no longer a desire, but a need. On-site repair or replacement of vehicle components in austere environments can be made possible with low energy, high material versatility processes like solid-state additive manufacturing (AM). Additive Friction Stir Deposition (AFSD) is a relatively new solid-state AM process. Sharing similar physics to friction stir welding, AFSD utilizes frictional heat, maintained under the melting point of the material, between a feedstock, hollow tool, and substrate surface to plastically deform the feedstock material and induce a mechanical bond between the material and the substrate. This thermo-mechanical process results in a layered, non-porous, near-net shape deposition. While many materials have been examined with this process, aluminum alloys are of particular interest due to their broad industrial applicability.

Aluminum alloy 5083 (AA5083) is a commercially available strain-hardened alloy that is often used in vehicle applications for its performance in and resistance to corrosive environments. For materials like AA5083, strain hardening, or work hardening, increases strength in the material by forming dislocations through plastic deformation [106]. The newly formed dislocations are then forced to move along slip planes until they reach an obstacle that prevents movement. The dislocation continues to flow until it is no longer free to move, often wrapping itself around the obstacle that created the pinning. When this occurs, a new dislocation is formed and the process repeats itself until the dislocations can no longer flow. When movement is impeded, strength is increased. Strain hardening, while increasing strength, allows for a loss in ductility and increases the potential for brittle failure.

Understanding the sensitivity of a material to varying strain rates is a critical component in material design applications. Dynamic, or high rate (HR), testing involves subjecting a specimen to an impact load to observe the dynamic flow stress of a material. This behavior can be used to simulate vehicle impact or a reaction to another high-impact event, such as an explosion or other critical

situations. The effect of AFSD processing on the dynamic resistance of aluminum alloys is largely unknown.

Recent studies have quantified the dynamic loading performance of AA5083-H131 in the compressive state. Huskins et al. [108] sought to determine the mechanical response and strain rate sensitivity as well as explore the strengthening mechanisms in AA5083-H131. Compression tests of varying strain rates (1000-6000s^{-1}) were performed using a Kolsky bar. In their study, uniform deformation was observed for all high strain rate specimens, while non-uniform shearing deformations were observed in many of the monotonic specimens. Additionally, strain hardening was observed with increasing strain rates. Further, dynamic strain aging (DSA), an interaction between flowing solute atoms and pinned dislocations, was determined to have occurred as indicated by the evidence of serrated flow and negative strain rate sensitivity of the monotonic compression loading. In another study, Tucker et al. [107] evaluated the plasticity, damage, and fracture characteristics of AA5083 at varying the stress states (tension, compression and torsion) and strain rates (monotonic and high rate) experimentally coupled with Internal State Variable (ISV) modeling. In their study, flow stress, damage and fracture were observed to be dependent on the stress state more so than on the strain rate.

This study quantifies the process-structure-property-dynamic performance relationships of AFSD-AD AA5083. Experimental data for wrought AA5083-H131 is compared to AFSD-AD AA5083 and is used in a history-dependent plasticity- damage modeling of strain rate dependence that is expanded upon from just the wrought material behavior, but is now calibrated to capture material with varying processing histories such as AFSD. Specifically, the ISV plasticity-damage theory model employed in this work captures damage from microstructural defects in the material and can be used to predict plastic deformation under various loading conditions.

5.14.1 Materials and Methods

Materials

In the present study, a 63.5 mm thick rolled plate of AA5083-H131 was machined into 9.53 x 9.53 x 254 mm square rods using wire electrical discharge machining (EDM) to use as feedstock for the AFSD process. Process parameters for the AA5083 AFSD build were as follows: tool rotational speed was 300 RPM, with a traversing speed along the longitudinal direction of 127 in/min, an actuator feedrate of 83 mm/min, with a layer thickness of 1 mm. Figure 5.117(a) depicts solid bar feedstock being forced through the rotating tool for the layer-by-layer deposition of the AFSD process. A featured tool with teardrop protrusions on the tool face to aid in material mixing of deposited layers, as depicted in Figure 5.117 (b), was used to create the AA5083 AFSD build.

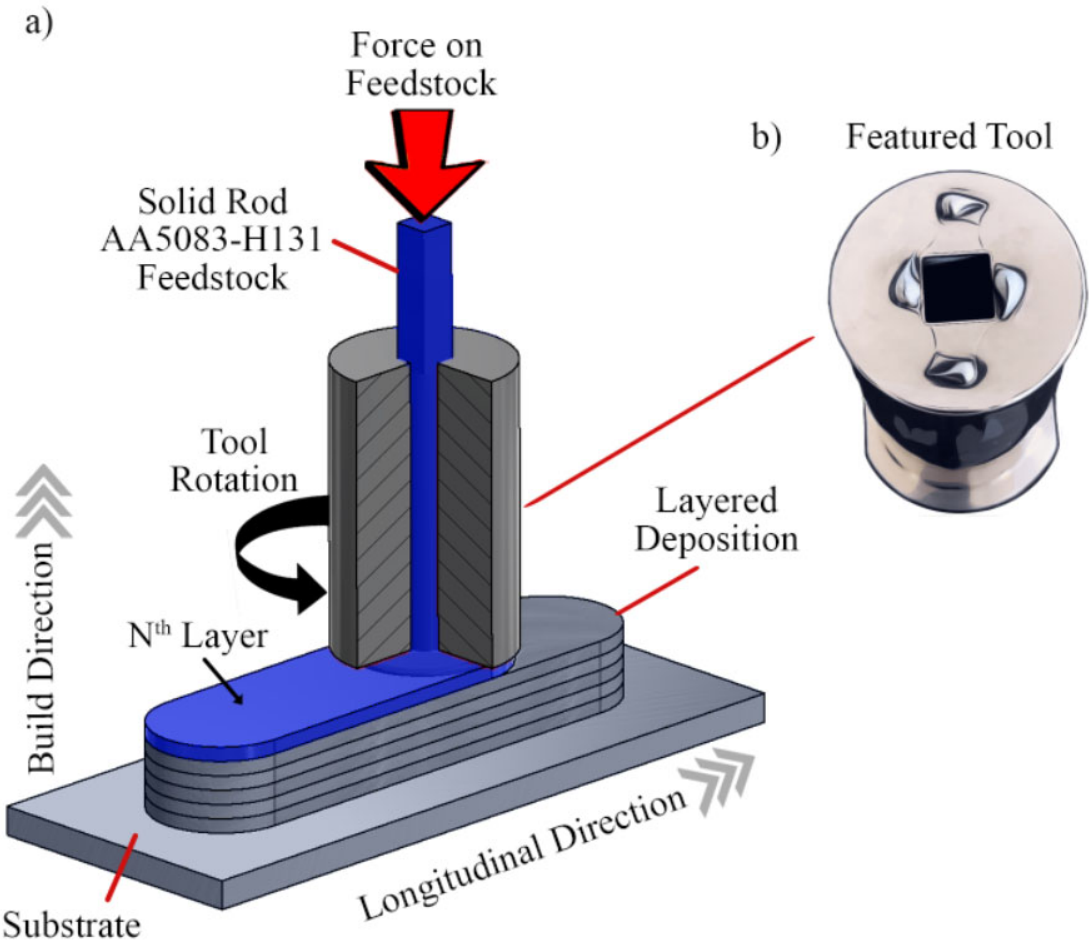

Figure 5.117 Representative images of (a) AFSD process using AA5083-H131 solid rod feedstock and (b) featured tool with "tear drop" protrusions on tool face that interacts with substrate surface.

Test Specimens and Experimental Methods

Figure 5.118 displays the resulting (a) AA5083 AFSD build, (b) the layout and orientation of specimens used in this study, and (d) the dimensions for the compression specimens used for both quasistatic and high-rate experiments. Test specimens were machined from the build as well as a wrought control AA5083-H131 plate via wire EDM. Additionally, material from both the AA5083-H131 wrought plate and AA5083 AFSD deposition were mounted, ground and polished to evaluate grain morphology using electron backscatter diffraction (EBSD) imaging equipped with a Tescan Lyra FE-SEM with EDAX Hikari Super EBSD camera.

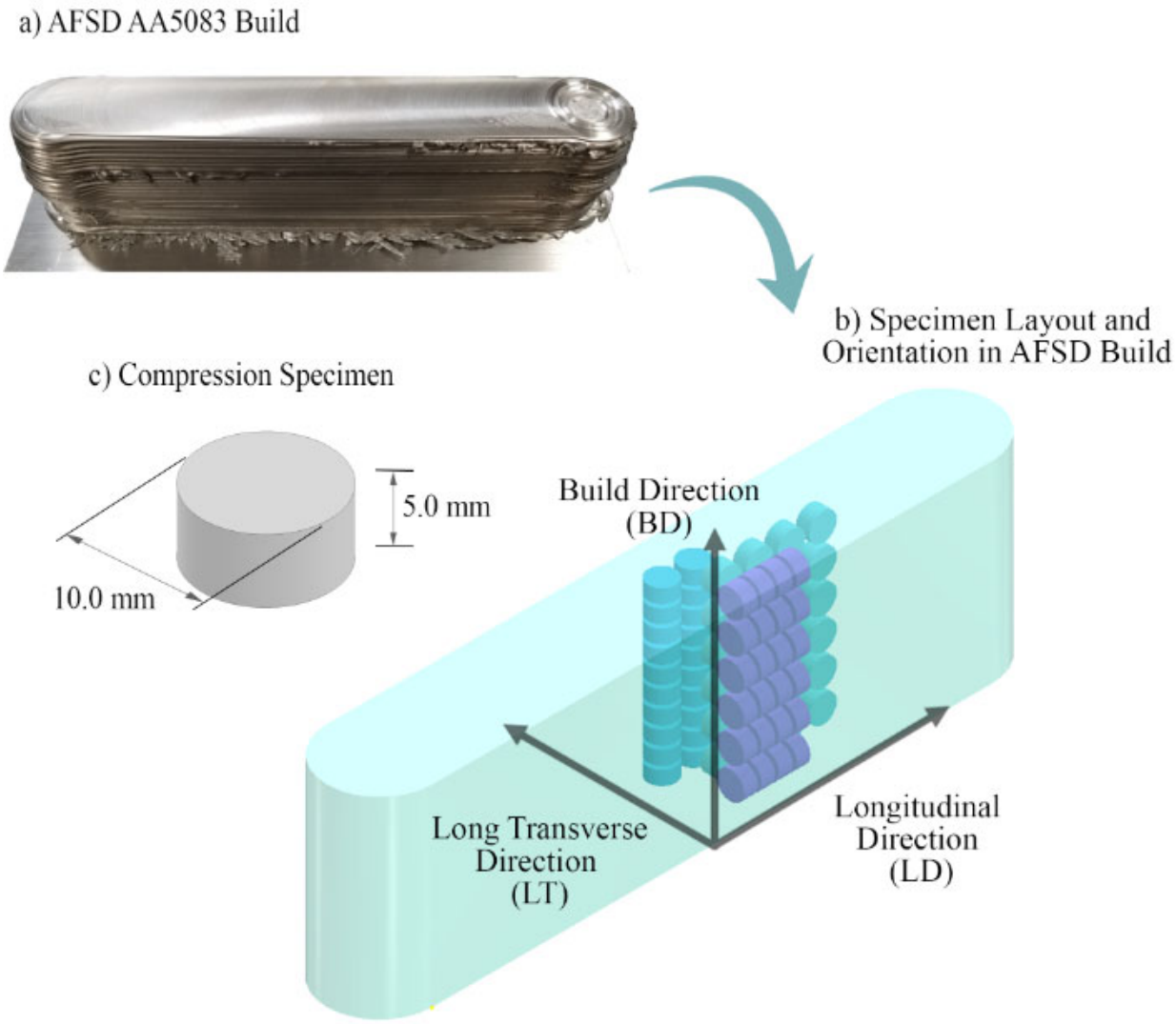

Figure 5.118 Representative a) image of AFSD AA5083 build, b) specimen layout and orientation in AFSD build, and c) compression specimen shape and dimensions.

Uniaxial quasistatic compression (QSC) loading was performed in triplicate on the wrought AA5083-H131 plate and the AA5083 AFSD samples at room temperature using a Gleeble thermomechanical simulator in displacement control with an approximate strain rate of $0.001s^{-1}$. The compression specimens had a cylindrical geometry with a diameter of 10 mm and a length of 5 mm, yielding an aspect ratio of 0.5 to allow for stress-state equilibrium on the front and back faces during high rate loading.

High rate compression (HRC) loading was also performed in triplicate on the wrought AA5083-H131 plate and the AA5083 AFSD samples at room temperature, using the same specimen dimensions as for QSC, and were tested at a strain rate of 2000 s^{-1} on a 12.7 mm diameter Inconel 718 tension-compression Kolsky apparatus, or Split-Hopkinson Pressure Bar (SHPB), that was used in previous research for dynamically testing wrought and additive materials [238], [239],

[291], [292]. The SHPB, illustrated in Figure 5.119, displays a compressive test setting, and consists of a striker bar, which strikes the incident bar, propelled by pressurized gas to achieve the desired strain rate, sending a compressive stress wave (generally a trapezoidal pulse) through the incident bar. The incident bar, then loads the test specimen, which is sandwiched between the incident bar and the transmitted bar. A strain gage on both the incident and transmitted bars detects wave propagation as the wave moves from the incident bar, through the sample, to the transmitted bar and is eventually reflected back into the incident bar. The incident and transmitted bars had an equal length of 2,413 mm, while the striker bar, which is comprised of 350 maraging steel, had a length of 458 mm. A commercially available grease was applied to the specimen faces prior to loading to reduce the interfacial friction between the specimens and the platens screwed in to either end of the bars where this lubrication mitigated barreling of the specimens so a uniaxial stress state was applied in the compression specimens. The platens were made of Inconel 718 and Teflon tape was applied along the shaft of the platen screw to minimize dispersion effects. The progression of deformation was filmed at 20,000 FPS using a Phantom® v611 high-speed camera. Strain data was collected with a Measurement Computing Data Acquisition (DAQ) system at 1 MHz via strain gages cemented to each bar in a full Wheatstone bridge configuration. The strain data was processed by the open-source Split Hopkinson Pressure Bar Graphical Analysis Tool MATLAB® code [293].

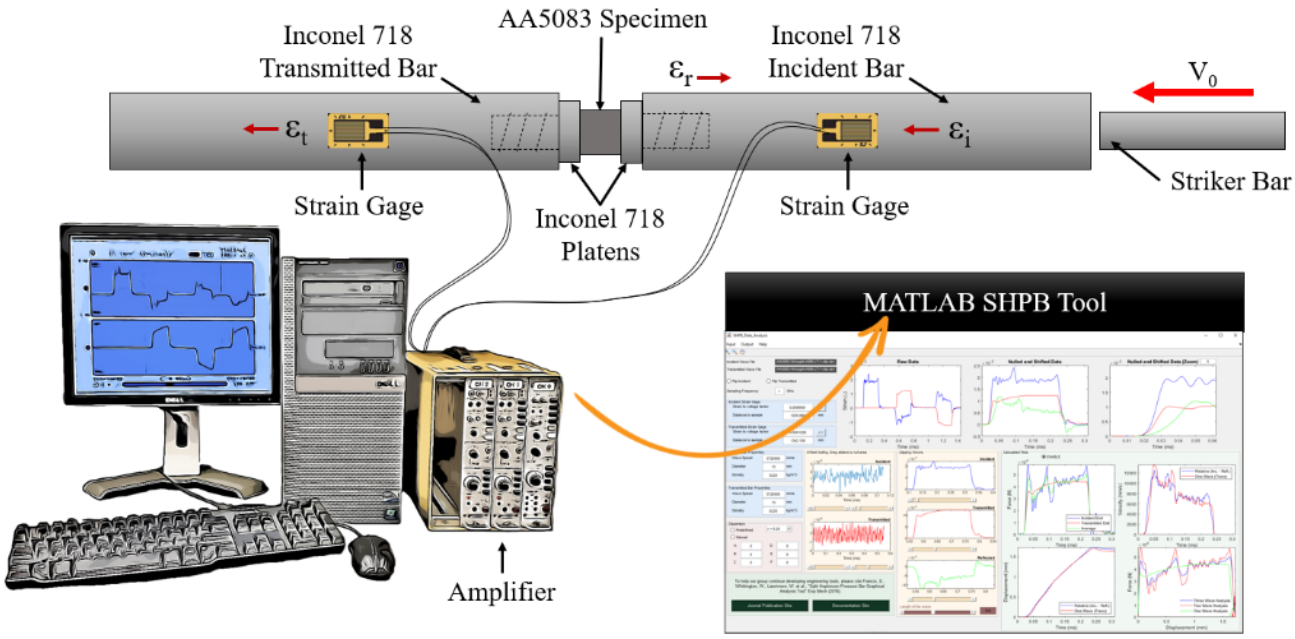

Figure 5.119 Graphical illustration of Split-Hopkinson Pressure Bar experiment setup including MATLAB Split-Hopkinson Pressure Bar Data Analysis Tool.

Internal State Variable Modeling:

The ISV plasticity-damage modeling approach has been implemented to capture the material history and resultant microstructural features and defects of wrought, cast, powder metal, and additive manufactured materials to incorporate stress-state, strain-rate, and temperature dependence deformation [166], [294]–[297].

The initial framework of the model proposed by Bammann et al. [298] is presented in Equation 15.14.1:

$$\underline{\mathring{\sigma}} = \underline{\dot{\sigma}} - \underline{W}^e\underline{\sigma} - \underline{\sigma}\,\underline{W}^e = \lambda tr\left(\underline{D}^e\right)\underline{I} + 2\mu\underline{D}^e \tag{15.14.1}$$

where λ is the Lamé constant, μ is the shear modulus, I is the second-order identity tensor, and the Cauchy stress σ is modified with elastic spin W^e. The D^e is the elastic deformation tensor given by Equation 2.

$$\underline{D}^e = \underline{D} - \underline{D}^{in} \tag{15.14.2}$$

where D^{in} is the inelastic flow rule given by the relationship,

$$\underline{D}^{in} = f(T)\sinh\left[\frac{\left\|\underline{\sigma} - \underline{\alpha}\right\| - \{R + Y(T)\}}{V(T)}\right]\frac{\underline{\sigma} - \underline{\alpha}}{\left\|\underline{\sigma} - \underline{\alpha}\right\|} \tag{15.14.3}$$

where α and R are prescribed in a hardening minus recovery format.

$$\underline{\dot{\alpha}} = \left\{h(T)\underline{D}^{in} - \left[\sqrt{\frac{2}{3}}r_d(T)\left\|\underline{D}^{in}\right\| + r_s(T)\right]\|\underline{\alpha}\|\underline{\alpha}\right\} \tag{15.14.4}$$

$$\dot{R} = \left\{H(T)\underline{D}^{in} - \left[\sqrt{\frac{2}{3}}R_d(T)\left\|\underline{D}^{in}\right\| + R_s(T)\right]R^2\right\} \tag{15.14.5}$$

The ISV plasticity-damage model contains specific functions to describe the inelastic response exhibited in a material and can be grouped into three distinct sections; yield function, isotropic hardening function, and kinematic hardening function. The temperature dependent (T) yield functions are given by

$$Y(T) = C_3\,exp\left(\frac{C_4}{T}\right) * \left(1 + \frac{tanh\left(C_{19}(C_{20} - T)\right)}{2}\right) \tag{15.14.6}$$

$$f(T) = C_5\,exp\left(-\frac{C_6}{T}\right) \tag{15.14.7}$$

$$V(T) = C_1\,exp\left(-\frac{C_2}{T}\right) \tag{15.14.8}$$

where Y(T) determines initial yielding independent of strain rate, f(T) determines the strain rate at which yielding becomes strain rate dependent, and V(T) determines the magnitude at which the material is strain rate sensitive. Isotropic hardening is governed by three distinct functions; isotropic hardening modulus (h(T)), static recovery of dislocations (r_s(T)), and dynamic recovery of dislocations (r_d(T)):

$$h(T) = (C_9 - C_{10}T)\left(1 + C_a\left(\frac{4}{27} - \frac{J_3'^2}{J_2'^3}\right) + C_b\frac{J_3'}{J_2'^{3/2}}\right) \quad (15.14.9)$$

$$r_s(T) = C_{11}\,exp\left(-\frac{C_{12}}{T}\right) \quad (15.14.10)$$

$$r_d(T) = C_7\left(1 - C_a\left(\frac{4}{27} - \frac{J_3'^2}{J_2'^3}\right) - C_b\frac{J_3'}{J_2'^{3/2}}\right)exp\left(-\frac{C_8}{T}\right) \quad (15.14.11)$$

Likewise, the kinematic hardening is governed by three distinct functions; kinematic hardening modulus (H(T)), static recovery of dislocations (R_s(T)), and dynamic recovery of dislocations (R_d(T))

$$H(T) = (C_{15} - C_{16}T)\left(1 + C_a\left(\frac{4}{27} - \frac{J_3'^2}{J_2'^3}\right) + C_b\frac{J_3'}{J_2'^{3/2}}\right) \quad (15.14.12)$$

$$R_s(T) = C_{25}\,exp\left(-\frac{C_{26}}{T}\right) \quad (15.14.13)$$

$$R_d(T) = C_{13}\left(1 - C_a\left(\frac{4}{27} - \frac{J_3'^2}{J_2'^3}\right) - C_b\frac{J_3'}{J_2'^{3/2}}\right)exp\left(-\frac{C_{14}}{T}\right) \quad (15.14.14)$$

where the model constants C_1-C_{26}, C_a, and C_b are calibrated to experimental data. In the present study, the ISV plasticity-damage model was calibrated through the similar process outlined by Mason et al [166].

The calibration of the ISV plasticity-damage model consists of five sets of constants: those that affect yield and yield adjustment, kinematic hardening and recovery, isotropic hardening and recovery, cyclic hardening and recovery, and damage. The parameters related to yielding (C1, C3, and C5) serve as the magnitude of the rate of dependence on yielding, the rate independent yield stress, and magnitude of rate dependence on yielding, respectively. The values corresponding to kinematic hardening and recovery (C7, C9, and C11), help to identify the kinematic dynamic recovery of dislocations, the isotropic hardening modulus, and the kinematic static recovery of dislocations, respectively. The isotropic hardening and recovery values (C13, C15, and C17), are related to the isotropic dynamic recovery of dislocations, the hardening modulus, and the isotropic static recovery of dislocations, respectively. The cyclic hardening and recovery constants (C21, C23, and C25) are used to calculate dynamic recovery. The damage constants were not considered for the present study, as the focus was on modeling the plasticity. There are also a set of even-numbered constants (C2-C26) that were not relevant to the current study as the temperature was not varied from room temperature.

In order to capture the mechanical gradient exhibited between the final layers and the initial layers of the AFS-D AA7050 component caused by the overgrowth of precipitates and increase of the size of PFZ along the grain boundary, the ISV plasticity-damage model was modification to incorporate heterogeneity in precipitate size and PFZ length throughout the AFS-D component. The modified equations are discussed below.

The yield functions, isotropic hardening functions, and kinematic hardening functions were modified to account for the increase in size of precipitates within the grain boundary and increase size of PFZ. The modifications are bolded in Equations 15.14.15-22.

$$Y(T) = C_3\, exp\left(\frac{C_4}{T}\right) * \left(1 + \frac{tanh\left(C_{19}(C_{20} - T)\right)}{2}\right) * (\mathbf{1} - \boldsymbol{C56} * (\boldsymbol{PFZ} + \boldsymbol{GI})) \quad (15.14.15)$$

$$V(T) = C_1\, exp\left(-\frac{C_2}{T}\right) * (\mathbf{1} - \boldsymbol{C57} * (\boldsymbol{PFZ} + \boldsymbol{GI})) \quad (15.14.16)$$

$$h(T) = (C_9 - C_{10}T)\left(1 + C_a\left(\frac{4}{27} - \frac{J_3'^2}{J_2'^3}\right) + C_b\frac{J_3'}{J_2'^{3/2}}\right) * (\mathbf{1} - \boldsymbol{C58} * (\boldsymbol{PFZ} + \boldsymbol{GI})) \quad (15.14.17)$$

$$r_s(T) = C_{11}\, exp\left(-\frac{C_{12}}{T}\right) * (\mathbf{1} - \boldsymbol{C59} * (\boldsymbol{PFZ} + \boldsymbol{GI})) \quad (15.14.18)$$

$$r_d(T) = C_7\left(1 - C_a\left(\frac{4}{27} - \frac{J_3'^2}{J_2'^3}\right) - C_b\frac{J_3'}{J_2'^{3/2}}\right) exp\left(-\frac{C_8}{T}\right) * (\mathbf{1} - \boldsymbol{C60} * (\boldsymbol{PFZ} + \boldsymbol{GI})) \quad (15.14.19)$$

$$H(T) = (C_{15} - C_{16}T)\left(1 + C_a\left(\frac{4}{27} - \frac{J_3'^2}{J_2'^3}\right) + C_b\frac{J_3'}{J_2'^{3/2}}\right) * (\mathbf{1} - \boldsymbol{C61} * (\boldsymbol{PFZ} + \boldsymbol{GI})) \quad (15.14.20)$$

$$R_s(T) = C_{25}\, exp\left(-\frac{C_{26}}{T}\right) * (\mathbf{1} - \boldsymbol{C62} * (\boldsymbol{PFZ} + \boldsymbol{GI})) \quad (15.14.21)$$

$$R_d(T) = C_{13}\left(1 - C_a\left(\frac{4}{27} - \frac{J_3'^2}{J_2'^3}\right) - C_b\frac{J_3'}{J_2'^{3/2}}\right) exp\left(-\frac{C_{14}}{T}\right) * (\mathbf{1} - \boldsymbol{C63} * (\boldsymbol{PFZ} + \boldsymbol{GI})) \quad (15.14.22)$$

where PFZ is the difference between the average length of the precipitate free zone along the grain boundaries in the given area and the average precipitate free zone length along the grain boundary in the area with the peak hardness. This is given by,

$$PFZ = PFZ_2 - PFZ_1 \quad (15.14.23)$$

where PFZ_2 is the average precipitate free zone length along the grain boundary in the given area and PFZ_1 is the average precipitate free zone length along the grain boundary for the area that contains the highest hardness. GI is the difference between the average secondary phase or precipitate within the grain for a given area and the average secondary phase or precipitate within the grain for the area that exhibits the highest hardness:

$$GI = GI_2 - GI_1 \quad (15.14.24)$$

where GI_2 is the average precipitate or secondary phase within the grain for a given area and GI_1 is the average precipitate or secondary phase within the grain for the area that contains the highest hardness.

The constants $C_{56\text{-}64}$ are material parameters that are calibrated to fit experimental data. As the value of a given constant is increased, the mechanical response for the given equation will decrease. The added equations will allow for the model to account for mechanical degradation exhibited in the material. To calibrate the modified ISV plasticity-damage model, the precipitate free zone length and precipitate and secondary phase size were evaluated for the highest and lowest hardness response areas. This was achieved through imaging TEM specimens from these areas. Then the model was calibrated to the mechanical response obtained from mechanical test specimens taken from the highest and lowest hardness response areas.

5.14.2 Results and Discussions

Microstructure

Figure 5.120 illustrates the microstructural morphology of the materials observed in this study. The AA5083-H131 wrought material displayed in Figure 5.120 (a), shows the microstructure in the rolling direction (RD) exhibited large, elongated grains, while the long transverse (LT) and short transverse (ST) directions both presented with a similar grain structure, still elongated, but with flattened pancake shaped grains. The wrought material had an average grain size of 250 μm. The AA5083 AFSD material, shown in Figure 5.120 (b), exhibited a refined microstructure with equiaxed grains and an average grain size of approximately 3 μm. Microstructure from the AA5083 AFSD longitudinal direction (LD), long transverse (LT) direction, and build direction (BD) all exhibited the highly refined, equiaxed grain structure. The refinement of grain

morphology is due to the dynamic recrystallization that occurs during the AFSD process[65]. Dynamic recrystallization is induced through the severe plastic deformation inherent to AFSD, allowing for the nucleation and growth of new grains to occur during the thermomechanical process.

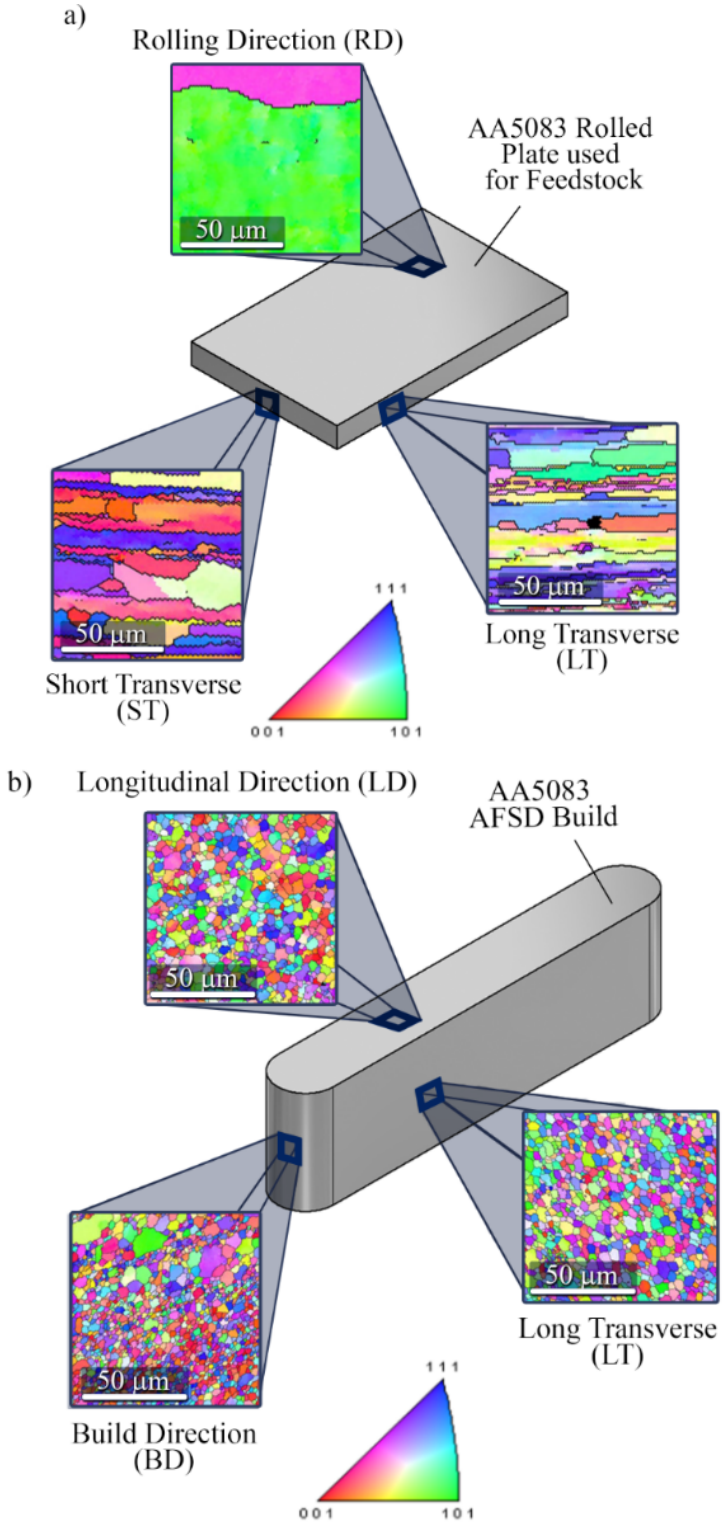

Figure 5.120 Representative grain structure of a) AA5083-H131 rolled plate wrought control in RD, ST, and LT directions and b) AFSD As-Deposited in LT, LD, and BD directions.

Compression Test Results

Figure 5.121 displays a representative sampling of raw data associated with the high rate performance of the AA5083-H131 wrought control material. The oscilloscope trace displays the amplified strain gage output voltage for the incident (blue dashed line), transmitted (red solid line), and reflected (green dotted line) waves in Figure 5.121 (a). The peak voltage registered from the strain gages by the DAQ was approximately 10 V for the transmitted, 3 V for the incident, and -2 V for the reflected. The voltage was converted to strain using a calculated [299] strain-to-voltage factor of 0.000614 e/V for the incident and reflective waves and 0.0001228 e/V for the transmitted wave. As shown Figure 5.121 (b) the incident experienced a strain of 0.002 mm/mm on average, the transmitted 0.001 mm/mm with a gradual slope upward toward 0.00125 mm/mm, and then a strain of 0.001 mm/mm trailing down to 0.005 mm/mm was reflected onto the incident bar. Specimen barreling is a common occurrence in compressive deformation. Friction between the compression platens and the specimen causes a delay in material flow, resulting in a bulging (or barreling) toward the center of the specimen. Adiabatic shear banding is a dynamic failure mechanism where shear bands are formed due to increased temperature and localized shear during high strain rate loading, and results in failure. Neither specimen barreling, nor adiabatic shear bands were observed during HRC of AA5083-H131, as has been observed in previous studies[300], [301], likely due to the lubricant applied on either end of the specimen to reduce frictional effects and the specimen geometry[302].

Looking at Figure 5.121 (b), the incident pulse exhibits the characteristic trapezoidal shape of the SHPB. Oscillations visible at the top of the incident wave in Figure 5.121 (b) are the result of wave dispersion, caused by a relatively small amount of stress from the compressive wave radiating outward in the radial direction in addition to the primary axial direction. The wave with a higher frequency has a tendency to lag behind the wave with a lower frequency, resulting in what is known as Pochhammer-Chree oscillations, producing a distorted waveform[303]. The dispersions are not as severe in the transmitted wave as the ductile specimen acts as a filter. The incident pulse shown in Figure 5.121 (b) presents a constant strain, aside from dispersions, of 0.002 mm/mm. As the wave flows through the specimen, a slight change in the shape of the wave is observed as it enters the transmitted bar. The transmitted wave shown in Figure 5.121 (b) exhibits an initial strain of 0.001 mm/mm and settles out a relatively constant strain of approximately 0.00125 mm/mm. This change is likely due to a small amount of strain hardening occurring in the AA5083-H131 specimen.

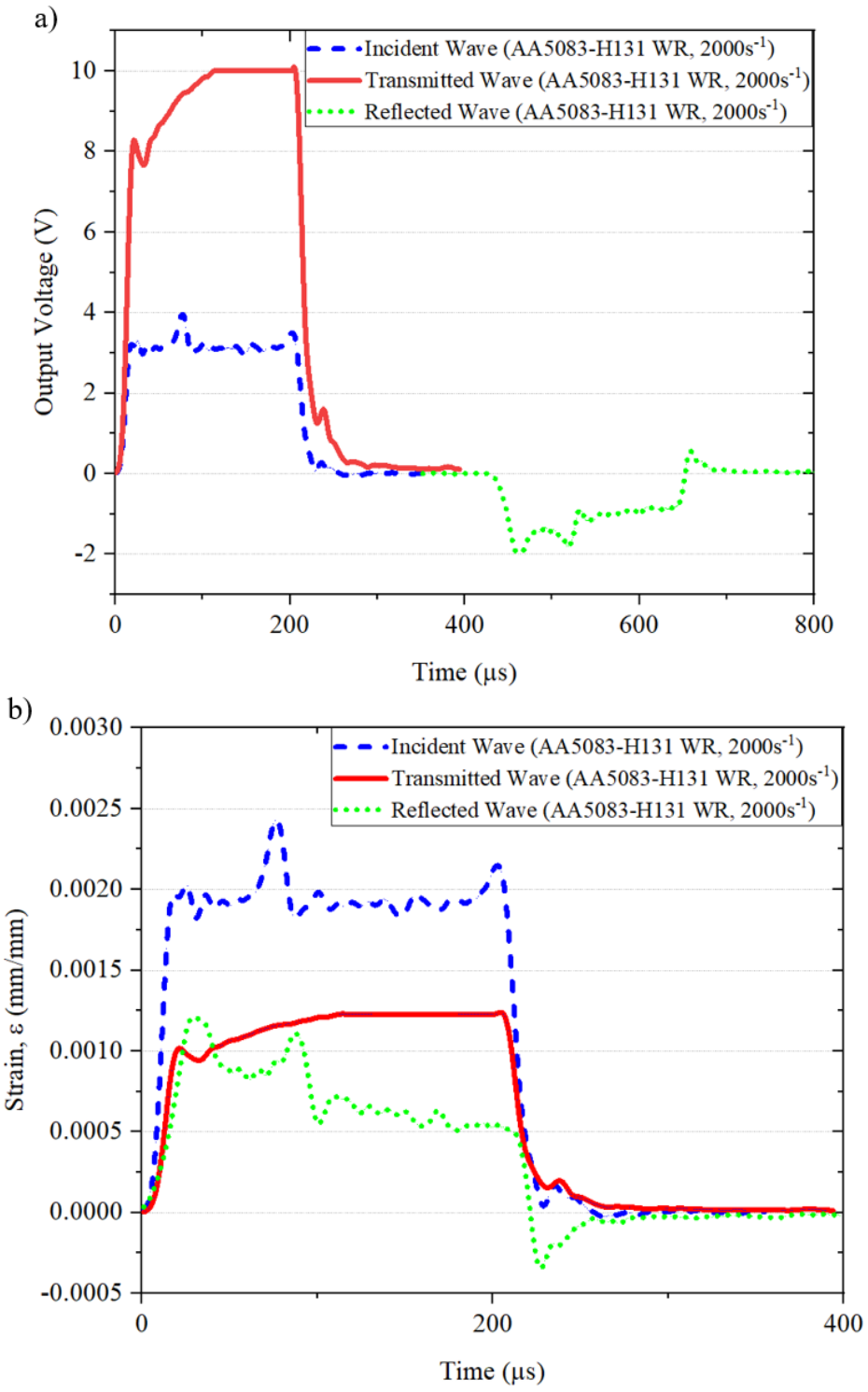

Figure 5.121 Representative sampling of raw data for AA5083-H131 wrought control including an a) oscilloscope trace displaying the amplified strain gage output voltage for the incident, transmitted, and reflected waves and b) oscilloscope trace converted to strain using strain-to-voltage factor 0.000614 e/V for incident and reflective waves and 0.0001228 e/V for transmitted wave.

Figure 5.122 displays a representative sampling of raw data associated with the high rate performance of the AA5083-AFSD material. The oscilloscope trace displays the amplified strain gage output voltage for the incident (blue dashed line), transmitted (red solid line), and reflected (green dotted line) waves in Figure 5.122 (a). The peak voltage registered from the strain gages by the DAQ was approximately 10 V for the transmitted, 3 V for the incident, and -2 V for the reflected. The voltage was converted to strain using the same calculated strain-to-voltage factor as in the wrought experiment of 0.000614 e/V for the incident and reflective waves and 0.0001228 e/V for the transmitted wave. As shown Figure 5.122 (b) the incident experienced a strain of 0.00175 mm/mm on average, the transmitted 0.0075 mm/mm with a slope upward toward 0.00125 mm/mm, and then a strain of 0.0015 mm/mm trailing down to 0.005 mm/mm was reflected onto the incident bar. It is also shown in Figure 5.122 (b) that the specimen was unloaded after approximately 200 s. Neither specimen barreling nor adiabatic shear bands were observed during HRC of AA5083 AFSD-LT, -LD, or -BD.

The incident pulse for the AA5083 AFSD HRC loading, shown in Figure 5.122 (b), is nearly identical to that of the AA5083-H131 experiment, presenting with the same incident wave dispersions. The transmitted wave, as displayed in Figure 5.122 (a), appears to have less of an initial spike in the dispersions and a larger slope increasing in voltage (5V–10V as opposed to 8V-10V as was observed in AA5083-H131). The variance in voltage corresponds to the increase in strain observed in the transmitted bar. The increase in strain from 0.005 mm/mm to ultimately 0.00125 mm/mm indicates additional strain hardening occurs in the AA5083 AFSD specimen, over the slight strain hardening observed in the AA5083-H131 specimen seen in Figure 5.121(b).

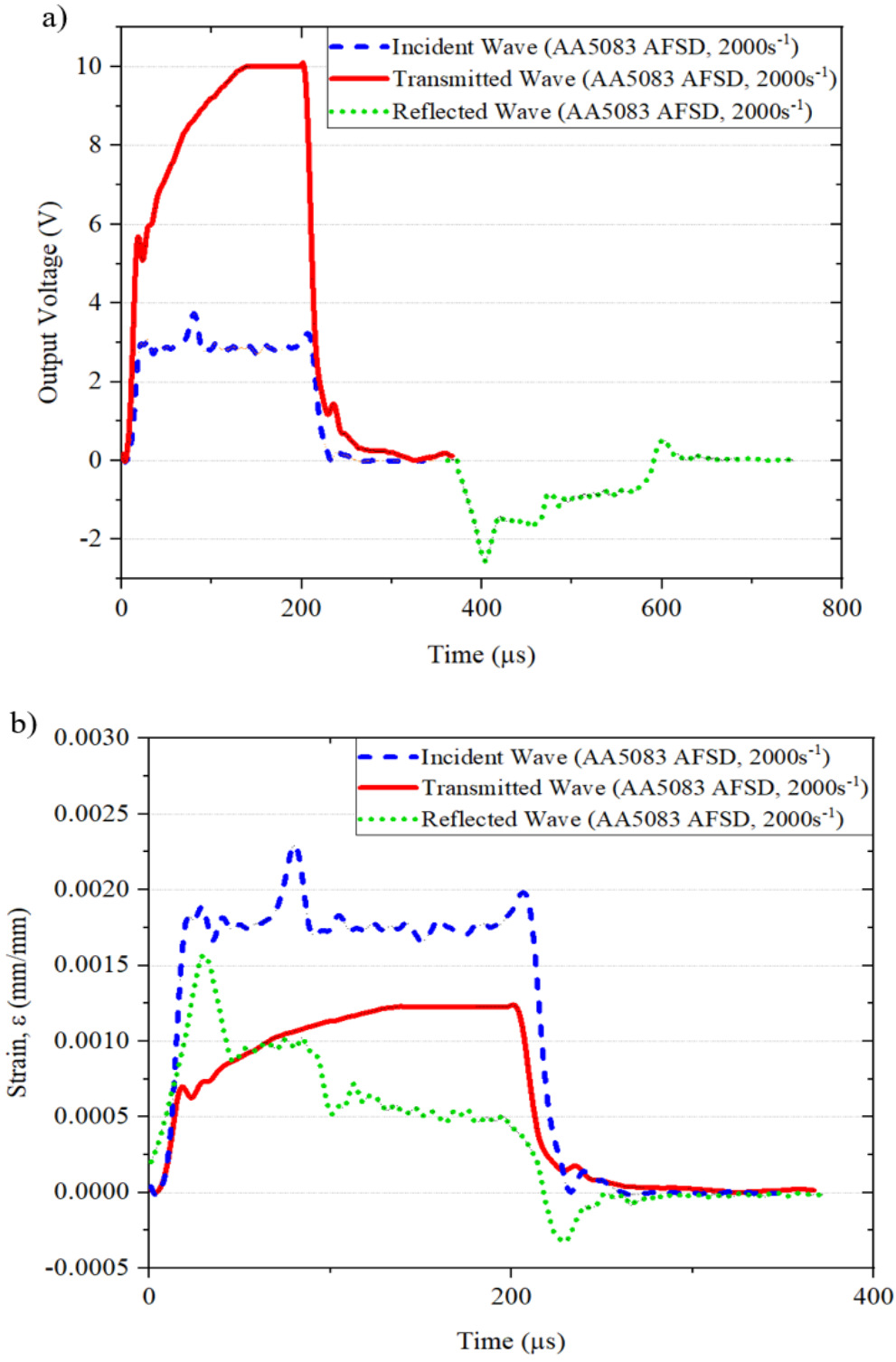

Figure 5.122 Representative sampling of raw data for AA5083-AFSD including an a) oscilloscope trace displaying the amplified strain gage output voltage for the incident, transmitted, and reflected waves and b) oscilloscope trace converted to strain using strain-to-voltage factor 0.000614 e/V for incident and reflective waves and 0.0001228 e/V for transmitted wave.

Figure 5.123 displays the results of the plastic deformation portion of the stress-strain response for AA5083-H131 and AA5083-AFSD-LT at room temperature for QSC ($0.001s^{-1}$), and AA5083-H131 and AA5083-AFSD-LT, -BD, and -LD at room temperature for and HRC ($2000s^{-1}$). The QSC of the AA5083-H131 wrought control (black solid line) exhibited very little strain hardening and a low ultimate stress of 304 MPa. The HRC response of the AA5083-H131 wrought control (black dotted line) showed slightly more strain hardening than in the QSC condition with an ultimate stress of 440 MPa. The AA5083-AFSD material presented with significantly more strain hardening for all directions in the HRC condition with ultimate flow stresses presented as follows: AA5083 AFSD-BD = 316 MPa, -LT = 373 MPa, and -LD = 388 MPa. The QSC response of AA5083 AFSD-LT exhibited similar strain hardening to what was observed for that direction in HRC, with an ultimate stress of 296 MPa. The AA5083-H131 wrought control exhibited a yield strength of 270 MPa under QSC, while the AA5083 AFSD-LT material exhibited a yield strength of 175 MPa. These results were congruent with a concurrent tensile study of AA5083 AFSD.

The results from the QSC and HRC for both the AA5083-H131 wrought control and the AA5083 AFSD material indicated both AA5083-H131 and AA5083-AFSD experienced positive strain rate sensitivity. Flow stress was observed to increase with increasing strain rates. The AA5083-H131 wrought control exhibited very little strain hardening due to the -H131 temper already applied to the material through a rolling process that increases dislocation wall strengthening and increases the strength of the material, leaving little room for additional strain hardening. The increased strain hardening in the AA5083 AFSD materials was expected due to the loss of critical strengthening mechanisms due to the thermo-mechanical processing of AFSD. It is likely that the grain boundary strengthening replaced dislocation wall, solution, and precipitation strengthening as the dominant and primary strengthening mechanism. Initially, when the compression loading began, the strength exhibited by the AA5083 AFSD is almost fully dependent on the size of the grains. As the AA5083 AFSD specimens undergo compression, dislocation density increases. An increase in the dislocation density would inevitably cause an increase in the interaction of dislocations with grain boundaries, which inhibits the dislocation motion, driving the flow stress upward.

While the AFSD material exhibits an isotropic microstructure, an orientation dependence was observed for the flow stress. The AA5083 AFSD-BD material exhibited a flow stress that was, on average, 75 MPa less than the AA5083 AFSD-LT and -LD material. A further reduction in flow stress would be expected for the QSC of AA5083 AFSD-BD, but additional testing would be required for confirmation. The rate of strain hardening under HRC, however, appeared consistent regardless of orientation within the AFSD build.

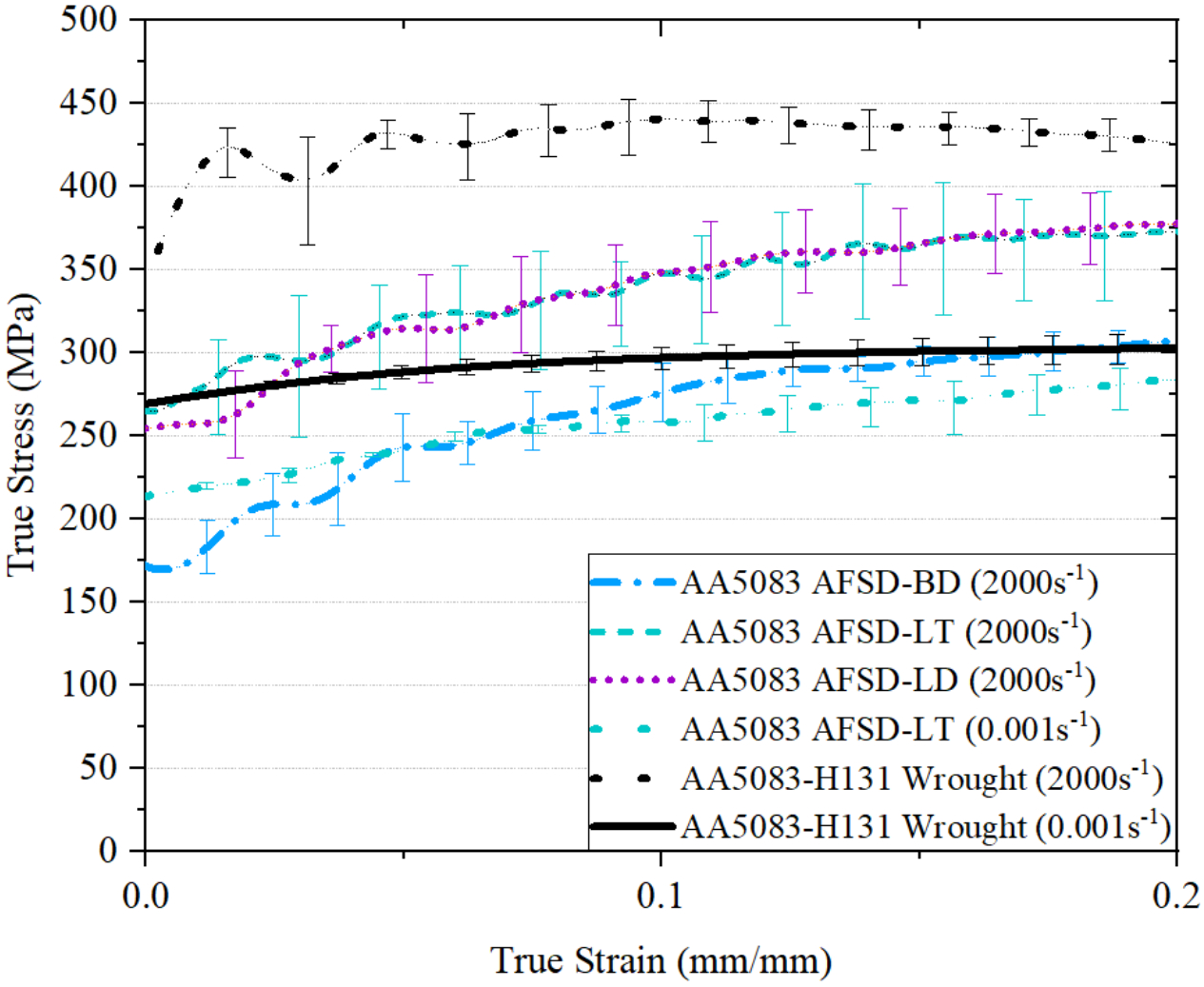

Figure 5.123 Plasticity stress-strain response for AA5083-H131 and AA5083-AFSD-BD, -LT, and -LD at room temperature for HRC ($2000s^{-1}$) and AA5083-H131 and AA5083-AFSD-LT for QSC ($0.001s^{-1}$) with error bars to represent the resultant range for each test condition.

Internal State Variable Modeling

As shown in Figure 5.124, the ISV model was able to capture the material behavior for both QSC and HRC and of AA5083-H131 and AA5083-AFSD materials at ambient temperature within the maximum and minimum ranges of the experimental data. While prior work in ISV modeling of AA5083-H131[107] was considered in selecting the plasticity constants for the ISV model, some variation was necessary to capture the unique history of experimental QSC and HRC loading, and was expected due to variance in mechanical performance of AA5083 AFSD material as compared to AA5083-H131. The evolution of flow stress, from yield to ultimate, was captured with the yield adjustment values and isotropic hardening values for both the AA5083-H131 wrought control and AA5083 AFSD. The compressive loading forces dislocation movement and this behavior was captured with the dynamic kinematic recovery coefficient in both materials as well. A reduced dynamic recovery rate was assumed for the AA5083 AFSD material, based on prior research by McCullough et al.[163] who determined an annealed AA6061 exhibited a lower dynamic recovery rate due to recrystallization along with some solutionizing that occurred during annealing. AFSD presents similar characteristics to annealed materials due to the severe plastic deformation and thermal cycling from successive deposited layers. Therefore a similar approach was taken for AA5083 AFSD.

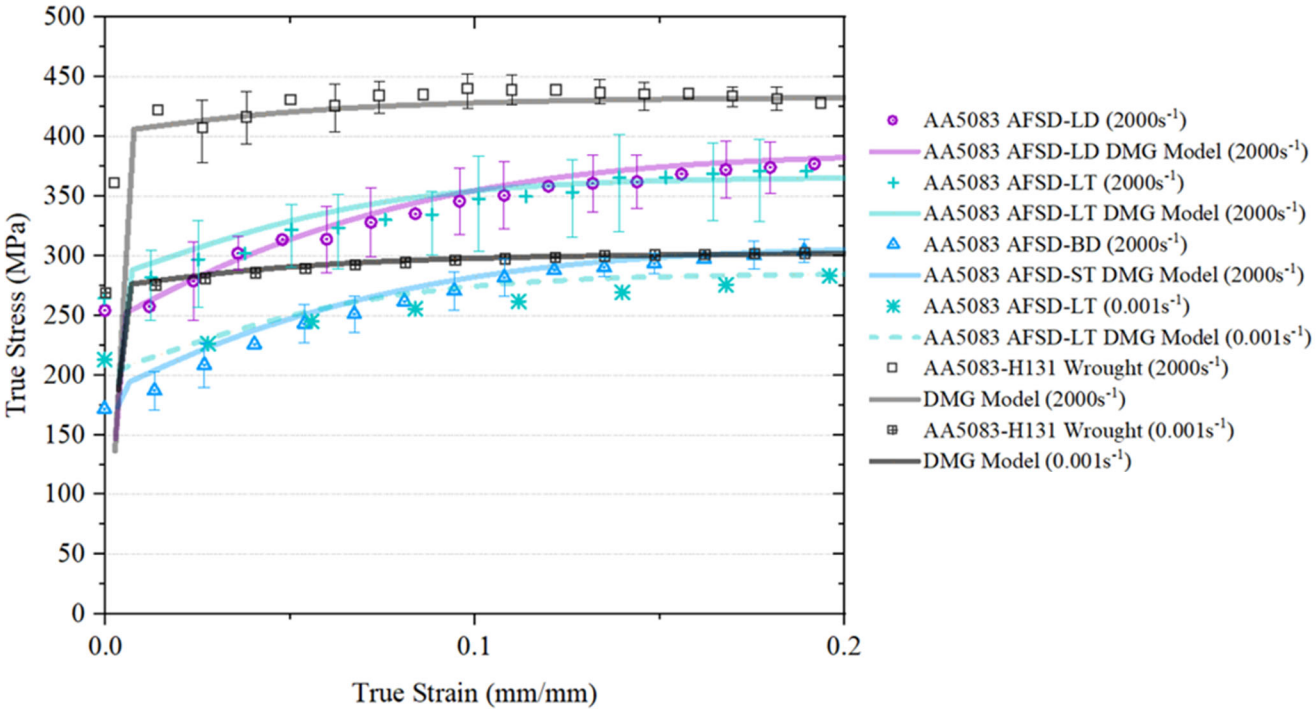

Figure 5.124 Comparison between ISV plasticity-damage model prediction and experimental data for a) QS compressive response at room temperature for AA5083-H131 wrought material and AA5083-AFSD-LT and b) HR compressive response at room temperature for AA5083-H131 wrought material and AA5083-AFSD-LT, -ST, and -LD directions.

The modeling parameters used to model the stress-strain dependence of the AA5083-H131 wrought control, AA5083 AFSD-LT, -LD, and -BD materials, capturing both the quasistatic and high rate compression behavior for each material with one set of constants, can be found in Table 5.14.2.

Table 5.14.2. ISV model parameters

	Constants	AA5083-H131 Wrought	AA5083 AFSD-LT	AA5083 AFSD-LD	AA5083 AFSD-BD	Units
Elastic and Thermal Constants	*Shear modulus, G*					MPa
	Bulk Modulus, K					MPa
	Init. Temperature	297	297	297	297	K
	Heat Gen. Coeff.	0.34	0.34	0.34	0.34	
Yield & yield adjustment constants	*C1*	9	6	6	6	MPa
	C3	260	200	200	100	MPa
	C5	0.005	0.005	0.005	0.005	1/MPa
Kinematic hardening & recovery constants	*C7*	0.6	0.05	0.05	0.05	1/MPa
	C9	100	100	100	500	MPa
Isotropic hardening & recovery constants	*C13*	2	2	2	2	1/MPa
	C15	100	500	500	500	MPa
Hardening & recovery constants	*Ca*	0	0	0	0	
	Cb	-0.05	-0.05	-0.05	-0.05	
McClintock void growth	*Void Growth Exp.*					
	Initi. Radius					
Dynamic Recovery						
Long Range Isotropic	*C21*	0	0	0	0	
Long Range Kinematic	*C23*	600	300	300	300	
Long Range Kinematic Static	*C25*	0	0	0	0	

* *C2, C4, C6, C8, C10, C12, C14, C16, C18, C20 = 0.*

Additionally, to capture the layer dependence with the ISV material model. The as-deposited AA6061 AFSD tensile results discussed in Section 5.4 were compared to model predictions for the different longitudinal bottom and top layer tensile experiments in Figure 5.125a and Figure 5.125b for the original ISV and modified ISV, respectively.

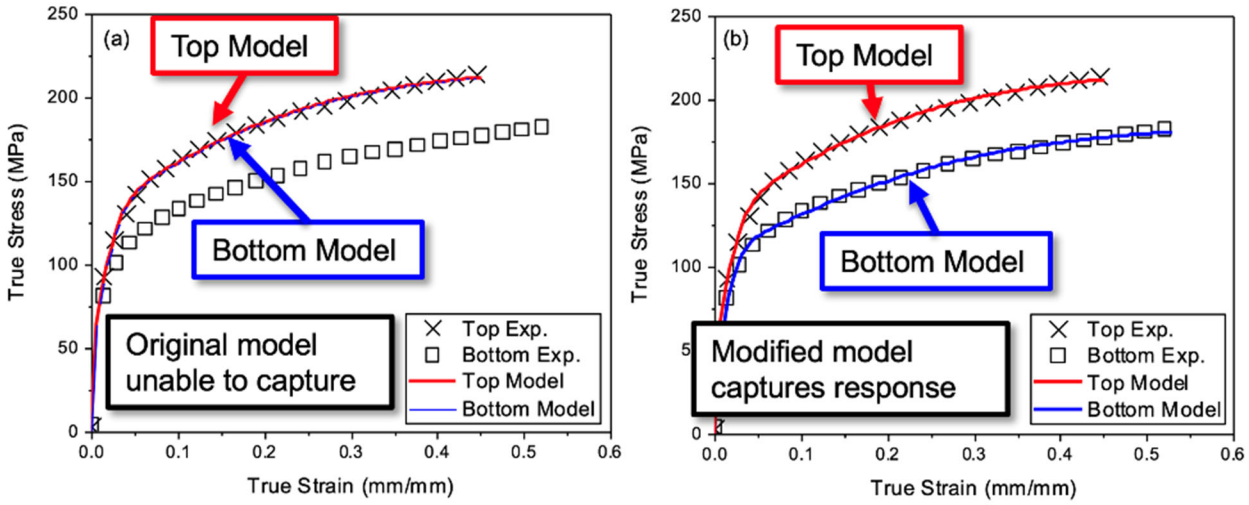

Figure 5.125 Comparison between the modified ISV plasticity model prediction and the experimental data for AFSD AA6061. **(a)** Comparison between the Original ISV plasticity model prediction and experimental data under the top and bottom longitudinal orientation. **(b)** Comparison between the modified ISV plasticity model prediction and experimental data under top and bottom longitudinal orientation able to capture the material behavior.

These modifications to the ISV plasticity-damage model as shown in Figure 5.125 resulted in a significantly more accurate prediction of the mechanical response of the as-built AFSD material that exhibited a mechanical gradient while using a universal set of material constants. Thus, the contribution of modified ISV plasticity-damage model provides a modeling pathway to capture the complex mechanical behavior gradients that can be exist in solid-state additive processes such as AFSD.

5.14.3 Conclusions

The objective of this study was to quantify the process-structure-property-performance relationships in order to elucidate the effect of thermomechanical processing on the strain-hardening observed in QSC and HRC of AFSD AA5083. Based on the results in the present study, the following conclusions can be drawn:

1. The AFSD process promoted a refined, equiaxed grain structure in the AA5083 AFSD material in the -LT, -LD, and -ST directions. The elongated 250 mm grains reduced to an average size of 3.2 mm through dynamic recrystallization inherent to the AFSD process.

2. Compression loading was performed for AA5083-H131 wrought control and AA5083-AFSD at a high rate condition ($2000s^{-1}$) and at a quasistatic condition ($0.001s^{-1}$) to evaluate the dependence of mechanical performance of AA5083 AFSD on strain rate. The results revealed increased strain hardening in AA5083 AFSD material over AA5083-H131. The increase was attributed to the exchange in strengthening mechanisms brought about by the dynamic recrystallization of the AFSD process that removed critical strengthening mechanisms and lessened dislocation density in an exchange for smaller grain sizes to promote grain boundary strengthening. The rate of strain hardening for the AA5083-H131 was consistent between QSC and HRC. Similarly, the rate of strain hardening of AA5083

AFSD in QSC was analogous to the HRC. The results from the compression loading also revealed that the AA5083-H131 wrought control and AA5083 AFSD-LT exhibited an increase in flow stress response with strain rate, indicating a positive strain rate sensitivity from the QS to the HR regime.

3. The ISV model was successfully calibrated for the AA5083-H131 wrought control as well as the unique history of the AA5083 AFSD-LT, -BD, and -LD materials as well as the AA6061 tensile data capturing builds exhibiting differences between loss of strengthening mechanisms between bottom and top layers.

Future work will include additional strain rates for the AA5083-H131 wrought control and AA5083 AFSD-LT, -BD, and -LD materials and experiment with pulse-shaping to provide a more thorough understanding and additional experimental data for ISV model calibration.

5.15 Airfield Landing Mat Strip Feedstock for Point-of-Need Manufacturing and Repair of Airfield Landing Mat Skin Punctures

In this work, the Direct Additive Recycling (DAR) paradigm of using damaged aluminum alloy (AA) components for Point-of-Need additive manufacturing and repair has been investigated through a multi-scale experimental approach. Specifically, X-ray Computed Tomography (CT) compared Additive Friction Stir Deposition (AFSD) deposits fabricated in open atmosphere from new AA6061 solid rod feedstock and a secondary feedstock from discrete stacked AA6061 strips extracted from damaged expeditionary airfield landing mats. The X-ray CT for both depositions showed fully dense builds regardless of solid rod or stacked strips feedstock. Vickers hardness maps of the deposited cross-sections and optical microscopy confirmed similar hardness and grain sizes for both depositions. Additionally, strips were extracted from damaged airfields mats to use as a secondary feedstock to repair simulated forklift puncture damage on the aluminum airfield mat core top extrusion skin. Four-point bend experiments of the repaired mat core confirmed no knockdown in performance when compared to new mat core four-point bend results. These results provide a starting point for the scientific community to begin assessing this new DAR paradigm for using battle-damaged material as secondary feedstock for Point-of-Need Manufacturing and Repair that eases logistic burdens. The paradigm also eliminates the challenges of high energy, atmosphere requirements, and/or powder handling requirements typical of some other AM processes.

In Figure 5.125, the DAR paradigm is described through this Point-of-Need Manufacturing and Repair Methodology for secondary feedstocks, specifically, battle damaged components such as expeditionary aluminum airfield matting (AM2) that also complements recycling of machine chips as previously reported by Jordon et al.

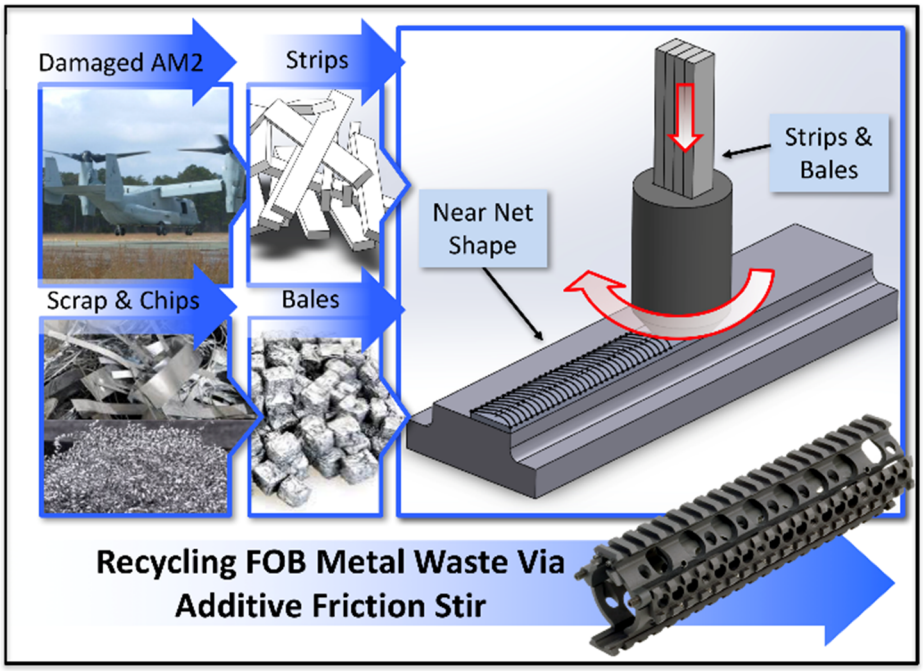

Figure 5.126 The Direct Additive Recycling (DAR) paradigm for recycling secondary feedstocks at forward operating bases (FOBs) processed through the Additive Friction Stir Deposition (AFSD) process.

Since the AFSD process depicted in Figure 5.125 is a low-power open atmosphere process that operates with similar technical skill to CNC machines. The process deposits the feedstock material (solid rod, discrete strips, compacted machine chips) through a hollow rotating tool layer-by-layer. This process is then able to make new components from the secondary feedstocks or even use the secondary feedstocks to repair broken or damaged components. Inherently, AFSD takes advantage of depositing material in the solid state, therefore, avoiding melt pool challenges typical to fusion-based processes.

The successful depositions of the recycled airfield matting feedstock is depicted in Figure 5.127 where the as-deposited morphology is compared between the secondary feedstock (damaged matting stacked strips) and the new solid rod feedstock AFSD builds. The airfield landing mats were previously tested as discussed by Rushing et al. For ease of laboratory machining, the strips were machined from smaller section using a water-jet cutting machine. The paint and non-skid coating was removed from the aluminum strips by using a handheld grinder.

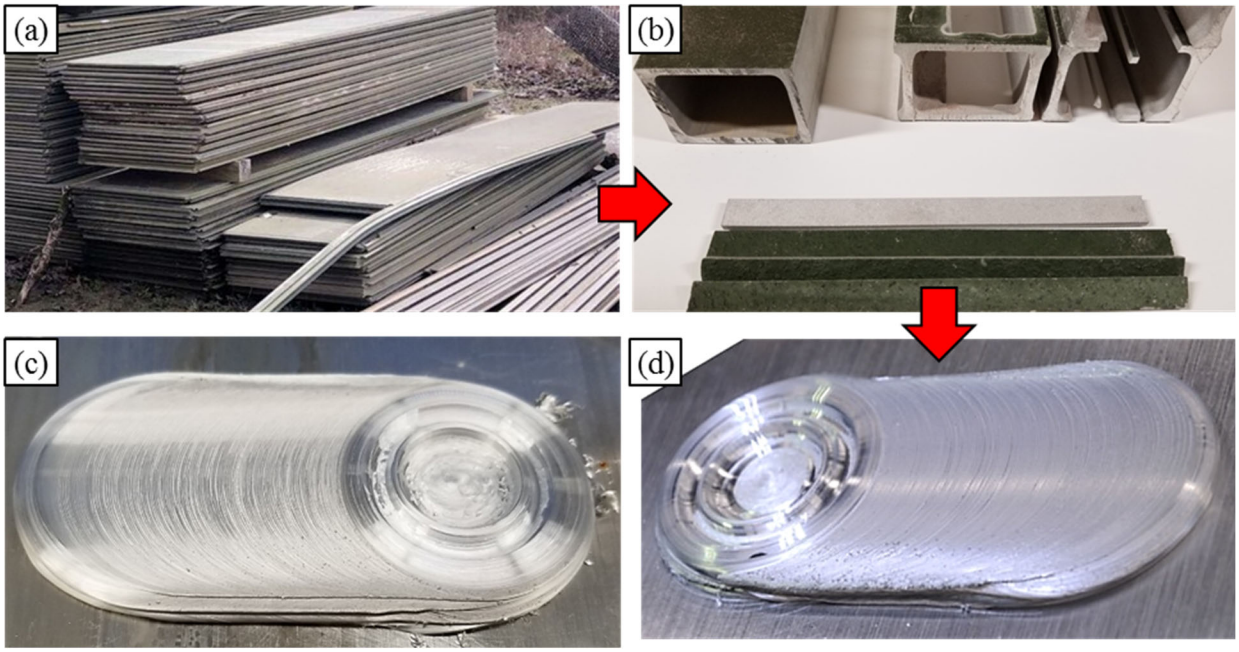

Figure 5.127 a) Battlefield scrap serving as bulk feedstock stream for subsequent deposition. b) Scrap recycled into compatible geometry for AFSD feedstock. c) Deposition using solid virgin material. d) Deposition using recycled strips from battlefield scrap. Both depositions exhibit similar build morphology and surface finish.

Using the same process parameters for an AA6061 deposition detailed in Phillips et al. that provided minimum flash or galling produced a similar four-layer deposition made from the recycled stacked strips in Figure 5.127b. The strip deposition was compared to the four-layer solid rod feedstock deposition in Figure 5.127c. Visually, the depositions appear very similar regardless of the use of recycled stacked strips feedstock or a monolithic solid rod feedstock.

Next, X-ray CT assessed the internal structure of the deposition fabricated from the discrete strips feedstock that is compared to the solid rod feedstock deposition is shown in Figure 5.128.

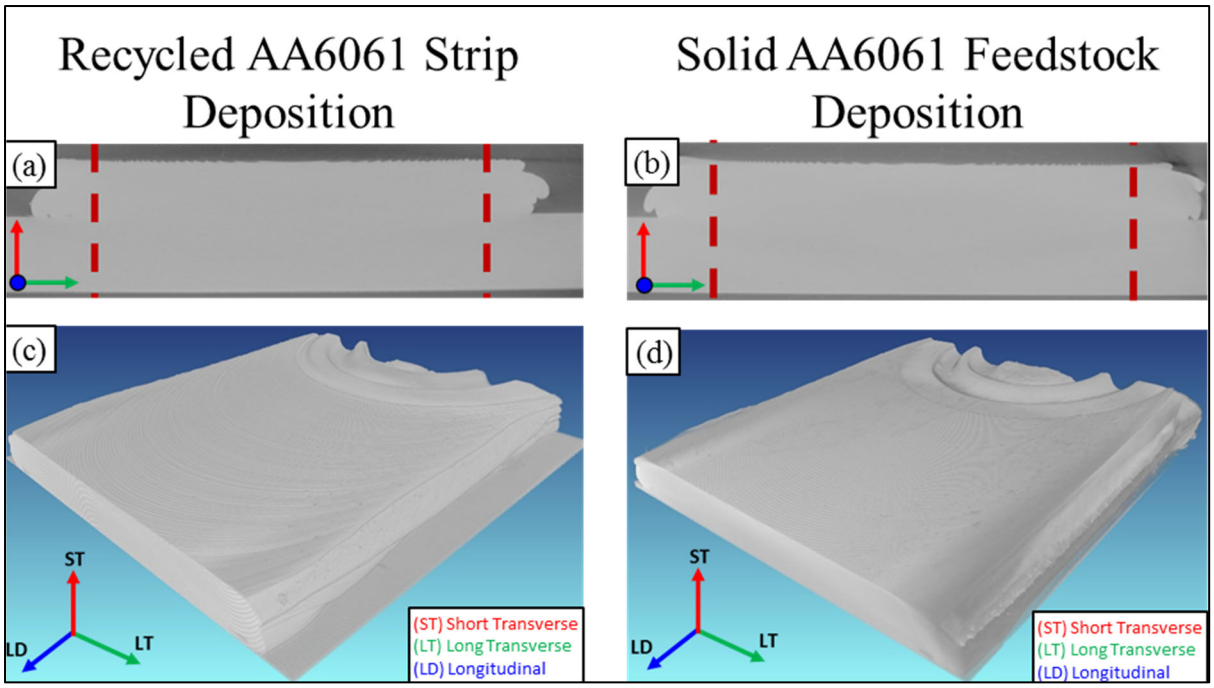

Figure 5.128 a,b) Cross-sectional X-ray CT confirming fully dense deposition for a) recycled strip deposition and b) solid feedstock deposition. c,d) Isometric X-ray CT confirming full density within near net shape deposit for c) recycled strip deposition and d) solid feedstock deposition.

X-ray CT results in Figure 5.128 shows cross-sections for both the stacked strip and solid rod feedstock depositions with fully dense builds within the near net shape additive builds. Additionally, the 3D scan view looks identical between the two feedstock depositions in Figure 5.128.

The EBSD results are compared in Figure 5.129 for the solid rod deposition and the recycled stacked strip deposition to assess the grain size and morphology.

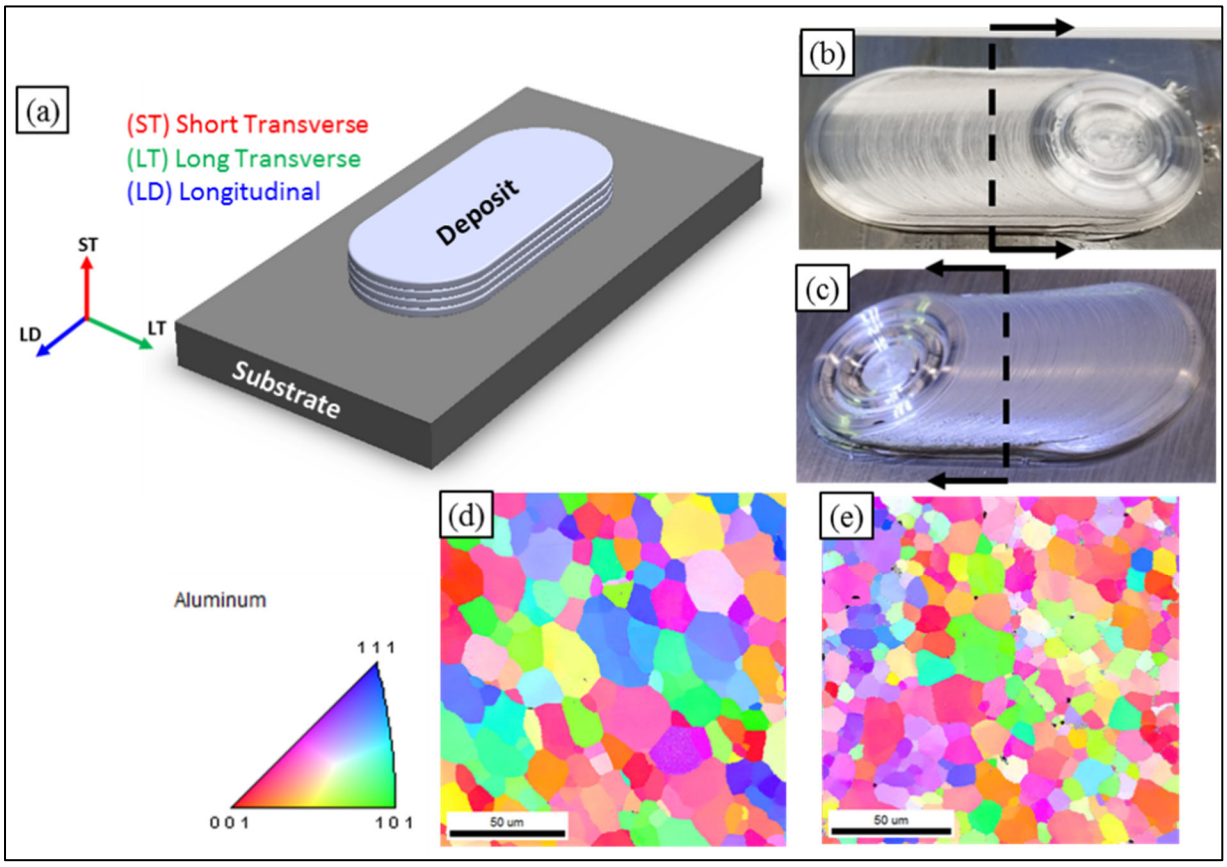

Figure 5.129 a) Schematic depicting the three principal directions of the deposit. b) Deposition utilizing solid feedstock. c) Deposition utilizing recycled stacked strips. (d,e) Representative Electron Backscatter Diffraction at denoted locations in d) solid feedstock deposition and e) recycled stacked strip deposition.

The EBSD analysis in Figure 5.129 confirmed a 15µm equiaxed grain structures evident in both deposits refined from the +100 µm feedstock grain size. Additionally, Vickers microhardness maps where performed on the material cross-sections. The as-deposited hardness for the solid rod depositions was 60.8 ± 3.2 HV and the recycled strip deposition hardness was 55.6 ± 4.0 HV. This correlates to near identical average hardness values between the two deposits when accounting for the scatter within the data.

As we envision transitioning this AFSD technology out of the lab and to manufacturing in austere locations such as FOBs, the types of damage such as a forklift blade puncture in the airfield matting skin is visually portrayed in Figure 5.130.

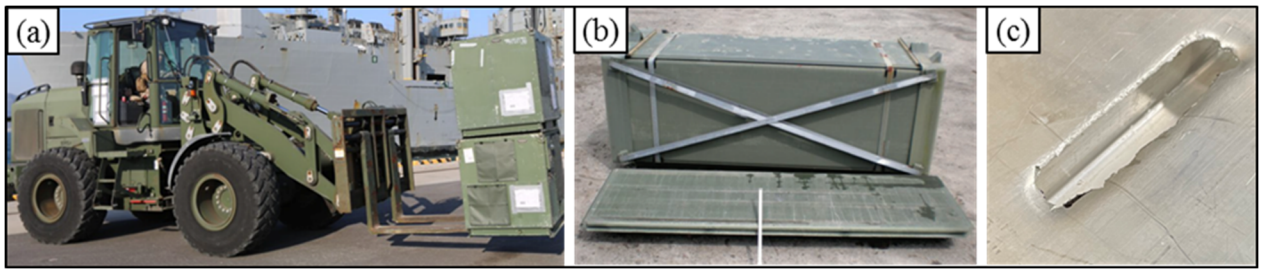

Figure 5.130 a) Representative 44.5 kN rough terrain forklift used to transport mat bundles [304] b) Typical mat bundle configuration [305] c) Simulated fork puncture in mat skin.

The forklift blade puncture shown in Figure 5.130 is a representative damage occurring in the field when the airfield matting is getting deployed at FOBs. These types of damage are currently not repaired in the field and render that matting panel useless since that damage could potentially be detrimental to an aircraft tire and makes the panel no longer water-tight. It should be noted that comparable skin damage can also occur due to arresting system cable rollovers or tailhook impacts during landing operations, and the repair methodology outlined below is similarly applicable to these damage mechanisms.

Therefore, Figure 5.131 depicts the sequence of operations to repair the damage puncture in the matting skin by depositing the same exact aluminum alloy material to repair the damage.

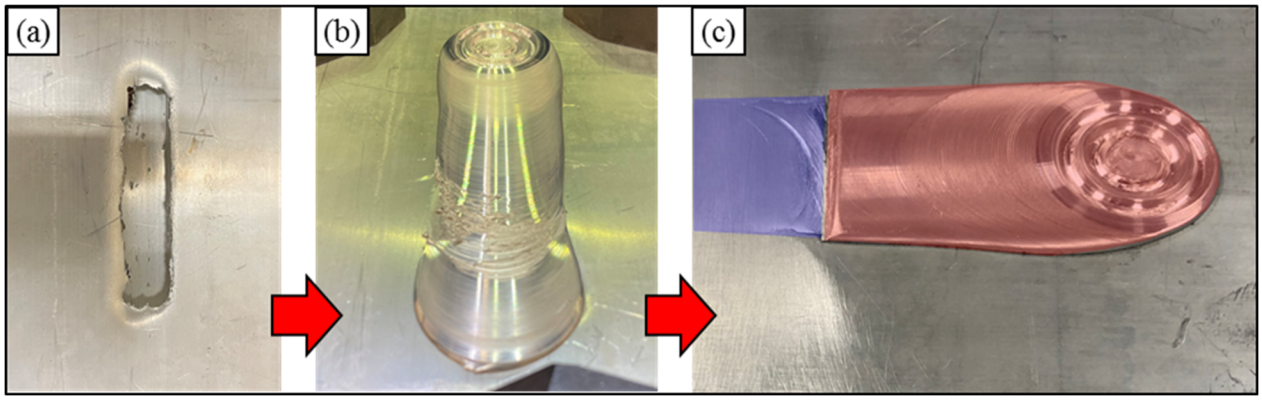

Figure 5.131 a) Skin damaged component fixtured in machine for repair. b) Repaired skin damage after solid-state deposition of material. c) As-deposited material (red) and post-deposition machining (blue) to restore original component geometry.

The repaired puncture in Figure 5.131 has the benefit of being repaired with the same exact filler material that eliminates galvanic coupling that could occur for repairs with dissimilar filler material. Additionally, after machining of the deposit back to the matting surface tolerance the damaged section is not able to be visually observed (Figure 5.131c). Additionally, without having to deal with challenges of melt pools and filler material in the liquid phase the large gaps of the simulated forklift puncture are able to be fully repaired.

To quantify the repair performance, the repaired mat compared to new matting material through a sub-component four-point bend analysis is shown in Figure 5.132 with the load-displacement results and corresponding test set-up insert.

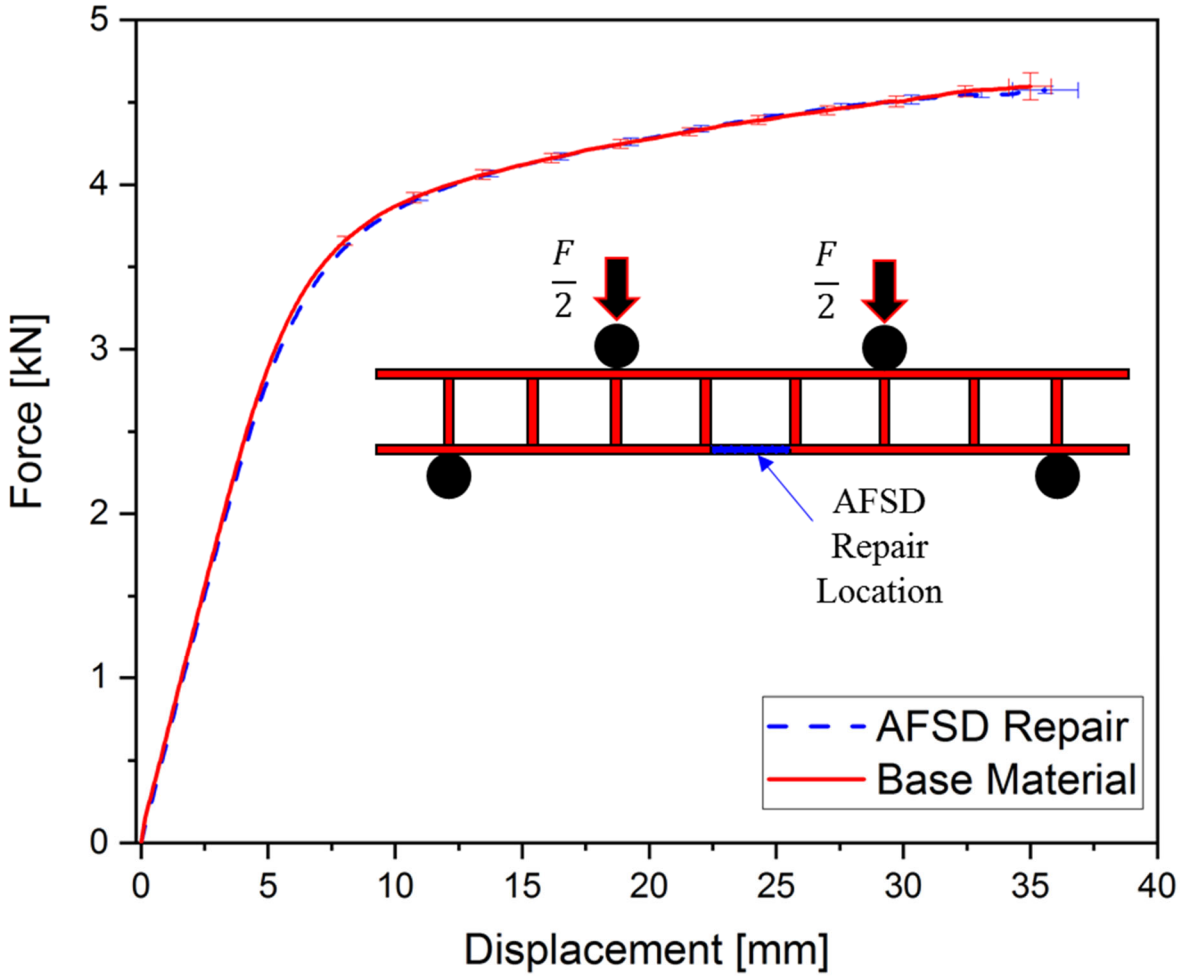

Figure 5.132 Subcomponent four-point bed results depicting similar mechanical behavior between new matting (Base Material) and repaired matting (AFSD Repair) cross-sections. The experimental setup and location of the repair is denoted schematically within the graph. The cross-sectional geometry of the component is not publicly available and has therefore been omitted.

The results comparing the new mat base material and the repaired mat core show similar behavior that highlights the benefits of this solid-state, low-heat input, nature of this process for repair of components. By taking advantage of depositing the recycled material below the melting point of the material, the repair allows for minimal distortion and minimized loss of strength to the component at the continuum scale.

In conclusion for recycling of secondary feedstocks, the X-ray CT confirmed the deposited material is fully dense, regardless of whether the feedstock is a solid rod or stacked strips of material. The resulting high magnification SEM/EBSD images also depict the robustness of this processing approach for AM and repair by confirming a uniform as-deposited grain refinement and morphology with Vickers hardness experiments also confirming similar behavior for both the stacked strip feedstock deposition and solid rod feedstock deposition. As we want to transition recycling of secondary feedstocks for Point-of-Need Manufacturing and Repair, the research here showed that large damaged sections such as forklift punctures in extruded skins of mat cores are able to be successfully repaired by the exact same material that eliminates corrosion challenges from dissimilar filler material repairs. Additionally, by using a solid-state process with low heat input when compared to traditional fusion-based approaches, the repair does not vaporize alloying elements or distort/damage the component being repaired.

6. CONCLUSIONS AND IMPLICATIONS FOR FUTURE RESEARCH

This research was the first investigation into assessing a Direct Additive Recycling (DAR) paradigm for multiple waste streams (machine chips and damaged scrap). This program completed the objective of understanding and confirming the viability of AFSD to use these waste streams to fabricate fully-dense components with robust material performance.

Specifically, the AFSD process has been demonstrated to breakup inclusions and constituent particles resulting from the high shear stresses and frictional heat generated, which is necessary for dispersion of any surface contaminants that hinder attaining a robust metallurgical bond between deposited layers.

Furthermore, the AFSD process does not suffer from significant tool wear issues for aluminum and magnesium alloys since the AFSD feed rod is consumed during the deposition. Additionally, due to AFSDs low power input (~5 kW), scalable in an ambient environment, capable of using a variety of materials as rod or powder, and independent of secondary processing, the near-net shape AFSD process provides a new path for reducing cost by alleviating the need for Hot Isostatic Press (HIP), and HAZ rework. Additionally, one of the greatest advantages of the solid-state AFSD process is the wide array of deposited materials available as well as the ability to join or repair dissimilar materials and produce functionally graded components. Additionally, maximum temperatures during this process are maintained well below the liquidous state ($T_d < T_m$) of the respective deposited material, preventing phase transformation during the deposition. Additionally, the lower temperatures during deposition allow for a lower amount of distortion for the substrate, in comparison to fusion-based additive manufacturing techniques, e.g.laser powder bed fusion (L-PBF) and EBM. The lower severity of thermal cycles reduces the residual stresses within the deposition and substrate, thus, residual stress induced distortion is minimized. The quality of the desired microstructure and fabrication rates are established through flexible process parameters such as spindle geometry, spindle speed, deposition rate, and substrate traversing rate.

Differences from Other Processes (Advantages, Disadvantages)

However, it is important to note that although AFSD may provide increased deposition rates in an open atmosphere (certain materials like Ti alloys require shielding) with low energy. Finish machining is required since components are generally more near net-shape with a comparison of build accuracy to deposition rates provided in Figure 6.1 that compares AFSD, DED, and PBF.

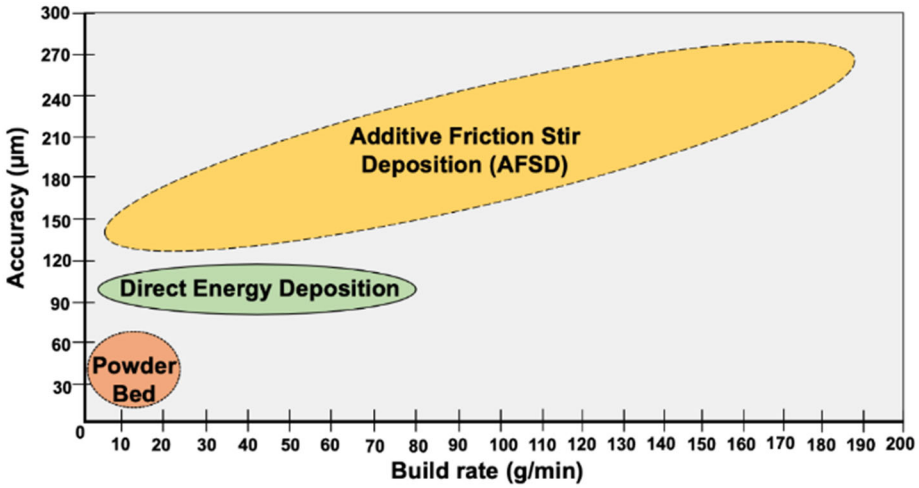

Figure 6.1 Comparison of build accuracy versus build rates for additive friction stir deposition (AFSD), powder bed, and direct energy deposition.

The current nascent state of the AFSD technology is commercially available from MELD Manufacturing that is constrained to square cross-section feedstocks. The process is controlled via operator written, traditional CNC G-code via the commercial MELD Manufacturing software, which translates the machine code into 3-axis movements and deposition rates. During operation, the software generated timestamped machine feedback at 1Hz is subsequently analyzed for temporal and material consumption examination. Tabulated position data for the machine head and linear actuator are determined by position sensors located in the AFSD machine, which are used to determine absolute distance and material consumption. Although not equipped to provide feedback control, force measurements are recorded at 1 Hz via electrical current required to maintain feedstock deposition velocity.

Companies such as Bond Technologies provide alternative AFSD machine platforms, referred to by Bond Technologies as Friction Stir Additive Manufacturing (FSAM), machine platforms that are now capable of depositing both round and square feedstock. These machines run off the same FSW platforms Bond has been providing to customers for several years, but now create a Hybrid AFSD machine capable of FSW, AFSD/FSAM, and machining with temperature and force feedback controls complementing displacement control processing.

Generically, the variable process parameters are tool geometry, spindle speed, filler feed rate, and substrate traverse rate. The tool design has been shown to have a large impact on the deposited layer thickness, and thus the volumetric deposition rate. The next most significant process parameter controlling the volumetric deposition rate is the traverse rate. The maximum traverse speed for a defect-free deposition is a function of tool design, filler feed rate, and spindle speed. The spindle speed is the most significant parameter in controlling the temperature for a given tool; on the other hand the filler feed rate is the most significant parameter in controlling the pressure for a given tool plunge depth. Hence, the interdependent process parameters need to be optimized for a given tool design to maximize the deposition rate for each material.

The procedure to produce deposits are methodological and can be summarized into individual steps by both the operator and machine. It is important to outline the various interactions to elucidate the effects of time and material management. For solid rod depositions, a 305 mm long graphite coated metal rod is first loaded into the raised tool similar to muzzle loading. Next, the operator lowers the machine head onto the surface of the substrate and sets a manual origin. The tool is then raised to a reload position, typically away from the origin, where the operator inserts a prepared feedstock rod through the bottom of the tool. The machine is then returned to the relative origin and carefully lowered to a marginal distance just above the substrate. Upon checking for clearance, the operator initiates tool rotation at a desired rotational speed. Once at the given RPM (200 or 300 RPM for aluminum alloys), the operator lowers the tool into the substrate, where the tool begins stirring material via the face and teardrop protrusions; thus, generating heat and severe plastic deformation. The operator then engages the actuator feed mechanism at a specified velocity to steadily deposit the rod into the substrate, generating mechanical and metallurgical cohesion between the two surfaces. The slow initial feed rate permits heat to adequately transfer to the feedstock, reducing the flow stress as a function of temperature and softening the material for plastic flow to progress. As material begins to deform, steady force is achieved as material begins to deform and the tool is slowly raised, manually by the operator, to the specified layer height. Once at the specified layer height, the operator engages the G-code to drive machine movements until the completion of a layer. Upon layer completion, the tool disengages with the freshly deposited material by raising to a set distance above the deposit before moving to a reload position away from the deposit. Data acquisition is then terminated as a remaining quantity of feedstock is ejected from the bottom of the tool, completing the full layer production sequence. For a deposition requiring multiple rods of feedstock, the head is required to be raised to load a new 305 mm long graphite coated rod before the dwell and start sequence is initiated over again. Layers that began after a length of downtime greater than 30 minutes for material such as AA6061. It has been observed that additional material is generally required during the dwell process and upon the production of the first layer. The lengthier downtime is significant as the material is permitted to convectively cool. As a result, the machine must be supplied with additional energy over consecutive layers, whether by extending the dwell time or heating the deposit externally, to adequately provide the necessary thermal softening to promote plastic deformation of both the existing layer and feedstock.

As an additive process, it is imperative to be able to determine the necessary inventory of material required to produce a desired part. By using actuator position and velocity data, measurements of material consumption during deposition is possible. The two governing process parameters that define deposition rate are the actuator feed rate, which governs the velocity that material is extruded through the bottom of the tool onto the workpiece, and the tool traversing velocity. These two machine parameters can be related to the length of feedstock required to deposit a layer of defined length and height by the Phillips-Avery Limits of Deposition (PALOD) equation,

$$L = \sum F_R \left(\frac{d_{xyz}}{V_{xyz}}\right) + L_{dwell} \tag{8}$$

where:

L is the length of feedstock required to produce a deposition.

F_R is the linear actuator speed; feed rate.

d_{xyz} is the Cartesian coordinate distance the tool travels.

V_{xyz} is the tool traversing velocity used to travel the respective distance.

L_{dwell} is the additional length of feedstock required to begin deposition following a reload.

To determine the total quantity of solid feedstock rods required for a given deposition path, the total number of layers at a predefined layer height can be multiplied by the PALOD equation.

Build Successes from Multiple Waste Streams

This research project has identified key barriers for deposition of recycled material. By learning from new feedstock deposition strategies, successful depositions for both recycled machine chips and strips of damaged material feedstock were achieved as depicted in Figure 6.2. and detailed in Section 5.15.

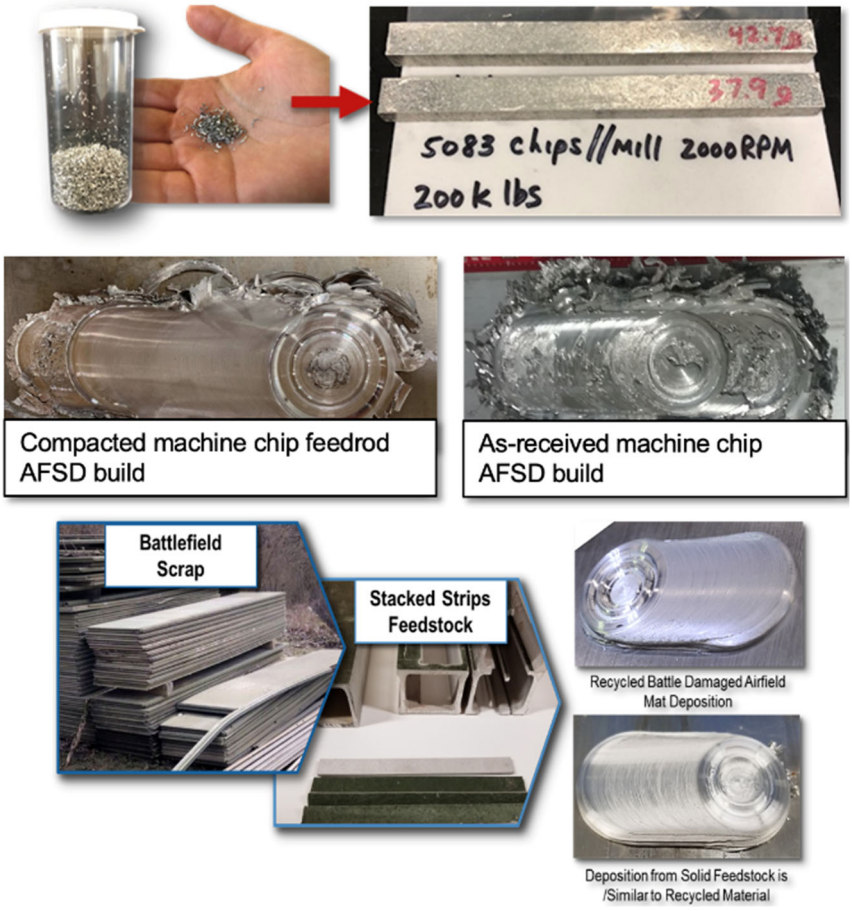

Figure 6.2 Successful AFSD depositions from recycled feedstock including compacted machine chips, loose machine chips, and strips of damaged material.

However, to achieve adequate compaction and deposition of machine chip feedstocks in Figure 6.2, the chips required an additional processing step of ball milling to sizes less than 30 um regardless of whether the chips were compacted into a rod fed AFSD machine or directly fed through the auger AFSD machine. From a FOB standpoint, the auger system is incapable of depositing hard alloys such as steel or titanium alloys, and would require time intensive machine modifications to switch between being able to do auger feedstock or rod feedstock. Therefore, the use of a continuous chip recycling machine as discussed later would be a more viable option to mitigate machine downtime from swapping out AFSD components.

Alternatively, strips of material instead of monolithic rods can be loosely deposited by the AFSD process by creating stacks of thin strips of a material together to fill the approximate geometry of traditional AFSD feedstock. With these stacked strip recycling depositions, exterior contaminants such as sand or other abundance of high friction particles will result in jamming of material in the tool and require extensive cleaning with machine downtime. Interestingly, the current SERDP research project was able to demonstrate the viability of depositing the strips of material with the non-skid coating or even internal sand embedded between layers to create a successful MMC deposition. Here, these depositions highlight the robustness of the process to fabricate parts using contaminated feedstock material.

Basic Limits of Technology

Currently, AFSD provides a complimentary process that can overcome barriers created by liquid-solid phase transformations of fusion-based AM processes, but there are still limits to the nascent technology. Specifically, additional research and development are required for items such as tooling advancements, process monitoring and feedback controls, and automatic feeding of solid rod feedstock.

For example, in the AA6061 build shown in Figure 6.3, that was a 64 mm tall build with a length of 152.4 mm the actual deposition rate was 0.25 kg/hr compared to the theoretical rate deposition rate of 1.03 kg/hr. The difference between the two values is that only 2 layers were able to be deposited per rod of feedstock. Therefore, the machine and tool had to cool down for a certain amount of time before the operator loads a new rod of feedstock. Additionally, since the machine was only able to deposit in position control there was no spatial-temporal information to provide feedback control from subsequent heat generation as the build height increased to the maximum height.

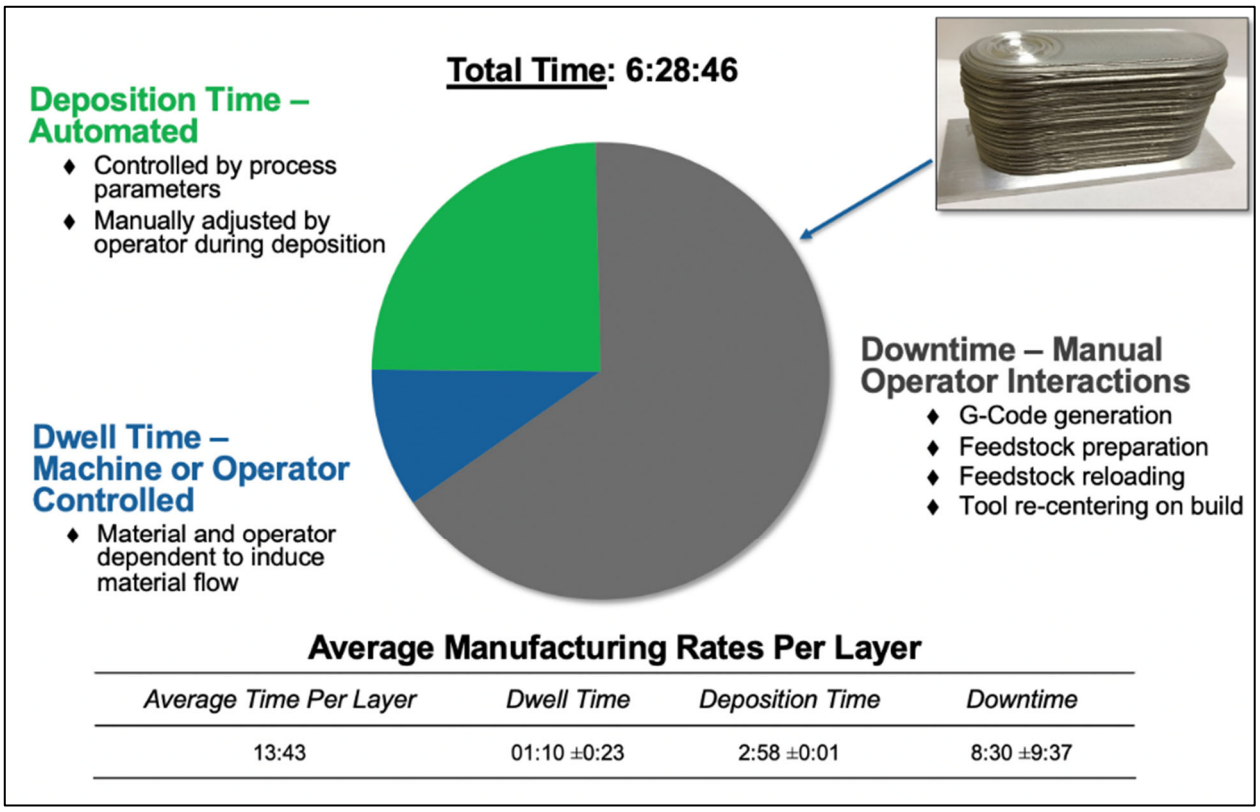

Figure 6.3 Limitations of current build comparing actual deposition time to machine downtime during a build.

Opportunities For Future Research (Continuous Feeding, Round Feedstock, Hard Alloys, Dem/Vals)

To-date, this project has demonstrated the ability for DAR of aluminum alloy secondary feedstocks. As AFSD is still in the early maturation stages there is still additional development required to transition this technology to the field. Particularly, automatic feeding is currently in development, which will significantly create improved microstructures and mechanical behavior by eliminating transient regions of starting/stopping the process to reload new feedstock. The AFSD process is at a stage where there are still more scientific discoveries to make as the process matures, but the process does offer key immediate benefits for production repair, specifically by fabricating and repairing long-lead time large aluminum alloy components at production facilities such as military depots. However, since fabricating the square feedstock is a significant limitation from a time and material standpoint, the ability to further investigate round feedstock depositions is highly beneficial to the user community. Limited investigations to-date for round feedstock demonstrate the ability to produce similar AFSD builds and properties to builds fabricated with square feedstock depositions (Figure 6.4).

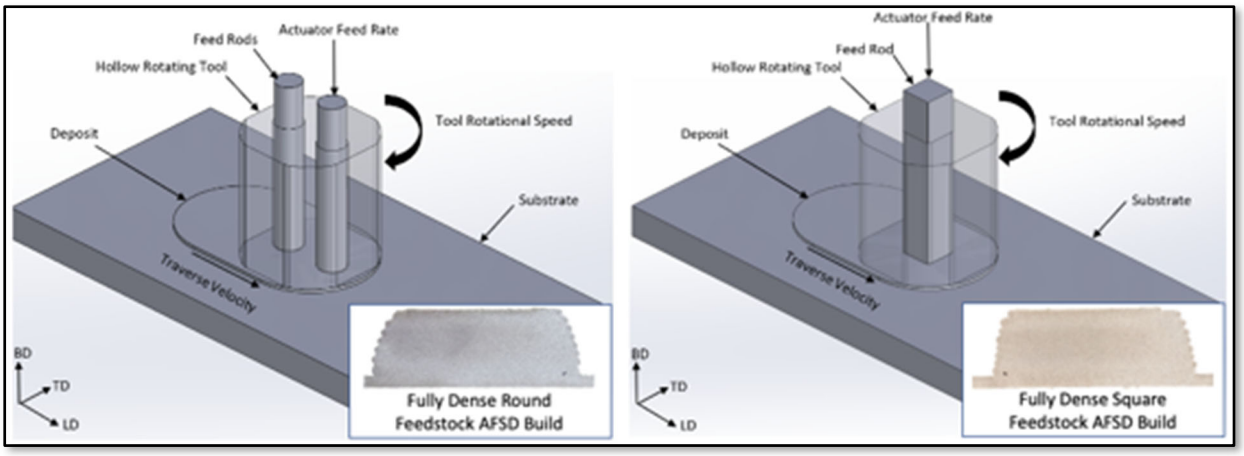

Figure 6.4 Comparison between round and square feedstock depositions that are both fully-dense.

The preliminary work in Figure 6.4 comparing round and square feedstock demonstrate the ability for AFSD to no longer be limited to square feedstock cross-sections, but to have a variable feedstock geometry that would significantly benefit harder materials such as steel, titanium, and Inconel alloys where round feedstock would be more economical and efficient to produce through extrusions instead of machining square cross-section feedrods from plates. However, to expand this research from recycling softer alloys such as aluminum, magnesium, and copper alloys to harder materials requires further research into process-structure-property relations.

The process steps to recycle materials such as machine chips or waste powders into an additive build would also benefit from a vertically integrated processing approach as depicted in Figure 6.5. Here, Friction Extrusion (FE) equipment that is currently used to recycle machine chips into solid rods or tubes is placed into a field portable ISO Container with an AFSD/FSAM with additive/subtractive machine capability to complement ISO Container machining centers at FOBs.

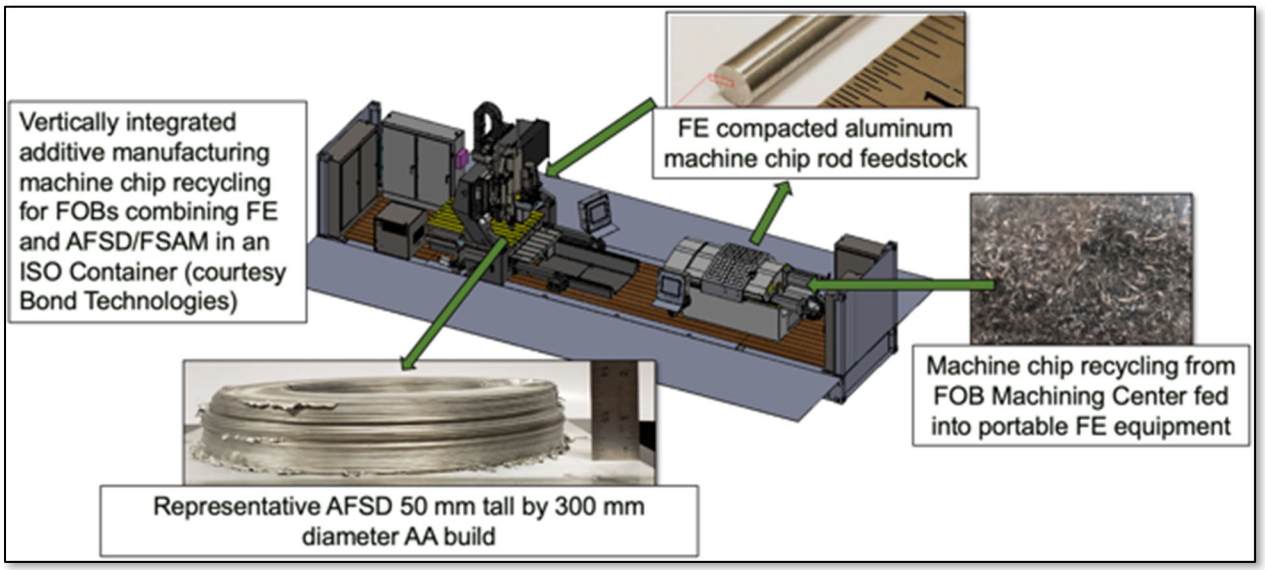

Figure 6.5 A vertically integrated Direct Additive Recycling (DAR) approach combining FE and AFSD/FSAM/Machining to fabricate or repair components without needing atomization of scrap in a field portable ISO container [306].

The aforementioned vertically integrated chip recycling approach depicted in Figure 6.5 benefits by not requiring AFSD machine component being swapped out between an auger fed system that is not suitable for hard alloys and requires refining of machine chips. Yet, this approach implements a commercially available Friction Extrusion (FE) machine that has already been demonstrated to fabricate tubes or solid rods for both soft and hard alloys from machine chips and powders. The consolidated rods are then able to be directly fed into the Hybrid AFSD/FSAM/Machining equipment also shown in Figure 6.5. This vertically integrated approach is field portable in an ISO Container that may be placed next to current FOB ISO Container machining centers to minimize logistical challenges at austere locations.

The strip recycling is a viable method to repair AA6061 components, but would greatly benefit from the development of a portable machine that could be placed on an expeditionary airfield for in-field repair at the point-of-need as detailed in Figure 6.6.

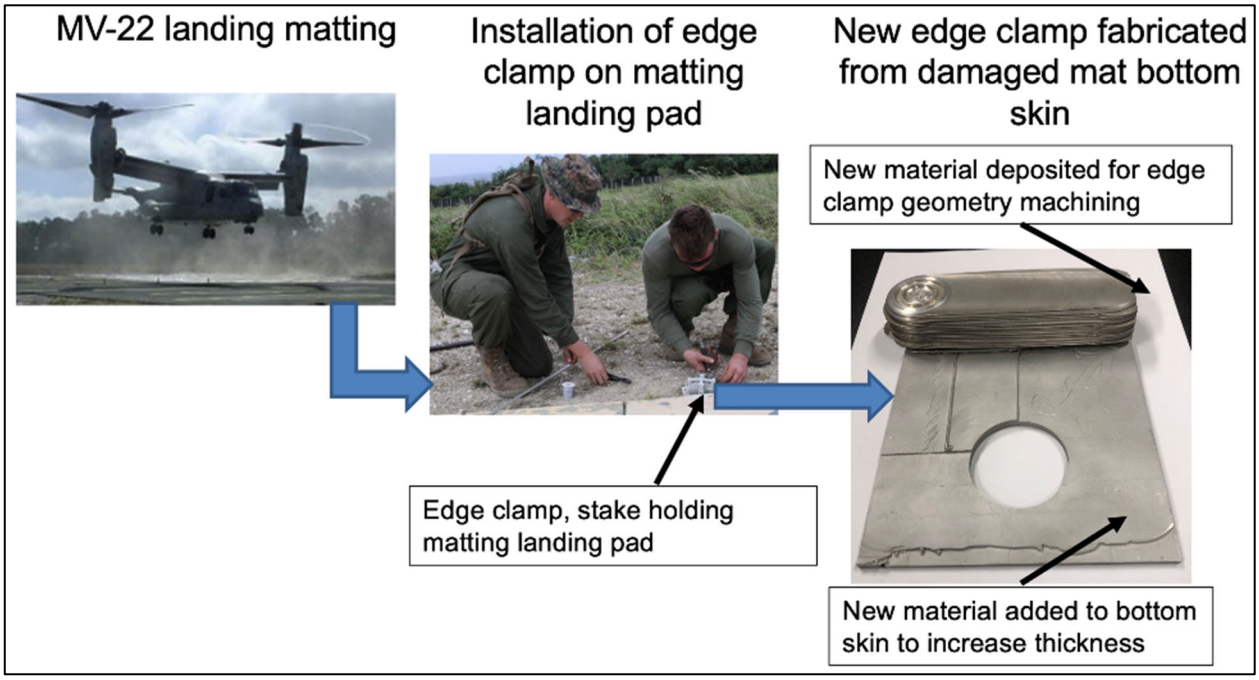

Figure 6.6 Use of AFSD for repairing airfield landing mat components such as edge clamps fabricated from mat core top skins where strips of damaged landing mat built up the component thickness to required sizes. Left image from [307]. Center image from [304].

The new edge clamp created in Figure 6.6 was fabricated from the damaged mat core extrusion skin that had the required component thickness increased from the thinner skin by using the damaged strips of material as the feedstock. Additionally, as depicted in Section 5.15 where the mat core was repaired using the damaged landing mat material as feedstock there is necessary machining required.

In conclusion, there is still additional development required for deployment to FOBs with this DAR AFSD approach and technology where the maturation of AFSD software needs to include automation of the AM process flow that would be integrated with a digitally driven approach for parameter prediction and optimization through a simulation based tool framework.

Literature Cited

[1] V. F. Medina, M. Wynter, S. Waisner, S. Cosper, and G. Rodriguez, "Sustainable Cities and Military Installations," in *Sustainable Cities and Military Installations*, I. Linkov, Ed. Springer Science, 2014, pp. 391–427.

[2] U.S. Army, "Technical Manual 3-34.56, Waste Management for Deployed Forces," no. July, 2013.

[3] G. Gerdes, "Studies Define Solid Waste Stream at Base Camps," *Engineer*, no. April, pp. 70–71, 2009.

[4] G. L. Gerdes, D. Curtin, and C. Gutkowski, "ERDC/CERL TR-08-13: Hydrothermal Processing of Base Camp Solid Wastes To Allow Onsite Recycling Construction Engineering," Champaign, IL, 2008.

[5] S. D. Cosper, H. G. Anderson, K. Kinnevan, and B. J. Kim, "ERDC/CERL TR-13-17: Contingency Base Camp Solid Waste Generation," Champaign, IL, 2013.

[6] V. F. Medina and S. A. Waisner, "Military Solid and Hazardous Wastes-Assessment of Issues at Military Facilities and Base Camps," *Waste*, pp. 357–376, 2011.

[7] M. Infante, "Subject : Date : From : To : CC : RE : Discard rate of AM2 at FOB ? Tuesday , December 13 , 2016 at 4 : 20 : 25 PM Central Standard Time," 2016. .

[8] D. Lamothe, "Landing pad blamed for Super Cobra crash," *Military Times*, 2013. [Online]. Available: http://www.militarytimes.com/story/military/archives/2013/03/22/landing-pad-blamed-for-super-cobra-crash/78535842/. [Accessed: 05-Jan-2017].

[9] E. Collier, "Joint Airfield Surfacing Workshop Minutes July 2015." .

[10] E. Collier, "The Expeditionary Airfield Capability: A Core USMC Competence for Global Operations," 2010. [Online]. Available: http://www.sldinfo.com/the-expeditionary-airfield-capability-a-core-usmc-competence-for-global-operations-2/.

[11] AFCESA/CES, "Engineering Technical Letter (ETL) 04-2 (Change 1): Standard Airfield Pavement Marking Schemes," ETL 04-2, 2004.

[12] P. G. Allison, T. W. Rushing, and L. Garcia, "ERDC/GSL-TR-14-18: Analysis of Lightweight Materials for the AM2 System," ENGINEER RESEARCH AND DEVELOPMENT CENTER, Vicksburg, MS, 2014.

[13] T. W. Rushing and J. S. Tingle, "ERDC/GSL TR-07-05: AM2 and M19 Airfield Mat Evaluation for the Rapid Parking Ramp Expansion Program Geotechnical and Structures Laboratory AM2 and M19 Airfield Mat Evaluation for the Rapid Parking Ramp Expansion Program," Vicksburg, MS, 2007.

[14] T. W. Rushing, I. L. Howard, J. B. Jordon, and P. G. Allison, "Laboratory Characterization of Fatigue Performance of AM2 Aluminum Airfield Matting," *http://dx.doi.org/10.1061/(ASCE)MT.1943-5533.0001620*, 2016.

[15] C. A. Donnahoe, "Reverse Logistics Operations in Afghanistan.," *Army Sustain.*, vol. 44, no. 6, pp. 28–32, 2012.

[16] J. M. Railsback, "Force Protection of Forward Operating Bases in Baghdad," *Engineer*, no. December, pp. 14–18, 2003.

[17] S. Palanivel, P. Nelaturu, B. Glass, and R. S. Mishra, "Friction stir additive manufacturing for high structural performance through microstructural control in an Mg based WE43 alloy," *Mater. Des.*, vol. 65, pp. 934–952, Jan. 2015.

[18] D. Manfredi *et al.*, "From Powders to Dense Metal Parts: Characterization of a Commercial AlSiMg Alloy Processed through Direct Metal Laser Sintering," *Materials (Basel).*, vol. 6, no. 3, pp. 856–869, Mar. 2013.

[19] W. E. Frazier, "Metal additive manufacturing: A review," *J. Mater. Eng. Perform.*, vol. 23, no. 6, pp. 1917–1928, 2014.

[20] T. DebRoy *et al.*, "Additive manufacturing of metallic components – Process, structure and properties," *Prog. Mater. Sci.*, vol. 92, pp. 112–224, Mar. 2018.

[21] C. Shen, Z. Pan, Y. Ma, D. Cuiuri, and H. Li, "Fabrication of iron-rich Fe–Al intermetallics using the wire-arc additive manufacturing process," *Addit. Manuf.*, vol. 7, pp. 20–26, Jul. 2015.

[22] C. E. Roberts, D. Bourell, T. Watt, and J. Cohen, "A novel processing approach for additive manufacturing of commercial aluminum alloys," in *Physics Procedia*, 2016, vol. 83, pp. 909–917.

[23] E. Brandl, U. Heckenberger, V. Holzinger, and D. Buchbinder, "Additive manufactured AlSi10Mg samples using Selective Laser Melting (SLM): Microstructure, high cycle fatigue, and fracture behavior," *Mater. Des.*, vol. 34, pp. 159–169, Feb. 2012.

[24] K. Schmidtke, F. Palm, A. Hawkins, and C. Emmelmann, "Process and Mechanical Properties: Applicability of a Scandium modified Al-alloy for Laser Additive Manufacturing," *Phys. Procedia*, vol. 12, pp. 369–374, Jan. 2011.

[25] T. Mukherjee, J. S. Zuback, A. De, and T. DebRoy, "Printability of alloys for additive manufacturing," *Sci. Rep.*, vol. 6, no. 1, p. 19717, Apr. 2016.

[26] I. Maskery *et al.*, "A mechanical property evaluation of graded density Al-Si10-Mg lattice structures manufactured by selective laser melting," *Mater. Sci. Eng. A*, vol. 670, pp. 264–274, Jul. 2016.

[27] E. Louvis, P. Fox, and C. J. Sutcliffe, "Selective laser melting of aluminium components,"

J. Mater. Process. Technol., vol. 211, no. 2, pp. 275–284, 2011.

[28] N. T. Aboulkhair, N. M. Everitt, I. Ashcroft, and C. Tuck, "Reducing porosity in AlSi10Mg parts processed by selective laser melting," *Addit. Manuf.*, vol. 1–4, pp. 77–86, Oct. 2014.

[29] B. A. Fulcher, D. K. Leigh, and T. J. Watt, "Comparison of AlSi10Mg and Al 6061 Processed Through DMLS," *Proc. 25th Solid Free. Fabr. Symp.*, pp. 404–419, 2014.

[30] S. Z. Uddin, L. E. Murr, C. A. Terrazas, P. Morton, D. A. Roberson, and R. B. Wicker, "Processing and characterization of crack-free aluminum 6061 using high-temperature heating in laser powder bed fusion additive manufacturing," *Addit. Manuf.*, vol. 22, pp. 405–415, Aug. 2018.

[31] E. O. Olakanmi, R. F. Cochrane, and K. W. Dalgarno, "A review on selective laser sintering/melting (SLS/SLM) of aluminium alloy powders: Processing, microstructure, and properties," *Prog. Mater. Sci.*, vol. 74, pp. 401–477, Oct. 2015.

[32] L. Thijs, K. Kempen, J.-P. Kruth, and J. Van Humbeeck, "Fine-structured aluminium products with controllable texture by selective laser melting of pre-alloyed AlSi10Mg powder," *Acta Mater.*, vol. 61, no. 5, pp. 1809–1819, Mar. 2013.

[33] J. R. Croteau *et al.*, "Microstructure and mechanical properties of Al-Mg-Zr alloys processed by selective laser melting," *Acta Mater.*, vol. 153, pp. 35–44, Jul. 2018.

[34] C. Brice, R. Shenoy, M. Kral, and K. Buchannan, "Precipitation behavior of aluminum alloy 2139 fabricated using additive manufacturing," *Mater. Sci. Eng. A*, vol. 648, pp. 9–14, Nov. 2015.

[35] R. Li *et al.*, "Selective laser melting of a novel Sc and Zr modified Al-6.2 Mg alloy: Processing, microstructure, and properties," *Powder Technol.*, vol. 319, pp. 117–128, Sep. 2017.

[36] O. G. Rivera, "Structure-Property Relationships of Solid State Additive Manufactured Aluminum Alloy 2219 and Inconel 625," The University of Alabama, 2017.

[37] H. Z. Yu *et al.*, "Non-beam-based metal additive manufacturing enabled by additive friction stir deposition," *Scr. Mater.*, vol. 153, Aug. 2018.

[38] O. G. Rivera *et al.*, "Microstructural Evolution and Mechanical Properties of Inconel 625 Manufactured by AFS Additive Manufacturing," *Acta Mater.*, pp. 1–15.

[39] D. Z. Avery *et al.*, "Fatigue Behavior of Solid-State Additive Manufactured Inconel 625," *Jom*, vol. 70, no. 11, pp. 2475–2484, 2018.

[40] O. G. Rivera *et al.*, "Influence of Texture and Grain Refinement on the Mechanical Behavior of AA2219 Depositions Fabricated by HIgh Shear Solid State Material Deposition," *Mater. Sci. Eng. A*, vol. 724, pp. 547–558, Mar. 2018.

[41] O. G. Rivera *et al.*, “Microstructures and mechanical behavior of Inconel 625 fabricated by solid-state additive manufacturing,” *Mater. Sci. Eng. A*, 2017.

[42] Y. S. Sato, F. Yamashita, Y. Sugiura, S. H. C. Park, and H. Kokawa, “FIB-assisted TEM study of an oxide array in the root of a friction stir welded aluminium alloy,” *Scr. Mater.*, vol. 50, no. 3, pp. 365–369, 2004.

[43] C. Zhou, X. Yang, and G. Luan, “Effect of oxide array on the fatigue property of friction stir welds,” *Scr. Mater.*, vol. 54, no. 8, pp. 1515–1520, 2006.

[44] S. Liu *et al.*, “Friction surface cladding: An exploratory study of a new solid state cladding process,” *J. Mater. Process. Technol.*, vol. 229, pp. 769–784, Mar. 2016.

[45] A. A. Van Der Stelt, T. C. Bor, H. J. M. Geijselaers, R. Akkerman, and A. H. van den Boogaard, “Cladding of Advanced Al Alloys Employing Friction Stir Welding,” *Key Eng. Mater.*, vol. 554–557, pp. 1014–1021, 2013.

[46] W. M. W. Thomas *et al.*, “Friction stir welding process developments and variant techniques,” 1991.

[47] R. I. Rodriguez *et al.*, “Microstructure, texture, and mechanical properties of friction stir spot welded rare-earth containing ZEK100 magnesium alloy sheets,” *Mater. Sci. Eng. A*, vol. 618, no. February, pp. 637–644, Nov. 2014.

[48] M. Koilraj, V. Sundareswaran, S. Vijayan, and S. R. Koteswara Rao, “Friction stir welding of dissimilar aluminum alloys AA2219 to AA5083 - Optimization of process parameters using Taguchi technique,” *Mater. Des.*, vol. 42, pp. 1–7, Dec. 2012.

[49] H. J. Aval, “Microstructure and residual stress distributions in friction stir welding of dissimilar aluminium alloys,” *Mater. Des.*, vol. 87, pp. 405–413, Dec. 2015.

[50] G. Padmanaban and V. Balasubramanian, “Selection of FSW tool pin profile, shoulder diameter and material for joining AZ31B magnesium alloy - An experimental approach,” *Mater. Des.*, vol. 30, pp. 2647–2656, Aug. 2009.

[51] M. Esmaily *et al.*, “Bobbin and conventional friction stir welding of thick extruded AA6005-T6 profiles,” *Mater. Des.*, vol. 108, pp. 114–125, Oct. 2016.

[52] H. J. Liu, J. C. Hou, and H. Guo, “Effect of welding speed on microstructure and mechanical properties of self-reacting friction stir welded 6061-T6 aluminum alloy,” *Mater. Des.*, vol. 50, pp. 872–878, 2013.

[53] L. Wan, Y. Huang, Z. Lv, S. Lv, and J. Feng, “Effect of self-support friction stir welding on microstructure and microhardness of 6082-T6 aluminum alloy joint,” *Mater. Des.*, vol. 55, pp. 197–203, 2014.

[54] B. Li, Y. Shen, and W. Hu, “The study on defects in aluminum 2219-T6 thick butt friction stir welds with the application of multiple non-destructive testing methods,” *Mater. Des.*,

vol. 32, no. 4, pp. 2073–2084, 2011.

[55] Y. C. Chen and K. Nakata, “Effect of tool geometry on microstructure and mechanical properties of friction stir lap welded magnesium alloy and steel,” *Mater. Des.*, vol. 30, no. 9, pp. 3913–3919, Oct. 2009.

[56] E. Salari, M. Jahazi, A. Khodabandeh, and H. Ghasemi-Nanesa, “Influence of tool geometry and rotational speed on mechanical properties and defect formation in friction stir lap welded 5456 aluminum alloy sheets,” *Mater. Des.*, vol. 58, pp. 381–389, Jun. 2014.

[57] A. Garg and A. Bhattacharya, “Strength and failure analysis of similar and dissimilar friction stir spot welds: Influence of different tools and pin geometries,” *Mater. Des.*, vol. 127, pp. 272–286, Aug. 2017.

[58] M. N. Avettand-Fènoël, A. Simar, R. Shabadi, R. Taillard, and B. de Meester, “Characterization of oxide dispersion strengthened copper based materials developed by friction stir processing,” *Mater. Des.*, vol. 60, pp. 343–357, Aug. 2014.

[59] H. B. Chen, J. F. Wang, G. D. Zhen, S. B. Chen, and T. Lin, “Effects of initial oxide on microstructural and mechanical properties of friction stir welded AA2219 alloy,” *Mater. Des.*, vol. 86, pp. 49–54, Dec. 2015.

[60] B. Xie, M. Sun, B. Xu, C. Wang, D. Li, and Y. Li, “Dissolution and evolution of interfacial oxides improving the mechanical properties of solid state bonding joints,” *Mater. Des.*, vol. 157, pp. 437–446, Nov. 2018.

[61] N. Guo, Y. Fu, Y. Wang, Q. Meng, and Y. Zhu, “Microstructure and mechanical properties in friction stir welded 5A06 aluminum alloy thick plate,” *Mater. Des.*, vol. 113, pp. 273–283, Jan. 2017.

[62] D. K. Yaduwanshi, S. Bag, and S. Pal, “Numerical modeling and experimental investigation on plasma-assisted hybrid friction stir welding of dissimilar materials,” *Mater. Des.*, vol. 92, pp. 166–183, Feb. 2016.

[63] D. Garcia *et al.*, “In situ investigation into temperature evolution and heat generation during additive friction stir deposition: A comparative study of Cu and Al-Mg-Si,” *Addit. Manuf.*, vol. 34, p. 101386, Aug. 2020.

[64] R. J. Griffiths *et al.*, “Solid-state additive manufacturing of aluminum and copper using additive friction stir deposition: Process-microstructure linkages,” *Materialia*, vol. 15, p. 100967, Mar. 2021.

[65] B. J. Phillips *et al.*, “Microstructure-deformation relationship of additive friction stir-deposition Al–Mg–Si,” *Materialia*, vol. 7, 2019.

[66] J. B. Jordon *et al.*, “Direct recycling of machine chips through a novel solid-state additive manufacturing process,” *Mater. Des.*, vol. 193, p. 108850, 2020.

[67] B. A. Rutherford *et al.*, “Effect of thermomechanical processing on fatigue behavior in solid-state additive manufacturing of Al-Mg-Si alloy,” *Metals (Basel).*, vol. 10, no. 7, pp. 1–17, Jul. 2020.

[68] D. Z. Avery *et al.*, “Influence of Grain Refinement and Microstructure on Fatigue Behavior for Solid-State Additively Manufactured Al-Zn-Mg-Cu Alloy,” *Metall. Mater. Trans. A Phys. Metall. Mater. Sci.*, vol. 51, no. 6, pp. 2778–2795, 2020.

[69] J. K. Yoder, R. J. Griffiths, and H. Z. Yu, “Deformation-based additive manufacturing of 7075 aluminum with wrought-like mechanical properties,” *Mater. Des.*, p. 109288, Nov. 2020.

[70] Z. McClelland *et al.*, “Microstructure and Mechanical Properties of High Shear Material Deposition of Rare Earth Magnesium Alloys WE43,” *Miner. Met. Mater. Ser.*, pp. 277–282, 2019.

[71] J. L. Chenot and E. Massoni, “Finite element modelling and control of new metal forming processes,” *Int. J. Mach. Tools Manuf.*, vol. 46, pp. 1194–1200, Sep. 2006.

[72] G. Buffa, J. Hua, R. Shivpuri, and L. Fratini, “A continuum based fem model for friction stir welding - Model development,” *Mater. Sci. Eng. A*, vol. 419, pp. 389–396, Mar. 2006.

[73] G. Buffa, L. Fratini, and R. Shivpuri, “Finite element studies on friction stir welding processes of tailored blanks,” *Comput. Struct.*, vol. 86, pp. 181–189, Jan. 2008.

[74] A. F. Hasan, C. J. Bennett, and P. H. Shipway, “A numerical comparison of the flow behaviour in Friction Stir Welding (FSW) using unworn and worn tool geometries,” *Mater. Des.*, vol. 87, pp. 1037–1046, Dec. 2015.

[75] Y. Zhu, G. Chen, Q. Chen, G. Zhang, and Q. Shi, “Simulation of material plastic flow driven by non-uniform friction force during friction stir welding and related defect prediction,” *Mater. Des.*, vol. 108, pp. 400–410, Oct. 2016.

[76] W. F. Noh, “CEL: A Time Dependent, Two Space Dimensional, Coupled Eulerian-Lagrange,” Livermore, CA, 1963.

[77] A. Ajri and Y. C. Shin, “Investigation on the Effects of Process Parameters on Defect Formation in Friction Stir Welded Samples Via Predictive Numerical Modeling and Experiments,” in *Proceedings of the ASME 2017 12th International Manufacturing Science and Engineering Conference*, 2017.

[78] A. W. Zhu and E. A. Starke, “Materials aspects of age-forming of Al-xCu alloys,” in *Journal of Materials Processing Technology*, 2001, vol. 117, no. 3, pp. 354–358.

[79] R. M. Franck and R. B. Lazarus, “Mixed Eulerian-Lagrangian Method,” *Methods Comput. Phys.*, vol. 3, pp. 47–67, 1964.

[80] J. G. Trulio, “Theory and Structure of the AFTON Codes,” Newbury Park, CA, 1966.

[81] a. a. van der Stelt, T. C. Bor, H. J. M. Geijselaers, W. Quak, R. Akkerman, and J. Huétink, "Comparison of ALE finite element method and adaptive smoothed finite element method for the numerical simulation of friction stir welding," in *The 14th International ESAFORM Conference on Material Forming*, 2011, pp. 1290–1295.

[82] B. Meyghani, M. B. Awang, S. S. Emamian, M. K. B. Mohd Nor, and S. R. Pedapati, "A Comparison of Different Finite Element Methods in the Thermal Analysis of Friction Stir Welding (FSW)," *Metals (Basel).*, vol. 7, no. 450, p. 450, Oct. 2017.

[83] N. Dialami, M. Cervera, M. Chiumenti, and A. Segatori, "Prediction of joint line remnant defect in friction stir welding," *Int. J. Mech. Sci.*, vol. 151, pp. 61–69, Feb. 2019.

[84] L. Traversoni, "Natural Neighbour Finite Elements.," *Trans. Ecol. Environ.*, vol. 8, pp. 291–297, 1994.

[85] N. Sukumar, B. Moran, and T. Belytschko, "The natural element method in solid mechanics," *Int. J. Numer. Methods Eng.*, vol. 43, pp. 839–887, Nov. 1998.

[86] I. Alfaro, L. Fratini, E. Cueto, and F. Chinesta, "Numerical Simulation of Friction Stir Welding by Natural Element Methods," *Int. J. Mater. Form.*, vol. 1, pp. 1079–1082, Apr. 2008.

[87] T. Belytschko, Y. Y. Lu, and L. Gu, "Element-free Galerkin methods," *Int. J. Numer. Methods Eng.*, vol. 37, pp. 229–256, Jan. 1994.

[88] C. T. Wu, W. Hu, H. P. Wang, and H. Lu, "A Robust Numerical Procedure for the Thermomechanical Flow Simulation of Friction Stir Welding Process Using an Adaptive Element-Free Galerkin Method," *Math. Probl. Eng.*, vol. 2015, pp. 1–16, 2015.

[89] R. A. Gingold and J. J. Monaghan, "Smoothed particle hydrodynamics: theory and application to non-spherical stars," *Mon. Not. R. Astron. Soc.*, vol. 181, pp. 375–389, 1977.

[90] L. B. Lucy, "A numerical approach to the testing of the fission hypothesis," *Astron. J.*, vol. 82, no. 12, 1977.

[91] J. J. Monaghan, "Smoothed particle hydrodynamics," *Reports on Progress in Physics*, vol. 68, no. 1703. IOP Publishing, Jul-2005.

[92] R. A. Gingold and J. J. Monaghan, "Kernel estimates as a basis for general particle methods in hydrodynamics," *J. Comput. Phys.*, vol. 46, no. 3, pp. 429–453, Jun. 1982.

[93] K. Fraser, L. Kiss, L. St-Georges, and D. Drolet, "Optimization of Friction Stir Weld Joint Quality Using a Meshfree Fully-Coupled Thermo-Mechanics Approach," *Metals (Basel).*, vol. 8, pp. 1–24, 2018.

[94] Y. Xi, M. Bermingham, G. Wang, and M. Dargusch, "SPH/FE modeling of cutting force and chip formation during thermally assisted machining of Ti6Al4V alloy," *Comput.*

Mater. Sci., vol. 84, pp. 188–197, Mar. 2014.

[95] C. Ravi and C. Wolverton, "First-principles study of crystal structure and stability of Al-Mg-Si-(Cu) precipitates," *Acta Mater.*, vol. 52, no. 14, pp. 4213–4227, 2004.

[96] D. Maisonnette, M. Suery, D. Nelias, P. Chaudet, and T. Epicier, "Effects of heat treatments on the microstructure and mechanical properties of a 6061 aluminium alloy," *Mater. Sci. Eng. A*, vol. 528, pp. 2718–2724, 2011.

[97] J. Osten, B. Milkereit, C. Schick, and O. Kessler, "Dissolution and Precipitation Behaviour during Continuous Heating of Al–Mg–Si Alloys in a Wide Range of Heating Rates," pp. 2830–2848, 2015.

[98] S. P. Ringer and K. Hono, "Microstructural evolution and age hardening in aluminium alloys: atom probe field-ion microscopy and transmission electron microscopy studies," *Mater. Charact.*, vol. 44, no. 1–2, pp. 101–131, 2000.

[99] L. Trueba, G. Heredia, D. Rybicki, and L. B. Johannes, "Effect of tool shoulder features on defects and tensile properties of friction stir welded aluminum 6061-T6," *J. Mater. Process. Technol.*, vol. 219, pp. 271–277, 2015.

[100] W. Boonchouytan, J. Chatthong, S. Rawangwong, and R. Burapa, "Effect of heat treatment T6 on the friction stir welded SSM 6061 aluminum alloys," *Energy Procedia*, vol. 56, no. C, pp. 172–180, 2014.

[101] A. H. Feng, D. L. Chen, and Z. Y. Ma, "Microstructure and low-cycle fatigue of a friction-stir-welded 6061 aluminum alloy," *Metall. Mater. Trans. A Phys. Metall. Mater. Sci.*, vol. 41, no. 10, pp. 2626–2641, 2010.

[102] J. Boonma, S. Khammuangsa, K. Uttarasak, J. Dutchaneephet, C. Boonruang, and N. Sirikulrat, "Post-weld heat treatment effects on hardness and impact strength of aluminum alloy 6061 friction stir Butt weld," *Mater. Trans.*, vol. 56, no. 7, pp. 1072–1076, 2015.

[103] R. Priya, V. Subramanya Sarma, and K. Prasad Rao, "Effect of post weld heat treatment on the microstructure and tensile properties of dissimilar friction stir welded AA 2219 and AA 6061 alloys," *Trans. Indian Inst. Met.*, vol. 62, no. 1, pp. 11–19, 2009.

[104] C. Huang, Z. Wu, R. Huang, W. Wang, and L. Li, "Mechanical properties of AA5083 in different tempers at low temperatures," *IOP Conf. Ser. Mater. Sci. Eng.*, vol. 279, no. 1, 2017.

[105] S. Kang and N. J. Grant, "Notch tensile testing as a measure of the toughness of aluminum alloys," *Mater. Sci. Eng.*, vol. 72, no. 2, pp. 155–162, 1985.

[106] A. Argon and A. S. Argon, "Strain Hardening," *Strength. Mech. Cryst. Plast.*, pp. 283–343, 2007.

[107] M. T. Tucker, M. F. Horstemeyer, W. R. Whittington, K. N. Solanki, and P. M. Gullett,

"The effect of varying strain rates and stress states on the plasticity, damage, and fracture of aluminum alloys," *Mech. Mater.*, vol. 42, no. 10, pp. 895–907, Oct. 2010.

[108] E. L. Huskins, B. Cao, and K. T. Ramesh, "Strengthening mechanisms in an Al-Mg alloy," *Mater. Sci. Eng. A*, vol. 527, no. 6, pp. 1292–1298, 2010.

[109] R. Abdi behnagh, M. K. Besharati Givi, and M. Akbari, "Mechanical properties, corrosion resistance, and microstructural changes during friction stir processing of 5083 aluminum rolled plates," *Mater. Manuf. Process.*, vol. 27, no. 6, pp. 636–640, 2012.

[110] M. Peel, A. Steuwer, M. Preuss, and P. J. Withers, "Microstructure, mechanical properties and residual stresses as a function of welding speed in aluminium AA5083 friction stir welds," *Acta Mater.*, vol. 51, no. 16, pp. 4791–4801, Sep. 2003.

[111] H. J. Liu and X. L. Feng, "Effect of post-processing heat treatment on microstructure and microhardness of water-submerged friction stir processed 2219-T6 aluminum alloy," *Mater. Des.*, vol. 47, pp. 101–105, 2013.

[112] J. Torzewski, K. Grzelak, M. Wachowski, and R. Kosturek, "Microstructure and low cycle fatigue properties of AA5083 H111 friction stir welded joint," *Materials (Basel).*, vol. 13, no. 10, 2020.

[113] P. Vilaça, N. Pépe, and L. Quintino, "Metallurgical and corrosion features of friction stir welding of AA5083-H111," *Weld. World*, vol. 50, no. 9–10, pp. 55–64, 2006.

[114] W. Hussein and M. A. Al-Shammari, "Fatigue and Fracture Behaviours of FSW and FSP Joints of AA5083-H111 Aluminium Alloy," *IOP Conf. Ser. Mater. Sci. Eng.*, vol. 454, no. 1, pp. 0–10, 2018.

[115] E. O. Olakanmi, "Selective laser sintering/melting (SLS/SLM) of pure Al, Al-Mg, and Al-Si powders: Effect of processing conditions and powder properties," *J. Mater. Process. Technol.*, vol. 213, no. 8, pp. 1387–1405, 2013.

[116] J. P. Kruth, L. Froyen, J. Van Vaerenbergh, P. Mercelis, M. Rombouts, and B. Lauwers, "Selective laser melting of iron-based powder," *J. Mater. Process. Technol.*, vol. 149, no. 1–3, pp. 616–622, 2004.

[117] S. Siddique, M. Awd, J. Tenkamp, and F. Walther, "High and very high cycle fatigue failure mechanisms in selective laser melted aluminum alloys," *J. Mater. Res.*, vol. 32, no. 23, pp. 4296–4304, 2017.

[118] J. Zhang, B. Song, Q. Wei, D. Bourell, and Y. Shi, "A review of selective laser melting of aluminum alloys: Processing, microstructure, property and developing trends," *Journal of Materials Science and Technology*, vol. 35, no. 2. Chinese Society of Metals, pp. 270–284, Feb-2019.

[119] C. Galy, E. Le Guen, E. Lacoste, and C. Arvieu, "Main defects observed in aluminum alloy parts produced by SLM: From causes to consequences," *Additive Manufacturing*,

vol. 22. Elsevier B.V., pp. 165–175, Aug-2018.

[120] M. Tang and P. C. Pistorius, "Oxides, porosity and fatigue performance of AlSi10Mg parts produced by selective laser melting," *Int. J. Fatigue*, vol. 94, pp. 192–201, 2017.

[121] S. Li, Q. Wei, Y. Shi, C. K. Chua, Z. Zhu, and D. Zhang, "Microstructure Characteristics of Inconel 625 Superalloy Manufactured by Selective Laser Melting," *J. Mater. Sci. Technol.*, vol. 31, no. 9, pp. 946–952, 2015.

[122] O. Zinovieva, A. Zinoviev, and V. Ploshikhin, "Three-dimensional modeling of the microstructure evolution during metal additive manufacturing," *Comput. Mater. Sci.*, vol. 141, pp. 207–220, Jan. 2018.

[123] Y. Li and D. Gu, "Parametric analysis of thermal behavior during selective laser melting additive manufacturing of aluminum alloy powder," *Mater. Des.*, vol. 63, pp. 856–867, 2014.

[124] K. Kempen, L. Thijs, J. Van Humbeeck, and J. P. Kruth, "Mechanical Properties of AlSi10Mg Produced by Selective Laser Melting," *Phys. Procedia*, vol. 39, pp. 439–446, 2012.

[125] E. Brandl, U. Heckenberger, V. Holzinger, and D. Buchbinder, "Additive manufactured AlSi10Mg samples using Selective Laser Melting (SLM): Microstructure, high cycle fatigue, and fracture behavior," *Mater. Des.*, vol. 34, pp. 159–169, 2012.

[126] E. Zaretsky, A. Stern, and N. Frage, "Dynamic response of AlSi10Mg alloy fabricated by selective laser melting," *Mater. Sci. Eng. A*, vol. 688, no. December 2016, pp. 364–370, 2017.

[127] T. M. Mower and M. J. Long, "Mechanical behavior of additive manufactured, powder-bed laser-fused materials," *Mater. Sci. Eng. A*, vol. 651, pp. 198–213, 2016.

[128] B. C. White, W. A. Story, L. N. Brewer, and J. B. Jordon, "Fracture mechanics methods for evaluating the adhesion of cold spray deposits," *Eng. Fract. Mech.*, vol. 205, pp. 57–69, Jan. 2019.

[129] V. K. Champagne, M. Trexler, Y. Sohn, and G. E. Kim, "Novel Cold Spray Nanostructured Aluminum," in *ICAA13 Pittsburgh*, 2012, pp. 993–998.

[130] D. L. Gilmore, R. C. Dykhuizen, R. A. Neiser, T. J. Roemer, and M. F. Smith, "Particle velocity and deposition efficiency in the cold spray process," *J. Therm. Spray Technol.*, vol. 8, no. 4, pp. 576–582, 1999.

[131] T. Liu, J. D. Leazer, and L. N. Brewer, "Particle deformation and microstructure evolution during cold spray of individual Al-Cu alloy powder particles," *Acta Mater.*, vol. 168, pp. 13–23, 2019.

[132] M. Bray, A. Cockburn, and W. O'Neill, "The Laser-assisted Cold Spray process and

deposit characterisation," *Surf. Coatings Technol.*, vol. 203, no. 19, pp. 2851–2857, 2009.

[133] A. C. Hall, L. N. Brewer, and T. J. Roemer, "Preparation of Aluminum Coatings Containing Homogenous Nanocrystalline Microstructures Using the Cold Spray Process," *J. Therm. Spray Technol.*, vol. 17, no. 3, pp. 352–359, Sep. 2008.

[134] M. R. Rokni, C. A. Widener, and V. R. Champagne, "Microstructural Evolution of 6061 Aluminum Gas-Atomized Powder and High-Pressure Cold-Sprayed Deposition," *J. Therm. Spray Technol.*, vol. 23, no. 3, pp. 514–524, Feb. 2014.

[135] M. R. Rokni, C. A. Widener, and V. R. Champagne, "Microstructural stability of ultrafine grained cold sprayed 6061 aluminum alloy," *Appl. Surf. Sci.*, vol. 290, pp. 482–489, Jan. 2014.

[136] M. R. Rokni, C. A. Widener, O. C. Ozdemir, and G. A. Crawford, "Microstructure and mechanical properties of cold sprayed 6061 Al in As-sprayed and heat treated condition," *Surf. Coatings Technol.*, vol. 309, pp. 641–650, 2017.

[137] B. Aldwell, E. Kelly, R. Wall, A. Amaldi, G. E. O'Donnell, and R. Lupoi, "Machinability of Al 6061 Deposited with Cold Spray Additive Manufacturing," *J. Therm. Spray Technol.*, vol. 26, no. 7, pp. 1573–1584, 2017.

[138] Y. Guo, H. Pan, L. Ren, and G. Quan, "An investigation on plasma-MIG hybrid welding of 5083 aluminum alloy," *Int. J. Adv. Manuf. Technol.*, vol. 98, no. 5–8, pp. 1433–1440, 2018.

[139] X. Fang *et al.*, "Correlations between microstructure characteristics and mechanical properties in 5183 aluminium alloy fabricated by wire-arc additive manufacturing with different arc modes," *Materials (Basel).*, vol. 11, no. 11, 2018.

[140] J. Gu *et al.*, "Deformation microstructures and strengthening mechanisms for the wire+arc additively manufactured Al-Mg4.5Mn alloy with inter-layer rolling," *Mater. Sci. Eng. A*, vol. 712, no. November 2017, pp. 292–301, 2018.

[141] C. Menzemer, P. C. Lam, T. S. Srivatsan, and C. F. Wittel, "Investigation of fusion zone microstructures of welded aluminum alloy joints," *Mater. Lett.*, vol. 41, no. 4, pp. 192–197, 1999.

[142] L. Wang, Y. Suo, Z. Liang, D. Wang, and Q. Wang, "Effect of titanium powder on microstructure and mechanical properties of wire + arc additively manufactured Al-Mg alloy," *Mater. Lett.*, vol. 241, pp. 231–234, 2019.

[143] L. Zhou *et al.*, "Microstructure and mechanical properties of Zr-modified aluminum alloy 5083 manufactured by laser powder bed fusion," *Addit. Manuf.*, vol. 28, no. May, pp. 485–496, 2019.

[144] A. B. Spierings, K. Dawson, K. Kern, F. Palm, and K. Wegener, "SLM-processed Sc- and Zr- modified Al-Mg alloy: Mechanical properties and microstructural effects of heat

treatment," *Mater. Sci. Eng. A*, vol. 701, no. May, pp. 264–273, 2017.

[145] A. B. Spierings *et al.*, "Microstructural features of Sc- and Zr-modified Al-Mg alloys processed by selective laser melting," *Mater. Des.*, vol. 115, pp. 52–63, 2017.

[146] ASTM, "Standard Practice for Determining Average Grain Size Using Electron Backscatter Diffraction (EBSD) in Fully Recrystallized Polycrystalline Materials," *ASTM Int.*, pp. 1–5, 2014.

[147] ASTM, "E384 -17 Standard Test Method for Microindentation Hardness of Materials," *ASTM Int.*, pp. 1–40, 2017.

[148] M. T. Hutchings, P. J. Withers, T. M. Holden, and T. Lorentzen, *Introduction to the Characterization of Residual Stress by Neutron Diffraction*, 1st ed. CRC Press, 2005.

[149] W. Woo, H. Choo, D. W. Brown, Z. Feng, and P. K. Liaw, "Angular distortion and through-thickness residual stress distribution in the friction-stir processed 6061-T6 aluminum alloy," *Mater. Sci. Eng. A*, vol. 437, no. 1, pp. 64–69, 2006.

[150] K. An, L. Yuan, L. Dial, I. Spinelli, A. D. Stoica, and Y. Gao, "Neutron residual stress measurement and numerical modeling in a curved thin-walled structure by laser powder bed fusion additive manufacturing," *Mater. Des.*, vol. 135, pp. 122–132, 2017.

[151] K. A. Fraser, "Adaptive smoothed particle hydrodynamics neighbor search algorithm for large plastic deformation computational solid mechanics," in *13th International LS-DYNA Users Conference*, 2014, no. April.

[152] X. Yang, M. Liu, and S. Peng, "Smoothed particle hydrodynamics modeling of viscous liquid drop without tensile instability," *Comput. Fluids*, vol. 92, pp. 199–208, 2014.

[153] K. C. Mills, *Recommended values of thermophysical proterties for commercial alloys*. Cambridge, UK: Woodhead Publishing Ltd, 2002.

[154] J. J. Valencia and P. N. Quested, "Thermophysical Properties," in *ASM Handbook vol 15*, 2008, p. 12.

[155] D. Tarwidi, "Smoothed particle hydrodynamics method for two-dimensional Stefan problem," in *5th International Symposium on Computational Sciences*, 2012.

[156] J. J. Monaghan, "SPH without a Tensile Instability," *J. Comput. Phys.*, vol. 159, pp. 290–311, 2000.

[157] J. P. Gray, J. J. Monaghan, and R. P. Swift, "SPH elastic dynamics," *Comput. Methods Appl. Mech. Eng.*, vol. 190, pp. 6641–6662, 2001.

[158] R. Vignjevic, J. R. Reveles, and J. Campbell, "SPH in a total lagrangian formalism," *C. - Comput. Model. Eng. Sci.*, vol. 14, no. 3, pp. 181–198, 2006.

[159] P. N. Sun, A. Colagrossi, S. Marrone, and A. M. Zhang, "The δplus-SPH model: Simple procedures for a further improvement of the SPH scheme," *Comput. Methods Appl. Mech. Eng.*, vol. 315, pp. 25–49, 2017.

[160] S. Marrone, A. Colagrossi, D. Le Touzé, and G. Graziani, "Fast free-surface detection and level-set function definition in SPH solvers," *J. Comput. Phys.*, vol. 229, pp. 3652–3663, Apr. 2010.

[161] G. Oger, S. Marrone, D. Le Touzé, and M. de Leffe, "SPH accuracy improvement through the combination of a quasi-Lagrangian shifting transport velocity and consistent ALE formalisms," *J. Comput. Phys.*, vol. 313, pp. 76–98, May 2016.

[162] G. R. Johnson and W. H. Cook, "A Constitutive Model and Data for Metals Subjected to Large Strains, High Strain Rates and High Temperatures," in *Proceedings of the Seventh International Symposium on "Ballistics,"* 1983, pp. 541–548.

[163] R. R. McCullough, J. B. Jordon, P. G. Allison, D. J. Bammann, L. Garcia, and T. W. Rushing, "Characterization of the Bauschinger effect in an extruded aluminum alloy," *Strength, Fract. Complex.*, vol. 10, no. 3–4, 2017.

[164] P. G. Allison, H. Grewal, Y. Hammi, H. R. Brown, W. R. Whittington, and M. F. Horstemeyer, "Plasticity and fracture modeling/experimental study of a porous metal under various strain rates, temperatures, and stress states," *J. Eng. Mater. Technol. Trans. ASME*, vol. 135, no. 4, 2013.

[165] P. G. Allison, Y. Hammi, J. B. Jordon, and M. F. Horstemeyer, "Modelling and experimental study of fatigue of powder metal steel (FC-0205)," *Powder Metall.*, 2013.

[166] C. J. T. Mason *et al.*, "Plasticity-Damage Modeling of Strain Rate and Temperature Dependence of Aluminum Alloy 7075-T651," *J. Dyn. Behav. Mater.*, vol. 5, no. 1, pp. 105–114, 2019.

[167] K. Fraser, "Robust and efficient meshfree solid thermo-mechanics simulation of friction stir welding," Université du Québec à Chicoutimi, 2017.

[168] D. L. McDowell, K. Gall, M. F. Horstemeyer, and J. Fan, "Microstructure-Based Fatigue Modeling of Cast A356-T6 Alloy," *Eng. Fract. Mech.*, vol. 70, pp. 49–80, 2003.

[169] Y. Xue, A. M. Wright, D. L. McDowell, M. F. Horstemeyer, K. Solanki, and Y. Hammi, "Micromechanics Study of Fatigue Damage Incubation Following an Initial Overstrain," *J. Eng. Mater. Technol.*, vol. 132, no. 2, p. 021010, 2010.

[170] Y. Xue, D. L. McDowell, M. F. Horstemeyer, M. H. Dale, and J. B. Jordon, "Microstructure-based multistage fatigue modeling of aluminum alloy 7075-T651," *Eng. Fract. Mech.*, vol. 74, no. 17, pp. 2810–2823, Nov. 2007.

[171] J. Jordon, J.B., Horstemeyer, M.F., Daniewicz, S.R., Badarinarayan, H., and Grantham, "Material Characterization and Modeling of Friction Stir Spot Welds in a Magnesium

AZ31 Alloy," *J. Eng. Mater. Technol.*, vol. 132, 2010.

[172] H. El Kadiri, Y. Xue, M. F. Horstemeyer, J. B. Jordon, and P. T. Wang, "Identification and modeling of fatigue crack growth mechanisms in a die-cast AM50 magnesium alloy," *Acta Mater.*, vol. 54, no. 19, pp. 5061–5076, 2006.

[173] B. Torries and N. Shamsaei, "Fatigue Behavior and Modeling of Additively Manufactured Ti-6Al-4V Including Interlayer Time Interval Effects," *JOM*, vol. 69, no. 12, pp. 2698–2705, Dec. 2017.

[174] B. Torries, A. Imandoust, S. Beretta, S. Shao, and N. Shamsaei, "Overview on Microstructure- and Defect-Sensitive Fatigue Modeling of Additively Manufactured Materials," *JOM*, vol. 70, no. 9. Minerals, Metals and Materials Society, pp. 1853–1862, Sep-2018.

[175] P. Biswas, D. A Kumar, and N. R. Mandal, "Friction stir welding of aluminum alloy with varying tool geometry and process parameters," *Proc. Inst. Mech. Eng. Part B J. Eng. Manuf.*, vol. 226, no. 4, pp. 641–648, 2012.

[176] P. Cavaliere, A. Squillace, and F. Panella, "Effect of welding parameters on mechanical and microstructural properties of AA6082 joints produced by friction stir welding," *J. Mater. Process. Technol.*, vol. 200, no. 1–3, pp. 364–372, 2008.

[177] W. K. Kim, B. C. Goo, and S. T. Won, "Optimal Design of Friction Stir Welding Process to Improve Tensile Force of the Joint of A6005 Extrusion," *Mater. Manuf. Process.*, vol. 25, no. 7, pp. 637–643, 2010.

[178] S. P. Jung, T. W. Park, and Y. G. Kim, "Fatigue strength optimisation of friction stir welded A6005-T5 alloy sheets," *Sci. Technol. Weld. Join.*, vol. 15, no. 6, pp. 473–478, 2010.

[179] F. C. Liu and Z. Y. Ma, "Influence of tool dimension and welding parameters on microstructure and mechanical properties of friction-stir-welded 6061-T651 aluminum alloy," *Metall. Mater. Trans. A Phys. Metall. Mater. Sci.*, vol. 39, no. 10, pp. 2378–2388, 2008.

[180] W. J. Arbegast, "A flow-partitioned deformation zone model for defect formation during friction stir welding," *Scr. Mater.*, vol. 58, no. 5, pp. 372–376, Mar. 2008.

[181] O. V. Flores *et al.*, "Microstructural issues in a friction-stir-welded aluminum alloy," *Scr. Mater.*, vol. 38, no. 5, pp. 703–708, 1998.

[182] G. Liu, L. E. Murr, C. S. Niou, J. C. McClure, and F. R. Vega, "Microstructural aspects of the friction-stir welding of 6061-T6 aluminum," *Scr. Mater.*, vol. 37, no. 3, pp. 355–361, 1997.

[183] R. I. Rodriguez, J. B. Jordon, P. G. Allison, T. Rushing, and L. Garcia, "Microstructure and mechanical properties of dissimilar friction stir welding of 6061-to-7050 aluminum

alloys," *Mater. Des.*, vol. 83, 2015.

[184] T. R. McNelley, S. Swaminathan, and J. Q. Su, "Recrystallization mechanisms during friction stir welding/processing of aluminum alloys," *Scr. Mater.*, vol. 58, no. 5, pp. 349–354, 2008.

[185] J. Humphreys, G. S. Rohrer, and A. Rollett, *Recrystallization and Related Annealing Phenomena*, 3rd ed. Cambridge: Elsevier Ltd, 2017.

[186] R. S. Mishra and Z. Y. Ma, "Friction stir welding and processing," *Mater. Sci. Eng. R Reports*, vol. 50, no. 1–2, pp. 1–78, 2005.

[187] D. R. Tobergte and S. Curtis, *Recrystallisation and Related Annealing Phenomena*, 2nd ed. Oxford: Elsevier, 2004.

[188] G. Nurislamova, X. Sauvage, M. Murashkin, R. Islamgaliev, and R. Valiev, "Nanostructure and related mechanical properties of an Al-Mg-Si alloy processed by severe plastic deformation," *Philos. Mag. Lett.*, vol. 88, no. 6, pp. 459–466, 2008.

[189] U. F. H. R. Suhuddin, S. Mironov, Y. S. Sato, and H. Kokawa, "Grain structure and texture evolution during friction stir welding of thin 6016 aluminum alloy sheets," *Mater. Sci. Eng. A*, vol. 527, no. 7–8, pp. 1962–1969, 2010.

[190] R. Nandan, G. G. Roy, T. J. Lienert, and T. Debroy, "Three-dimensional heat and material flow during friction stir welding of mild steel," *Acta Mater.*, vol. 55, no. 3, pp. 883–895, 2007.

[191] R. Nandan, G. G. Roy, and T. Debroy, "Numerical simulation of three-dimensional heat transfer and plastic flow during friction stir welding," *Metall. Mater. Trans. A*, vol. 37, no. 4, pp. 1247–1259, Apr. 2006.

[192] M. Murayama and K. Hono, "Pre-precipitate clusters and precipitation processes in Al-Mg-Si alloys," *Acta Mater.*, vol. 47, no. 5, pp. 1537–1548, Mar. 1999.

[193] L. Cao, P. A. Rometsch, and M. J. Couper, "Clustering behaviour in an Al-Mg-Si-Cu alloy during natural ageing and subsequent under-ageing," *Mater. Sci. Eng. A*, vol. 559, pp. 257–261, 2013.

[194] Y. Aruga, M. Kozuka, Y. Takaki, and T. Sato, "Evaluation of Solute Clusters Associated with Bake-Hardening Response in Isothermal Aged Al-Mg-Si Alloys Using a Three-Dimensional Atom Probe," *Metall. Mater. Trans. A Phys. Metall. Mater. Sci.*, vol. 45, no. 13, pp. 5906–5913, 2014.

[195] V. Fallah, B. Langelier, N. Ofori-Opoku, B. Raeisinia, N. Provatas, and S. Esmaeili, "Cluster evolution mechanisms during aging in Al-Mg-Si alloys," *Acta Mater.*, vol. 103, pp. 290–300, 2016.

[196] A. Serizawa, S. Hirosawa, and T. Sato, "Three-Dimensional atom probe characterization

of nanoclusters responsible for multistep aging behavior of an Al-Mg-Si alloy," *Metall. Mater. Trans. A Phys. Metall. Mater. Sci.*, vol. 39, no. 2, pp. 243–251, 2008.

[197] C. G. Rhodes, M. W. Mahoney, W. H. Bingel, R. a. Spurling, and C. C. Bampton, "Effects of friction stir welding on microstructure of 7075 aluminum," *Scr. Mater.*, vol. 36, no. 1, pp. 69–75, Jan. 1997.

[198] M. E. J. Perry, R. J. Griffiths, D. Garcia, J. M. Sietins, Y. Zhu, and H. Z. Yu, "Morphological and Microstructural Investigation of the Non-Planar Interface Formed in Solid-State Metal Additive Manufacturing by Additive Friction Stir Deposition," *Addit. Manuf.*, no. May, p. 101293, 2020.

[199] H. Okamura, K. Aota, M. Sakamoto, M. Ezumi, and K. Ikeuchi, "Behaviour of oxides during friction stir welding of aluminium alloy and their effect on its mechanical properties," *Weld. Int.*, vol. 16, no. 4, pp. 266–275, 2002.

[200] H. J. Liu, Y. C. Chen, and J. C. Feng, "Effect of zigzag line on the mechanical properties of friction stir welded joints of an Al-Cu alloy," *Scr. Mater.*, vol. 55, no. 3, pp. 231–234, 2006.

[201] S. R. Ren, Z. Y. Ma, and L. Q. Chen, "Effect of initial butt surface on tensile properties and fracture behavior of friction stir welded Al-Zn-Mg-Cu alloy," *Mater. Sci. Eng. A*, vol. 479, no. 1–2, pp. 293–299, Apr. 2008.

[202] Z. Y. Ma, S. R. Sharma, and R. S. Mishra, "Effect of multiple-pass friction stir processing on microstructure and tensile properties of a cast aluminum–silicon alloy," *Scr. Mater.*, vol. 54, no. 9, pp. 1623–1626, May 2006.

[203] A. H. Baghdadi, A. Rajabi, N. F. M. Selamat, Z. Sajuri, and M. Z. Omar, "Effect of post-weld heat treatment on the mechanical behavior and dislocation density of friction stir welded Al6061," *Mater. Sci. Eng. A*, vol. 754, pp. 728–734, Apr. 2019.

[204] X. Sauvage, A. Dédé, A. C. Muñoz, and B. Huneau, "Precipitate stability and recrystallisation in the weld nuggets of friction stir welded Al–Mg–Si and Al–Mg–Sc alloys," *Mater. Sci. Eng. A*, vol. 491, no. 1–2, pp. 364–371, Sep. 2008.

[205] A. Dorbane, G. Ayoub, B. Mansoor, R. Hamade, G. Kridli, and A. Imad, "Observations of the mechanical response and evolution of damage of AA 6061-T6 under different strain rates and temperatures," *Mater. Sci. Eng. A*, vol. 624, pp. 239–249, Jan. 2015.

[206] A. Ghahremaninezhad and K. Ravi-Chandar, "Ductile failure behavior of polycrystalline Al 6061-T6," *Int. J. Fract.*, vol. 174, no. 2, pp. 177–202, 2012.

[207] H. Bin Chen, K. Yan, T. Lin, S. Ben Chen, C. Y. Jiang, and Y. Zhao, "The investigation of typical welding defects for 5456 aluminum alloy friction stir welds," *Mater. Sci. Eng. A*, vol. 433, no. 1–2, pp. 64–69, 2006.

[208] R. J. Griffiths *et al.*, "A Perspective on Solid-State Additive Manufacturing of Aluminum

Matrix Composites Using MELD," *J. Mater. Eng. Perform.*, vol. 28, no. 2, pp. 648–656, 2019.

[209] G. Ipekoglu, S. Erim, and G. Cam, "Investigation into the influence of post-weld heat treatment on the friction stir welded AA6061 Al-Alloy plates with different temper conditions," *Metall. Mater. Trans. A Phys. Metall. Mater. Sci.*, vol. 45, no. 2, pp. 864–877, 2014.

[210] I. Charit and R. S. Mishra, "Abnormal grain growth in friction stir processed alloys," *Scr. Mater.*, vol. 58, no. 5, pp. 367–371, 2008.

[211] M. M. Attallah and H. G. Salem, "Friction stir welding parameters: A tool for controlling abnormal grain growth during subsequent heat treatment," *Mater. Sci. Eng. A*, vol. 391, no. 1–2, pp. 51–59, 2005.

[212] J. K. Yoder, R. J. Griffiths, and H. Z. Yu, "Deformation-based additive manufacturing of 7075 aluminum with wrought-like mechanical properties," *Mater. Des.*, vol. 198, pp. 2020–2022, 2021.

[213] M. Products and A. Products, "Standard Practice for Heat Treatment of Wrought Aluminum Alloys 1," pp. 1–15, 2018.

[214] "ASTM E2627 - 13 Standard Practice for Determining Average Grain Size Using Electron Backscatter Diffraction (EBSD) in Fully Recrystallized Polycrystalline Materials." .

[215] C. Ravi and C. Wolverton, "First-principles study of crystal structure and stability of Al–Mg–Si–(Cu) precipitates," *Acta Mater.*, vol. 52, no. 14, pp. 4213–4227, Aug. 2004.

[216] H. Tanihata, T. Sugawara, K. Matsuda, and S. Ikeno, "Effect of casting and homogenizing treatment conditions on the formation of Al–Fe–Si intermetallic compounds in 6063 Al–Mg–Si alloys," *J. Mater. Sci.*, vol. 34, no. 6, pp. 1205–1210, 1999.

[217] A. L. Dons, E. K. Jensen, Y. Langsrud, E. Trømborg, and S. Brusethaug, "The alstruc microstructure solidification model for industrial aluminum alloys," *Metall. Mater. Trans. A*, vol. 30, no. 8, pp. 2135–2146, Aug. 1999.

[218] G. Sha, K. O'Reilly, B. Cantor, R. Hamerton, and J. Worth, "Effect of Grain Refiner on Intermetallic Phase Formation in Directional Solidification of 6xxx Series Wrought Al Alloys," *Mater. Sci. Forum*, vol. 331–337, pp. 253–258, May 2000.

[219] T. . Srivatsan, M. Al-Hajri, M. Petraroli, B. Hotton, and P. . Lam, "Influence of silicon carbide particulate reinforcement on quasi static and cyclic fatigue fracture behavior of 6061 aluminum alloy composites," *Mater. Sci. Eng. A*, vol. 325, no. 1–2, pp. 202–214, Feb. 2002.

[220] C. A. W. Olea, L. Roldo, J. F. dos Santos, and T. R. Strohaecker, "A sub-structural analysis of friction stir welded joints in an AA6056 Al-alloy in T4 and T6 temper conditions," *Mater. Sci. Eng. A*, vol. 454–455, pp. 52–62, Apr. 2007.

[221] J. E. Hatch, “Aluminum: Properties and physical metallurgy,” in *American Society of Metals*, 1984, p. 424.

[222] D. Lassance, D. Fabrègue, F. Delannay, and T. Pardoen, “Micromechanics of room and high temperature fracture in 6xxx Al alloys,” *Prog. Mater. Sci.*, vol. 52, no. 1, pp. 62–129, Jan. 2007.

[223] A. Perovic, D. D. Perovic, G. C. Weatherly, and D. J. Lloyd, “Precipitation in aluminum alloys AA6111 and AA6016,” *Scr. Mater.*, vol. 41, no. 7, pp. 703–708, 1999.

[224] ASM International. Handbook Committee., *ASM handbook*. .

[225] R. R. McCullough, J. B. Jordon, P. G. Allison, T. Rushing, and L. Garcia, “Fatigue crack nucleation and small crack growth in an extruded 6061 aluminum alloy,” *Int. J. Fatigue*, vol. 119, 2019.

[226] A. R. Cisko *et al.*, “A parametric investigation on friction stir welding of Al-Li 2099,” *Mater. Manuf. Process.*, pp. 1–8, Jun. 2020.

[227] P. M. G. P. Moreira, T. Santos, S. M. O. Tavares, V. Richter-Trummer, P. Vilaça, and P. M. S. T. de Castro, “Mechanical and metallurgical characterization of friction stir welding joints of AA6061-T6 with AA6082-T6,” *Mater. Des.*, vol. 30, no. 1, pp. 180–187, 2009.

[228] R. I. Stephens, A. Fatemi, R. R. Stephens, and H. O. Fuchs, *Metal Fatigue in Engineering*. John Wiley & Sons, 2000.

[229] G. İpekoğlu and G. Çam, “Effects of initial temper condition and postweld heat treatment on the properties of dissimilar friction-stir-welded joints between AA7075 and AA6061 aluminum alloys,” *Metall. Mater. Trans. A Phys. Metall. Mater. Sci.*, vol. 45, no. 7, pp. 3074–3087, 2014.

[230] D. Rao, K. Huber, J. Heerens, J. F. dos Santos, and N. Huber, “Asymmetric mechanical properties and tensile behaviour prediction of aluminium alloy 5083 friction stir welding joints,” *Mater. Sci. Eng. A*, vol. 565, pp. 44–50, 2013.

[231] M. N. James, G. R. Bradley, H. Lombard, and D. G. Hattingh, “The relationship between process mechanisms and crack paths in friction stir welded 5083-H321 and 5383-H321 aluminium alloys,” *Fatigue Fract. Eng. Mater. Struct.*, vol. 28, no. 1–2, pp. 245–256, Jan. 2005.

[232] O. G. Rivera *et al.*, “Influence of Texture and Grain Refinement on the Mechanical Behavior of AA2219 Depositions Fabricated by Solid State Additive Manufacturing,” *Mater. Des.*

[233] C. Menzemer and T. S. Srivatsan, “The quasi-static fracture behavior of aluminum alloy 5083,” *Mater. Lett.*, vol. 38, no. 5, pp. 317–320, 1999.

[234] J. Yan and A. M. Hodge, “Study of β precipitation and layer structure formation in Al

5083: The role of dispersoids and grain boundaries," *J. Alloys Compd.*, vol. 703, pp. 242–250, 2017.

[235] R. S. Mishra, Z. Y. Ma, and I. Charit, "Friction stir processing: A novel technique for fabrication of surface composite," *Materials Science and Engineering A*, vol. 341, no. 1–2. 2003.

[236] H. N. B. Schmidt, T. L. Dickerson, and J. H. Hattel, "Material flow in butt friction stir welds in AA2024-T3," *Acta Mater.*, vol. 54, no. 4, pp. 1199–1209, Feb. 2006.

[237] O. L. Rodriguez, P. G. Allison, W. R. Whittington, H. El Kadiri, O. G. Rivera, and M. E. Barkey, "Strain rate effect on the tension and compression stress-state asymmetry for electron beam additive manufactured Ti6Al4V," *Mater. Sci. Eng. A*, vol. 713, pp. 125–133, Jan. 2018.

[238] O. L. Rodriguez *et al.*, "Dynamic tensile behavior of electron beam additive manufactured Ti6Al4V," *Mater. Sci. Eng. A*, vol. 641, pp. 323–327, 2015.

[239] C. J. T. Mason, P. G. Allison, J. B. Jordon, M. Barkey, and R. Amaro, "PLASTICITY-DAMAGE MODELING OF STRAIN RATE AND TEMPERATURE DEPENDENCE OF ALUMINUM ALLOY 7075-T651," 2018.

[240] K. Anderson-Wedge *et al.*, "Characterization of the fatigue behavior of additive friction stir-deposition AA2219," *Int. J. Fatigue*, vol. 142, no. January 2020, p. 105951, 2021.

[241] S. C. Beck *et al.*, "The effect of solutionizing and artificial aging on the microstructure and mechanical properties in solid-state additive manufacturing of precipitation hardened Al–Mg–Si alloy," *Mater. Sci. Eng. A*, vol. 819, no. April, p. 141351, 2021.

[242] J. C. Pang, S. X. Li, Z. G. Wang, and Z. F. Zhang, "General relation between tensile strength and fatigue strength of metallic materials," *Mater. Sci. Eng. A*, vol. 564, no. May 2020, pp. 331–341, 2013.

[243] J. L. Walley, E. J. Lavernia, and J. C. Gibeling, "Low-cycle fatigue of ultra-fine-grained cryomilled 5083 aluminum alloy," *Metall. Mater. Trans. A Phys. Metall. Mater. Sci.*, vol. 40, no. 11, pp. 2622–2630, 2009.

[244] D. Samantaray, S. Mandal, and A. K. Bhaduri, "A comparative study on Johnson Cook, modified Zerilli-Armstrong and Arrhenius-type constitutive models to predict elevated temperature flow behaviour in modified 9Cr-1Mo steel," *Comput. Mater. Sci.*, vol. 47, no. 2, pp. 568–576, 2009.

[245] A. S. Khan and S. Huang, *Continuum Theory of Plasticity*, 1st ed. Wiley-Interscience, 1995.

[246] J. Lemaitre and J.-L. Chaboche, *Mechanics of Solid Materials*, 1st ed. Avon: The Bath Press, 1990.

[247] J. Lemaitre, “A Continuous Damage Mechanics Model for Ductile Fracture,” *J. Eng. Mater. Technol.*, vol. 107, p. 83, Jan. 1985.

[248] J. A. Bannantine, J. J. Comer, and J. L. Handrock, *Fundamentals of Metal Fatigue in Engineering*, 1st ed. Pearson, 1989.

[249] T. Børvik, O. S. Hopperstad, and K. O. Pedersen, “Quasi-brittle fracture during structural impact of AA7075-T651 aluminium plates,” *Int. J. Impact Eng.*, vol. 37, pp. 537–551, 2010.

[250] D. Dwivedi, A. Kumar, S. Priyadarshi, P. K. Jain, and P. Tandon, “Numerical prediction of Fracture in Parts Formed with Incremental Sheet Forming Process,” in *Simulations for Design and Manufacturing*, U. S. Dixit and R. Kant, Eds. Singapore: Springer Nature, 2016.

[251] M. Sima and T. Özel, “Modified material constitutive models for serrated chip formation simulations and experimental validation in machining of titanium alloy Ti-6Al-4V,” *Int. J. Mach. Tools Manuf.*, vol. 50, no. 11, pp. 943–960, 2010.

[252] F. Al-Badour, N. Merah, A. Shuaib, and A. Bazoune, “Thermo-mechanical finite element model of friction stir welding of dissimilar alloys,” *Int. J. Adv. Manuf. Technol.*, vol. 72, no. 5–8, pp. 607–617, 2014.

[253] R. A. Behnagh, N. Shen, M. A. Ansari, M. Narvan, M. K. B. Givi, and H. Ding, “Experimental Analysis and Microstructure Modeling of Friction Stir Extrusion of Magnesium Chips,” *J. Manuf. Sci. Eng.*, vol. 138, pp. 1–11, 2016.

[254] F. J. Zerilli and R. W. Armstrong, “Dislocation-mechanics-based constitutive relations for material dynamics calculations,” *J. Appl. Phys.*, vol. 61, no. 5, pp. 1816–1825, Mar. 1987.

[255] K. J. Laidler, “The development of the Arrhenius equation,” *J. Chem. Educ.*, vol. 61, p. 494, 1984.

[256] C. Zener and J. H. Hollomon, “Effect of strain rate upon plastic flow of steel,” *J. Appl. Phys.*, vol. 15, pp. 22–32, Jan. 1944.

[257] S. F. Medina and C. A. Hernandez, “General expression of the Zener-Hollomon parameter as a function of the chemical composition of low alloy and microalloyed steels,” *Acta Mater.*, vol. 44, no. 1, pp. 137–148, Jan. 1996.

[258] M. Chiumenti, M. Cervera, C. Agelet de Saracibar, and N. Dialami, “Numerical modeling of friction stir welding processes,” *Comput. Methods Appl. Mech. Eng.*, vol. 254, pp. 353–369, 2013.

[259] W. Pan, D. Li, A. M. Tartakovsky, S. Ahzi, M. Khraisheh, and M. Khaleel, “A new smoothed particle hydrodynamics non-Newtonian model for friction stir welding: Process modeling and simulation of microstructure evolution in a magnesium alloy,” *Int. J. Plast.*, vol. 48, pp. 189–204, 2013.

[260] G. G. Stubblefield, K. Fraser, B. J. Phillips, J. B. Jordon, and P. G. Allison, "A meshfree computational framework for the numerical simulation of the solid-state additive manufacturing process, additive friction stir-deposition (AFS-D)," *Mater. Des.*, vol. 202, 2021.

[261] R. J. Griffiths, D. T. Petersen, D. Garcia, and H. Z. Yu, "Additive Friction Stir-Enabled Solid-State Additive Manufacturing for the Repair of 7075 Aluminum Alloy," *Appl. Sci.*, vol. 9, no. 17, p. 3486, Aug. 2019.

[262] B. J. Phillips *et al.*, "Examination of Parallel Deposition Path Microstructure and Material Flow on Interface Tensile Behavior for Aluminum Alloy Al-Mg-Si Additive Friction Stir-Deposition," *J. Mater. Process. Technol.*, p. 117169, Apr. 2021.

[263] G. R. Johnson and W. H. Cook, "Fracture characteristics of three metals subjected to various strains, strain rates, temperatures and pressures," *Eng. Fract. Mech.*, vol. 21, no. 1, pp. 31–48, 1985.

[264] F. Al-Badour, N. Merah, A. Shuaib, and A. Bazoune, "Coupled Eulerian Lagrangian finite element modeling of friction stir welding processes," *J. Mater. Process. Technol.*, vol. 213, no. 8, pp. 1433–1439, 2013.

[265] N. K. Sanjeev, V. Malik, and H. S. Hebbar, "Verification of Johnson-Cook Material Model Constants of AA2024-T3 for Use in Finite Element Simulation of Friction Stir Welding and Its Utilization in Severe Plastic Deformation Process Modelling," *Int. J. Res. Eng. Technol.*, vol. 3, no. 6, pp. 98–102, 2014.

[266] C. M. Sellars and J. M. Tegart, "Hot Workability," *Int. Metall. Rev.*, vol. 17, no. 1, 1972.

[267] T. Sheppard and D. S. Wright, "Determination of flow stress: Part 1 constitutive equation for aluminium alloys at elevated temperatures," *Met. Technol.*, vol. 6, no. 1, pp. 215–223, Jan. 1979.

[268] K. Kuykendall, T. Nelson, and C. Sorensen, "On the selection of constitutive laws used in modeling friction stir welding," *Int. J. Mach. Tools Manuf.*, vol. 74, pp. 74–85, 2013.

[269] R. Nandan, G. G. Roy, and T. Debroy, "Numerical simulation of three dimensional heat transfer and plastic flow during friction stir welding," *Metall. Mater. Trans. A*, vol. 37, pp. 1247–1259, Apr. 2006.

[270] P. A. Colegrove and H. R. Shercliff, "3-Dimensional CFD modelling of flow round a threaded friction stir welding tool profile," *J. Mater. Process. Technol.*, vol. 169, pp. 320–327, Nov. 2005.

[271] A. H. Ammouri and R. F. Hamade, "On the selection of constitutive equation for modeling the friction stir processes of twin roll cast wrought AZ31B," *Mater. Des.*, vol. 57, pp. 673–688, May 2014.

[272] C. Hamilton, M. S. Węglowski, and S. Dymek, "A Simulation of Friction-Stir Processing

for Temperature and Material Flow," *Metall. Mater. Trans. B Process Metall. Mater. Process. Sci.*, vol. 46, no. 3, pp. 1409–1418, 2015.

[273] F. Khodabakhshi, A. P. Gerlich, A. Simchi, and A. H. Kokabi, "Hot deformation behavior of an aluminum-matrix hybrid nanocomposite fabricated by friction stir processing," *Mater. Sci. Eng. A*, vol. 626, pp. 458–466, Feb. 2015.

[274] A. N. Albakri, B. Mansoor, H. Nassar, and M. K. Khraisheh, "Thermo-mechanical and metallurgical aspects in friction stir processing of AZ31 Mg alloy - A numerical and experimental investigation," *J. Mater. Process. Technol.*, vol. 213, pp. 279–290, Feb. 2013.

[275] H. W. Nassar and M. K. Khraisheh, "Simulation of Material Flow and Heat Evolution in Friction Stir Processing Incorporating Melting," *J. Eng. Mater. Technol.*, vol. 134, pp. 1–7, Oct. 2012.

[276] H. Zhang, N. P. Jin, and J. H. Chen, "Hot deformation behavior of Al-Zn-Mg-Cu-Zr aluminum alloys during compression at elevated temperature," *Trans. Nonferrous Met. Soc. China (English Ed.*, vol. 21, no. 3, pp. 437–442, 2011.

[277] H. R. Rezaei Ashtiani, M. H. Parsa, and H. Bisadi, "Constitutive equations for elevated temperature flow behavior of commercial purity aluminum," *Mater. Sci. Eng. A*, vol. 545, pp. 61–67, May 2012.

[278] C. Shi, W. Mao, and X. G. Chen, "Evolution of activation energy during hot deformation of AA7150 aluminum alloy," *Mater. Sci. Eng. A*, vol. 571, pp. 83–91, Jun. 2013.

[279] Z. Wang, K. Guan, M. Gao, X. Li, X. Chen, and X. Zeng, "The microstructure and mechanical properties of deposited-IN718 by selective laser melting," *J. Alloys Compd.*, vol. 513, pp. 518–523, Feb. 2012.

[280] W. H. Van Geertruyden, W. Z. Misiolek, and P. T. Wang, "Grain structure evolution in a 6061 aluminum alloy during hot torsion," *Mater. Sci. Eng. A*, vol. 419, pp. 105–114, Mar. 2006.

[281] H. E. Vatne, T. Furu, R. Ørsund, and E. Nes, "Modelling recrystallization after hot deformation of aluminium," *Acta Mater.*, vol. 44, no. 11, pp. 4463–4473, Nov. 1996.

[282] P. Z. Zhao and T. Tsuchida, "Effect of fabrication conditions and Cr, Zr contents on the grain structure of 7075 and 6061 aluminum alloys," *Mater. Sci. Eng. A*, vol. 499, pp. 78–82, Jan. 2009.

[283] T. Morishige, T. Hirata, M. Tsujikawa, and K. Higashi, "Comprehensive analysis of minimum grain size in pure aluminum using friction stir processing," *Mater. Lett.*, vol. 64, pp. 1905–1908, Sep. 2010.

[284] *The Metals Handbook Volume 4-Heat Treating*, 9th ed. American Society for Metals.

[285] A. Dorbane, G. Ayoub, B. Mansoor, R. Hamade, G. Kridli, and A. Imad, "Observations of the mechanical response and evolution of damage of AA 6061-T6 under different strain rates and temperatures," *Mater. Sci. Eng. A*, vol. 624, pp. 239–249, Jan. 2015.

[286] S. Y. Jin and W. Altenhof, "Control of load/displacement responses of AA6061-T6 and T4 circular extrusions under axial compressive loads," *Int. J. Impact Eng.*, vol. 38, pp. 1–12, Jan. 2011.

[287] D. F. Fields and W. A. Backofen, "Determination of strain-hardening characteristics by torsion testing," in *Proceedings ASTM*, 1957, pp. 1259–1272.

[288] B. Allen, "Creep and Elevated Temperature Mechanical Properties of 5083 and 6061 Aluminum," Virginia Polytechnic Institute, 2012.

[289] P. G. Allison, Y. Hammi, and M. F. Horstemeyer, "Determination of microstructure-property relations for performance and design optimization of the pm process," in *Advances in Powder Metallurgy and Particulate Materials - 2007, Proceedings of the 2007 International Conference on Powder Metallurgy and Particulate Materials, PowderMet 2007*, 2007.

[290] J. B. Jordon, M. F. Horstemeyer, K. Solanki, and Y. Xue, "Damage and stress state influence on the Bauschinger effect in aluminum alloys," *Mech. Mater.*, vol. 39, no. 10, pp. 920–931, Oct. 2007.

[291] O. G. Rivera *et al.*, "Interrupted Quasi-static and Dynamic Tensile Experiments of Fully Annealed 301 Stainless Steel."

[292] O. G. Rivera, P. G. Allison, L. N. Brewer, J. B. Jordon, O. L. Rodriguez, and Z. Mcclelland, "Microstructural Evolution and Strain Rate Dependence of Thermo-mechanical Additive Manufactured Inconel 625," *Mater Sci Eng A*, pp. 1–16.

[293] D. Francis, W. R. Whittington, W. B. LawrimoreII, P. G. Allison, S. A. Turnage, and J. J. Bhattacharyya, "Split Hopkinson Pressure Bar Graphical Analysis Tool," vol. 57, pp. 179–183, 2017.

[294] M. F. Horstemeyer, *Integrated Computational Materials Engineering (ICME) for Metals*. Hoboken, New Jersey: John Wiley & Sons, Inc, 2012.

[295] P. G. Allison, M. F. Horstemeyer, Y. Hammi, H. R. Brown, M. T. Tucker, and Y.-K. Hwang, "Microstructure–property relations of a steel powder metal under varying temperatures, strain rates, and stress states," *Mater. Sci. Eng. A*, vol. 529, pp. 335–344, Nov. 2011.

[296] J. B. Jordon, M. F. Horstemeyer, K. Solanki, J. D. Bernard, J. T. Berry, and T. N. Williams, "Damage characterization and modeling of a 7075-T651 aluminum plate," *Mater. Sci. Eng. A*, vol. 527, no. 1–2, pp. 169–178, Dec. 2009.

[297] M. F. Horstemeyer, J. Lathrop, A. M. Gokhale, and M. Dighe, "Modeling stress state

dependent damage evolution in a cast Al–Si–Mg aluminum alloy," *Theor. Appl. Fract. Mech.*, vol. 33, no. 1, pp. 31–47, Feb. 2000.

[298] D. J. Bammann, M. L. Chiesa, M. F. Horstemeyer, and L. I. Weingarten, "Failure in ductile materials using finite element methods," in *Structural Crashworthiness and Failure*, Belfast, 1993.

[299] H. Di Donato, J. P. Garbezza, A. Infante, and R. Lopez, "STRIKER MECHANISM UPGRADE FOR THE SPLIT-HOPKINSON PRESSURE BAR EXPERIMENT," pp. 1–100, 2013.

[300] "Dynamic Impact Behavior of 6061-T6 and 5083-H131 Aluminum alloys," pp. 1–9.

[301] B. Beglarzadeh and B. Davoodi, "Investigating of Mechanical Behavior of AA5083 in the Pressing Process Using Finite Element Analysis," *Mod. Appl. Sci.*, vol. 11, no. 9, p. 51, 2017.

[302] A. J. Holzer and R. H. Brown, "Specimen Geometry and Friction in Dynamic Compression," *CIRP Ann. - Manuf. Technol.*, vol. 29, no. 1, pp. 135–139, 1980.

[303] B. Chen, Weinong; Song, *Split Hopkinson (Kolsky) Bar*. New York: Springer Science+Business Media, LLC, 2011.

[304] K. Peacock, "Ryukyu Warriors repair sole LHD deck in Pacific." DVIDS, 2011.

[305] L. Garcia, J. Fisher, T. W. Rushing, and J. S. Tingle, "AM2 Brickwork Pattern Evaluation," ERDC/GSL TR-16-34, U.S. Army Engineer Research and Development Center, Vicksburg, MS, 2016.

[306] S. A. Whalen *et al.*, "High ductility aluminum alloy made from powder by friction extrusion," *Materialia*, vol. 6, no. December 2018, 2019.

[307] T. W. Rushing and I. L. Howard, "Prediction of soil deformation beneath temporary airfield matting systems based on full-scale testing," *J. Terramechanics*, vol. 58, pp. 1–9, Apr. 2015.

Appendix

List of Publications:

1. G.G. Stubblefield, K.A. Fraser, D. Van Iderstine, S. Mujahid, H. Rhee, J.B. Jordon, P.G. Allison, "Elucidating the influence of temperature and strain rate on the mechanics of AFS-D through a combined experimental and computational approach," Journal of Materials Processing Technology, V. 305, pp. 117593, 2022.
2. C.J.T. Mason, D.Z. Avery, B.J. Phillips, J.B. Jordon, P.G. Allison, "Strain rate dependent plasticity modeling for precipitate hardened aerospace aluminum alloy produced with solid-state additive manufacturing," Journal of Dynamic Behavior of Materials, V. 8, pp214-230, 2022.
3. B.J. Phillips, C.J. Williamson, R.P. Kinser, J.B. Jordon, K.J. Doherty, P.G. Allison, "Microstructural and Mechanical Characterization of Additive Friction Stir-Deposition of Aluminum Alloy 5083 Effect of Lubrication on Material Anisotropy," Materials, 14 (21), pp. 6732, 2021.
4. N. Zhu, D.Z. Avery, B.A. Rutherford, B.J. Phillips, P.G. Allison, J.B. Jordon, L.N. Brewer, "The Effect of Anodization on the Mechanical Properties of AA6061 Produced by Additive Friction Stir-Deposition," Metals 11 (11), 1773, 2021.
5. S.C. Beck, B.A. Rutherford, D.Z. Avery, B.J. Phillips, H. Rao, M.Y. Rekha, L.N. Brewer, P.G. Allison, J.B. Jordon "The effect of solutionizing and artificial aging on the microstructure and mechanical properties in solid-state additive manufacturing of precipitation hardened Al-Mg-Si alloy," *Mat. Sci. Eng. A,* pp. 141351, 2021.
6. B. J. Phillips, C. J. T. Mason, S. C. Beck, D. Z. Avery, K. J. Doherty, P. G. Allison, J. B. Jordon "Effect of parallel deposition path and interface material flow on resulting microstructure and tensile behavior of Al-Mg-Si alloy fabricated by additive friction stir deposition," *J. Mat. Proc. Tech.,* vol. 295, pp. 117169, 2021.
7. G. G. Stubblefield, K. Fraser, B. J. Phillips, J. B. Jordon, P. G. Allison, "A meshfree computational framework for the numerical simulation of the solid-state additive manufacturing process, additive friction stir-deposition (AFS-D)," *Mat. & Des.,* vol. 202, pp. 109514, 2021.
8. B. Rutherford, D. Z. Avery, B. J. Phillips, K. J. Doherty, L. N. Brewer, P. G. Allison, J. B. Jordon, "Effect of thermomechanical processing on fatigue behavior in solid-state additive manufacturing of Al-Mg-Si alloy," *Metals,* vol. 29, no. 8, pp. 4928-4933, 2020.
9. J. B. Jordon, P. G. Allison, B. J. Phillips, D. Z. Avery, R. P. Kinser, L. N. Brewer, C. Cox, K. Doherty, "Direct recycling of machine chips through a novel solid-state additive manufacturing process," *Mat. & Des.,* vol. 193, pp. 108850, 2020.
10. B. J. Phillips, D. Z. Avery, T. Liu, O. L. Rodriguez, C. J. T. Mason, J. B. Jordon, L.N. Brewer, P. G. Allison, "Microstructure-deformation relationship of additive friction stir-deposition Al-Mg-Si," *Materialia*, vol. 7, pp. 100387, 2019.
11. N. Zhu, D. Z. Avery, P.G. Allison, J.B. Jordon, K. An, Y. Chen, L.N. Brewer, "Residual Stress Distributions in AA6061 Material Produced by Additive Friction Stir-Deposition," Submitted for publication.
12. K. Anderson, Z. Balrow, P.G. Allison, S. Daniewicz, "Fatigue crack growth resistance of additive friction stir deposited AA6061," Submitted for publication.

List of Presentations:

1. "AM Innovation Panel: Utilizing Advanced Materials & Manufacturing Methods to Enhance the Durability & Speed at Which Military Aircraft Parts are Delivered to the Battlespace, Panel Moderator: Dr. Mark Benedict, AM Lead, Air Force Research Laboratory," Additive Manufacturing for Defense 2021, Tampa, FL, USA, July 28th, 2021.

2. "Point-of-Need Manufacturing: Machine Chip Recycling Through Friction Stir Additive Manufacturing," ASETS Defense, Washington D.C. - Virtual, USA, August 4, 2020.

3. "Point-of-Need Manufacturing through Direct Additive Recycling of Metal Waste," TMS 149th International Symposium, San Diego, CA, USA, February 23, 2020.

4. "Direct Additive Recycling to Support Expeditionary Manufacturing of Portable Airfields," Air Force Civil Engineering Command, Tyndall AFB, USA, January 9, 2020.

5. "Recycling and Reuse of Metal Alloys by a Single Solid-State Additive Manufacturing and Repair Process," SERDP-ESTCP Symposium 2019 - Enhancing DoD's Mission Effectiveness, Washington D.C., USA, December 4, 2019.

6. "Direct Recycling of Metal Scrap Through Solid Phase Additive Manufacturing," 4th ASTM Symposium on Structural Integrity of Additive Manufactured Materials & Parts, ASTM International, Washington D.C., USA, October 9, 2019.

7. "Microstructure-Sensitive Fatigue Modeling of Friction Stir Welded Aluminum Alloy 6061," ASME 2015 International Mechanical Engineering Congress and Exposition, Phoenix, AZ, USA, November 2015.

8. "AFSD Manufacturing of Functionally Graded and Advanced Materials," NASA Breakthrough Materials Workshop, Huntsville, AL, USA, April 23, 2019.

9. "A Computational and Experimental Approach to Solid-State Additive Manufacturing of Metal Waste by Direct-Recycling of Manufacturing Chips and Metal Strips," NASA-MSFC Additive and Welding Working Group, Huntsville, AL, USA, February 20, 2019.

10. "AM Innovation Panel: Developing the Next Generation of 3D Printing and Processes in Support of the Warfighter, Panel Moderator: Dr. Alan Pentz, AM Lead, Deputy Assistant Secretary of the Navy, Pentagon," Additive Manufacturing for Defense 2019, Tampa, FL, USA, February 6, 2019.

13. "Direct Recycling of Metal Waste by Additive Friction Stir Deposition (AFSD)" Friction Stir Welding & Processing, September 2019

14. "Direct Recycling of Metal Scrap Through Solid Phase Additive Manufacturing" ASTM Additive Manufacturing Symposium

15. "Smoothed Particle Hydrodynamics Simulation of Additive Friction Stir Manufacturing of Aluminum Alloy 6061" Materials Science & Technology, 2019

16. "Microstructural-Mechanical Property Relationship of Additive Friction Stir-Deposition Al-Mg-Si-Cu" Materials Science & Technology, 2019

17. “Point-of-Need Manufacturing through Direct Additive Recycling of Metal Waste” TMS Annual Conference, San Diego, CA, February 2020
18. “Fatigue Mechanisms of Aluminum Alloys Fabricated by Additive Friction Stir-Deposition” TMS Annual Conference, San Diego, CA, February 2020
19. “Smoothed Particle Hydrodynamic Modeling of Solid State Additively Manufactured Aluminum Alloy 6061” TMS Annual Conference, San Diego, CA, February 2020
20. “Mechanical Property and Characterization of Anodized AA6061 after Additive Friction Stir-deposition” TMS Annual Conference, San Diego, CA, February 2020
21. “Material Flow Behavior Prediction of Additive Friction Stir Deposition Using Smoothed Particle Hydrodynamics” TMS Annual Conference, Anaheim, CA, February 2022